Metal Oxide Chemistry and Synthesis

From Solution to Solid State

JEAN-PIERRE JOLIVET
Université Pierre et Marie Curie, Paris

In collaboration with

MARC HENRY
Université de Strasbourg

and

JACQUES LIVAGE
Université Pierre et Marie Curie, Paris

Translated by

ERIC BESCHER
University of California, Los Angeles

DropBooks

JOHN WILEY & SONS, LTD
Chichester · New York · Weinheim · Brisbane · Singapore · Toronto

Originally published in French as *De la Solution à l'Oxyde* 3rd Edition. © Masson, Paris, 1994

Authorised English translation published with the help of the Ministère de la Culture
Copyright © 2000 John Wiley & Sons Ltd,
Baffins Lane, Chichester,
West Sussex PO19 1UD, England

National 01243 779777
International (+44) 1243 779777
e-mail (for orders and customer service enquiries): cs-books@wiley.co.uk
Visit our Home Page on http://www.wiley.co.uk
or http://www.wiley.com

All Rights Reserved. No part of this publication may be reproduced, stored in a retrieval system, or transmitted, in any form or by any means, electronic, mechanical, photocopying, recording, scanning or otherwise, except under the terms of the Copyright Designs and Patents Act 1988 or under the terms of a licence issued by the Copyright Licensing Agency, 90 Tottenham Court Road, London W1P 9HE, UK, without the permission in writing of the Publisher.

Other Wiley Editorial Offices

John Wiley & Sons, Inc., 605 Third Avenue,
New York, NY 10158-0012, USA

WILEY-VCH Verlag GmbH, Pappelallee 3,
D-69469 Weinheim, Germany

Jacaranda Wiley Ltd, 33 Park Road, Milton,
Queensland 4064, Australia

John Wiley & Sons (Asia) Pte Ltd, Clementi Loop #02-01,
Jin Xing Distripark, Singapore 129809

John Wiley & Sons (Canada) Ltd, 22 Worcester Road,
Rexdale, Ontario M9W 1L1, Canada

British Library Cataloguing in Publication Data

A catalogue record for this book is available from the British Library

ISBN 0 471 97056 5

Typeset on 10/12 Times by Thomson Press (India) Ltd, New Delhi
Printed and bound in Great Britain by Antony Rowe, Chippenham, Wilts

This book is printed on acid-free paper responsibly manufactured from sustainable forestry, in which at least two trees are planted for each one used for paper production.

Contents

Preface xi

Introduction xiii

Part I INORGANIC CONDENSATION

1 Water and Cations in Aqueous Solution 3

1.1 Properties of Water as a Solvent 4
1.1.1 Electronic Structure of the Water Molecule. 4
1.1.2 Structure of Liquid Water 6
1.1.3 Hydration of Ions and the Structure of Solutions 9
(a) First Hydration Sphere 9
(b) Outer Solvation Spheres 11
(c) Structure of Solutions 11
1.2 Acid–Base Properties of Ions in Aqueous Solution 12
1.3 Model of the Acid–Base Behavior of Cations 15
1.4 Mechanism and Kinetics of Hydroxylation 19
1.5 Water Under Hydrothermal Conditions 20
1.6 References 23

2 Condensation and Precipitation in Aqueous Solution 25

2.1 Mechanism of the Condensation Reactions 26
(a) Initiation 27
(b) Propagation 27
(c) Termination 32
2.2 Model of Cation Condensation in Aqueous Solutions 34
2.3 Kinetics of Solid Formation: Nucleation, Growth, Aging 37
2.3.1 Steps of Formation of a Solid 37
2.3.2 Nucleation 39

2.3.3 Growth . . . 42
(a) Diffusion-limited Growth . . . 43
(b) Growth Limited by a Surface Reaction . . . 43
2.3.4 Aging . . . 45
(a) Increase in Particle Size . . . 45
(b) Change in Crystal Type . . . 47
(c) Changes in Morphology . . . 48
2.4 References . . . 51

3 Olation: Polycations and Solid Phases . . . 53

3.1 The Olation Reaction . . . 53
3.1.1 Mechanism . . . 53
3.1.2 Structure . . . 55
3.1.3 Growth . . . 57
3.2 Condensation of Trivalent Elements . . . 58
3.2.1 Oligomeric Species: Polycations . . . 60
3.2.2 Large Polycations . . . 63
3.2.3 Solid Phases: Hydroxides, Oxyhydroxides, Oxides . . . 67
(a) Hydroxylation via the Addition of a Base at Room Temperature . . . 67
(b) Thermohydrolysis . . . 74
3.3 Condensation of Divalent Elements . . . 78
3.3.1 Polycations . . . 78
3.3.2 Solid Phases . . . 79
3.4 Condensation of Tetravalent Elements . . . 80
3.4.1 Polycations . . . 81
3.4.2 Solid Phases . . . 82
3.5 Mixed-valence Systems . . . 86
3.6 References . . . 90

4 Oxolation: Polyanions and Solid Phases . . . 93

4.1 Oxolation Reaction . . . 93
4.2 p-Block Elements Having Their Maximum Coordination in the Monomer . . . 96
4.2.1 Si(IV): Silicates . . . 96
(a) Aluminosilicates . . . 101
4.2.2 Sb(V): Antimonates . . . 105
4.2.3 B(III): Borates . . . 108
4.3 Transition Metals for which Condensation Leads to an Increase in Coordination Number . . . 111
4.3.1 V(V): Vanadates . . . 114
(a) Polyanions . . . 115

(b) Solid Phase . . . 119
(c) Other Vanadic Polyanions . . . 121
4.3.2 Mo(VI): Molybdates; W(VI): Tungstates . . . 125
(a) Molybdic Polyanions . . . 126
(b) Tungstic Polyanions . . . 128
(c) Solid Phases: Tungstic and Molybdenic Oxides and Hydrates . . . 132
4.4 References . . . 137

5 Complexation and Condensation . . . 141

5.1 Complexation of Cations . . . 142
5.2 Basic Salts of Zirconium(IV) . . . 145
5.3 Complexation by the Phosphate Anion . . . 149
5.3.1 Zirconium . . . 150
5.3.2 Antimonate . . . 151
5.3.3 Tungstates . . . 152
5.4 Influence of the Anion on the Structure of the Oxide . . . 160
5.4.1 Iron(III) Oxyhydroxides . . . 160
5.4.2 Titanium Oxides . . . 161
5.5 Control of the Size Distribution and Morphology of Oxide Particles . . . 163
5.5.1 Chromium Oxide . . . 163
5.5.2 Iron Oxide . . . 165
5.5.3 Zinc Oxide . . . 169
5.6 Synthesis of Polymetallic Oxides . . . 170
5.6.1 Spinel Ferrites AB_2O_4 . . . 171
5.6.2 Hexagonal Ferrites $BaFe_{12}O_{19}$ . . . 173
5.6.3 Perovskite Oxides ABO_3 . . . 174
5.6.4 Superconducting Cuprates . . . 176
5.7 References . . . 178

Appendix to Part I Partial Charges Model and Applications to Aqueous Chemistry . . . 183

A.1 Ionocovalent Bonding, Partial Charges and Electronegativity . . . 184
A.1.1 Ionocovalent Bonding and Partial Charges . . . 184
A.1.2 Electronegativity . . . 185
A.2 Partial Charges Model . . . 189
A.2.1 Dependence of Electronegativity on the Charge . . . 189
A.2.2 Electronegativity Equalization Principle . . . 190
A.2.3 Calculation of the Average Electronegativity . . . 190
A.2.4 Approximations used in the Model . . . 191
A.2.5 Guidelines for the Use of the Model . . . 194

DropBooks

A.3 Application of the Model to the Acid–Base Properties of Cations . . . 195
A.3.1 pH–Electronegativity Relationship . . . 195
A.3.2 Hydrolysis of Cations . . . 196
A.3.3 Acid–Base Properties of Elements in Aqueous Solution . . . 197
(a) Acid Behavior . . . 198
(b) Basic Behavior . . . 198
A.4 Application of the Model to the Condensation of Cations in Solution . . . 199
A.5 Application of the Model to the Complexation of Cations in Solution . . . 201
A.6 References . . . 208

Part II SURFACE CHEMISTRY OF OXIDES

6 Oxide–Solution Interface . . . 211

6.1 Origins of the Surface Charge . . . 211
6.2 Solvation and Structure of the Interface . . . 214
6.2.1 Solvation of the Particles . . . 214
6.2.2 Surface–Electrolyte Interactions . . . 215
6.3 Effect of Ionic Strength and Determination of the PZC . . . 217
6.4 Components of the Surface Countercharge . . . 220
6.5 References . . . 221

7 Modeling of the Oxide–Solution Interface . . . 223

7.1 Surface Acidity . . . 223
7.1.1 Surface Acidity Instrinsic Constants: the Multisite Complexation (MUSIC) Model . . . 225
7.1.2 Evaluation of the PZC . . . 231
7.1.3 Point of Zero Charge or Isoelectric Point? . . . 233
7.2 Surface Charge–Potential Relationship . . . 235
7.2.1 Inner Part of the Double Layer . . . 235
7.2.2 Diffuse Part of the Double Layer . . . 237
7.2.3 Interfacial Capacitance . . . 240
7.3 Models of the Oxide–Solution Interface . . . 241
7.3.1 Basic Model (Two-Layer) . . . 242
7.3.2 Site Complexation Model (Triple-Layer) . . . 243
7.3.3 Applications of the MUSIC Model . . . 249
7.3.4 Other Models of the Oxide–Solution Interface . . . 251
(a) Gel Models . . . 251
(b) Model with Variable PZC . . . 252
7.4 References . . . 254

8 Stability of Colloidal Dispersions . . . 256

8.1 Kinetic Stability of the Dispersions. Control of Particle Aggregation . . . 257
8.1.1 Electrostatic Forces . . . 257
(a) Static Aspect of the Interactions . . . 257
(b) Dynamic Aspect of the Interaction . . . 261
8.1.2 Van der Waals Forces . . . 263
8.1.3 Total Potential Energy of the Interaction . . . 264
8.1.4 Kinetics of Flocculation . . . 268
8.1.5 Characterization of the Oxide–Solution Interface by the Flocculation Kinetics . . . 271
8.2 Thermodynamic Stability of the Dispersions. Control of Particle Size . . . 273
8.2.1 Surface Energy (Tension) and Interfacial Energy . . . 275
8.2.2 Decrease in Interfacial Energy owing to Adsorption . . . 276
8.2.3 Control of the Particle Size of Oxides . . . 279
8.3 References . . . 282

9 Interface Reactions and Adsorption . . . 284

9.1 Adsorption of Metal Cations . . . 284
9.1.1 Electrostatic Interaction and Outer Sphere Complexes . . . 285
9.1.2 Chemisorption and Inner Sphere Complexes . . . 286
(a) Structural Considerations . . . 288
(b) Electrophoretic Mobility . . . 290
(c) Adsorption Isotherms . . . 293
(d) Models . . . 294
9.1.3 Cation Adsorption and Interface Transfers . . . 295
9.2 Anion Adsorption . . . 301
9.3 Polymer Adsorption . . . 309
9.3.1 Non-ionic Macromolecules . . . 310
9.3.2 Charged Polymers . . . 311
9.3.3 Polymer Grafting . . . 313
9.4 References . . . 315

Index . . . 319

Preface

This book was written for researchers and engineers interested in the precipitation of oxides and the physicochemical properties of their surfaces. Oxides play an important role in the blooming science of finely divided materials.

The main objectives of this book are twofold:

- to describe the logic behind the formation of oxides from solutions,
- to introduce the basics of the physics and chemistry of oxide surfaces, which are at the core of the behavior of small particles in suspension.

DropBooks

In spite of the extensive scientific literature, there are few books on this topic. Precipitation is usually discussed using the macroscopic concept of solubility product. From this angle, the behavior of cations in solution appears very confusing. Moreover, the physics and chemistry of aqueous oxide solutions are an equally important topic from both fundamental and practical standpoints. They are seldom included in university curricula.

I wrote this book, at Jacques Livage's instigation, using the classes I teach at the University Pierre and Marie Curie in Paris as a blueprint. I have also included Marc Henry's partial charges model, based on the principle of electronegativity equalization as demonstrated by Sanderson. The pedagogical interest of this model is its simplicity. Like any model, its use requires a full understanding of its limitations. The second part of the book contains results of our research with Elisabeth Tronc. I wish to thank her and express the great esteem I have held her in throughout our collaboration. I am also grateful to the students we have supervised together: Philippe Belleville, Christophe Barbé, Philippe Prené, Colette Levraud, Martine Richard, Lionel Vayssières, Virginie Boulet, Corinne Chanéac.

I am greatly indebted to Elisabeth Tronc, Clément Sanchez and François Ribot for their support and the time they have spent reading and reviewing this manuscript. I have also greatly appreciated the many discussions I have had with Roland Contant on tungsten polyanions and phosphate–tungsten anions.

I would like to thank the editors as well as the French and foreign colleagues who have allowed reproduction of their documents, in particular M. Figlarz (Amiens),

E. Matijevic (Potsdam), C.J. Brinker (Albuquerque), T. Sugitomo (Sendai) and C.J. Serna (Madrid).

I wish to thank my wife, Arlette, for her patience during many evenings and weekends spent working on this book, and for her support during the past few years.

I also wish to thank Jean Lefebvre, and acknowledge the memories of Gaston Charlot and Pierre Souchay. Their teachings initiated me into the science of solutions. They are, without doubt, the foundation of my interest in the phenomena discussed here.

J.P. JOLIVET
Paris, July 1994

Introduction

Metal oxides have long generated technological and industrial interest because of their very diverse properties (optical, electrical, magnetic, etc.), combined with their overall characteristics of hardness, thermal stability and chemical resistance. Silica SiO_2 is now one of the most widely used materials in the world because of its optical properties, characteristics as an electrical and thermal insulator, hardness and chemical stability. Ferrimagnetic iron oxides (spinel ferrite γ-Fe_2O_3, hexaferrite $BaFe_{12}O_{19}$) are the materials of choice for data storage and transmission. Some oxides with variable electron mobility are used as semiconductors (V_2O_5) or superconductors ($YBa_2Cu_3O_7$). Materials with high ion mobility have a promising future as solid electrolytes and cathodes for batteries. Ferroelectric or dielectric oxides of perovskite structure ($BaTiO_3$, $PbZrTiO_3$) are extensively used in electronic devices.

'Nanomaterials' also generate interest because of the specific properties linked to the nanometer size of the particles. Some unusual optical and electrical properties are due to a phenomenon known as quantum confinement. The large surface/volume ratio also leads to the use of some of these materials in catalysis. The excellent sintering characteristics of fine powders are useful in the fabrication of ceramics and composites. The dispersion of small particles in various solvents allows the fabrication of thin films and antireflection coatings, or improvements in the optical performance of mirrors.

Various techniques are used in the processing of oxide micro- or nanoparticles. They include dividing a bulk solid through mechanical abrasion (crushing), electrical or thermal erosion (laser ablation) or condensing ions or molecules. Gas phase compounds are deposited and condensed on to various substrates by CVD (Chemical Vapor Deposition). Precipitation and co-precipitation of ions from solutions have been used for many years in most industrial production of fine powders for ceramics or catalyst supports. The Bayer process for the synthesis of alumina is based on the precipitation of gibbsite $Al(OH)_3$ from aluminate solutions. Titanium oxide pigments (TiO_2) are synthesized through controlled hydrolysis of $TiCl_4$ solutions. Zirconia ZrO_2 is prepared from oxychloride $ZrOCl_2$ solutions.

Precipitation from solutions is also used in hydrothermal synthesis. It is also involved in geochemical phenomena and even some biological processes such as calcification and kidney stone formation.

Solution chemistry offers many possible routes for 'chemical manipulations' and allows various combinations in the synthesis of solids of diverse structures, compositions and morphologies. It is also referred to as 'soft chemistry', since it frequently takes place at room temperature or around 200–300 °C under standard hydrothermal conditions, conditions which also allow the synthesis of metastable phases. The control of the texture of the solid (porosity and surface area) is also much easier than in classical high-temperature processing techniques.

Controlling the method requires a good understanding of the formation process of colloidal particles, i.e. how the ions go from the solution to the solid. This is a complex phenomenon from chemical and structural standpoints because it involves a set of chemical reactions, and the experimental conditions (concentration, acidity, temperature, nature of the anions, etc.) also have a strong influence on the structural, morphological and dimensional characteristics of the solid phase. Precipitation is the result of a process of inorganic polycondensation involving the hydrolysis of metal ions in solution and the condensation of hydroxylated complexes:

$$M{-}OH + M{-}OH \longrightarrow M{-}OH{-}M, \qquad M\begin{matrix}\diagup OH \\ \diagdown OH\end{matrix}M, \qquad M{-}OH{-}M$$

The various stages involved make this indeed a complicated process. There is a wide diversity in the behavior of various elements, as shown in the following examples:

- Pentavalent vanadium forms polyanions of various degrees of condensation in solution, in which the coordination of vanadium varies from 4 to 6. Under certain conditions of acidity, the oxide precipitates and forms entangled ribbons. Phosphorus (V), however, stays in solution as a monomer in the form of phosphate anions.
- Aluminum forms the hydroxide $Al(OH)_3$, whereas in the case of iron the $Fe(OH)_3$ phase is unstable. It dehydrates spontaneously and crystallizes as α-Fe_2O_3 hematite or α-FeOOH goethite. The isostructural α-AlOOH (diaspore) forms only under hydrothermal conditions.
- Chromium(VI) and tungsten(VI) exhibit different behavior. The chromate ion $[CrO_4]^{2-}$ forms the dimer $[Cr_2O_7]^{2-}$ in solution at any acidification level and does not precipitate a solid phase. The tungstate ion $[WO_4]^{2-}$, however, forms upon acidification a series of polyanions of variable degrees of condensation in which tungsten is hexacoordinated. It may also, unlike chromium(VI) and molybdenum(VI), form the oxide WO_3 by precipitation.

Hydrolysis, condensation and complexation reactions of cations in aqueous solution are the phenomena involved in the formation of the solid by precipitation. These are

the focus of Part I in this book. Analysis of the behavior of the elements allows the identification of the structural relationships between species in solution and the solid, and it allows for an interpretation of the transformations taking place during ageing of suspensions.

Part II is concerned with a very important aspect of the physicochemistry of oxide particles: the oxide–solution interface and its reactivity. The high surface/volume ratio of submicron particles gives the solid a specific surface area that can reach several hundred square meters per gram. The behavior of particles in the dispersion is therefore controlled to a large extent by the characteristics of their surface:

- The formation of sols, gels or aggregates depends on the repulsive or attractive forces between the surfaces.
- The growth of particles is controlled by the forces exerted on their surfaces.
- Adsorption or grafting depends on the interactions between the surface and the ions or molecules in the solution.

Since these various forces are directly related to the physicochemical conditions of the medium, it is possible to control these phenomena by adjusting the concentration of the solution. Some of the unique properties of the solid are also due to the small size of the particles, and hence to the large oxide–solution interface. For example, some reactions on the surface, such as ion or electron transfer across the interface, may trigger a response in the core of the particles.

DropBooks

Part I

INORGANIC CONDENSATION

1

Water and Cations in Aqueous Solution

Water is the most widely used dispersion liquid in inorganic chemistry because of its exceptional ability to dissolve mineral salts. It is safe, chemically stable and remains liquid over a wide temperature range. It is the solvent of choice for metallic cations because it is the most convenient reaction medium, in the laboratory as well as on an industrial scale. The ability of water to dissolve ionic and ionocovalent solids stems from two main characteristics: the high *polarity* of the water molecule ($\mu = 1.84$ debye) and the high *dielectric constant* of the liquid ($\varepsilon = 78.5$ at 25 °C).

The polarity of the water molecule is responsible for its good solvation power, i.e. its ability to attach itself on to ions as a result of electrical dipolar interactions. Water is also an ionizing liquid, i.e. able to polarize a covalent bond because of its Lewis base (electron donor) character. For example, the solvolysis phenomenon allows the ionization of the HCl molecule.

The high dielectric constant makes water a dissociating medium because the decrease in electrostatic forces between solvated cations and anions allows their easy dispersion in water (the attractive force F between two charges q and q' separated by a distance r is given by Coulomb's law $F = qq'/\varepsilon r^2$). Both characteristics are seldom found simultaneously in usual liquids. For example, the dipole moment of the ethanol molecule ($\mu = 1.69$ debye) is of the order of magnitude of that of water, but the dielectric constant is smaller ($\varepsilon = 24.3$). Therefore, this alcohol is solvating but poorly dissociating, as it stabilizes solvated ions in pairs, and therefore it is a poor solvent for ionic compounds.

The effect of water on an ionic solid such as an alkali halogen MX is limited to the simple dispersion of solvated ions as $M^+ \cdot nH_2O$ $(4 < n < 8)$ and $X^- \cdot mH_2O$ $(m = 6)$ at any pH. Cations of higher charges, transition metals most notably, strongly retain a number of water molecules around them and form true aquo complexes $[M(OH_2)_N]^{z+}$ with well-defined geometry. Water molecules are true ligands because a σ donor effect towards the empty orbitals of the cation adds to water–cation dipolar interactions. In such complexes, solvation water molecules may be more or less stable, depending upon the size and charge of the cation, and the acidity of the medium. Some water molecules lose protons spontaneously and

DropBooks

are transformed into hydroxo (OH^-) or oxo (O^{2-}) ligands. The acid–base character of cations in solution is due to proton exchange between the solvated complex and water. The degree of protonation of the oxygenated ligands, governed by hydrolysis equilibria, directly influences the reactivity of metal cations as far as condensation phenomena are concerned. Therefore, it is important to know, under specific conditions (pH, concentration, temperature, etc.) the nature of the coordination sphere of the cation in the various complexes in solution.

1.1 PROPERTIES OF WATER AS A SOLVENT

1.1.1 ELECTRONIC STRUCTURE OF THE WATER MOLECULE

The symmetry of the water molecule is C_{2v}. Its molecular orbitals (MOs) are formed by linear combination of the atomic orbitals (AOs) of the oxygen atoms (2s, 2p) and of the hydrogen atom (1s) according to the LCAO method. They exhibit one of the symmetries that correspond to the four irreducible representations of the C_{2v} group (A_1, A_2, B_1, B_2). Theoretical calculations give the following expressions for the four MOs of lowest energy [1]:

$$2a_1 \quad 0.85(2s) + 0.13(2p_z) + 0.81(1s_a + 1s_b), \qquad E = -36\,\text{eV}$$

$$1b_2 \quad 0.54(2p_y) + 0.78(1s_a - 1s_b), \qquad E = -19\,\text{eV}$$

$$3a_1 \quad 0.46(2s) - 0.83(2p_z) - 0.33(1s_a + 1s_b), \qquad E = -14\,\text{eV}$$

$$1b_1 \quad (2p_x), \qquad E = -12\,\text{eV}$$

Each of the occupied MOs contains two electrons, whereas the antibonding MOs of higher energy ($4a_1$, $2b_2$) are empty (Figure 1.1a). The photoelectronic spectrum of water, obtained via UV excitation with the He(I) line of helium (21.2 eV), shows the bonding nature of the $1b_2$ and $3a_1$ MOs (presence of fine vibrational structure), whereas the b_1 MO is strictly non-bonding owing to symmetry limitations [1].

The main properties of the water molecule may be predicted from its electronic structure.

- The high polarity, which explains the solvation of ions, is due to the electronegativity difference between oxygen and hydrogen. The propensity of oxygen to attract the electronic charge is much greater than that of hydrogen. The high coefficients of the oxygen AOs in the expression for the occupied MOs point to the fact that the electron density is shifted towards oxygen [2] (Figure 1.1b). The electronic charge carried by each of the atoms (partial charge) may be calculated from the above-mentioned expression for the MOs. The 'partial' charge of an atom in a combination is defined (see Appendix to Part I) by the total atomic population, which includes its formal charge (degree of oxidation) and half the overlap charge due to bonds with other atoms, the overlap charge being considered localized on to the atoms [1].

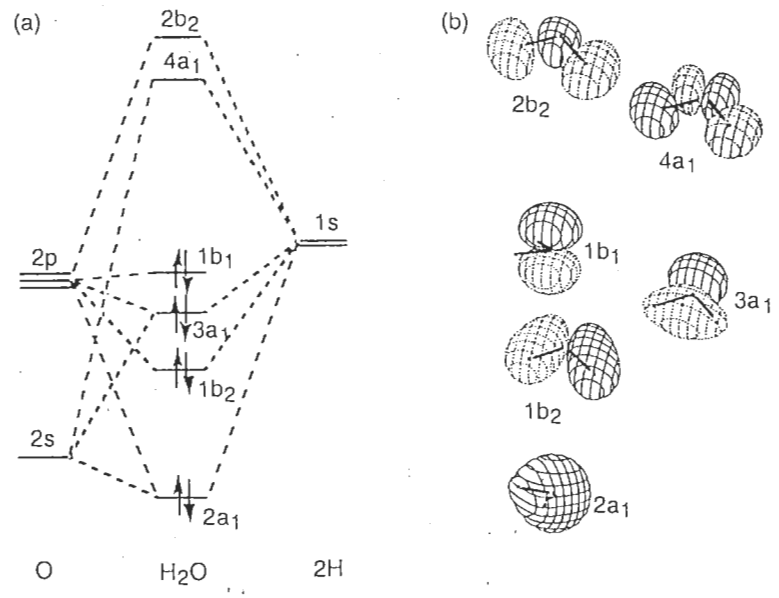

Figure 1.1 (a) Molecular orbital diagram of the water molecule and (b) electronic probability of presence. Reproduced by permission Academic Press from [2]

The calculation of the partial charge is a complex task because it requires knowledge of the overlap integrals for each occupied MO. It leads to extremely variable results depending on the method of calculation. For the sake of simplicity, we have chosen to use the model presented in the Appendix, which is based on the principle of electronegativity equalization within a compound. Although the model is relative and approximate, it does provide a simple estimation of the charges on atoms in a combination.

According to (A.10), the average electronegativity χ of the water molecule is

$$\chi = \frac{2\sqrt{\chi_H^*} + \sqrt{\chi_O^*}}{(2/\sqrt{\chi_H^*}) + (1/\sqrt{\chi_O^*})} = 2.49$$

and from (A.8)

$$\delta(H) = \frac{\chi - \chi_H^*}{1.36\sqrt{\chi_H^*}} = +0.2, \qquad \delta(O) = \frac{\chi - \chi_O^*}{1.36\sqrt{\chi_O^*}} = -0.4$$

It is useful to point out that the relationship between the ionic character of bonds and the dipole moment of a molecule is not trivial. The ionic moments of the bonds are only one of the contributions to the molecular dipole moment. The size difference between atoms, as well as the dipole moments of free pairs, must also be taken into

consideration [3]. Assessment of the effective charges on atoms based solely on the molecular dipole moments is therefore subject to controversy.

• The Lewis base character is due to the electrons in the $3a_1$ MO. This MO is essentially built on the hybridization of the 2s and $2p_z$ AOs of oxygen. It is strongly delocalized towards the outside of the molecule, as indicated by the high coefficients of the corresponding AOs and their negative contributions in the combination. The water molecule behaves like a donor ligand of a σ pair, which explains its ionizing properties and its aptitude to coordinate Lewis acids (complexing properties). However, the non-bonding b_1 MO entirely localized on oxygen (Figure 1.1b), exhibits a very weak π donor character and does not allow the creation of a bond.

1.1.2 STRUCTURE OF LIQUID WATER

Compared with similar compounds (H_2S, H_2Se, H_2Te), liquid water has very peculiar properties: its boiling and melting points are unusually high, the volume change at the melting point is negative and the density maximum is found at around 4 °C; the diffusion of protons and hydroxyls in water is particularly fast compared with other ions. Such peculiarities are the result of associations between water molecules through hydrogen bonds. Such interaction occurs when the hydrogen atom, bound to a highly electronegative atom (F,O,N), is associated to another electronegative atom:

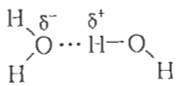

Within this bond, the hydrogen atom may occupy two positions of identical minimal energy, each of which is very close to the oxygen atom. A small potential barrier separates both positions, but the hydrogen atom may cross it by tunneling. The energy of the hydrogen bond is about 20–40 kJ mol^{-1}.

Under usual conditions, water crystallizes as hexagonal ice. In this structure, the hydrogen bonds, which are strongly directional, allow each oxygen atom to surround itself with hydrogen atoms in an almost symmetrical tetrahedron (Figure 1.2a).

As ice melts, the breakdown of a number of hydrogen bonds decreases the geometrical constraints between water molecules. They become mobile and able to get closer to each other. This is why the density increases and goes through a maximum at around 4 °C, above which thermal agitation dominates and causes dilatation of the liquid. Molecular dynamics calculations [5,6] show that, at ambient conditions, the number of isolated molecules in the liquid is very small (Figure 1.2b). The molecules form, on average, 2–3 hydrogen bonds and primarily form polygonal assemblies of tetrahedral geometry. Such limited-size associations have a very short lifetime of 10^{-10} s but they form constantly. The structure of the liquid is therefore not topologically related to that of hexagonal water. The liquid may be considered as a disordered three-dimensional network of hydrogen

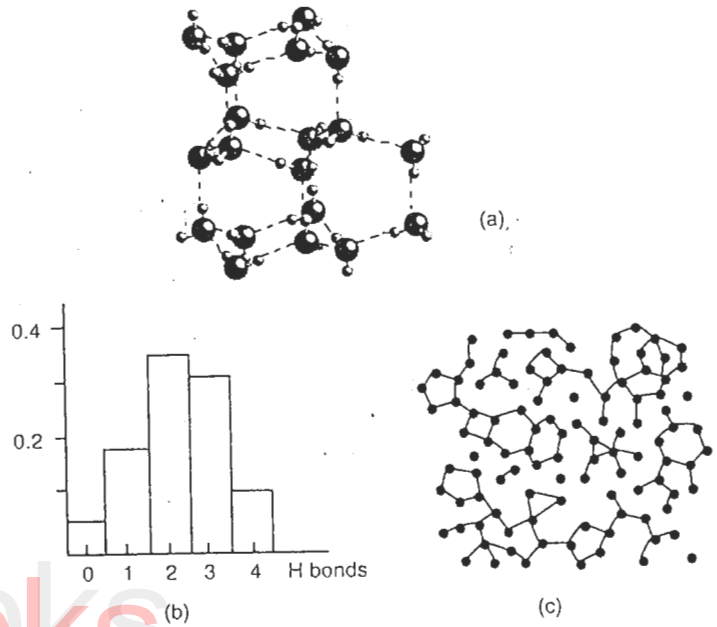

Figure 1.2 (a) Structure of hexagonal ice (bond length O···H···O 2.76 Å, O–H 1 Å, O···H 1.75 Å, angles H–O–H 109.5° [4]), (b) fraction of the molecules involved in various numbers of H bonds in liquid water at 10 °C [5]) and (c) hydrogen bond network in liquid water (molecules are shown as points). Reprinted with permission from [5]. Copyright 1973 American Chemical Society

bonds, which form statistical connections allowing fast proton and hydroxyl transfers [6,7].

The ionizing and dissociating power of liquid water leads to appreciable self-dissociation of the molecules:

$$2HO \longleftrightarrow H_3O^+_{solvated} + HO^-_{solvated} \quad K_e = [H_3O^+][OH^-] = 10^{-14} \text{ at } 25\,^\circ C$$

Hence, water molecules are amphoteric in nature. The liquid is a protic solvent for which the acid–base concept is linked to the proton exchange between water and any proton acceptors (bases) or donors (acids).

The structure of the oxonium ion H_3O^+ has been investigated by NMR on monohydrated crystals of strong acids ($HClO_4 \cdot H_2O$, $HNO_3 \cdot H_2$, $H_2SO_4 \cdot H_2O$) [8,9]. The results indicate a planar or slightly pyramidal geometry involving H–O–H bond angles of 120 or 118 ° respectively, with H–H distances of 1.72 Å.

Solvation of the oxonium ion by water molecules occurs through hydrogen bonds and creates $[H_3O \cdot nH_2O]^+$ entities. The degree of solvation, i.e. the number of water molecules forming the 'coordination sphere', varies depending on whether

DropBooks

the ion is in aqueous solution or involved in a solid network. The di-aquo hydrogen ion $[H_2O{-}H{-}OH_2]^+$ ($n = 1$) was identified using neutron and X-ray diffraction in crystals of $HBr \cdot 2H_2O$ and in some complexes such as *trans*$[Co(en)_2Cl_2]Cl \cdot 2H_2O$, HCl [10]. The O–O distances in the di-aquo ion are about 2.40 Å, the hydrogen atoms being approximately in a central position with respect to oxygen atoms.

In solution, the structural information obtained using diffraction techniques (X-ray, neutrons) points to the presence of four water molecules in the immediate surroundings of the H_3O^+ ion ($n = 4$) [11,12]. Neutron diffraction indicates a tetrahedral configuration of the oxonium ion solvated in aqueous molar solutions of HCl or HBr [13], whereas the analysis of the radial distribution functions obtained via X-ray diffraction on concentrated HCl solutions reveals a pyramidal geometry [14]. Three solvation molecules form short hydrogen bonds (O–O distance 2.44 Å). The fourth molecule of water, much further away (O–O distance 2.90 Å, similar to that observed in pure water), is located at the corner of a trigonal pyramid (Figure 1.3a). The techniques give different results because neutron diffraction gives an average O–O distance [14]. The energy of short bonds, calculated by the LCAO method, is about 190 kJ mol^{-1} [15], while that of the long bond is almost zero. Therefore, one of the water molecules interacts very weakly, and it is possible to consider the solvated proton as a 'molecular' entity $[H_9O_4]^+$, itself solvated by other water molecules through weaker hydrogen bonds, of the order of 20–40 kJ mol^{-1}.

The hydroxyl ion, HO^-, present in the structure of many complexes in the monosolvated state $[HO{-}H{-}OH]^-$ (O–O distance 2.29 Å), exists in solution as a 'molecular' entity $[H_7O_4]^-$, itself solvated by other water molecules [10] (Figure 1.3b). This ion is the strongest Brönsted base in water. This is why self-dissociation of molecules is weak and why the O^{2-} ion is never present in aqueous solution. It follows that oxides never dissolve in water without an acid–base protonation reaction of O^{2-} ions.

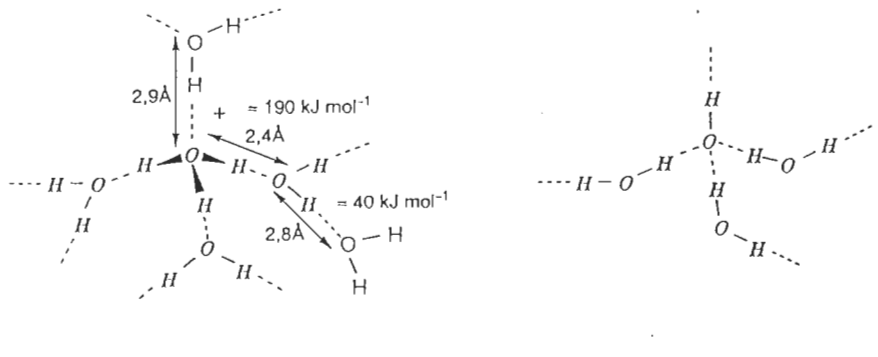

Figure 1.3 Probable structure of hydrated ions: (a) $[H_9O_4]^+$; (b) $[H_7O_4]^-$. From [14]

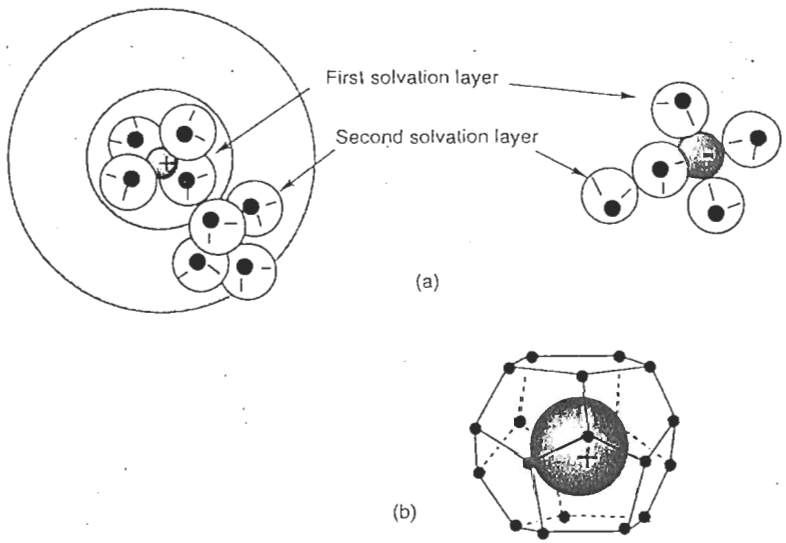

Figure 1.4 Hydration schemes (a) of hydrophilic cations and anions in aqueous solution and (b) of hydrophobic cations

1.1.3 HYDRATION OF IONS AND THE STRUCTURE OF SOLUTIONS

The dissolution of ionic or polar solutes is explained by the polarity and the high dielectric constant of water. The solvation of ions allows their separation in solution. The structure of solvated ions is investigated using spectroscopy techniques (EXAFS, XANES, NMR, infrared, Raman), or diffraction and diffusion techniques (X-ray, neutrons) [11,12]. Such techniques have shown that solvated cations and anions are linked to water molecules through the oxygen and hydrogen atoms respectively (Figure 1.4a).

The number of water molecules involved in the solvation of a cation increases with its polarizing strength, i.e. as the cation charge z increases and its radius r decreases. The polarizing strength of an ion is defined as the z/r^2 ratio. The attraction and organization of water molecules around ions subjected to dipolar interactions occur over several layers, and it is convenient to distinguish the first hydration 'sphere', which contains the water molecules in contact with the cation, from the outer and more distant layers.

(a) First Hydration Sphere

Monovalent cations such as alkaline ions are surrounded by a first hydration sphere, the geometry and composition of which are poorly defined. The Li^+ ion, the smallest and most polarizing in the series, is surrounded by a tetrahedron of water molecules. The larger and less polarizing ions (Na^+, K^+, Cs^+) have a first solvation

Table 1.1 Hydration enthalpies (kJ mol^{-1}, 25 °C) and ionic radii (Å) of a few ions [16]

Ion	$-\Delta H°$	Radius	Ion	$-\Delta H°$	Radius
H^+	1100	–			
Li^+	522	0.78	Cr^{2+}	1930	0.80
Cs^+	285	1.65	Fe^{2+}	1956	0.83
Mg^{2+}	1940	0.78	Ni^{2+}	2120	0.78
Ba^{2+}	1320	1.43	Cr^{3+}	4620	0.65
Al^{3+}	4700	0.57	Fe^{3+}	4450	0.67

Table 1.2 Exchange rate constant for the water molecule in the first hydration sphere of metal cations [16]

Ion	k (s^{-1})	Ion	k (s^{-1})
Ca^{2+}, Sr^{2+}, Ba^{2+}	$\approx 5\times10^8$–5×10^9		
Li^+, Na^+, K^+, Cs^+	$\approx 5\times10^8$–5×10^9		
Mg^{2+}	10^5	Be^{2+}	10^2
Cr^{2+}	3×10^8	Al^{3+}	≈ 1
Fe^{2+}	3×10^6	Fe^{3+}	10^2
Ni^{2+}	4×10^4	Cr^{3+}	3×10^{-6}

sphere of 6–8 water molecules. The symmetry of the solvation sphere of these cations cannot be defined precisely because the electrostatic interactions with the water molecules are relatively weak (Table 1.1) and the solvation molecules are exchanged rapidly with those from the medium [12] (Table 1.2). In addition, the number of water molecules that form the first hydration sphere of these cations varies with the concentration, the temperature and the nature of anions present in solution.

Small-size, high-charge cations develop stronger electrostatic interactions with water and have strong hydration energy (Table 1.1). Therefore, the geometry of such hydrated cations is well defined. Structural investigations [11,12] point to a tetrahedral symmetry for the tetra-aquo $[Be(OH_2)_4]^{2+}$ ion, an octahedral symmetry for the $[M(OH_2)_6]^{2+}$ (M = Mg, Ca, Zn, Cd, Hg, Pb, etc.) and $[Al(OH_2)_6]^{3+}$ hexa-aquo ions and a square-base antiprism geometry for $[Sr(OH_2)_8]^{2+}$, for example. The coordination of cations is directly related to their size.

All divalent and trivalent ions from the first transition series are hexacoordinated. The octahedral coordination of these ions is in agreement with crystal field theory. The interactions between the water molecules and these cations are clearly the result of the σ-donor ligand role of the water molecules, through the overlap of the $3a_1$ MO with the d orbitals of the cation. Hence, the bond exhibits a strong covalent character and the hydrated cations are really coordination complexes. Some distortions of the hydration sphere are observed with Cr^{2+} and Cu^{2+} owing to the Jahn–Teller effect. The labile character of the water molecule, when coordinated to transition elements, is very variable (Table 1.2). Some hexa-aquo complexes, which

are strongly stabilized by the crystal field, are inert towards substitution reactions. This is the case for $[Ni(OH_2)_6]^{2+}$ and $[Cr(OH_2)_6]^{3+}$ of electronic configurations $t_{2g}^6 e_g^2$ and $t_{2g}^3 e_g^0$ respectively, for which formation of the transition state during the substitution causes the most energetically costly change in electronic configuration (see Chapter 2).

It is difficult to predict the degree of solvation for ions with a charge higher than three, because they are subject to hydrolysis reactions and, except in a highly acidic medium, the hexa-aquo forms are mostly unstable.

(b) Outer Solvation Spheres

The second solvation sphere is more difficult to characterize because of the rapid exchange with the water molecules from within the solution. Studies undertaken according to the aforementioned techniques and via simulations imply that, for the majority of cations, the immediate environment of the solvated ions consists of 12 water molecules. The average O–O distance between the oxygen atoms of the first and second hydration spheres, which is about 2.7 Å, is shorter than the average intermolecular distance between water molecules in pure water (about 2.9 Å) [11,12]. The number of layers of water molecules attracted and oriented by a cation increases with its polarizing strength.

(c) Structure of Solutions

The presence of a cation in solution induces local ordering of the water molecules owing to dipolar interactions propagating beyond the second solvation sphere. Four or five layers of water molecules are influenced by the diffusion of ions in solution. One may define the hydration of an ion by the number of water molecules it carries with it in its movements through the solution, whereas its coordination corresponds to the number of water molecules in direct contact with it in the first hydration sphere. The orientation and order of the hydration layer modify appreciably the structure of the solvent [17]. An LiCl solution is more viscous (1.146 cP at 20 °C, 0.1 mol l^{-1}) than water at the same temperature (1 cP), whereas a CsCl solution (0.947 cP at 20 °C, 0.1 mol l^{-1}) is less viscous than water. Small ions with a high charge density are able locally to alter the primitive structure of water through the rupture of hydrogen bonds and the reorganization of numerous solvent layers, forming a completely different structure from the pure liquid. Such behavior is typical of ions such as Li^+, Na^+, Mg^{2+}, F^- and HO^-. These are called 'type I structuring ions'.

Ions of intermediate size and charge develop interactions with water that are strong enough to break the hydrogen bonds locally, but they cannot keep many solvent molecules around them. The loss of the primitive structure of water is not counterbalanced by the restructuring of the water molecules around the ion. This is the case for K^+, Cs^+, NH_4^+, NO_3^- and ClO_4^-, which are called 'destructuring' or

DropBooks

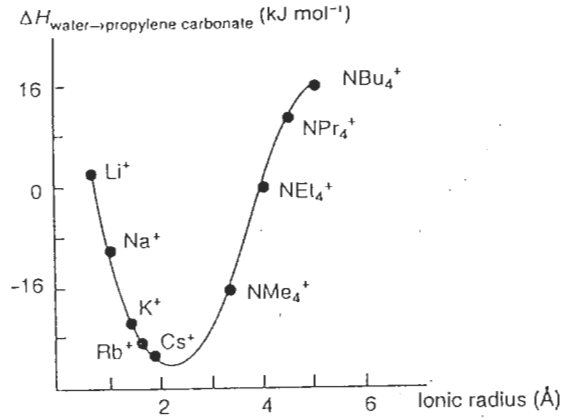

Figure 1.5 Transfer enthalpy for ions of various sizes from water towards propylene carbonate. Reprinted with permission from [19]. Copyright 1969 American Chemical Society

'breaking' ions. Solvation of these ions is much weaker than for structuring ions, which explains the decrease in viscosity of a Cs^+ solution compared with a solution of Li^+ ions.

Weakly polarizing ions such as quaternary ammonium cations $[NR_4]^+$ ($R = CH_3$, C_2H_5, etc.) are not able to break the network of hydrogen bonds but, rather, are incorporated within the liquid, thereby altering its local architecture drastically. Around these ions, the liquid forms polyhedral cages similar to those found in clathrates [7,18] (Figure 1.4b). This type of interaction is sometimes called 'hydrophobic interaction', in contrast to the hydrophilic structuring ions of type I. These are called 'type II structuring ions'.

These three types of behavior are clearly separated on the transfer enthalpy from water to propylene carbonate for monovalent ions of various sizes [19] (Figure 1.5). The breaking ions, which develop weaker interactions with water, have the smallest transfer energy.

1.2 ACID–BASE PROPERTIES OF IONS IN AQUEOUS SOLUTION

The overlap of valence orbitals between the solvated ion and the water molecules allows an electron transfer from the $3a_1$ MO of water to the AOs of the cation, which are either empty or partially filled. The transfer is more significant (the M–O bond is stronger) if the cation is strongly polarizing, i.e. if its charge is high and its ionic radius is small.

The $M \leftarrow OH_2$ transfer decreases the electronic density in the bonding $3a_1$ MO and weakens the O–H bond. The ionic character of the O–H bond increases and the

Table 1.3 Distribution of the partial charges δ in $[M(OH_2)_6]^{z+}$ complexes, as calculated using the partial charges model in the Appendix

Complex	χ	δ(M)	δ(O)	δ(H)	δ(H_2O)
$[Mn(OH_2)_6]^{2+}$	2.657	+0.59	−0.33	+0.28	+0.23
$[Cr(OH_2)_6]^{3+}$	2.762	+0.68	−0.29	+0.34	+0.39
$[Ti(OH_2)_6]^{4+}$	2.848	+0.98	−0.25	+0.38	+0.51
$[V(OH_2)_6]^{5+}$	2.983	+0.84	−0.20	+0.45	+0.70

positive charge on hydrogen increases. Concurrently, the positive charge on the cation decreases (Table 1.3).

Coordinated water molecules are stronger acids than water molecules in the solvent itself. They tend to de-protonate according to

$$[M{-}OH_2]^{z+} \overset{H_2O}{\Longleftrightarrow} [M{-}OH]^{(z-1)+} + H^+_{aq} \overset{H_2O}{\Longleftrightarrow} [M{-}O]^{(z-2)+} + 2H^+_{aq} \qquad (1.1)$$

The acidity of the aquo-ion is directly dependent on the magnitude of the σ transfer, and the cation may be coordinated to three types of ligands: aquo (H_2O), hydroxo (HO^-) and oxo (O^{2-}).

The elements of small formal charge ($z = 1, 2$) do not polarize oxygen very strongly. They form aquo cations in a large domain of acidity. The oxides of such elements are ionic and exhibit basic behavior in water:

$$Li_2O + 9H_2O \longrightarrow 2[Li(OH_2)_4]^+ + 2HO^-_{aq}$$

On the other extreme of the classification, elements of high charge ($z = 5, 6, 7$) polarize oxygen very strongly and form anionic oxo complexes. The oxides are covalent and acidic in water:

$$z = 5 \quad N_2O_5 + H_2O \longrightarrow 2NO_3^- + 2H^+_{aq}$$
$$z = 6 \quad SO_3 + H_2O \longrightarrow SO_4^{2-} + 2H^+_{aq}$$
$$z = 7 \quad Cl_2O_7 + H_2O \longrightarrow 2ClO_4^- + 2H^+_{aq}$$

Some metals have several degrees of oxidation. Their oxides may therefore exhibit two types of behavior:

$$Cr^{III}_2O_3 + 15H_2O \xrightarrow{H_2O} 2[Cr(OH_2)_6]^{3+} + 6OH^-_{aq}$$
$$Cr^{VI}O_3 + H_2O \longrightarrow [CrO_4]^{2-} + 2H^+_{aq}$$

Equilibria (1.1) are the hydrolysis equilibria of the cation [20]. They depend on its intrinsic characteristics (formal charge, size, nature of the element) and may be displaced by changing the medium acidity. Therefore, it is possible, to a certain extent, to modify the nature of the coordination sphere of the cation.

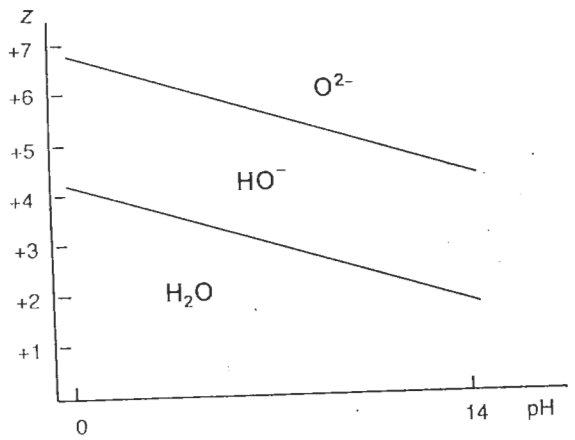

Figure 1.6 Nature of the ligands in the coordination sphere of a cation as a function of its formal charge z and the pH of the medium. Reproduced by permission of Academic Press from [2]

The possible modifications are shown on an experimental diagram indicating which ligand is present as a function of the charge of the cation and the pH [21,22] (Figure 1.6).

In the aquo domain, all coordinated water molecules keep their proton, whereas in the oxo domain, oxygen cannot be protonated. In the hydroxo domain, at least one hydroxo ligand is present within the coordination sphere.

Hence, the Mn(IV) ion may exist as the oxo form $[MnO_4]^-$ at any pH. This form does not exhibit any basic character because of the small charge density on the oxygen atoms, which are strongly polarized by the cation (see Chapter 4, Section 4.3). In other words, MnO_3OH is a strong acid in water. The hydroxo and aquo forms of the cation do not exist in water, within usual acidity domains [20]. On the other hand, the Mn(II) ion exhibits a poorly defined acidic character in water. At $pH < 6$, it forms the hexa-aquo complex $[Mn(OH_2)_6]^{2+}$. The addition of a base allows the formation of aquo–hydroxo complexes, but the Mn(II) cation is unable to polarize oxygen enough to break the OH bond of the hydroxo ligand and form O^{2-} in solution.

The Cr(VI) ion is present in water at $pH > 7$ as the oxo form $[CrO_4]^{2-}$. At $pH < 7$, protonation is possible because the polarization of oxygen by the Cr(VI) ion is weaker than by the Mn(VII) ion. $[CrO_3(OH)]^-$ exists in solution around pH 4. In a more acidic medium, the $CrO_2(OH)_2$ form predominates in very dilute solution. However, it is impossible to obtain cationic forms of Cr(VI) corresponding to an additional protonation of the oxygen bound to chromium. This occurs with Cr(III) which forms the $[Cr(OH_2)_6]^{3+}$ aquo complex at $pH < 2$. Around pH 4–5, the hydroxo form $Cr(OH)_3(OH_2)_3$ leads to the hydroxide which redissolves in the alkaline medium into $[Cr(OH)_4(OH_2)_2]^-$, but the oxo ligand does not appear in

Table 1.4

	$Si^{IV}(OH)_4$	$P^{V}O(OH)_3$	$S^{VI}O_2(OH)_2$	$Cl^{VII}O_3(OH)$
pK_1	9.8	2.1	(−1)	(−9)

Table 1.5

s	r(Å)	N	Most acidic form
Ti^{4+}	0.68	6	aquo–hydroxo $[Ti(OH)(OH_2)_5]^{3+}$
Si^{4+}	0.41	4	aquo–hydroxo $[Si(OH)_3(OH_2)]^+$
C^{4+}	0.15	3	oxo–hydroxo $[CO(OH)_2]^0$

Table 1.6

	HClO	$HClO_2$	$HClO_3$	$HClO_4$
z(Cl)	+1	+3	+5	+7
$\delta(Cl)^a$	−0.05	0.04	0.09	0.12
$\delta(H)^a$	0.33	0.42	0.47	0.51
pK	7.3	2	0	(−9)

[a] Charges calculated for the protonated form using the partial charges model.

DropBooks

the coordination sphere of Cr(III) owing to the excessively weak polarization of oxygen by the cation.

The increase in polarization of oxygen by the cation of increasing charge is clearly illustrated by the series of tetrahedral compounds in Table 1.4. As the charge of the cation increases, the number of oxo ligands bound to the central element increases at the expense of the hydroxo ligands, which see their acidic character increase [23]. The oxo ligands, which cannot be protonated, do not have a basic character because they are in fact bound to the cation through σ and π bonds (Chapter 4, Section 4.3).

The decrease in size of the cation decreases its coordination number N and increases its polarizing strength. This effect is clearly seen on the more acidic forms of the elements in Table 1.5 [20].

Both size and charge factors intervene together, since the size of the ion depends on its charge. The simultaneous effect of both factors is clearly seen in the chlorine oxides (Table 1.6) [18].

1.3 MODEL OF THE ACID–BASE BEHAVIOR OF CATIONS

The behavior of cations toward hydrolysis is very well known. It is described by thermodynamic equilibrium constants [20,23–26]. They allow the calculation of

the distribution of species as a function of the pH and the solution concentration. They can be combined with the complexing constants of the cation for any ligand [24]. However, the situation is very complex whenever condensation reactions occur because the relevant thermodynamic data are almost non-existent in the literature. The partial charges model, presented in the Appendix, is a simple quantitative approach to the problem. Let us summarize below the main conclusions of the model to acid–base equilibria.

The problem is the definition of the nature of the coordination sphere of a cation of charge z and coordination N as a function of the pH of the medium. This is equivalent to calculating the hydrolysis ratio h of this element in the equilibrium:

$$[M(OH_2)_N]^{z+} \overset{H_2O}{\Longleftrightarrow} [M(OH)_h(OH_2)_{N-h}]^{(z-h)+} + hH^+_{solvated}$$

Intuitively, it is logical to assume that an increase in the charge on the hydrogen of the water molecules coordinated to the cation (first solvation sphere) weakens the O–H bond. In a manner similar to the equalization of electronegativities of atoms in a chemical bond through electron transfer, it is generally accepted that a chemical reaction allows equalization of the average electronegativities of the reactants through a change in composition (see the Appendix). Therefore, the deprotonation reaction of the aquo complex occurs in order to equalize the electronegativities of the hydroxylated complex and water. A criterion may be set in order to find the composition of species in equilibrium as a function of the pH (A.14). The principle is described in the Appendix (A3.2). The conclusions are summarized in the following equations, which allow the determination of the limiting forms of the cations in solution.

At pH = 0, the hydrolysis ratio h of the complex $[M(OH_2)_N]^{z+}$ is given by

$$h = 1.36z - 0.24N - \frac{(2.621 - \chi^*_M)}{\sqrt{\chi^*_M}} \qquad (A17)$$

whereas at pH 14 we obtain

$$h = 1.14z + 0.25N' - \frac{0.836(2.341 - \chi^*_M)}{\sqrt{\chi^*_M}} \qquad (A18)$$

The results from equations (A.17) and (A.18) (Table 1.7) are in good agreement with the experiments [20].

One may note that in equations (A.17) and (A.18) the acidic nature of a cation is governed by three parameters: the charge z, the size (via the coordination number N) and the electronegativity. The most important factor is the formal charge of the cation. The limits of the existence domain of the aquo–hydroxo $[M(OH_2)_{N-1}(OH)]^{(z-1)+}$ and oxo–hydroxo $[MO_{N-1}(OH)]^{(2N-z-1)-}$ forms as a function of z and the pH are easily calculated using $h = 1$ or $h = 2N - 1$ in the general expression (A.16). The experimental pH–charge diagram is easily confirmed.

Table 1.7 Results of equations (A.17) and (A.18), showing the most acidic and basic forms of some elements in aqueous solution

M	z	N	χ^*	h	Acid forms	N'	h	Basic forms
Mn	7	4	1.63	7.8	$MnO_3(OH)$	4	8.5	MnO_4^-
Cr	6	4	1.59	6.4	$CrO_2(OH)_2$	4	7.3	CrO_4^{2-}
P	5	4	2.11	5.5	$PO(OH)_3$	4	8	PO_4^{3-}
V	5	6	1.56	4.5	$VO_2(OH_2)_4^+$	4	6.2	$VO_3(OH)^{2-}$
Ti	4	6	1.32	2.9	$Ti(OH)_2(OH_2)_4^{2+}$	4	4.8	$TiO(OH)_3^-$
Zr	4	8	1.29	2.4	$Zr(OH)_2(OH_2)_6^{2+}$	6	5	$Zr(OH)_5(OH_2)^-$
Si	4	4	1.74	3.8	$Si(OH)_3(OH_2)^+$	4	5.1	$SiO_2(OH)_2^{2-}$
Fe	3	6	1.72	1.9	$Fe(OH)(OH_2)_5^{2+}$	4	4	$Fe(OH)_4^-$
B	3	3	2.02	2.9	$B(OH)_2(OH_2)^+$	4	4.2	$B(OH)_4^-$
Mn	2	6	1.63	0.5	$Mn(OH_2)_6^{2+}$	4	2.8	$Mn(OH)_3(OH_2)^-$
Ag	1	2	1.68	0.1	$Ag(OH_2)_2^+$	2	1.2	$Ag(OH)_3^-$
Li	1	4	0.97	−1.2	$Li(OH_2)_2^+$	4	0.9	$Li(OH)(OH_2)_3$

The cation is considered here in its standard state (activity = 1). The h values relatives to other conditions (such as concentration) could be obtained using an empirical constant in the hardness calculation [equation (A.6)].

Generally, cations of formal charge z lower or equal to 4 form aquo–hydroxo complexes $[M(OH)_h(OH_2)_{N-h}]^{(z-h)+}$ in an acid or neutral medium ($h \leqslant z$). In an alkaline medium, they may exist in hydroxo forms $[M(OH)_x]^{(x-z)-}$. Elements of high formal charge (higher than 4), form oxo–hydroxo anions $[MO_{h-N}(OH)_{2N-h}]^{(h-z)-}$.

It must be clearly stressed that, owing to the approximations of the model, no information regarding the respective amounts of species in solution may be obtained (see the Appendix). In a molecular entity, atoms of similar chemical nature are treated similarly. Consequently, the results are mere estimations that must be used with caution, particularly if structural peculiarities are present. This is the case of the shortening of bonds owing to π overlap, a frequent phenomenon in the case of small cations of high formal charge ($z \geqslant 4$). Vanadium ($r = 0.54$ Å) is a typical example. The $[V(OH_2)_6]^{5+}$ species does not exist in aqueous solution, even in an extremely acidic medium. Its spontaneous hydrolysis ratio is 4 and the main species in an acidic medium is the *cis*-dioxo vanadic ion $[VO_2(OH_2)_4]^+$ [20,23,27]. Formation of the dioxo–aquo configuration is favored compared with the $[VO(OH)_2(OH_2)_3]^+$ or $[V(OH)_4(OH_2)_2]^+$ configurations, because the cation, which is strongly polarizing, forms V–O bonds of strong π character, thereby allowing a decrease in its partial charge and the ionicity of bonds in the complex. This results in a strong distortion of the environment of the cation. This effect is not as strong in the case of vanadium(IV), of smaller oxidation state and larger size ($r = 0.59$ Å). V(IV) forms $[VO(OH_2)_5]^{2+}$ which contains only one short V–O bond (1.6 Å) [28,29]. The π character of the short bonds sharply lowers the basicity of the oxo ligand and is responsible for the stability of the monomeric forms of the vanadic and vanadyl cations in solution. It must be stressed that the water molecules in *trans* of the

Table 1.8 Exchange rate constants k (s^{-1}, 25 °C) for water molecules in various hydroxylated species of iron(III) [32,33]

a	$[Fe(OH_2)_6]^{3+}$	$[Fe(OH)(OH_2)_5]^{2+}$	$[Fe(OH)_2(OH_2)_4]^{+}$
k	1.7×10^2	4.5×10^5	10^6
$\delta(H_2O)$	+0.40	+0.29	+0.16

Table 1.9 Partial charge on the water molecule in the coordination sphere of aluminum, as a function of the hydrolysis ratio of the cation

	$[Al(OH_2)_6]^{3+}$	$[Al(OH)(OH_2)_5]^{2+}$	$[Al(OH)_2(OH_2)_4]^{+}$	$[Al(OH)_3(OH_2)_3]$	$[Al(OH)_4(OH_2)_2]^{-}$
χ	2.754	2.675	2.588	2.487	2.373
δ_{H_2O}	+0.37	+0.26	+0.14	0	−0.16

short V–O bonds are very far from the vanadium (V–O = 2.4 Å in the vanadyl ion), which explains their high lability and the multiple coordination of V(IV) and V(V) ions [30,31] (see Chapter 4, Section 4.3). Titanium Ti(IV), with radius $r = 0.61$ Å slightly larger than V(IV), does not seem to form such oxo bonds. The $[Ti(OH)_2(OH_2)_4]^{2+}$, which is strongly acidic, forms $[Ti(OH)_3(OH_2)_3]^{+}$ and $[Ti(OH)_4(OH_2)_2]^{0}$ which are not stable as monomers (see Chapter 3).

Another interesting point is the decrease in coordination of some small-charge cations ($z < 4$), soluble in a basic medium as anionic hydroxo forms. This reduction in coordination is explained by the decrease in polarization of the coordinated water with the decrease in overall charge of the complex. The increased exchange rate for these water molecules can be correlated with the decrease in their partial charge (Table 1.8).

In the zero-charge species $M(OH)_z(OH_2)_{N-z}$, the water molecules carry a near-zero partial charge, so it is difficult to say that they act as ligands. These molecules may be considered as belonging to the second hydration sphere. With aluminum for example, the partial charge of the water molecules in the hexacoordinated complex of various hydration ratios decreases steadily until it becomes negative (Table 1.9). The latter situation is of course unrealistic because it would mean an electron transfer from the cation to the water molecule. In fact, ^{27}Al NMR spectra do show Al in coordination 4 in an alkaline medium [34], which confirms that, in these conditions, water molecules have lost their nucleophilic character owing to the decrease in the partial charge of the cation.

Transition metal cations of high formal charge ($z > 4$), highly polarizing and hexacoordinated in an acidic medium, adopt a tetrahedral configuration in an alkaline medium for other reasons. Because of their small size, and the presence of empty low-energy d orbitals, the tetra-oxo forms are stabilized by a system of π bonds. This point is discussed in some detail in Chapter 4, Section 4.3.

Aside from structural characteristics specific to complexed cations, the partial charges model is useful in explaining the general behavior of elements in solution.

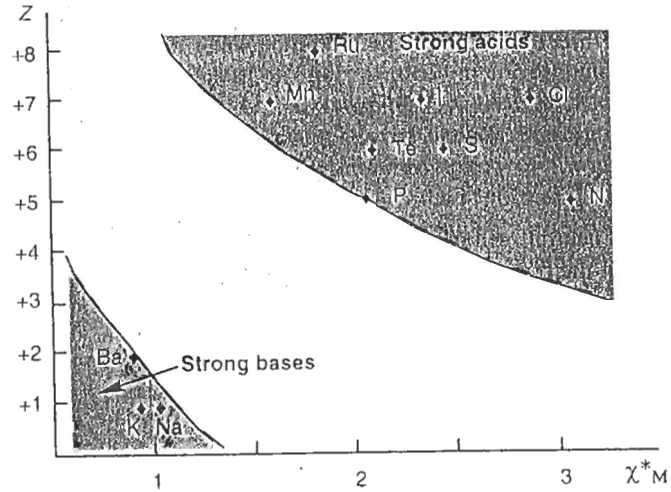

Figure 1.7 Charge–electronegativity diagram obtained from (A.19) and (A.20), showing the strong acidic or basic behavior of elements

In particular, the strong acid or strong base behavior may be explained using the formal charge and the electronegativity (see the appendix, Section A.3.3). The results of the model, summarized in Figure 1.7, are in accordance with experimental observations.

1.4 MECHANISM AND KINETICS OF HYDROXYLATION

Owing to the strong lability of water observed for aquo complexes (Tables 1.2 and 1.8), hydroxylation through neutralization may be treated as a ligand exchange reaction by substitution:

$$M(OH_2)_N^{z+} + HO_{aq}^{-} \longrightarrow M(OH)(OH_2)_{N-1}^{(z-1)+} + H_2O$$

However, the hydrogen bond network in the liquid ensures fast diffusion paths for the proton and the HO^- ion, so that the reaction may as well proceed though a direct attack of the aquo ligand by the hydroxyl:

This mechanism probably occurs in the case of hydroxylation of the oxo forms. It is somewhat unlikely that the oxo ligand, which is strongly nucleophilic and has low

PropBooks

basicity, could be substituted by the hydroxyl ion. Therefore, the reaction must proceed through direct reaction of the proton or water on the oxo ligand:

$$MO_{N'}^{q-} + H_{aq}^{+} \longrightarrow MO_{N'-1}(OH)^{(q-1)-} + H_2O$$

The kinetics of neutralization are extremely fast [20] and diffusion-controlled, which means that the reaction rate is limited only by the approach of the reactants.

Hydrolysis is, strictly speaking, a neutralization carried out by the water molecule:

$$[M(OH_2)_N]^{z+} + hH_2O \longrightarrow [M(OH)_h(OH_2)_{N-h}]^{(z-h)+} + hH^+_{solv}$$

For this reaction [20]

$$\Delta H^\circ(75.2 - 9.6z)\ \text{kJ mol}^{-1}, \qquad \Delta S^\circ = (-148.4 + 73.1z)\ \text{J mol}^{-1}$$

from which $\Delta G^\circ_{298} = (119.5 - 31.35z)\ \text{kJ mol}^{-1}$.

The reaction is spontaneous ($\Delta G^\circ < 0$) for elements of charge equal to or greater than 4. Therefore, at room temperature, tetravalent elements do not exist as purely aquo complexes, even in a strongly acidic medium. For elements with a charge z smaller than 4, ΔG° becomes negative only if the temperature is higher than 298 K. Therefore, it is necessary to heat the solution in order to carry out hydrolysis of the cation (forced hydrolysis or thermohydrolysis). This technique is used in the preparation of particles of narrow size distribution [35]. Indeed, neutralization of a solution by addition of a base inevitably leads to local pH gradients, causing inhomogeneities in the hydrolysis products, which condense in an anarchical manner. Often, they lead to amorphous solids and, under such conditions, the particle size is very heterogeneous because of the overlap of nucleation and growth kinetics in the solid phase (see Section 2.3). Heating of a solution to ca 50–100 °C makes it possible, particularly with trivalent elements (Al, Fe, Cr) [35], to carry out the hydrolysis homogeneously, in conditions close to thermodynamic equilibrium. Under such conditions, the slow speed of formation of the hydrolyzed precursors allows decoupling of the nucleation and growth steps from a kinetic standpoint. This allows narrow particle size distributions. Many examples of the usefulness of thermohydrolysis are given below.

1.5 WATER UNDER HYDROTHERMAL CONDITIONS

The thermohydrolysis of cations in solution involves heating temperatures that do not exceed the boiling temperature of the solutions at atmospheric pressure. As discussed previously, the increase in temperature allows water to act as a reactant in

hydrolysis. It also allows acceleration of the kinetics of various reactions such as the transformation of solids in suspension.

The hydrothermal conditions of an aqueous medium correspond to temperatures and pressures higher than 100 °C and 1 bar respectively. Such conditions allow considerable modifications of the chemistry of cations in solution. They favor the formation of metastable structures, more complex, of lower symmetry and involving smaller enthalpy and entropy changes than 'normal' conditions [36,37]. Hydrothermal conditions also pertain to the geological processes during which many minerals have been formed. In the laboratory, such conditions are realized by heating a solution in a closed system (autoclave or 'pressure bomb') at temperatures ranging from 200 to 400 °C. Zeolites are a good example of the use of such synthesis conditions [38]. Other examples will be discussed later in this book (see Chapter 4).

Although at this time, no systematic understanding has emerged to account for the role of such conditions in the nature of the reaction products, it is likely that the properties of the solvent play a fundamental role because these properties are significantly influenced by temperature and pressure. The thermodynamic properties of water for temperatures of up to 1000 °C and pressures of several tens of kilobars are well known [36]. Quantitative data are summarized in various review articles [36,39]. Three main points must be stressed:

(a) The dielectric constant of water decreases as temperature increases. It increases with increasing pressure [40] (Figure 1.8). Hydrothermal solutions are therefore characterized by low dielectric constants and electrolytes completely dissociated under normal conditions will preferentially form ion pairs or complexes of small electrostatic charge.

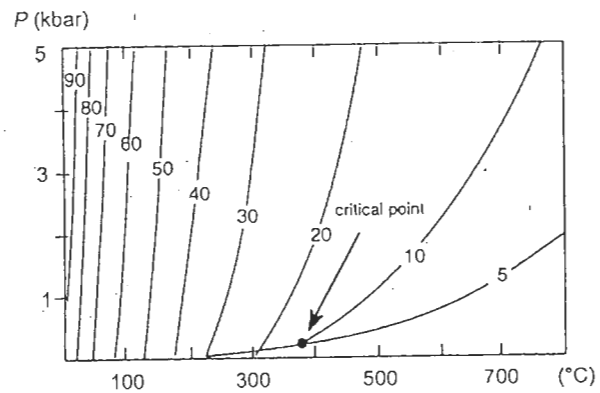

Figure 1.8 Change in the dielectric constant of water as a function of temperature and pressure. Reproduced by permission of Elsevier Science Ltd, The Boulevard, Langford Lane, Kidlington, OX5 1GB, UK from [40]

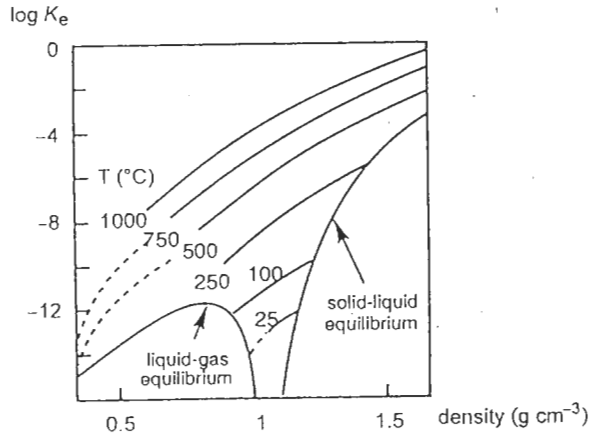

Figure 1.9 Ionic product of water as a function of temperature and density of the liquid. Reproduced with permission from [42]

(b) The viscosity of water decreases with increasing temperature [41], which leads to an increased mobility of the dissolved species compared with normal conditions.

(c) The ionic product of water increases strongly with temperature [42] (Figure 1.9). Conductivity measurements allow the determination of the law of variation of the ionic product with temperature:

$$\log K_e = -(3018/T) - 3.55$$

The increase in temperature enhances the dissociation of water and leads to a decrease in its acidity scale (defined by $-\log K_e$). The strength of acids and bases is therefore appreciably modified compared with 'normal' conditions. Concurrent with the decrease in the dielectric constant of the medium, the effect of hydrothermal conditions on the behavior of acid–base couples of the type HA/A^- and HB^+/B may therefore be very different. This is the case for solvents such as water or alcohol, for example [43]. This explains why the basicity of the chlorine ion is much higher under hydrothermal conditions. In water at 500 °C and 2 kbar, the equilibrium constant of

$$Cl^- + H_2O \Longleftrightarrow HCl + HO^-$$

is 9 orders of magnitude higher than for normal conditions [41]. It is perhaps for this reason that quaternary ammonium cations $[R_4N]^+$ and some amines $R-NH_2$, R_2-NH and R_3-N (where R is a hydrocarbon chain) play a unique role in the hydrothermal synthesis of compounds with a zeolitic structure [38,44,45]. Such amines form acid–base couples of the HB^+/B type and are able, like $[R_4N]^+$ cations, to involve steric effects and hydrophilic/hydrophobic balances tunable by

DropBooks

the structure of the R groups. They also involve electrostatic interactions and hydrogen bonds with several ionic or molecular entities in solution.

Under mild hydrothermal conditions, around 200 °C in the presence of a liquid phase, an increase in pressure of up to 10 bar does not seem to have a marked effect on the nature of the products obtained. On the other hand, thermal effects, which act by decreasing kinetic barriers, mostly influence the physicochemical properties of the solvent, favoring electrostatic interaction and the formation of hydrogen bonds. These interactions, that play a major role in the molecular recognition that characterizes the formation of cryptates [46,47], are probably the cause of the very surprising structures observed under those conditions (see Chapter 4, Section 4.3.1). However, the state of current knowledge of these reactions requires some caution in the interpretation of the mechanisms involved under such conditions.

1.6 REFERENCES

1. M. Chabanel, P. Gressier, *Liaison Chimique et Spectroscopie*, Marketing Ed., Paris (1991).
2. W.L. Jorgensen, L. Salem, *The Organic Chemist's Book of Orbitals*, Academic Press, New York (1973).
3. J.E. Huheey, *Inorganic Chemistry, Principles of Structure and Reactivity*, 2nd ed., Harper and Row, New York (1978), p. 174.
4. F.A. Cotton, G. Wilkinson, *Advanced Inorganic Chemistry*, 4th ed., J. Wiley & Sons, New York (1980), p. 224.
5. A. Rahman, F.H. Stillinger, *J. Am. Chem. Soc.* **95**, 7943 (1973).
6. F.H. Stillinger, *Science* **209**, 4455 (1980).
7. M.C.R. Symons, *Acc. Chem. Res.* **14**, 179 (1981).
8. R.E. Richards, J.A.S. Smith, *Trans. Faraday Soc.* **47**, 1261 (1951).
9. D.E. O'Reilly, E.M. Peterson, J.M. Williams, *J. Chem. Phys.* **54**, 96 (1971).
10. M. Ardon, A. Bino, *Structure and Bonding*, Vol. 65, 1, Springer-Verlag, Berlin (1987).
11. M. Magini, G. Licheri, G. Paschina, G. Pinna, *X-Ray Diffraction of Ions in Aqueous Solutions: Hydration and Complex Formation*, CRC Press, Boca Raton (1988).
12. H. Ohtaki, T. Radnai, *Chem. Rev.* **93**, 1157 (1993).
13. N. Ohtomo, K. Arakawa, M. Takeuchi, T. Yamaguchi, H. Ohtaki, *Bull. Chem. Soc. Jpn* **54**, 1314 (1981).
14. H.G. Lee, Y. Matsumoto, T. Yamaguchi, H. Ohtaki, *Bull. Chem. Soc. Jpn* **56**, 443 (1983).
15. R. Grahn, *Arkv. Fysik* **1**, 13 (1962).
16. F. Basolo, R.G. Pearson, *Mechanism of Inorganic Reactions*, 2nd ed., J. Wiley & Sons, New York (1958).
17. H.S. Franck, W.Y. Wen, *Disc. Faraday Soc.* **24**, 133 (1957).
18. A.F. Wells, *Structural Inorganic Chemistry*, 5th ed., Clarendon Press, Oxford (1991).
19. C.V. Krishnan, H.L. Friedman, *J. Phys. Chem.* **73**, 3934 (1969).
20. C.F. Baes, R.E Mesmer, *The Hydrolysis of Cations*, J. Wiley & Sons, New York (1976).
21. C.K. Jorgensen, *Inorganic Complexes*, Academic Press, New York (1963), p. 15.
22. D.L. Kepert, *The Early Transition Metals*, Academic Press, New York (1972).
23. G. Charlot, *L'Analyse Qualitative et les Réactions en Solution*, 6th ed., Masson, Paris (1969).
24. A. Ringbom, *Les complexes en Chimie Analytique*, Dunod, Paris (1967).

25. L.G. Sillen, *Stability Constants of Metal–Ion Complexes*, The Chemical Society, London, Special Publication No. 17 (1964) and No. 25 (1971).
26. J. Kragten, *Atlas of Metal Ligand Equilibrium in Aqueous Solution*, E. Horswood Ed., J. Wiley & Sons, Chichester (1978).
27. M.T. Pope, *Heteropoly and Isopoly Oxometalates*, Springer-Verlag, Berlin (1983), p. 35.
28. C.J. Ballhausen, H.B. Gray, *Inorg. Chem.* 1, 111 (1962).
29. L. Kevan, *J. Phys. Chem.* 88, 327 (1984).
30. L.V. Boas, J.C. Pessoa, in *Comprehensive Coordination Chemistry*, Sir G. Wilkinson Ed., Pergamon Press, Oxford (1987), p. 498.
31. F.A. Cotton, G. Wilkinson, *Advanced Inorganic Chemistry*, 4th ed., J. Wiley & Sons, New York (1980), p. 716.
32. H.W. Dodgen, G. Liu, J.P. Hunt, *Inorg. Chem.* 20, 1002 (1981).
33. M. Grant, R.B. Jordan, *Inorg. Chem.* 20, 55 (1981).
34. J.W. Akitt, *Progress in NMR Spectroscopy* 21, 1 (1989).
35. E. Matijevic, *Pure and Appl. Chem.* 52, 1179 (1980).
36. A. Rabenau, *Angew. Chem. Int. Ed. Engl.* 24, 1026 (1985).
37. A. Stein, S.W. Keller, T.E. Mallouk, *Science* 259, 1558 (1993).
38. R.M. Barrer, *Hydrothermal Chemistry of Zeolites*, Academic Press, London (1982).
39. L. Haar, J.S. Gallagher, *NBS/NRC Steam Tables*, Hemisphere Publ. (1984).
40. T.M. Seward, *Chemistry and Geochemistry of Solutions at High Temperatures and Pressures*, D. Rickard, F. Wickman Eds, Physics and Chemistry of the Earth, Vol. 13/14, Pergamon Press, New York (1981), pp. 113–132.
41. K. Tödheide, *Water, A Comprehensive Treatise*, Vol. 1, F. Francks Ed., Plenum, New York (1972), pp. 463–514.
42. W. Holzapfel, E.U. Franck, *Ber. Bunsenges.* 70, 1105 (1966).
43. G. Charlot, *Chimie Analytique Générale, Solutions Aqueuses et Non Aqueuses*, Masson, Paris (1967).
44. J.L. Guth, P. Caullet, *J. Chim. Phys.* 83, 155 (1986).
45. T. Loiseau, Thesis, Université du Maine, Le Mans (1993).
46. J.M. Lehn, (Chimie) Supramoléculaire, *Encyclopœdia Universalis*, Vol. 21, Paris (1989), p. 855.
47. B. Dietrich, P. Viout, J.M. Lehn, *Aspects de la Chimie des Composés Macrocycliques*, InterEditions, Paris (1991), p. 183.

2

Condensation and Precipitation in Aqueous Solution

The condensation of ions in aqueous solution creates entities in which identical or dissimilar cations are linked through various types of oxygenated bridge like HO^- or O^{2-}. The precipitation of hydroxides through the addition of a base to aquo complexes, such as

$$[Al(OH_2)_6]^{3+} + 3HO^-_{solvated} \longrightarrow Al(OH)_3 + 6H_2O$$

or the synthesis of oxides through the addition of an acid to an anion complex

$$[SiO_2(OH)_2]^{2-} + 2H^+_{solvated} \longrightarrow SiO_2 + 2H_2O$$

are classical examples. Within the solid, Al^{3+} and Si^{4+} are linked by hydroxo or oxo bridges respectively. The solid is obtained as submicron particles.

Under other conditions of acidity, the condensation reaction may lead to discrete and soluble entities, polycations or polyanions of various size, depending on the degree of condensation:

$$13[Al(OH_2)_6]^{3+} + 32HO^- \longrightarrow [Al_{13}O_4(OH)_{24}(OH_2)_{12}]^{7+} + 70H_2O$$
$$4[SiO_2(OH)_2]^{2-} + 4H^+_{solvated} \longrightarrow [Si_4O_{12}]^{4-} + 4H_2O$$

The propensity of an element to condense and precipitate in solution depends on its nature and on the physicochemical characteristics of the medium. For example, acidification of the chromate ion does not cause precipitation. A mere change in the color of the solution is observed, from yellow to orange, which corresponds to the formation of the bichromate ion, made up of two corner-sharing tetrahedra:

$$2[CrO_4]^{2-} + 2H_3O^+ \longrightarrow [Cr_2O_7]^{2-} + 3H_2O$$

The condensation of chromium(VI) stops at the dimer stage, irrespective of the extent of acidification. On the other hand, tungsten(VI) condenses to a much larger extent but increases its coordination. Acidification around pH 4 of the tungstate

$[WO_4]^{2-}$ leads to the dodecatungstic polyanion in which the coordination of tungsten is octahedral [1,2]:

$$12[WO_4]^{2-} + 18H_3O^+ \longrightarrow [H_2W_{12}O_{40}]^{6-} + 26H_2O$$

Coordination 4 Coordination 6

Under more acidic conditions, condensation of the tungstate ion proceeds to the hydrated oxide $WO_3 \cdot nH_2O$. However, there is no direct structural relationship between the solid and the polyanion.

Similarly, weak alkalinization of aquo cations causes the formation of polycations:

$$2[Cr(OH_2)_6]^{3+} + 2HO^- \longrightarrow [Cr_2(OH)_2(OH_2)_8]^{4+} + 2H_2O$$

Under stronger alkalinization, chromium forms a series of increasingly condensed polycations [3], and then a hydrated hydroxide gel $Cr(OH)_3(OH_2)_3$ [4]. Different behavior is observed for iron(III) and aluminum(III). Aluminum forms the stable hydroxide $Al(OH)_3$ (gibbsite, bayerite) [5], whereas the '$Fe(OH)_3$' hydroxide has never been identified. It transforms very rapidly to an oxyhydroxide through spontaneous dehydration [6].

These examples show that the condensation of metal cations is directly linked to their acid–base characteristics, but also that elements with similar characteristics may have very different behavior. In all cases, condensation may be more or less advanced, and precipitation represents the last stage of the reaction.

Precipitation of cations is often considered a simple phenomenon because it is so common. However, the transition of the ion in solution to the solid comprises complex phenomena that are true inorganic polymerization (polycondensation) reactions. From a certain angle, the reactions are analogous to organic polymerization, but a systematic analysis is more difficult in inorganic chemistry because of the wider diversity of the elements involved. It is indispensable, however, to analyze the processes involved in solution during formation of the solid, because they will govern some of the chemical, structural and morphological characteristics of the resulting solid. Understanding these phenomena would allow control of the characteristics of finely divided oxide powders (alumina, zirconia, titanium dioxide, iron oxide, etc.) which are used in many applications [7,8].

Before examining the specific behavior of a few elements, this chapter will identify the main characteristics of condensation and precipitation reactions in aqueous solution.

2.1 MECHANISM OF THE CONDENSATION REACTIONS

By analogy to organic polymerization processes, one may identify several steps in the condensation processes of metallic elements in solution.

(a) Initiation

Condensation occurs when an acid is added to an oxo species ($[CrO_4]^2$, for example) or if a base is added to an aquo form $\{[Cr(OH_2)_6]^{3+}\}$. This leads to the formation of the hydroxo ligand on the monomer:

$$[M{-}O]^- + H_3O^+ \longrightarrow M{-}OH + H_2O \longleftarrow [M{-}OH_2]^+ + HO^-$$

Hydroxylation of the metal cation may be obtained through an acid–base reaction (neutralization, thermolysis, etc.) or through an oxidation–reduction reaction. The charge–pH diagram (Figure 1.6) shows that reduction and oxidation of cations as oxo and aquo species, respectively, allows them to reach the stability domain of hydroxo forms. Hydroxylation is the initiation stage of the process and the hydroxylated complex is the precursor of the condensation products.

(b) Propagation

As soon as a hydroxylated species appears in the solution, condensation may take place and lead to oxygenated bridges between cations.

If the coordination of the precursor is not saturated, as is sometimes the case with some metallic elements present in an alkaline medium as hydroxo $\{[Al(OH)_4]^-\}$ or oxo $\{[VO_4]^{3-}, [WO_4]^{2-}\}$ ions, extension of the cation coordination may occur via nucleophilic addition (see Chapter 4, Section 4.3):

$$-M{-}OH + -M{-}OH \longrightarrow -M{-}OH{-}M{-}OH$$

$$[-M{-}O]^- + -M{-}OH \longrightarrow [-M{-}O{-}M{-}OH]^-$$

In an acidic medium, the maximum cation coordination is always achieved in the aquo–hydroxo monomeric complex, and hence the reaction must proceed though nucleophilic substitution. This reaction may take place via one of three simple mechanisms: dissociation, association and a concerted mechanism or direct displacement [9].

Dissociative substitution is a two-step process involving the formation of a reduced-coordination intermediate. The starting complex has enough thermal energy spontaneously to break a bond and release the leaving group. In the second step, the nucleophile completes the cation coordination (Figure 2.1a).

Associative substitution is also a two-step process, this time involving a high coordination intermediate. The creation of a bond with the nucleophile (first step) occurs prior to the release of the leaving group (second step). From an energy standpoint, this release is favored by the formation of a bond with the entering group in the transition state (Figure 2.1b). In a concerted or direct displacement mechanism, the substitution is a one-step process, in which the leaving group and the nucleophile contribute simultaneously to the formation of the transition state. The formation of the bond with the nucleophile and the breaking of the bond with the leaving group are synchronous (Figure 2.1c). The associative and direct

DropBooks

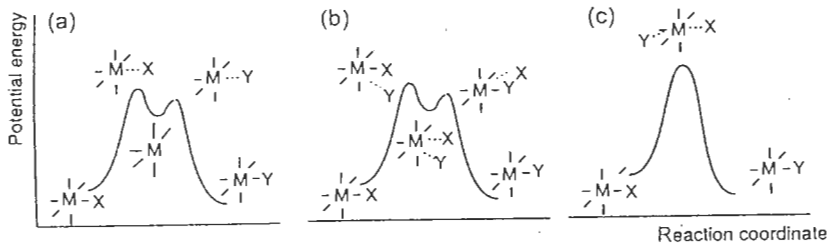

Figure 2.1 Reaction paths for nucleophilic substitution reactions: (a) dissociative; (b) associative; (c) direct displacement

displacement mechanisms are often difficult to distinguish, unless an intermediary compound can be identified directly.

In each of the mechanisms, the transition states are very reactive. Therefore, the first step is rate-controlling and the dissociative process is called unimolecular nucleophilic substitution SN_1. The associative and direct displacement mechanisms, which require two partners in the transition state, are called bimolecular nucleophilic substitutions SN_2.

Condensation by substitution requires a charge donor, the nucleophile, which is able to attack the metal cation, which bears a positive charge and is an electron acceptor. The cation must also possess a coordinated group which may be eliminated (leaving group). Ligands most easily removable bear a positive charge δ^+. In a non-complexing medium, three types of ligand are likely to exist in the coordination sphere of the cation: the aquo (H_2O), hydroxo (OH) and oxo (O) ligands. What is their role in nucleophilic substitution reactions?

(i) Let us consider the aquo species $[M(OH_2)_N]^{z+}$. The partial charges on the metal and the aquo ligand are positive:

$[Mn(OH_2)_6]^{2+}$ $\quad \chi = 2.657$ $\quad \delta(Mn) = +0.59$ $\quad \delta(H_2O) = +0.23$

$[Cr(OH_2)_6]^{3+}$ $\quad \chi = 2.756$ $\quad \delta(Cr) = +0.68$ $\quad \delta(H_2O) = +0.39$

The aquo ligand has no nucleophilic character and may only play the role of a leaving group. Condensation of the aquo species alone does not occur since the water molecule never acts as a nucleophile.

(ii) In oxo species $[MO_N]^{(2N-z)-}$, the partial charge on the metal is positive while that on the oxo ligand is highly negative:

$[MnO_4]^-$ $\quad \chi = 2.533$ $\quad \delta(Mn) = +0.52$ $\quad \delta(O) = -0.38$

$[CrO_4]^-$ $\quad \chi = 2.055$ $\quad \delta(Cr) = +0.27$ $\quad \delta(O) = -0.57$

The oxo ligand could be an excellent nucleophile. In fact, the calculated charges on oxo ligands are probably incorrect since the M–O bonds have a strong π character

in the oxo species. The basic character, and hence the nucleophilic strength, of the oxygen atoms is probably much smaller than would be expected from such values of partial charges. The π character of the bonds does not allow the oxo ligands to act as leaving groups. Therefore, purely oxo species cannot condense.

(iii) In the aquo–hydroxo $[M(OH)_h(OH_2)_{N-h}]^{(z-h)+}$ and oxo–hydroxo $[MO_{N-h}(OH)_h]^{(2N-h-z)-}$ forms, both nucleophile (OH^-) and leaving (H_2O) groups are present. Usually, the hydroxo ligand bears a negative partial charge. If the partial charge were positive, the ligand would be acidic and would lose its proton. Indeed, the charge on oxygen is always negative and would not be sufficient to shield the cation–proton repulsion. Therefore, the hydroxo ligand is a nucleophile and the presence of the aquo ligand allows the condensation reaction to occur. Under these conditions, the reaction leads to the formation of hydroxo bridges:

$$M{-}OH + M{-}OH_2 \longrightarrow M{-}OH{-}M + H_2O$$

Since the aquo ligand is usually very labile (see Section 3.1), the reaction proceeds through a dissociative SN_1 mechanism with the formation of a reduced-coordination intermediate. The rupture of the $M{-}OH_2$ bond occurs before the formation of the M–OH–M bond. However, in the case of transition metal ions highly stabilized in octahedral symmetry by the crystal field (Cr^{3+}, Ni^{2+}), the lability of coordination water is very low and the condensation must proceed via an associative mechanism with temporary formation of the $[H_3O_2]^-$ bridging ligand.

The bridging OH groups are called 'ol' in order to distinguish them from terminal hydroxo ligands [10,11]. The reaction leading to the formation of a hydroxo bridge is called 'olation'.

In the absence of aquo ligands within the coordination sphere, a hydroxo ligand may act as a leaving group if, through proton transfer in the transition state of a SN_2 mechanism, the formation of an aquo ligand is possible. The proton in the ol bridge of the transition state is more acidic than that of terminal hydroxo ligands and may migrate on one of them to form the aquo ligand. This ligand may be eliminated if its partial charge is positive. In this case, condensation occurs with the formation of oxo bridges and proceeds through oxolation [10]:

$$M{-}OH + M{-}OH \longrightarrow M{-}\overset{\overset{H}{|}}{O}{-}M{-}OH \longrightarrow M{-}O{-}M + H_2O$$

Assuming that there are no labile groups within the coordination sphere of the reactants, the oxolation reaction mechanism is associative. The coordination of the transition state must increase by one unit before a leaving group can be released.

Experimentally, oxolation is often much slower than olation. For example, condensation via oxolation of silicic acid $Si(OH)_4$ around pH 3 is much slower than condensation via olation of aquo–hydroxo complexes of titanium and zirconium. It is possible that the difference in mechanism would make olation intrinsically faster than oxolation. A comparison is difficult because it would require the

study—everything else being equal—of the kinetics of each reaction with the *same* chemical element. In addition, the generation of a leaving group during oxolation is often heavily dependent on the acidity of the medium, which makes the reaction very sensitive to acid–base equilibrium. This effect is particularly pronounced with silicates (see Section 4.1.1).

Therefore, the presence of a hydroxo ligand bearing a negative charge (a nucleophile) in the cation coordination sphere is required for condensation to take place. However, this is not a sufficient requirement. Nucleophilic attack by the hydroxo ligand may only take place if the cation can be subjected to it, in other words, if its electrophilic character is high enough. Generally, many examples have shown that condensation occurs only if the partial charge on the cation in the precursor is equal to or higher than 0.3 (*when the charge is calculated with the model presented in the Appendix*). This empirical value defines the threshold for the onset of condensation, whatever the partial charge on the hydroxo ligand. Therefore, the criterion for condensation in solution is the double condition

$$\delta(\mathrm{OH}) < 0, \qquad \delta(\mathrm{M}) > +0.3$$

The validity of this requirement may be demonstrated with a few examples. In the $[Cr(OH)(OH_2)_5]^{2+}$ ion, $\delta(OH) = -0.02$ and $\delta(Cr) = +0.64$. The monomer may condense and various polycations are observed in solution [3] (see Section 3.2.1).

With phosphates, the calculations give

$[PO_3(OH)]^{2-}$	$\chi = 2.18$	$\delta(P) = +0.03$	$\delta(OH) = -0.48$
$[PO_2(OH)_2]^{-}$	$\chi = 2.49$	$\delta(P) = +0.19$	$\delta(OH) = -0.20$
$[PO(OH)_3]$	$\chi = 2.71$	$\delta(P) = +0.35$	$\delta(OH) = 0.0$

Condensation of anionic species does not occur because the electrophilic character of the cation is too weak. Phosphoric acid does not condense, because the OH ligand does not have a nucleophilic character. In fact, the first acidity of phosphoric acid is quite high and the OH ligand is unstable. Condensation of the phosphate cannot occur spontaneously in aqueous solution [12]. Soluble polyphosphates are metastable and more or less rapidly hydrolyzed in an acidic medium. Their condensation is obtained in the solid state only and through heating in order to force dehydration [13].

The hydrolysis ratio of the cation, which controls the number of hydroxo ligands in its coordination sphere, may be understood as the functionality of the precursor. The most frequent oxo or hydroxo bridges are

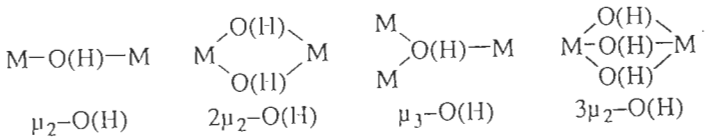

μ_2–O(H) $2\mu_2$–O(H) μ_3–O(H) $3\mu_2$–O(H)

The hydroxo ligand is able to form one, two or three bonds through the weakly bonding 3σMOs and the non-bonding π orbitals (Figure 2.2).

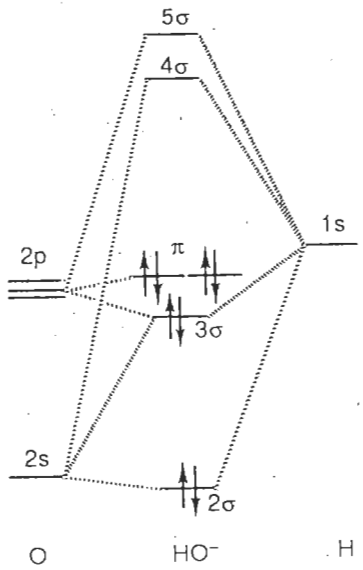

Figure 2.2 Molecular orbital diagram for the HO^- ion

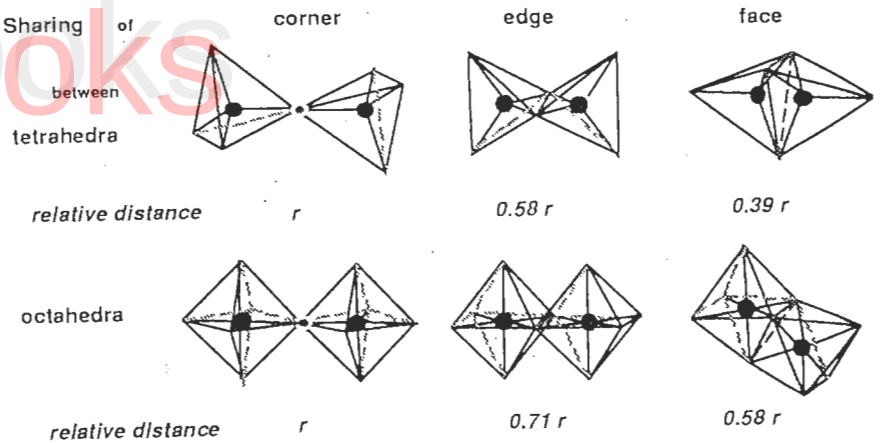

Figure 2.3 Relative distances between cations in octahedral and tetrahedral environments sharing a corner, an edge or a face

The simple μ_2–O(H) bridge corresponds to corner-sharing coordination polyhedra, whereas the $2\mu_2$–O(H) double bridge corresponds to edge-sharing polyhedra. Connectivity of the coordination polyhedra through a face [$3\mu_2$–O(H) bridge] is rare. The μ_3–O(H) bridge, which links three polyhedra through single hydroxo or oxo bridges, is often observed. Figure 2.3 shows the relative distances between cations for associations of tetrahedra and octahedra.

DropBooks

As the number of shared corners grows, the electrostatic repulsion between cations becomes increasingly strong. Electrostatic repulsions are very high in edge-sharing tetrahedra. Face sharing tetrahedra are never observed, either in solution or in the solid state. The repulsion is not as strong between octahedra and edge sharing in this case is rather frequent, although face sharing is still rare.

(c) Termination

Under given acid–base conditions, spontaneous interruption of the growth of an object in solution may occur at various stages. Condensation may be limited to the formation of oligomers or continue until the precipitation of a solid. Chromium(VI) does not go beyond the stage of the $[Cr_2O_7]^{2-}$ dimer and never precipitates in solution. Chromium(III), on the other hand, forms a series of soluble polycations as long as the hydrolysis ratio h is smaller than 2.5 (see Chapter 3), and the oxide precipitates for $h \approx 3$.

Condensation of hydroxylated and electrically charged complexes *always* ends at a more or less advanced stage, leaving discrete species in solution, either polycations or polyanions, depending on whether the monomeric complex is a cation or an anion. Indeed, one cannot indefinitely accumulate electrical charges on a polymer. When should condensation stop? As soon as conditions allowing nucleophilic substitution are no longer present. Because condensation causes water elimination, the change in composition of the reaction product modifies its average electronegativity, causing charge redistribution within its structure and, therefore, a change in the reactivity of the functional groups. Hence, OH ligands in the polymer may lose their nucleophilic character [$\delta(OH) > 0$] and cations may lose their electrophilic character [$\delta(M) < +0.3$]. Usually, the nucleophilic character of hydroxo ligands cancels itself out in polycations, and the nucleophilic character of the cation cancels itself out in polyanions.

However, condensation of electrically neutral ions continues indefinitely until the precipitation of a solid (hydroxide, oxyhydroxide or more or less hydrated oxide) or of a basic salt in the presence of complexing ligands. Elimination of water never leads to a sufficient change in the average electronegativity to cancel the reactivity of functional groups.

In theory, a hydroxide $M(OH)_z$ is formed via endless condensation of aquo–hydroxo complexes. However, the hydroxide may not be stable. Its spontaneous dehydration, more or less rapid and extensive, generates an oxyhydroxide $MO_x(OH)_{z-2x}$ or a hydrated oxide $MO_{z/2} \cdot xH_2O$. The reaction takes place via oxolation in the solid phase with elimination of water from hydroxo ligands. The reaction is associated with structural changes in order to preserve the coordination of the cation. One can formally predict the likelihood of dehydration, considering that, if water molecules can form in the hydroxide, they may be eliminated when they are no longer subject to interactions with the cations from the solid. The formation of water molecules in the solid requires that the charge on the oxygen of the hydroxo

Table 2.1 Partial charge of water in a few hydroxides

Hydroxide	$\delta(H_2O)$	Identified phases
$Mn(OH)_2$	−0.06	$Mn(OH)_2$, MnO
$Fe(OH)_2$	−0.01	$Fe(OH)_2$, FeO
$Cr(OH)_3$	+0.01	$Cr(OH)_3(OH_2)_3$, $Cr(OH)_3$ $CrO(OH)$, Cr_2O_3
$Fe(OH)_3$	+0.07	$FeO(OH)$, Fe_2O_3
$Zr(OH)_4$	+0.002	$ZrO_{2-x}(OH)_{2x} \cdot nH_2O$ ZrO_2
$Ti(OH)_4$	+0.01	TiO_2

be not excessively negative in order to allow proton migration. Then, the stability of the hydroxide is simply related to the charge on water in the hydroxide.

If $\delta(H_2O) < 0$ *in the hydroxide*, the hydroxo ligands are too negative and hence too weakly polarized by the cations for water to form. The hydroxide is stable. If $\delta(H_2O) > 0$ *in the hydroxide*, oxygen in the hydroxo ligands is highly polarized by the cations. The formation of oxo bridges is favored. A structural change leads to the formation and elimination of water.

A calculation of the partial charge on the water in a few hydroxides shows that, as long as $\delta(H_2O) < 0$, the hydroxide is indeed obtained. However, if $\delta(H_2O) > 0$, the hydroxide is unstable and forms an oxyhydroxide or a hydrated oxide in aqueous solution (Table 2.1). This means that in stable hydroxides the metal–oxygen bond is strongly ionic. An increase in the covalent nature of the bond favors the formation of oxyhydroxides or oxides.

Usually, elements with a +2 charge precipitate as hydroxides, and those with a +3 charge as oxyhydroxides (the final stage of evolution is the oxide). Those of higher charge form oxides of various levels of hydration [15]. This sequence is a clear illustration of the increasing polarization of the hydroxo ligands by the cation, which is associated to the covalent nature of the metal–oxygen bond. One must point out the case of chromium(III), for which the $Cr(OH)_3(OH_2)_3$ and $Cr(OH)_3$ phases, which will be described later, are obtained owing to the particularly inert chemical nature of this element [16]. After heat treatment, an oxide is always obtained.

In summary, condensation of cations in solution is initiated when the acidity allows the presence of the hydroxo ligand in the coordination sphere of the cation. This occurs through the addition of a base to aquo complexes of elements of formal charge equal to or smaller than 4, or through the addition of an acid to oxo complexes of elements of charge equal to or greater than 4 (Figure 2.4). Two reactions, olation and oxolation respectively, ensure the development of condensation. The condensation of cationic and anionic hydroxylated complexes is always limited. It leads to polycations and polyanions respectively. The formation of a solid requires the presence of zero-charge complexes. It is also possible (although less common) to involve redox phenomena in order to decrease the formal charge

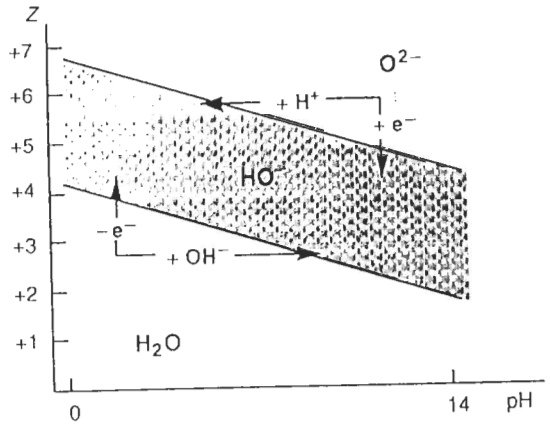

Figure 2.4 Possible initiation mechanisms for condensation reactions of metal cations in solution

on the metal and force the appearance, under given acidic conditions, of the hydroxo ligand in the coordination sphere of the cation.

The very rough classification suggested in Figure 2.4 must be somewhat mitigated, particularly for elements carrying a formal charge between +3 and +5. Parameters such as electronegativity, size and electronic configuration affect the acid–base properties and must be taken into account in order to clarify the behavior of such elements. Boron and aluminum, for example ($z = +3$), have radically different behavior in solution. This is also the case for silicon and titanium ($z = +4$) or phosphorus, antimony and vanadium ($z = +5$). Examples will be discussed in Chapters 3 and 4.

2.2 MODEL OF CATION CONDENSATION IN AQUEOUS SOLUTIONS

The behavior of chemical elements with respect to condensation and precipitation may appear very disparate at first glance. In fact, a study of reaction mechanisms and reaction products allows the extraction of a few general rules of behavior. The analysis may be refined by the inclusion of a few criteria leading to a simple and general rationale explaining the behavior of elements in solution. The general approach will be described below, and the quantitative treatment is presented in the Appendix.

The study of the condensation mechanisms of dissolved cations in solution has shown that the presence of a hydroxo ligand in the coordination sphere was required for the reaction to take place. This imposes restrictions on the electronegativity of the element involved. For example, the zero-charge molecular form MO_NH_{2N-z} of

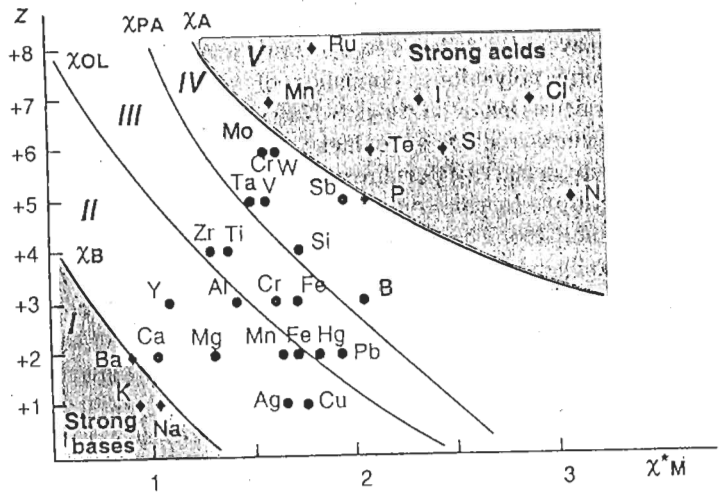

Figure 2.5 Charge–electronegativity diagram drawn using equations (A.15) to (A.18), showing five classes of behavior for the zero-charge MO_NH_{2N} form of a M^{z+} cation. In domains I and V, the element remains monomeric and soluble. Elements in domain II condense by olation only, and those in field IV by oxolation. Both condensation processes may be simultaneous for elements in field III

an element carrying a formal charge z will behave as a strong base if the electronegativity χ^*_M of M is lower than the limit $\chi_{B,z}$, or as a strong acid if χ^*_M is higher than the $\chi_{A,z}$ limit. Under such conditions, condensation in solution cannot occur and the element will exist as a monomeric cation or anion (domains I and V in Figure 2.5).

If $\chi_{B,z} < \chi^*_M < \chi_{A,z}$, hydroxo ligands in zero-charge MO_NH_{2N-z} are 'stable' because their negative charge prevents their acidic dissociation. Condensation is not hampered and a solid is formed. If coordination water molecules are present in the precursor, condensation via olation leads to the hydroxide $M(OH)_z$. Otherwise, an oxide $MO_{z/2}$ may be formed via oxolation. One may assume that dehydration of the hydroxide leads to formation of the oxide. This remark makes it possible to set a criterion on hydroxide stability, taking into account the possibility of water elimination through internal dehydration (see Section 2.1). The criterion will be obtained using $\delta(H_2O) = 0$ in the charge balance equation of the precursor or of the hydroxide [equation (A.17)]. An electronegativity $\chi_{OI,z}$ emerges, which limits the domain ($\chi_{B,z} \leq \chi^*_M < \chi_{OI,z}$) within which cations may condense via olation only and form stable hydroxides from zero-charge precursors. Such elements have moderate electronegativities for low oxidation levels: Ag(I), Ca(II), Mg(II), Mn(II), Al(III) (Figure 2.5, domain II).

If $\chi^*_M > \chi_{OI,z}$, hydroxides are not stable. Oxyhydroxides or oxides are obtained via dehydration if olation and oxolation are competing mechanisms. If there is no

DropBooks

aquo ligand in the coordination sphere of the monomeric precursor, only condensation by oxolation may occur. It leads to the formation of often poorly condensed polyacids which form polyanions. Formation of polyanions is a result of the interruption of condensation at a stage when hydroxo ligands become acidic [$\delta(OH) \geqslant 0$]. Such considerations again make it possible to separate two types of behavior in the electronegativity domain: $\chi_{OI,z} < \chi^*_M < \chi_{A,z}$.

As long as the hydroxo ligand remains negatively charged in the growing entity, condensation does not stop. The formation of a solid oxide phase is possible. As soon as the hydroxo ligand acquires a zero or negative charge, condensation ceases and leads to the formation of polyacids of various degrees of condensation. The $\delta(OH)=0$ criterion, introduced in the charge balance equation of the MO_NH_{2N-z} species [equation (A.18)] gives a value for χ_{PA} such that, if $\chi_{OI,z} < \chi^*_M < \chi_{PA,z}$, condensation via olation and oxolation leads to oxyhydroxides or to oxides (Figure 2.5, domain III). The term depends on the relative kinetics of both reactions. If oxolation is fast compared with olation, the solid is an oxide [Zr(IV), Ti(IV)] [17,18]. If it is slow, the coexistence of oxo and hydroxo bridges leads to an oxyhydroxide [Fe(III), Cr(III)] which may later form an oxide through ageing or calcination [15]. Hydration may occur in such compounds owing to water trapped in the pores of the material or adsorbed on the particles (hydrated oxides), or as hydroxo groups (ol bridges) in the oxyhydroxides.

Elements for which $\chi_{PA,z} < \chi^*_M < \chi_{A,z}$ (Figure 2.5, domain IV) form polyacids of various degrees of condensation. Some high-charge transition metals [V(V), Cr(VI), Mo(VI), W(VI)] strongly polarize the hydroxo ligands in the complexes formed during stoichiometric acidification ($MO_{N'}^{z-} + xH^+$) and their condensation via oxolation stops fairly early. The condensed entities are strong acids that form polyanions [1,2]. In a way, these entities are the last stage of evolution for condensation via oxolation. However, some of these elements [V(V), W(VI)] are able to form solids after ageing (hours or days) of the solutions. Polyanions are not directly involved because there is no relationship between the structure of the solid and that of the polyanion. Quite to the contrary, growth of the solid always seems to involve at least an olation step between monomeric or oligomeric species resulting from decondensation equilibrium of the polyanion. Some examples of possible formation mechanisms of oxyhydrates such as $V_2O_5 \cdot nH_2O$, $WO_3 \cdot H_2O$ or $WO_3 \cdot 2H_2O$ are discussed in Chapter 4.

Antimony(V) and tin(IV) form polyacids and oxides by oxolation (Figure 2.5) (see Chapter 4), but one or several olation steps are also involved. Zero-charge complexes such as $Sb(OH)_5(OH_2)$ or $Sn(OH)_4(OH_2)_2$ contain aquo ligands. Hydrated antimony oxide $HSbO_3 \cdot H_2O$ precipitated in solution is a strong acid in which the solvated protons in the three-dimensional oxide network are mobile and can be substituted by cations [19]. In the case of silicon(IV), although the $Si(OH)_4$ precursor is able to condense via oxolation only, a solid is formed: $SiO_2 \cdot nH_2O$ [20a]. In silica, the terminal hydroxo ligands exhibit a rather strong acid character and the solid may be described as a high molecular weight polyacid. In fact, the

charge of the hydroxo groups on the growing polymer becomes positive at a late stage of condensation and the polyanions gel or flocculate by aggregation in aqueous solution.

In the case of boron, the hydroxo ligands in $B(OH)_3$ bear a negative partial charge. However, boric acid does not condense because the partial charge on the cation is too small. The monomeric form $B(OH)_3$ is stable in solution. The solid phase, obtained after drying, is made of monomeric units connected by hydrogen bonds [15,21]. Boron appears to be a unique element in the respect that the coordination 3 in boric acid is stabilized by the strong π character of the B–OH bonds. After alkalinization, borates are in tetrahedral coordination and are able to form polyanions with boric acid (see Chapter 4).

Figure 2.5 summarizes the acid–base properties and possible condensation behaviors in solution for all elements of the periodic table. It is possible to predict and understand the main trends on the basis of their electronegativity and their oxidation level. The next chapters are concerned with the specific behavior differences for elements within one class.

2.3 KINETICS OF SOLID FORMATION: NUCLEATION, GROWTH, AGING

Hydroxide, oxyhydroxide or hydrated oxide solid phases obtained via precipitation are made of particles whose average size may range from a few tens of ångstrom to a few microns. Particle morphology may vary depending on synthesis conditions, and aging in aqueous solution may bring about significant dimensional, morphological and structural changes. In order to understand how small particles form and what influence experimental parameters have on their characteristics and evolution, it is useful to review the kinetic aspect of condensation mechanisms.

2.3.1 STEPS OF FORMATION OF A SOLID

The precipitation of a solid involves four kinetic steps [22–25].

(i) *Formation of the zero-charge precursor* $[M(OH)_z(OH_2)_{N-z}]^0$, which is able to condense and form a solid phase. Hydroxylation of the cation is a very fast acid–base reaction, but the speed of formation of the zero-charge precursor in solution is very variable depending on whether the reaction starting from cationic complexes, for example, takes place through the addition of a base, thermohydrolysis or the thermal decomposition of a base such as urea.

(ii) *Creation of nuclei* through condensation (olation or oxolation) of zero-charge precursors. The condensation rate is a function of the precursor concentration and, as long as it is small at the onset of cation hydroxylation, the rate is almost zero (zone I, Figures 2.6 and 2.7). Beyond a critical concentration C_{min}, the condensation

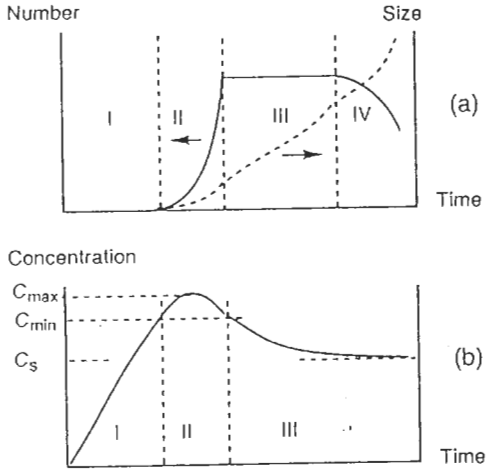

Figure 2.6 Change (a) in the number and sizes of particles formed in solution and (b) in the concentration C of the soluble precursor of the solid phase [23] during precipitation. The condensation rate, which is zero for $C < C_{min}$, becomes infinite for $C \geqslant C_{max}$. C_S is the solubility of the solid phase

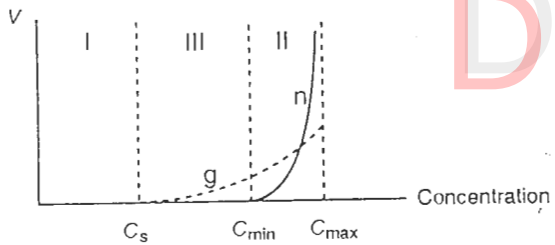

Figure 2.7 Nucleation rate n and growth rate c as a function of the precursor concentration in solution. Zones labeled I, II and III correspond to those in Figure 2.6

rate increases abruptly and polynuclear entities–the nuclei–are formed in an 'explosive' manner throughout the solution (zone II, Figures 2.6 and 2.7). Indeed, nucleation is an abrupt kinetic phenomenon because, since its order is high compared with the precursor concentration (see later), it is either extremely fast or non-existent within a narrow concentration range (Figure 2.7). If the rate of generation of the precursor is significantly smaller than the condensation rate, nucleation sharply reduces the precursor concentration and the condensation rate decreases equally rapidly. When the precursor condensation is again close to C_{min}, formation of new nuclei is no longer possible.

(iii) *Growth of the nuclei* through the addition of matter, until the primary particle stage is reached. This step follows the same chemical mechanisms as nucleation:

olation or oxolation. However, for a concentration close to C_{min}, the nucleation rate is very small and precursors condense preferentially on existing nuclei, which causes their growth until the precursor concentration reaches solution saturation, in other words the solubility limit of the solid phase (zone III, Figure 2.6). Growth, which has a kinetics of first or second order, is a somewhat faster process. Precursor condensation during precipitation is a function of the respective rates of precursor generation and nucleation. Nucleation and growth phases could therefore be consecutive or overlap and occur simultaneously if the precursor concentration stays higher than C_{min}.

The number, and therefore the size, of the primary particles that form from a given quantity of matter is linked to the relative nucleation and growth rates. In order to obtain particles of homogeneous size, it is necessary that the nucleation and growth steps be separated to ensure that a singular nucleation stage takes place, and that their growth, via accumulation of all remaining matter, be controlled. This implies that the nucleation rate should be much greater that the rate at which the precursor is generated. Under these conditions, nucleation is very brief and clearly decoupled from the growth phase. If the nucleation rate is not high enough compared with the rate of generation of the precursor, the precursor concentration remains higher than C_{min} throughout the reaction, and nucleation and growth are simultaneous. The growth of the first nuclei is much larger than that of the younger ones, which leads to a large particle size distribution.

(iv) *Ageing of the particles in suspension* leads to various possible modifications of the primary particles after their growth. 'Ostwald ripening' leads to an increase in the average particle size, and possible aggregation (zone IV, Figure 2.6). Ageing may also trigger a change in morphology and crystalline structure or even cause crystallization of amorphous particles. In fact, ageing is one of the most important phenomena which must be considered, because it determines the characteristics of the particles after precipitation.

The following sections explore the main characteristics of nucleation and growth, as well as various ageing mechanisms.

2.3.2 NUCLEATION

Nucleation corresponds to the first stages of precursor condensation and solid formation. What are the parameters that affect the size of nuclei and their rate of formation?

The free enthalpy change of nuclei P_n, formed from n precursors P, includes a term due to the chemical potential difference $(\mu_S - \mu_L)$ of the P entity in the solution and in the solid, respectively, as well as a term representing the energy required for formation of the surface of the nucleus [22]:

$$\Delta G = n(\mu_S - \mu_L) + A\gamma \qquad (2.1)$$

DropBooks

where γ is the interfacial tension or energy, $\gamma = \partial G/\partial A$, and A is the surface area of the solid (see Section 8.2.1).

Assimilating activity and concentration, the chemical potential difference may be written as $(\mu_S - \mu_L) = kT \ln(c_S/c_L) = -kT \ln S$, where c_L is the precursor concentration in the solution, c_S is the solubility of the solid phase and $S = c_L/c_S$ is the supersaturation ratio of the solution.

The radius r of nuclei (assumed to be spherical), formed from n precursors of molecular volume v, is $r = (3nv/4\pi)^{1/3}$. The surface of the nucleus is $A = n^{2/3}(36\pi v^2)^{1/3}$ and the free enthalpy of nucleation is

$$\Delta G = -nkT \ln S + n^{2/3}(36\pi v^2)^{1/3}\gamma \tag{2.2}$$

The surface tension γ is usually positive and the solution is usually supersaturated ($S > 1$). The first term of equation (2.2) is negative and the second one is positive. Under these conditions of spontaneous precipitation, the formation of nuclei in homogeneous solution requires passage through a maximum in the free enthalpy of reaction (Figure 2.8). This maximum corresponds to the formation of the activated complex in the transition state of any chemical reaction.

The activation energy required for nucleation corresponds to that of the maximum change in ΔG as a function of n. The number of precursor molecules n^* in 'critical' nuclei is given by $\partial(\Delta G)/\partial n = 0$, or

$$n^* = \frac{32\pi\gamma^3 v^2}{3(kT \ln S)^3} \tag{2.3}$$

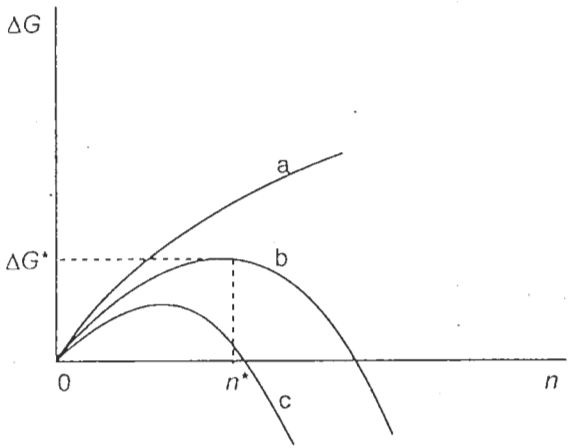

Figure 2.8 Variation in the free enthalpy of formation of nuclei as a function of the number of precursor molecules n associated in the nucleus. Curve a for a solution that is not supersaturated ($S < 1$); curves b and c are for a supersatured solution, with $S_c > S_b > 1$

and the corresponding change in free enthalpy is

$$\Delta G^* = \frac{n^*}{2} kT \ln S = \frac{16\pi\gamma^3 v^2}{3(kT \ln S)^2} \tag{2.4}$$

The radius of the critical nucleus is given by the Gibbs–Kelvin equation:

$$r^* = (3n^* v/4\pi)^{1/3} = \frac{2\gamma v}{kT \ln S} \tag{2.5}$$

The size of the critical nuclei is smaller for higher supersaturation and smaller surface tension. For a given solid, the latter is a strong function of the physicochemical conditions of the medium (see Chapter 8). The critical nuclei are in an unstable equilibrium with the solution. They correspond to a maximum of $\Delta G = f(n)$, which means that a small change in their size leads to either dissolution or growth because $\partial(\Delta G)/\partial n < 0$ in either case. In fact, the probability of growth of the nuclei is higher than that of dissolution, and precipitation is spontaneous.

From a kinetic standpoint, the nucleation rate J represents the number of nuclei formed per unit time per unit volume. It is expressed as [22]

$$J = J_0 \exp\left(\frac{-\Delta G_N}{kT}\right) \tag{2.6}$$

where J_0 is the frequency of collisions between precursor molecules (usually between 10^{10} and $10^{35}\,cm^{-3}\,s^{-1}$) and ΔG_N is the nucleation activation energy, which includes two major contributions. The first is the height of the energy barrier ΔG^* required for the formation of a nucleus large enough to be stable [equation (2.4)]. The second component, ΔG^R, is related to the type of chemical reaction (olation and/or oxolation) involved in the process. It is usually of the order of $35\,kJ\,mol^{-1}$. Basic or acid catalysis in oxolation (see Chapter 4) decreases the activation energy of the reaction to a few $kJ\,mol^{-1}$ [26].

Hence, the nucleation rate may be written as

$$J = J_0 \exp\left[\frac{\Delta G^* + \Delta G^R}{kT}\right] = J_0' \exp\left[\frac{16\pi\gamma^3 v^2}{3(kT)^3(\ln S)^2}\right] \tag{2.7}$$

with $J_0' = J_0 \exp(-\Delta G^R/kT)$.

Nucleation phenomena are difficult to investigate experimentally because their rate changes very abruptly with concentration. At 300 K, with usual parameters for oxides ($\gamma = 100\,mJ\,m^{-2}$, $v = 2 \times 10^{-5}\,m^3\,mol^{-1}$, $J_0' = 10^{30}\,cm^{-3}\,s^{-1}$), 10^5 nuclei are formed per $1\,cm^3\,s^{-1}$ for $S = 100$. The reaction is instantaneous, whereas for $S = 10$ a single nucleus is formed every 10^{70} s and nucleation is impossible. Nuclei are also very difficult to detect owing to their small size (the degree of condensation n^* is typically a few tens of units). Usually, an 'induction time' t_{ind} is determined via light scattering, t_{ind} being the time at which the intensity of the scattered light changes sharply [27]. From the final size and amount of matter

formed, one may calculate the number of particles and determine a pseudo nucleation rate $J = N/t_{ind}$. Measurements for various supersaturation conditions S allow estimation of the pre-exponential term J_0' and of the surface tension of the solid, γ [22,28,29].

Strictly speaking, nucleation does not have a definite kinetic order, although experimental $\log J = f(\log S)$ curves do fit approximately on a straight line over a few decades of J [22]. Within a small concentration range, it is possible to write $J = k_n C^n$, where n is roughly equal to n^*, the number of monomers in the critical nucleus. This is only an approximation because n^* is itself a function of S [equation (2.3)], and the probability of a simultaneous collision between n^* monomeric precursors is zero. More probably, the formation of the critical nucleus is the result of consecutive bimolecular steps. However, it may depend on an n^*th power of the concentration, considering that, since all steps are very fast, they all contribute to the global equilibrium [30].

When crystals of a solid are present in the precipitation medium, nucleation is often sharply accelerated. This is a typical catalytic effect due to a decrease in activation energy. The latter is a function of the solid–liquid surface energy γ [equation (2.7)], and, when the surface of the foreign solid is compatible with that of the precipitating solid surface because of the presence of adsorption sites (see Chapter 9) or structural similarities (see Section 4.3.2), the solid–solid surface tension γ' is smaller than the solid–solution tension γ [22]. Nucleation on the surface of the foreign solid occurs more easily. The nucleation is called heterogencous, and it is used in the seeding process, in which crystals of the desired solid are placed in the solution [31,32]. The very small energy barrier allows epitaxial growth of the nuclei even at small supersaturation levels. Heterogeneous nucleation also allows the coating of particles with a different oxide, avoiding homogeneous nucleation of the seed. Oxide particles [chromium, iron (hematite), titanium, silicon] can be coated with other oxides (aluminum, chromium, yttrium, etc.) [33–35]. Heterogeneous nucleation can also be avoided using ultrafiltration and careful washing of the particles before precipitation, in order to avoid the presence of nuclei or heterogeneities [22].

Nucleation is usually difficult to control using the concentration of the precursor, but it may nevertheless be efficiently controlled by a modification of the solid–liquid surface tension. Effects of the adsorption of anions or cations, pH variations and the ionic strength of the precipitation medium will be discussed in Chapter 8.

2.3.3 GROWTH

The unstable nature of critical-size nuclei formed during the nucleation stage leads to their growth through incorporation of the precursor molecules, which continue to be generated after nucleation. The average size of the final particles depends on the number of nuclei and the amount of matter available during the synthesis, but the width of the particle size distribution is linked to the mechanism

of nuclei growth. The kinetic step that limits the growth rate may be either the diffusion of the precursor towards the surface or a surface reaction prior to incorporation [22].

(a) Diffusion-limited Growth

It takes place when the chemical reaction of incorporation is very fast. The change in particle size with time is given by [22,36]

$$\frac{dr}{r} = \frac{D(C - C_s)v}{r} \tag{2.8}$$

where r is the radius of the particle (assumed spherical), D is the diffusion coefficient of the solute of molar volume v and concentration C, and C_s is the solubility of the solid.

The width of the size distribution Δr is given by [22,36]

$$\frac{\Delta r}{r} = \left(\frac{r_0}{r}\right)^2 \frac{\Delta r_0}{r_0} \tag{2.9}$$

where r_0 and Δr_0 are the nuclei size and the width of the size distribution respectively. The larger the growth, the smaller is the relative width of the distribution $\Delta r/r$. When the size of the particles is very large, of the order of 10 µm, their movement in the solution creates turbulence and convection currents that lower the concentration gradients near their surface and accelerate their growth. It is rare, however, for diffusion-limited growth to lead to monodispersed solutions because, under high supersaturation, nucleation and growth steps overlap and the formation of nuclei is continuous during a large part of precipitation.

(b) Growth Limited by a Surface Reaction

The kinetic step is the incorporation of the precursor on the surface of the nuclei, and a new nucleation step, this time on the surface, must take place in order to form two-dimensional nuclei (Figure 2.9a).

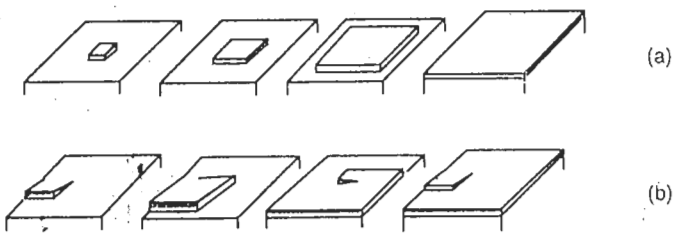

Figure 2.9 (a) Surface nucleation with two-dimensional growth of the nuclei. The hatched area represents the surface created by the formation of the nucleus. (b) Spiral growth around a defect

DropBooks

Primary homogeneous nucleation and surface nucleation are analogous phenomena, but the activation energy of the latter is smaller because only the outer limits of the nucleus participate in the creation of the surface. If the surface nucleation rate is much smaller than the two-dimensional growth rate for the surface nucleus, each new layer comes from a single nucleus. Growth takes place according to a 'mononuclear' mechanism which is a function of the surface area. If surface nucleation and growth rates are similar, several nuclei form simultaneously and may fit into one another. New layers begin to form prior to the previous ones being completely covered. This 'polynuclear' growth mechanism is independent of the surface area [22,36].

Quantitative analysis shows that, for the mononuclear mechanism [22], the growth rate of the particles is

$$\frac{dr}{dt} = k_m r^2 C^m \tag{2.10}$$

where k_m is the rate constant, and m is the approximate number of precursor molecules contained in the surface nuclei. Because their growth rate is proportional to the surface area, the larger particles grow faster. This mechanism leads to a broadening of the relative size distribution of the particles:

$$\frac{\Delta r}{r} = \left(\frac{r}{r_0}\right)\frac{\Delta r_0}{r_0} \tag{2.11}$$

The polynuclear growth rate is

$$\frac{dr}{dt} = k_p C^{(m+2)/3} \tag{2.12}$$

and the relative width of the size distribution is written as

$$\frac{\Delta r}{r} = \left(\frac{r_0}{r}\right)\frac{\Delta r_0}{r_0} \tag{2.13}$$

Other growth mechanisms may take place, such as spiral growth. It takes place from a structural defect such as a dislocation formed during nucleation or during the initial steps of growth. Subsequent growth maintains the defect by wrapping itself around it (Figure 2.9b). This mechanism allows the growth of particles on a singular defect, since it creates little or no increase in the solid–liquid interface and therefore the activation energy is very small and this mechanism may occur at very low supersaturation ($S \approx 1$).

Growth mechanisms do not obey the same power laws of concentration and particle size [equation (2.8), (2.10) and (2.12)]. Therefore, they will occur as the predominant mechanism in different concentration ranges (Figure 2.10). However, as precipitation progresses, the medium concentration decreases and the particle size increases. Several mechanisms contribute to growth, and composite rate laws [22,37] must be used to describe the evolution of the system.

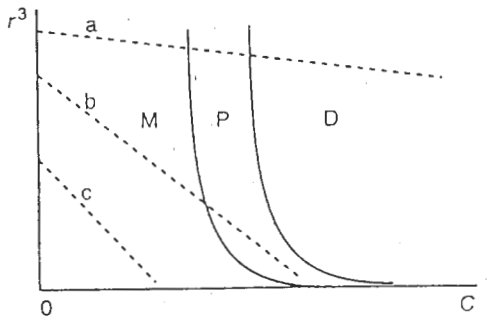

Figure 2.10 Domains of predominance of the main growth mechanisms: M mononuclear; P polynuclear; D diffusion. The evolution of r^3 (dashed lines) with concentration is approximately linear during precipitation initiated through mechanisms 1 (a), 2 (b) and 3 (c). From [22]

2.3.4 AGING

Nucleation and growth steps create particles under kinetics control following a reaction path of minimum activation energy under conditions imposed on the system (acidity, concentration, temperature), but the products are not necessarily thermodynamically stable. Aging of the suspensions, which may take place over a very large time scale (hours, days or months), allows the system to tend towards or to reach stability, and this is why ageing is often associated with modifications of some physical or chemical characteristics of the particles. Some of the most frequently observed phenomena are described below.

(a) Increase in Particle Size

This is manifested by a shift in particle size distribution owing to the disappearance of the smaller molecules and the formation of larger ones (Figure 2.11a). This evolution is possible because, if the liquid–solid interfacial tension is positive, true thermodynamic stability is reached when all precipitated matter is gathered in a single particle. The surface area of the solid is therefore at a minimum [equation (2.1)]. From another point of view, the Gibbs–Kelvin equation (2.5) shows that, for a concentration corresponding to saturation, only particles with radius r are in equilibrium with the solution. For particles with $r < r$ the solution does not appear to be saturated and they must redissolve. For those particles with $r > r$ the solution is supersaturated and the particles must grow ($\partial \Delta G/\partial n < 0$). The process involves transport of matter through the solution in what are referred to as 'dissolution–crystallization' mechanisms. This process can be very slow, because it occurs for very low concentrations ($S \approx 1$) and because, as is the case for hydroxides or oxides, it requires breaking of hydroxo or oxo bridges. This secondary growth must proceed through surface nucleation or spiral growth.

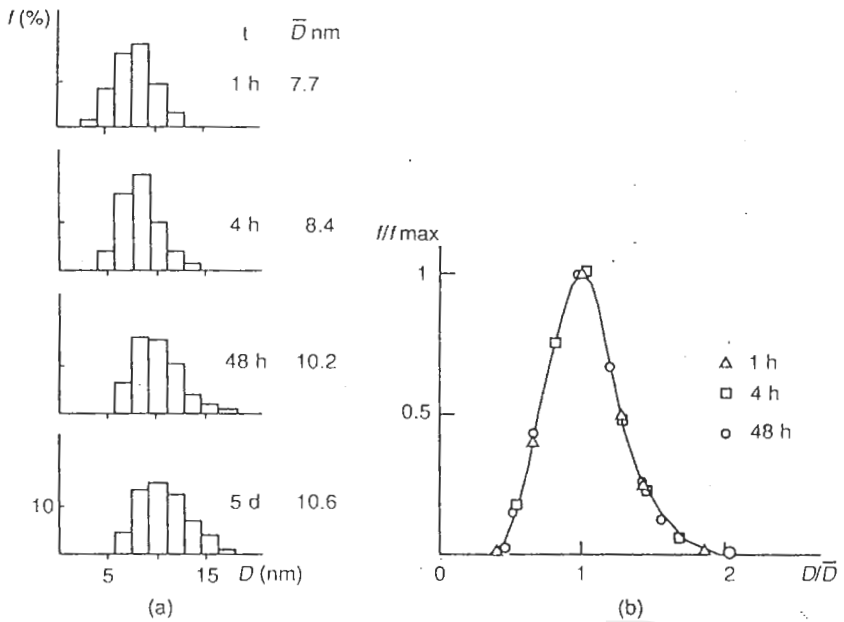

Figure 2.11 (a) Particle size distribution of Fe_3O_4 magnetite during aging and (b) Size distribution normalized for various times. From [39]

A quantitative treatment of the kinetics of the phenomenon [22,37,38] shows that this secondary growth process leads to a change in the absolute particle size distribution, but the normalized particle size remains unchanged (Figure 2.11b). This peculiarity is one way of confirming that secondary growth follows the laws of Ostwald ripening, without involving other phenomena such as aggregation or coalescence. In practice, the evolution of the system stops before all particles are transformed because the increase in the size of the particles decreases the rate of dissolution, and a pseudo-equilibrium is soon reached.

A decrease in the area of the solid–liquid interface may also occur via particle aggregation. It is favored by the physicochemical conditions of the medium (pH, ionic strength) which minimize the surface electrical charge of the particles (see Chapters 6 and 8). In the absence of an electrical double layer, particles attract each other and aggregation allows, more easily and rapidly than crystalline growth, a decrease in the area of the oxide–solution interface, and hence the attainment of a pseudo-stable state.

One must note that aggregation does not necessarily occur at a specific stage of the evolution of the system. It may occur as early as the onset of nucleation, or at any stage during growth, causing formation of dendrites, mosaic crystals or fractal structures [40].

Aggregation of primary particles bolsters the dissolution–crystallization equilibria because the areas close to the contact point between particles (concave surfaces) have smaller solubilities than the areas of positive curvatures (convex surfaces). Gibbs–Kelvin equation (2.5) may be rewritten as

$$\frac{S_r}{S_\infty} = \exp\left(\frac{2\gamma v}{kTr}\right) \qquad (2.14)$$

where S_r and S_∞ are the solubility of a particle with radius r and of a flat surface (infinite radius) respectively. Therefore, the contact zones between particles fill themselves until the solubility difference between the different zones is appreciably decreased. The phenomenon is more predominant as the size of the primary particles is small. This may lead to coalescence, i.e. 'fusion' of the primary particles, chain stiffening of spherical particles and even their transformation into fibers or sticks. Such morphological transformations are observed with aggregates of silica [20b] and tin oxide particles [41], for example.

(b) Change in Crystal Type

In the case of a crystal that may exhibit various allotropes, the least stable and most soluble phase usually precipitates first. This metastable phase is transformed during ageing into a more thermodynamically stable phase. This phenomenon, known as the Stranski rule [42], is explained using kinetic considerations.

Equations (2.5) and (2.7) show respectively that, for a given supersaturation level S, the nucleus size is smaller and the nucleation rate is larger for a smaller solid–solution interfacial energy γ. Since solubility is inversely proportional to interfacial tension [43], precipitation of the most soluble phase is favored kinetically (it is the least stable thermodynamically). Because of its solubility and metastable nature, this phase is of course more prone to ageing, which leads to recrystallization of the more stable phases, usually through heterogeneous nucleation [31]. This phenomenon is typical of many hydrates, such as titanium oxide TiO_2 which forms the anatase and rutile phases consecutively (see Section 3.2.3b), or aluminum hydroxide for which the amorphous phase $Al(OH)_3 \cdot xH_2O$ is transformed into boehmite first and bayerite later [44,45], or again amorphous iron oxyhydroxides (ferrihydrites) which form goethite α-FeOOH or hematite α-Fe_2O_3 (see Section 3.2.1c).

At times, heavily hydrated metastable phases, either amorphous or weakly crystalline, are formed initially during neutralization of cations such as Al(III) and Fe(III). The particles seem to form by aggregation of very small nuclei, rather than by crystal growth. In fact, the first stages of hydrolysis and condensation can lead very rapidly to polycationic entities that are very hydrated and chemically inert. They do not act as a reservoir for monomers but, rather, they aggregate because of the cancellation of their charge during neutralization, causing the formation of a solid without structure. Internal modifications (dehydration, crystal rearrangement)

DropBooks

allow subsequent nucleation of more stable phases [31,46,47]. Some examples are discussed in the following chapters (see Section 3.2.3a).

Preferential precipitation of the least stable phases may be used as a means of controlling and regulating the nucleation processes in order to form particles of homogeneous size. The initial precipitation of a basic salt, for example, containing ligands other than hydroxo or oxo, forms a reservoir which releases the metallic cation slowly and maintains its low concentration in solution. This favors nucleation of the stable phase of the oxide and allows growth of monodispersed particles. In these conditions, an 'ideal' separation of the nucleation and growth steps may be obtained. The synthesis of chromium oxide particles from a basic sulfate is a perfect example of this mechanism [48] (see Section 5.5.1).

(c) Changes in Morphology

The morphology of particles formed by precipitation is very intricately connected to the experimental conditions of the synthesis. Recrystallization of a solid in suspension into a more thermodynamically stable species is frequently associated with a change in the shape of the particles. It is difficult to predict the shape of the particles in a solid because the same crystal structure may exist under various morphologies.

A sphere is, from a thermodynamic point of view, the most favored geometry because its minimal surface/volume ratio decreases the free enthalpy of nucleation [equation (2.1)]. Small particles of many solids are very often spheroidal. However, particle anisotropy develops during growth, for structural or chemical reasons. Growth may be favored along preferential axes or crystallographic planes because the chemical reactivity of surface groups, on which the precursors bind, depends on many parameters such as local structure and electrostatic charge, as well as aggregation of primary particles. The last two factors are strongly linked to the pH of the solution and to the presence of complexing ions. Hematite (α-Fe_2O_3) particles of various morphologies are obtained through recystallization of akaganeite (β-FeOOH) under various experimental conditions [49] (Figures 2.12 and 2.13) or in the presence of various complexing agents [50] (cf. Section 5.4). The role of such parameters is discussed in more detail in Chapters 5 to 8.

In summary, the precipitation in solution of small solid particles follows four main kinetic stages. For most fundamental studies or applications, it is usually desirable to obtain particles of homogeneous size. This imposes a control over the relative rates of these stages via a control of the essential parameters on which they depend: precursor concentration and solid–solution interfacial tension (at a given temperature).

The precursor concentration (supersaturation level) must be maintained as low as possible after nucleation, in order to prevent, as far as possible, simultaneous occurrence of nucleation and growth. Several techniques may be used to this effect.

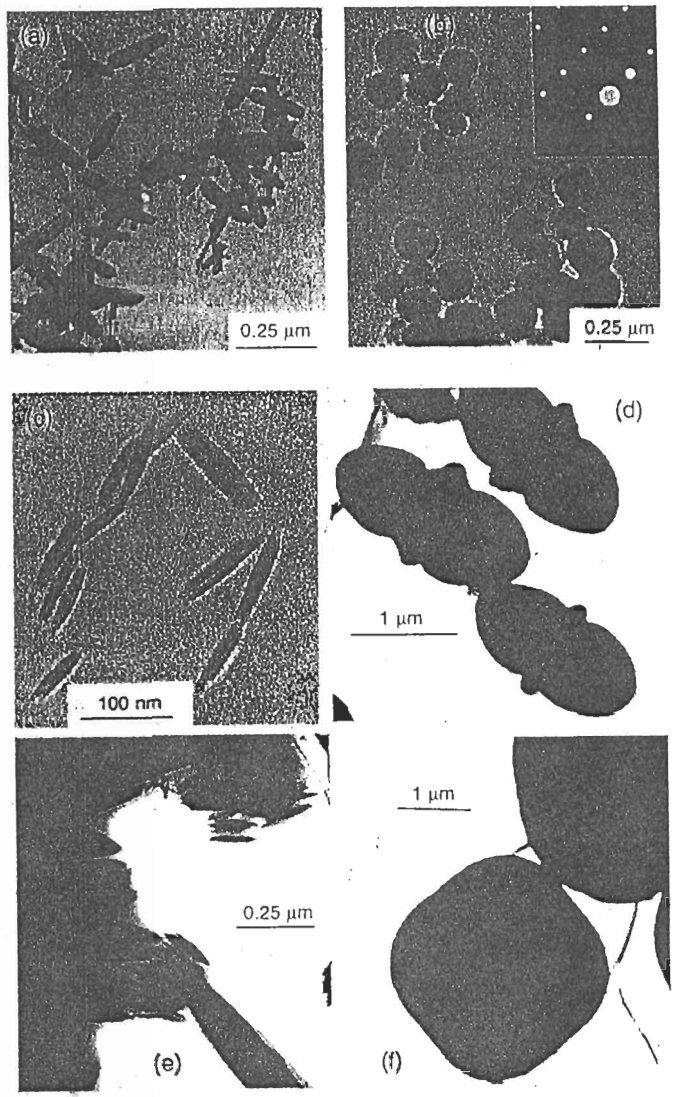

Figure 2.12 (a) Akaganeite particles formed by treatment of a solution of $FeCl_3$ ($0.018\,mol\,l^{-1}$) and HCl ($0.01\,mol\,l^{-1}$) at 100 °C for 12 h and (b) transformation into pseudospherical hematite particles after 1 week of heating; (c) akaganeite particles formed by heat treatment of a solution of $FeCl_3$ ($0.018\,mol\,l^{-1}$) and HCl ($0.05\,mol\,l^{-1}$) at 100 °C for 1 h and (d) transformation into double ellipsoidal hematite after 1 week of heat treatment; (e) aggregates of akaganeite particles obtained by heat treatment of a solution of $FeCl_3$ ($0.45\,mol\,l^{-1}$) and HCl ($0.01\,mol\,l^{-1}$) at 150 °C for 13 min and (f) transformation into particles of cubic hematite after 24 h of heat treatment. Reproduced by permission of Academic Press from [49]

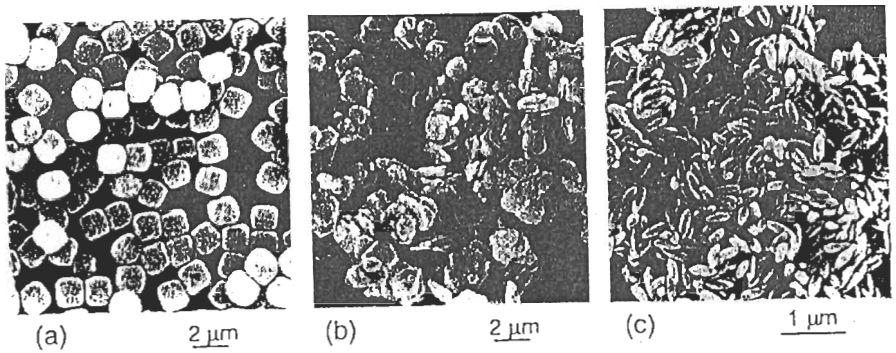

Figure 2.13 Hematite particles obtained by addition of sodium hydroxide to an $FeCl_3$ solution (final Fe concentration 1 mol l^{-1}): (a) pseudocubic particles obtained after heat treatment at 100 °C for 8 days of a suspension of ($OH^-/Fe = 5.4$); (b) platelets obtained after heat treatment at 180 °C for 2 h of a suspension of ($OH^-/Fe = 8$); (c) spindle-shaped particles obtained by heat treatment at 100 °C for 2 days of a solution of 2×10^{-2} mol l^{-1} in $FeCl_3$ and 3×10^{-4} mol l^{-1} in NaH_2PO_4. Reproduced by permission of Academic Press from [50]

When a reaction takes place under a set of fixed constraints (composition, concentration, acidity, temperature, etc.), it is necessary to study the way in which these constraints are applied to the system. Let us consider, for example, an acidic solution of a cation at fixed temperature and concentration. At pH < 1, hexa-aquo ions are predominant and stable as monomers. Precipitation of the solid requires the presence of hydroxylated complexes which are obtained by increasing the pH of the solution. From a thermodynamic point of view, it is easy to link the rate of hydrolysis of the cation to the pH of the solution, and therefore it is easy to know the form(s) present in the medium and to predict which species will be formed: polycations, polyanions or solid phase(s), and it is possible to adjust the pH accordingly. From a kinetics point of view, the situation is complex because a destabilization of the solution may occur in different ways.

(i) *Addition of a Base*

During the addition of a droplet of a base in the solution, a strong pH gradient exists locally around the droplet because the mixing and homogenezation are relatively slow (of millisecond order in a turbulent medium) compared with the rate of exchange of the protons with the aquo complex ($k \approx 10^{10}$ mol^{-1} s^{-1}). Before reaching equilibrium, a collection of species of variable hydrolysis ratios is formed, each of which with its own reactivity. Condensation via olation of these various forms occurs in an anarchical manner, in time and in space, which results in particles of very different sizes that do not necessarily correspond to thermodynamic equilibrium if kinetic constraints are involved.

(ii) *Thermohydrolysis*

Rather than modifying the composition of the system abruptly, it is preferable to work near equilibrium, in a homogeneous system. This may be achieved by generating the reactant (the base) within the solution while heating. The reactant may be water itself during thermohydrolysis (see Section 1.4), or a thermally unstable molecule such as urea:

$$(NH_2)_2C{=}O + 2H_2O \longrightarrow 2NH_4^+ + CO_3^{2-}$$

which acts as a buffer and maintains the solution around pH 7.8.

These reaction rates may be adjusted thermally, and it is possible to tune both the extent and the rate of hydrolysis, thereby controlling nucleation. This results in a narrow particle size distribution. Similarly, thermal decomposition of metallic complexes or basic salts allows regulation of the precursor concentration and control of the precipitation of the solid. Matijevic's research [35,51] clearly demonstrates the efficiency of such techniques.

Another factor, which is seldom considered, is the oxide–solution surface tension. This quantity can vary considerably for a given solid, depending on chemical composition and surface electrical charge density. These values are controlled by the pH and the ionic strength of the medium. Tuning these values allows, for a given metal concentration and in particularly favorable cases, modification of the respective rates of nucleation and growth, as well as the control of aggregation and ageing processes [52]. Further discussion on this topic, which requires a detailed description of the oxide–solution interface, can be found in Chapter 8.

2.4 REFERENCES

1. P. Souchay, *Ions Minéraux Condensés*, Masson, Paris (1969).
2. M.T. Pope, *Heteropoly and Isopolyoxometalates*, Springer-Verlag, Berlin (1983).
3. H. Stünzi, W. Marty, *Inorg. Chem.* 22, 2145 (1983).
4. K.K. Singh, P.R. Sarode, P. Ganguly, *J. Chem. Soc. Dalton Trans.* 1895 (1983).
5. R.F. Giese Jr, *Acta Cryst.* B32, 1719 (1976).
6. C.M. Flynn Jr, *Chem. Rev.* 84, 31 (1984).
7. W.D. Kingery, H.K. Bowen, D.R. Uhlman, *Introduction to Ceramics*, 2nd ed., John Wiley & Sons, New York (1975).
8. C.J. Brinker, G.W. Scherer, *Sol Gel Science*, Academic Press, San Diego (1990).
9. F. Basolo, R.G. Pearson, *Mechanisms of Inorganic Reactions*, 2nd ed., J. Wiley & Sons, New York (1958).
10. C.L. Rollinson, *Chemistry of the Coordination Compounds*, Vol. 131, Am. Chem. Soc. Master Ser., Bailar Ed., New York (1956), p. 448.
11. V. Baran, *Coord. Chem. Rev.* 6, 65 (1971).
12. C.F. Baes, R.E. Mesmer, *The Hydrolysis of Cations*, J. Wiley & Sons, New York (1976).
13. J.R. Van Wazer, *Phosphorus and its Compounds*, Interscience, New York (1958).
14. C.S.G. Philips, R.J.P. Williams, *Inorganic Chemistry*, Vol. 1, Clarendon Press, Oxford (1966), p. 158.

DropBooks

15. A.F. Wells, *Structural Inorganic Chemistry*, 5th ed., Clarendon Press, Oxford (1991).
16. L. Spiccia, W. Marty, *Inorg. Chem.* **25**, 266 (1986).
17. L.I. Bekkerman, I.P. Dobrovol'skii, A.A. Ivakin, *Russ. J. Inorg. Chem.* **21**, 223 (1976).
18. E. Narita, H. Takeuchi, N. Horiguchi, T. Okabe, *Bull. Chem. Soc. Jpn.* **57**, 1388 (1984).
19. L.H. Baestle, D. Huys, *J. Inorg. Nucl. Chem.* **30**, 1968 (1968).
20. R.J. Iler, *The Chemistry of Silica*, J. Wiley & Sons, New York (1979).
21. N.N. Greenwood, A. Earnshaw, *Chemistry of the Elements*, Pergamon Press, Oxford (1984).
22. A.E. Nielsen, *Kinetics of Precipitation*, Pergamon Press, Oxford (1964).
23. V.K. La Mer, R.H. Dinegar, *J. Am. Chem. Soc.* **72**, 4847 (1950).
24. T. Sugimoto, *Adv. Colloid Interface Sci.* **28**, 65 (1987).
25. M. Haruta, B. Delmon, *J. Chim. Phys.* **83**, 859 (1986).
26. H. Krüger, *Chem. Soc. Rev.* **11**, 227 (1982).
27. J.K.G. Dhont, C. Smits, H.N.W. Lekkerkerker, *J. Colloid Interface Sci.* **152**, 386 (1992).
28. A. Mersmann, *J. Cryst. Growth* **102**, 841 (1990).
29. P. Bennema, O. Söhnel, *J. Cryst. Growth* **102**, 547 (1990).
30. W. Stumm, J.J. Morgan, *Aquatic Chemistry*, Wiley-Interscience, New York (1970), p. 232.
31. H. Füredi-Milhofer, *Pure Appl. Chem.* **53**, 2041 (1981).
32. N.H.G. Penners, L.K. Koopal, *Colloids and Surf.* **19**, 337 (1986).
33. S. Kratohvil, E. Matijevic, *Adv. Ceramic Mater.* **2**, 798 (1987).
34. A. Garg, E. Matijevic, *Langmuir* **4**, 38 (1988).
35. E. Matijevic, *Pure Appl. Chem.* **60**, 1479 (1988).
36. J.Th.G. Overbeek, *Adv. Colloid Interface Sci.* **15**, 251 (1982).
37. A.E. Nielsen, *Crystal Growth*, H.S. Peiser Ed., Pergamon Press, London (1967), p. 419.
38. W.J. Dunning, *Particle Growth in Suspension*, A.L. Smith Ed., Academic Press, London (1973), p. 3.
39. P. Belleville, Thesis Université P. & M. Curie, Paris (1991).
40. *On Growth and Form, Fractal and Non-Fractal Patterns in Physics*, H.E. Stanley, N. Ostrowsky Eds, NATO Series E: Applied Sciences No. 100, Martinus Nijhoff Pub., Dordrecht (1986).
41. S.H. Pulcinelli, C.V. Santilli, J.P. Jolivet, E. Tronc, *J. Non-Cryst. Solids* **170**, 21 (1994).
42. I.N. Stranski, D. Totomanov, *Naturwissenschaften* **20**, 905 (1933).
43. A.E. Nielsen, O. Söhnel, *J. Cryst. Growth* **11**, 233 (1971).
44. H.A. Van Straten, B.T.W. Holtkamp, P.L. De Bruyn, *J. Colloid Interface Sci.* **98**, 342 (1984).
45. H.A. Van Straten, P.L. De Bruyn, *J. Colloid Interface Sci.* **102**, 260 (1984).
46. G.C. Bye, K.S.W. Sing, *Particle Growth in Suspension*, A.L. Smith Ed., Academic Press, London (1973), p. 29.
47. M.A. Blesa, E. Matijevic, *Adv. Colloid Interface Sci.* **29**, 173 (1989).
48. E. Matijevic, A. Bell, *Particle Growth in Suspension*, A.L. Smith Ed., Academic Press, London (1973), p. 179.
49. J.K. Bailey, C.J. Brinker, M.L. Mecartney, *J. Colloid Interface Sci.* **157**, 1 (1993).
50. T. Sugimoto; A. Muramatsu, K. Sakata, D. Shindo, *J. Colloid Interface Sci.* **158**, 420 (1993).
51. E. Matijevic, *Langmuir* **2**, 12 (1986).
52. J.P. Jolivet, E. Tronc, L. Vayssières, in *Nanophase Materials*, G.C Hadjipanayis, R.W. Siegel Eds, NATO ASI Series, Series E, Vol. 260, Kluwer Academic Pub., Dordrecht (1994), p. 45.

3

Olation: Polycations and Solid Phases

Condensation of cations by olation takes place by formation of hydroxo bridges (ol bridges) [1]. The OH ligand acts as the nucleophile in the nucleophilic substitution reaction. It only undergoes a change in coordination as it goes from terminal ligand in a monomer to bridging ligand in a condensed species. Therefore, this mechanism requires the pre-existence of a leaving aquo group, in order to prevent deprotonation of the OH ligand (see Section 2.1). Thus this reaction concerns neutral ($h \leqslant z$) or charged aquo–hydroxo complexes $[M(OH)_h(OH_2)_{N-h}]^{(z-h)+}$ formed by elements with an oxidation number smaller than or equal to 4. Condensation leads to soluble polycations if $h < z$, or to solids if $h = z$. The solid is an oxide or an oxyhydroxide as the formal charge of the cation increases. The formation of an oxide requires that an oxolation step should follow the olation reaction.

3.1 THE OLATION REACTION

3.1.1 MECHANISM

The olation reaction between aquo–hydroxo complexes, or between aquo–hydroxo and aquo complexes, may be schematically written as

$$-M-OH + -M-OH_2 \longrightarrow -M-OH-M- + H_2O$$

The reaction involves elimination of the aquo ligand. It is kinetically controlled by the lability of the $M-OH_2$ bond, which is usually rather high (Table 1.2). The lability of the $M-OH_2$ bond increases as the formal charge z of the cation decreases and its size increases (owing to the small polarizing power of the cation) [2,3]. In this case, condensation proceeds via a dissociative (SN_1) mechanism involving an intermediate compound of reduced coordination number. In the absence of other specific factors such as the presence of complexing ligands or steric effects, the olation reaction is usually very fast, and is essentially diffusion-controlled.

Transition elements for which the crystal field stabilization energy (CFSE) in octahedral configuration is high (Cr^{3+} d^3, Ni^{2+} d^8) form aquo complexes of very low reactivity, i.e. inert towards substitution [4]. The large change in CFSE owing to symmetry changes contributes to the activation energy of the reaction. For the formation of a pentacoordinated intermediary compound with C_{4v} symmetry:

$$[M(OH_2)_6]^{3+} \longrightarrow [M(OH_2)_5]^{3+} + H_2O$$

Symmetry O_h C_{4v}

the change in CFSE is $\delta_{CFSC} = CFSE_{C_{4v}} - CFSE_{O_h}$. For Fe^{3+}, $\delta_{CFSE} = 0$. The Fe–OH_2 bond is very labile and the rate constant of the reaction is approximately 10^2 s^{-1}. It is about 10^{-6} s^{-1} for Cr^{3+}, for which $\delta_{CFSE} = +0.2\Delta_0$.

For these elements, the reaction mechanism is probably more complex. Analysis of the structure of condensed Co(III) compounds in low spin configuration, as well as studies of Cr(III) cations strongly stabilized by the crystal field, reveal the existence of the bridging ligand $[H_3O_2]^-$ [5] (Figure 3.1). This ligand is formed by a strong hydrogen bond between the OH of one cation and the H_2O of the other. The $[H_3O_2]^-$ is unstable, but its existence, albeit temporary, shows that condensation proceeds,

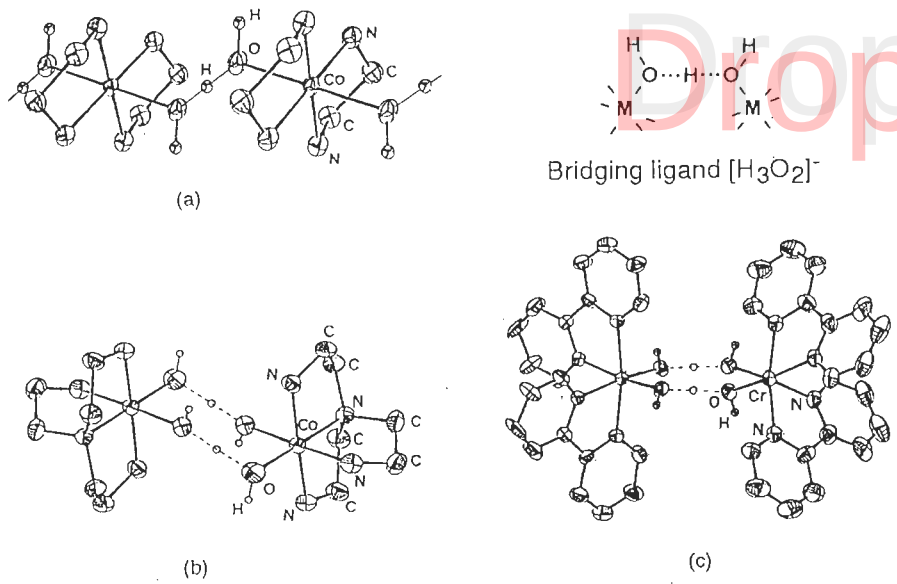

Figure 3.1 (a) Fragment of the chain of *trans*-$[Co(en)_2(H_3O_2)]_n^{2n+} \cdot 2n\,ClO_4^-$ bearing the $[H_3O_2]^-$ ligand in which the proton appears approximately in the central position along the O–O axis (distances O–O 2.44 Å, O–H 1.22 Å, $O–H_{non\text{-}bridging}$ about 0.95 Å). Crystal structures of (b) $[(tren)Co(H_3O_2)_2–Co(tren)]^{4+}$ and (c) *cis*-$[(bipy)_2Cr(H_3O_2)_2Cr(bipy)_2]^{4+}$, where en = ethylenediamine, bipy = bipyridine and tren = triaminotriethylamine. From [5] with permission

for these elements, according to an associative mechanism with the formation of an outer sphere complex or the formation of an ion pair during the transition state:

$$M–OH + H_2O–M \longrightarrow M–\overset{H}{O}\cdots H–O–M$$

This step is followed by breaking of the M–OH_2 bond and elimination of the aquo ligand:

$$M–\overset{H}{O}\cdots H–O–M \longrightarrow M–OH–M + H_2O$$

The $[H_3O_2]^-$ bridges have a rather long lifetime because of the chemical inertia of the cations, but they are not very stable. With more reactive elements, the OH bridge forms immediately and such intermediate compounds cannot be isolated.

Condensation of monohydroxylated species may lead to the formation of chains of corner-sharing polyhedra, or to the formation of dimers in which the polyhedra share edges via a double ol bridge. This type of bridge is formed via intramolecular olation after the formation of the first bridge. If a hydroxo ligand maintains a sufficiently high nucleophilic strength, the same mechanism may occur once more with a third cation, causing the formation of a μ_3–OH bridge. Large complexing ligands do limit edge or corner sharing of the coordination polyhedra by steric effects (Figure 3.1).

3.1.2 STRUCTURE

The structure of condensed species is controlled by several factors:

- *The hydrolysis ratio, h*, controls the number of ligands able to form single, double or triple ol bridges (Figure 3.2). The hydrolysis ratio characterizes, in a first approximation, the functionality of the cation in the condensation process.
- *The geometry of the condensation polyhedron* limits the mode of association because sharing corners, edges or faces involves increasingly short distances between cations (Figure 2.1). Edge sharing of octahedra is the most common geometry. Face sharing is rare. It does occur in some amino–hydroxo complexes of Co(III) (Figure 3.2). However, these compounds do not form via hydrolysis, owing to the chemical inertia of Co^{3+} (d^6 low spin), but via oxidation of Co(II) complexes [6,7]. Face-sharing octahedra are more commnonly seen in the oxide corundum structures formed by trivalent elements.
- *Cyclization* stabilizes the μ_2–OH corner bridge. This bridge is usually unstable and is found in a few polycations (for divalent and trivalent cations) such as Be^{3+} and Au^{3+} [8] (Figure 3.2). $[Bi_6(OH)_{12}(OH_2)_x]^{6+}$ is an interesting structure

DropBooks

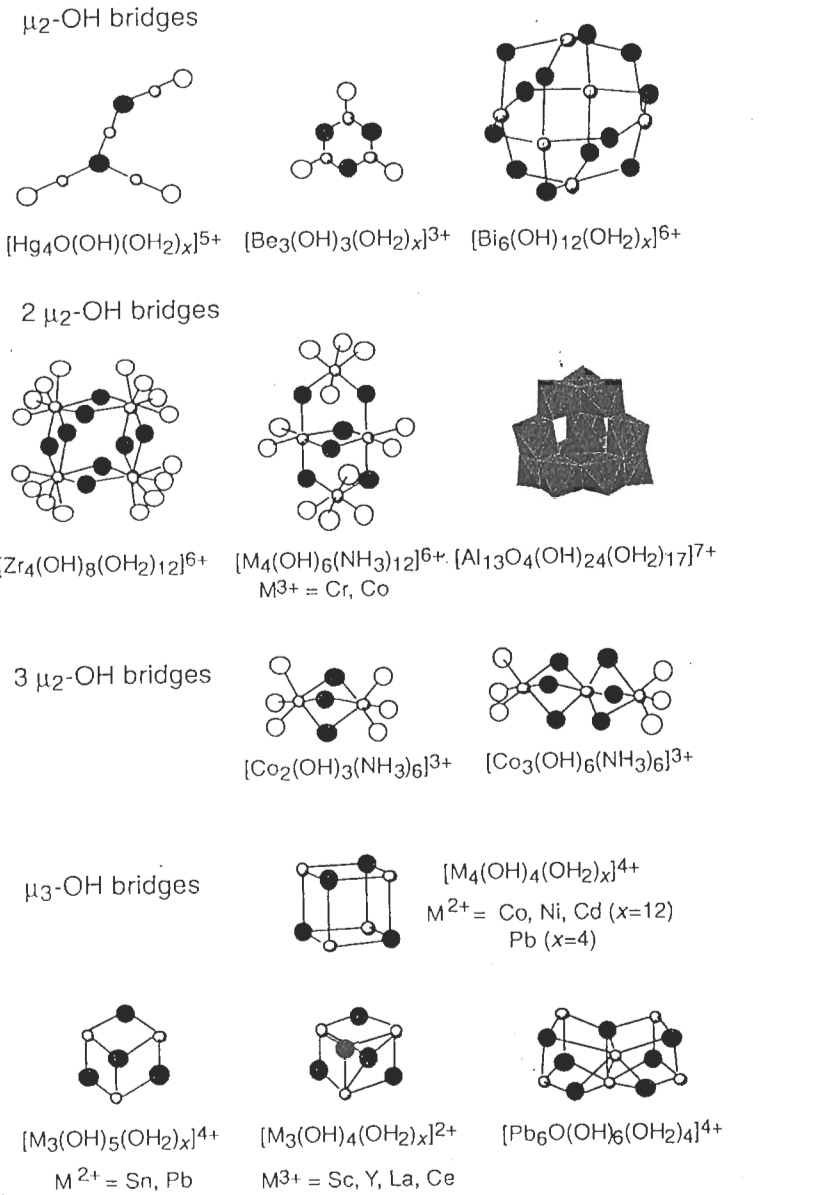

Figure 3.2 Several polycations with various modes of connection between coordination polyhedra

(Figure 3.2), consisting of simple hydroxo bridges forming the edges of an octahedra of bismuth atoms. It appears that *metal–metal interactions* ($d_{Bi-Bi} = 3.71$ Å) might play a role in the stabilization of this geometry [9]. Perhaps is it also the case for the Pb^{2+} polycation $[Pb_6O(OH)_6(OH_2)_4]^{4+}$, where one distance is very short ($d_{Pb1-Pb2} = 3.44$ Å, Figure 3.2) whereas the others vary from 3.67 to 4.09 Å [10]. In the absence of such factors, the corner bridge is poorly stable and edge sharing is more frequent. For entropy and structural reasons, the formation of the double hydroxo bridge in discrete species is more likely than a chain condensation creating high molecular mass species.

3.1.3 GROWTH

The condensation of aquo–hydroxo cationic complexes $[M(OH)_h(OH_2)_{N-h}]^{(z-h)+}$ $h < z$ is always limited. It stops spontaneously when a finite degree of condensation is reached. The condensed species remain soluble as polycations, which are usually entities of molecular size.

As the degree of condensation increases, accumulation of electric charges on the condensed species, as well as compositional changes due to dehydration, decrease the nucleophilic character of the hydroxo ligands. Both factors increase the average electronegativity of the polycation, which in turn increases the charges δ(OH) and δ(M) and the condensation stops as soon as condensation criteria are no longer met (Section 2.1b). Therefore, it makes sense that the degree of condensation would increase with the hydrolysis ratio of the complexes because the hydroxo ligands, which are more numerous in complexes of lower charge, maintain their nucleophilic activity until the late stages of condensation.

For example, chromium(III) hydrolyzed at $h = 1$ forms the dimer [11]

$$2[Cr(OH)OH_2)_5]^{2+} \rightleftharpoons [(H_2O)_4Cr(OH)_2Cr(OH_2)_4]^{4+} + 2H_2O$$

For the $h = 1$ monomer: $\chi = 2.69$, $\delta(Cr) = +0.64$, $\delta(OH) = -0.02$; for the dimer: $\chi = 2.73$, $\delta(Cr) = +0.66$, $\delta(OH) = +0.01$. Subsequent condensation of the dimer cannot take place.

The hydrolysis ratio $h = 1.33$ corresponds to the presence of $h = 1$ and $h = 2$ forms. They undergo more extensive condensation [11]:

$$2[Cr(OH)(OH_2)_5]^{2+} + [Cr(OH)_2(OH_2)_4]^{+} \rightleftharpoons \left[\begin{array}{c} OH \\ Cr \\ HO \end{array}\!\!\begin{array}{c} OH \\ OH \\ Cr \end{array}\!\!\begin{array}{c} OH \\ Cr \\ OH \end{array}\right]^{5+} + 4H_2O$$

For the $h = 2$ monomer: $\chi = 2.60$, $\delta(Cr) = +0.59$, $\delta(OH) = -0.10$; for the trimer: $\chi = 2.72$, $\delta(Cr) = +0.66$, $\delta(OH) = +0.01$. Here again, condensation stops at this stage.

On the other hand, condensation of neutral complexes $M(OH)_z(OH_2)_{N-z}$ ($h = z$) is not limited. Colloids can form, i.e. solid fragments from a few tens or hundreds of ångstroms to a few microns. The increase in average electronegativity in the growing species is due only to dehydration, and this increase is never sufficient to make the hydroxo ligands lose their nucleophilic character. As a result, a solid phase precipitates, usually a hydroxide $M(OH)_z$. This phase may be unstable and may spontaneously dehydrate by internal oxolation to form oxyhydroxides MO(OH) or hydrated oxides $MO_{z/2} \cdot nH_2O$ (Section 2.3).

It must be stressed that the polycations are not usually the nuclei from which the solid forms. During the slow alkalinization of the solution, when the conditions are met for the formation of the hydroxide, the structure of the transient polycation(s) changes so that there is usually no structural relationship between polycations and solid. This is probably due to the lability of the polycations, which also causes great difficulty in understanding their chemistry and their structure. The most inert ones {chromium(III) trimer and aluminum polycations, such as $[Al_{13}O_4(OH)_{24}(OH_2)_{12}]^{7+}$} maintain their structure during charge cancellation by alkalinization, and they flocculate as disorganized solids. These condensed, aggregated entities in the metastable 'amorphous' phase [formed under kinetic control (see Section 2.3) during rapid precipitation] may reorganize during ageing, causing crystallization of the solid.

During thermolysis of acid solution, the thermal effect and the acidity of the medium often allow direct synthesis of thermodynamically stable phases which may be different from those formed by neutralization. Frequently, these are oxyhydroxides or oxides. In some cases, their structure may be described in terms of a building block of similar topology to that of the polycations (Section 3.2.3). Under experimental conditions allowing control of nucleation kinetics, crystallization of the solid may correspond to an extension of the short range order of the polycation. This control usually involves control of the rate of generation of the precursor and control of the activation energy. In this case, it is tempting to consider that polycations are the structural templates for the nuclei. This may also be the case during ageing by dissolution–crystallization of some metastable phases. We shall now discuss a few examples.

3.2 CONDENSATION OF TRIVALENT ELEMENTS

The solution chemistry of trivalent elements is very complex because of the large number of polycations and solid phases they may form. It serves, however, as a good illustration of the previous considerations.

In spite of the structural similarities between their oxides M_2O_3 and oxyhydroxides MOOH [12a,b], chromium, iron and aluminum exhibit very different behaviors in solution.

Chromium forms small polycations, usually kinetically stable [11,13], whereas iron polycations are very labile and form colloids very easily [14–17]. Among these three elements, only aluminum is able to form the very peculiar 'Al_{13}' polycation (Figure 3.2) [18–20].

Isostructural solids are formed in very different conditions. Precipitation of chromium leads to strongly hydrated hydroxide gels $Cr(OH)_3(OH_2)_n$ [21–25]. Aluminum also forms amorphous gels [26,27] and transforms into various crystalline forms of $Al(OH)_3$ (gibbsite, nordstrandite, bayerite) [28] or oxyhydroxide γ-AlOOH (boehmite), depending on the acidity. Diaspore, α-AlOOH, can be obtained only by hydrothermal synthesis, and corundum, α-Al_2O_3, is obtained by heating hydroxides or oxyhydroxides at high temperature after the formation of 'transition aluminas'. The hydroxide $Fe(OH)_3$ does not exist. It dehydrates spontaneously, at any temperature, and forms in suspension, depending on acidity and temperature, α-FeOOH (goethite) isostructural with diaspore, or α-Fe_2O_3 (hematite) isostructural with corundum [17]. γ-FeOOH (lepidocrocite) isostructural with boehmite results from the oxidation of ferrous hydroxide in suspension [17,64]. In the presence of chloride ions, β-FeOOH (akaganeite) forms spontaneously. This phase does not exist with aluminum.

Such differences in behavior appear to be linked to the size and electronic configuration of the cations.

The acidity in solution of these elements increases in the sequence Cr, Al, Fe, as shown by measurement of the pH at the onset of precipitation (Figure 3.3). Table 3.1 contains some characteristics of the ions.

Hydroxylation of aquo cations as

$$[M(OH_2)_6]^{3+} + H_2O \Longleftrightarrow [M(OH)(OH_2)_5]^{2+} + H^+_{solvated}$$

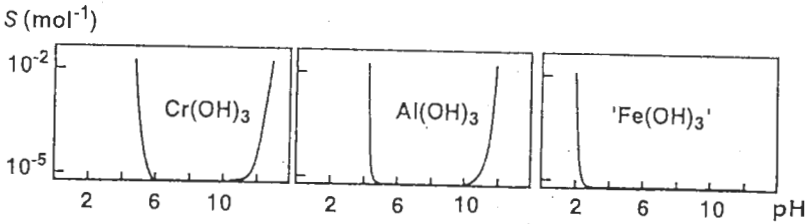

Figure 3.3 Precipitation of Cr(III), Al(III) and Fe(III). From [29a]

Table 3.1 Characteristics of a few trivalent elements

	Al^{3+}	Cr^{3+}	Fe^{3+}
Electronic structure	$2p^6$	$3d^3$	$3d^5$
Ionic radius (Å)	0.53	0.65	0.64
χ^*_M	1.47	1.59	1.72

DropBooks

is fast in all three cases ($k \approx 10^5\,s^{-1}$) [30]. Hydrolysis is a simple acid–base reaction involving proton exchange between the solvent and the coordinated water molecules. Its activation energy is very small (see Section 1.4).

The lability of coordination water is, on the other hand, very variable [2–4]. Exchange of the ligand by a dissociative nucleophilic substitution reaction requires an activation energy corresponding to the formation of a pentacoordinated intermediate compound (see Section 2.1) [4]. The rate constants for coordination water exchange are of the order of 10^{-6}, 1 and $10^2\,s^{-1}$ for Cr^{3+}, Al^{3+} and Fe^{3+} respectively [4]. Chromium(III), whose d^3 configuration is strongly stabilized in octahedral symmetry by the crystal field, is inert towards substitution reactions (see Section 3.1.1). For Fe(III) of high-spin d^5 configuration in an oxygen environment, the CFSE is zero for any symmetry. This explains the good lability of coordination water. Al^{3+} (Table 3.1) is a smaller ion, and its coordinated water molecules are more polarized. The differences in the lability of coordination water for these three elements leads to large differences in the kinetics of olation reactions.

3.2.1 OLIGOMERIC SPECIES: POLYCATIONS

Although a study of the condensation of Cr(III) in solution is complicated by the slow reaction rates, this chemical inertia is actually beneficial in the analysis and separation of the species formed. Several species are isolated on ion-exchange resin from solution hydrolyzed at $h = HO^-/Cr \approx 1$ at a pH close to 4. These species are oligomers with the acidity constants shown in Table 3.2.

The addition of a base causes the creation of a pH gradient, and several hydrolyzed species may coexist because of their poor reactivity. Although the structure of these species cannot be resolved by diffraction because of the absence of crystals, a study of the solution indicates the most probable configurations.

The formation of the dimer from the $h = 1$ precursor may be written as

$$2[Cr(OH)(OH_2)_5]^{2+} \rightleftharpoons [(H_2O)_4Cr(OH)_2Cr(OH_2)_4]^{4+} + 2H_2O$$

Table 3.2 Acidity of chromium(III) polycations [13]

Complexes	pK
$[Cr(OH_2)_6]^{3+}$	4.3
$[Cr_2(OH)_2(OH_2)_8]^{4+}$	3.7
$[Cr_3(OH)_4(OH_2)_9]^{5+}$	4.3
$[Cr_4(OH)_6(OH_2)_{10}]^{6+}$	3.5
$[Cr_4O(OH)_5(OH_2)_{10}]^{5+}$	0.9

We discussed earlier that this dimer is stable in solution since the bridging OH groups do not exhibit nucleophilic character. The crystal structure of the dimer has been obtained via X-ray diffraction after dissolution of the hydroxide (see Section 3.2.3) in paratoluenesulfonic acid or in mesitylene-2-sulfonic acid [22].

The early condensation stages of Cr(III) proceed by the formation of binuclear outer sphere complexes involving the bidentate ligand $[H_3O_2]^-$ formed by an intramolecular hydrogen bond (Figure 3.4). Elimination of a water molecule forms the dimer in which polyhedra share corners. Elimination of a second water molecule leads to the di-μ–OH ion in which the polyhedra share edges [31,32]. These transformations are associated with a color change: the precursor $h = 0$ and the

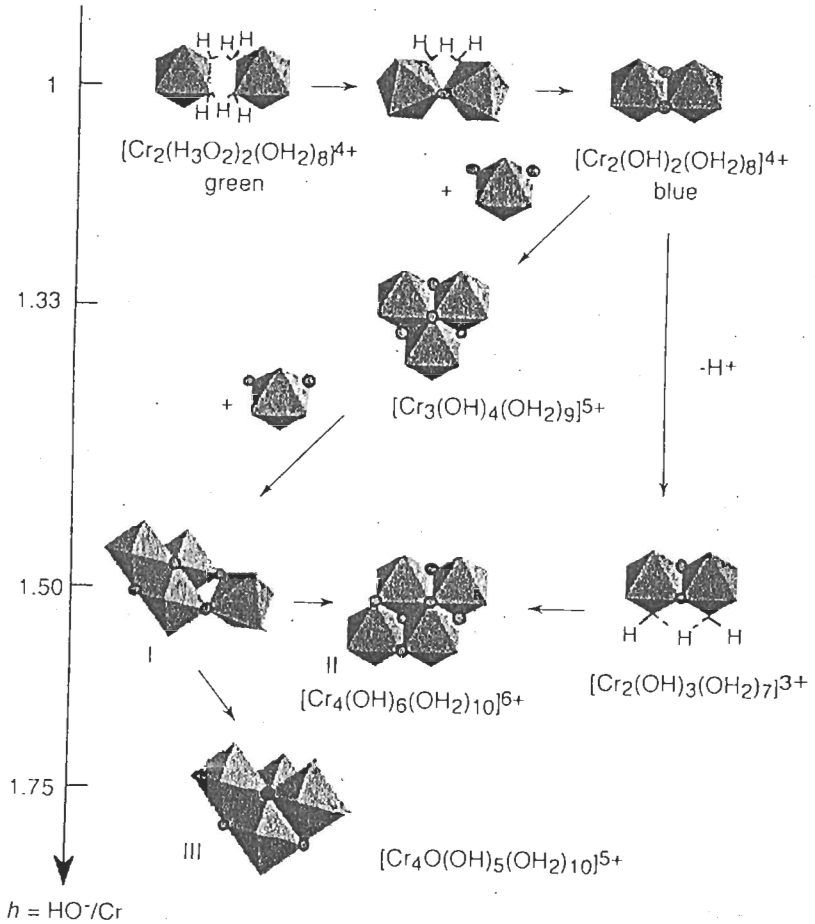

Figure 3.4 Cr(III) polycations in aqueous solution

hydrated binuclear dimer are green, whereas the di-μ–hydroxo ion is blue [33]. The monomer–dimer equilibria have been characterized thermodynamically [34].

The acidity of the $[Cr_2(OH)_2(OH_2)_8]^{4+}$ dimer is stronger than that of the monomer (Table 3.2) because of an intramolecular hydrogen bond beween two water molecules in *cis* configuration with respect to the equatorial plane of the compound. This bond tends to stabilize the deprotonated form $[Cr_2(OH)_3(OH_2)_7]^{3+}$ with the bridging ligand $[H_3O_2]^-$ (Figure 3.4). The same is true of the *cis* form $[Cr_2(OH)_2(OH_2)_2(NH_3)_6]^{4+}$, which is more acidic than the *trans* form and cannot form intramolecular hydrogen bonds [33].

The deprotonated dimer $[Cr_2(OH)_3(OH_2)_7]^{3+}$ forms other polycations with an identical overall hydrolysis ratio because a decrease in its charge increases the nucleophilic character of hydroxo groups [$\chi = 2.68$, $\delta(OH) = -0.03$]. It may react in several ways: with the $h = 1$ complex, the trimer $[Cr_3(OH)_4(OH_2)_9]^{5+}$ forms, containing three μ_2–OH bridges and a central μ_3–OH bridge (Figure 3.4). This is the most inert chromium polycation [11,13,23,35]; it may also dimerize and form a planar tetramer $[Cr_4(OH)_6(OH_2)_{10}]^{6+}$ (structure II, Figure 3.4).

The same planar tetramer can be formed from the trimer and an $h = 2$ precursor via an intermediate form $[Cr_4(OH)_6(OH_2)_{11}]^{6+}$ (form I, Figure 3.4) [11]. Internal olation leads to the planar tetramer $[Cr_4(OH)_6(OH_2)_{10}]^{6+}$. At higher pH, deprotonation of the μ_3–OH bridge in form I leads by internal olation to the tetramer $[Cr_4O(OH)_5(OH_2)_{10}]^{5+}$ (structure III, Figure 3.4). Reaction kinetics has shown that interconversion between forms (II) and (III) depends on the acidity of the medium [36].

This structural analysis is confirmed by the fact that acidification of the tetramer leads to a monomer–tetramer mixture, irrespective of how it was formed. The tetramer synthesized by reaction of a ^{51}Cr-tagged monomer with a large excess of a non-tagged trimer (to prevent formation of the tetramer from the monomer alone) yields, after separation on an ion-exchange resin and degradation in an acid medium, a mixture of monomer and trimer both containing the same amount of ^{51}Cr [11]. This result allows the exclusion of other configurations that could not allow ^{51}Cr exchange, such as

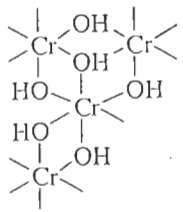

Similar polycations probably exist with Al and Fe, but the trimer $[Al_3(OH)_4(OH_2)_{12}]^{5+}$ is the only one to have been observed using potentiometric titration [37]. ^1H, ^{17}O and ^{27}Al NMR have recently confirmed that the di-μ_2 hydroxo dimer is not formed in appreciable amounts by neutralization of acid solutions [19,20].

A sulfate of the dimer does crystallize from sulfuric acid solutions [38], but ^{27}Al NMR shows that, when crystals are dissolved in pure water, the monomer $[Al(OH_2)_6]^{3+}$ and a trimer of unknown structure form, at the expense of the dimer [19]. Solution dilution leads directly and rapidly to the $[Al_{13}O_4(OH)_{24}(OH_2)_{12}]^{7+}$ [19,20] polycation (see below).

Iron polycations are not as well known as chromium or aluminum polycations because of the lability of ferric complexes. Only a few polycations (dimers, trimers) have been characterized in acidic solutions (pH < 1.5) [39]. $[Fe_2(OH)_2]^{4+}$ and $[Fe_2O]^{4+}$ dimers are present in organic complexes such as $L_3(H_2O)Fe(OH)_2$-$Fe(OH_2)L_3$ and $L_5FeOFeL_5$, where the L_3 ligand is a tridentate picolinate and L_5 a tridentate amine [16,40,41]. Other polydentate ligands, such as proteins, are able to stabilize many polynuclear iron complexes [42–45]. The existence of the aquo complexes $[(H_2O)_4Fe_2(OH)_2(OH_2)_4]^{4+}$ and $[(H_2O)_5Fe_2O(OH_2)_5]^{4+}$ is very probable in spite of the lack of structural data.

3.2.2 LARGE POLYCATIONS

The three elements behave quite differently near a hydrolysis ratio of 2.5. Chromium forms inert tetramers, whereas aluminum forms the unusual polycation $[Al_{13}O_4(OH)_{24}(OH_2)_{12}]^{7+}$ having a Keggin-type structure. Twelve AlO_6 octahedra divided into four trimer groups surround a central AlO_4 tetrahedron [18,19] (Figure 3.5). At a similar hydrolysis level, iron forms colloidal species with a much higher degree of condensation ($n \approx 100$) [16].

These differences in behavior may be ascribed to differences in the electronic configuration of the cations. One may assume that the three elements form, at least temporarily, the trimer $[M_3(OH)_4(OH_2)_9]^{5+}$ (M = Al, Fe, Cr). This trimer is seen in many systems since it is the most able to minimize electrostatic repulsions because of its geometry. It may act as an intermediate species for condensation at a later stage. In this entity, the oxygen atom in the μ_3–OH bridge forms three bonds with cations and a fourth one with the proton (Figure 3.5).

The small Al(III) cation has a larger polarizing effect on the oxygen of the μ_3–OH bridge than on the oxygen from the μ_2–OH, and therefore the μ_3–OH bridge is more acidic (Figure 3.5). This causes dissociation of the μ_3–OH bridge [46]:

$$[Al_3(OH)_4(OH_2)_9]^{5+} + H_2O \longrightarrow [Al_3O(OH)_3(OH_2)_9]^{4+} + H_3O^+$$

and makes the water molecules in *cis* (with respect to the μ_3–O bridge) more acidic than the molecules in *trans*. Formation of the $[H_3O_2]^-$ ligand (Figure 3.5) can also favor deprotonation of the aquo ligands in *cis* under moderate hydrolysis conditions ($h < 2.6$):

$$[Al_3O(OH)_3(OH_2)_9]^{4+} + 3OH^- \longrightarrow [Al_3O(OH)_3(O_2H_3)_3(OH_2)_3]^+ + 3H_2O$$

DropBooks

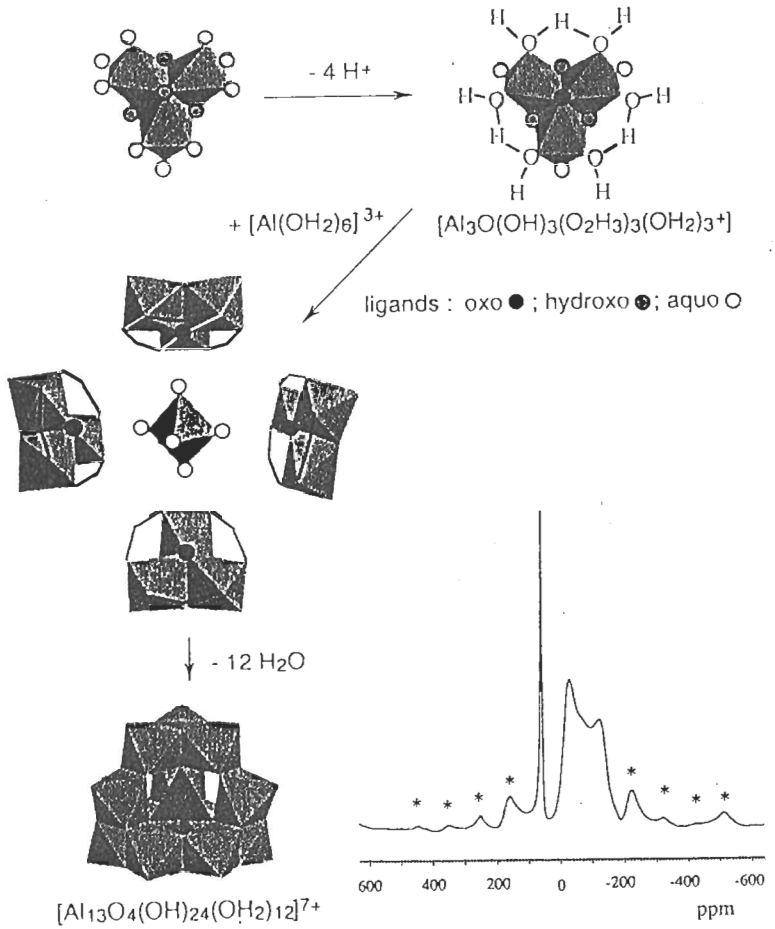

Figure 3.5 Possible formation mechanism of $[Al_{13}O_4(OH)_{24}(OH_2)_{12}]^{7+}$ and ^{27}Al MAS-NMR spectrum of the sulfate salt of the polycation Al_{13} measured at 9.4 T, with spinning speed of 15 kHz; *spinning sidebands (J. Hernandez and J.P. Jolivet, unpublished results)

The μ_3–O bridge of the trimer becomes able to act as a nucleophile towards a $h = 0$ monomer but, because of steric effects, the central element cannot reach coordination 6 and Al adopts a tetrahedral coordination. In the end, the following complex forms:

$$[Al(OH_2)_6]^{3+} + 4[Al_3O(OH)_3(O_2H_3)_3(OH_2)_3]^{+} \longrightarrow \{Al[Al_3O(OH)_3(O_2H_3)_3(OH_2)_3^{+}]_4\}^{7+} + 6H_2O$$

The four trimers coordinated to the central aluminum atom may subsequently undergo intramolecular condensation by olation, with elimination of water

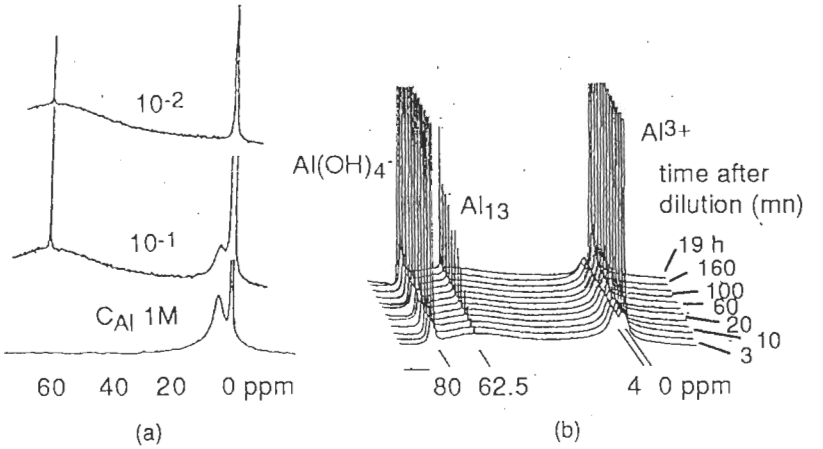

Figure 3.6 (a) ^{27}Al NMR spectra of $AlCl_3$ solutions hydrolyzed at $h = 0.5$. The peak at around 4 ppm is due to oligomers (di-, tri- or tetramers). (b) ^{27}Al NMR spectra of a solution of $AlCl_3$ (1 mol l^{-1}) hydrolyzed at $h = 1$ and diluted 10 times rapidly with water. $[Al(OH)_4]^-$ at 80 ppm is used as a reference. From [19] with permission

molecules in *cis*:

$$\{Al[Al_3O(OH)_6(OH_2)_6]_4\}^{7+} \longrightarrow [Al_{13}O_4(OH)_{24}(OH_2)_{12}]^{7+} + 12H_2O$$

This last step ensures the stability of the cation. It is further favored by heating the $h = 2.6$ aluminum solution around 80 °C. Under such conditions, it is possible to probe the polycation by NMR [20]. Distortion of the AlO_6 octahedra is significant, as indicated by the very large peak on the MAS-NMR spectrum of the polycation at solid state (Figure 3.5).

This reaction mechanism is in agrement with ^{1}H, ^{17}O and ^{27}Al NMR of moderately hydrolyzed solutions [19] (Figure 3.6), which indicate that only small oligomers, probably trimers, condense directly without intermediates during the formation of Al_{13}.

This type of M_{13} polycation is not observed with chromium or iron. The main reason seems to be the difficulty these ions have in adopting the tetrahedral coordination, even if the Fe(III) ion can be tetrahedrally coordinated in some complexes in solution and in solids such as spinels (see Section 5.6). In addition, when the d orbitals of the cation are partially occupied, the donor effect of the oxygen in the μ_3–OH bridge of the trimer $[M_3(OH)_4(OH_2)_9]^{5+}$ is not as large as with aluminum. Hence, deprotonation of the bridge is probably more difficult. On the other hand, one may consider that the d orbitals of iron and chromium are more diffuse than the p orbitals of aluminum, allowing a better overlap with the orbitals of oxygen of the μ_3–OH bridge. Therefore, the acidity of the OH ligand is high and

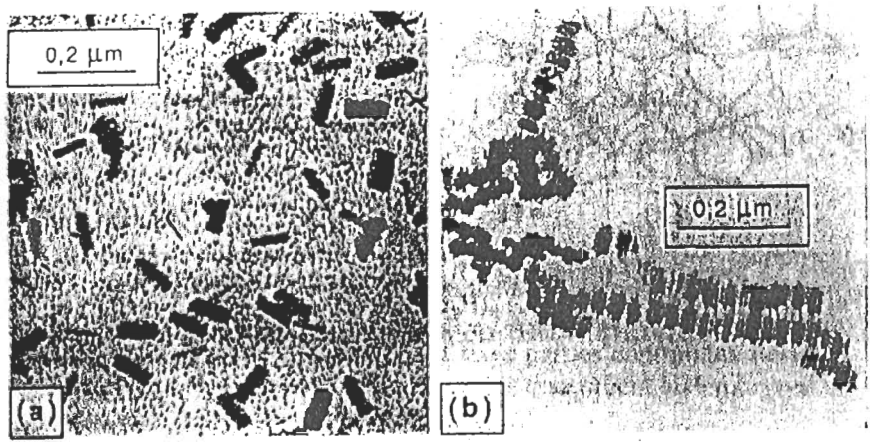

Figure 3.7 (a) Sol (Fe^{3+} 6.25×10^{-3} mol l^{-1}) after 1 year of ageing (pH = 1.95), containing 20–40 Å colloids and goethite particles. (b) In a more concentrated medium (Fe^{3+} 6×10^{-2} mol l^{-1}, pH = 1.50), the particles aggregate as tactoids. Reproduced by permission of Elsevier Science Ltd from [49]

the nucleophilic character of the oxo ligand is very low. It is, however, difficult to compare the acidity of the μ_3–OH bridge in different trimers because specific distortions for each cation may change the acidic properties. Consequently, reaction of the iron or chromium trimer with the non-hydrolyzed precursor must lead preferentially to the tetramer (forms II or III, Figure 3.4).

Contrary to Cr(III) condensation in solution, the condensation of ferric ions at $h < 2.5$ is difficult to control because of their labile nature. Fast condensation proceeds until the formation of polymers or colloids (red sols made of ≈ 30 Å particles [16,39]). X-ray absorption (XANES, EXAFS) [47] indicates that Fe(III) is always in 6-coordination. FeO_6 polyhedra share edges and corners via oxo and hydroxo bridges. The local environment around Fe is nonetheless similar to the one observed in goethite α-FeOOH and akaganeite β-FeOOH (see below). The particles aggregate very slowly in solution, in an orderly fashion, and form tactoids that recrystallize as goethite (Figure 3.7) [38,47–49].

Stabilization of iron polycations requires strongly complexing and bulky ligands forcing a reduction in the reactivity and functionality of the cation [42–45]. Large oxo–hydroxo polycations can be stabilized by N-(2 hydroxyethyl)iminodiacetic acid $N(CH_2COOH)_2(CH_2CH_2OH)$, a tetradentate ligand that coordinates the cation with carboxylic groups, the alkoxy ligand and the nitrogen [50] (Figure 3.8).

These are the largest iron polycations known to date, containing 17 and 19 metal cations. It should be noted that the core of the ferric clusters contains μ_3–OH bridges only, with a topology close to that of the tetramer involved temporarily in the formation of goethite (see below).

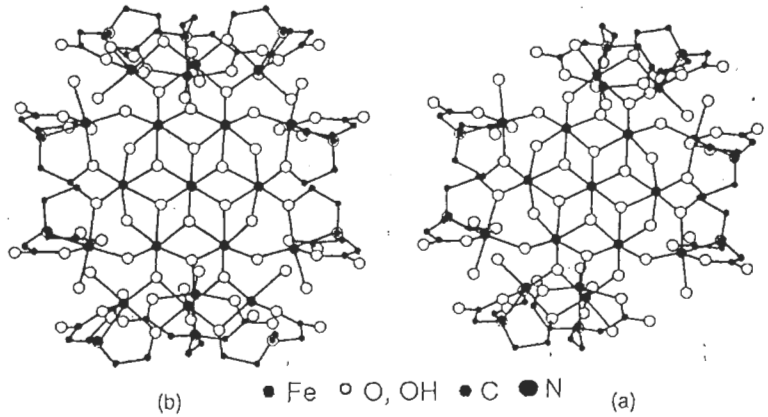

Figure 3.8 Structure of (a) $[Fe_{17}(\mu_3\text{–}O)_4(\mu_3\text{–}OH)_6(\mu_2\text{–}OH)_{10}(L)_8(H_2O)_{12}]^{3+}$ and (b) $[Fe_{19}(\mu_3\text{–}O)_6(\mu_3\text{–}OH)_6(\mu_2\text{–}OH)_8(L)_{10}(H_2O)_{12}]^{+}$, where $L = N(CH_2COOH)_2(CH_2CH_2OH)$. From [50] with permission

3.2.3 SOLID PHASES: HYDROXIDES, OXYHYDROXIDES, OXIDES

The formation of solid phases of trivalent elements occurs around $h \approx 2.5$. Above this value, the concentration in a zero-charge precursor is sufficiently high for nucleation to take place. Hydroxylation of the cation can occur via the addition of a base, thermohydrolysis (see Section 1.4) or hydrothermally (see Section 1.5). Most often, different processing techniques lead to different crystal structures and morphologies. Kinetic and/or thermodynamic factors, as well as the solvent, are likely to affect the behavior of complexes in solution and orient the reaction mechanism.

(a) Hydroxylation via the Addition of a Base at Room Temperature

Alkalinization of an aluminum nitrate solution around pH 6–7 with sodium hydroxide or ammonia causes the immediate formation of a translucent amorphous gel. This unstable gel crystallizes more or less rapidly and forms different crystalline phases depending on the acidity of the medium: at pH 6 or 7, it leads to the oxyhydroxide γ-AlOOH (boehmite), whereas at pH < 5 or pH ⩾ 8, $Al(OH)_3$ gibbsite or bayerite forms, respectively. The reaction path during transformation of the gel is related to changes in the solubility of aluminum with the pH of the medium (Figure 3.9).

The amorphous gel formed immediately upon neutralization of acidic solutions [55] is a metastable and poorly defined phase. It is probably due to aggregation of intermediate and inert species such as the Al_{13} polycation. During the evolution of the gel at room temperature, the NMR peak characteristic of Al(III) in tetrahedral

DropBooks

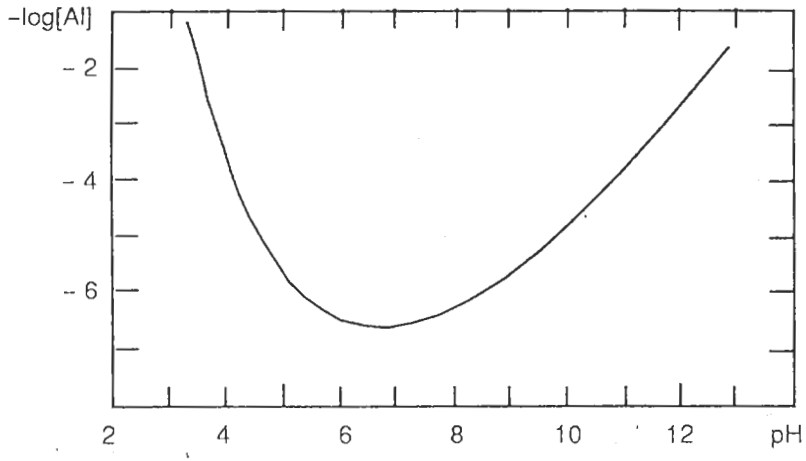

Figure 3.9 Solubility diagram of an amorphous aluminic gel (data obtained from [29b])

coordination disappears as crystallization takes place [26]. This metastable nature is due to the amorphous structure of the solid particles: as the particles become crystalline, lattice energy is released and the free enthalpy of the system decreases. How the crystal structure develops is a function of the conditions of the system.

At pH 6–7, i.e. at the solubility minimum of aluminum, matter transport through the solution is difficult and reorganization of Al_{13}-type entities is more easily accomplished within the solid. The transformation involves partial dehydration and leads to γ-AlOOH boehmite, in which the oxygen lattice is f.c.c. and similar to that of Al_{13}. Although boehmite is not the thermodynamically most stable phase at room temperature, it is probably kinetically stabilized because the system is constrained to evolve without heating and transforms on the lowest activation energy path.

For $pH < 6$, and $pH > 8$, solubility of aluminum is appreciable. Gel transformation can occur via matter transport in the solution, in a dissolution–crystallization process (see Section 2.3.4). Slowly generated soluble species in small concentration, probably monomers, feed the formation of $Al(OH)_3$ which is more stable than boehmite at room temperature ($\Delta G^0_{f\,298\,K}$ kJ mol^{-1}): $Al(OH)_3 = -546$, γ-AlOOH $= -436$).

At $pH > 8$, the precursor of the hydroxide phase is probably the tetrahedral $[Al(OH)_3(H_2O)]^0$. Indeed, alkaline solutions contain mostly aluminate ions $[Al(OH)_4]^-$, as confirmed by ^{27}Al NMR [56]. This complex ion is stable as a monomer. Through acidification or reaction with water:

$$[Al(OH)_4]^- + H_3O^+(H_2O) \Longleftrightarrow [Al(OH)_3(OH_2)]^0 + H_2O(HO^-)$$

it forms a zero-charge entity that may condense rapidly by addition. Addition and solvation cause an increase in the coordination of the Al^{3+} cations, which leads to

the formation of oligomers in which Al^{3+} is once again in coordination 6:

$$2[Al(OH)_3(OH_2)]^0 + 2H_2O \Longleftrightarrow [Al_2(OH)_6(OH_2)_4]^0$$

We may then consider a reaction mechanism involving octahedral dimers $[Al_2(OH)_6(OH_2)_4]^0$ whose further condensation by olation leads simply and directly to the planes characteristic of the structure of the hydroxide (Figure 3.10). At $pH < 6$, the soluble species are octahedral, so that the dimer $[Al_2(OH)_6(OH_2)_4]^0$ may form directly to allow formation of the hydroxide from the gel along the same reaction path.

Depending on the pH of the medium, aluminum hydroxide crystallizes as gibbsite or as bayerite. Both structures are based on the stacking of identical layers of edge-sharing $Al(OH)_6$ octahedra (Figure 3.10). In gibbsite, the order of the stacking is of the ABBA type (oxygen atoms of two adjacent sheets are face-to-face), whereas in bayerite, stacking is of the ABAB type (oxygen atoms form a hexagonal close-packed structure) [28,12c]. Within the sheets, hydrogen bonds between OH groups maintain the cohesiveness. It is probable that, depending on the pH, the charge on OH groups on the surface of the sheets could be somewhat different, which would tend to modify their solvation. As a consequence, their interaction through the hydrogen bonds is modified, thereby favoring one structure or the other. Gibbsite appears to be slightly more stable than bayerite (enthalpies of formation $\Delta H^0_{f,\,298\,K}$ are respectively -612.5 and -610.1 kJ mol^{-1}). Contrary to what is expected, the Bayer process (using bauxites) produces gibbsite. In this process, cooled and neutralized alkali aluminate solutions are seeded with gibbsite, and the growth of this phase is due to a heterogeneous nucleation process.

The addition of a base to a solution of ferric nitrate causes the formation of a gelatinous precipitate in acidic media (pH 2–2.5). We have previously discussed the fact that it is difficult to limit the condensation of ferric ions because of their high lability. Ferric gels are made of oxyhydroxides of various degrees of hydration (ferrihydrites). Several wide reflections observed by XRD are characteristic of planar sheets of edge-sharing octahedra [two-line or six-line ferrihydrite depending on the degree of ordering within and between layers, of approximate composition $Fe_4(O, OH, H_2O)_{12}$ and $Fe_{4.6}(O, OH, H_2O)_{12}$] [47,58–60]. Analysis of the gels using EXAFS [47] shows two Fe–O distances at 1.92 and 2.08 Å corresponding to the Fe–O and Fe–OH bonds respectively. The local order around iron seems to be the same as in goethite α-FeOOH and akaganeite β-FeOOH (See Chapter 5, Figure 5.16). The amorphous nature of ferric gels and polymers is due only to the small size of the coherent diffraction domains.

Ageing of ferric gels (ferrihydrites) in suspension at room temperature or heated at moderate temperatures leads mostly to hematite α-Fe_2O_3 at $5 \leqslant pH \leqslant 10$ [39,60–62]. Outside of this pH range, and particularly during precipitation in an alkaline medium ($pH \geqslant 10$) [60], the suspensions mostly contain goethite α-FeOOH. Ferric hydroxide $Fe(OH)_3$ does not exist as such in the precipitation products. This phase has only been identified in a very rare mineral, bernalite, found in the Broken

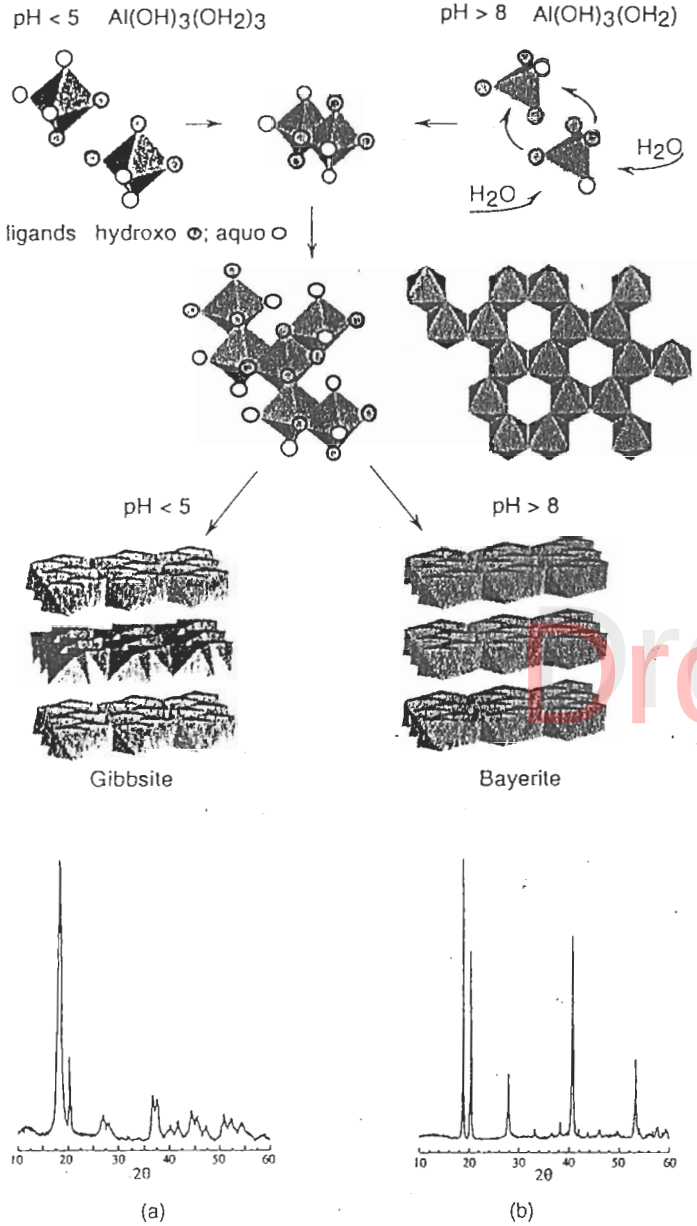

Figure 3.10 Possible reaction mechanisms for the formation of $Al(OH)_3$ (gibbsite, bayerite) during evolution of the aluminic gel at pH < 5 and pH > 8. XRD of the solids precipitated at pH 10 and aged (a) at pH 4.5 for 1 month (gibbsite) and (b) at pH 10 for 1 week (bayerite) (J. Hernandez and J.P. Jolivet, unpublished results)

Hill mine in Australia. Its structure is quite surprising for a hydroxide, since it is made of corner-sharing $Fe(OH)_6$ octahedra. In this perovskite structure, some water molecules occupy a few large voids in the lattice [115]. Ferric gels evolve, following both types of mechanisms already described in the case of aluminum gels.

The transformation of ferric gels into hematite occurs within the acidity range where the solubility of Fe(III) is minimum, and therefore the dissolution–recrystallization equilibria are not favored. Under these conditions, formation of the oxide stems from dehydration of the gel and *in situ* structural reorganization. This mechanism was shown in EXAFS investigations of ferric gels precipitated at pH 6.5 at room temperature and aged at 92 °C [62]. The electron density radial distribution functions around iron in the freshly made gel (Figure 3.11) show iron–iron distances characteristic of corner-sharing octahedra (3.45 Å) and edge-sharing octahedra (3.05 Å), which indicate short-range order. Up to 6 h ageing time, hematite crystals are not observed by XRD, but a peak appears on the radial distribution functions, indicating Fe–Fe distances at 2.86 Å characteristic of face-sharing octahedra. The intensity of the peak increases with time and hematite peaks appear on the XRD spectrum after 6 h ageing time. Crystallization of ferric gels into hematite is therefore the result of a solid state process initiated by octahedra sharing faces, and is favored by aggregation and dehydration of the solid [63]. The acidity range in which iron solubility is minimum corresponds to the range in which the surface charge on the particles is the smallest and where aggregation and internal dehydration of the solid are most favored (see Chapter 7). Dehydration is kinetically enhanced at higher temperatures and leads directly to the thermodynamically stable phase. Thermolysis of diluted ferric solutions (0.06 mol l^{-1}), in the absence of

DropBooks

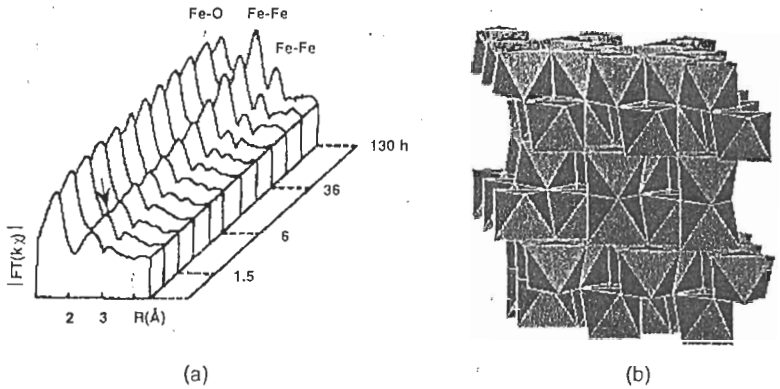

Figure 3.11 (a) Radial distribution function around Fe during crystallization of a ferric gel into hematite at 92 °C. The arrow indicates the appearance of the shoulder characteristic of Fe–Fe distances of 2.86 Å. (Reproduced from [62] 1990 by permission of Elsevier Science Ltd The Boulevard, Langford Lane, Kidlington OX5 1GB, UK (b) Structure of hematite α-Fe_2O_3

previous precipitation of ferric gel, causes the formation of hematite according to a process very similar to the one just discussed [61] (see the discussion below).

Under acid conditions where, at room temperature, the solubility of Fe increases slightly, the ferric gel tends to form goethite. A dissolution–recystallization process seems to be involved. Under these conditions, nucleation of the solid phase takes place through condensation of zero-charge species formed in a process similar to the formation of polycations. Growth of the solid may be interpreted as taking place from the planar tetramer $[M_4(OH)_{12}(OH_2)_4]^0$; this process indeed appears highly probable for Fe(III) (Section 3.2.2). Condensation of these species by olation can lead directly to embryos of double chains of octahedra, characteristic of the structure of goethite. The chains connect by oxolation because of the relative kinetics of each reaction. Connection between the double chains occurs through μ_3–O bridges and hydrogen bonds between the chains (Figure 3.12). Growth of the chains may take place later in a dissolution–recrystallization process, resulting in particles of high anisotropy where the largest dimension corresponds to the direction of the chains. In a more acidic medium (pH $\leqslant$ 4), processes of formation

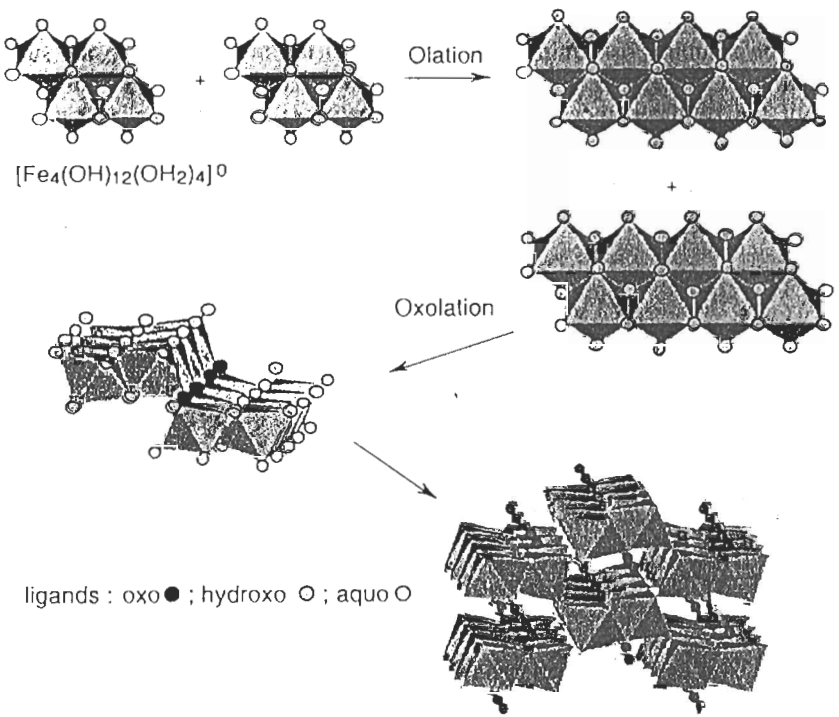

Figure 3.12 Possible formation mechanism of goethite α-FeOOH in solution, via ageing or thermohydrolysis

of goethite and hematite compete [60]. Although the solubility of the ferric complexes increases, their charge is also much higher {$[Fe(OH)(OH_2)_5]^{+}$ and $[Fe(OH)_2(OH_2)_4]^{2+}$ complexes}, and therefore the nucleation of goethite is more difficult. In addition, the acidity facilitates oxolation within the solid ferrihydrite precursor (see Section 4.1). Under these conditions, the formation of hematite is favored by the kinetics.

Chromium(III) differs from aluminum and iron in its exceptional chemical inertia. The fast addition of a base in a solution of Cr^{3+} ions also causes the formation of a gel owing to cancellation of the charge on the aquo complexes or polycations. Various hydrated hydroxides are formed, and they are made of aggregates of species that previously existed in solution.

The addition of a base to the monomer $[Cr(OH_2)_6]^{3+}$ causes the precipitation of the grey-blue hydrated hydroxide $Cr(OH)_3(OH_2)_3$, in which $Cr(OH)_3(OH_2)_3$ octahedra are connected by double $[H_3O_2]^-$ bridges formed by hydrogen bonds between hydroxo and aquo ligands [21,25]. The solid contains planar hexagons similar to those observed in aluminum hydroxides $Al(OH)_3$ (Figure 3.13).

The formation of this phase may be described from the monomeric precursors $[M(OH)_3(OH_2)_3]^0$ or $[M(O_2H_3)_3]^0$ in which the $[H_3O_2]^-$ groups are chelating in nature:

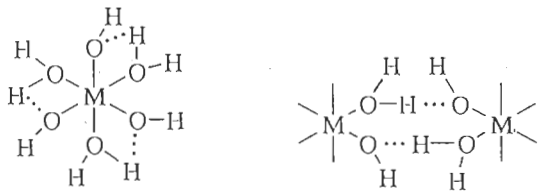

The mode of coordination of the $[H_3O_2]^-$ ligands may become bridging quite easily, after a simple change in the orientation of hydrogen bonds between the OH

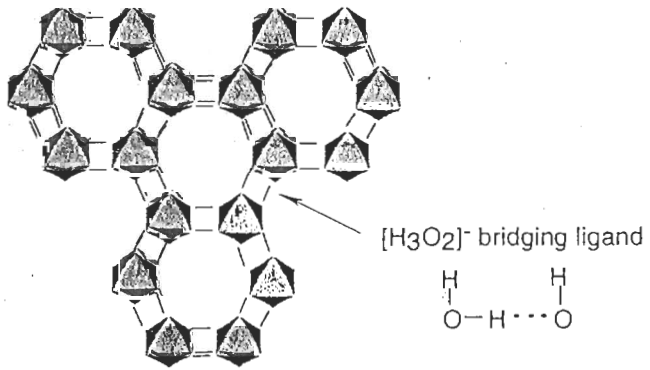

Figure 3.13 Planes of chromium hydroxide $Cr(OH)_3(OH_2)_3$. $[Cr(OH)_3(OH_2)_3]$ octahedra are connected by the bridging ligand $[H_3O_2]^-$

and the OH_2 groups. The formation of chains and rings is therefore possible. Their size is controlled by steric factors imposed by the bridging ligands. The rings aggregate easily and form the embryos of the solid phase.

The structure of polycationic dimers and trimers (Figure 3.4) is preserved during neutralization in a pyridine buffer (pH ≈ 6.9) because of their poor chemical reactivity. The hydroxides $Cr_2(\mu\text{–}OH)_2(OH)_4(OH_2)_4 \cdot 2H_2O$ [22] (blue-green) and $Cr_3(\mu\text{–}OH)_4(OH)_5(OH_2)_4 \cdot 4H_2O$ [23] (light green) form, in which the dimers and trimers, respectively, are connected by the $[H_3O_2]^-$ ligand.

The kinetic stability of these compounds towards dehydration is quite low. They usually transform spontaneously as early as 60 °C or through ageing at room temperature into the green amorphous phase characteristic of chromium gels [24], and later into oxyhydroxides CrOOH and into the more or less hydrated oxide Cr_2O_3 [21,23,51–54]. Chromium hydroxide can also be obtained by acidification of strongly alkaline solutions of chromite $[Cr(OH)_4(OH_2)_2]^-$ [23]. From a thermodynamic point of view, the instability of hydroxides appears to be due to the positive charge on the water molecule (Table 2.1).

In summary, hydroxylation of cations in solution by the addition of a base generates almost instantaneously a large amount of zero-charge entities, and therefore condensation is very fast. The speed of the process does not leave enough time for the crystal to form and the resulting solid is amorphous. Crystallization is not immediate because inert species can form very rapidly, causing flocculation when their charge is cancelled (Al_{13} with aluminum and chromium complexes, for example). In fact, the species can be so labile that their condensation takes place in an anarchical manner without the formation of long-range crystalline order (ferrihydrites). The driving force behind the evolution of such poorly structured solids is the formation of a more thermodynamically stable crystalline phase because of the enthalpy gain associated with the release of lattice energy. Depending on acidity (i.e. solubility) conditions, the transformation of a metastable phase may involve one of the following mechanisms: dehydration–structuring *in situ* or dissolution–crystallization. In the latter scenario, the difference in thermodynamic stability between the solid phases and the differences in their solubilities create a continuous flux of matter at very low concentrations through the solution, which allows the slow transformation of the entire amount of initial material (gel or gelatinous precipitate) into an organized phase.

(b) Thermohydrolysis

Hexa-aquo complexes of trivalent elements are stable in an acidic medium at room temperature. Hydroxylation of these complexes by water may, however, take place by heat treatment (see Section 1.4). Heating of an acid solution of Al(III) ions to about 80–100 °C causes the formation of boehmite γ-AlOOH [67,68]. In similar conditions, Fe(III) forms hematite. Thermolysis of acid solutions of chromium causes the formation of oxyhydroxides of poorly defined structure, as well as

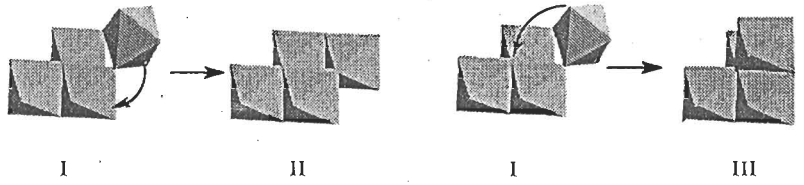

Figure 3.14 Possible forms of the tetramer for M(III) elements

the hydrated oxide Cr_2O_3 [54]. Hydrothermal techniques also allow the synthesis of other oxyhydroxides such as α-AlOOH diaspore isostructural with goethite, α-CrOOH brucite [69], β-CrOOH isostructural with InOOH [70] and a variety named 'γ-CrOOH' although it is amorphous by XRD [71].

During the thermolysis process, deprotonation is slow. Species in solution may therefore condense during slow hydroxylation, forming intermediate species of similar structure to polycations. These entities may aggregate and condense to form a crystallized solid, as in the case of the dissolution–crystallization process.

It is reasonable to assume that boehmite may form by thermolysis of aluminum solutions, starting from $[Al_4O(OH)_{10}(OH_2)_5]^0$ or $[Al_4(OH)_{12}(OH_2)_4]^0$ tetramers. These are good structural models for the oxyhydroxide nuclei and they may be considered in a first approximation as the building blocks of the solid phase.

During studies of the early stages of condensation of trivalent elements, it was observed that two forms of tetramer may result from an octahedron fixed on the compact $[M_3(OH)_4(OH_2)_9]^{5+}$ flipping in one direction or another (Figure 3.14). The tetramer with a μ_4–O bridge (form III) appears favored in the case of aluminum because of the nucleophilic character of the μ_3–OH bridge (see Section 3.2.2). Condensation of $[Al_4O(OH)_{10}(OH_2)_5]^0$ by olation and oxolation could lead directly to the formation of corrugated sheets of AlO(OH) containing μ_4–O and μ_2–OH bridges. These sheets are characteristic of the γ-AlOOH phase and are linked by hydrogen bonds between the hydroxo groups on adjacent sheets (Figure 3.15). Another reaction mechanism could involve the formation of boehmite from the planar tetrameric precursor rapidly forming double chains of octahedra, in a process similar to the formation of goethite (Figure 3.12). Connections between these chains could take place by oxolation between the μ_3–OH of one chain and the terminal ligands of another. This seems rather unlikely because the growth of 'fibrillar' boehmite particles is preferential along their c axis perpendicular to the corrugated planes of the lattice, rather that in the direction of the chains. Diaspore, isostructural with goethite, forms only under hydrothermal conditions [around 400 °C, 6 kbar, conditions in which the physicochemical properties of water are very different from the standard conditions (see Section 1.5), and can affect drastically the structure and acidity of the oligomers]. Therefore, the formation of double chains of octahedra from the planar precursor $[Al_4(OH)_{12}(OH_2)_4]^0$ appears difficult.

DropBooks

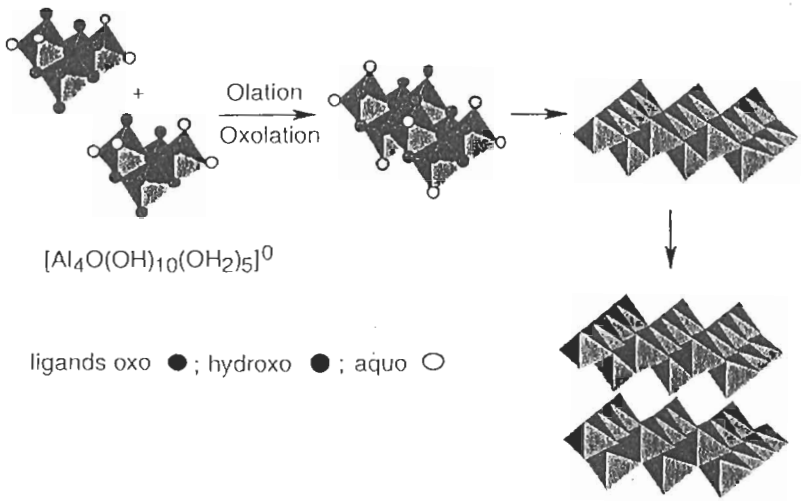

Figure 3.15 Possible formation mechanism of boehmite γ-AlOOH by thermolysis

In the cases of chromium and iron, we have discussed the fact (see Section 3.2.2) that the planar configuration of the tetramer (form II, Figure 3.14) is strongly favored. However, the strong lability of the ferric species probably forces a very rapid condensation, even if the formation of hydroxylated species is slow. During the first hours of thermolysis at 100 °C, at a pH close to 2, the six-line ferrihydrite is obtained as small particles a few tens of ångstroms in diameter. The particles aggregate to form, after a few hours, much larger monocrystalline particles of hematite. The size of the hematite particles decreases when the pH of the thermolyzed solution increases from 2 to about 4. This would suggest that the formation of hematite from ferrihydrite takes place by *in situ* recrystallization of the aggregates and by dissolution–crystallization, the latter process being favored at low pH when the solubility of Fe is higher. Under these conditions, goethite does not form as it does at room temperature (Figure 3.12). An increase in temperature probably increases the reactivity of the ferric tetramer and the tendency towards oxolation (which is already high at room temperature) and leads to the formation of the most thermodynamically stable phase. The situation is somewhat different in the case of chromiun(III). The planar precursor $[Cr_4(OH)_{12}(OH_2)_4]^0$ is able to condense by olation and oxolation, as in the case of goethite. However, because of the low lability of coordinated water, both reactions become kinetically competitive and, instead of forming chains by rapid olation as in the case of goethite at room temperature, the simultaneous reactions lead to the formation of sheets containing μ_3–OH and μ_3–O bridges characteristic of the α-CrOOH phase (Figure 3.16). The sheets are connected by hydrogen bonds and form structures similar to that of CdI_2.

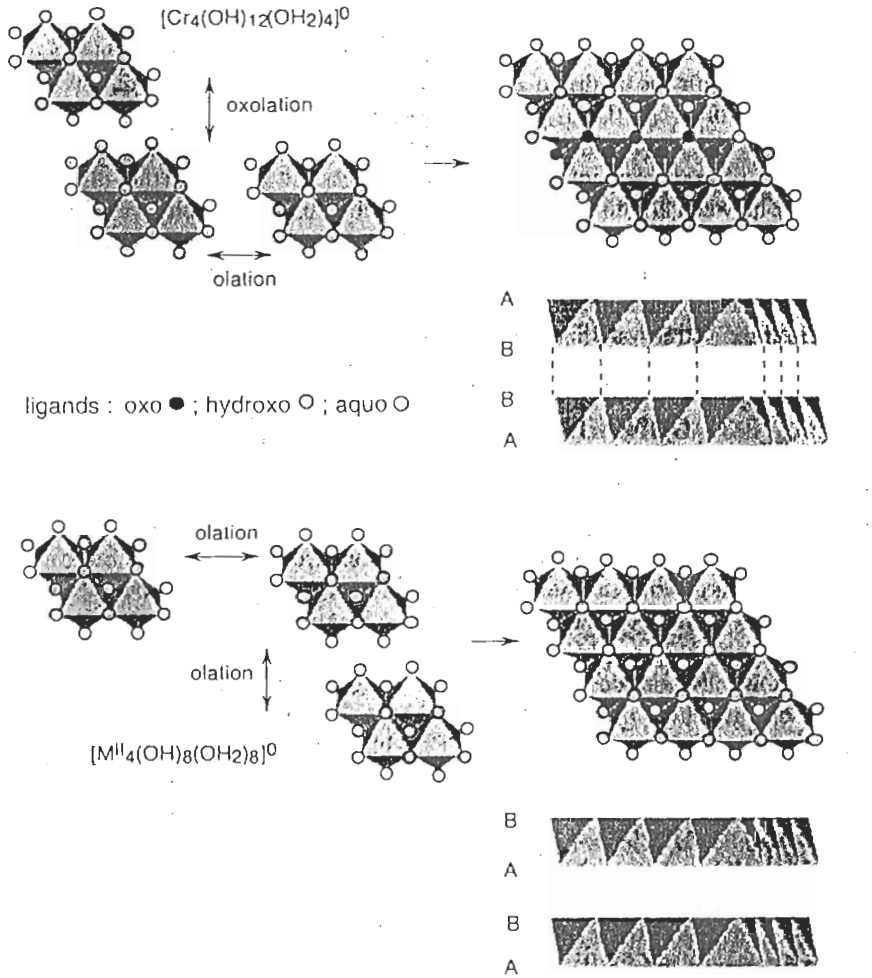

Figure 3.16 Possible reaction mechanism for the formation of chromium oxyhydroxide α-CrOOH and hydroxides $M(OH)_2$ of brucite structure

It is clear that, in spite of a few analogies, Al(III), Fe(III) and Cr(III) each have their own behavior in solution. The spontaneous tendency of the hydroxylated form of iron to undergo rapid dehydration probably explains the poor solubility in an alkaline medium. With aluminum or chromium, for which oxolation is less likely, hydroxo bridges are relatively stable with respect to dehydration in the hydroxides. However, they are easily dissolved in an alkaline medium because free hydroxyls are better nucleophiles than hydroxo bridges in the solid. However, iron and aluminum oxides are poorly soluble in an alkaline medium because oxo bridges are

much more stable than hydroxo bridges. In addition, because of its small size, aluminum can easily acquire a coordination of 4 that can be further stabilized by π interactions with the hydroxo ligands. Therefore, aluminum can dissolve as the anionic monomer $[Al(OH)_4]^-$ or, in a concentrated and very strongly alkaline medium, as the polyanion $[Al_4(OH)_{16}]^{4-}$ [65]. The treatment of bauxites and the separation of both elements in the Bayer process are based on this difference in behavior between aluminum and iron [66]. In the mineral, which owes its red color to the presence of hematite, aluminum is present as boehmite γ-AlOOH (French bauxites) or gibbsite $Al(OH)_3$ (American or African bauxites). After treatment in a strongly alkaline medium at about 200–250 °C, aluminum is dissolved, separated from iron oxide, recrystallized as hydroxide and calcined to obtain alumina Al_2O_3.

3.3 CONDENSATION OF DIVALENT ELEMENTS

3.3.1 POLYCATIONS

For a similar hydrolysis ratio, polycations formed by divalent ions must attain a higher degree of condensation than those formed by trivalent ions, owing to the smaller formal charge of the cation and the higher nucleophilic character of the hydroxo ligands. For a hydrolysis ratio $h = 1$, the olation reaction for divalent elements usually goes beyond the stage of the $[M_2(OH)_2(OH_2)_8]^{2+}$ dimer [30]. The partial charge on the μ_2–OH bridge is negative in this dimer, whereas it is positive in those of trivalent elements forming stable dimers (Table 3.3). Condensation must therefore proceed, and the easiest route is an olation reaction converting all μ_2–OH bridges into μ_3–OH bridges (Figure 3.17). Very compact polycations $[M_4(OH)_4(OH_2)_n]^{4+}$ [$n = 4$, Pb(II), or 12, Ni(II)] are produced, in which μ_3–OH bridges are located above the faces of the tetrahedron formed by the metal cations.

Such polycations exist with Pb(II) (XRD) [72] and Ni(II) (measurements of reaction kinetics) [73]. In spite of a lack of structural data, similar species are also assumed to exist for Co(II), Cd(II) and Mg(II) [30].

The compactness of the tetramers may cause magnetic coupling of the cations (Ni, Co) or metal–metal interactions (Pb). These interactions are favored by the fact that aquo and hydroxo ligands are located outside the metallic cluster. The

Table 3.3 Partial charge on the μ_2–OH bridge in dimers of divalent and trivalent elements

$z = +2$	δ(OH)	$z = +3$	δ(OH)
$[Mn_2(OH)_2(OH_2)_8]^{2+}$	−0.11	$[Fe_2(OH)_2(OH_2)_8]^{4+}$	+0.03
$[Co_2(OH)_2(OH_2)_8]^{2+}$	−0.10	$[Cr_2(OH)_2(OH_2)_8]^{4+}$	+0.01
$[Ni_2(OH)_2(OH_2)_8]^{2+}$	−0.09	$[Al_2(OH)_2(OH_2)_8]^{4+}$	0.00

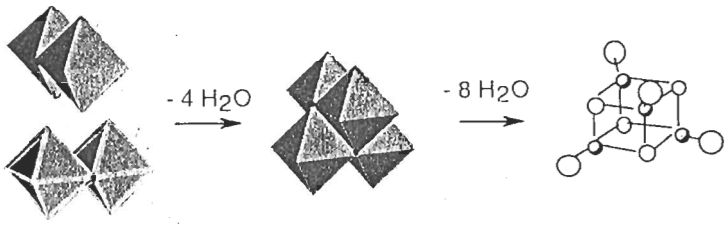

Figure 3.17 Tetrameric polycations formed by $[M_2(OH)_2(OH_2)_8]^{2+}$ dimers

coordination number of the cation can vary from 6 (Ni, Co) to 4 (Pb) via elimination of water molecules, without affecting the geometry.

Little data are available on the hydrolysis of elements like Pd^{2+} and Pt^{2+} [30]. These d^8 elements, usually larger than Ni^{2+}, are usually subject to a strong crystal field and adopt the square–planar coordination [74].

Cu(II) forms linear polycations rather than compact tetramers [75]. Owing to the Jahn–Teller effect typical of a d^9 ion in an octahedral field, the decrease in the symmetry of the coordination polyhedron ($O_h \rightarrow C_{4v}$) is due to the lengthening of two Cu bonds in *trans* (from 1.94 to 2.38 Å) [76]. These two water molecules are therefore less acidic than the others, so that hydrolysis and condensation must involve the ligands located in the equatorial plane of the coordination polyhedron (Figure 3.18). The $[Cu_2(OH)(OH_2)_{10}]^{3+}$ dimer (corner-sharing) which probably exists for pH < 3 [77] forms linear polycations $[Cu_n(OH)_{2n-2}(OH_2)_{2n+4}]^{2+}$ with edge bridges [75,78], at higher pH.

3.3.2 SOLID PHASES

Neutralization of divalent elements around $h = 2$ leads to the rapid formation of stable hydroxides $M(OH)_2$ (Table 2.1) which usually exhibit the lamellar brucite structure (CdI_2 structure) with μ_3–OH bridges on both sides of the cationic sheets [12d] (Figure 3.16).

There is no structural relationship between the compact tetramers of Figure 3.17 and the hydroxide. The nuclei of the solid phase could be planar tetramers $[M_4(OH)_8(OH_2)_8]^0$ formed by olation between neutral species $[M(OH)_2(OH_2)_4]^0$. Zero-charge dimers similar to those involved in the formation of compact tetramers can create μ_3–OH bridges as they are forming the planar tetramer. The growth of nuclei, always by olation, must take place rapidly in the plane and lead to the layered brucite-type structure seen in many hydroxides of divalent elements.

Copper hydroxide $Cu(OH)_2$ exhibits a different structure, isotypical of boehmite γ-AlOOH. Its formation may be explained by the addition of zero-charge chains $[Cu(OH)_2(OH_2)_2]^0_n$ coming from the neutralization of linear polycations (Figure 3.18). Therefore, μ_4–OH bridges form in the hydroxide [79]. These bridges where oxygen is pentacoordinated are obviously unstable towards oxolation. This is why

DropBooks

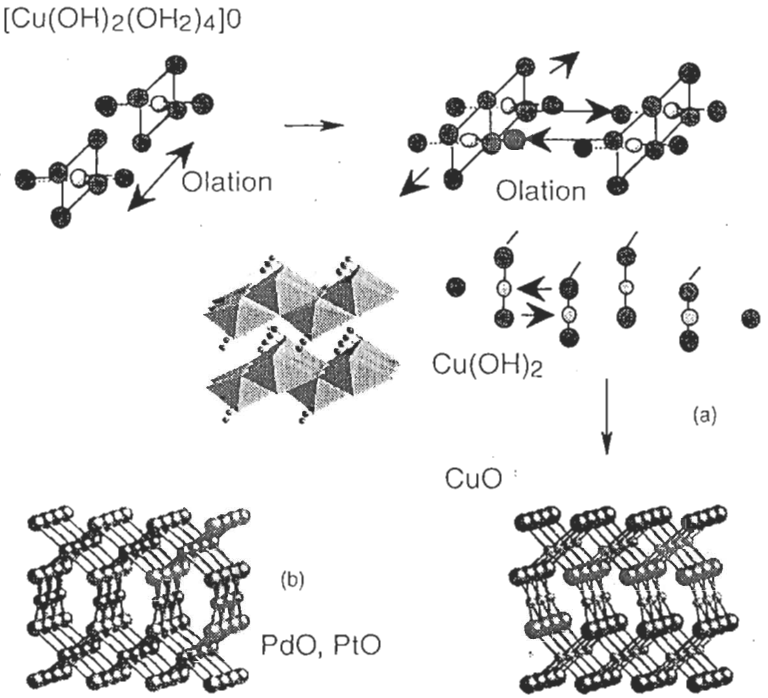

Figure 3.18 (a) Possible reaction mechanism of the formation of copper hydroxide $Cu(OH)_2$ isostructural to boehmite. In CuO_6 octahedra highly distorted by the Jahn–Teller effect, there are four Cu–OH bonds of 1.94 Å and two of 2.63 Å. (b) Structure of CuO tenorite and of PdO and PtO

the blue hydroxide tranforms into black CuO tenorite after moderate heating or at high pH [80]. Its structure is made of chains in which copper is in square–planar coordination and surrounded by μ_4–O bridges [12e]. Pd^{2+} and Pt^{2+} exhibit a similar behavior, i.e. their hydroxides are unstable. PdO and PtO have higher symmetry than CuO (Figure 3.18) [12e]. Hydroxides with the brucite structure are stable even in a strongly basic medium. They form MO oxides (NaCl structure) above 300 °C [81].

3.4 CONDENSATION OF TETRAVALENT ELEMENTS

Tetravalent elements are soluble only within narrow acidity ranges, which causes their chemistry to be complicated and poorly known. These elements belong to two families of very distinct electronegativities, the d-block and the p-block, which have very different characteristics (Table 3.4).

Table 3.4 Characteristics of a few tetravalent elements

	Ti	Zr	Hf	Ce	Th	(V)	Si	Ge	Sn	Pb
χ_M^*	1.32	1.29	1.36	1.17	1.24	(1.56)	1.74	2	1.89	1.92
Electronic configuration	.....	.....	d^0	.....	.....	(d^1)	$2p^6$	.....	d^{10}	.....
Ionic radius (Å)	0.60	0.72	0.71	1.03	1.0	(0.59)	0.26	0.54	0.69	0.77
Coordination	6	.....	(7)8	.....	.....	(5–6)	4	4–6	6	6
Solubility	.....	.....	pH < 0.5–1	.....	.....	.....	.....	.....	pH > 10–12	.....

The weakly electronegative d^0 elements are soluble only in a strongly acidic medium, where they undergo spontaneous hydrolysis. They exist as monomeric or aquo–hydroxo condensed cations. The high electronegativity of p-block elements allows their solubility only in a strongly alkaline medium, as anions or oxo or oxo–hydroxo polyanions [29,30]. This difference in behavior, which is due to the large electronegativity difference, is clearly seen in the charge–pH and charge–electronegativity diagrams (Figures 1.1 and 2.5).

The median position of the elements on the scale of formal charges on the charge–pH diagram allows their coordination by two of the three aquo, hydroxo or oxo ligand types. The hydroxo ligand is predominant in the coordination sphere over a wide pH range, and these elements have a strong propensity to precipitate. The charge-electronegativity diagram (Figure 2.3) predicts the formation of oxides (Ti, Zr, Hf, Ce, Th) and polyanions (Si, Ge, Sn, Pb). The hydroxides $M(OH)_4$ are usually unstable. They spontaneously dehydrate to form hydrated oxides $MO_2 \cdot nH_2O$ which are frequently polymorphous.

The behavior of these elements is illustrated by the difference between titanium and zirconium, and titanium and tin. The latter does exist in an alkaline medium as stannates and, as with silicates, condenses mostly by oxolation. These elements are studied in Chapter 4.

3.4.1 POLYCATIONS

Because of their high formal charge, tetravalent cations undergo spontaneous hydrolysis even in a strongly acidic medium [30]. Ti(IV) exists at pH = 0 as $[Ti(OH)(OH_2)_5]^{3+}$. The positive charge on the OH ligand ($\delta = +0.06$) does not allow condensation, and therefore this acidic ion is in equilibrium with the $[Ti(OH)_2(OH_2)_4]^{2+}$ complex. This species, in which hydroxo ligands carry a small negative charge ($\delta = -0.01$), appears to remain monomeric in solution [82,83], in equilibrium with the titanyl ion $[TiO(OH_2)_5]^{2+}$ formed via intramolecular oxolation (see Section 1.3). To the author's knowledge, however, there is no experimental evidence proving the existence of this ion in a non-complexing medium. In media of lower acidity, $[Ti(OH)_3(OH_2)_3]^+$ probably condenses, but very little data are

available concerning the condensation of titanium(IV) in solution, other than studies of $[Ti_8O_8(OH)_{12}(OH_2)_x]^{4+}$, an octamer of unknown structure [84,85].

Zr(IV) is larger than Ti(IV) and its coordination number is higher. In solution it acquires the square–antiprismatic 8-coordination. Zirconium is consequently less acidic than titanium. $[Zr(OH_2)_8]^{4+}$ ($pK \approx -0.3$) is nonetheless a strong acid that hydrolyzes spontaneously in water to form $[Zr(OH)(OH_2)_7]^{3+}$. In this complex, the charge on the hydroxo ligand is almost zero ($\delta(OH) = -0.007$). The complex is acid and forms the dihydroxo complex $[Zr(OH)_2(OH_2)_6]^{2+}$, which condenses by olation [$\delta(OH) = -0.007$] and forms, in the absence of complexing ions, a cyclical tetramer with double hydroxo bridges:

$$4[Zr(OH)_2(OH_2)_6]^{2+} \longrightarrow [Zr_4(OH)_8(OH_2)_{16}]^{8+} + 8H_2O$$

This tetramer is stable in solution. It has been characterized using various techniques, in solution [86–88] and in the solid state [89,90]. Zirconium maintains its antiprismatic coordination number 8 (Figure 3.22). The geometry and the high coordination number of Zr^{4+} ions do not allow formation of compact oligomers as in the case of trivalent and divalent elements. This is probably why the polycation forms rings and limits its condensation.

3.4.2 SOLID PHASES

Tetravalent ions are too polarizing to form stable $M(OH)_4$ hydroxides. Spontaneous dehydration via oxolation leads to the oxide MO_2 (Table 3.1)

$$M(OH)_4MO(OH)_2(OH_2) \longrightarrow MO(OH)_2 + H_2O \longrightarrow MO_2 + 2H_2O$$

There are several crystal structures for TiO_2: rutile is thermodynamically stable, whereas anatase is metastable. In these phases, oxygen lattices are hexagonal close-packed and face-centered cubic respectively. TiO_6 octahedra share edges and corners in rutile, but only share edges in anatase (Figure 3.20). The anatase–rutile transition takes place between 400 and 1200 °C. It is strongly influenced by the type of anions in the precipitation medium (Chapter 5). There are other polymorphs of TiO_2: brookite is formed under hydrothermal conditions [91], and TiO_2 B is obtained by heating $Ti_4O_7(OH)_2$ around 500 °C (itself obtained from $K_2Ti_4O_9$ in an acidic medium [92]). These phases will not be studied here.

In a poorly complexing or non-complexing medium, depending on the precipitation conditions (chlorohydric or nitric acid), titanium forms TiO_2 rutile in a highly acidic medium and at high temperatures. The anatase form is obtained for lower acid and temperature conditions (Figure 3.19) [93–95].

The behavior of titanium may be explained by taking into account that the first stage of condensation (by olation) of the zero-charge precursor $[Ti(OH)_4(OH_2)_2]^0$ is the formation of the dimer $[Ti_2(OH)_8(OH_2)_2]^0$ in which both octahedra share an edge (double hydroxo bridge). The growth of this embryo by olation with monomers

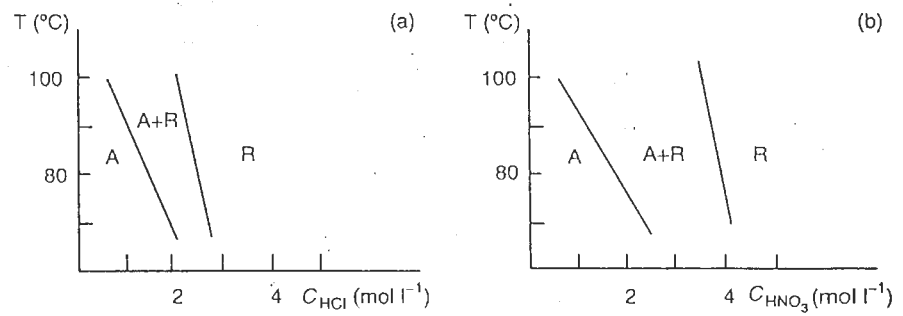

Figure 3.19 Precipitation of TiO_2 rutile R and anatase A as a function of medium acidity and temperature (a) With HCl; (b) with HNO_3. From [93]

may lead to nuclei of various geometries, for example straight or curved small chains (Figure 3.20).

Subsequent condensation of these embryos by oxolation is likely to trigger crystallization of rutile or anatase respectively. Given the respective possible positions of water molecules in the dimer, the probability that the growth of the embryo would take place through edge sharing in the same plane to form straight small chains is much smaller than the probability of edge sharing in different planes, leading to curved or bent chains. Therefore, crystallization of anatase appears far more likely than that of rutile, under any experimental conditions. However, since rutile is the thermodynamically stable phase, its formation probably takes place through a dissolution–crystallization mechanism (Ostwald ripening) at the expense of anatase. Strongly acidic media and high temperatures favor these equilibria (Figure 3.19). Indeed, anatase crystallizes as small particles at low temperature in a low acidity medium, where the solid is the least soluble. In a more acidic medium, it is probable that anatase would form first, but the higher solubility of the oxide promotes the dissolution–crystallization equilibria which then allows growth of rutile. The considerable increase in particle size with time during thermohydrolysis shows clearly that this mechanism does take place [94] (Figure 3.21). In addition, hydrolysis of $TiCl_4$ in vapor phase always exclusively forms anatase [95]. In these conditions, the absence of solvent does not allow a transition to the rutile phase.

The formation of anatase in solution appears to be linked to kinetic (rate of precipitation) and thermodynamic (solubility) considerations. Other tetravalent elements that also adopt 6-coordination (V, Sn, Pb) only form the rutile variety of their oxides [12f]. The precipitation of SnO_2 (cassiterite) probably involves a precursor similar to that of titanium, $Sn(OH)_4(OH_2)_2$, during hydrolysis of $SnCl_4$ [96,97] or acidification of stannate $[Sn(OH)_6]^{2-}$ [98] (see Section 4.3.1). It is possible that kinetics (lability) and thermodynamics (solubility) could favor the fast redissolution–crystallization equilibria, which do not allow an intermediate anatase phase to form prior to crystallization of cassiterite.

DropBooks

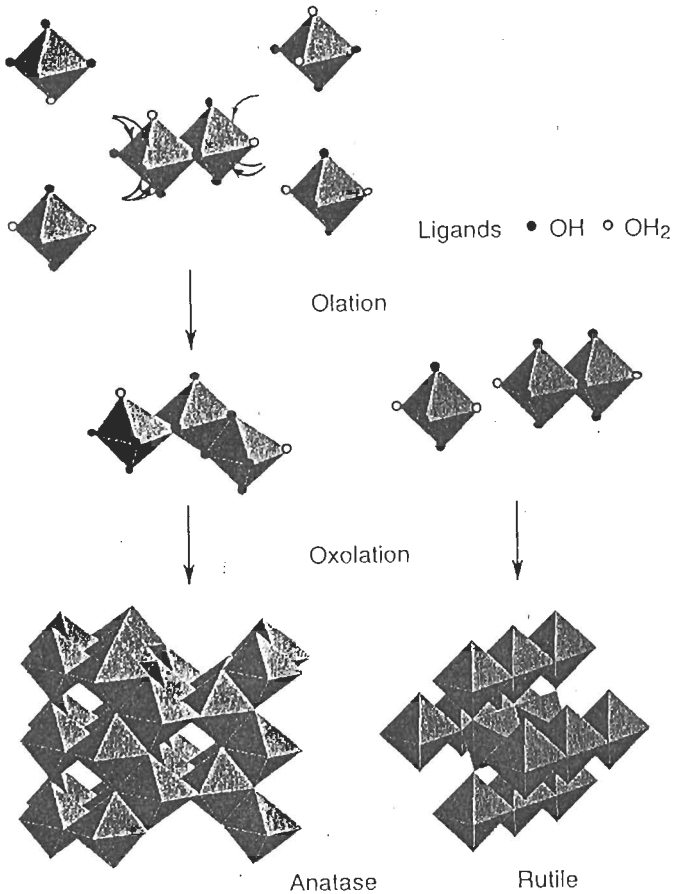

Figure 3.20 Possible formation mechanisms of TiO_2 rutile and anatase from aqueous solutions

Zirconium(IV), because of its large size and coordination number, never forms rutile but forms a gelatinous precipitate of the oxyhydroxide $ZrO_{2-x}(OH)_{2x} \cdot yH_2O$. X-ray and neutron diffractions suggest that this amorphous phase has a two-dimensional structure [99]. Crystallization around 400 °C forms the metastable tetragonal ZrO_2 phase (Figure 3.22).

Around pH 4–5, the amorphous solid could be the product of flocculation or of rapid condensation by olation of the neutralized tetramer $[Zr_4(OH)_{16}(OH_2)_8]^0$:

$$n Zr_4(OH)_{16}(OH_2)_8 \longrightarrow [Zr_4(OH)_{16}]_n + 8nH_2O$$

The unstable solid phase dehydrates slowly (slow oxolation).

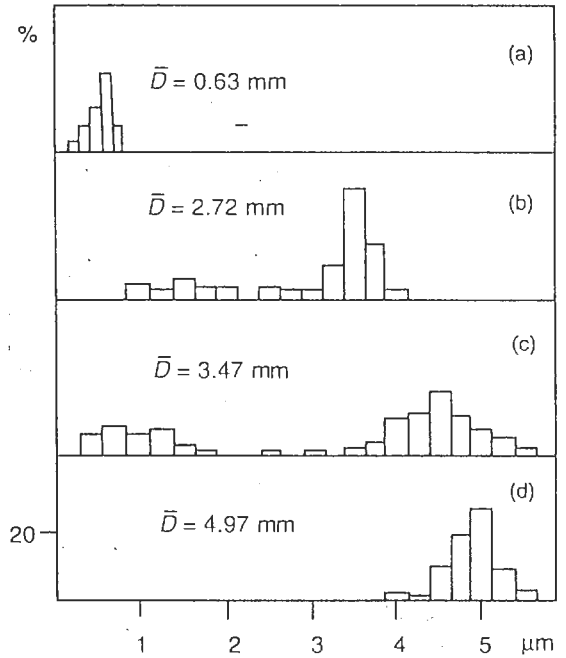

Figure 3.21 Size distribution of rutile particles as a function of the heating time at 95 °C. Duration (a) 0, (b) 1 h, (c) 3 h, (d) 6 h; (HCl 2.13 mol l^{-1}, Ti 0.22 mol l^{-1}. From [94] by permission

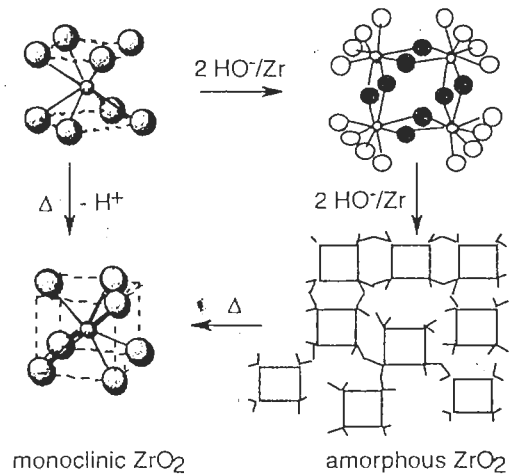

Figure 3.22 Formation of solid phases of zirconium oxides from solution, with the corresponding coordination polyhedra

Prolonged reflux of solutions around pH 2.5 leads, after about 20 h, to sols of monoclinic ZrO_2 (distorted fluorite structure) [100,101]. It does not appear that the tetramer $[Zr_4(OH)_{16}(OH_2)_8]^0$ is involved in the reaction. Indeed, the geometry of the coordination polyhedron of zirconium is not the same in the tetramer (antiprismatic, 8-coordination) and in monoclinic zirconium (7-coordination, Figure 3.22). In addition, acidification of the medium by thermohydrolysis (the pH decreases from 2.5 to 0.4 after 40 h reflux) [100] probably destroys the tetramer, and it is likely that the growth of the solid takes place via a mechanism of acidic oxolation between monomers (see Chapter 4).

Amorphous zirconia boiled in a strongly basic medium forms cubic zirconia [100]. It is stable up to 650 °C. As for monoclinic zirconia, it does not appear that the tetramer is involved in its formation.

3.5 MIXED-VALENCE SYSTEMS

The coprecipitation of different cations leads, in most cases, to segregation into separate phases (see Chapter 5). If the cations are chemically identical but exhibit various degrees of oxidation, this is not necessarily the case and mixed-valence crystalline phases may be obtained. These phases are usually not formed by one type of cation alone. The Fe(III)–Fe(II) pair is a typical example.

We have seen above (Section 3.2) that precipitation of ferric ions in solution forms an oxyhydroxide that turns into goethite (α-FeOOH) or hematite (α-Fe_2O_3) through very different reaction mechanisms. In the presence of ferrous ions, ferric ions form a spinel oxide over a wide range of compositions. Alkalinization at pH > 9 of a Fe(II)/Fe(III) = 0.5 mixture forms stoichiometric magnetite Fe_3O_4 [102–104]. Small quantities of ferrous ions [Fe(II)/Fe(III) $\geqslant$ 0.1] lead to a similar structure but containing vacancies [105,106].

Fe_3O_4 magnetite crystallizes in an inverse spinel structure where all ferrous ions and half of the ferric ions occupy half the octahedral sites of the f.c.c. oxygen lattice. The other half of the ferric ions occupy 1/8th of the tetrahedral sites [12g]. The unit cell may be written $[Fe^{3+}]_{tetra}[Fe^{3+}\ Fe^{2+}]_{octa}O_4$. The spinel lattice can accommodate large non-stoichiometries, from Fe_3O_4 to γ–Fe_2O_3 (maghemite). The latter may also be written $[Fe^{3+}]_{tetra}[Fe^{3+}_{5/3}L_{1/3}]_{octa}O_4$ (where L represents cation vacancies in the octahedral sublattice). The octahedral sublattice is subject to electron delocalization between Fe(II) and Fe(III) [107–109]. At room temperature, Mössbauer spectroscopy has shown octahedral cations with a +2.5 charge. The fast electronic exchange between Fe(III) and Fe(II) in the solid seems to be responsible for the spinel crystallization.

The crystallization of magnetite during precipitation of a stoichiometric mixture of Fe(III) and Fe(II) is too rapid to allow an analysis of the mechanism (Figure 3.23e). Crystallization is slower for substoichiometric mixtures.

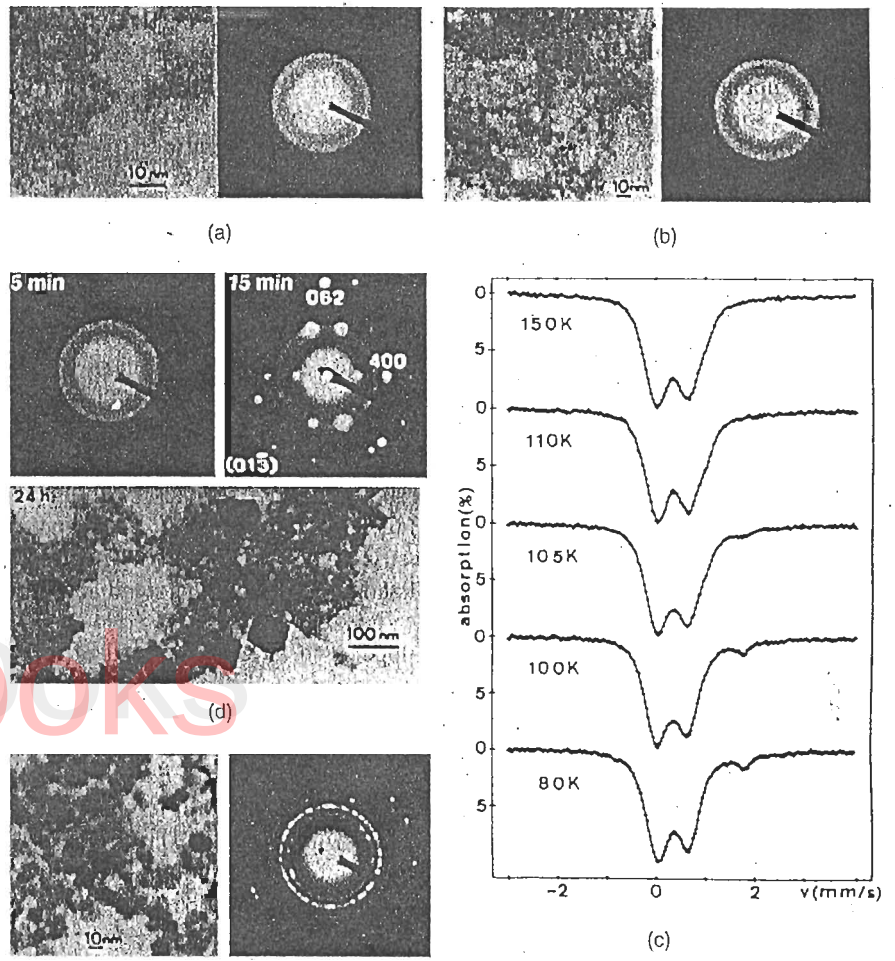

Figure 3.23 Micrographs and electron diffraction patterns of suspensions x = Fe(II)/Fe(III) for various reaction times (a) $x = 0$, $t = 5$ min (ferric ferrihydrite); (b) $x = 0.15$, $t = 1$ min; (c) Mössbauer spectra at various temperatures for $x = 0.15$ and $t = 1$ min; (d) $x = 0.15$, $t = 5$ min, $t = 15$ min, $t = 24$ h; (e) $x = 0.5$, $t = 1$ min. Reprinted with permission from [106]. Copyright 1992 American Chemical Society

The Fe(II)/Fe(III) = 0.15 mixture initially forms particles about 25–30 Å in diameter, very similar to the particles observed in the ferric gel or the ferrihydrite (Section 3.2.3, Figure 3.23a). The wide diffraction rings (Figure 3.23b) suggest a local two-dimensional organization of the anions and some correlation between the layers. At low temperatures, between 80 and 105 K, the Mössbauer spectra exhibits

DropBooks

two components due to Fe(III) and Fe(II) ions. Above 105 K, the Fe(II) contribution disappears and a valence 2.5 contribution appears (Figure 3.23c). The relative area of this component is double that of Fe(II) below 105 K, indicating that all ferrous ions in the solid are involved in the electron exchange before a long-range spinel lattice forms [106]. Crystallization occurs during room-temperature ageing of the non-stoichiometric material. The presence of Fe(II) appears necessary for the formation of the spinel structure, which also seems stabilized by the electron delocalization. Other divalent ions (Mn, Zn, Cu, Ni, Co) that do not cause electron delocalization may also form the spinel lattice, but they usually require large M^{2+} concentrations and higher processing temperatures [111–113].

Ageing of a suspension of the solid Fe(II)/Fe(III) = 0.15 causes the formation of two distinct families of particles [105]. The first type are Fe(II)-deficient [Fe(II)/Fe(III) $\approx$ 0.07] and preserve their original size. The other type grow to 1000–1500 Å after about 24 h (Figure 3.23d) and are richer in Fe(II) [Fe(II)/Fe(III) $\approx$ 0.33]. These large particles are formed via a process of dissolution–crystallization, and their composition indicates that mixed Fe(III)–Fe(II) complexes, with Fe(II)/Fe(III) = 0.3, are involved in their growth. For Fe(II)/Fe(III) < 0.3, both types of particle coexist in various proportions because Fe(II) is immediately extracted from the solid via the dissolution–crystallization equilibria that feed the large particles.

The driving force behind crystallization appears to be the formation of mixed ferric–ferrous entities rich in Fe(II), which ensure the stability of the structure. The crystallization of small particles poor in Fe(II) is the result of *in situ* dehydration and local structural reorganization without change in particle size. This type of transformation requires a minimum Fe(II) content because, if Fe(II)/Fe(III) is smaller than 0.1 in the entire mixture, small 30 Å particles form temporarily but transform into goethite after a few weeks [105]. When Fe(II)/Fe(III) reaches 0.3, all the Fe(III) may now be involved in the processes of redissolution. The particles grow but they remain homogeneous in size and composition.

The development of the inverse spinel structure of magnetite can be described as starting with tetramers such as $[Fe_4(OH)_{10}(OH_2)_6]^0$, for example. They are ferric–ferrous compounds formed by the dissolution equilibria in the initial material (Figure 3.24). In such a very compact tetramer containing only μ_3–OH, the electron delocalization is optimized. The Fe(II)–Fe(III) electron transfer is allowed by the overlap of d orbitals, which requires short metal–metal distances [110]. This entity may be a model of the nuclei of the solid. Condensation by olation forms chains and planes rather rapidly, and the connection between planes can be made by any excess octahedral ferric ions $Fe(OH)_3(OH_2)_3$. They act as hinges, forming Fe–O–Fe bridges by oxolation (Figure 3.24). This imposes steric constraints on Fe(III) ions. Since there is no crystal field stabilization energy, they can easily switch to a coordination number 4 characteristic of the inverse spinel structure. This process is somewhat similar to the one involved in the formation of the Al_{13} polycations (see Section 3.2.2).

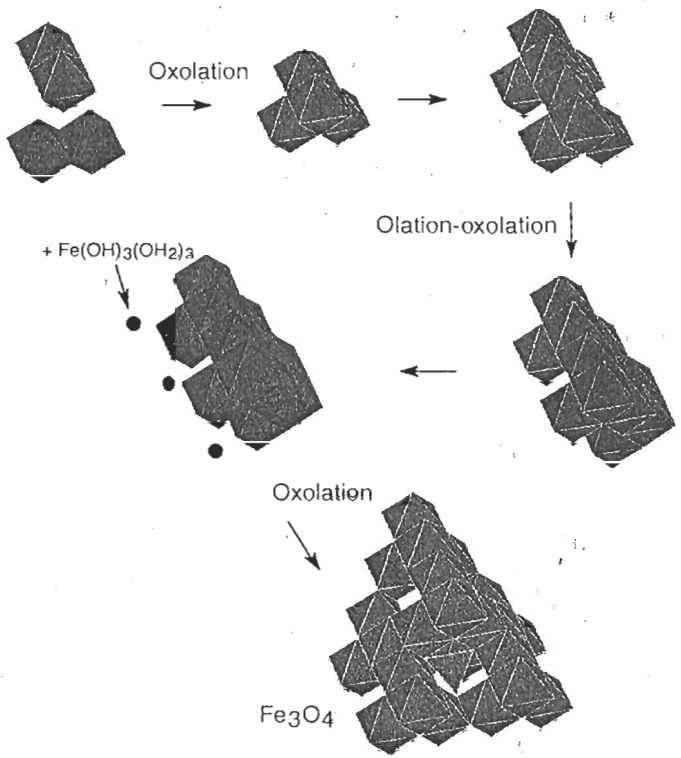

Figure 3.24 Possible reaction mechanism for the formation of the spinel lattice of Fe_3O_4 magnetite from a solution of ferric and ferrous ions

The Fe(II)–Fe(III) electron transfers, which allow the formation of iron oxide spinel, also play a role in the crystallization of the ferric gel adsorbed on the surface of colloidal particles of magnetite [114] (see Chapter 9). The electron mobility in the magnetite lattice is also responsible for the transformation to γ-Fe_2O_3 maghemite (see Chapter 9).

Ferrous ions act as dehydrating and structuring agents for ferric ions. Indeed, dehydration of ferrous hydroxide is not spontaneous. Dehydration of ferric gels is slow. The electron delocalization occurring during the association of both types of cation alters their behavior and allows the stabilization of a particular structure.

The formation of solid phases and the behavior of some elements may thus be interpreted directly from the analysis of phenomena in solution. In Chapter 5, we shall see that modification of the nature of the coordination sphere of the precursor by complexing in solution can greatly influence reactivity and allows control of the

formation of other crystalline phases or modification of the morphology of the particles.

3.6 REFERENCES

1. C.L. Rollinson, *Chemistry of the Coordination Compounds*, Vol. 131, Am. Chem. Soc. Master Ser., Bailar Ed., New York (1956), p. 148.
2. M. Eigen, *Pure and Appl. Chem.* 6, 97 (1963).
3. H. Kruger, *Chem. Soc. Rev.* 11, 227 (1982).
4. F. Basolo, R.G. Pearson, *Mechanisms of Inorganic Reactions*, 2nd ed., J. Wiley & Sons, New York (1958).
5. M. Ardon, A. Bino, *Structure and Bonding*, Vol. 65, 1, Springer-Verlag, Berlin (1987).
6. M.N. Jones, *Elementary Coordination Chemistry*, Prentice Hall, Englewood Cliffs (1964), pp. 23–26.
7. K.F. Purcell, J.C. Kotz, *Inorganic Chemistry*, Holt-Saunders, Japan (1985), p. 684.
8. V. Baran, *Coord. Chem. Rev.* 6, 65 (1971).
9. V.A. Maroni, T.G. Spiro, *Inorg. Chem.* 7, 183 (1968).
10. T.G. Spiro, D.H. Templeton, A. Zalkin, *Inorg. Chem.* 8, 856 (1968).
11. H. Stünzi, W. Marty, *Inorg. Chem.* 22, 2145 (1983).
12. A.F. Wells, *Structural Inorganic Chemistry*, 5th ed., Clarendon Press, Oxford (1991): (a) p. 638; (b) p. 544; (c) p. 635; (d) p. 258; (e) p. 539; (f) p. 540.
13. H. Stünzi, L. Spiccia, F.P. Rotzinger, W. Marty, *Inorg. Chem.* 28, 66 (1989).
14. D.L. Segal, *J. Chem. Techn. Biotechnol.* 34A, 25, 355 (1984).
15. G.H. Khoe, P.L. Brown, R.N. Sylva, R.G. Robins, *J. Chem. Soc. Dalton Trans.* 1901 (1986).
16. C.M. Flynn Jr, *Chem. Rev.* 84, 31 (1984).
17. M.A. Blesa, E. Matijevic, *Adv. Colloid Interface Sci.* 29, 173 (1989).
18. G. Johansson, *Arkiv. Kemi* 20, 305 (1963).
19. J.W. Akitt, J.M. Elders, *J. Chem. Soc. Dalton Trans.* 1347 (1988).
20. A.R. Thompson, A.C. Kunwar, H.S. Gutowsky, E. Oldfield, *J. Chem. Soc. Dalton Trans.* 2317 (1987).
21. L. Spiccia, W. Marty, *Inorg. Chem.* 25, 266 (1986).
22. L. Spiccia, H. Stoeckli-Evans, W. Marty, R. Giovanoli, *Inorg. Chem.* 26, 474 (1987).
23. L. Spiccia, W. Marty, R. Giovanoli, *Inorg. Chem.* 27, 2660 (1988).
24. K.K. Singh, P.R. Sarode, P. Ganguly, *J. Chem. Soc. Dalton Trans.* 1895 (1983).
25. R. Giovanoli, W. Stadelman, W. Feitknecht, *Helv. Chim. Acta*, 56, 839 (1973).
26. M. Axelos, D. Tchoubar, J.Y. Bottero, F. Fiessinger, *J. Physique* 46, 1587 (1985).
27. J.Y. Bottero, M. Axelos, D. Tchoubar, J.M. Cases, J.J. Fripiat, F. Fiessinger, *J. Colloid Interface Sci.* 117, 47 (1987).
28. R.F. Giese Jr, *Acta Cryst.* B32, 1719 (1976).
29. (a) G. Charlot, L'Analyse Qualitative et les Réactions en Solution, 6th ed., Masson, Paris (1969); (b) L.G. Sillen, A.E. Martell, *Stability Constants of Metal-Ion Complexes*, Special Publ. No. 17, The Chemical Society, London (1964).
30. C.F. Baes, R.E. Mesmer, *The Hydrolysis of Cations*, J. Wiley & Sons, New York (1976).
31. M. Thompson, R.E. Connick, *Inorg. Chem.* 20, 2279 (1981).
32. F.P. Rotzinger, H. Stünzi, W. Marty, *Inorg. Chem.* 25, 489 (1986).
33. L. Mønsted, O. Mønsted, J. Springborg, *Inorg. Chem.* 24, 3496 (1985).
34. T. Merakis, L. Spiccia, *Aust. J. Chem.* 42, 1579 (1989).
35. J.E. Finholt, M.E. Thompson, R.E. Connick, *Inorg. Chem.* 20, 4151 (1981).
36. H. Stünzi, F.P. Rotzinger, W. Marty, *Inorg. Chem.* 23, 2160 (1984).

37. P.L. Brown, R.N. Sylva, G.E. Batley, J. Ellis, *J. Chem. Dalton Trans.* 1967 (1985).
38. G. Johansson, *Acta Chem. Scand.* 16, 403 (1962).
39. J.H.A. Van Der Woude, P.L. De Bruyn, *Colloids and Surf.* 8, 55 (1983).
40. A. Coda, B. Kamenar, K. Prout, J.R. Carrothers, J.S. Rollett, *Acta Cryst.* B31, 1438 (1975).
41. C.C. Ou, R.G. Wollmann, D.N. Hendrickson, J.A. Potenza, H.J. Schugar, *J. Am. Chem. Soc.* 100, 4717 (1978).
42. S.J. Lippard, *Angew. Chem. Int. Ed. Engl.* 27, 344 (1988).
43. J.B. Vincent, G.L. Olivier-Lilley, B.A. Averill, *Chem. Rev.* 90, 1447 (1990).
44. R.G. Wilkins, *Chem. Soc. Rev.* 171 (1992).
45. K.S. Hagen, *Angew. Chem. Int. Ed. Engl.* 31, 1010 (1992).
46. H.T. Evans, *Inorg. Chem.* 5, 967 (1966).
47. J.M. Combes, A. Manceau, G. Calas, J.Y. Bottero, *Geochemica Cosmochem. Acta* 53, 583 (1989).
48. J.H.A. Van Der Woude, J.B. Rijnbout, P.L. De Bruyn, *Colloids and Surf.* 11, 391 (1984).
49. J.H.A. Van Der Woude, P.L. De Bruyn, J. Pieters, *Colloids and Surf.* 9, 173 (1984).
50. S.L. Heath, A.K. Powell, *Angew. Chem. Int. Ed. Engl.* 31, 191 (1992).
51. L. Spiccia, W. Marty, R. Giovanoli, *Helv. Chim. Acta* 70, 1737 (1987).
52. L. Spiccia, W. Marty, *Inorg. Chem.* 25, 266 (1987).
53. I.P. Saraswat, A.C. Vajpei, *J. Mater. Sci. Lett.* 3, 515 (1984).
54. V. Swayambunathan, Y.X. Liao, D. Meisel, *Langmuir* 5, 1423 (1989).
55. P.H. Hsu, *Clays Clay Minerals* 36, 25 (1988).
56. J.W. Akitt, W. Gessner, *J. Chem. Soc. Dalton Trans.* 147 (1984).
57. G. Ervin Jr, *Acta Cryst.* 5, 103 (1952).
58. R.A. Eggleton, R.W. Fitzpatrick, *Clays Clay Minerals* 36, 111 (1968).
59. M. Magini, *J. Inorg. Nucl. Chem.* 39, 409 (1977).
60. U. Schertmann, E. Murad, *Clays Clay Minerals* 31, 277 (1983).
61. J.H. Johnston, D.G. Lewis, *Geochemica Cosmochem. Acta* 47, 1823 (1983).
62. J.M. Combes, A. Manceau, G. Calas, *Geochemica Cosmochem. Acta* 54, 1083 (1990).
63. W.R. Fischer, U. Swertmann, *Clays Clay Minerals* 23, 33 (1975).
64. T. Misawa, K. Hashimoto, S. Shimodaira, *Corros. Sci.* 14, 131 (1974); S. Hamada, K. Kuma, *Bull. Chem. Soc. Jpn* 49, 3695 (1976).
65. L.S. Dent Glasser, R. Giovanoli, *Acta Cryst.* B28, 519 (1972).
66. W.H. Gitzen, *Alumina as a Ceramic Material*, American Ceramic Society, Columbus, Ohio (1970).
67. B.R. Baker, R.M. Pearson, *J. Catal.* 33, 265 (1974).
68. B.E. Yoldas, *J. Appl. Chem. Biotech.* 23, 409 (1977).
69. W.C. Hamilton, J.A. Ibers, *Acta Cryst.* 16, 1209 (1963).
70. A.N. Christensen, *Inorg. Chem.* 5, 1452 (1966).
71. A.N. Christensen, *Acta Chem. Scand.* A30, 133 (1976).
72. G. Johansson, A. Olin, *Acta Chem. Scand.* 22, 3197 (1968).
73. G.B. Kolski, N.W. Kildahl, D.W. Margerum, *Inorg. Chem.* 8, 1211 (1969).
74. F.A. Cotton, G. Wilkinson, *Advanced Inorganic Chemistry*, 3rd ed., Interscience Pub., New York (1972), p. 1031.
75. D.D. Perrin, *J. Chem. Soc.* 3189 (1960).
76. H. Ohtaki, T. Yamagushi, M. Maeda, *Bull. Chem. Soc. Jpn* 49, 701 (1976).
77. E. Neher-Neumann, *Acta Chem. Scand.* A38, 517 (1984).
78. R.N. Sylva, M.R. Davidson, *J. Chem. Soc. Dalton Trans.* 232 (1979).
79. H. Jaggi, H.R. Ostwald, *Acta Cryst.* 14, 1041 (1961).
80. H.B. Weiser, *J. Phys. Chem.* 27, 501 (1923).
81. I.F. Hazell, R.J. Irving, *J. Chem. Soc. (A)* 669 (1966).

DropBooks

82. J.D. Ellis, A.G. Sykes, *J. Chem. Soc. Dalton Trans.* 537 (1973).
83. J.D. Ellis, A.K. Thompson, A.G. Sykes, *Inorg. Chem.* **15**, 3172 (1976).
84. H. Einaga, *J. Chem. Soc. Dalton Trans.* 1917 (1979).
85. H. Einaga, Y. Komatsu, *J. Inorg. Nucl. Chem.* 43, 2443 (1981).
86. J.S. Johnson, K.A. Kraus, *J. Am. Chem. Soc.* **78**, 3937 (1956).
87. G.M. Muha, P.A. Vaughan, *J. Chem. Phys.* 33, 194 (1960).
88. M. Aberg, *Acta Chem. Scand.* B31, 171 (1977).
89. A. Clearfield, P.A. Vaughan, *Acta Cryst.* **9**, 555 (1956).
90. T.C.W. Mak, *Can. J. Chem.* **46**, 3493 (1968).
91. I. Keesmann, *Z. Anorg. Allg. Chem.* **346**, 30 (1966).
92. R. Marchand, L. Brohan, M. Tournoux, *Mat. Res. Bull.* **15**, 1129 (1980).
93. L.I. Bekkerman, I.P. Dobrovol'skii, A.A. Ivakin, *Russ. J. Inorg. Chem.* **21**, 223 (1976).
94. E. Narita, H. Takeuchi, N. Horiguchi, T. Okabe, *Bull. Chem. Soc. Jpn* **57**, 1388 (1984).
95. L.I. Segrov, *Russ. J. Phys. Chem.* 4 (1963).
96. M. Ocana, E. Matijevic, *J. Mater. Res.* 5, 1083 (1990).
97. R.S. Hiratsuka, S.H. Pulcinelli, C.V. Santilli, *J. Non Cryst. Solids* **121**, 76 (1990).
98. J.D. Donalson, M.J. Fuller, *J. Inorg. Nucl. Chem.* 30, 1083 (1968).
99. J. Livage, K. Doi, C. Mazières, *J. Am. Ceram. Soc.* **51**, 349 (1968).
100. A. Clearfield, *Inorg. Chem.* 3, 146 (1964).
101. A. Clearfield, *Rev. Pure and Appl. Chem.* 14, 91 (1964).
102. W.C. Elmore, *Phys. Rev.* 54, 309 (1938).
103. R. Massart, *C.R. Acad. Sc. Paris* 291C, 1 (1980).
104. J.P. Jolivet, R. Massart, J.M. Fruchart, *Nouv. J. Chim.* 7, 325 (1983).
105. J.P. Jolivet, P. Belleville, E. Tronc, J. Livage, *Clays Clay Minerals* 40, 531 (1992).
106. E. Tronc, P. Belleville, J.P. Jolivet, J. Livage, *Langmuir* 8, 313 (1992).
107. C. Kittel, *Introduction of Solid State Physics*, J. Wiley & Sons, New York (1966).
108. G.C. Allen, P.M. Tucker, P.K. Wild, *Philos. Mag.* B46, 411 (1982).
109. C. Gleitzer, J.B. Goodenough, *Structure and Bonding*, Vol. 61, Springer-Verlag, Berlin (1985), p. 1.
110. D.M. Shermann, *Phys. Chem. Miner.* **14**, 355 (1987).
111. R.M. Cornell, *Clay Miner.* 23, 329 (1988).
112. R.M. Cornell, R. Giovanoli, *Polyhedron* 7, 385 (1988).
113. R.M. Cornell, R. Giovanoli, W. Schneider, *J. Chem. Tech. Biotechnol.* **53**, 73 (1992).
114. P. Belleville, J.P. Jolivet, E. Tronc, *J. Livage, J. Colloid Interface Sci.* **150**, 453 (1992).
115. W.D. Birch, A. Pring, A. Reller, H. Semalle, *Naturwissenschaft* 79, 509 (1992); *Am. Min.* 78, 827 (1993).

4

Oxolation: Polyanions and Solid Phases

Oxolation is the process of creation of oxo bridges between cations that do not have aquo ligands in their coordination sphere [1]. Therefore, this reaction occurs only with elements of high formal charge ($z \geqslant 4$), which exist in a dilute alkaline or neutral medium as oxo anions or oxo–hydroxo monomers [Si(IV), Cr(VI)] (see Section 1.1, charge–pH diagram).

Some of these elements (Section 2.2, Figure 2.5), such as Sn(IV) and Sb(V), exist as monomeric hydroxo forms in an alkaline medium $\{[Sn(OH)_6]^{2-}, [Sb(OH)_6]^{-}\}$ [2]. After acidification, the aquo ligand appears in the coordination sphere of the cation and the initial condensation steps of $[Sn(OH)_4(OH_2)]^{-}$, $[Sn(OH)_4(OH_2)_2]^{0}$ and $[Sb(OH)_5(OH_2)]^{0}$ take place by olation. However, because the coordination sphere contains one or two aquo ligands only, most of the condensation process in fact occurs by oxolation.

The case of boron(III), which also condenses via oxolation, is somewhat unique. In an alkaline medium, boron exists as borate $[B(OH)_4]^{-}$, but it is one of the few elements to undergo a coordination number reduction upon acidification, leading to monomeric boric acid $B(OH)_3$ [3]. Therefore, condensation between boric acid and borates takes place by oxolation only.

Transition metals of high formal charge, such as V(V), Nb(V), W(VI) and Mo(VI), also undergo oxolation. However, their behavior is also somewhat peculiar, because the coordination of tetraoxo species $[MO_4]^{(8-z)-}$ changes from tetrahedral in an alkaline medium to octahedral at some stage of the acidification and condensation processes [2].

Such examples are evidence of a large diversity in behavior. The specific behavior of some typical elements will now be examined.

4.1 OXOLATION REACTION

The ligands of an anionic form carry a highly negative partial charge. For an oxo bridge to form between such entities where the maximum cation coordination is

satisfied, a substitution must occur, which implies formation of a leaving group such as a water molecule. This molecule does not exist in the coordination sphere of the initial entities. Therefore, it is likely that the oxolation reaction occurs via a two-step SN_2 associative mechanism:

(i) nucleophilic addition with formation of an ol bridge:

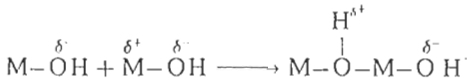

leading to an unstable transition state because of the coordination increase.

(ii) proton transfer from the ol bridge to a terminal OH ligand, forming a leaving aquo ligand:

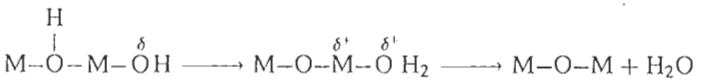

The leaving water is present initially in the coordination sphere as an OH ligand and not as coordination water (aquo ligand). This tends strongly to tie the oxolation rates to the acidity of the medium, contrary to what happens in the case of olation. The reaction can be catalyzed, and it is possible to distinguish basic, acid or neutral oxolation from a kinetics standpoint. Neutral oxolation is usually the slowest of the three, as evidenced in the case of silicates. Their condensation rates are 10 times faster at pH 1 than at pH 2, the slowest at pH 3 and 100 times faster at pH 6 than at pH 4 [4].

Basic catalysis is due to hydroxyl ions from the medium reacting on positively charged centers of the reactants [5], such as the cations themselves, or the protons of the hydroxo ligands of the cation. Since we are considering oxo–hydroxo or hydroxo forms of cations with saturated coordination, the protons themselves will be attacked by the hydroxyls. The negative charge on the nucleophilic oxygen is increased, and the first step of oxolation is eased. This is illustrated by the following concerted mechanism involving hydroxyl ions and water molecules:

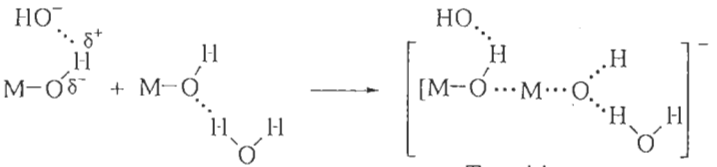

Transition state

$$\longrightarrow \quad M{-}O{-}M + HO^- + 2H_2O$$

An increase in pH has two opposite effects. It strengthens the catalysis by favoring deprotonation of hydroxo groups, thereby increasing their nucleophilic strength. In

doing so, it also decreases the number of hydroxo ligands in the precursors (the hydrolyis rate increases). Since the number of groups decreases, the progression of the reaction, and hence the growth, is limited.

Acid catalysis of oxolation takes place on the negatively charged centers of the reactants. Protonation of hydroxo ligands facilitates the formation of expendable aquo ligands in the transition state, and strengthens the acidity of the ol bridge. The second step of the reaction is therefore favored:

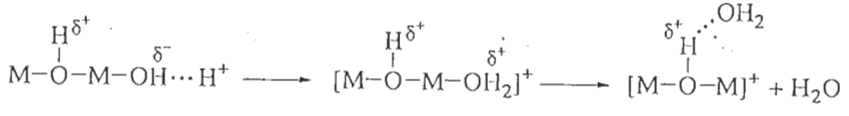

Transition state

$$\longrightarrow \quad M{-}O{-}M + H_3O^+$$

If the medium acidity increases, the formation of positively charged aquo–hydroxo species is possible. Such species are even more prone to nucleophilic attack by the hydroxo forms. Elimination of the proton, which allows a decrease in the charge of the transition state, is also favored. However, an excessive amount of acid inhibits the nucleophilic power of the hydroxo ligand and therefore limits the reaction.

Oxolation may occur over a wide range of pH. The reaction rate will be at a minimum when the reactants carry no charge (neutral oxolation). This is not the case for the olation reaction, which involves aquo–hydroxo forms for which condensation rates are limited only by the lability of the water molecule.

Some high-charge, small-size transition metals exist in solution as tetraoxo forms for which the maximum coordination is not satisfied [V(V), Mo(VI), W(VI)]. At a certain stage, which depends on the metal, condensation is associated with an increase in the coordination number. Then it takes place by nucleophilic addition, as described in Section 4.3.

It has been established (see Chapter 3) that, for cationic species, condensation by olation is always limited. The same applies to condensation by oxolation between anionic or neutral forms.

(i) Condensation may stop because all hydroxo ligands have reacted and there are no expendable groups left on the growing polymer. Condensation is limited by the acidification rate of the precursors, as in the case of vanadates acidified at $H^+/V = 1$:

$$2[VO_3(OH)]^{2-} \longrightarrow [V_2O_7]^{4-} + H_2O$$

Further condensation of pyrovanadates requires higher acidification. For $H^+/V = 2$, the reaction proceeds until the formation of metavanadates:

$$4[VO_2(OH)_2]^- \longrightarrow [V_4O_{12}]^{4-} + 4H_2O$$

DropBooks

(ii) Hydroxo ligands of a condensed species may become excessively acid. The reaction stops, again for lack of expendable groups:

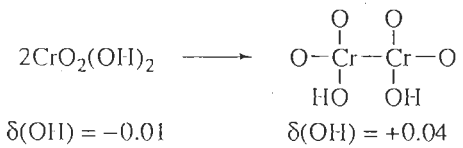

The dimer is a strong acid ($[Cr_2O_7]^{2-}$, $2H^+$). Hydroxo groups are dissociated and condensation stops, leaving polyanions in the solution. This is also observed in the case of V(V), Mo(VI), W(VI), etc. Dehydration causes an increase in the average electronegativity, and hence an increase in the partial charge on hydroxo ligands and the loss of their nucleophilic power.

One may anticipate that the oxolation reaction between $[MO_NH_{2N-z}]^0$ zero-charge species would not be limited and would lead to the formation of an oxide, in a manner similar to the formation of hydroxides via olation (Chapter 3). This is not the case because hydroxo ligands always become strongly acidic at some stage of the condensation. The oxolation reaction *alone* always leads to strong polyacids which, depending on their degree of condensation, are either soluble (in the case of high formal charge transition metals) or insoluble [Si(IV)] (see Section 2.2). Strongly acidic oxides, of varying levels of hydration, are formed whenever condensation begins by an olation step [Sn(IV), Sb(V) and some high formal charge transition elements]. This is a significant difference in behavior between oxo–hydroxo and aquo–hydroxo forms.

The most widely encountered oxo bridge is the μ_2–O bridge, which corresponds to corner-sharing polyhedra. This is the case for chromates, borates, phosphates and silicates (CN = 4), and for niobates and antimonates (CN = 6).

These few generalities will now be discussed further in a few characteristic examples.

4.2 p-BLOCK ELEMENTS HAVING THEIR MAXIMUM COORDINATION IN THE MONOMER

4.2.1 Si(IV): SILICATES

In most of its oxygenated compounds, silicon is found in coordination 4. The basic unit is the SiO_4 tetrahedron which may share corners but cannot share edges [6]. Sharing edges would create exceedingly high Si–Si repulsions. Silicates are very well known in the solid state, but their chemistry in solution is still poorly known owing to the large number of species and the complexity of the equilibria involved [2,4].

Silicate solutions are obtained by dissolving metasilicate Na_2SiO_3, which is made of infinite chains of SiO_4 tetrahedra [6]. Breaking of the chains is almost immediate in water, and dissolution is fast.

Table 4.1 Characteristics of monomeric silicates in solution

s	From	pK	χ	δ(OH)	δ(Si)
$h = 6$	$[SiO_2(OH)_2]^{2-}$		2.10	−0.55	+0.20
		13			
$h = 5$	$[SiO(OH)_3]^-$		2.37	−0.30	+0.35
		9.9			
$h = 4$	$[Si(OH)_4]^0$		2.58	−0.12	+0.47
		2			
$h = 3$	$[Si(OH)_3(OH)_2]^+$		2.74	+0.03	+0.56

The possible silicic monomers in solution are summarized in Table 4.1. By convention, the hydrolysis ratio h is expressed with respect to the aquo form chosen as a reference, whether it exists or not (see Section A.3.2).

The $h = 6$ species is a very strong base which exists in water only for very alkaline medium. Conversely, the $h = 3$ species is a strong acid existing only in very acidic medium [2].

At pH ≈ 12 (hydrolysis ratio $h = 5.5$), condensation of $h = 5$ and $h = 6$ species is limited to the dimer (pyrosilicate) made of two corner-sharing tetrahedra:

$$[SiO(OH)_3]^- + [SiO_2(OH)_2]^{2-} \longrightarrow [Si_2O_4(OH)_3]^{3-} + H_2O$$

The dimer is stable because of the exceedingly weak electrophilic character of the cation ($\chi = 2.183$, $\delta(Si) = +0.25$, $\delta(OH) = -0.22$).

The $h = 5$ form [$\delta(OH) \ll 0$, $\delta(Si) > 0.3$] is highly prone to condensation:

$$2[SiO(OH)_3]^- \longrightarrow [Si_2O_3(OH)_4]^{2-} + H_2O$$

In the dimer, $\chi = 2.346$, $\delta(OH) = -0.33$ and $\delta(Si) = +0.34$. Condensation should not stop at this stage. Corner-sharing tetrahedra tend to form rings and lead to oligomers with degrees of condensation between 3 and 8 [7]. The cyclic tetramer is the most abundant species for pH between 11 and 12. These species are the metasilicates. Within this pH range, equilibria are fast owing to the basic catalysis of oxolation.

The structure and distribution of polysilicates in solution has been determined, prior to the advent of ^{29}Si NMR, using a very elegant method, trimethylsilylation [9]. The technique converts labile silicates into inert derivatives by abrupt acidification in the presence of trimethylsilane chloride $ClSi(CH_3)_3$. Silicates are converted into the corresponding silicic acids and the very reactive silanol end groups are rendered inert by the trimethyl silanes:

$$-Si-O^- + H^+ \longrightarrow -Si-OH \xrightarrow{ClSi(CH_3)_3} -Si-O-Si-Me_3 + HCl$$

Assuming that such reactions do not trigger structural rearrangements of the silicates, the distribution of the silylated species reflects the composition of the initial

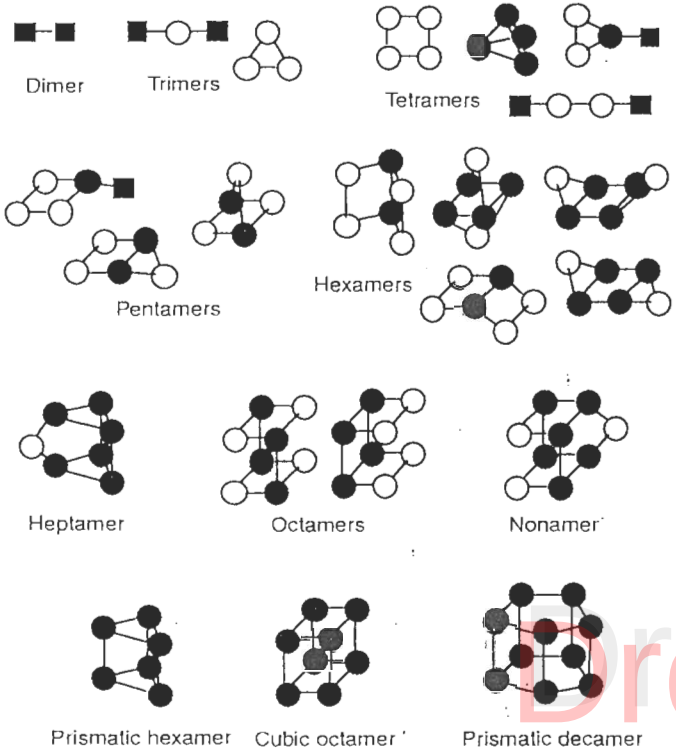

Figure 4.1 Main structures of silicates in aqueous solution (silicon concentration 1.5 mol l^{-1}, KOH/Si = 1, 22 °C). SiO_4 tetrahedra, shown using different symbols, share 1 (■), 2 (○) or 3 (●) corners. The double cages are stabilized in solution by tetraalkylammonium cations. Reproduced from [7] with permission

solution. Of course, acidification is the critical step. The compounds formed are extracted from the aqueous phase in an appropriate solvent [hexamethyldisiloxane $(CH_3)_6Si_2O$] and analyzed using gas phase chromatography for the most volatile derivatives, or using gel permeation and mass spectrometry for the heavier ones.

High resolution NMR techniques have allowed *in situ* characterization of concentrated solutions [7,9–14]. Figure 4.1 shows the structure of the most probable species.

The nature of the cation in solution has a profound influence on the structure of cyclical oligomers. With tetraalkylammonium ions $[NR_4]^+$ (R = CH_3, C_2H_5, C_3H_7, etc.), cages made of double cycles of 3–5 SiO_4 tetrahedra are stabilized and have been observed in solution [15–20]. Tetramethylammonium hydroxide promotes formation of the cubic octamer $[Si_8O_{20}]^{8-}$ (Figure 4.1), which is obtained indirectly after the prismatic hexamer $[Si_6O_{15}]^{6-}$. This species corresponds to the final evolution of the solution in the presence of tetraethylammonium hydroxide. If tetrabutylammonium hydroxide is used, the decamer $[Si_{10}O_{25}]^{10-}$ seems to form preferably.

The crystalline structure of these various species has been determined via X-ray diffraction, using various ethylenediamine complexes of transition metals as cations.

The effect of tetraalkylammonium ions has not been clearly determined yet. It could be due to the particular structuring role of this type of ions on the solvent, and/or to a polarization effect on the anions. In the presence of $[N(CH_3)_4]^+$, 80% of silicates exist in solution as the double cycles of four silicon atoms ($[Si_8O_{20}]^{8-}$). The addition of Na^+ swiftly replaces the cubic units with simple $[Si_4O_{12}]^{4-}$ cycles. Transverse bonds between cycles are broken, probably because of the strong affinity of the solvated Na^+ for the basic oxygen in the silicate.

Between pH 3 and pH 9, the neutral $Si(OH)_4$ is predominant in dilute solution [2]. Oxolation leads to gels of amorphous 'hydrated silica' $[SiO_2 \cdot xH_2O]_n$ [4]. In fact, the oxide itself does not form. A heavily hydrated polymeric gel does instead, with many terminal Si–OH groups of high acidic character (pK around 2). One may consider that the gel is made of large-size polyanions which aggregate by 'secondary' condensation of silanols from different units.

In the domain of predominance of $Si(OH)_4$, around pH 3, condensation is slow. It is accelerated strongly when the pH of the medium deviates from a value of 3. Variations in the rate of consumption of monomer reflect the acid or basic catalysis with the acidity domain [21] (Figure 4.2).

Around pH 7–8, gelation is instantaneous. The catalysis is due to the presence of $[SiO(OH)_3]^-$. At pH < 2, the presence of $[Si(OH)_3(OH_2)]^+$ accelerates the reaction.

Particles formed in alkaline or acidic media exhibit very different morphologies [4,21]. At pH > 3, the molecular weight of the species in solution increases rapidly immediately from the onset of the reaction. Chains are highly branched and form a three-dimentional network leading to spherical particles a few hundred ångstroms in diameter and forming particulate gels. At pH < 3, molecular weights remain

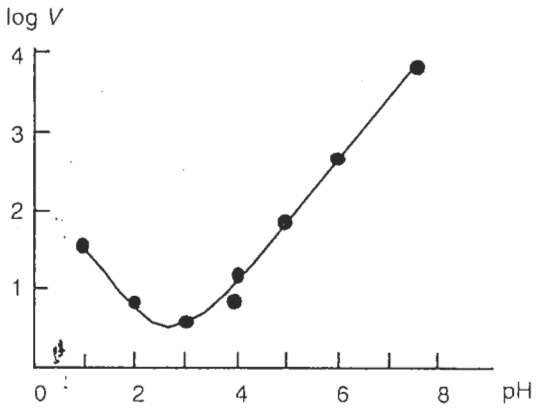

Figure 4.2 Rate of disappearance of the monomer at various pH (Si concentration 6 g/l in SiO_2, temperature 20 °C). From [21]

DropBooks

relatively small throughout the process. Condensation mostly generates oligomers (a degree of condensation of 2–6) which aggregate and gel slowly, forming diffuse aggregates of very small particles about 50 Å in diameter (polymeric gels). The influence of medium acidity on the morphology of the particles may be explained using the previously described mechanism for oxolation catalysis.

It is possible to predict the overall structure of the polymer, considering that, at an early stage of condensation, a branched chain contains several types of groups:

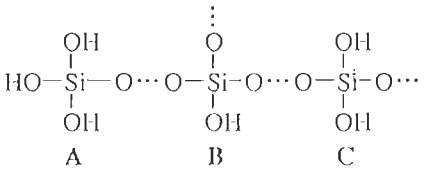

Let us consider the three different types of groups: $Si(OH)_3(OX)$ [A], $Si(OH)(OX)_3$ [B] and $Si(OH)_2(OX)_2$ [C], where X represents the rest of the chain of average chemical composition $SiO(OH)_2$. The X group is also a ligand with average electronegativity: $\chi(X) = \chi[SiO(OH)_2] = 2.63$. Partial charges on sites A, B and C are given in Table 4.2.

In an alkaline medium, catalysis involves the first step of the condensation mechanism, i.e. nucleophilic attack by the anionic forms (or OH^-). It can be seen that the charge on all Si of the growing chain is higher than on the monomer [$\delta(Si) = 0.47$]. Therefore, nucleophilic attack by silicic anions must take place on the chain, and preferentially on sites with highest partial charge, i.e. in the middle of the chain (sites B and C). Condensation creates many nodes, in agreement with experimental observation.

In an acid medium, catalysis impacts the second step of condensation. Elimination of the proton in the -ol bridge in the transition state is eased by the protonation of an OH ligand, which favors formation of the leaving group (aquo ligand). The OH groups concerned are those located at the ends of chains, which bear the highest negative partial charge, or even those of the $Si(OH)_4$ monomer. As a result, poorly crosslinked and poorly condensed chains are formed. Therefore, the morphology of the particles is heavily dependent upon the conditions of acidity in which condensation takes place.

Particles and polymers may remain dispersed in the medium, forming sols, or they can agglomerate and gel more or less rapidly. In general, oxide colloidal particles exhibit a stability minimum when the surface charge σ is zero (see

Table 4.2

Site	χ	δ(Si)	δ(OH)
A	2.64	+0.50	−0.06
B	2.78	+0.58	+0.06
C	2.71	+0.54	0

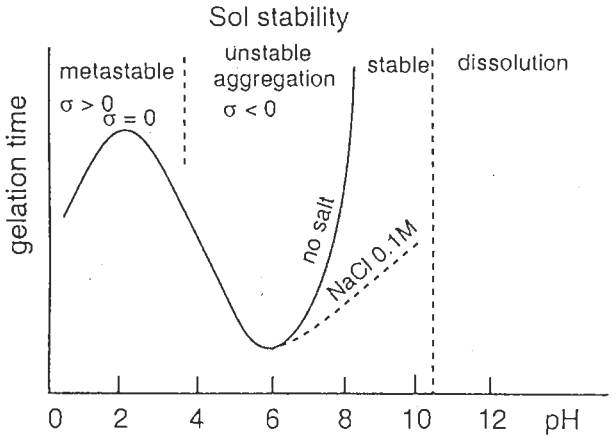

Figure 4.3 Gelation time and stability range for 'silica' sols as a function of pH. From [4] with permission

Chapter 6). The attractive forces between particles (Van der Waals forces) are no longer compensated for by the repulsion due to charged surface groups, and the particles flocculate. When the acidity of the medium allows existence of a positive or negative surface charge, collisions between particles caused by Brownian motion become inefficient. Particles repel each other and the sol is stable. The behavior of silica is quite different. Stability is at a maximum at the point of zero charge (pH = 2) because gelation is also the slowest [4] (Figure 4.3).

On either side of pH = 2, gelation is faster because acid or base catalysis accelerates the condensation rate of Si–OH groups between particles. At pH < 2, the surface charge is too small to provide efficient repulsion between particles. At pH > 2, base catalysis of oxolation has the same effect, which is maximum for pH = 6. For pH > 6, the surface charge is high enough for the sol to remain stable.

(a) Aluminosilicates

Silicon is, after oxygen, the most abundant element in the earth's crust, which explains why soil, rocks, clay and sand are almost entirely made of silicates which include most metallic elements in extraordinarily diverse one-, two- or three-dimensional crystalline structures. Aluminosilicates are an important class of materials owing to their properties and their importance in geology, mineralogy, agronomy, ceramic science, catalysis and many industrial appplications.

Aluminosilicates are also likely to form by condensation of silicate and aluminate complexes. Silicates can react with many elements, and with aluminum as the aluminate ion $[Al(OH)_4]^-$ in particular. The aluminate ion has a very low propensity towards condensation but it can be incorporated easily in polysilicates: silicates

behave as polymerizable ligands, allowing the formation of mixed compounds, and aluminum adopts the same tetrahedral coordination as silicon in an alkaline medium. In addition, Al–O–Si–O–Al chains are energetically favored in comparison with Al–O–Al bonds [95]—there are no direct bonds between AlO_4 tetrahedra in natural aluminosilicates. Mixed polyanions are certainly formed by oxolation between aluminate and various silicates $[SiO_{4-x}(OH)_x]^{(4-x)-}$ $(I \leqslant x \leqslant 4)$:

$$-Si-OH + HO-Al(OH)_3^- \longrightarrow -Si-O-Al(OH)_3^- + H_2O$$

The structure of species in solution depends on numerous parameters (pH, temperature, nature of the cation of the base, Al/Si ratio, etc.) and remains uncertain. The interpretation of ^{27}Al and ^{29}Si NMR spectra is complicated and uncertain because of the high lability of Al–O–Si bonds, 2–3 orders of magnitude higher than that of Si–O–Si bonds [96,97]. In the presence of alkaline cations (Na^+, Cs^+), the complexes: $[(HO)_3AlOSi(OH)_2OSiO_3H_{3-x}]^{(x+1)-}$ and $[(HO)_3AlOSiO_3H_{3-x}]^{(x+1)-}$ are detected in solution. With tetraalkylammonium cations, cages similar to those observed in silicate solution were found with different substitution ratios of silicon by aluminum.

Depending on the reaction conditions (composition, acidity, temperature, pressure, etc.), they can lead to the formation of many compounds [6]. The following provides some structural information on two large classes of aluminosilicates.

• Clays are natural compounds formed in geological layers under hydrothermal conditions. Their structures, which are usually two-dimensional, are based on the stacking of sheets of SiO_4 tetrahedra (Si layers) and AlO_6 octahedra (Al layers). Van der Waals forces between the sheets ensure the stability of the structure. The organization of the layers may vary. Substitution of Si by Al in the Si layers and/or of Al by divalent cations [often Mg(II)] in Al layers gives the network a negative charge balanced by cations (Na^+, K^+, H^+, Ca^{2+}, etc.) located between the sheets [6,22a,b]. The result is a very large number of structures and chemical compositions. For exemple, the sheets of kaolinite $Si_2O_5Al_2(OH)_4$ and its substituted derivatives contain one Si layer and one Al layer (Figure 4.4a). Derivatives of pyrophyllite $Si_4O_{10}Al_2(OH)_2$ contain an Al layer between two Si layers (Figure 4.4b). Substitutions within Al layers lead to the formation of montmorillonites of generic formula $Si_4O_{10}(Al_{2-x}M_x^{2+})(OH)_2$, C_x where C is the exchangeable hydrated cation, most likely calcium (Figure 4.4d). If C is sodium, the compounds are called bentonites. Substitutions within Si layers form the beidellites $(Si_{4-x}Al_x)O_{10}Al_2(OH)_2$, C_x. Muscovite (mica) is the compound for which $x = 1$ and $C = K^+$ (Figure 4.4c).

Substitutions taking place simultaneously in both types of layer lead to vermiculites $(Si_{4-x}Al_x)O_{10}M_{3-y}^{2+}M_y'^{3+}(OH)_2$, C_{x-y} or to saponites $(Si_{4-x}Al_x)O_{10}M_3^{2+}(OH)_2$, C_x. The latter are derivatives of talc $Si_4O_{10}Mg_3(OH)_2$. Some of these clays can swell (montmorillonites, saponites) because water may place itself between the sheets and separate them since they are held together by the electrostatic forces of the solvated exchangeable cations (Figure 4.4d).

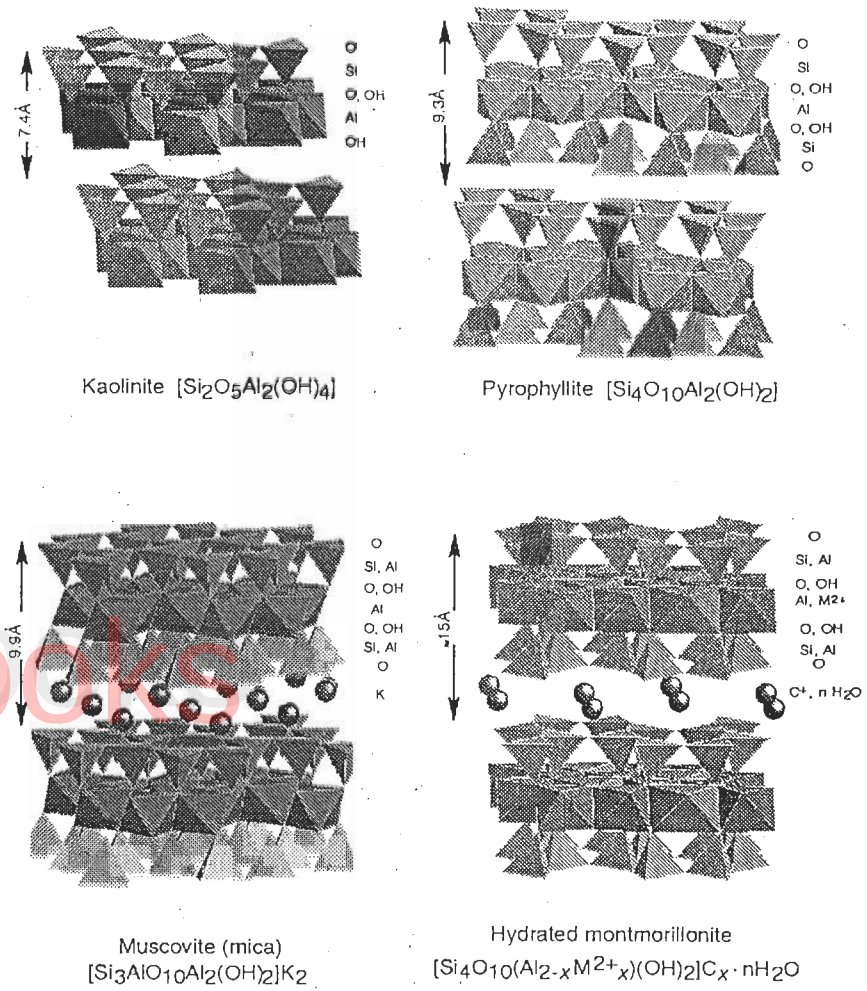

Kaolinite $[Si_2O_5Al_2(OH)_4]$

Pyrophyllite $[Si_4O_{10}Al_2(OH)_2]$

Muscovite (mica) $[Si_3AlO_{10}Al_2(OH)_2]K_2$

Hydrated montmorillonite $[Si_4O_{10}(Al_{2-x}M^{2+}{}_x)(OH)_2]C_x \cdot nH_2O$

Figure 4.4 Structures of a few clays

• Zeolites are another class of aluminosilicates in which corner-sharing SiO_4/AlO_4 tetrahedra form giant, very open polyhedral structures (Figure 4.5). Zeolites are formed via precipitation or hydrothermal synthesis [23a,b,24]. Their synthesis requires the presence of quaternary ammonium cations or that of crown ether complexes which act as templates and orient the structure. Many crystalline varieties can be obtained, depending on the composition (Si/Al), the nature of the charge-balancing cation and the type of complex initially formed in the solution.

The structure of zeolites is characterized by the existence of large channels and voids where the charge-balancing cations are located. These cations may be

DropBooks

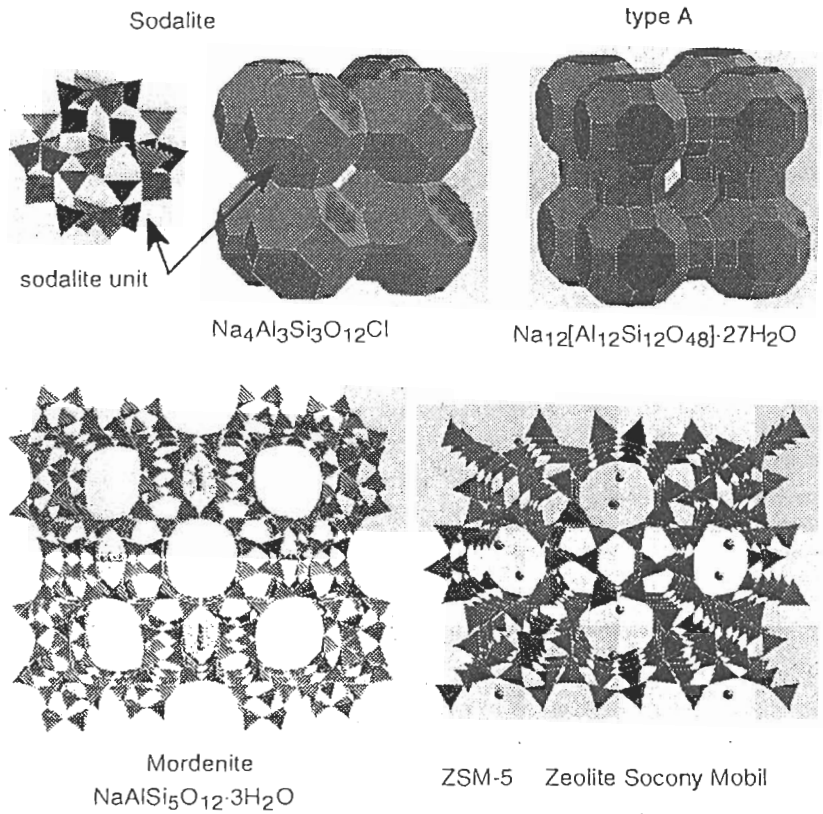

Figure 4.5 Structure of a few zeolites. These structures are based on corner-sharing SiO_4 and AlO_4 tetrahedra forming various motifs such as the sodalite unit (6.6 Å in diameter) shaped as a cuboctahedron. This unit contains 2.2 Å wide openings on hexagonal faces. The structure of the zeolite is formed by stacking such cuboctahedra to form small cubic or hexagonal prismatic voids. These voids may be connected to one another directly (sodalite) or through prismatic channels (zeolites of type A, for example). The large voids contain the charge-compensating cations and account for about 20–50% of the total volume of the crystal. Mordenite, the most silica-rich natural zeolite, contains large parallel channels formed by cycles of twelve tetrahedra (9.5 Å in diameter) and smaller channels (8-tetrahedra channels) trapping water molecules. The channels are connected by other perpendicular channels formed by 5- or 6-tetrahedra channels. In the ZSM-5 zeolite, a synthetic zeolite widely used as a catalyst, the Si/Al ratio is higher than 20. The larger the Si/Al ratio, the lower is the number of exchangeable cations and the network becomes hydrophobic

exchanged for other cations, and hence the widespread use of zeolites as ion-exchange materials. H^+ zeolites play a considerable role as catalysts, particularly in the cracking of oil because of the large number of acid sites in the structure [23a,24]. In the dry state, the cavities are able to contain many different molecules. Zeolites may be used as molecular sieves for adsorption and separation of gas mixtures.

Because of its electrical charge, the aluminosilicate network is hydrophilic and is used to dry non-aqueous solvents. The aluminate ion may be removed from the structure without significant modification of the framework, giving the network a hydrophobic character. The resulting material is used as a molecular sieve for the separation of paraffins: linear molecules are adsorbed in the network whereas branched molecules are excluded from it.

4.2.2 Sb(V): ANTIMONATES

Antimony(V), always hexacoordinated in solution, exists in an alkaline medium as $[Sb(OH)_6]^-$. This species is stable as a monomer owing to the weak electrophilic character of the cation. A calculation gives $\chi = 2.478$, $\delta(OH) = -20.21$ and $\delta(Sb) = +0.26 < 0.3$.

Acidification of antimonate in solution leads to condensation phenomena culminating in the formation of polyanions and antimonic acid gels.

Antimonic polyanions are poorly known. Potentiometry seems to indicate that, for an acidification ratio H/Sb of 0.6, a species condensed 12 times is in equilibrium with the monomer $[Sb(OH)_6]^-$ and with the protonated forms of the polyanion [25] of unknown nature.

Acidification of potassium antimonate $KSb(OH)_6$ in solution by K^+/H^+ ion-exchange on a resin (in order to avoid an increase in the ionic strength of the medium) leads immediately to the formation of an opalescent suspension which becomes clear after about 30 min at room temperature. After about 24 h, a crystalline gel of antimonic acid particles $HSbO_3 \cdot 1.5H_2O$, of pyrochlore structure, is formed [26,27,28]. The structure contains corner-sharing SbO_6 octahedra (Figure 4.6).

The protons of antimonic acid can exchange easily with alkaline cations or the silver ion [26,27,29,30]. Ionic conductivity measurements [31,32] show that the protons are very mobile in the network. A study of the dehydration linked to the exchange [30], as well as ^1H NMR of antimonic acid [32], seems to indicate that exchangeable protons do exist as H_3O^+-solvated ions within the channels of the structure, so that the solid may be represented by $[H_3O^+][SbO_3]^- \cdot 0.5H_2O$.

Formation of the solid phase cannot result from an oxolation reaction alone. It turns out that acidification of antimonate leads to the neutral hydroxo–aquo species $Sb(OH)_5(OH_2)$ which can condense by olation [$\chi = 2.60$, $\delta(Sb) = +0.32$, $\delta(OH) = -0.10$, $\delta(H_2O) = +0.16$]. This form can rapidly lead to amorphous particles of various sizes, such as entangled polymer chains of corner-sharing octahedra, which are responsible for the opalescence observed upon acidification. Disappearance of the opalescence is probably due to the rearrangement of these species into smaller-size entities, as indicated by the decrease in molecular weight of the soluble compounds [28]. Such entities are susceptible to becoming the nuclei of the crystallized solid. In fact, if the ageing process is halted (through freezing of the suspension in alcohol, for example), various types of hydrated amorphous antimonic acid are obtained [33,34].

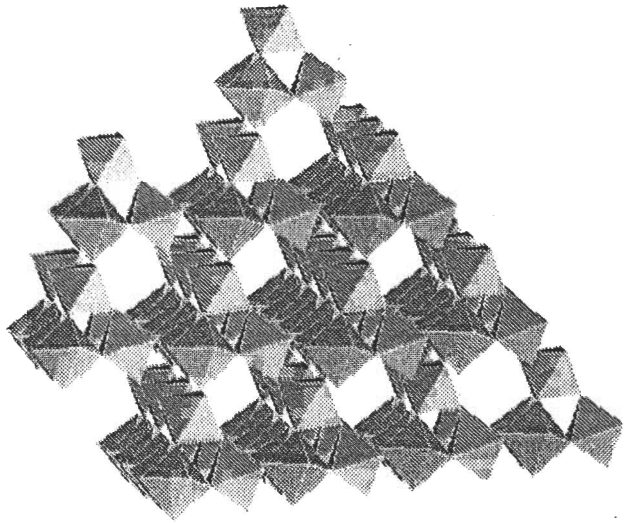

Figure 4.6 Pyrochlore structure of antimonic acid. SbO_6 octahedra are connected by oxo bridges (corner sharing). The solvated protons are distributed in the hexagonal channels of the structure

Hence, the reaction mechanism in Figure 4.7 is proposed, which explains the development of the crystalline structure and the presence of exchangeable protons in the network.

The $[Sb(OH)_5(OH_2)]^0$ species, which contains one molecule of water only, allows the formation of small rings of corner-sharing octahedra, rather than the formation of chains. The smallest units that appear to be at the origin of the final structure are the $Sb_3(OH)_{15}$ rings (species I). The nucleophilic activity of the hydroxo ligands ($\chi = 2.635$, $\delta(OH) = -0.07$) allows these rings to bind, by olation and oxolation, to the remaining antimonate from the initial amorphous precipitate, and form intermediate compound II, $Sb_4O_2(OH)_{16}$. Its topology seems to be the most favorable for the stabilization of rings, which are therefore capped by a fourth octahedron.

At this stage, a condensation by olation is no longer possible. Intermediate compound II may, however, condense by oxolation ($\chi = 2.658$, $\delta(OH) = -0.05$) and form a pyrochlore network quite easily. Not all the hydroxo ligands in units II are removed during condensation, and the overall chemical formula of the solid is $SbO_2(OH)$. In fact, the hydroxo ligands in the solid are highly acidic: $\chi = 2.819$, $\delta(OH) = +0.10$. Therefore, these ligands have a tendency to undergo acid dissociation when in contact with the hydration water from the solid. The solid is probably more accurately described by the formula $[H_3O^+, SbO_3^-] \cdot nH_2O$. Although this proposed mechanism is speculative, it is simple and logical and does account for the phenomena observed. It must be stressed that both olation and oxolation are involved in the formation of the hydrated oxide.

DropBooks

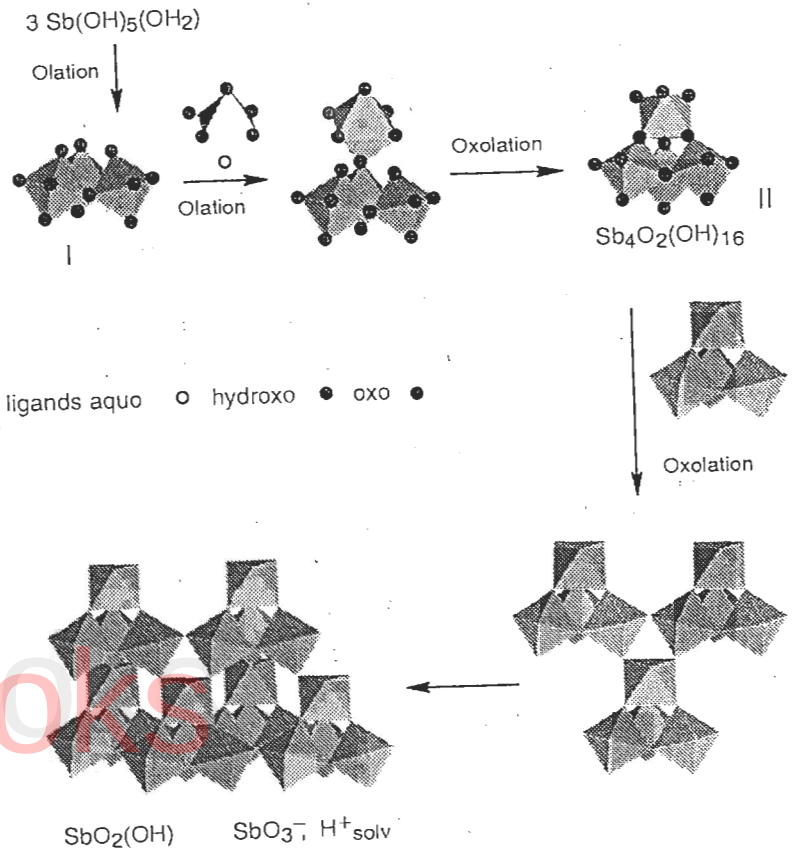

Figure 4.7 Possible reaction mechanism for the solution synthesis of antimonic acid (pyrochlore structure)

A similar reaction mechanism is seen for tin(IV). Hydrated tin oxide is usually formed by the addition of a base to $SnCl_4$ solutions [35,36,37] or by acidification of sodium stannate [38]. In either case, condensation leads to $SnO_2 \cdot nH_2O$ (cassiterite) of the rutile-type crystal structure (see Section 3.2.3b).

The essential structural difference between the pyrochlore lattice of antimonate (corner-sharing MO_6 octahedra) and the rutile lattice of the stannate (edge and corner-sharing MO_6 octahedra) appears to be due to the difference in formal charge between the two elements. The octahedral coordination of tin(IV) [2] in the neutral species $Sn(OH)_4(OH_2)_2$ leads to the presence of two water molecules which allow the onset of condensation by olation, as in the case of antimony (V). However, electrostatic repulsions between Sn(IV) cations are smaller than between Sb(V) cations. Therefore, in the case of tin, SnO_6 octahedra share edges (double hydroxo bridges) and tend not to form rings. Chains link up at a later stage by oxolation,

forming a rutile-type structure. In Section 3.2.3b, we have seen that an anatase structure of SnO_2 is never obtained.

As in the case of many systems, the morphology of the oxide or oxohydroxide particles is strongly dependent on the experimental conditions. However, it seems that small spherical crystalline particles (about 20 Å in diameter) are always formed initially [37,35]. Aggregation and dissolution–crystallization equilibria eventually lead to a change in morphology (from spheres to short sticks), as well as to higher crystallinity.

4.2.3 B(III): BORATES

Boron is a highly electronegative element ($\chi_B^* = 2.02$) which forms a very small cation B^{3+} (ionic radius 0.27 Å). In aqueous solution, boron exhibits two coordination modes: tetrahedral in the borate, $[B(OH)_4]^-$, or trigonal in boric acid, $B(OH)_3$. The pK_a of the couple is 9.5 [2]. Both forms are stable as the monomer, the borate for $pH > 11$ and boric acid for $pH < 7$.

Contrary to what is usually observed, acidification of the borate leads to a reduction in coordination number. This is why boric acid acts as a Lewis acid, behaving as an OH^- acceptor rather than a proton donor:

$$B(OH)_3 + OH^- \longrightarrow [B(OH)_4]^-$$

or

$$B(OH)_3 + H_2O \longrightarrow [B(OH)_4]^- + H^+_{solvated}$$

One could consider that a water molecule in the coordination sphere of boric acid could act as a proton donor:

$$B(OH)_3(OH_2) + H_2O \longrightarrow [B(OH)_4]^- + H_3O^+$$

In fact, ^{11}B liquid NMR [39,40] and the structure of the solid [3] show boron D_{3h} symmetry in boric acid. This is why the $B(OH)_3$ form is proposed. The decrease in coordination of boron during acidification in aqueous solution is, to our knowledge, a phenomenon never observed with any other element. It could be due to a π donor effect from the three hydroxo ligands, as in the BX_3 halogens [41].

The $[B(OH_4)]^-$ ion exhibits a T_d symmetry. Its MO diagram is shown in Figure 4.8a. The π donor character of the ligands is small and the π symmetry AOs of the ligands remain non-bonding [41].

Protonation of the borate forms a H_2O ligand, and causes an increase in the B–O bond length and a decrease in the symmetry ($T_d \rightarrow C_{3v}$). The $B(OH)_3(OH_2)$ complex is not stable, and water is easily eliminated from the coordination sphere. Boron is too small to maintain four-coordination ($r_{B3+}/r_{O^{2-}} = 0.19 < 0.225$, the characteristic value of tetrahedral coordination in the ionic model). In addition, a switch to D_{3h} symmetry allows the three hydroxo ligands to establish $p_\pi - p_\pi$ interactions between the empty p_z orbital of boron and an orbital of π symmetry

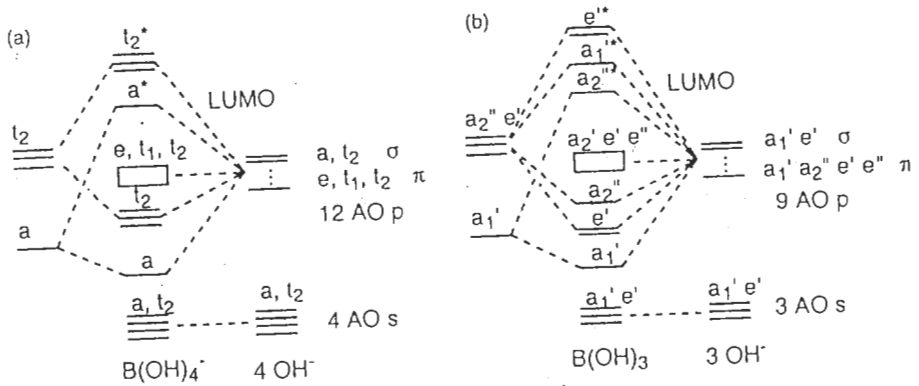

Figure 4.8 MO diagram for (a) $[B(OH)_4]^-$ and (b) $B(OH)_3$. The diagrams are drawn by analogy with the diagrams of BX_4^- and BX_3 respectively. From [41]

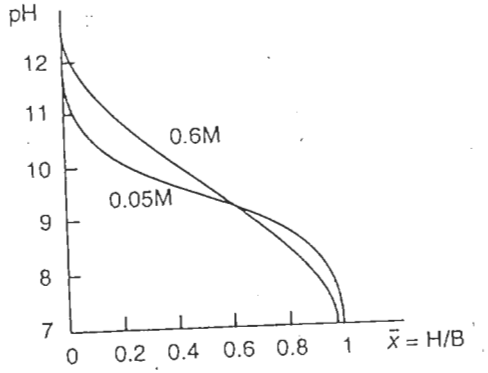

Figure 4.9 Protometric titration curves of borate for various concentrations, showing an intersection point corresponding to a maximum of condensation. Reproduced from [42]

from each ligand (Figure 2.2). As a result, three strong σ bonds (labeled a_1' and e' in Figure 4.8b) and one π bond (labeled a_2'') are formed. The formation of π bonds in boric acid causes a decrease in the partial charges on boron and the hydroxo ligands, compared with those derived from σ bonds alone. This is probably the reason why boric acid does not condense in solution or in the solid. (*It is also why the partial charges model cannot be used in a discussion of these species in solution*).

Potentiometry measurements [42,43] show that the borate and boric species may co-condense. The acidification ratio of the borate must be between 0 and 1 for both species to coexist in solution ($11 > pH > 7$). Condensation goes through a maximum for an intermediate pH value. This is shown by the intersection of the protometric titration curves [42–44] (Figure 4.9).

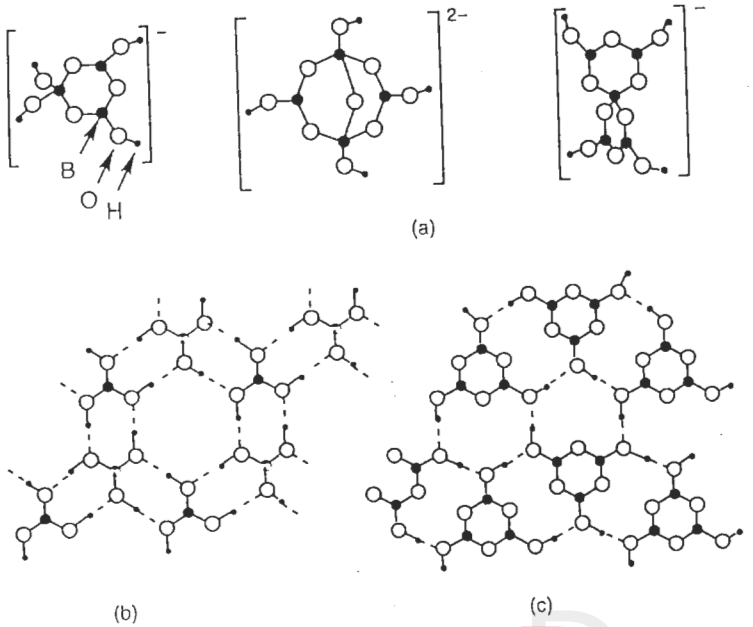

Figure 4.10 Structures of (a) polyborates, (b) boric acid and (c) metaboric acid

Potentiometric measurements show that acidification of borate forms, in sequence, the following species: a dimer in diluted solution, a tetramer in a concentrated solution of acidity $p = H^+_{added}/B = 1/2$ and a trimer ($p = 2/3$).

For $p = 1/2$, the formation of the dimer is

$$[B(OH)_4]^- + B(OH)_3 \longrightarrow [B_2O(OH)_5]^- + H_2O$$

For a high concentration ($\approx 0.4\ mol\ l^{-1}$), the dimer itself dimerizes to form the cyclic tetramer $[B_4O_5(OH)_4]^{2-}$ (Figure 4.10):

$$2[B_2O(OH)_5]^- \longrightarrow [B_4O_5(OH)_4]^{2-} + 3H_2O$$

For a higher acid content ($p = 2/3$), the trimer is formed:

$$[B(OH)_4]^- + 2B(OH)_3 \longrightarrow [B_3O_3(OH)_4]^- + 2H_2O$$

This species is stable in solution owing to cyclization (Figure 4.10).

For $p > 2/3$, the system decondenses and the boric acid monomer is predominant in solution. It would seem that, around $p = 4/5$, condensation proceeds as far as the pentamer (Figure 4.10):

$$[B(OH)_4]^- + 4B(OH)_3 \longrightarrow [B_5O_6(OH)_4]^- + 6H_2O$$

The existence of this species in solution deduced from NMR investigations is still controversial [39,40]. Its lifetime in solution is probably very short since the hydrated potassium pentaborate $K[B_5O_6(OH)_4]\cdot 2H_2O$ is rapidly hydrolyzed in solution.

In most condensed boron compounds, the basic structure is a six-membered ring (three boron atoms and three oxygen atoms) which always contains one or two tetrahedral borons that form connections between rings [6] (Figure 4.10).

Cyclization explains condensation in solution. In the solid, boric acid forms rings linked together by hydrogen bonds. Since boron adopts a trigonal configuration, a layer structure develops (Figure 4.10b).

Metaboric acid HBO_2 forms various crystal structures by dehydration of the trimer ($T > 100\,°C$). The orthorhombic form, obtained by quenching, is made of trimer rings linked by hydrogen bonds in a layered structure (Figure 4.10c). The monoclinic form is made of chains $[B_3O_4(OH)(OH_2)]_n$ in which 3- and 4-coordinated boron coexist. In the cubic form, BO_4 tetrahedra are linked by hydrogen bonds [6].

Metallic polyborates have important industrial applications: millions of tons of borax $Na_2B_4O_5(OH)_4\cdot 8H_2O$ (tetramer chains linked by hydrogen bonds) are produced each year. This material is widely used in the synthesis of ceramics, glass fibers, thermal insulators, enamels, fire retardants, etc. Boron oxide B_2O_3 (partially ordered network of B_3O_3 rings) is used mostly in the fabrication of borosilicate glasses (Pyrex). Owing to its small thermal expansion coefficient, the resulting glass exhibits good resistance to thermal shock.

DropBooks

4.3 TRANSITION METALS FOR WHICH CONDENSATION LEADS TO AN INCREASE IN COORDINATION NUMBER

In their maximum oxidation state, V(V), Cr(VI), Mo(VI), W(VI) and Mn(VII) have the d^0 electron configuration, carry a high charge and are relatively small. In an alkaline medium, they exist as tetraoxo $[MO_4]^{(8-z)-}$ monomers [2] (see Section I.1, charge–pH diagram).

These complexes condense by protonation, the extent of their condensation being inversely proportional to their acidity. In the series $[VO_4]^{3-}$, $[CrO_4]^{2-}$, $[MnO_4]^-$, the strength of the conjugated acids $[MO_{3-x}(OH)_x]^{(8-z-x)-}$ increases with the charge of the cation, and hence the extent of the condensation is decreased (Table 4.3). Mn(VII) exists only as the monomer $[MnO_4]^-$. Polarization of the OH group is extremely high and the $MnO_3(OH)$ acid does not exist in diluted solution [2].

For identical formal charges, the degree of condensation increases from Cr(VI) to W(VI). In this series, the strength of the acid decreases, but the variation in condensation cannot be justified by this simple fact because the size of the cation increases, and, moreover, Mo(VI) and more importantly W(VI) do not form condensed species from the tetrahedral motif [45,46].

For some transition elements, the transition from 4-coordination to 6-coordination observed during protonation and condensation may be qualitatively explained by considering π bonding with the ligands (see the case of boron, Section 4.2.3).

Table 4.3 Characteristics of a few d^0 transition elements of high oxidation state

Form	VO_4^{3-}	CrO_4^{2-}	MnO_4^-	MoO_4^{2-}	WO_4^{2-}
pK	13.2	5.6	(−2)	3.9	4
	7.5	0.8	—	3.9	4
Ionic radius (Å)	0.56	0.52	0.46	0.62	0.67
$R_M R_O$[a]	0.40	0.37	0.33	0.44	0.48
Coordination	4–5–6	4	4	4–6	4–6
Condensation	10	2	1	7–8	7–12

[a] The radius of O^{2-} is assumed equal to 1.40 Å for the calculation of R_M/R_O. The radius of cations is from Shannon and Prewitt [47].
[b] Highest degree of condensation of polyanions in aqueous solution.

In their tetraoxo form, d^0 transition metals may involve their d and p atomic orbitals in π bonds with the oxo ligands. The ligands of e symmetry are the ones involved, since the t_2 (d and p) are already involved in σ bonds and can only participate in small overlaps (Figure 4.11) [41,48,49]. π bonds can be very strong in oxoanions, in particular in $[MnO_4]^-$ [48,49], owing to the strong polarizing power of Mn(VII) caused by its small size and high charge. Therefore, oxo ligands in $[MnO_4]^-$ are not basic and cannot be protonated, even in a strongly acid medium.

With larger and more highly charged d^0 cations, tetrahedral coordination is still favored because the antibonding orbitals are empty, but the π overlaps are less pronounced than in the case of Mn(VII). Therefore, the basic character of the oxo ligands is stronger. Protonation becomes possible and the formation of hydroxo ligands further weakens the π transfers. Under such conditions, the steric demand of the largest cations is no longer balanced by sufficiently strong π bonds, and a change in coordination occurs. This change occurs via condensation with the addition of tetrahedra, or by solvation in a diluted (and/or acidic) medium. The cation acquires the octahedral coordination of symmetry O_h, D_{4h} or C_{4v}—even with a single σ system, which has more favorable crystal field stabilization than in coordination 4 with σ and π bonds. By comparison, the size of Ti(IV) is similar to that of Mo(VI) and W(VI), but its charge is smaller, and therefore it cannot form π bonds, and formation of the oxo ligand does not occur. Titanium remains in coordination 6 in the aquo–hydroxo form, which is insoluble in an alkaline medium.

The stage of protonation for which a change in coordination takes place is a direct function of the charge and size of the cation, because the basic character of oxo ligands is inversely proportional to the polarizing strength of the cation. For V(V), a change from coordination 4 to 6 is observed for $H^+/V=3$ which corresponds to the species $[VO(OH)_3]^0$. For Mo(VI) and W(VI), the coordination expansion occurs earlier, at $1<H^+/M<2$, which corresponds to $[MO_3(OH)]^-$ and $[MO_2(OH)_2]^0$ species (see Section 4.3.2). This explains why W(VI), or very rarely Mo(VI), does not form condensed species from tetrahedral motifs. Cr(VI) and Mn(VII) are too small to expand their coordination beyond 4. A change in coordination would require a cation/oxygen radius ratio close to 0.414, which corresponds

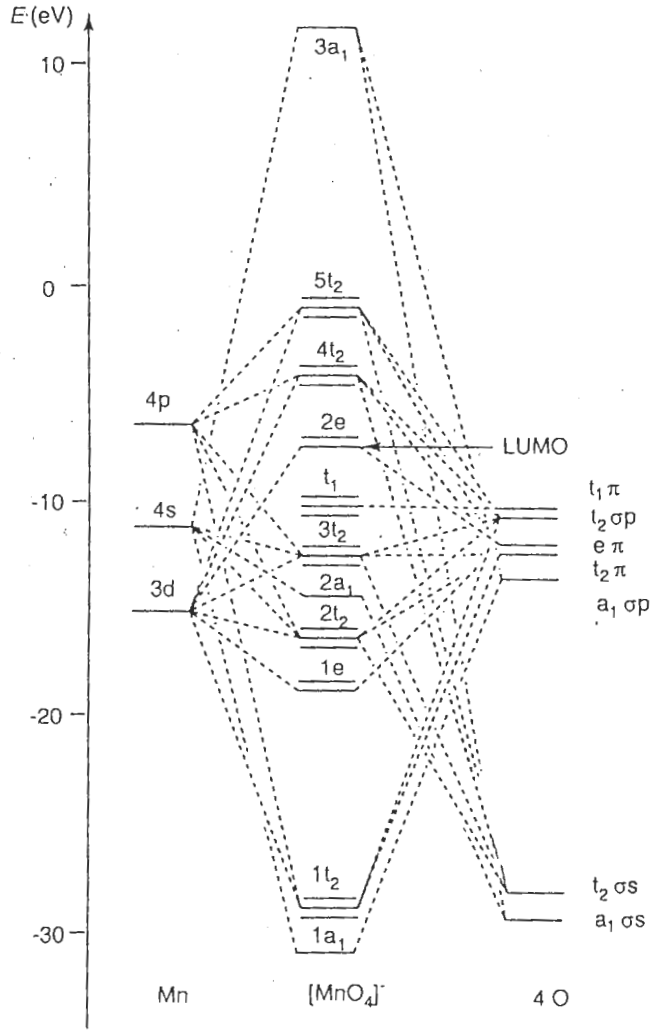

Figure 4.11 Molecular orbital diagram for $[MnO_4]^-$. From [49]

to the size of octahedral sites in a close-packed stacking of oxygen atoms (Table 4.3). It is probable that the inability of these two elements to exceed coordination 4 is responsible for their limited solution chemistry.

Extension of cation coordination may take place through two different mechanisms, according to acidity conditions:

(i) When the acidity of the medium allows the existence of $[MO_a(OH)_b]^{x-}$ anions, nucleophilic addition of these protonated moeities may take place by condensation

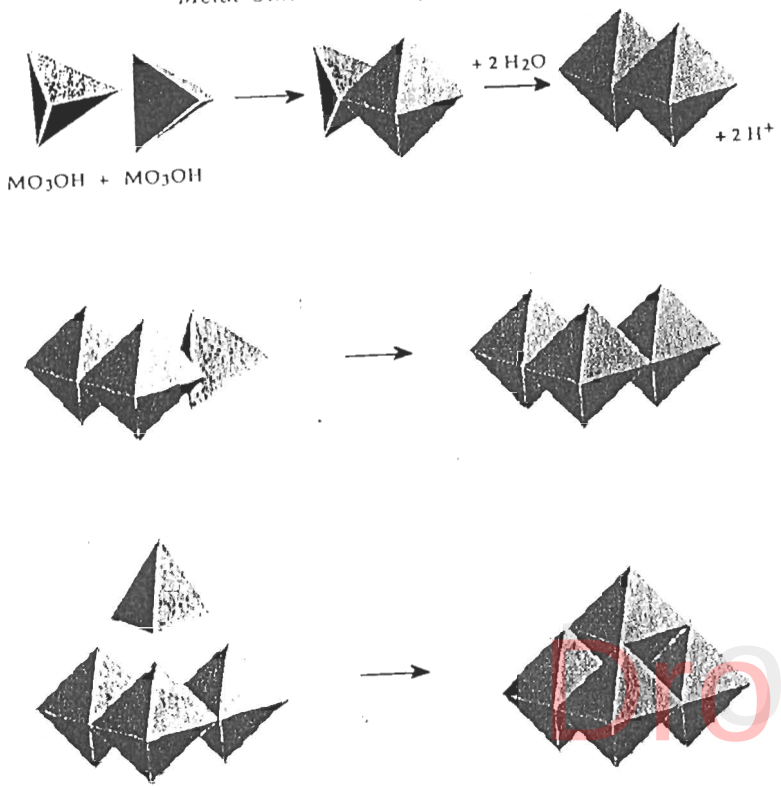

Figure 4.12 Tetrahedra addition with formation of chains and rings

[V(V), Mo(VI), W(VI)]. Protonation increases the length and decreases the π character of the M–OH bonds. The mechanism leads to edge-sharing polyhedra and the formation of rings or chains [50–52] (Figure 4.12).

(ii) In the acidity range where zero-charge species are formed, a coordination increase may take place by solvation, i.e. via the addition of aquo ligands on the tetrahedral mocities. Under such conditions, water is a better nucleophilic agent than the OH ligands on these entities. This mechanism explains the formation of vanadium and tungsten oxides, as will be discussed in the following sections.

4.3.1 V(V): VANADATES

It is interesting to draw a parallel between the behavior of phosphates and that of vanadates. The central element has the same formal charge, in a similar tetraoxo environment. However, whereas phosphates may only condense via thermal dehydration of the solid [53] (see Section 2.1), vanadates condense spontaneously

in solution in acid conditions. The difference in the behavior of V(V) and P(V) is due to the smaller size of phosphorus which increases its polarizing strength. Therefore, P–O bonds have a higher covalent character than V–O bonds, and phosphorus is considerably less electrophilic than vanadium.

(a) Polyanions

The condensation of vanadates is seen very clearly in the shift of proton titration curves as a function of vanadate concentration [2,5] (Figure 4.13). In addition, the various stages are clearly differentiated by distinct equivalent points.

From $p = H^+_{added}/V = 0-1$, the shift in titration curves is such that $\Delta pH/\Delta \log C > 0$ [5]. Condensation occurs and the equivalent point indicates the formation of pyrovanadate:

$$2[VO_4]^{3-} + 2H^+ \longrightarrow [V_2O_7]^{4-} + H_2O$$

or

$$2[VO_3(OH)]^{2-} \longrightarrow [V_2O_7]^{4-} + H_2O$$

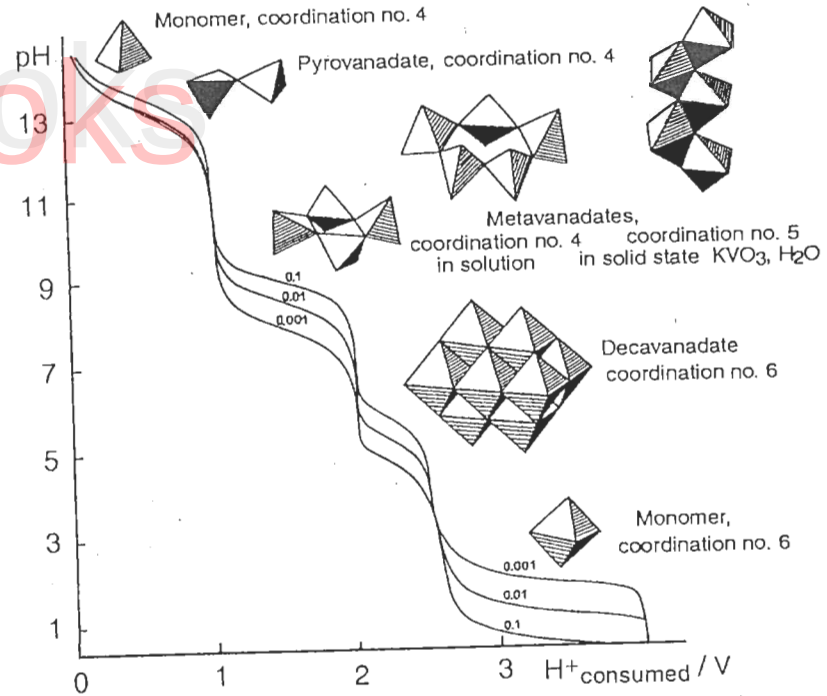

Figure 4.13 Titration curves of vanadate solutions for various vanadium concentrations. Reproduced by permission of John Wiley & Sons from [2]

DropBooks

The structure of pyrovanadate consists of two corner-sharing tetrahedra, similar to $[P_2O_7]^{4-}$ and $[Cr_2O_7]^{2-}$. Under such acid conditions (pH > 12), the pyrovanadate ion is stable.

From $p = 1$ to $p = 2$ ($9 > pH > 6$), the $\Delta pH/\Delta \log C$ term is positive and the second equivalent point indicates the formation of metavanadates $[V_4O_{12}]^{4-}$, tetramer rings (Figure 4.13):

$$4[VO_3]^{4-} + 8H^+ \longrightarrow [V_4O_{12}]^{4-} + 4H_2O$$

or

$$4[VO_2(OH)_2]^- \longrightarrow [V_4O_{12}]^{4-} + 4H_2O$$

In fact, the structure of metavanadate solutions is more complex, as indicated by ^{51}V NMR spectroscopy coupled to potentiometry investigations [54].

In a very alkaline medium, a single peak is observed, assigned to $[VO_4]^{3-}$ (Figure 4.14a). During acidification, additional peaks appear (Figure 4.14b). The displacement of the chemical shift of these peaks with pH shows the presence of protonated forms of vanadate ($[HVO_4]^{2-}$, $[H_2VO_4]^-$) and pyrovanadate ($[HV_2O_7]^{3-}$, $[H_2V_2O_7]^{2-}$). However, the peaks remain singular because protonation equilibria are faster than NMR observation time, and an average situation is observed.

Within the formation range of the metavanadate ($9 > pH > 6$), two peaks appear, with a chemical shift independent of pH. The corresponding species do not participate in protonation equilibria, and hence such peaks are assigned to the tetramer $[V_4O_{12}]^{4-}$ and to the pentamer $[V_5O_{15}]^{5-}$. The small width of the peaks suggests high symmetry around structurally identical vanadium atoms: four and five corner-sharing VO_4 tetrahedra forming a ring. A small peak at 570 p.p.m.

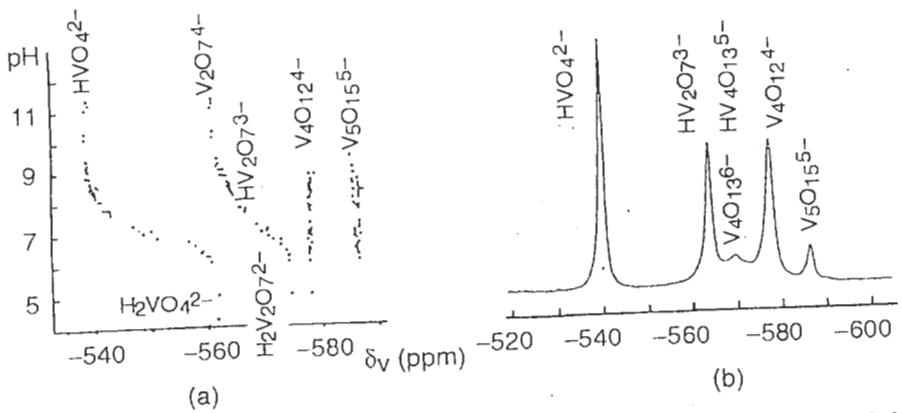

Figure 4.14 (a) ^{51}V NMR chemical shifts of the main vanadium species as a function of pH and (b) ^{51}V NMR spectrum of a solution at pH 8.3 ($C_V = 10^{-2}$ mol l^{-1}). Reproduced from [54] with permission

(Figure 4.14a), which may be assigned to a linear tetramer $[V_4O_{13}]^{6-}$ and its protonated form $[HV_4O_{13}]^{5-}$, overlaps at pH < 9, with the peak assigned to $[V_4O_{12}]^{4-}$ rings.

In the solid, metavanadates have linear anionic structures [46,55]: infinite chains of corner-sharing (KVO_3) tetrahedra, or distorted trigonal bipyramids ($KVO_3 \cdot H_2O$), in which vanadium is pentacoordinated (Figure 4.13).

By acidification above $p = 2$, vanadate solutions become orange and the shift in titration curves with concentration is such that $\Delta pH/\Delta \log C > 0$. Condensation proceeds and the equivalent point around pH = 3 ($H^+/V = 2.5$) indicates the formation of decavanadate:

$$10[VO_4]^{3-} + 25H^+ \longrightarrow [HV_{10}O_{28}]^{5-} + 12H_2O$$

or

$$5[VO_2(OH)_2]^- + 5[VO(OH)_3]^0 \longrightarrow [HV_{10}O_{28}]^{5-} + 12H_2O$$

The addition of tetrahedra allowing octahedral coordination of vanadium occurs within this acidity range, where the equilibria are slow.

The structure of decavanadate consists of 10 edge-sharing VO_6 octahedra (Figure 4.15). ^{51}V NMR investigations have shown that the decavanadic ion maintains

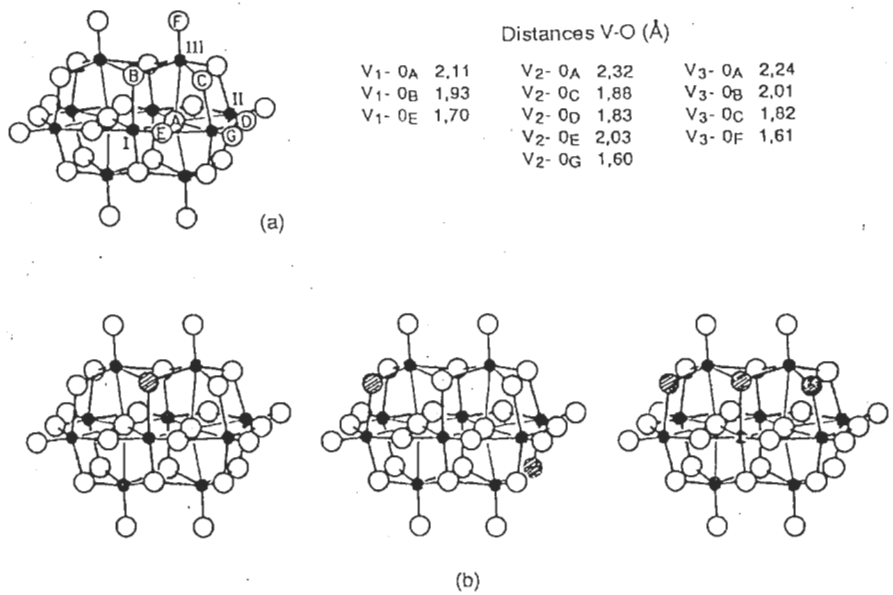

Figure 4.15 (a) Structure of the $[V_{10}O_{28}]^{6-}$ ion and bond lengths and (b) protonation sites for $[HV_{10}O_{28}]^{5-}$ and $[H_2V_{10}O_{28}]^{4-}$ in water and for $[H_3V_{10}O_{28}]^{3-}$ in H_2O/CH_3CN. Reprinted with permission from [56]. Copyright 1987 American Chemical Society

the same structure in solution and in the solid [56]. Three types of vanadium ion (labeled I, II and III in Figure 4.15a) are present in the ratios 1/2/2. Their coordination polyhedra share seven, four and five edges respectively.

Such compact stacking of octahedra creates significant repulsions between vanadium atoms, which find themselves appreciably shifted towards the outside of the polyanion. V–O bond lengths vary from 1.60 Å (V–$O_{terminal}$) to 2.32 Å (V–$O_{central}$) (Figure 4.15a). The strong distortion of the coordination polyhedron causes the poor basic nature of the external oxygens. In water, the most protonated form of decavanadate is $[H_2V_{10}O_{28}]^{4-}$ (equivalent point $H^+/V=2.6$, Figure 4.13). In a water/acetonitrile mixture ($\varepsilon_{CH_3CN} = 36.2$), a medium less dissociative than pure water, it is possible to obtain $[H_3V_{10}O_{28}]^{3-}$ [56]. Various protonated sites have been identified via X-ray diffraction and polynuclear NMR (^1H, ^{17}O, ^{51}V) [56]. The terminal oxygens of the very short V=O bonds cannot be protonated. In $[HV_{10}O_{28}]^{5-}$ the oxygen in μ_3 is the most basic and reacts with the proton. As a result, the V–O bond is stretched (+0.1 Å), and an important charge redistribution occurs in the polyanion, so that subsequent protonation sites will not be the same (Figure 4.15b).

$[H_2V_{10}O_{28}]^{4-}$ may undergo easy deprotonation and form $[V_{10}O_{28}]^{6-}$ by the addition of sodium hydroxide. The slowness of the equilibria prevents rapid evolution to the metavanadates [45].

Upon stronger acidification ($H^+/V>2.6$), $[H_2V_{10}O_{28}]^{4-}$ does not form the protonated species that one would expect. Within this acid range, the $\Delta pH/\Delta \log C$ term is negative (Figure 4.13) and the system decondenses to give the octahedral vanadic cation $[VO_2(OH_2)_4]^+$ [2,45]:

$$[H_2V_{10}O_{28}]^{4-} + 14H_3O^+ + 18H_2O \Longleftrightarrow 10[VO_2(OH_2)_4]^+$$

The intersection of the titration curves at $H^+/V=2.6$ indicates a maximum of condensation.

Decondensation of the system in this acidity range may be explained by the nature of the coordination sphere of V(V) in the monomer. We noted previously (Section 1.3) that, because of the high polarizing nature of V(V), vanadium appears to be better stabilized in a dioxo–aquo form $[VO_2(OH_2)_4]^+$ involving π bonds than in oxo–hydroxo–aquo $[VO(OH)_2(OH_2)_3]^+$ or hydroxo–aquo $[V(OH)_4(OH_2)_2]^+$ forms:

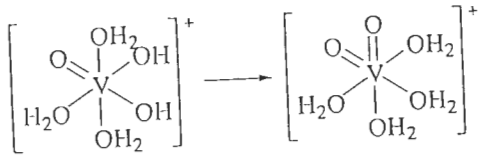

Hence, condensation is inhibited because both oxo groups are involved in very short V–O bonds which destroy the nucleophilic character of such ligands, leaving them poorly basic and not prone to protonation.

(b) Solid Phase

During the titration of sodium or ammonium vanadate at a high ionic strength, no solid phase is formed around $H^+/V=3$ corresponding to the existence of the zero-charge species. The decavanadate is in equilibrium with the non-condensed cation $[VO_2(OH_2)_4]^+$ and the kinetic phenomena are such that there is a direct transition from one form to the other [2,50].

However, if a solution acidified at $H^+/V=3$ with a low ionic strength is aged (acidification taking place via an ion-exchange resin) [57,58], the solution gels in a few hours if the vanadium concentration is higher than 0.1 mol l^{-1}. The vanadium oxide gel, $V_2O_5 \cdot nH_2O$, is made of entangled ribbon-shaped fibers, several thousand ångstroms in length, about 1000 Å wide and 10 Å thick [59] (Figure 4.16).

The structure of the fibers (Figure 4.17) is very different from that of the decavanadic polyanion formed immediately after acidification. The oxide is therefore not the result of aggregation of polyanions. Rather, it is the result of polyanion decondensation equilibria during which zero-charge precursors are formed and removed from the solution via unlimited condensation. In fact, the solid forms only if acidification takes place in a medium of weak ionic strength favoring weakly charged species [60].

The formation of V_2O_5 may be explained by considering the zero-charge monomers $[VO(OH)_3(OH_2)_2]^0$ and $[VO_2(OH)(OH_2)_3]^0$ in equilibrium with the decavanadate. As soon as they appear in solution, these entities condense by olation since both hydroxo and aquo ligands are present. The formation of chains is the result of the structure of the precursors: short V=O bonds prevent condensation

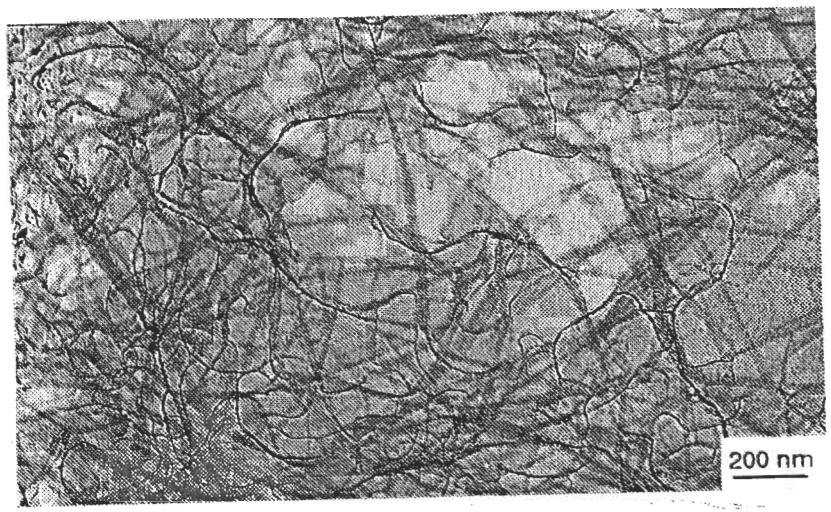

Figure 4.16 TEM micrograph of a vanadium oxide gel $V_2O_5.nH_2O$ obtained via acidification of sodium metavanadate on an ion-exchange resin

DropBooks

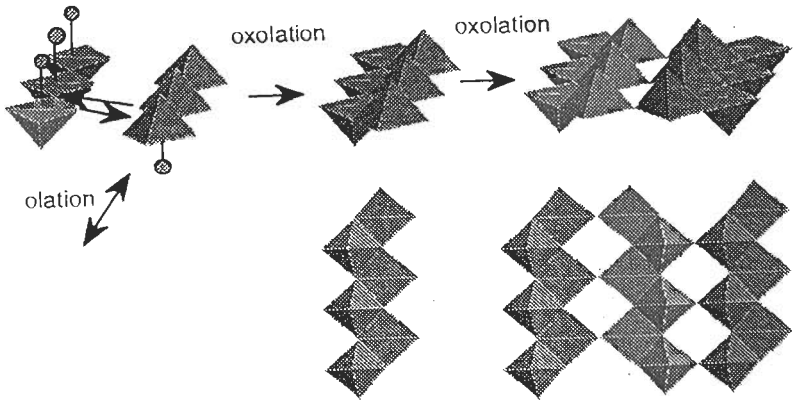

Figure 4.17 Possible formation mechanism of a $V_2O_5.nH_2O$ gel from the neutral precursor $VO(OH)_3(OH_2)_2$

along their axis. Several possible chain structures are possible, depending on the precursor:

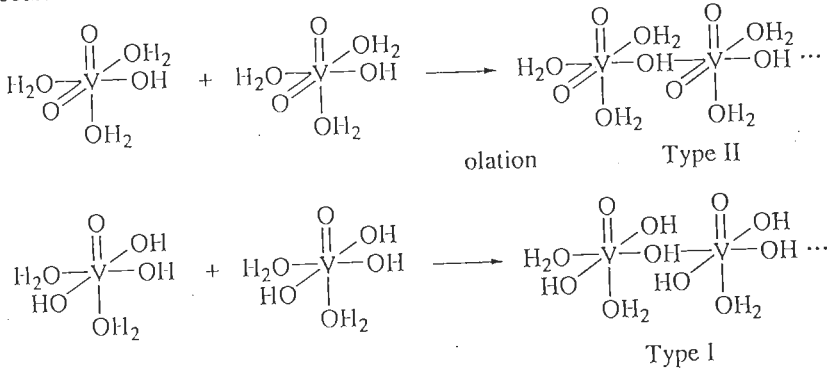

Type II chains formed by the dioxo precursor cannot link to each other. However, subsequent condensation by oxolation of type I chains stabilizes μ_2–OH bridges into μ_3–O bridges, leading to the formation of ribbons connected by hydrogen bonds [61] (Figure 4.17). Upon thermal dehydration, V_2O_5 crystallizes.

This reaction mechanism is oversimplified because gelation of vanadic acid requires the presence of traces of V(IV), which appear spontaneously during acidification with an ion-exchange resin or with addition of alcohol [58,62]. The role of V(IV) as a catalyst is not quite clear yet [63]. It may act as an initiator of the initial condensation, either by olation of vanadic complexes or in the oxolation of the chains. Indeed, the nucleophilic power of the hydroxo ligands in the species formed by V(IV), $[VO(OH)_2(OH_2)_3]^0$, is probably greater than that of the hydroxo

ligands present in the correponding forms of V(V), because of the smaller formal charge on the cation.

The conductivity of vanadic gels has both ionic and electronic components. Ionic conductivity stems from the mobility of protons in the water-swollen space between the sheets, and it occurs in wet gels. Electronic conductivity is due to the mobility of electrons between V(IV) and V(V) sites in the lattice, and occurs only in dry gels [64]. This leads to interesting applications such as the fabrication of antistatic strips on photographic film, for example [65].

Although qualitative, the proposed mechanism stresses that the formation of vanadium oxide does not stem from an oxolation reaction alone. This is also true for other elements [Sn(IV), Sb(V), W(VI), etc.). The formation of solid phases of metal oxides by precipitation always involves at least one olation step, because oxolation *alone* leads only to the formation of polyanions (see Chapter 2).

(c) Other Vanadic Polyanions

The decavanadic ion is the largest isopolyanion formed in water by pentavalent vanadium in the presence of alkali or protons. A change of solvent and/or cation may allow formation of other species, some of which exhibit very surprising structures.

We have already discussed the effect that the nature of the solvent and the presence of some cations, particularly quaternary ammonium cations, have on the reactivity of many systems. Silicates are one such system. It is also the case for polyoxometalates, and in particular polyoxovanadates. Furthermore, the formation of V(IV)/V(V) mixed-valence polyanions also increases the number of structural varieties. Recent studies by A. Müller in Germany and W.G. Klemperer in the United States, have shown spectacular results in the chemistry of polyoxovanadates. In the following sections, the synthesis and structure of some of these compounds are discussed.

i *Vanadium V compounds*

After refluxing the decavanadate $V_{10}O_{28}H_z[N(nBu)_4]_4$ in acetonitrile for 1–2 min, it is possible to extract the $[CH_3CN.V_{12}O_{32}]^{4-}$ anion [66] as a tetraphenylphosphonium salt. The compound contains vanadium atoms in pyramidal 5-coordination, and exhibits a very open 'basket' structure holding a molecule of acetonitrile almost in its entirety (Figure 4.18a).

Prolonged reflux of $V_{10}O_{28}H_3[N(nBu)_4]_3$ in acetonitrile yields a very compact polyanion $[V_{13}O_{34}]^{3-}$ with a structure based on extremely distorted VO_6 octahedra [67] (Figure 4.18b). The structure is reminiscent of Keggin's description of the tungstic polyanions (Figure 4.24), but the trivanadic groups and the thirteenth atom of vanadium form a much more compact two-layer configuration.

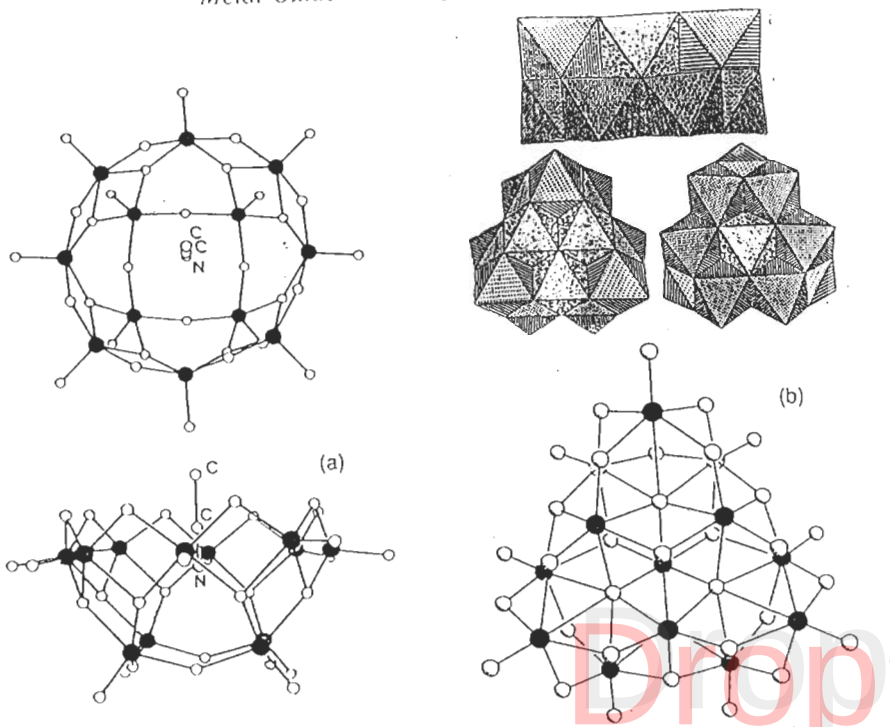

Figure 4.18 (a) Structure of $[V_{12}O_{32}]^{4-}$ (the vanadium atoms are shown as filled circles). Reprinted with permission from [66]. Copyright 1989 American Chemical Society from [66]. (b) Structure of $[V_{13}O_{34}]^{3-}$. Reprinted with permission from [67]. Copyright 1992 American Chemical Society from [67]

ii *V(IV) compounds and V(IV)/V(V) mixed-valence compounds*

Some V(IV) oxopolyvanadates or some mixed-valence (V(IV)/V(V)) compounds formed in aqueous solution are a very unique family of compounds. Their architecture appears to be controlled by a template around which the structure develops.

Vanadium(IV) forms $[V_{18}O_{42}]^{12-}$ from $VOSO_4$ in an alkaline medium (pH 14). Corner- and edge-sharing VO_5 pyramids form a 4.5 Å diameter shallow sphere [68] (Schlemper's structure, Figure 4.19a) which traps a water molecule within its volume. In the structure, V(IV) atoms (d^1) are separated by an average of 2.95 Å and exhibit antiferromagnetic coupling.

Reduction of KVO_3 by hydrazine hydroxide followed by the addition of HCl, HBr or HI yields the compounds $K_9[H_4V^{IV}_{18}O_{42}(X)]\cdot 16H_2O$ with X=Cl, Br or I [69]. The halogen ion is also at the center of the hollow sphere (symmetry is close to D_{4d}). The structure is very similar to Schlemper's (Figure 4.19b). A similar cage

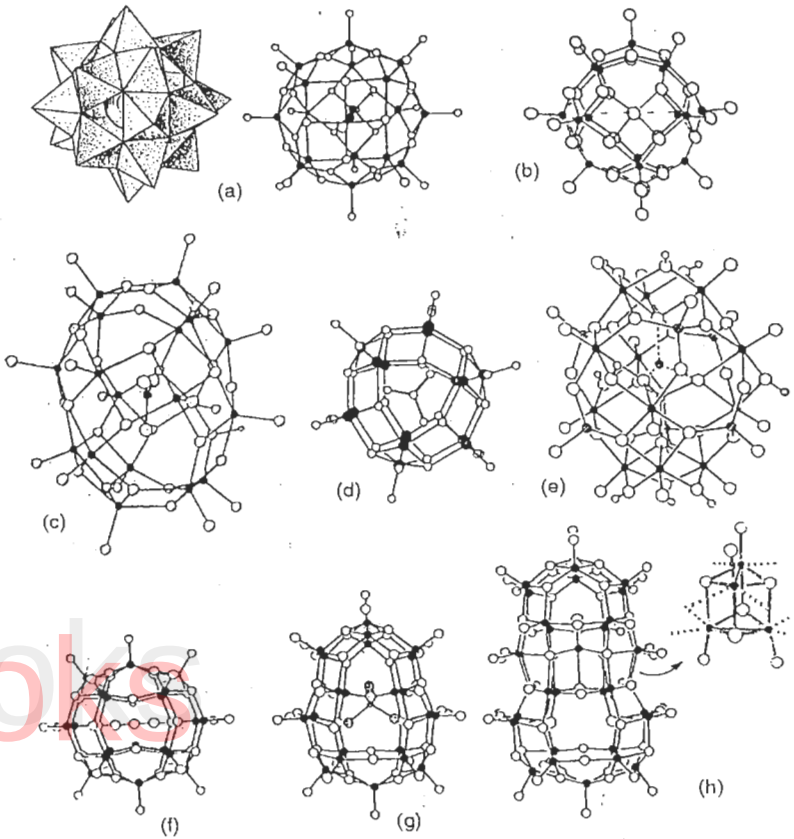

Figure 4.19 Cage structures of polyoxovanadic ions: (a) $[V_{18}O_{42}(H_2O)]^{12-}$ (reproduced by permission of the American Chemical Society from [68]); (b) $[H_4V_{18}O_{42}(X)]^{9-}$ (X=Cl, Br, I); (c) $[HV_{18}O_{42}(NO_3)]^{10-}$; (d) $[V_{15}O_{36}(CO_3)]^{7-}$; (e) $[V_{19}O_{41}(OH)_9]^{9-}$; (f) $[H_2V_{18}O_{44}(N_3)]^{5-}$; (g) $[HV_{22}O_{54}(ClO_4)]^{6-}$; (h) $[V_{34}O_{82}]^{10-}$. (Peproduced by permission of VCH from [69,70,71,72])

[70] containing a citrate ion also exists in $[HV^{IV}_{12}V^{V}_{6}O_{42}(NO_3)]^{10-}$ (Figure 4.19c). Treating V_2O_5 with $LiCO_3$ and later with hydrazine sulfate gives the compound $Li_7[V^{IV}_8V^{V}_7O_{36}(CO_3)]\cdot 39H_2O$. The $V_{15}O^{5-}_{36}$ shell (Figure 4.19d) contains the carbonate [69].

Partial reduction of NH_4VO_3 by hydrazine sulfate in aqueous solution forms $[V_{19}O_{41}(OH)_9]8NH_4\cdot 11H_2O$. Twelve octahedra $V^{IV}O_6$ and six tetrahedra $V^{V}O_4$ form an ellipsoid surrounding a $V^{V}O_4$, tetrahedron which itself shares corners with four octahedra from the shell [71] (Figure 4.19e). This compound heated at 75 °C in aqueous solution in the presence of NEt_4BF_4 and NaN_3 forms $[H_2V^{IV}_8V^{V}_{10}O_{44}(N_3)]\cdot(NEt_4)_5$ [72] (Figure 4.19f).

DropBooks

The hollow cage has D_{2h} symmetry and contains the N_3^- ions. If treated with NEt_4ClO_4 under the same conditions, the V_{19} compound forms $[HV_8^{IV}V_{14}^{V}O_{54}(ClO_4)](NEt_4)_6$ [72] (Figure 4.19g). The hollow cage (symmetry D_{2d}) encapsulates the perchlorate ion. Finally, the reduction of KVO_3 at 90 °C in an aqueous solution of hydrazine hydroxide forms $K_{10}[V_{34}O_{82}]\cdot 20H_2O$. Its cage structure contains 30 atoms of vanadium [12V(IV), 18V(V)] in pyramidal 5-coordination, and contains a $[V_4^{IV}O_4]O_4$ [73] core (Figure 4.19h).

It is interesting to note that in these structures the encapsulated anions (ClO_4^-, N_3^-, NO_3^-) are not an integral part of the framework. Their position within the cavity is controlled by weak interactions with vanadium and oxygen atoms of the shell, which do not affect the crystalline structure [72]. There is no ionocovalent bond between vanadium and oxygen or between vanadium and nitrogen. In $[H_2V_{18}O_{44}(N_3)]^{5-}$, the shortest N···O distances are 3.05 Å. In $[HV_{22}O_{54}(ClO_4)]^{6-}$, the shortest V···O($ClO_3$) distances are 2.96 Å.

The $[V_{12}^{IV}V_2^{V}O_{22}(OH)_4(OH_2)_2(C_6H_5PO_3)_8]^{6-}$ [74] anion exhibits an even more interesting structure. The shell contains $C_6H_5PO_3$ ligands (Figure 4.20) and traps two Cl^-, two NH_4^+ ions and two water molecules. The ions form a planar cycle within the cage, and the distance between them are similar to that observed in the NH_4Cl lattice. Hydrogen bonds within the cavity appear to make a contribution to the electrostatic interactions creating the organized structure.

From a strictly topological standpoint, this family of polyoxovanadates (Figure 4.21) illustrates a very peculiar process of molecular organization in inorganic chemistry. Encapsulation of anions of molecules within shells themselves anionic in nature appears to influence and control the architecture of the system, and hence the use of the terms 'template' or 'guest–host' supercomplexes, which are reminiscent of the chemistry of zeolites or of supramolecular organic chemistry [75].

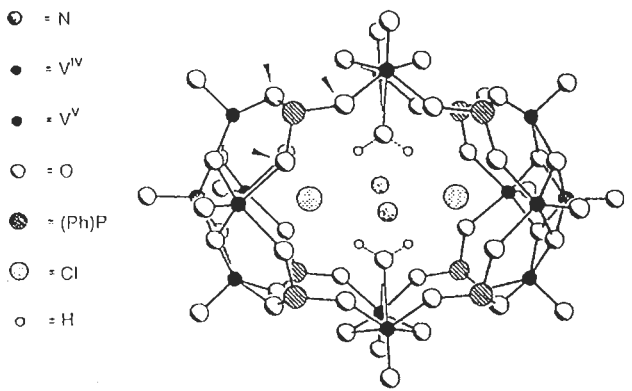

Figure 4.20 Structure of $[V_{14}O_{22}(OH)_4(OH_2)_2(C_6H_5PO_3)_8]^{6-}$. (Reproduced by permission of VCH from [74]

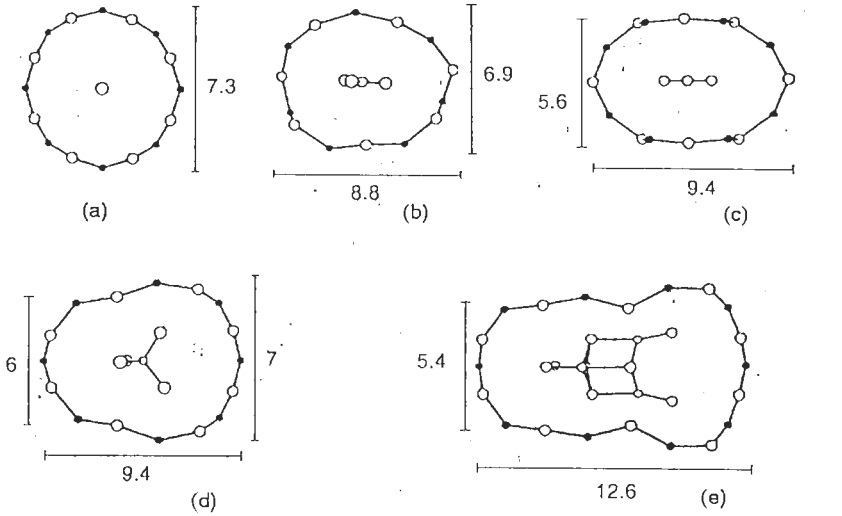

Figure 4.21 Simplified polyvanadic structures built by template effect (lengths in Å): (a) $[H_4V_{18}O_{42}(X)]^{9-}$ (X=Cl, Br or I); (b) $[HV_{18}O_{42}(NO_3)]^{10-}$; (c) $[H_2V_{18}O_{44}(N_3)]^{5-}$; (d) $[HV_{22}O_{54}(ClO_4)]^{6-}$; (e) $[V_{34}O_{82}]^{10-}$. Reproduced by permission of VCH from [72]

The causes of this effect are not well understood at this time. This shell type of structure in which the building block is a pyramid is probably imposed by the large anions (halogen, nitrate, perchlorate, V_4O_4). They are likely to combine the weak repulsion with vanadium-coordinated oxygen and the attraction with the cation itself. These interactions are possible because of the pyramidal coordination of vanadium and the *trans* effect of the terminal V=O group. This type of structure does not occur with tungstate and molybdate, since both of them prefer octahedral coordination.

This architecture is probably possible because V(IV) and V(V) can have several coordination numbers. This results in strong magnetic and/or electronic coupling owing to the presence of V(IV) in d^1 electron configuration. Although the contribution of such couplings to the overall energy of the system is small, they may influence the cohesion of the hollow sphere. This sphere does not form with V(V) alone, although this ion can also adopt the same pyramidal geometry as V(IV).

4.3.2 MO(VI): MOLYBDATES; W(VI): TUNGSTATES

At pH>7, molybdates and tungstates exist in solution as tetraoxo ions MO_4^{2-}. Upon acidification, they form many polyanions [2,45,46]. These are complex systems and we shall limit our discussion to a few of the most stable compounds.

Molydbates in solution reach equilibrium much faster than tungstates, which may take a few days or a few months at room temperature [45]. Thermodynamically

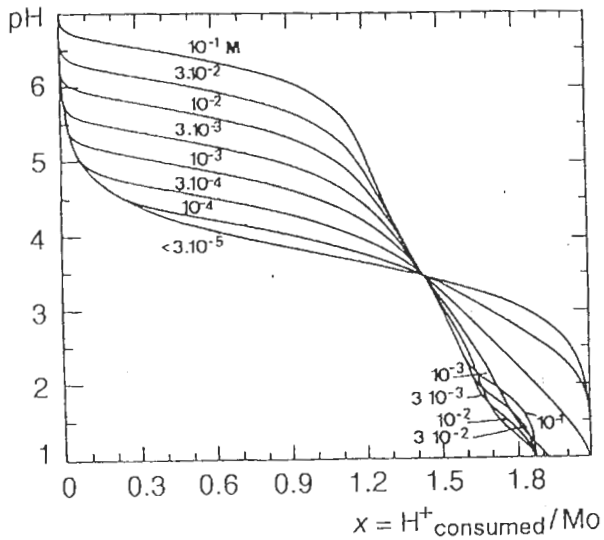

Figure 4.22 Protometric titration of $[MoO_4]^{2-}$ for different molydenum concentrations. Reproduced by permission of John Wiley & Sons from [2]

stable tungstates are formed only after many intermediate compounds are formed [46]. In both cases, 6-coordination is reached during acidification. A few polyanions of Mo(VI) contain both MoO_4 tetrahedra and MoO_6 octahedra. Polyanions of W(VI) contain only WO_6 octahedra [45,46].

(a) Molybdic Polyanions

A titration curve of a molydbate solution does not exhibit a clear equivalent point, only a rather flat equivalence zone around $H^+/Mo = 1.5$ [45] (Figure 4.22). This is due to the presence of many different equilibria and species in solution.

The predominant species is a heptamolybdate (paramolybdate) formed according to the following reaction:

$$7[MoO_4]^{2-} + 8H^+ \longrightarrow [Mo_7O_{24}]^{6-} + 4H_2O$$

This species has been the focus of many studies [46]. No intermediate compound with $1 < n < 7$ has been observed. Between pH 5 and 3, this species coexists with its protonated forms $[HMo_7O_{24}]^{5-}$ (pK = 4.4), $[H_2Mo_7O_{24}]^{4-}$ (pK = 3.5) and $[H_3Mo_7O_{24}]^{3-}$ (pK = 2.5).

The paramolybdate structure is an assemblage of edge-sharing octahedra (addition mechanism) (Figure 4.23). One may consider that it derives from the structure of the decavanadate $M_{10}O_{28}$, from which three octahedra would have been removed [76].

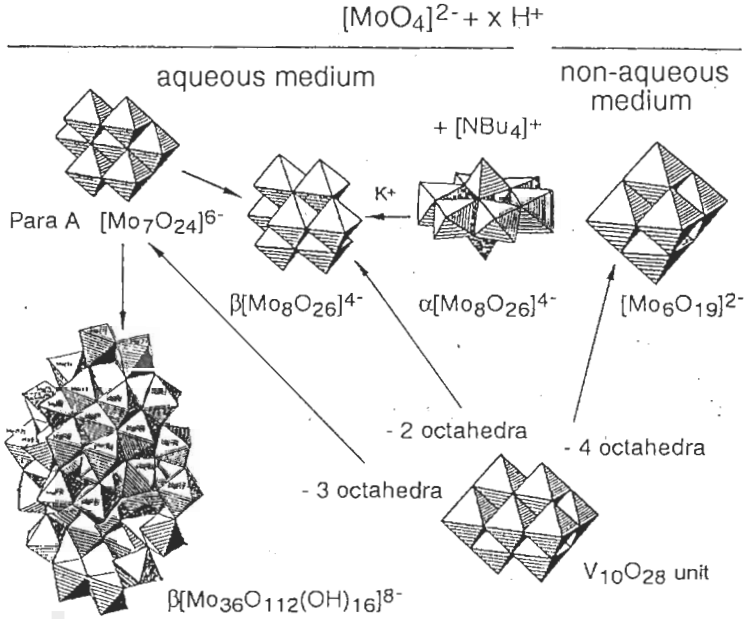

Figure 4.23 Structure of a few molybdic ions

The composition of more acid solutions (pH 2–3, $H^+/Mo = 1.5$) is even more unclear at this time. Investigations point to a series of protonated heptamolybdates, or a mixture of hepta- and octamolybdates $[Mo_8O_{26}]^{4-}$ [46]. The latter has been isolated; its structure (β-$[Mo_8O_{26}]^{4-}$) is also a derivative of the $V_{10}O_{28}$ motif from which two octahedra would have been removed [76] (Figure 4.23). It is possible to stabilize an α isomer of the octamolybdate in the presence of tetrabutylammonium. This polyanion contains a six-atom ring of octahedral molybdenum, capped on each side by two tetrahedral molydenum atoms (Figure 4.23). The addition of a cation such as K^+ triggers $\alpha \rightarrow \beta$ isomerization probably by solvent structuring effects [46].

In non-aqueous media (DMF, DMSO), acidification of the molybdate forms a very compact hexa-condensed structure, $[Mo_6O_{19}]^{2-}$ (Figure 4.23). This structure is common to many systems, [W(VI), Nb(V), Ta(V)] and contains highly deformed octahedra in which Mo–O distances can vary greatly: $Mo–O_{terminal}$ 1.68 Å, $Mo–O_{bridging}$ 1.93 Å, $Mo–O_{central}$ 2.32 Å [46]. The metal atoms are, as is usually the case in most polyanions, strongly pushed towards the exterior of the structure.

A very large polyanion condensed 36 times has been observed in a more acid medium ($H^+/Mo = 1.8$) [77] (Figure 4.23). It probably exists in small concentrations only. This polyanion contains two identical Mo_{18} units each made up of a crown of 11 molybdenum atoms surrounding a Mo_7 group in which two Mo

DropBooks

atoms have a coordination of 7. Both Mo_{18} are connected by four shared oxygen atoms.

At higher acidification ($H^+/Mo > 2$), soluble polycations are formed without the formation of solid phases [78,79]. The molybdic hydrates obtained in strong acid media are described below. Upon the addition of a base, these compounds decompose rapidly to form the $[MoO_4]^{2-}$ monomer.

(b) Tungstic Polyanions

Acidification of tungstate in an aqueous medium leads to a large number of polytungstates [45,46], only two of which are thermodynamically stable:

- paratungstate B, condensed 12 times and formed at around pH 6:

$$12[WO_4]^{2-} + 14H^+ \longrightarrow [H_2W_{12}O_{42}]^{10-} + 6H_2O$$

- α-metatungstate, also condensed 12 times but formed at around pH 4:

$$12[WO_4]^{2-} + 18H^+ \longrightarrow [H_2W_{12}O_{40}]^{6-} + 8H_2O$$

These two polyanions represent the final stage of evolution for acidification $H^+/W = 1.17$ and 1.5 respectively. Paratungstate B crystallizes after 1–2 days at room temperature. α-Metatungstate is completely formed in 15 days at 50 °C.

The structure of these compounds (Figure 4.24) contains W_3O_{14} linear groups and W_3O_{13} rings made up of edge-sharing octahedra. These groups share corners: two linear groups and two rings form paratungstate B; four rings form the α-metatungstate (Keggin structure) [46,55]. In both cases, tritungstic groups form a central cavity where two protons fit. These protons have been studied using neutron diffraction and NMR [46]. They are attached to the most basic oxygen atom, shared by the three octahedra in the rings (μ_3–O bridges). In α-metatungstate, it is not possible to titrate the protons, and it is also impossible to exchange them with the solvent [80] since they are not accessible. The internal protons of the para B are more accessible and can be exchanged with water [81].

In the structure of α-meta, the four oxygen atoms in μ_3 bridges form a tetrahedral cage which may only be occupied by P(V), Si(IV) or Ge(IV) to form Keggin-type heteropolyanions [45,46]. A few phosphatotungstates are described in Chapter 5.

Both polyanions (para B, α-meta) are the product of a very complex series of transformations. Some intermediate compounds have only recently been characterized in solution, using ^{183}W and ^{17}O [82,83] NMR. The complexity of the system is due to the large differences in the reaction kinetics of several equilibria. Some equilibria are attained in seconds or minutes, whereas others require days or weeks [45,46].

Acidification of $[WO_4]^{2-}$ at around pH 6 ($H^+/W = 1.15$; $8H^+/7W$) forms, very rapidly, paratungstate A, $[W_7O_{24}]^{6-}$:

$$7[WO_4]^{2-} + 8H^+ \xrightarrow{\text{fast}} [W_7O_{24}]^{6-} + 4H_2O$$

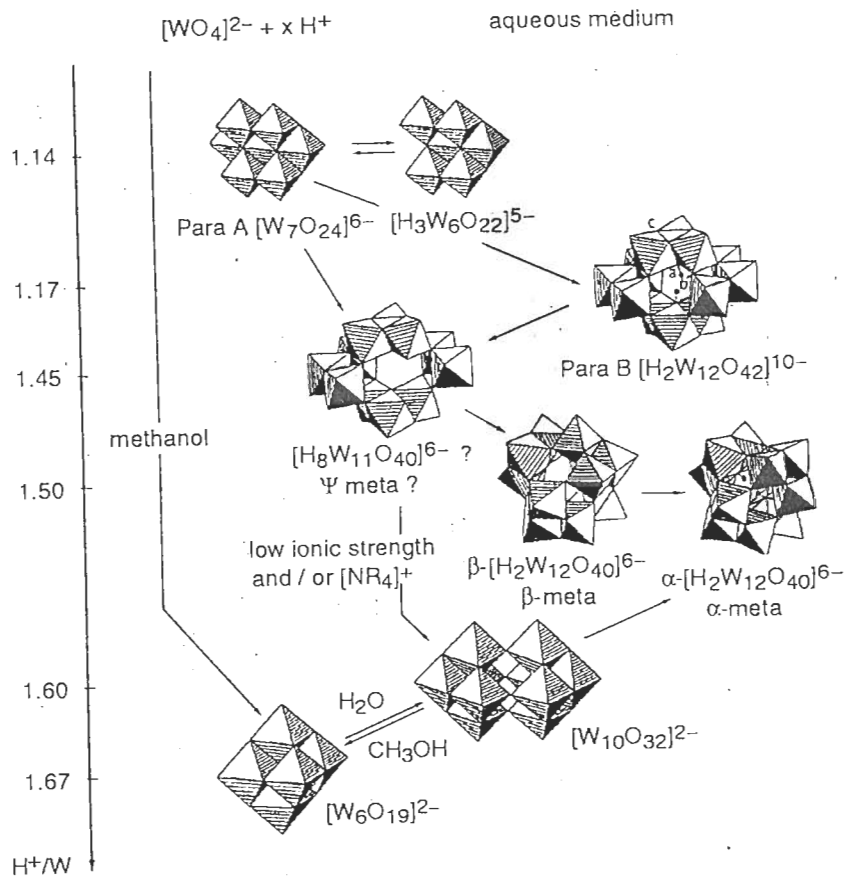

Figure 4.24 Structure of a few tungstic ions

The crystal structure of the polyanion, obtained from the piperidinium salt $(C_5H_{10}NH_2)_6[W_7O_{24}]$ [84], is similar to that of the paramolybdate. It has long been assumed that paratungstate A was an hexatungstate [45]. After a long controversy, it was established that its most probable form was that of an heptatungstate [84]. Although a hexatungstate $[H_3W_6O_{22}]^{5-}$ has recently been identified in solution via IR and Raman spectroscopies, and characterized by XRD as a sodium salt, it seems to be present only in small concentrations [85] (Figure 4.24). This gives an idea of the number of possible species present in solution within such a narrow acidity range. It also illustrates the complexity of the equilibria involved.

It is impossible to protonate para A (NMR peaks are stable as a function of pH [83]), at least until pH 5.5, after which a transformation into para B occurs. The mechanism is probably very complex.

The formation of α-metatungstate in a more acid medium is not direct either. It seems to take place after rapid formation of para A, which then transforms itself into an unknown species, the Ψ-metatungstate. This compound would in turn form the β-metatungstate isomer that would slowly transform into the stable α-metatungstate. The α and β isomers differ by a 120° rotation of one tritungstic group around the C_3 axis (Figure 4.24).

Tungsten and oxygen NMR investigations of the acidification of para B solutions [83] show that it adds an additional proton ($pK_a = 4.59$) to form $[H_3W_{12}O_{42}]^{9-}$. Previously, we described the presence of two protons on μ_3–O bridges within the central cavity of the polyanion (sites a). The shift in NMR peak positions with the pH is very complex. It appears that the later protonation sites are predominantly b-type μ_2–O bridges which are internal to the polyanion, as well as c-type external sites μ_2–O (Figure 4.24). The existence of several protonated isomers $[H_3W_{12}O_{42}]^{9-}$ is also a source of speculation. Some carry three internal protons, with two of these on b sites, which causes the displacement of one of the protons on μ_3–O bridges. The same phenomenon is observed with the decavanadate (Figure 4.15), in which the second and third protonation stages modify all the protonation sites. Other isomers of $[H_3W_{12}O_{42}]^{9-}$ would carry the third proton in rapid exchange on external c-type μ_2–O sites. The conversion from one isomer to another appears to be limited by the exchange of the proton between internal and external sites of the polyanion. These species are metastable. They evolve towards an intermediate compound lacking symmetry. This species seems to be a derivative compound of para B, $[H_7W_{11}O_{40}]^{7-}$, resulting from the elimination of one WO_6 octahedron from one of the linear groups [83] (Figure 4.24). This species could be one of the intermediates responsible for the transformation into α-metatungstate or yellow decatungstate $[W_{10}O_{32}]^{2-}$, the only colored isopolytungstate.

The latter is formed in water in more acid conditions ($H^+/W > 1.5$, $pH < 2$), or in a weak ionic strength medium and/or in the presence of quaternary ammonium cations [45] (Figure 4.24). The decatungstate is metastable in water and slowly transforms into α-metatungstate. It can be stabilized in a non-aqueous medium (methanol, DMSO). Acidification of tungstate in methanol leads to a very compact hexatungstate $[W_6O_{19}]^{2-}$ with a structure similar to that of the molybdate, niobate or tantalate (Figure 4.24). The addition of water causes rapid transformation into decatungstate $[W_{10}O_{32}]^{2-}$ (the half-reaction time is 8 min at 25 °C). The reverse transformation of decatungstate in methanol is much slower ($t_{1/2} = 4$ days at 35 °C). In mixed solvents (addition of water), both ions are at equilibrium [45,46].

Similarly to vanadates and molybdates, WO_6 octahedra in polytungstates are very distorted [46]: in the rings, the $W{-}O_{terminal}$ bond is particularly short (1.70 Å) and the $W{-}O_{central}$ located in *trans* position is very long (2.26 Å). The cation is shifted towards the exterior of the polyanion because of the π character of the $W{-}O_t$ bond. This short bond creates a layer of oxygen atoms strongly polarized towards the inside of the polyanion owing to $d\pi{-}p\pi$ interactions (as in $V_{10}O_{28}$). Hence, oxygen atoms are poorly basic and limit their protonation. This prevents

subsequent condensation via elimination of water. One may also consider that, if condensation were to continue, it would become much more difficult for metal cations to move in order to reduce any repulsion: no edge sharing would then be possible. Therefore, the smaller the metal, the easier it is for interactions to relax, and hence the larger the number of edge-sharing octahedra per polyanion unit:

$$R_{V(V)} > R_{Mo(VI)} \approx RW_{(VI)}$$

$$[V_{10}O_{28}]^{6-}\ [Mo_8O_{26}]^{4-}\ [W_7O_{24}]^{6}$$

It is possible for larger tungsten and molybdenum polyanions to form, such as ($[H_2W_{12}O_{40}]^{6-}$ or $[Mo_{36}O_{112}(H_2O)_{16}]^{8+}$), but they involve corner-sharing of octahedra in order to alleviate electrostatic repulsions between metal cations.

It is important to stress an important difference between Mo(VI) and W(VI). There are very few isostructural polymolybdates and polytungstates: the para A $[M_7O_{24}]^{6-}$ and the compact hexa $[M_6O_{19}]^{2-}$. Most molybdates are of the *cis*-dioxo type (two terminal oxygens in *cis*), whereas most tungstates are of the mono-oxo type (only one terminal oxygen per octahedron). Only the *cis*-dioxo tungstate (para A) is unstable compared with the molybdate. It is very difficult to understand this difference in behavior. Since single M–O bonds have the same length in tungstic and molybdic polyanions, (1.92 Å), one would think, as Pope [46] speculated, that better orbital overlap would occur with tungsten, since the reach of the 5d orbital is larger than that of the 4d. The molybdates could therefore compensate the weakness of single bonds by an increase in the number of multiple π bonds.

The difference in electronic configuration also has interesting consequences regarding the possible reduction of the metal. The distortion of the WO_6 octahedron imposes the C_{4v} symmetry in the polyhedron because of the shortening of the $W{-}O_t$ bond. This bond is too short to exhibit σ character and may be considered a double π bond. A simplified molecular orbitals diagram (Figure 4.25) shows that, for this symmetry, the d_{xy} orbital is still non-bonding, whereas in the case of molybdenum the same orbital is used to create a second π bond corresponding to the *cis*-dioxo configuration.

It is now easier to understand why the two-electron reduction is reversible in the tungstic polyanion: electrons occupy the empty d_{xy} orbital. Its non-bonding character has little influence on the structure. However, in the *cis*-dioxo configuration, electrons must place themselves in the available orbitals, which are antibonding, causing important structural modifications and, in most cases, irreversibility of the reduction [86,87].

The reversible nature of the reduction in tungstic polyanions gives them an important role as catalysts. The polyanions ensure electron transfer during redox reactions in solution. The initial form is regenerated by reoxidation upon exposure to air [46]. The importance of polyoxometallates in this field is strengthened by their high Brönsted acidity. The biological activity of some polyoxometallates also makes them good candidates for medical applications: heteropolyanions [88] are

PropBooks

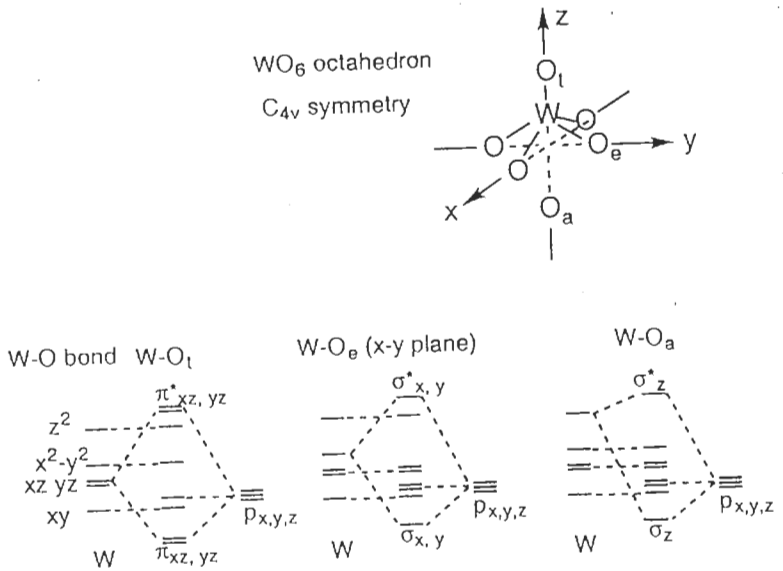

Figure 4.25 Simplified molecular orbital diagram for a C_{4v} WO_6 complex in a tungstic polyanion

particularly interesting since they form a large and diverse family of compounds. A study of these compounds, although undoubtedly fascinating, would be beyond the scope of this book. However, a few phosphatotungstic polyanions are described in Chapter 5.

(c) Solid Phases: Tungstic and Molybdenic Oxides and Hydrates

The difference in behavior of Mo(VI) and W(VI) in polyanions is also observed in the solid hydrated phases. The greater versatility of tungsten is reflected in the larger diversity of its oxides, as nicely shown in work by Figlarz *et al.* [89,90].

As in the case of the vanadates, ageing or heating of tungstic acid solutions of weak ionic strength (acidification by resin exchange) leads to the formation of an opaque solution and of a precipitate after a few hours. For $C_W < 0.5\,mol\,l^{-1}$, the pale yellow precipitate is $WO_3 \cdot 2H_2O$. If $C_W > 0.7\,mol\,l^{-1}$, it is a dark yellow $WO_3 \cdot H_2O$ [91]. The particles observed look like ordered or tactoidal platelets [92,93] (Figure 4.26). These hydrates are also obtained by acidification of $NaWO_4$ with concentrated HCl ($HCl \approx 3\,mol\,l^{-1}$) [94]. The $WO_3 \cdot 2H_2O$ hydrate precipitates at room temperature and $WO_3 \cdot H_2O$ forms at 100 °C.

Acidification of tungstate on a resin immediately causes formation of the decatungstate in equilibrium with the octahedral monomer $[WO(OH)_4(OH_2)]^0$. Only one molecule of water is present in the coordination sphere, in *trans* position from

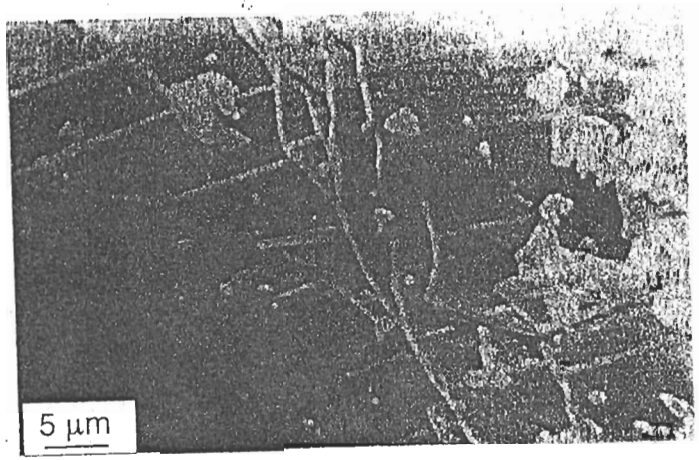

Figure 4.26 SEM micrograph of a tungstic gel of $WO_3 \cdot H_2O$ formed by acidification of sodium tungstate on a resin. From [92]

the oxo group. This is different from what happens with the vanadate. Condensation along this axis is therefore blocked and the only possible reaction is oxolation by two-dimensional growth and the formation of μ_2–O bridges. The sheets obtained are piled on top of each other, in a more or less ordered manner, and are bound together via hydrogen bonds between water molecules and oxo groups on each side of the tungstic sheets.

$MoO_3 \cdot 2H_2O$ precipitates very slowly, after about 3 weeks, from a solution of sodium molybdate in concentrated nitric acid ($\approx 4\,mol\,l^{-1}$) at room temperature. Through dissolution of the hydrate in $12\,mol\,l^{-1}$ hydrochloric acid, followed by dilution to $3\,mol\,l^{-1}$, $MoO_3 \cdot H_2O$ crystallizes. Both hydrates are made of sheets of corner-sharing octahedra and are isomorphous of their tungstic homologues [89]. However, their formation is more difficult since more brutal synthesis conditions are required for octahedra to share corners. This behavior is similar to the behavior of tungstic and molybdenic polyanions.

Hydrothermal treatment at 120 °C of a tungstic gel, or of a suspension of $WO_3 \cdot 2H_2O$, forms the hydrate $WO_3 \cdot 1/3H_2O$. Depending on the nature of the precursor used, it forms either needles or platelets (Figure 4.27) [89,90].

The orthorhombic structure of the hydrate $WO_3 \cdot 1/3H_2O$ consists of planes of corner-sharing octahedra. These planes are slightly offset from one another and are connected by the corners of some octahedra. Some water molecules are at the corner of some octahedra (Figure 4.28).. $WO_3 \cdot 1/3H_2O$, stable until 250 °C, dehydrates at higher temperatures to form the hexagonal oxide WO_3. Its structure is similar to that of the hydrate but the planes coincide on top of each other (Figure 4.28). Therefore, the lattice contains hexagonal channels in which hydrogen or alkaline atoms can be inserted to form the family of hexagonal bronzes M_xWO_3

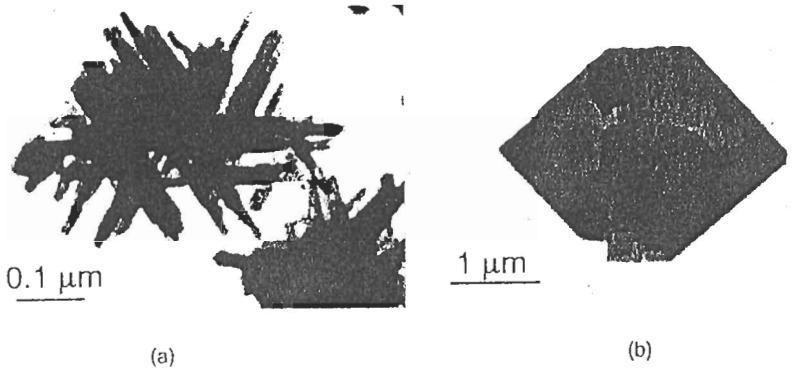

Figure 4.27 $WO_3 \cdot 1/3H_2O$ obtained by hydrothermal synthesis (a) as needles if obtained from tungstic gel and (b) as octagonal platelets if obtained from $WO_3 \cdot H_2O$. Reproduced from [90] Copyright 1989 with permission from Elsevier Science Ltd, The Boulevard, Langford Lane, Kidlington OX5 1GB, UK

[90]. Chemical intercalation of *n*-butylLi or naphthaleneLi(Na) is reversible until $x = 1$. Beyond this level, insertion forces the oxide to become amorphous.

The pseudomorphous transformation of $WO_3 \cdot 1/3H_2O$ into hexagonal WO_3 preserves the initial particle morphology. Although a direct parental relationship could be seen between both phases, the transformation actually takes place via complete reconstruction of the structure [90]. Elimination of water forces the rearrangement of W–O bonds, but the organization of the bonds is similar in the 001 planes in each phase. Therefore, the nucleation energy of the metastable hexagonal crystal is minimum and oxide nuclei appear first on the 001 plane of the hydrate. The transformation proceeds via progressive and oriented displacement of the oxide–hydrate interface. Around 400 °C, hexagonal WO_3 transforms into monoclinic WO_3 (Figure 4.28). This transformation is non-pseudomorphous but it also takes place via preferential orientation of the nucleation of the thermodynamically stable phase.

Hydrothermal treatment at 110 °C of a solution of molybdic acid obtained by acidification of molybdate on a resin or by dissolution of $MoO_3 \cdot 2H_2O$ also causes the formation of the hydrate $MoO_3 \cdot 1/3H_2O$. Its morphology is different from that of its tungstic homologue (Figure 4.29) but both are isostructural [94].

On the other hand, dehydration of $MoO_3 \cdot 1/3H_2O$ at 300 °C forms the monoclinic oxide MoO_3. Transformation of $MoO_3 \cdot 1/3H_2O$ into the monoclinic oxide proceeds according to a mechanism of preferentially oriented nucleation and growth. However, in molybdic phases, the common arrangement of Mo–O bonds is of the ReO_3 type, which explains why the monoclinic phase of MoO_3 would have the lowest nucleation energy. Nevertheless, this phase is metastable and transforms at 400 °C in the orthorhombic variety (Figure 4.30). In this structure, molybdenum exhibits the *cis*-dioxo configuration characteristic of the stable Mo(VI) polyanions.

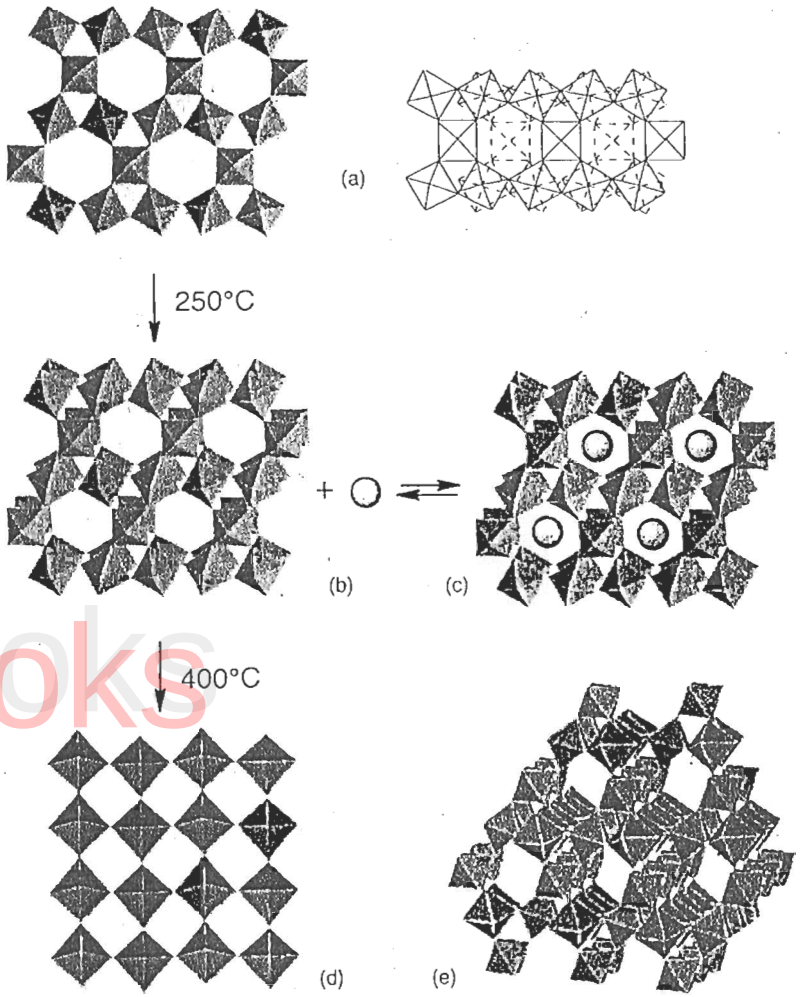

Figure 4.28 Structures of tungstic hydrates and oxides: (a) $WO_3 \cdot 1/3H_2O$ (001) plane and connection between 001 planes; (b) hexagonal WO_3 with one-dimensional channels along the c axis; (c) hexagonal bronze M_xWO_3; (d) monoclinic WO_3; (e) pyrochlore WO_3 (111 planes)

The difference in behavior between tungstic and molybdic hydrates and oxides probably stems from a difference in the π interactions in the W–O and Mo–O bonds [46,90].

The effect of the cations on the development of the structure is clearly seen with tungsten, which forms, in the presence of Cs^+ or Rb^+, a pyrochlore phase of tungstic oxide $(M_2O)_xW_2O_6$, with $M = Cs^+$, Rb^+ and $0.3 < x < 0.5$ [90]. The

DropBooks

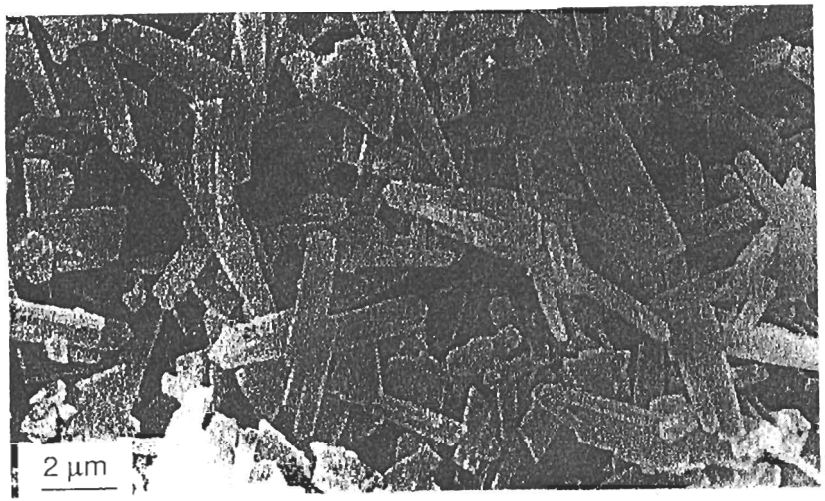

Figure 4.29 Particles of $MoO_3 \cdot 1/3H_2O$ obtained by hydrothermal synthesis. Reproduced from [90] Copyright 1989 with permission from Elsevier Science Ltd, The Boulevard, Langford Lane, Kidlington OX5 1GB, UK

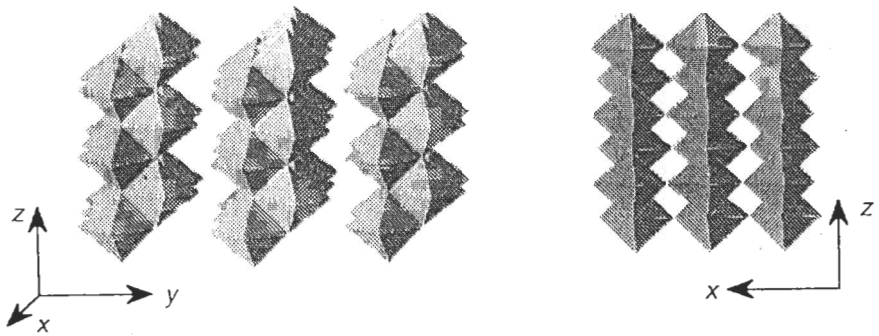

Figure 4.30 Structure of orthorhombic MoO_3

synthesis involves heating an acid (pH 3) solution of sodium tungstate and cesium or rubidium carbonate at 90 °C. Another processing route involves boiling the carbonate/tungstate solution in polyethylene glycol with acetic acid [90]. The reaction is complete after 20 h. Heating paratungstate B $(NH_4)_2W_{12}O_{41} \cdot 5H_2O$ under similar conditions forms the pyrochlore phase $(NH_4O)_{0.5}W_2O_6$. Three-dimensional channels in the pyrochlore structure allow easy and complete exchange of the ammonium ions for the protons in an acid medium. The Cs^+ and Rb^+ ions are more difficult to exchange because of their size. Contrary to antimonic acid of similar pyrochlore structure (see Section 4.2.2), atmospheric water in the exchanged

phase $WO_3 \cdot 0.5H_2O$ is very mobile and weakly bound to the electrically neutral lattice [90].

Such examples of condensation of oxo–hydroxo and hydroxo species illustrate different types of behavior leading either to infinite networks or to discrete species (polyanions). Two parameters appear to be essential: the size of the cation and its ability to be a good π acceptor.

The latter parameter is a consequence of the ability of an element to involve low-energy, empty d orbitals in the metal–oxygen bond. Metal–oxygen π bonds in which the oxygen loses almost entirely its properties as a base are therefore terminal bonds with no possibility of condensation to oligomers (polyoxoanions). This behavior is typical of transition metal oxides. For these elements, the size of the metal ion also limits the condensation: the small size of Cr(VI) forbids an increase in its coordination number.

Elements such as Si(IV), Sn(IV), Ge(IV), Sb(V) and Te(VI), for example, have sizes comparable with Mo(VI) and W(VI). However, they cannot form π bonds with oxygen (no terminal oxygen) since they lack accessible d orbitals. Some polyoxoanions formed under specific acid conditions may protonate upon increased acidification, and may increase their condensation by aggregation or oxolation between particles. This leads to large chains or planar structures, or even networks of tetrahedra (Si) or octahedra (Sn, Sb, Te). There is no short M–O bond in the coordination polyhedron to hinder protonation and condensation. This might be an opportune time to point out the case of P(V): the presence of the P=O double bond decreases the electrophilic character of the cation and prevents its condensation in solution. In addition, if the oxolation reaction is the only one to occur in solution, condensation is always limited and causes the formation of polyacids. The formation of solid phases is usually the result of a double condensation process, oxolation and olation.

Although we have stressed the 'aqueous chemistry' aspect in this chapter, all condensation processes are influenced by some countercations and by the solvent. The few examples discussed here show that these factors are likely to open the way for new synthesis routes for many applications such as the control of the formation of oligomers by the cationic (or anionic) template effect.

4.4 REFERENCES

1. C.L. Rollinson, *Chemistry of the Coordination Compounds*, Vol. 131, Am. Chem. Soc. Master Ser., Bailar Ed., New York, (1956), p. 448.
2. C.F. Baes, R.E. Mesmer, *The Hydrolysis of Cations*, J. Wiley & Sons, New York (1976).
3. J.B. Farmer, *Adv. Inorg. Chem. Radiochem.* 25, 187 (1982).
4. R.J. Iler, *The Chemistry of Silica*, J. Wiley & Sons, New York (1979).
5. P. Souchay, J. Lefebvre, *Equilibres et Réactivité des Complexes en Solution*, Masson, Paris (1969).
6. A.F. Wells, *Structural Inorganic Chemistry*, 5th ed., Clarendon Press, Oxford (1991).

7. C.T.C. Knight, *J. Chem. Soc. Dalton Trans.* 1457 (1988).
8. L.S. Dent Glasser, E.E. Lachowski, *J. Chem. Soc. Dalton Trans.* 393 (1980); 399 (1980).
9. R.K. Harris, R.H. Newman, *J. Chem. Soc. Faraday Trans. II* 73, 1204 (1977).
10. R.K. Harris, C.T.C. Knight, W.E. Hull, *J. Am. Chem. Soc.* 103, 1577 (1981).
11. R.K. Harris, C.T.C. Knight, W.E. Hull, *Am. Chem. Soc. Symp. Ser.* 194, 79 (1982).
12. R.K. Harris, C.T.C. Knight, *J. Chem. Soc. Faraday Trans. II* 79, 1525 (1983); 79, 1539 (1983).
13. R.K. Harris, M.J. O'Connor, E.H. Curzon, O.W. Howarth, *J. Magn. Reson.* 57, 115 (1984).
14. C.T.C. Knight, R.J. Kirkpatrick, E. Oldfield, *J. Chem. Soc. Chem. Comm.* 919 (1989).
15. D. Hoebbel, W. Wieker, *Z. Anorg. Allg. Chem.* 384, 43 (1971).
16. R.K. Harris, C.T.C. Knight, *J. Mol. Struct.* 78, 273 (1982).
17. D. Hoebbel, G. Garzo, G. Engelhardt, R. Ebert, E. Lippmaa, M. Alla, *Z. Anorg. Allg. Chem.* 465, 15 (1980).
18. D. Hoebbel, G. Garzo, G. Engelhardt, A. Varga, *Z. Anorg. Allg. Chem.* 494, 31 (1982).
19. C.T.C. Knight, R.J. Kirkpatrick, E. Oldfield, *J. Chem. Soc. Chem. Comm.* 66 (1986).
20. D. Hoebbel, W. Wieker, P. Francke, A. Otto, *Z. Anorg. Allg. Chem.* 418, 35 (1975).
21. M. Coudurier, B. Baudru, J.B. Donnet, *Bull. Soc. Chim. Fr.* 9, 3147 (1971); 9, 3154 (1971); 9, 3161 (1971).
22. (a) S. Caillère, S. Hénin, M. Rautureau, *Minéralogie des Argiles*, Vols 1 and 2, Masson, Paris (1982); (b) L.G. Berry, B. Mason, *Mineralogy, Concepts, Description, Determination*, 2nd Ed., W.H. Freeman, San Francisco (1972).
23. (a) D. Barthomeuf, *La Recherche* 11, 908 (1980); (b) R.M. Barrer, *Hydrothermal Chemistry of Zeolites*, Academic Press, London (1982).
24. D.W. Breck, *Zeolite Molecular Sieves. Structure, Chemistry and Uses*, J. Wiley & Sons, New York (1974).
25. J. Lefebvre, H. Maria, *C. R. Acad. Sci. Paris* 256, 3121 (1963).
26. M. Abe, T. Ito, *Bull. Chem. Soc. Jpn* 41, 333 (1968).
27. A. Clearfield, *Inorganic Ion Exchange Materials*, CRC Press, Inc., Boca Raton, Florida (1982).
28. J. Lemerle, *Rev. Chim. Min.* 9, 863 (1972); 10, 431 (1973).
29. L.H. Baestle, D. Huys, *J. Inorg. Nucl. Chem.* 30, 1968 (1968).
30. J.P. Jolivet, J. Lefebvre, *Rev. Chim. Min.* 9, 845 (1972).
31. W.A. England, M.G. Cross, A. Hamnett, P.J. Wiseman, J.B. Goodenough, *Solid State Ionics* 1, 231 (1980).
32. U. Chowdhry, J.R. Barkley, A.D. English, A.W. Leight, *Mat. Res. Bull.* 17, 917 (1982).
33. S. Cahuzac, J. Lefebvre, *Bull. Soc. Chim. Fr.* 771 (1969).
34. J.M. Colin, J. Lefebvre, *C.R. Acad. Sci. Paris* 268, 1760 (1969).
35. M. Ocana, E. Matijevic, *J. Mater. Res.* 5, 1083 (1990).
36. R.S. Hiratsuka, S.H. Pulcinelli, C.V. Santilli, *J. Non Cryst. Solids* 121, 76 (1990).
37. S.H. Pulcinelli, C.V. Santilli, J.P. Jolivet, E. Tronc, *J. Non Cryst. Solids* 170, 21 (1994).
38. J.D. Donalson, M.J. Fuller, *J. Inorg. Nucl. Chem.* 30, 1083 (1968).
39. R.K. Momii, N.H. Nachtrieb, *Inorg. Chem.* 6, 1189 (1967).
40. H.D. Smith Jr, R.J. Wiesenma, *Inorg. Chem.* 11, 1152 (1972).
41. K.F. Purcell, J.C. Kotz, *Inorganic Chemistry*, Holt Saunders Japan Intern. Ed., Philadelphia (1985).
42. J. Lefebvre, *J. Chim. Phys.* 567 (1957).
43. N. Ingri, *Acta Chem. Scand.* 16, 439 (1962).
44. R.E. Messmer, C.F. Baes, F.H. Sweeton, *Inorg. Chem.* 11, 537 (1972).
45. P. Souchay, *Ions Minéraux Condensés*, Masson, Paris (1969).
46. M.T. Pope, *Heteropoly and Isopolyoxometallates*, Springer-Verlag, Berlin (1983).

47. R.D. Shannon, C.T. Prewitt, *Acta Cryst.* B25, 925 (1969).
48. B.N. Figgis, *Introduction to Ligand Fields*, Interscience Publishers, J. Wiley & Sons, New York (1966).
49. C.J. Ballhausen, H.B. Gray, *Molecular Orbital Theory*, W.A. Benjamin Inc., New York (1964).
50. D.L. Kepert, *Prog. Inorg. Chem.* 4, 199 (1962).
51. K.H. Tytko, O. Glemser, *Adv. Inorg. Chem. Radiochem.* 19, 239 (1976).
52. A. Goiffon, B. Spinner, *Bull. Soc. Chim. Fr.* 11–12, 2435 (1975); 11–12, 1081 (1977).
53. J.R. Van Wazer, *Phosphorus and its Compounds*, Vol. 1, Interscience, New York (1958).
54. E. Heath, O.W. Howard, *J. Chem. Soc. Dalton Trans.* 1105 (1981).
55. D.L. Kepert, *The Early Transition Metals*, Academic Press, New York (1953).
56. V.W. Day, W.G. Klemperer, D.J. Maltbie, *J. Am. Chem. Soc.* 109, 2991 (1987).
57. J.F. Hazel, W.M. McNabb, R. Santini, *J. Phys. Chem.* 57, 681 (1953).
58. N. Gharbi, C. Sanchez, J. Livage, J. Lemerle, L. Nejem, J. Lefebvre, *Inorg. Chem.* 21, 2758 (1982).
59. J.J. Legendre, J. Livage, *J. Colloid Interface Sci.* 94, 75 (1983).
60. P. Souchay, *Thermodynamique Chimique*, 3rd ed., Masson, Paris (1968).
61. J.J. Legendre, P. Aldebert, N. Baffier, J. Livage, *J. Colloid Interface Sci.* 94, 84 (1983).
62. J. Lemerle, L. Nejem, J. Lefebvre, *J. Inorg. Nucl. Chem.* 42, 17 (1980).
63. G.A. Poznarsky, A.V. McCormick, *Chem. Mater.* 6, 380 (1994).
64. C. Sanchez, F. Babonneau, R. Morineau, J. Livage, *Phil. Mag.* B47, 279 (1983).
65. Kodak-Pathé, French Patent (BF) 2318442 (1977) and BF 2429252 (1979).
66. V.W. Day, W.G. Klemperer, O.M. Yaghi, *J. Am. Chem. Soc.* 111, 5959 (1989).
67. D. Hou, K.S. Hagen, C.L. Hill, *J. Am. Chem. Soc.* 114, 5864 (1992).
68. G.K. Johnson, E.O. Schlemper, *J. Am. Chem. Soc.* 100, 3645 (1978).
69. A. Müller, M. Penk, R. Rohlfing, E. Krickemeyer, J. Döring, *Angew. Chem. Int. Ed. Engl.* 29, 926 (1990).
70. A. Müller, *Nature* 352, 115 (1991).
71. A. Müller, M. Penk, E. Krickemeyer, H. Bögge, H.J. Walberg, *Angew. Chem. Int. Ed. Engl.* 27, 1719 (1988).
72. A. Müller, E. Krickemeyer, M. Penk, R. Rohlfing, A. Armatage, H. Bögge, *Angew. Chem. Int. Ed. Engl.* 30, 1674 (1991).
73. A. Müller, R. Rohlfing, J. Döring, M. Penk, *Angew. Chem. Int. Ed. Engl.* 30, 588 (1991).
74. A. Müller, K. Hovemeier, R. Rohlfing, *Angew. Chem. Int. Ed. Engl.* 31, 1192 (1992).
75. B. Dietrich, P. Viout, J.M. Lehn, *Aspects de la Chimie des Composés Macrocycliques*, InterEditions, Paris (1991), p. 183.
76. D.L. Kepert, *Inorg. Chem.* 8, 1556 (1969).
77. B. Krebs, I. Paulat-Böschen, *Acta Cryst.* B38, 1710 (1982).
78. E. Richardson, *J. Inorg. Nucl. Chem.* 25, 575 (1959).
79. Y. Doucet, S. Bugnon, *J. Chim. Phys.* 54, 155 (1957).
80. M.T. Pope, G.M. Varga Jr, *J. Chem. Soc. Chem. Comm.* 653 (1966).
81. J.P. Launay, M. Boyer, F. Chauveau, *J. Inorg. Nucl. Chem.* 38, 243 (1976).
82. R.I. Maksimovskaya, K.G. Burtseva, *Polyedron* 4, 1559 (1985).
83. J.J. Hasting, O.W. Howarth, *J. Chem. Soc. Dalton Trans.* 209 (1992).
84. J. Fuchs, E.P. Flindt, *Z. Naturforsch.* 34, 412 (1979).
85. H. Hartl, R. Palm, J. Fuchs, *Angew. Chem. Int. Ed. Engl.* 32, 1492 (1993).
86. J.P. Launay, Thesis, Université P. et M. Curie, Paris (1974).
87. J.P. Launay, *J. Inorg. Nucl. Chem.* 38, 807 (1976).
88. M.T. Pope, A. Müller, *Angew. Chem. Int. Ed. Engl.* 30, 34 (1991).
89. M. Figlarz, *Rev. Chim. Min.* 22, 177 (1985).
90. M. Figlarz, *Prog. Solid State Chem.* 19, 1 (1989).

DropBooks

91. D.L. Kepert, J.M. Kyle, *J. Chem. Soc. Dalton Trans II* 133 (1978).
92. A. Chemseddine, M. Henry, J. Livage, *Rev. Chim. Min.* 21, 487 (1984).
93. A. Chemseddine, F. Babonneau, J. Livage, *J. Non Cryst. Solids* 91, 271 (1987).
94. M.L. Freedman, *J. Am. Chem. Soc.* 81, 3834 (1959).
95. K. P. Schröder, J. Sauer, *J. Phys. Chem.* 97, 6579 (1993).
96. R.F. Mortlock, A.T. Bell, A.K. Chakraborty, C.K. Radke, *J. Phys. Chem.* 95, 4501 (1991).
97. T.W. Swaddle, J. Salerno, P.A. Tregloan, *Chem. Soc. Rev.* 319 (1994).

5

Complexation and Condensation

Up to this point, hydrolysis and condensation have been analyzed taking into account the role of aquo, hydroxo and oxo ligands in the coordination sphere of the cation. However, some of these ligands can often be substituted by molecules or anions from the solution. The modification of the coordination sphere of the cation can strongly affect its behavior during condensation and precipitation.

Depending on the conditions of acidity and temperature, thermohydrolysis of hydrochloric or nitric solutions of Ti(IV) leads to the formation of either the rutile or anatase forms of TiO_2 (see Section 3.4.2). In a sulfuric medium, anatase is always obtained, under any experimental condition [1]. Thermohydrolysis of chromium(III) in a perchloric acid solution gives soluble products only, whereas in the presence of sulfate, sulfate-free Cr_2O_3 monodisperse particles are obtained [2]. Some anions also have a significant influence on the size and the morphology of particles of a given compound (spheres, platelets, needles, etc.), as was nicely shown by Matijevic [3].

The role of anions is very variable because the complexation of a cation can have varying efficiencies, and may take place at various stages of hydrolysis and condensation. Anions or molecules possessing electron donor atoms (Lewis bases) compete with aquo, hydroxo or even oxo ligands to form the coordination sphere (inner sphere complexes). The stability of the complex depends on the relative nucleophilic character of the ligands under given acid–base conditions.

Polydentate molecules or anions (acid–alcohols, polyamines, aminocarboxylates), strongly bound to the cation by several coordination bonds, are able to form very stable chelates, in particular with transition metal ions [4]. Such ligands may replace all others and shield the cation from other reactants. In particular, the cation becomes almost insensitive to pH variations, in wide acidity ranges, and remains soluble as a monomer [5,6]. Some strong monodentate σ donor ligands (NH_3) and σ/π donors (CN^-) play a similar role. These ligands are well known and they are used very frequently in analytical chemistry in order to prevent precipitation.

Some mono or polydentate anions can affect permanently only part of the coordination sphere of the cation if they do not prevent hydrolysis and condensation. Phosphates, chromates, sulfates, carbonates and sometimes chlorides and nitrates are good examples. They form basic salts in which the complexed anions are an integral part of the structure of the solid.

Under certain conditions, particularly in an acid medium, some anions or molecules are able to form a temporary complex with the cation, at specific stages of hydrolysis and condensation when the cation is in monomeric or oligomeric form. Even if the anion is not present in the final solid, complexation often guides the behavior of the purely aquo–hydroxo or oxo–hydroxo form of the cation, thereby influencing some characteristics of the solid such as structure, morphology and particle size.

A similar effect is sometimes observed with weakly complexing anions that only form ion pairs with the cation (outer sphere complexes). Weak electrostatic interactions or steric effects may be responsible for important structural changes such as those observed in the template effect or in vanadic polyanions (see Section 4.3.1c). Some cations play a similar role in the construction of anionic cages (silicates, Section 4.2.1), as they intervene by forming ion pairs and/or causing a particular structuring effect of the solvent (Section 1.1.3). Examples of these effects are discussed in the following sections, with the examples of iron and some phosphato-tungstic polyanions.

If the anions are involved at the end of the condensation process, complexation takes place on the surface of the particles and therefore acts only on the stability of the dispersion (sol or flocculate) by affecting the structure of the electrical double layer (see Part II).

Examples of the influence of anions on the behavior of metallic elements are numerous in the literature. In this chapter, we shall briefly describe the role of the main physicochemical parameters in cation complexation. We shall give examples of some of the consequences of complexation on the behavior of cations in solution and on the characteristics of the resulting products.

DropBooks

5.1 COMPLEXATION OF CATIONS

The complexation of an aquo cation in solution by a X^{n-} species of coordination number α may be written as

$$[M(OH_2)_N]^{z+} + aX^{n-} \Longleftrightarrow [MX_a(OH_2)_{N-\alpha a}]^{(z-an)+} + \alpha a\, H_2O$$

The stability of the complex depends on the donor character of the various competing ligands (Lewis bases). From a purely thermodynamic standpoint, the stability of the complex is characterized by its stability constant K_f:

$$K_f = \frac{[MX_a(OH_2)_{N-\alpha a}^{(z-an)+}]}{[M(OH_2)_N][X^{n-}]^a}$$

The values of these constants have been published [4–6].

The stability constant of the complex is independent of the equilibria of other species in solution, and is not always representative of the effective complexation.

Indeed, anions are Brönsted bases and are likely to protonate, thereby losing their ability to coordinate the cation. Because of the acidity of the aquo ligand, hydroxo ligands may be better Lewis bases than the X^{n-} ligands. Frequently, the acidity of the medium affects the complexation equilibrium, and the acid–base reactions of hydroxylation of the cation and protonation of the X^{n-} anion become side reactions parasitic to complexation. Therefore, the complexation equilibrium of the cation must be characterized by an 'apparent' or 'conditional' constant taking into account these parasitic reactions [6].

A quantitative analysis of complexation requires knowledge of the thermodynamic constants of all equilibria involved. Some data are available in the literature [4–6], but when it comes to the complexation of condensed species, very little data are in fact available. It is possible, however, to use a simple model in order to establish simple criteria allowing a qualitative description of the aptitude of a ligand to coordinate a monomeric or oligomeric cation.

The complexation of an aquo metallic cation by a species X (monodentate of formal charge -1 for simplification purposes) can be written as

$$[M(OH_2)_N]^{z+} + X^- \longrightarrow [MX(OH_2)_{N-1}]^{(z-1)+} + H_2O$$

This problem (see the Appendix, Section A.5) relies on the establishment of criteria related to the stability of the M–X bond in the complex. The overall approach is summarized below.

First, the M–X bond must resist ionic dissociation. This means that the ligand X must be an electron donor (σ donor) and therefore that its charge must be greater (less negative) than -1. This condition is not sufficient because the M–X bond must also resist protonation of the ligand or hydrolysis of the cation. Therefore, the charge of the protonated ligand must remain negative in the following forms of the complex:

$$[MX(OH_2)_{N-1}]^{(z-1)+} \Longleftrightarrow [M(XH)(OH)(OH_2)_{N-2}]^{(z-1)+}$$

These conditions may be expressed with the criteria $\delta(X) > -1$ and $\delta(HX) < 0$ in the complex. If introduced in the expression of the average electronegativity of the complex $[MX(OH_2)_{N-1}]^{(z-1)+}$, the criteria are converted (see the Appendix, Section A.5) into values of average electronegativity, χ_{Diss} and χ_{Hyd}, corresponding respectively to the ionic dissociation of the complex and to its dissociation via hydrolysis of the cation and protonation of the ligand X:

$$\chi(X) < \chi_{Diss} = \chi[M(OH_2)_{N-1}^{z+}]$$

and

$$\chi(HX) > \chi_{Hyd} = \chi[M(OH)(OH_2)_{N-2}^{(z-1)+}]$$

The following is an example applied to the behavior of bidentate anions on Fe(III) as a function of medium acidity.

Table 5.1 Average critical electronegativities for complexation of Fe(III)

h	χ_{Hyd}	pH_{Hyd}	χ_{Diss}	pH_{Diss}
0	$\chi[Fe(OH)(OH_2)_3^{2+}] = 2.80$	−1.9	$\chi[Fe(OH_2)_4^{3+}] = 2.90$	−4.8
1	$\chi[Fe(OH)_2(OH_2)_2^{+}] = 2.68$	×1.5	$\chi[Fe(OH)(OH_2)_3^{2+}] = 2.80$	−1.9
2	$\chi[Fe(OH)_3(OH_2)^{0}] = 2.53$	×5.8	$\chi[Fe(OH)_2(OH_2)_2^{+}] = 2.68$	×1.5
3	$\chi[Fe(OH)_4^{-}] = 2.34$	11	$\chi[Fe(OH)_3(OH_2)^{0}] = 2.53$	×5.8

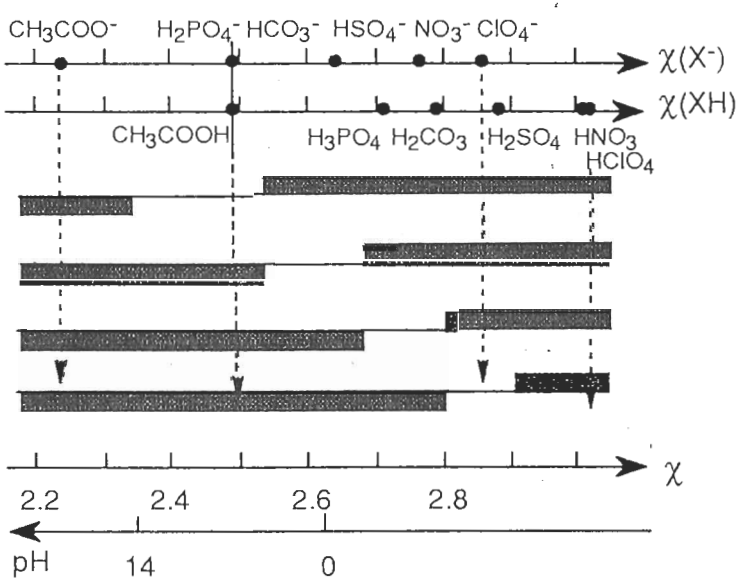

Figure 5.1 Complexation ranges of the hydrolyzed forms of Fe(III)

The overall equilibrium of complexation of iron by a ligand X^- is

$$[Fe(OH)_h(OH_2)_{6-h}]^{(3-h)+} + X^- \Longleftrightarrow [Fe(OH)_hX(OH_2)_{4-h}]^{(2-h)+} + 2H_2O$$

The limit values of χ_{Hyd} and χ_{Diss} for various hydrolysis ratios are calculated in Table 5.1.

Figure 5.1 shows the domains of electronegativity in which the ligands are likely to complex the various hydrolyzed forms of iron(III). $[ClO_4]^-$ can only form a complex with the $h = 0$ species of iron. For higher hydrolysis ratios, ionic dissociation takes place. This indicates that a stable bond can form in solution only between partners of reasonably similar electronegativity. Complexation of the cation by $[ClO_4]^-$ occurs only in a strongly acid medium allowing the existence of the most electronegative cation form, and hence the form most likely to accept the ligand → cation electron transfer. The $h = 0$ form of iron can also be complexed by

nitrate and sulfate ions, but not by the carbonate nor the acetate. Within this acid range, anions are protonated and these weak acids are eliminated. The complex is destroyed by hydrolysis. The $h = 1$ form could be complexed by the sulfate or carbonate ion. The $h = 2$ form can be complexed only by the sulfate and the carbonate. Both the carbonate and the acetate can form a complex with the $h = 3$ form.

The relationship between average electronegativity and pH, applied to χ_{Diss} and χ_{Hyd}, allows an estimation of the approximate acidity range of the complexation range (see the Appendix, Section A.5). The sulfate, as $[HSO_4]^-$, will form complexes with forms $h = 0$, 1 and 2 of iron from very acidic media up to pH ≈ 3 (Figure 5.1). Above pH 3, $[SO_4]^{2-}$ will react on the $h = 2$ and 3 forms of iron.

A generalization of this approach, taking into account the role of medium acidity on cation hydrolysis and ligand protonation, allows the design of electronegativity–pH plots which indicate the acidity range in which a cation (or one of its condensed forms) is likely to form a complex (see the Appendix, Section A.5).

It must be stressed that such diagrams are only qualitative. They allow a determination of whether or not an anion may act as a ligand, but are of no help in describing the extent of the reaction, i.e. the amount of cation that has formed the complex. These diagrams must therefore be handled with extreme caution. They may, however, be useful, in the absence of thermodynamic data, to take into account possible complexation phenomena in a solution.

5.2 BASIC SALTS OF ZIRCONIUM(IV)

A few strong complexing ions are able to remain coordinated to the cation throughout hydrolysis and condensation. They are therefore included in the structures of the solid. Since these structures include ions other than oxo or hydroxo ions, they are called 'basic salts'. In a way, these anions play a role in the formation of the network since, under similar acid conditions, no solid is formed in their absence. Most metallic elements form basic salts in nature, such as carbonates, sulfates and phosphates, which play an important role in mineralogy. A few structurally interesting zirconium(IV) compounds are discussed below.

In an acid medium, zirconium exists mostly as the polycation $[Zr_4(OH)_{8+x}(OH_2)_{16-x}]^{(8-x)+}$ (see Section 3.2.3). One may consider, in a first approximation, that this species can form complexes with several anions in solution. The electronegativity–pH diagram of the polycation is shown in Figure 5.2.

$[ClO_4]^-$ ions are highly electronegative ($\chi[ClO_4^-] = 2.85$) and play no complexing role within the usual pH range, independently of the coordination.

Complexation by chlorine takes place between pH 5 and 11. In acid solution, both anions behave as counterions of the tetramer units of zirconium (Figure 5.3a).

This is confirmed by XRD, which has shown that crystals of $ZrOClO_4 \cdot 8H_2O$ and $ZrOCl \cdot 8H_2O$ are indeed made of $[Zr_4(OH)_8(OH_2)_{16}]^{8+}$ tetramers and ClO_4^- or Cl^-

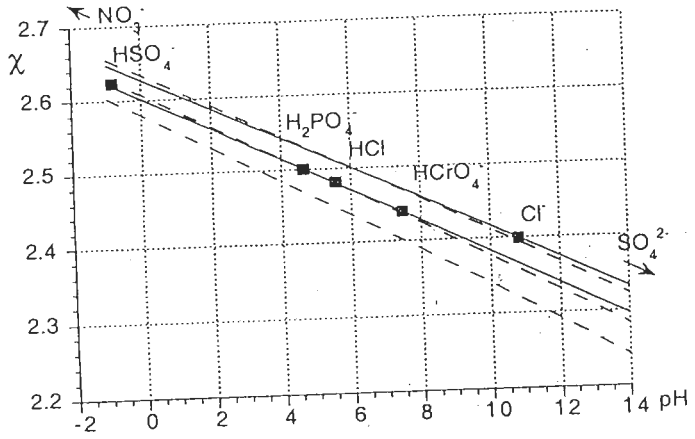

Figure 5.2 Electronegativity–pH diagram for the complexation of $[Zr_4(OH)_8(OH_2)_{16}]^{8+}$ by monodentate anions (solid lines) or bidentate anions (dotted lines)

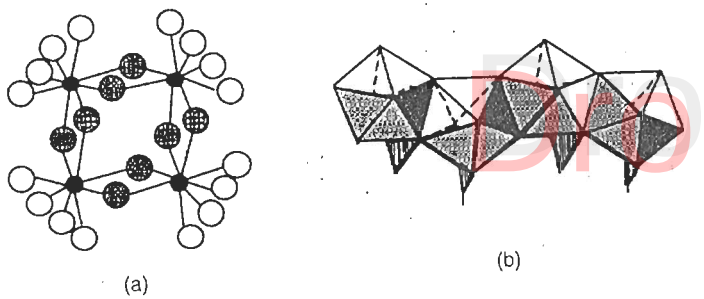

Figure 5.3 Structures of (a) $ZrOCl_2 \cdot 8H_2O$ and (b) $Zr(OH)_2(NO_3)_2 \cdot 4.7H_2O$

anions are not directly connected to the polycation [7,8]. Thus, when a solution of $ZrOCl_2$ is heated and refluxed in an acidic medium (pH < 2.5), the chlorine ions are not involved in the formation of monoclinic zirconia (see Section 3.2.3) [9]. However, when amorphous zirconia precipitates at higher pH, significant amounts of anions are found in the solid [7]. The amount of chlorine ions retained in the solid depends on the pH and decreases as the precipitation pH increases.

In a first approximation, the nitrate ion does not form complexes with zirconium, except under highly acidic conditions. Therefore, in moderately acidic media, zirconium should form the tetramer polycation as in the case of the perchlorate or the chloride [10]. However, after dissolution of zirconia in concentrated nitric acid, the basic salt $Zr(OH)_2(NO_3)_2 \cdot 4.7H_2O$ crystallizes. Its structure consists of chains of $[Zr(OH)_2(OH_2)_2(NO_3)^+]_n$ built with Zr in coordination 8 (dodecahedra), themselves linked by double OH bridges. Each atom of zirconium contains a bidentate nitrate

group in its coordination sphere (Figure 5.3b). The chains are connected in the solid via other nitrate ions and via hydrogen bonds with water molecules [11,12].

The sulfate ion is more complexing than the nitrate and forms many basic salts over a wide pH range (Figure 5.2). In these salts, the various coordinations of the sulfate lead to networks of varying dimensionality. The basic sulfates of zirconium exhibit a very large structural diversity depending on the thermohydrolysis conditions.

In an acid medium, for the hydrolysis ratio $h = 1$, the compound $Zr_2(OH)_2(SO_4)_3(H_2O)_4$ is obtained. In its structure, sheets contain dimers of Zr in coordination 8 connected by SO_4 bridges. Each sulfate group is linked to three dimers. The double bridges on the dimers ensure connectivity between sheets [13] (Figure 5.4a).

For a hydrolysis ratio $h = 2$, hydrated chains of pentagonal bipyramids sharing two edges are bridged by sulfate groups in the compound $Zr(OH)_2(OH_2)(SO_4)$ [14] (Figure 5.4b). Upon elimination of a water molecule, the structure changes. In the compound $Zr(OH)_2(SO_4)$, chains of antiprisms connected by edges and tetrahedra are connected by other sulfate groups [15] (Figure 5.4c).

In a strongly acid medium, around hydrolysis ratio $h = 0$, sulfates will form instead of basic salts. $Zr(SO_4)_2 \cdot 7H_2O$, stable at low temperatures, is made of $Zr_2(\mu\text{-}SO_4)_2(OH_2)_8(SO_4)_2$ dimers. The cation is in dodecahedral coordination 8. It is linked to two bridging and two chelating sulfates [16] (Figure 5.5a).

At room temperature in $Zr(SO_4)_2 \cdot 4H_2O$, the chelating sulfate groups become bridging. The structure includes sheets in which zirconium is in antiprismatic

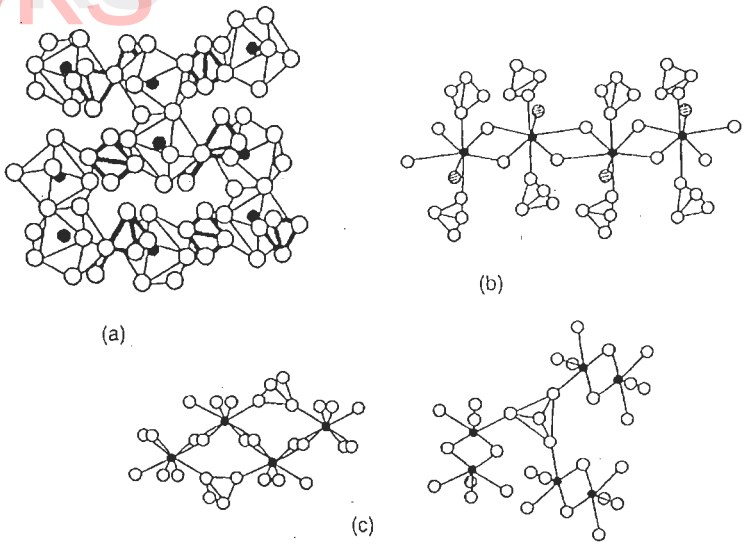

Figure 5.4 Structures of basic sulfates of zirconium: (a) $Zr_2(OH)_2(SO_4)_3(OH_2)_4$; (b) $Zr(OH)_2(OH_2)(SO_4)$; (c) $Zr(OH)_2(SO_4)$

DropBooks

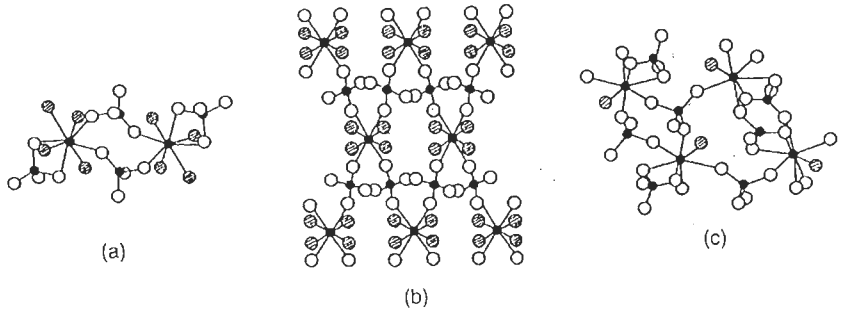

Figure 5.5 Structures of some zirconium sulfates: (a) $Zr(SO_4)_2 \cdot 7H_2O$; (b) $Zr(SO_4)_2 \cdot 4H_2O$; (c) $Zr(SO_4)_2 \cdot H_2O$

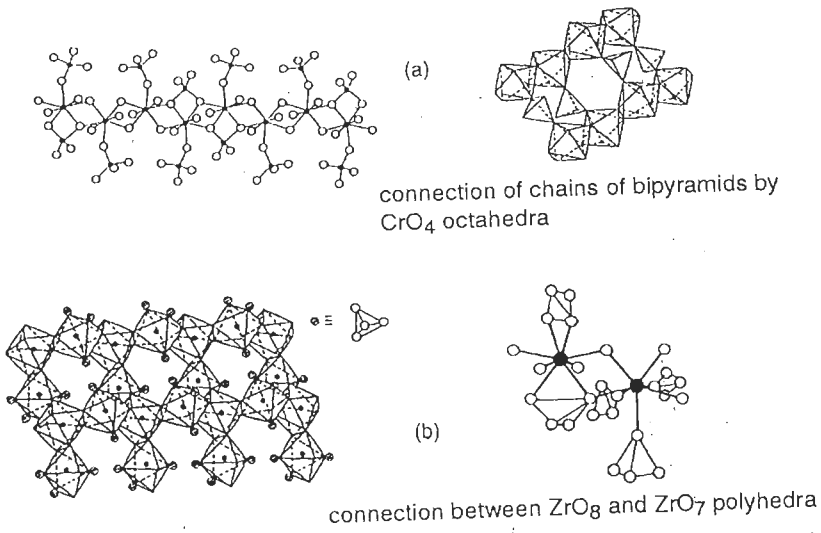

Figure 5.6 Structures of basic zirconium chromates: (a) $Zr_8(OH)_{10}(CrO_4)_{11} \cdot 2H_2O$; (b) $Zr(OH)_2(CrO_4)$

coordination 8 [17] (Figure 5.5b). At 100 °C, bridging increases at the expense of hydration: in $Zr(SO_4)_2 \cdot H_2O$, new sheets are observed in which zirconium is in coordination 7 [18] (Figure 5.5c). Above 300 °C, dehydration is complete and bridging is maximum in the three-dimensional compound $Zr(SO_4)_2$ [18].

Various basic salts are also formed by zirconium and chromate. The latter is slightly more complexing than sulfate. The compound $Zr_8(OH)_{10}(CrO_4)_{11} \cdot 2H_2O$, formed around $h = 1.25$, includes chains of $[Zr_8(OH)_{10}(CrO_4)_3]^{16+}$ where CrO_4 groups are both bridging and chelating [19] (Figure 5.6a).

In the solid $Zr(OH)_2(CrO_4)$, sheets of $[Zr_3(OH)_6(CrO_4)]_n^{4n+}$ include zirconium in coordination 8 (dodecahedral) and 7 (pentagonal bipyramidal) bound to chromates

[20] (Figure 5.6b). Both types of zirconium atom are connected with double OH bridges, and the sheets are connected by CrO_4 tetrahedra.

These examples illustrate the gradual structuring role of anions as a function of their complexing nature: the ClO_4^- ion has no nucleophilic character and can only act as the counterion of polycations in solution. The nitrate, in certain circumstances, allows opening of a cyclical polycation and the formation of independent chains. Chains and sheets are obtained with the sulfate and the chromate.

5.3 COMPLEXATION BY THE PHOSPHATE ANION

The complexing ability of the phosphate ion on metal cations is much more pronounced than that of the sulfate. The complex stability constants and solubility products are much higher than with the sulfate [4–6], and phosphate complexation occurs over the entire accessible pH range.

Complexation of a metallic cation by an oxygenated anion such as the phosphate or the sulfate ions may be seen as a heterocondensation reaction. There is no fundamental difference between these reactions, which proceed following the same path of nucleophilic substitution and lead to the formation of oxo M–O–P(S) bridges. In Section 2.2b, we discussed the fact that polyphosphates and polysulfates do not form in solution because the electrophilic character of the central element [P(V) or S(VI)] is too weak. This is due to the high formal charge and the small size of the element, leading to extreme polarization of the oxygen atoms. In addition to the four σ bonds in the tetrahedron, these elements form π bonds with oxygen. These bonds are made possible, in the T_d symmetry, by the overlap of the $2p_\pi$ orbitals of oxygen with the $3d_\pi$ (d_{z2}, d_{x2-y2}) orbitals of the phosphorous or the sulfur [21,22]. Chlorine in the perchlorate ion is in the same situation. For boron, the energy difference between the 2p and 3d orbitals of the cation is too large for π bonds to occur in $[B(OH)_4]^-$ (Section 4.2.3).

The formation of a system of π electrons in the tetrahedron decreases the partial charge of the central element, as well as that of the oxo ligands, compared with a σ system. They do not exhibit basic characteristics. However, hydroxo ligands of the anion can be sufficiently nucleophilic to bond to a cation. The nucleophilic character of the hydroxo ligands depends on the number of π bonds in the tetrahedron, i.e. on the formal charge of the element. The formation of complexes and of basic salts may therefore be understood as a condensation of bridging anions

$$[PO_{4-x}(OH)_x]^{(3-x)-} \quad \text{or} \quad [SO_{4-x}(OH)_x]^{(2-x)-}$$

with cations more or less hydrated. Depending on the pH of the medium, this reaction will be an olation or an oxolation, and the principles of condensation may be applied directly to complexation by polydentate oxygenated anions. Since there is only one π bond in the PO_4 tetrahedron, instead of two in the SO_4 tetrahedron, the nucleophilic character of the phosphate is superior to that of the sulfate. The ability

of the phosphate to form complexes is therefore greater. Moreover, the phosphate can be tri- or tetracoordinated, whereas the sulfate is generally dicoordinated. For these reasons, phosphates are a very diverse family of minerals. The same reasoning explains why $[ClO_4]^-$, which has almost no basic and nucleophilic characters, almost never forms any complex. Conversely, the absence of a π bond in SiO_4 allows the silicates to condense by themselves and to constitute, with many other metal cations, a family of compounds even more diverse than the phosphates (see Section 4.2, aluminosilicates).

In the following section, we describe a few compounds formed with the phosphate and elements of increasing formal charge [Zr(IV), Sb(V), W(VI)]. All these elements can be strongly complexed by the phosphate, but the formation of extended networks requires at least one step of condensation by olation (see Section 2.2). As in the case of oxo–hydroxo forms of cations, oxolation alone between complexes leads to heteropolyanions. This is observed in the case of high formal charge elements such as Sb(V) and W(VI).

5.3.1 ZIRCONIUM

The acid phosphate of zirconium $Zr(HPO_4)_2 \cdot H_2O$, written α-ZrP, has attracted attention because of its lamellar structure (Figure 5.7). This type of framework gives the material some ion exchange properties as well as the possibility of intercalation of various molecules [23].

Figure 5.2 shows that the phosphate can complex zirconium over the entire pH range. The addition of zirconium to phosphoric acid in solution [with $PO_4/Zr = 2$

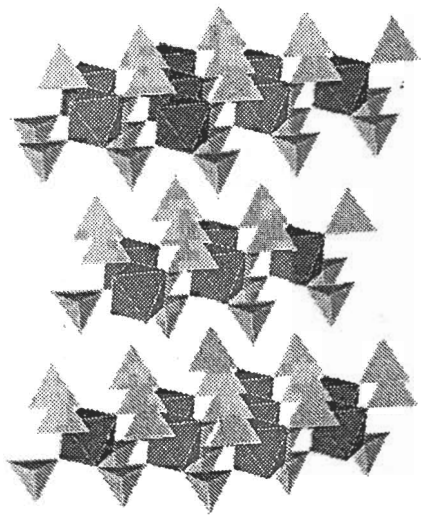

Figure 5.7 Structure of α-$Zr(HPO_4)_2 \cdot H_2O$

to prevent the presence of basic salts $Zr(OH)_x(HPO_4)_{2-x/2}$] forms a gel. The quasi-amorphous particles of the gel crystallize after reflux in concentrated phosphoric acid [23].

The phosphate in the network allows the formation of planes in which the zirconium is in coordination 6 owing to six phosphate bridging ligands, each PO_4 being coordinated to three metal ions (Figure 5.7).

Neutron diffraction shows that each phosphoric tetrahedron includes an OH bond [24]. Therefore, it is the $[HPO_4]^{2-}$ form that is involved in the formation of the solid, which may be thought of as being formed by precursors of the type $[Zr(HPO_4)_2(OH_2)_x]^0$ condensing by olation. Cohesion between the planes is due to hydrogen bonds between the POH groups and the water molecules present between the sheets [25]. The interlayer cohesion is rather strong but also allows swelling of the material in aqueous solution, as in the case of vanadium gels and contrary to what happens in the case of antimonic acid gels whose framework is three-dimensional (see Section 4.1.3). The protons can be exchanged by various cations (alkalis in particular), but $Zr(HPO_4)_2 \cdot H_2O$ is a poor proton conductor ($\approx 2 \times 10^{-5}\,\Omega\,cm^{-1}$ at 300 K) owing to the localization of the proton in the structure [26]. In the slightly more hydrated phases $[Zr(HPO_4)_2 \cdot 3.6H_2O]$, the mobility of protons is increased by the swelling and the solvation, and the conductivity increases ($\approx 2 \times 10^{-3}\,\Omega\,cm^{-1}$ at 300 K). It remains inferior to that of antimonic acid ($\approx 5 \times 10^{-3}\,\Omega\,cm^{-1}$ at 300 K) [26] in which the protons are highly mobile because they are not localized (see Section 4.1.3).

Similar structures are formed by Hf(IV) and other tetravalent elements such as Ti(IV), Ge(IV), Sn(IV) or Pb(IV) [23]. Their stability in water is reduced because M–O–P bridges are prone to hydrolysis. Ce(IV) phosphate of similar stoichiometry appears to form a different (unknown) structure, and the material is fibrous rather than lamellar [27].

5.3.2 ANTIMONATE

Complexation of antimony(V) by phosphates leads, within some composition ranges, to the opposite effect to that observed with zirconium: the formation of a network is avoided, but phosphatoantimonic polyanions are formed. The presence of phosphate in the coordination sphere of antimony no longer allows the presence of water. Therefore, condensation by oxolation alone is limited. In fact, the phosphate acts as a stabilizing or depolymerizing agent.

The addition of phosphoric acid to freshly made antimonic acid (see Section 4.1.3) prevents precipitation of the pyrochlore phase and allows stabilization of phosphatoantimonic high polymers as sols [28]. Incorporation of phosphates in the high polymers alters their crystal structure [29] and leads to a significant reduction in their size and quantity, to the benefit of phosphatoantimonic polyanions. The ratio $P/Sb = 0.5$ is the threshold for the existence of high polymers in solution. The composition and degree of condensation of the polyanions are functions of the pH

DropBooks

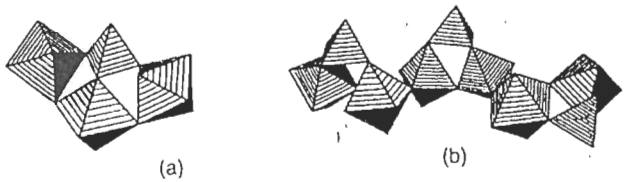

Figure 5.8 Configurations of phosphatoantimonic anions: (a) $[Sb_3(OH)_{11}O_2(PO_4)]^{3-}$ formed at pH > 7; (b) $[Sb_6(OH)_{20}O_5(PO_4H)_3]^{6-}$ formed at pH < 4. From [30] and [31]

of the medium. Between pH 9 and 7, a trimer of composition P/Sb = 0.33 forms, and at pH < 4, a hexamer of composition P/Sb = 0.5 [30,31]. Probable configurations of these polyanions are shown in Figure 5.8.

The formation of basic phosphatoantimonic salts is possible under very energetic synthesis conditions. In a highly concentrated phosphate medium, (85% H_3PO_4), the $HSb(PO_4)_2 \cdot xH_2O$ acid is formed [32]. Its structure is close to that of α-ZrP [33], because the presence of Sb(V) instead of Zr(IV) increases the polarization of oxygen by the cation and decreases the electrostatic charge on the anionic sheets. Hydrogen bonds between sheets are also weaker and the material swells more than α-ZrP in water.

In the solid state, potassium phosphatoantimonates are formed by calcination of mixtures of KNO_3, Sb_2O_3, and $NH_4H_2PO_4$ for 2–3 days at temperatures ranging from 900 to 1000 °C [34–36]. The structures of the compounds $K_5Sb_5O_{12}(PO_4)_2$ and $K_3Sb_3O_6(PO_4)_2$ are shown in Figure 5.9. The corresponding phosphatoantimonic acids are obtained by K^+/H^+ exchange in an acid medium [33].

It is interesting to note that the depolymerizing role of the phosphate occurs during solution synthesis as well as in the solid state. In solution, an increase in phosphate concentration causes the formation of polyanions. In the solid, it decreases the functionality of the compounds. In $H_5Sb_5O_{12}(PO_4)_2$, $H_3Sb_3O_6(PO_4)_2$, (Figure 5.9) and in $HSb(PO_4)_2$ (Figure 5.7), where the phosphate content increases (P/Sb = 0.4, 0.66, 2), the degree of connectivity of the SbO_6 decreases gradually. In the latter compound, as in α-ZrP, isolated SbO_6 octahedra are only connected via PO_4 tetrahedra. The same effect is observed in Ti(IV) phosphates [23].

The lamellar phosphatoantimonic acids have good potential as catalysts because of their high acidity and the possible intercalation of various molecules between the sheets [33].

5.3.3 TUNGSTATES

Many anionic species, silicates, germanates, arsenates, borates and, in particular, phosphates can be incorporated in the structure of polyanions of high formal charge transition elements (see Section 4.2). They can form heteropolyoxoanions [37,38]. The phosphate is the heteroanion that forms the largest variety of compounds with Mo(VI), W(VI) and V(V). Phosphatotungstates are interesting because the presence

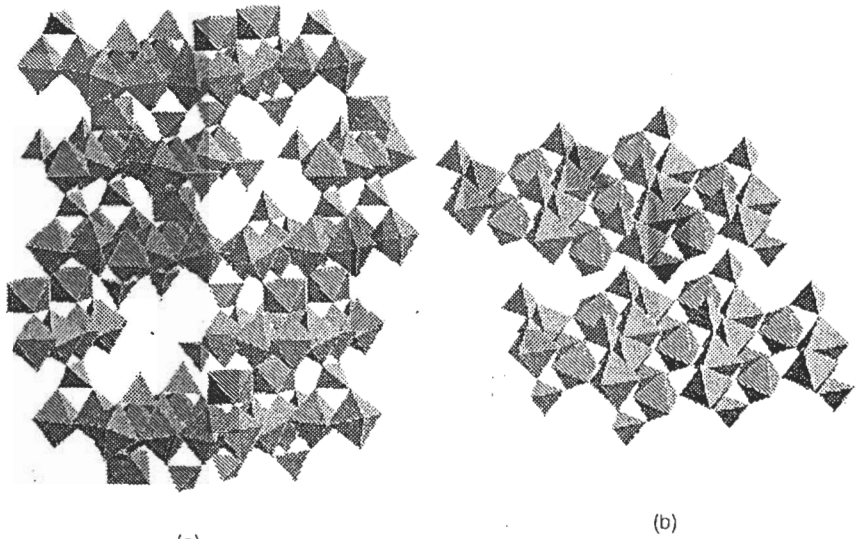

Figure 5.9 Structure of (a) $K_5Sb_5O_{12}(PO_4)_2$ and (b) $K_3Sb_3O_6(PO_4)_2$ from data in [34] and [36]

of the phosphate increases the number of possible structures of the isopolyanions. These structures have been studied by ^{31}P and ^{183}W NMR, and some have been examined by XRD.

As with many other iso- and heteropolyoxometallates, phosphatotungstates contain fragments made of edge-sharing WO_6 octahedra. These fragments are connected by corners-sharing octahedra in many different ways. The WO_6 octahedra are always highly distorted. The length of the W–O bonds varies from 2.4 Å (μ_3 bridging oxygen) to 1.7 Å (terminal oxygen). The short bond, which has the character of a multiple bond, decreases the basicity of oxygen so that it cannot accept a proton. This limits the ability of octahedra to share edges and prevents the formation of large compact entities (see Section 4.3.2). In the more stable species, the PO_4 tetrahedron is most often tetracoordinated. The P–O distances are usually identical in the tetrahedron and vary from 1.5 to 1.6 Å.

Many factors are involved in the solution equibria (see Section 4.3.2): the acidity of the medium, the nature of the acid, stoichiometry P/W, concentration, temperature and the nature of the solvent and of the cations. In addition, polyanions are very labile and frequently lead to isomers. As a result, their chemistry is extremely complex, and the variety of species formed is so large that many have not been identified yet. Therefore, it is difficult to follow their transformations, but it is possible to attempt to describe the topology of the system.

Most phosphatotungstates belong to three structural types. The first type is that of the Keggin polyanion α-$[PW_{12}O_{40}]^{3-}$ [39] (Figure 5.10). Its structure is analogous to

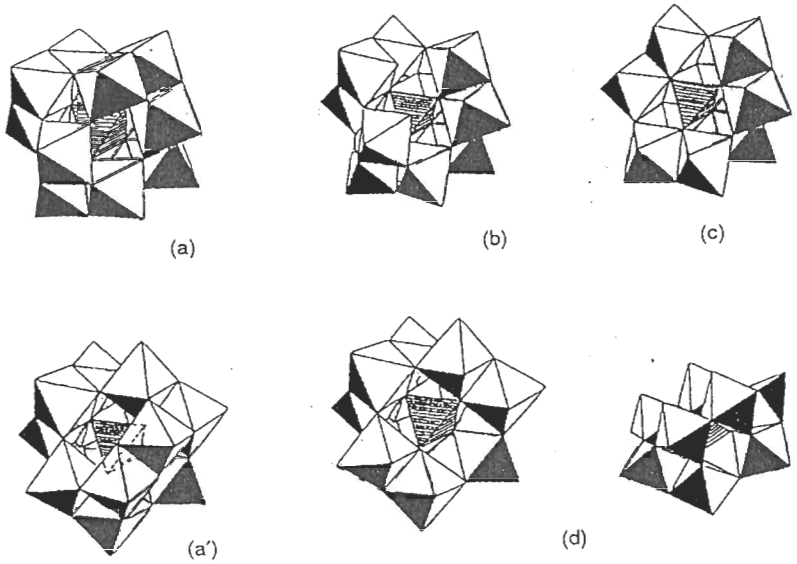

Figure 5.10 Structure of (a) α-$[PW_{12}O_{40}]^{3-}$ (Keggin structure) and derivatives (b) α-$[PW_{11}O_{39}]^{7-}$ and (c) Aα-$[PW_9O_{34}]^{9-}$. (a') γ isomer of Keggin's polyanion (two W_3O_{13} groups have rotated 60°). From [37] by permission. (d) Vacancy compound $[PW_{10}O_{36}]^{7-}$ Reprinted with permission from [42]. Copyright 1981 American Chemical Society

DropBooks

that of α-metatungstate $[H_2W_{12}O_{40}]^{6-}$ (Figure 4.24), but the central cage is occupied by the phosphoric tetrahedron linked on each corner to the four oxygen atoms in μ_3 of the cage. The polyanion is formed by the addition of excess phosphoric acid to sodium tungstate Na_2WO_4 dissolved in hot water, after the addition of hydrochloric acid. Crystallization occurs upon cooling of the solution [38a].

There are five possible isomers of the Keggin α-polyanion, created by a $\pi/3$ rotation of 1, 2, 3 or 4 tritungstic groups and forming the β, γ, δ and ε isomer respectively. The α form is the most stable because the cation–cation repulsions are minimized and the $d\pi-p\pi$ overlap is favored [37]. The γ isomer is rare and the δ form is unknown [the Al_{13} polycation (Figure 3.5) represents the ε isomer where the four M_3O_{13} groups have turned; the broadened ^{27}Al NMR signal indicates the strong distortion of the environment of cations owing to edge sharing between trimetallic groups in the polycation].

α-$[PW_{12}O_{40}]^{3-}$ is very soluble in water. However, its stability range is limited (pH < 1). It is converted into a vacancy compound upon loss of tungsten atoms. It is also parent to a family of heteropolyanions of similar structure to Keggin's. By alkalinization, it leads rapidly and irreversibly to the following species [40]:

$$\alpha\text{-}[PW_{12}O_{40}]^{3-} \Longleftrightarrow \alpha\text{-}[PW_{11}O_{39}]^{7-} \Longleftrightarrow A\alpha\text{-}[PW_9O_{34}]^{9-}$$
$$\Longleftrightarrow [HPO_4]^{2-} + [WO_4]^{2-}$$

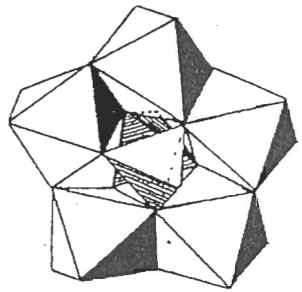

Figure 5.11 Structure of the $[P_2W_5O_{23}]^{6-}$ anion. Reproduced with permission from [42]. Copyright 1981 American Chemical Society

Their structures (Figure 5.10) have been obtained for the most part from investigations in solution [40] as well as from ^{31}P NMR [41]. All species can be synthesized by direct acidification of mixtures of tungstate and phosphate ions [40].

The treatment of tungstic acid by cesium hydroxide followed by neutralization of the solution up to pH 7 by phosphoric acid leads to the compound $Cs_6P_2W_5O_{23}$ with the very surprising structure shown in Figure 5.11. It is made of a ring of edge-sharing WO_6 octahedra, except for two of them which share only corners. The phosphoric tetrahedra are tricoordinated [42]. Heated in water at 100°C, this compound rapidly forms the $[PW_{10}O_{36}]^{7-}$ ion (Figure 5.10) which derives from Keggin's structure by a $\pi/3$ rotation of two tritungstic groups and the removal of two octahedra [42]. These structural modifications reveal the great complexity of equilibria in solution and stress the importance of the nature of the cation. In the presence of sodium or potassium instead of cesium, the synthesis leads to $[PW_9O_{34}]^{9-}$. The second structural type is that of the α-$[P_2W_{18}O_{62}]^{6-}$ polyanion (Dawson's structure) [43,44] formed by connecting two α-PW_9 units by the corners of octahedra (Figure 5.12). It is obtained by refluxing sodium tungstate in the presence of excess phosphoric acid. In the β isomer, one polar group W_3O_{13} has rotated by 60° [45,47]. Both isomers can be separated by fractional crystallization of the ammonium salts [38b].

After alkalinization, α-P_2W_{18} forms a series of vacancy compounds through elimination of polar octahedra [46] (Figure 5.12):

$$\alpha\text{-}[P_2W_{18}O_{62}]^{6-} \Longleftrightarrow \alpha\text{-}[P_2W_{17}O_{61}]^{10-}$$
$$\Longleftrightarrow \alpha\text{-}[P_2W_{15}O_{56}]^{12-} \longrightarrow [HPO_4]^{-} + [WO_4]^{2-}.$$

After the loss of equatorial and polar octahedra, α-$[P_2W_{17}O_{61}]^{10-}$ forms $[H_2P_2W_{12}O_{48}]^{12-}$ (Figure 5.12). In a lithium acetate/acetic acid buffer solution and in the presence of potassium ions exclusively, this ion causes the formation of crystals of $K_{28}Li_5H_7P_8W_{48}O_{184}$ [47]. In fact, $[P_2W_{17}O_{61}]^{10-}$ and $[H_7P_8W_{48}O_{184}]^{33-}$ ions form simultaneously during acidification of α-P_2W_{12}, following a series of complex equilibria involving several species and isomerization.

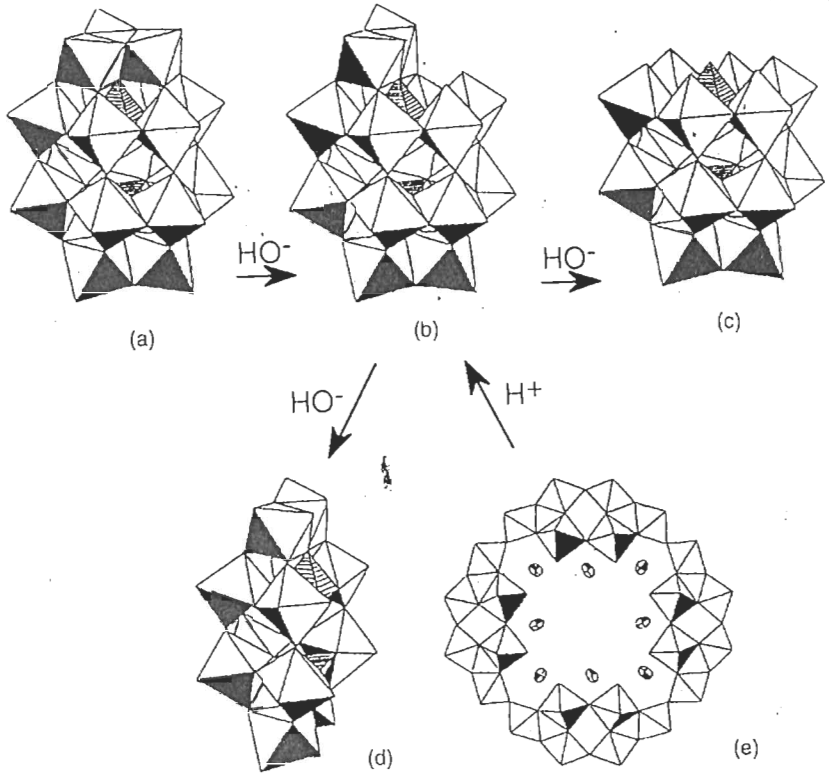

Figure 5.12 Structures of (a) α-$[P_2W_{18}O_{62}]^{6-}$ (Dawson's structure) and of the vacancy compounds (b) α-$[P_2W_{17}O_{61}]^{10-}$, (c) α-$[P_2W_{15}O_{56}]^{12-}$, (d) $[H_2P_2W_{12}O_{48}]^{12-}$ and (e) $[P_8W_{48}O_{184}]^{40-}$ (potassium ions within the crown are shown as ellipsoids). Reprinted with permission from [47]. Copyright 1985 American Chemical Society

The cyclical structure of $[H_7P_8W_{48}O_{184}]^{33-}$ (Figure 5.12) is formed by the connection of four P_2W_{12} units. The cycle contains eight potassium cations located at varying distances (2.7–3.1 Å) from internal oxygens. The remaining charge of the cation is compensated by K^+ and Li^+ located outside the crown. The polycation does not form only in the presence of potassium ions, but also in the presence of other alkalis (K^+, Li^+). Potassium ions can therefore play a key role in the synthesis. The phenomenon seems analogous to what is observed for polyvanadic cages (see Section 4.3.1c), and it is possible that its formation is due to a template effect.

The Preyssler anion $[NaP_5W_{30}O_{110}]^{14-}$ is another example of a phosphatotungstic cage [48,49] (Figure 5.13). The cycle contains a Na^+ ion appearing to be essential to its formation. It is statistically distributed on two sites on the C_5 axis of the ring (Figure 5.13). Both sites are separated by 2.5 Å and can be occupied simultaneously

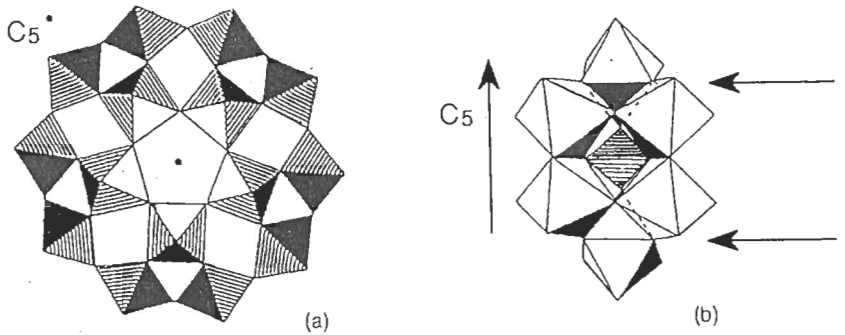

Figure 5.13 (a) Structure of $[NaP_5W_{30}O_{110}]^{14-}$. (b) PW_6O_{32} fragment shown parallel to the C_5 axis. The arrows perpendicular to the C_5 axis indicate the planes where sodium is located within the crown. Reprinted with permission from [49]. Copyright 1985 American Chemical Society

by sodium only. The sodium ion cannot be exchanged by protons but may be exchanged by calcium after heat treatment at 120 °C for several hours. This anion appears to be a by product of the synthesis of P_2W_{18} [48].

The third type of phosphatotungstic compound is the polyanion $[H_6P_2W_{21}O_{74}]^{6-}$. Its structure derives from P_2W_{18} by the insertion of three 6-coordinated atoms of tungsten between the two PW_9 halves [50] (Figure 5.14a).

The three internal oxygen atoms in the equatorial plane and separated by 2.40 Å interact and create a disorder in the positions of the three tungsten atoms to which they are connected (Figure 5.14b). One of these atoms (W_c) is pushed out towards the outside of the polyanion and is coordinated to an internal oxygen atom that in fact belongs to a water molecule. The protons undergo slow exchange with the solvent and form hydrogen bonds with the two other oxygen atoms in the same plane [50]. Each of the two other tungsten atoms in the equatorial plane carry one coordination water molecule so that the global formula of the compound is $[P_2W_{21}O_{71}(OH_2)_3]^{6-}$.

The polyanion is formed by acidification of α-$K_9PW_9O_{34}$ or $K_7PW_{11}O_{39}$ with the stoichiometric amount of tungstate [38c,40,50]. The presence of potassium or rubidium is necessary [46]. The polyanion is stable in an acid medium (pH < 2) but degrades at higher pH into $[P_2W_{20}O_{70}(OH_2)_2]^{10-}$ and $[P_2W_{19}O_{69}(OH_2)]^{14-}$ [40]. Their structure derives from P_2W_{21} by elimination of one and later two tungsten atoms joining the two PW_9 halves (Figure 5.14).

In P_2W_{20} ions, one of the PW_9 groups undergoes a rotation of 60° (Figures 5.14c and d). The ions are also unique because coordinated water molecules are located in *trans*-dioxo configuration on the tungsten atoms [40,51]. One of these ions (Figure 5.14c) behaves as a tetradentate ligand of transition elements such as Co^{II}, with cobalt occupying the tungsten vacancy [40]. Owing to its structure, the other 'isomer' does not form complexes with metal ions.

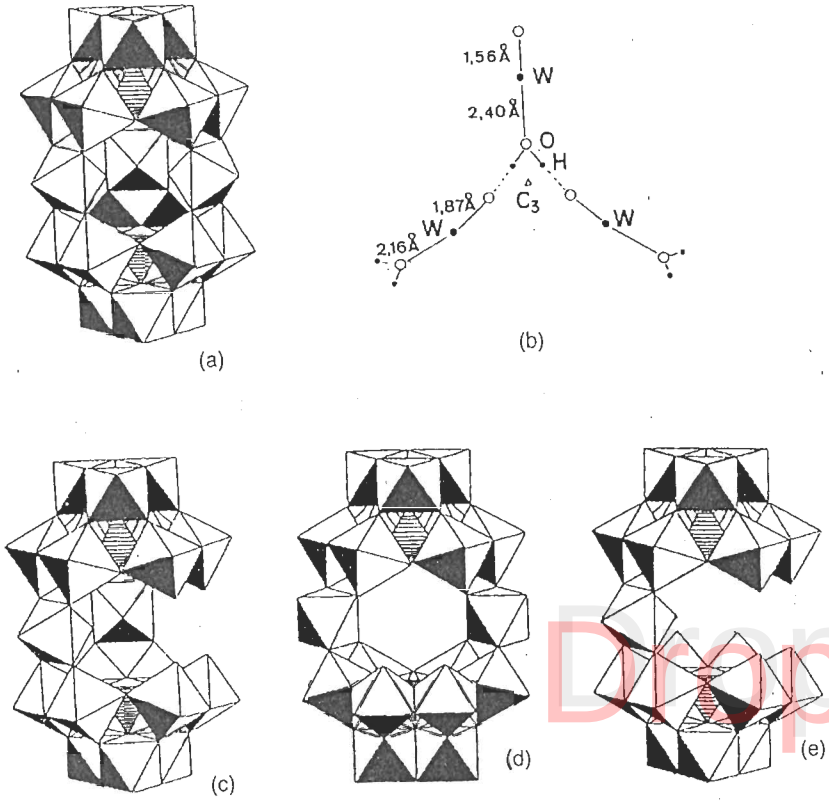

Figure 5.14 (a) Structure of the polyanion $[P_2W_{21}O_{71}(OH_2)_3]^{6-}$ and (b) arrangement of tungsten and oxygen atoms and water molecules near the equatorial plane of the anion. From [50] by permission. Structure of vacancy compounds (c) $[P_2W_{20}O_{70}(OH_2)_2]^{10-}$ and (d) $[P_2W_{20}O_{72}]^{14-}$. (e) Proposed structure for $[P_2W_{19}O_{69}(OH_2)]^{14-}$. Reproduced by permission of Conseil National de la Recherche du Canada from [40]

$[P_2W_{19}O_{69}(OH_2)]^{14-}$ is the product of the alkalinization of P_2W_{20} at around pH 7 [52,40] or the acidification at a pH slightly lower than 7 of a boiling, stoichiometric mixture of tungstate and phosphate in the presence of potassium [52]. The ion is poorly stable (it decomposes as PW_{11}) but nonetheless forms complexes with Co^{II} [52]. Like the other polyanions in this series, it requires the presence of potassium to form. Since there is only one junction tungsten atom (Figure 5.14e), the presence of these cations within the polyanion allows the structure to be stable by keeping both jaws of the polyanion open [53].

Finally, there are a few phosphate-rich phosphatotungstates such as $[P_5W_{18}O_{75}(OH)_3]^{20-}$ [54], $[P_4W_{14}O_{58}]^{12-}$ [54,55], $[P_6W_{18}O_{79}]^{20-}$ [54] and $[P_4W_8O_{40}]^{12-}$ [56] (Figure 5.15).

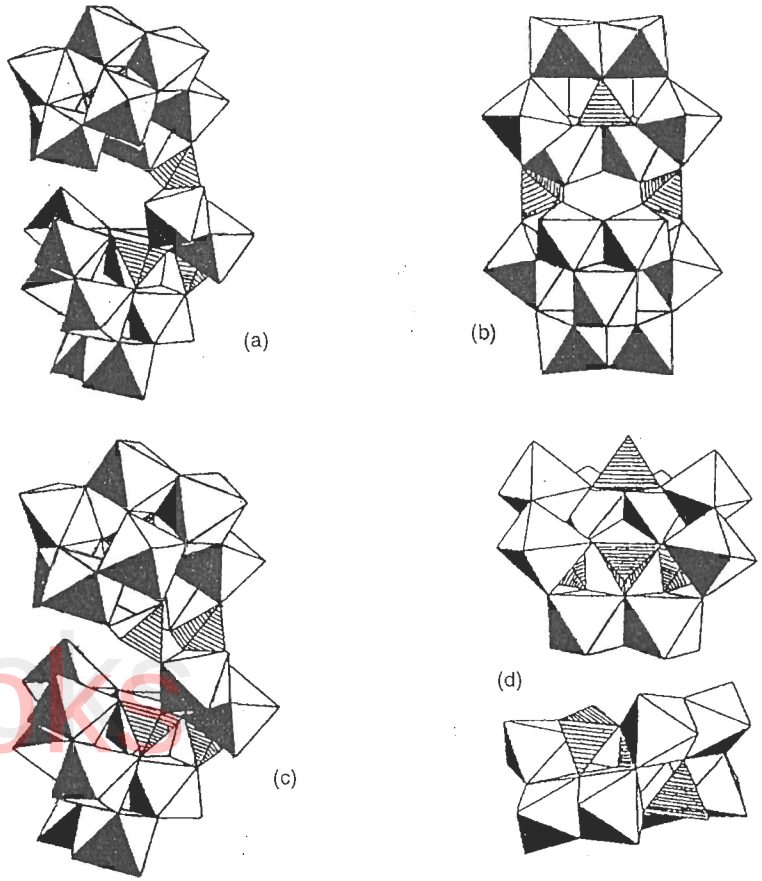

Figure 5.15 Structures of (a) $[P_5W_{18}O_{75}(OH)_3]^{20-}$ (from [54] by permission) (b) $[P_4W_{14}O_{58}]^{12-}$ (reprinted with permission from [55]. Copyright 1988 American Chemical Society), (c) $[P_6W_{18}O_{79}]^{20-}$ (from [54] by permission) and (d) $[P_4W_8O_{40}]^{12-}$ (reproduced from [56] by permission)

These polyanions are formed in concentrated solutions of mixtures of Na_2WO_4 and Na_2HPO_4 (ratio 3/1), acidified with acetic or perchloric acid in various solvents. Their structure is based on edge- and corner-sharing distorted octahedra and does not seem to be related to any of the previously described families. Although it is always possible to identify fragments of Keggin structure in these structures, they contain different tetra- or tricoordinated phosphoric groups.

These examples of phosphatotungstic polyanions are a good illustration of the structural diversity caused by a tri- or tetrabridging ion such as the phosphate. Like antimonates in solution, the phosphate does not form networks because it forms complexes of high formal charge cations, which condense exclusively by oxolation.

DropBooks

This does not occur in the case of titanium or zirconium, which maintain their ability to condense, at least by olation, in spite of the complexation. In the case of antimony, the formation of basic salts means that condensation must be forced by heat treatment. This is also the case for polyphosphates, which can only be obtained by heat treatment of the acid forms, since polyphosphates are metastable in aqueous solution [57].

5.4 INFLUENCE OF THE ANION ON THE STRUCTURE OF THE OXIDE

Unlike strongly complexing anions which usually form basic salts, some anions can force the oxide or the oxyhydroxide to form a specific structure, without even being present—at least stoichiometrically—in the final solid. Complexation takes place only at specific stages of precipitation. Two characteristic examples are discussed here: Fe(III) and Ti(IV).

5.4.1 IRON(III) OXYHYDROXIDES

The precipitation of ferric ions by the addition of a base or via thermohydrolysis in nitric or perchloric solutions leads to the oxyhydroxide α-FeOOH (goethite) or to the oxide α-Fe_2O_3 (hematite) (see Section 3.2.1c). In Chapters 2 (Section 2.3.4) and 3 (Section 3.2.3), we saw that the nature of the solid phase, as well as the size and morphology of the particles, depends largely on the experimental conditions (iron concentration, pH, temperature, ageing time and ionic strength of the medium).

Precipitation of ferric chloride in solution (at an iron concentration higher than 4×10^{-2} mol l^{-1}) by the addition of a base or thermohydrolysis leads to the oxyhydroxide β-FeOOH (akaganeite) [58–61a]. Its structure is a parent of goethite. Double chains of octahedra are present in both structures, but they connect differently (Figure 5.16). β-FeOOH has much wider channels containing variable amounts of chloride ions [58,62]. Unlike basic salts where polydentate ions are usually incorporated in the crystal structure, they are not part of the structure here, and can be exchanged with other ions [63–65].

The chloride ion does not have a very strong complexing character for iron [4–6]. EXAFS shows that two Cl^- in *trans* (distance 2.31 Å) form the coordination sphere of iron with four atoms of oxygen (distance 2.01 Å) in a weakly hydrolyzed solution ($h = HO^-/Fe \leqslant 0.3$) [66,67]. The Cl^- ions are gradually displaced as the hydrolysis ratio increases. During the initial stages of condensation, Fe–Fe distances at 3.45 Å and 3.01 Å appear, corresponding to octahedra sharing Fe–O–Fe corners and Fe–$(OH)_2$–Fe edges. These early stages are similar to what would occur in the presence of non-complexing ions (NO_3^-, ClO_4^-). At $h > 2$, no chlorine is detected in the coordination sphere of iron in the polymers. However, some Cl^- must remain trapped in the polymers and the chains formed by olation (see Section 3.2.3). In

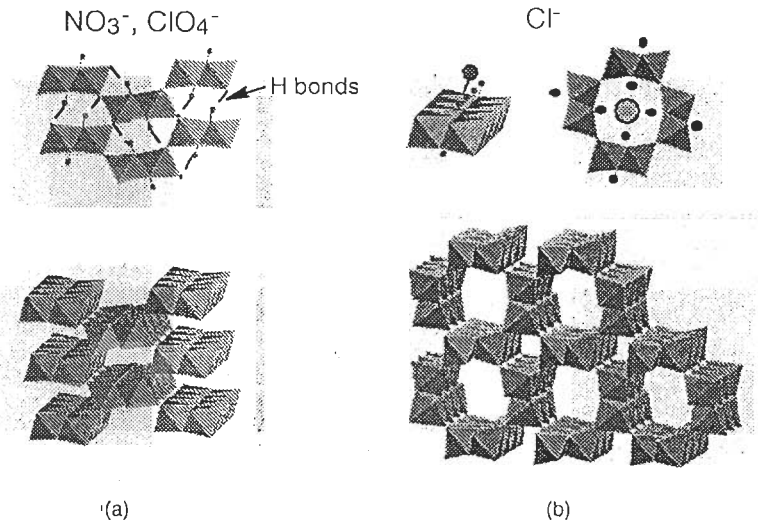

Figure 5.16 Structures of (a) goethite α-FeOOH and (b) akaganeite β-FeOOH

these chains, the charge of the proton on μ_3–OH bridges, which is probably quite high and positive, may cause strong interactions and the formation of outer sphere complexes $(Fe^{3+})_3$–O–$H^{\delta+} \cdots Cl^{\delta-}$. Therefore, hydrogen bonds cannot form between the polymer fragments. The large size (1.81 Å) of the chloride ions could therefore lead, by steric effects, to a less compact chain structure than the one observed in goethite. The weak complexing nature of chloride on the hydrolysis products of iron(III) also explains why FeOCl oxychloride is practically not obtained by precipitation in conditions similar to that of the formation of β-FeOOH. It should also be noted that the structure of FeOCl is very similar to the layered structure of γ-FeOOH [62]. FeOCl is obtained by reacting α-Fe_2O_3 with $FeCl_3$ around 400 °C in a closed container [68,69].

The oxyhydroxide β-FeOOH is a metastable phase forming spontaneously during the early stages of precipitation of $FeCl_3$. After high-temperature ageing of the suspensions, dissolution–crystallization equilibria lead to the formation of hematite [60,67,68] (see Sections 2.3.4 and 5.5.2).

5.4.2 TITANIUM OXIDES

In the presence of chloride or titanium, thermohydrolysis around 100 °C of acid solutions of Ti(IV) leads to the rutile or anatase forms of TiO_2 (see Section 3.4.2). Strongly acid media (> 2 mol l^{-1}) and a higher temperature favor the formation of rutile at the expense of anatase. It appears that anatase does form in the early stages, since statistically the most probable configuration of the coordination sphere of the

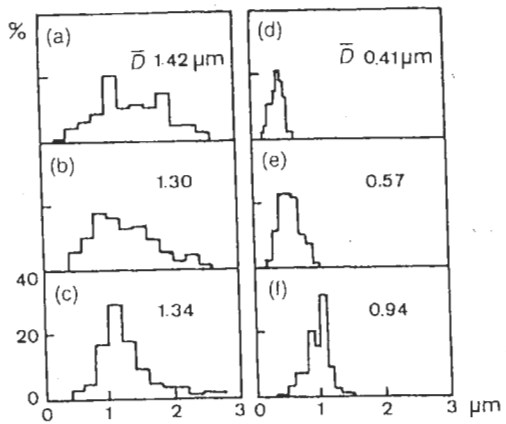

Figure 5.17 Particle size distribution of anatase as a function of the heating time at 95 °C (a–c) in a sulfate medium Na_2SO_4 (0.48 mol l^{-1}) and (d–f) in a fluoride medium NaF (0.11 mol l^{-1}). Heat treatment time: (a), (d) 1 h; (b), (e) 3 h; (c), (f) 6 h. HCl 2.13 mol l^{-1}, Ti 0.22 mol l^{-1}. Reproduced from [72] by permission

precursors allows non coplanar edges to be shared (Section 3.4.2). However, experimental conditions tend to favor dissolution–precipitation equilibria which allow nucleation of the thermodynamically stable phase into perfectly spherical particles. These particles grow with thermolysis time (Figure 3.19).

In the presence of sulfate or fluoride in solution, the reaction produces anatase only, as small irregular platelets. With the sulfate, their average size stays practically unchanged during ageing. With fluorine, the particles are smaller but tend to grow during ageing [72] (Figure 5.17).

Since thermodynamic data are not available, the electronegativity–pH diagram (Figure 5.18) shows that complexation of titanium by sulfate and fluoride ions may take place in a strongly acid medium. It cannot take place with chloride ions. The zero-charge complex precursor is $[Ti(OH_3)X(OH_2)_n]^0$ ($X = [HSO_4]^-, F^-$), with $n = 2$ or 1 if the ligand is bi- or monodentate respectively.

With the monodentate fluoride ion, it is difficult to have two H_2O ligands in *trans* allowing condensation of opposed coplanar edges. This mode of condensation is possible only with a bidentate ligand ($[HSO_4]$) which leaves only one water molecule in the coordination sphere. As a result, only anatase can form. In both cases, this mechanism may only take place if the complexes are sufficiently stable. Equilibria between various species are probably involved. Under these conditions, it is difficult to know what is the precursor of the solid. Since the oxide always contains some amount of sulfate difficult to remove, it is reasonable to speculate that the complexes are rather stable and that the formation of the solid takes place by incorporation of the sulfated titanium complexes by olation. This is also probably the case with the fluoride. Therefore, the complexing ions of titanium

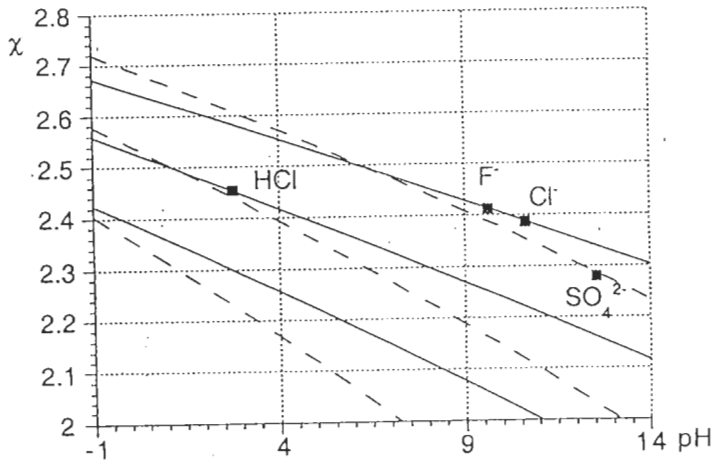

Figure 5.18 Electronegativity–pH diagram for the complexation of Ti(IV)

prevent dissolution–crystallization equilibria from taking place, thereby stabilizing anatase.

DropBooks

5.5 CONTROL OF THE SIZE DISTRIBUTION AND MORPHOLOGY OF OXIDE PARTICLES

The production of monodisperse particles is very important for industry (production of ceramics, catalysts, pigments, etc.) and for fundamental investigations of the dynamic behavior and stability of dispersions [73–75]. Monodisperse particles are usually obtained if there is only one nucleation step followed by uniform growth. It is therefore necessary to control the kinetics of nucleation and growth. This is rarely accomplished when a base is added to a solution of metal ions. It is usually preferable to use thermohydrolysis, which does not require mixing reactants [75,76] (see Section 2.3). The essential parameters are temperature, heating time and pH. The examples below also stress the importance of the nature of the cation on the morphology and the particle size distribution.

5.5.1 CHROMIUM OXIDE

Monodisperse particles of hydrated chromium oxide Cr_2O_3 can be obtained by prolonged heating around 75 °C of diluted solutions of $KCr(SO_4)_2 \cdot 16H_2O$ [2,77] (Figure 5.19). The specific role of sulfate is clear since, under similar conditions, chromium nitrate or perchlorate yield only soluble hydrolysis products.

There are two disctinct kinetic steps during the process. First, a filamentous veil appears (Figure 5.19). Analyses show that it contains sulfates. Spherical oxide

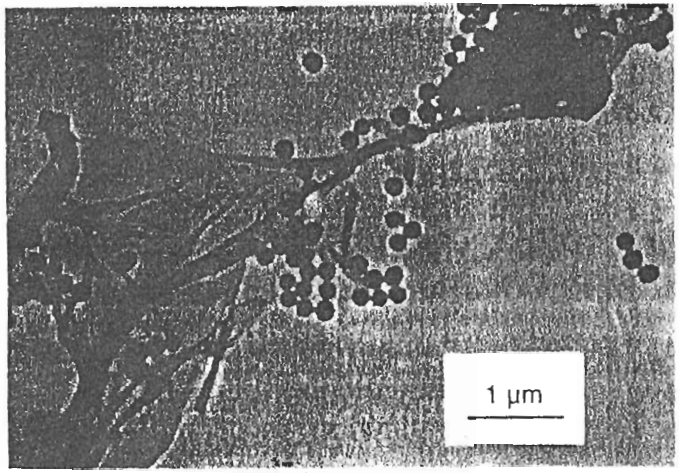

Figure 5.19 TEM micrograph of thermohydrolysis products at 75 °C of $KCr(SO_4)_2$ (4×10^{-4} mol l^{-1}, initial pH 3.7, final pH 3.3). Reproduced by permission of Academic Press from [2b]

particles form later at the expense of the veil. The particles are sulfate-free and have a narrow size distribution. The complexing role of the sulfate towards chromium is therefore only temporary.

The potential precursors of a solid phase are the zero-charge complexes $[Cr(OH)(SO_4)(OH_2)_3]^0$, $[Cr(OH)_2(HSO_4)(OH_2)_2]^0$ and $[Cr(OH)_3(OH_2)_3]^0$. The sulfated complexes are stable ($\chi = 2.653, \delta(SO_4) = -1.25, \delta(HSO_4) = -0.97$) and may condense by olation, with a maximum functionality of 1 or 2, to form linear polymers. As they entangle, they form the filamentous veil. In polymers such as $[Cr(OH)(SO_4)(OH_2)_2]_n^0$ (which contains μ_2–OH bridges) and $[Cr(OH)_2(HSO_4)]_n^0$ (which contains $2\mu_2$–OH bridges):

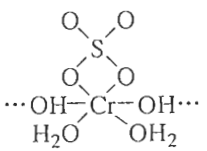

$\chi = 2.688 \quad \delta(SO_4) = -1.18$

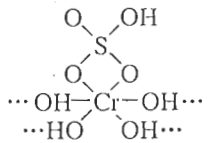

$\chi = 2.745 \quad \delta(HSO_4) = -0.73$

complexation of chromium by the sulfate must remain effective, as shown by the partial charge on the sulfate ligands.

As the polymers precipitate, the chromium concentration in the solution decreases, and most notably the concentration in $[Cr(OH)_3(OH_2)_3]^0$, which becomes unable to form the oxide by homogeneous nucleation. Heterogenous nucleation may therefore take place. It occurs by reaction with the sulfated polymers but requires elimination of the sulfate. Indeed, taking as an example the dimer produced by such

a reaction

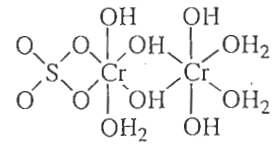

a HSO_4 ligand [$\chi = 2.597, \delta(HSO_4) = -1.11$] loses its ability to form a complex ($\delta < -1$). The sulfate is gradually removed during dissolution and the crystallization of sulfate-free oxide nuclei takes place on the surface of the polymer. The initial precipitation of the sulfated polymers allows regulation of the nucleation of the oxide by limiting the quantity of soluble species. The growth of the nuclei takes place in a uniform and isotropic manner and results in the formation of monodisperse, spherical particles.

5.5.2 IRON OXIDE

When particles of the same oxide can exhibit various morphologies, this is frequently the result of temporary complexation. Matijevic [3,60,73,76,78] has described these phenomena. An excellent example are the various morphologies of hematite (α-Fe_2O_3) particles formed by thermohydrolysis of acid solutions of chlorides, nitrates or ferric perchlorates [60] or of alkaline solutions of iron chelates with triethanolamine [78a,b] (Figure 5.20). Additional examples are shown in Figures 2.12 and 2.13.

As a rule, it is difficult to predict the effects of experimental conditions (pH, temperature, concentration, type of anion, etc.) on the morphology of the particles, because the factors that most strongly influence the preferential growth of one crystal face rather than another are difficult to comprehend. The photographs in Figure 5.20 show that α-Fe_2O_3 particles are increasingly anisotropic as the complexing nature of the anion increases.

It seems that complexation plays a role both during the nucleation step (regulation of the amount and nature of the precursors in solution) as well as during the growth stage. Since the oxide is free of complexing anions, it is likely that complexation takes place only on the surface of the particles (see Chapter 7). The most complexed faces must be less able to attach additional matter during growth, which results in these faces being larger than the less complexed ones.

Thermohydrolysis of ferric chloride solutions causes the formation of acicular particles of β-FeOOH initially (see Section 5.4.1). At iron concentrations of 2×10^{-2}–4×10^{-2} mol l^{-1}, they slowly transform by dissolution–crystallization into spherical or ellipsoidal particles of α-Fe_2O_3 [61,70] (Figures 5.20, 5.21 and 2.12). The chloride ions are not complexing enough to cause preferential orientiation during the growth of the highly anisotropic particles. The size and morphology of the hematite particles are more dependent upon the size and aggregation of the initial particles of β-FeOOH which act as substrates for heterogeneous nucleation

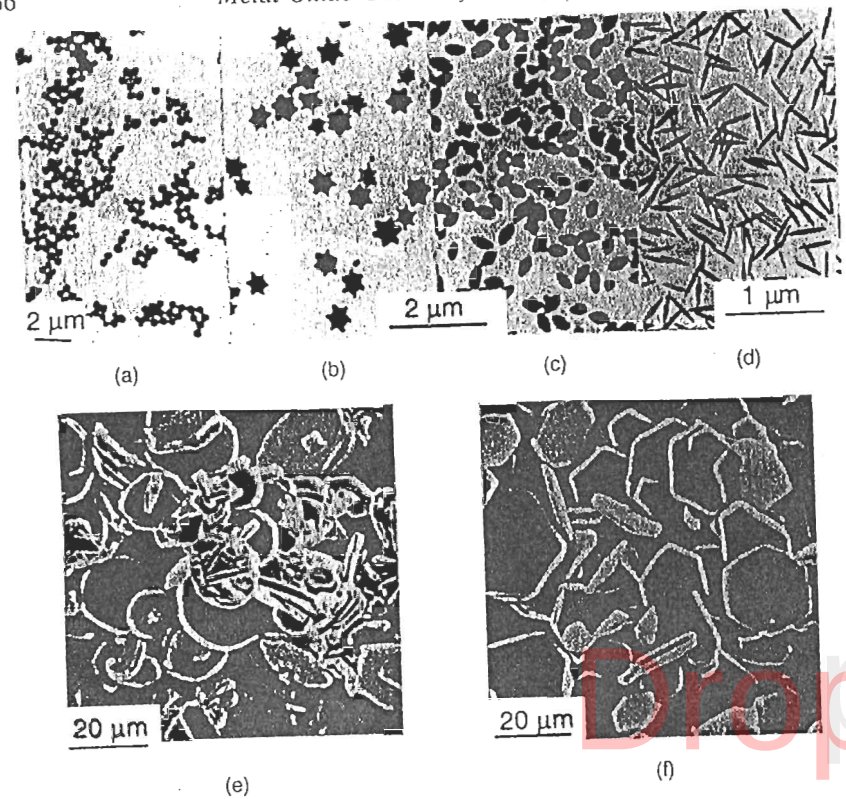

Figure 5.20 α-Fe_2O_3 particles formed by the thermohydrolysis of acidic solutions of Fe(III) (100 °C, pH 0.5–2.5) in the presence of ions (a) Cl^-, (b) ClO_4^-, (c) NO_3^- and (d) $H_2PO_4^-$, and by the thermohydrolysis of alkaline solutions of Fe(III)–triethanolamine chelates (250 °C, NaOH 1.2 mol l^{-1}) in media (e) ClO_4^- and H_2O_2 and (f) NO_3^- and CH_3COO^-. Reproduced by permission of E. Matijevic

[70]. At a high chloride concentration, iron complexation must be too important and the recrystallization equilibria of hematite are no longer involved. Akaganeite is the only phase obtained during ageing of the solutions [61].

In the presence of nitrates, hematite forms according to a different process. Thermohydrolysis first forms goethite α-FeOOH which subsequently induces crystallization of the remaining iron as hematite: after 3 h at 100 °C for solutions containing 2×10^{-2} mol l^{-1} $Fe(NO_3)$ and 5×10^{-2} mol l^{-1} HNO_3, goethite represents 48% of the solid, whereas there is only 8% left after 32 h when iron has almost completely precipitated [61b]. The particles are about 0.5 µm long and 0.3 µm wide, with an aspect ratio of 1.6. Electron diffraction confirms their composite nature. Towards the extremities, the diffraction pattern corresponds to monocrystalline hematite, whereas the pattern for the center of the particle shows

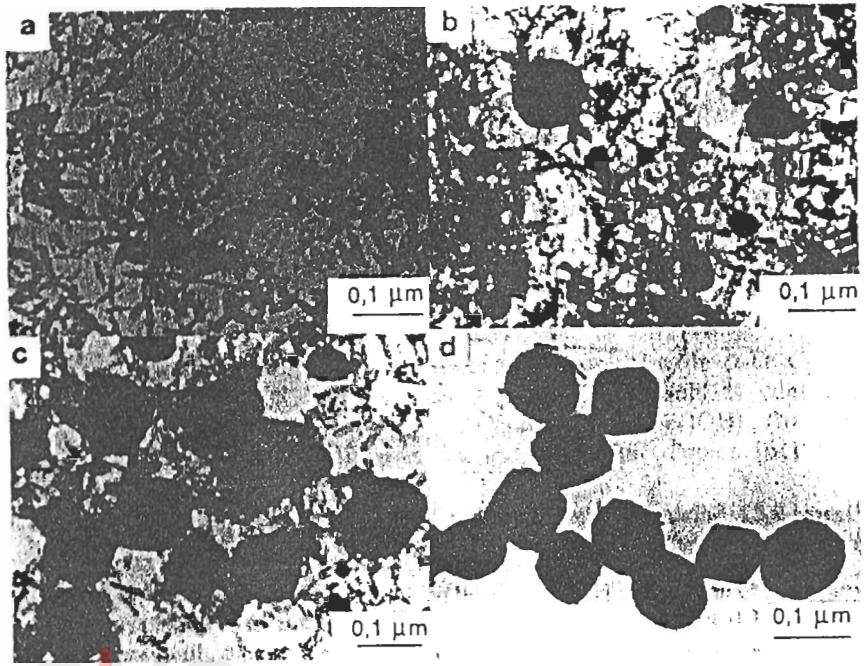

Figure 5.21 Formation steps of spherical particles of α-Fe_2O_3 by the thermohydrolysis at 100 °C of $FeCl_3$ solutions (0.02 mol l^{-1}): (a) onset of turbidity (β-FeOOH); (b) after 5 h; (c) after 1 day; (d) after 2 days. Reproduced from [61] by permission

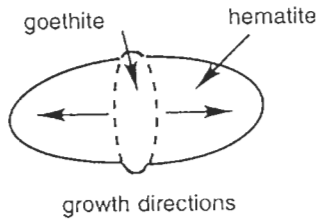

Figure 5.22 Anisotropic growth of hematite on a goethite nucleus. From [61b]

additional spots due to goethite [61b]. Thermohydrolyis under similar conditions but for more diluted solutions (6×10^{-2} mol l^{-1}) yields hematite exclusively, but the particles are heterogeneous in shape. The ellipsoidal morphology of hematite does seem to be the result of a template effect caused by the goethite formed originally. Heterogeneous nucleation and growth of hematite take place on an oblong nucleus of goethite (Figure 5.22).

A similar mechanism is probably responsible for the formation of the doubly ellipsoidal particles of hematite seen in Figure 2.12d. The large initial particles of β-FeOOH act as a substrate for recrystallization by heterogeneous nucleation.

DropBooks

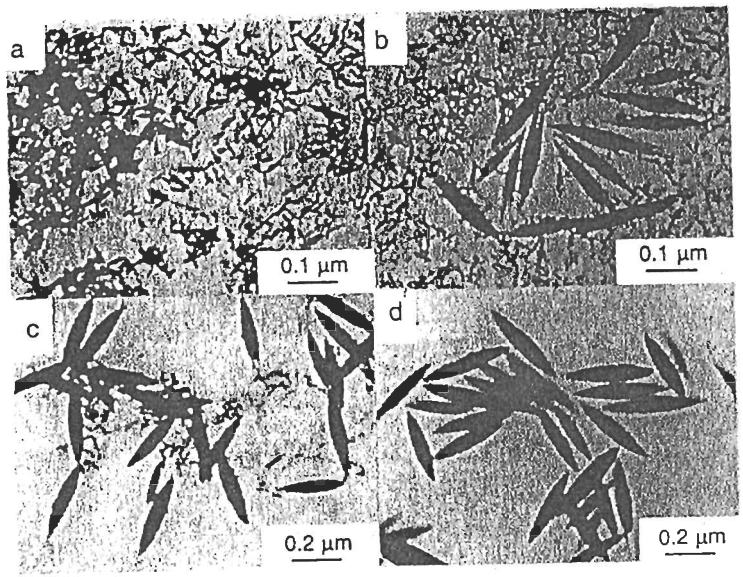

Figure 5.23 Formation steps of ellipsoidal particles of α-Fe_2O_3 by the thermohydrolysis at 100 °C of $FeCl_3$ solutions (0.02 mol l^{-1}) containing KH_2PO_4 (4.5×10^{-4} mol l^{-1}): (a) onset of turbidity (β-FeOOH); (b) after 2 days; (c) after 4 days; (d) after 6 days. From [61] by permission

Hematite forms at the expense of β-FeOOH but the dissolution–crystallization equilibria are not able completely to resorb the akageneite in the presence of a high concentration of chlorides [70].

The anisotropy of the hematite particles is more pronounced in the presence of phosphate (Figure 5.23). The aspect ratio reaches 6 (Figure 5.23d) and increases with increasing phosphate concentration [61,71].

The process also starts with the formation of β-FeOOH particles, but the growth of α-Fe_2O_3 particles during dissolution–crystallization is limited by adsorption of the phosphate. Cancellation of the surface charge (Chapter 7) causes aggregation of the particles in a direction parallel to their long axis. Aggregation, which causes interactions between surfaces and their desolvation, as well as medium acidity are factors favoring the slow desorption of the phosphate. This causes the recrystallization of tactoidal polycrystalline aggregates into monocrystals [61a,b]. The monodisperse characteristics of α-Fe_2O_3 particles obtained from aggregation phenomena remain difficult to explain.

A complexing ion such as the citrate also allows, in small concentration (Cit/Fe < 0.1 mol%) the formation of hematite particles. The particles are obtained by thermohydrolysis of ferric chloride solutions and exhibit a well-controlled cubic morphology [79]. However, because the citrate forms stable and charged iron chelates, high citrate concentrations cause the dissolution of the hematite particles [80,81].

5.5.3 ZINC OXIDE

Control of the morphology of oxide particles depends on the kinetics of formation of the zero-charge precurors, i.e. on the hydrolysis and condensation steps. The nature and the amount of complexing cations in the solution are also important. For elements of charge +III and +IV, kinetic control is attained by thermohydrolysis or forced hydrolysis. In this process, cation hydrolysis is carried out by water itself through an increase in temperature (see Section 1.4) in order to obtain a negative change in the free enthapy of the reaction. For elements of formal charge +II in an acid medium, the temperature required to obtain deprotonation of the aquo cation would be too high. Control of the kinetics of the reaction can be achieved through generation of controlled amounts of a base into the medium, or through the slow release of metal cations in a basic solution (see Section 2.3). This can be done by thermal decomposition of compounds like urea, formamide [76] or soluble metallic chelates in an alkaline medium (Figure 5.20). The production of zinc oxide particles by thermal decomposition of hexamethylenetetramine complexes is an example of the technique [82] (Figure 5.24d).

ZnO würtzite is obtained as prisms and needles. In the presence of a strongly complexing ligand such as hexamethylenetetramine, the chloride or nitrate ions

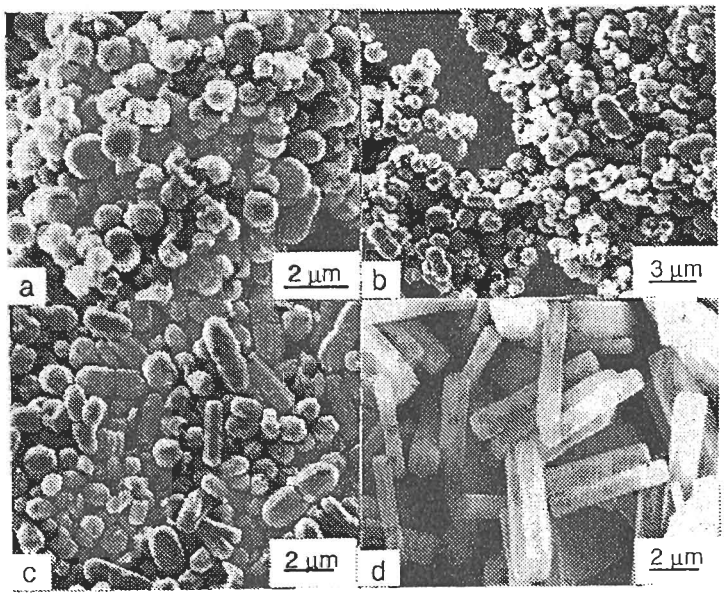

Figure 5.24 Change in the morphology of ZnO single crystals formed in a solution of $Zn(NO_3)_2$ (0.05 mol l^{-1}) and hexamethylenetetramine (0.05 mol l^{-1}) heated at 100 °C: (a) onset of turbidity; (b) after 3 min; (c) after 7 min; (d) after 30 min. Reproduced from [82] with permission

from the initial salt have very little influence on the characteristics of the particles. Both morphologies can be obtained in similar concentration and temperature conditions, and therefore they are probably strongly affected by kinetic factors only [82]. It is interesting to point out that spheres are formed at the beginning of thermohydrolysis (Figure 5.24a). They aggregate and appear to coalesce to form embryos of elongated crystals (Figures 5.24b and c). These embryos grow by dissolution–crystallization (Figure 5.24d). Under slow kinetic conditions (low temperatures, in particular), prismatic particles with clearly defined faces are favored at the expense of cylindrical acicular particles. Some prisms formed by thermohydrolysis at 80 °C transform into needles after heating at 100 °C.

5.6 SYNTHESIS OF POLYMETALLIC OXIDES

Using several examples, we have established that rigorous control of the chemistry of cations in solution permits the modification of the characteristics of the final products. When several cations are involved, problems are far more complicated because polycondensation of different elements can only take place if several specific conditions are met simultaneously. From a thermodynamic point of view, mixed compounds should be more stable than the compounds formed by each of the cations. From a kinetic point of view, the mixed phase must form at least as rapidly as the phases formed by each cation. Each cation must also have similar condensation rates. Incorporation of several elements in one network, without bringing in high activation energies since the reactions occur at low temperatures, imposes criteria on size, coordination and charges that are probably more stringent than a high temperature dry process would impose.

Coprecipitation of different cations sometimes leads to the thermodyanically stable mixed oxide, or to metastable mixed phases. It also often leads to segregation of metallic elements in separate phases. The activation energy required for crystallization of the mixed phase must be provided by heat treatment, as in the classical routes of solid state chemistry. However, there are a few advantages to working in solution. Precipitation most likely would produce nanometer-size particles. Small-size powders tend to make homogeneous mixtures, and the particles are very reactive owing to their large surface area. Even if the synthesis *per se* requires heat treatment, lower temperatures and lower processing times are usually required compared with the use of micrometer-size powders. In addition, grinding of coarse powders is avoided, which also prevents contamination issues.

The complexation of cations in solution plays an important role in the synthesis of polymetallic oxides. It can allow an adjustment in the reactivity of different elements via a modification of their coordination sphere or, more simply, by bringing together cations in complexes.

This would ease the formation of mixed oxide phases during hydrolysis and condensation. A few examples are described below.

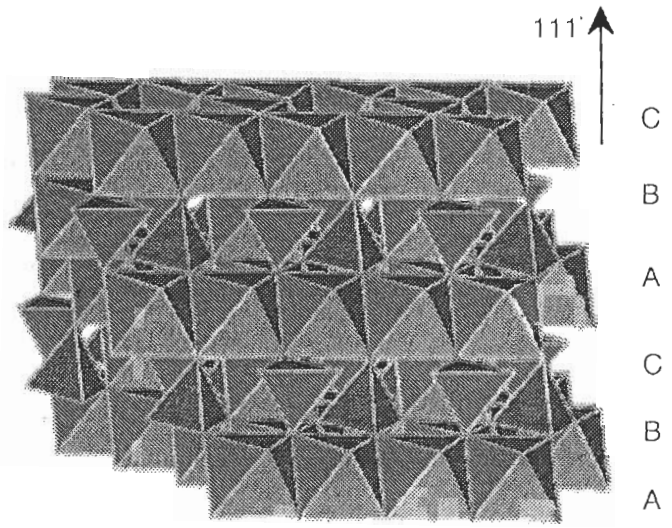

Figure 5.25 Spinel structure. A, B and C are conventional designations of the oxygen planes

5.6.1 SPINEL FERRITES AB_2O_4

The spinel structure $A^{II}B^{III}{}_2O_4$ (Figure 5.25) is formed by many pairs of elements A and B [83]. The structure is called normal or inverse, depending on whether the divalent cations occupy the tetrahedral sites or some octahedral sites of the oxygen f.c.c. network, respectively (see Section 3.5). This type of oxide usually exhibits interesting ferrimagnetic properties resulting from antiferromagnetic coupling between the magnetic moments of the ions on the tetrahedral and octahedral sublattices [84]. These materials are used as a magnetic recording medium.

Magnetite Fe_3O_4 is easily formed by coprecipitation of ferric and ferrous ions in stoichiometric ratio (see Section 3.5). Although Fe^{3+} and Fe^{2+} have very different acid–base characteristics [85], the spinel is formed almost immediately upon coprecipitation by a base [86, 87]. We have seen that electron delocalization plays a role in favoring the spinel structure and seems to be the 'catalyst' in the crystallization process. Electron transfer also appears to be involved in other preparation routes of magnetite: oxidation of ferrous hydroxide gels in an alkaline medium by air or nitrate ions [88,89], adsorption and reaction of ferrous ions on lepidocrocite γ-FeOOH [90] or maghemite γ-Fe_2O_3 [91] and adsorption of ferric ions on magnetite itself [92] (see Chapter 9). The required presence of divalent and trivalent cations in the formation of the spinel structure explains why maghemite γ-Fe_2O_3, whose structure contains only ferric ions, cannot be formed by a direct precipitation route. γ-Fe_2O_3 can be obtained under various experimental conditions from oxidation of magnetite (see Chapter 9). It can also

DropBooks

be obtained by reduction with hydrogen from hematite, followed by reoxidation [93]. This technique offers the advantage of preserving the morphology of the hematite particles, which allows the fabrication of acicular particles of high coercive field, particularly useful in magnetic recording media. However, these particles exhibit microstructural defects (mosaic crystals, porosity) which affect their performance.

The synthesis of $M^{II}Fe_2O_4$ ferrites by coprecipitation of Fe^{3+}, Co^{2+}, Ni^{2+} or Mn^{2+} ions is possible within the 50–100 °C temperature range [94–97]. Crystallization of the spinel is not immediate as in the case of Fe^{2+}. It involves dissolution–recrystallization processes from a poorly organized or amorphous precipitate consisting of hydroxides of the bivalent cation and ferric hydroxyhydroxide [96,97]. The lack of electron mobility between Co^{2+}, Mn^{2+} or Ni^{2+} and Fe^{3+}, owing to the redox potential of Fe^{3+}/Fe^{2+} being inferior to that of M^{3+}/M^{2+}, is probably responsible for the slow crystallization.

Coprecipitation of ferric ions and divalent ions such as Mg^{2+}, Cd^{2+}, Zn^{2+} and Pb^{2+} does not lead to the spinel structure, but to $M(OH)_2$ and the oxyhydroxide FeOOH [98]. The synthesis of the spinel requires heat treatment of the corresponding hydroxides or carbonates. Spinel ferrites partially replaced with divalent elements are prepared indirectly by precipitation of Fe^{2+} and M^{2+} as hydroxides, followed by oxidation of the suspension at 65 °C in air [99–103]. The stoichiometric phases are never obtained, however, except in the case of zinc. Precise conditions of acidity and composition (M^{2+}/Fe^{2+}) must be chosen in order to prevent precipitation of hydroxides or basic salts of the divalent element and formation of the oxyhydroxide α-FeOOH.

Replacement of Fe^{3+} by Cr^{3+} in the octahedral sublattice of the inverse spinel structure cannot be achieved during coprecipitation of Fe^{2+}, Fe^{3+} and Cr^{3+}. It may be achieved by forming a gel containing a mixture of the hydroxides $M(OH)_3$ in an alkaline medium. The mixed oxide $Cr_xFe_{2-x}O_3$ is precipitated by hydrothermal treatment of the gel, followed by heat treatment around 400 °C under hydrogen [104]. The chromium present in the starting gel is not entirely incorporated in the ferrite particles. The chromium content seems to be a function of the heat teatment time of the gel. This is probably due to the difference in crystallization kinetics between iron oxides and chromium oxides, which might cause heterogeneities in the composition of the spinel. A similar chrome-substituted ferrite is formed from thermal decomposition of the mixed oxalate complex $(NH_3)_3[Fe_{1-y}Cr_y(C_2O_4)_3]_3 \cdot H_2O$ [105–107]. Low-temperature reduction of the solid solution $(Fe_{1-y}Cr_y)_2O_3$ under hydrogen forms the mixed spinel.

The difficulties in synthesizing the mixed spinel seem related to both thermodynamic and kinetic issues. Hydroxides (and/or basic salts) of divalent elements are more stable than the ferrite at low temperatures. The large reactivity difference between iron and chromium explains the rapid crystallization of iron oxides or oxyhydroxides compared with the chromium compounds, as well as the segregation of both elements.

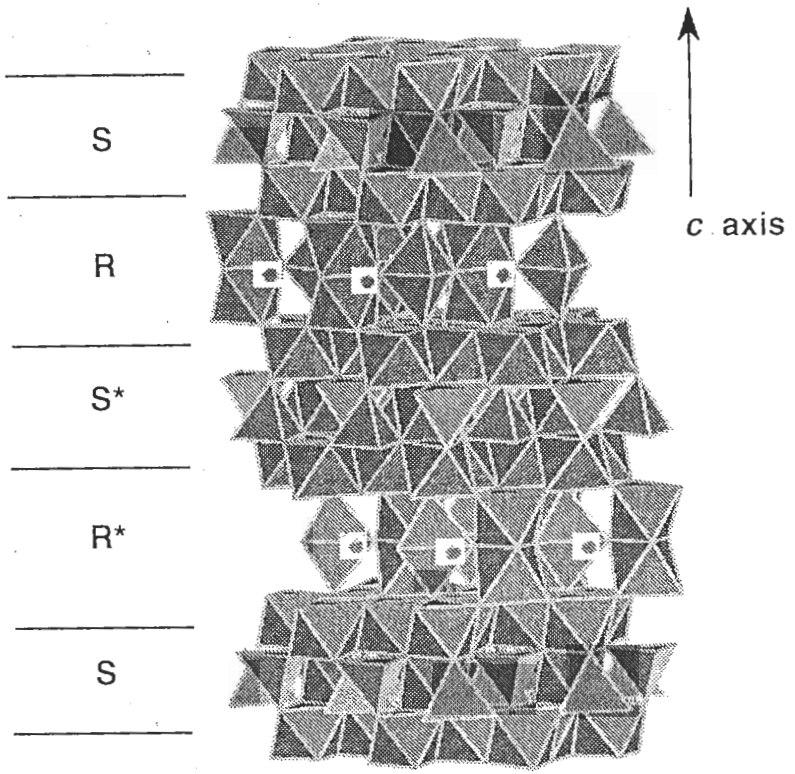

Figure 5.26 Structure of barium hexaferrite $BaFe_{12}O_{19}$. R and S blocks with an asterisk have rotated by 180° around the c axis

5.6.2 HEXAGONAL FERRITES $BaFe_{12}O_{19}$

Hexagonal ferrites (or hexaferrites) are magnetic oxides containing several blocks in their structure [62,108]. The $BaFe_{12}O_{19}$ structure (Figure. 5.26) contains blocks of half unit cell of spinel (blocks S) connected to blocks containing three layers of h.c.p. oxides (blocks R). These blocks do not belong to a particular structural type. They simply link the S blocks together. In other types of hexagonal ferrites, T blocks containing four layers of h.c.p. oxides also act as links between S blocks. Changing the stacking sequence of two or three types of block leads to an entire family of hexaferrites, the most simple of which is $BaFe_{12}O_{19}$.

In these structures, iron is in coordination 4 and 6 in the spinel blocks, and in coordination 5 and 6 in the R blocks (Figure 5.26). These compounds are ferrimagnetic. In $BaFe_{12}O_{19}$, magnetization is unaxial and parallel to the c axis of the unit cell. The high magnetocrystalline anisotropy of hexaferrites is responsible

for their high remanent magnetization and high coercivity, i.e. high resistance to demagnetization. These materials are used in the fabrication of permanent magnets [109].

Conventional synthesis of $BaFe_{12}O_{19}$ requires a high temperature (1100 °C) reaction between iron oxide and barium carbonate. The material is shaped after grinding and sintering at 1200 °C. This process causes the creation of many defects in the stoichiometry or in the stacking sequence. It also causes local precipitation of Fe_2O_3 which decreases the coercive forces [109]. To avoid such problems, it is possible to synthesize the material at lower temperatures from solutions.

Coprecipitation of ferric chloride in excess NaOH and in the presence of barium carbonate forms a mixture of mixed hydroxides and basic carbonates which, upon calcination at 710 °C, form the barium ferrite. The magnetic properties are optimized by subsequent heat treament at 950 °C. This method produces platelet-shaped particles with an average size of 0.3 μm [110]. Another technique involves oxidation of ferrous oxalate by hydrogen peroxide in the presence of excess oxalic acid. The addition of barium carbonate (Ba/Fe = 1/12) forms mixed complexes of Fe^{3+} and Ba^{2+}. The complexes are destroyed in an alkaline medium (carbonate buffer) and form a mixed hydroxide gel. The hexaferrite crystallizes as circular platelets after heat-treatment at 700 °C [110].

The easy magnetization axis of the platelets is perpendicular to the large faces. Micrometer-size (0.1–0.3 μm) particles allow the fabrication of high-density storage materials which use the vertical component of the magnetic field of the recording head. For longitudinal recording, acicular particles with the easy magnetization axis parallel to the axis of the needle are more suitable, but this morphology is not frequently found in hexaferrites. An indirect technique can be used to obtain such materials starting from acicular particles of goethite α-FeOOH. A gel of these particles is treated with barium ethoxide $Ba(C_2H_5O)_2$ in alcohol. Elimination of the alcohol upon reaction of the alkoxide with the hydroxyl groups on the surface of goethite causes adsorption of the barium. Upon heat treatment, barium diffuses inside the particles and crystallization of hexaferrite occurs at 750 °C, preserving the morphology of the starting particles [110,111].

5.6.3 PEROVSKITE OXIDES ABO_3

Many compounds of perovskite structure (Figure 5.27) exhibit intersting ferro- or piezoelectric properties. They are widely used in the fabrication of multilayer ceramic capacitors ($BaTiO_3$, $PbTiO_3$, $PbZr_{1-x}Ti_xO_3$, $PbFe_{0.5}Nb_{0.5}O_3$, etc.) [112]. Some perovskites such as $PbZr_{0.5}Ti_{0.5}O_3$ and $(Pb_{1-x}La_xZr_yTi_{1-y})_{1-x/4}O_3$ exhibit electro-optic properties used in the modulation of light by an electric field. $LiNbO_3$ exhibits non-linear optical properties [113].

Traditional synthesis of $BaTiO_3$ and of many other titanates involves grinding and calcination above 1000 °C of titanium oxide and barium carbonate [112,114].

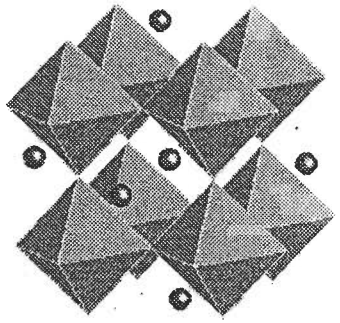

Figure 5.27 Perovskite structure ABO_3

The main difficulty is in avoiding the formation of the very stable pyrochlore phase, which lowers the dielectric performance of the material. This is why many parameters such as the stoichiometry of the mixture, the method and duration of grinding (i.e. the particle size) and the duration and temperature of heat treatment are involved in the process. Abrasion of the grinding medium causes unavoidable contamination. High sintering temperatures require the use of expensive heating elements, palladium for example, in the fabrication of capacitors. Although some improvements have been made in solid state synthesis [114], other methods based on coprecipitation of titanium and barium now allow the synthesis of the perovskite phase at much lower temperatures, with higher purity and as small particles. It is possible to fabricate thin films for capacitors simply by depositing the suspension or the gel on the metal electrode. The small particle size allows sintering at lower temperatures with inexpensive copper or nickel electrodes.

A possible synthesis route is the formation of mixed titanium–barium complexes such as oxalates or citrates [115,116]. These anions are able to form complexes with many metal cations, allowing their simultaneous dissolution and homogenous precipitation at the molecular scale. A mixed citrate $BaTi(C_6H_5O_7)_3 \cdot 6H_2O$ crystallizes by the acidification at pH ⩽ 2.6 of a solution of both citrates, at any stoichiometry [116]. Thermal decomposition of the compound leads, after many steps, to the formation of $BaTiO_3$ between 600 and 700 °C. It is interesting to note that the pyrolysis forms barium carbonate at 360 °C and a $BaCO_3$–TiO_2 mixture around 500 °C (identified by XRD and TGA). This shows that barium titanate does not crystallize directly upon heat treatment of the coprecipitate, but that the stable phases (barium carbonate and titanum oxide) form first. The perovskite appears by solid state reaction at 700 °C, a temperature well below that required when coarse powders are used, and without the formation of the pyrochlore. The decrease in crystallization temperature is due to the reactivity of the particles, allowing diffusion over a shorter distance.

It is also possible to synthesize $BaTiO_3$ in 'soft' conditions by heating aqueous supensions of $Ba(OH)_2$ and TiO_2 at 90 °C [117]. The reaction takes place only with

DropBooks

fine powders of anatase (7 m^2/g) or titanium oxide B (72 m^2/g). The B variety is obtained by treatment of $K_2Ti_4O_9$ in an acid medium, followed by heat treatment at 500 °C [118] (see Section 3.4.2). Conversion of TiO_2 B into barium titanate is complete after 24 h at 90 °C. It is only 50% complete with TiO_2 anatase and 15% with rutile under the same conditions. Similar results are obtained under hydrothermal synthesis (250 °C, 3.5 MPa). Crystallization of the titanate occurs by reaction of the barium on the surface of the TiO_2 particles. Conversion of the oxide requires diffusion of the barium through the titanate layer, and the reaction is much faster if the oxide particles have a less stable crystalline structure and a large surface area, therefore if they are small [117,119].

Many other perovskites are also prepared from organometallic precursors such as $Ti(OR)_4$, $Zr(OR)_4$, $Nb(OR)_5$ and $Ba(OR)_2$, $Sr(OR)_2$, where R is an aliphatic hydrocarbon [120]. A stoichiometric mixture of barium and titanium alkoxides in alcoholic or benzenic solution is first refluxed ($\approx$ 90 °C) and hydrolyzed with water. The titanate precipitates as 50–150 Å particles. Refluxing alkoxides leads, upon elimination of ether R_2O, to oxoalkoxide clusters where Ba–O–Ti bonds are stable towards hydrolysis. Hydrolysis occurs in order to eliminate the organic ligands located on the outside of the clusters and to facilitate their condensation. Crystallization of the material occurs at the synthesis temperature.

Since alkoxides of low formal charge metals are highly condensed and therefore poorly reactive, the synthesis of many perovskites (titanium, zirconium, niobium, barium, strontium or lead) can take place by hydrolysis of the alkoxide by an aqueous suspension of hydroxide (Ba, Sr) [121] or by an aqueous solution of a lead complex such as the acetate [122]. Iron is introduced as acetylacetonate in the case of $PbFe_{0.5}Nb_{0.5}O_3$ [123]. The calcination temperature varies with the nature of the metallic cation. It must be adjusted if the formation of undesirable phases is possible, such as the pyrochlore phase in the case of $PbMg_{0.33}Nb_{0.66}O_3$ and $PbZr_{1-x}Ti_xO_3$ [122]. A fast ramp rate prevents or minimizes its formation.

5.6.4 SUPERCONDUCTING CUPRATES

The crystal structure of high T_c (90 K) superconducting cuprates is based on a perovskite lattice with an orthorohombic distortion [124] (Figure 5.28). In the various families of these compounds, copper ions exhibit various coordinations: four planar–square, five pyramidal, six octahedral. In all cases the four bonds in the perovskite layers are shorter that the Cu–O bonds between layers.

The most studied phase, $YBa_2Cu_3O_{7-x}$, can be synthesized using traditional ceramic processing by calcination of barium carbonate, yttrium oxide and copper oxide. Because of the stability of the barium and since the reaction takes place by diffusion in the solid state, temperatures of the order of 950 °C and reaction times of at least 48 h are required in order to obtain well-crystallized phases. The main difficulty is to obtain a dense powder allowing high critical currents. Sintering at temperatures ranging from 900 to 950 °C causes grain growth without densification.

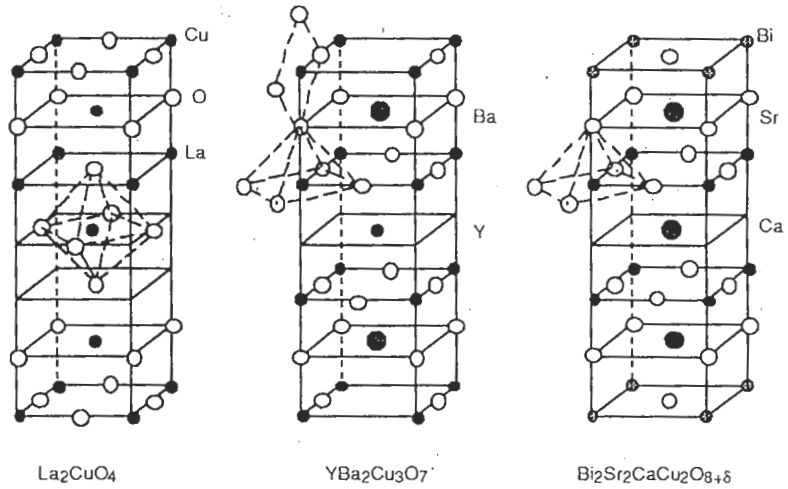

Figure 5.28 Structures of three copper-based superconductors

As a result, grain boundaries seriously alter the superconducting properties owing to the penetration of magnetic flux between the grains [125].

These difficulties call for a technique allowing a decrease in the processing temperature. This can be achieved starting from mixtures of the elements in solution. Two routes can be used: coprecipitation and fast drying of solutions. The superconducting phases are obtained, depending on which route was chosen, between 650 and 850 °C. However, the advantage of these techniques—forming small particles to improve the homogeneity and reactivity of the compounds—is a major problem because the small size decreases the Meissner effect. It is necessary eventually to sinter the particles and therefore to use high temperatures. The advantages of the processing route are therefore somewhat lost because of the poor properties of the material. There is, however, still an advantage in the synthesis of thin film for electronic applications. The coprecipitate or initial gel is deposited on an MgO, $SrTiO_3$ or ZrO_2 substrate. The crystallization temperature of the film prevents strong interactions with the substrate and diffusion of impurities along grain boundaries. However, film/substrate interactions can texture the sample, i.e. align the particles so that the c axis of the perovskite is perpendicular to the substrate. This allows an increase in critical current density and improves the properties of the material [125].

Coprecipitation of yttrium, copper and barium is most often done with carboxylates (citrates, oxalates, acetates) from solutions of nitrates. Control of the pH, temperature and concentration make the precipitation as quantitative as possible in order to preserve the stoichiometry of the mixture [126–129]. Long-chain carboxylates (2-ethylhexanoate, neodecanoate) ensure the solubility of metals in volatile solvents such as xylene or xylene–pyridine mixtures, in order to make drying at

low temperatures (150 °C) possible on various substrates [130–132]. Chelation of metal cations by ethyleneglycol [133] produces viscous solutions able to form films.

The formation of the perovskite phase requires heat treatment of the precipitate or gel. The organic components are removed between 200 and 400 °C and the metallic elements segregate as oxides (Y_2O_3, CuO) and carbonate Ba_2CO_3. Since the small size of the particles causes short-range heterogeneities only, crystallization of the perovskite occurs around 850–900 °C [134,135]. These methods are interesting in the fabrication of thin textured films.

No truly superconducting film can be processed below 900 °C because of the poor reactivity of the intermediate phases. Also, the heat treatment time must be kept below 20 min in order to prevent diffusion of impurities between the film and the substrate. The use of carbon-free reactants prevents the formation of carbonates and decreases heat treatment times.

A mixture of nitrates in solution can be sprayed directly on a hot substrate (200 °C), subsequently heated at 800 °C and reheated (for a few minutes) around 900 °C. This technique was applied to the synthesis of $YBa_2Cu_3O_7$ [136–139], $Bi_2(Sr, Ca)_3Cu_2O_8$ [135,140] and $Tl_2Ba_2Ca_2Cu_3O_{10}$ [135].

The presence of carbon can also be prevented by precipitating the hydroxides at a high pH around 60 °C, which decreases the solubility of the hydroxides, and most notably barium hydroxide. The hydroxides are then decomposed at 600 °C and form $YBa_2Cu_3O_{6+x}$ around 850 °C [141]. Heat treatment at 920 °C allows sintering of the ceramic.

The examples shown in this chapter illustrate the important role of anions in the condensation and precipitation of cations in solution. The choice of anion must be made carefully in order to synthesize the chosen phase and in order to obtain particles of the chosen structure or morphology. Complexation does not play as clear a role in the synthesis of polymetallic oxides. Indeed, heterocondensation in solution does not always allow the formation of mixed solids. Judicious use of complexation reactions may allow the control of both the functionality and the electrophilic character of the cations through a modification of the coordination sphere.

5.7 REFERENCES

1. L.I. Bekkerman, I.P. Dobrovol'skii, A.A. Ivakin, *Russ. J. Inorg. Chem.* **21**, 223 (1976).
2. (a) A. Bell, E. Matijevic, *J. Inorg. Nucl. Chem.* **37**, 907 (1975); (b) E. Matijevic, A. Bell, *Particle Growth in Suspension*, A.L. Smith Ed., Academic Press, London (1973), p. 179.
3. E. Matijevic, *Ann. Rev. Mater. Sci.* **15**, 483 (1985).
4. L.G. Sillen, *Stability Constants of Metal–Ion Complexes*, The Chemical Society, London, Special Publication No. 17 (1964) and No. 25 (1971).
5. G. Charlot, *L'analyse Qualitative Minérale, 6th ed., Masson, Paris (1969).*
6. A. Ringbom, *Les Complexes en Chimie Analytique, Dunod, Paris (1967).*
7. A. Clearfield, *Rev. Pure and Appl. Chem.* **14**, 91 (1964).
8. A. Clearfield, P.A. Vaughan, *Acta Cryst.* **9**, 555 (1956).
9. A. Clearfield, *Inorg. Chem.* **3**, 146 (1964).

10. B.I. Nabivanets, *Russian Inorg. Chem.* (English Transl.) **6**, 586 (1961).
11. D.B. Mc Whan, G. Lundgren, *Acta Cryst.* **16**, A36 (1963).
12. P. Bénard, M. Louër, D. Louër, *J. Solid State Chem.* **94**, 27 (1991).
13. W. Mark, G. Lundgren, *Inorg. Chem.* **5**, 284 (1966).
14. M. Hansson, *Acta Chem. Scand.* **27**, 2614 (1973).
15. M. Brahimi, J. Durand, L. Cot, *Eur. J. Solid State Inorg. Chem.* **25**, 185 (1988).
16. I.J. Bear, G.W. Mumme, *Acta Cryst.* **B25**, 1558, 1566, 1572 (1969).
17. J. Singer, D.T. Cromer, *Acta Cryst.* **12**, 719 (1959).
18. I.J. Bear, G.W. Mumme, *Acta Cryst.* **B26**, 1125, 1131, 1140 (1969).
19. W. Mark, *Acta Chem. Scand.* **27**, 177 (1973).
20. W. Mark, *Acta Chem. Scand.* **26**, 3744 (1972).
21. F.A. Cotton, G. Wilkinson, *Advanced Inorganic Chemistry*, 4th ed., J. Wiley & Sons, New York (1980).
22. D.E.C. Corbridge, *Phosphorus, An Outline of its Chemistry, Biochemistry and Technology*, 3rd ed., Elsevier, Amsterdam (1985).
23. A. Clearfield, *Inorganic Exchange Materials*, CRC Press, Inc., Boca Raton (1982).
24. J. Albertsson, Å. Oskarsson, R. Tellgren, J.O. Thomas, *J. Phys. Chem.* **81**, 1574 (1977).
25. J.M. Troup, A. Clearfield, *Inorg. Chem.* **16**, 3311 (1977).
26. U. Chowdhry, J.R. Barkley, A.D. English, A.W. Leight, *Mat. Res. Bull.* **17**, 917 (1982).
27. R.G. Herman, A. Clearfield, *J. Inorg. Nucl. Chem.* **37**, 1697 (1975).
28. J.P. Jolivet, J. Lefebvre, *Bull. Soc. Chim. Fr.* 11-12, 2409 (1975).
29. J.P. Jolivet, J. Lemerle, J. Lefebvre, *Bull. Soc. Chim. Fr.* 11-12, 2415 (1975).
30. J.P. Jolivet, J. Lefebvre, *Bull. Soc. Chim. Fr.* 1-2, 27 (1977).
31. J.P. Jolivet, J. Lefebvre, *Bull. Soc. Chim. Fr.* 1-2, 34 (1977).
32. A. Winkler, E. Thilo, *Z. Anorg. Allg. Chem.* **92**, 346 (1966).
33. A. Galarneau, Thesis, Université de Nantes, 1993.
34. Y. Piffard, A. Lachgar, M. Tournoux, *J. Solid State Chem.* **58**, 253 (1985).
35. Y. Piffard, S. Oyetola, S. Courant, A. Lachgar, *J. Solid State Chem.* **60**, 209 (1985).
36. Y. Piffard, A. Lachgar, M. Tournoux, *Mat. Res. Bull.* **21**, 1231 (1986).
37. M.T. Pope, *Heteropoly and Isopoly Oxometalates*, Springer-Verlag, Berlin (1983).
38. P. Souchay, *Ions Minéraux Condensés*, Masson, Paris (1969); (a) p. 92; (b) p. 106; (c) p. 98.
39. J.F. Keggin, *Proc. Roy. Soc. A* **144**, 75 (1934).
40. R. Contant, *Can. J. Chem.* **65**, 568 (1987).
41. R. Massart, R. Contant, J.M. Fruchart, J.P. Ciabrini, M. Fournier, *Inorg. Chem.* **16**, 2916 (1977).
42. W.H. Knoth, R.L. Harlow, *J. Am. Chem. Soc.* **103**, 1865 (1981).
43. B. Dawson, *Acta Cryst.* **6**, 113 (1953).
44. H. D'Amour, *Acta Cryst.* **B32**, 729 (1976).
45. R. Acerete, S.P. Harmalker, C.F. Hammer, M.T. Pope, L.C.W. Baker, *J. Chem. Soc. Chem. Comm.* 777 (1979).
46. R. Contant, J.P. Ciabrini, *J. Chem. Res.* 2601 (1977).
47. R. Contant, A. Tézé, *Inorg. Chem.* **24**, 4610 (1985).
48. C. Preyssler, *Bull. Soc. Chim. Fr.* 30 (1970).
49. M.H. Alizadeh, S.P. Harmalker, Y. Jeannin, J. Martin-Frère, M.T. Pope, *J. Am. Chem. Soc.* **107**, 2662 (1985).
50. C.M. Tourné, G.F. Tourné, T.J.R. Weakley, *J. Chem. Soc. Dalton Trans.* 2237 (1986)
51. J. Fuchs, R. Palm, *Z. Naturforsch.* **39b**, 757 (1984).
52. C. Tourné, A. Revel, G. Tourné, *Rev. Chim. Min.* **14**, 537 (1977).
53. R. Contant, Personal communication (1992)
54. J. Fuchs, R. Palm, *Z. Naturforsch.* **43b**, 1529 (1988).

DropBooks

55. R. Thouvenot, A. Tézé, R. Contant, G. Hervé, *Inorg. Chem.* **27**, 524 (1988).
56. B.M. Gatehouse, A.J. Jozsa, *Acta Cryst.* C39, 658 (1983).
57. J.R. Van Wazer, *Phosphorus and its Compounds*, Vol. 1, Interscience, New York (1958).
58. C.M. Flynn, *Chem. Rev.* **84**, 31 (1984).
59. M.A. Blesa, E. Matijevic, *Adv. Colloid Interface Sci.* **29**, 173 (1989).
60. E. Matijevic, P. Scheiner, *J. Colloid Interface Sci.* **63**, 509 (1978).
61. (a) M.P. Morales, T. Gonzales-Carreno, C.J. Serna, *J. Mater. Res.* **7**, 2538 (1992); (b) C.J. Serna, Personal Communication; M. Ocana, M.P. Morales, C.J. Serna, in preparation.
62. A.F. Wells, *Structural Inorganic Chemistry*, 5th ed., Clarendon Press, Oxford (1991).
63. R. Paterson, H. Rahman, *J. Colloid Interface Sci.* **94**, 60 (1983).
64. R. Paterson, H. Rahman, *J. Colloid Interface Sci.* **97**, 423 (1984).
65. R. Paterson, H. Rahman, *J. Colloid Interface Sci.* **98**, 494 (1984).
66. J.M. Combes, A. Manceau, G. Calas, J.Y. Bottero, *Geochim. Cosmochim. Acta* **53**, 583 (1989).
67. J.Y. Bottero, A. Manceau, F. Villieras, D. Tchoubar, *Langmuir* **10**, 316 (1994).
68. G. Rousseau, *C.R. Acad. Sci. Paris* **110**, 1032 (1890).
69. S. Goldsztaub, *C.R. Acad. Sci. Paris* **198**, 667 (1934).
70. J.K. Bailey, C.J. Brinker, M.L. Mecartney, *J. Colloid Interface Sci.* **157**, 1 (1993).
71. T. Sugimoto, A. Muramatsu, K. Sakata, D. Shindo, *J. Colloid Interface Sci.* **158**, 420 (1993).
72. E. Narita, H. Takeuchi, N. Horiguchi, T. Okabe, *Bull. Chem. Soc. Jpn* **57**, 1388 (1984).
73. E. Matijevic, *Acc. Chem. Res.* **14**, 22 (1981).
74. J. Th. G. Overbeek, *Adv. Colloid Interface Sci.* **15**, 251 (1982).
75. T. Sugimoto, *Adv. Colloid Interface Sci.* **28**, 65 (1987).
76. E. Matijevic, *Langmuir* **2**, 12 (1986).
77. R.I. Larson, E.F. Fullam, A.D. Lindsay, E. Matijevic, *AIChE J.* **19**, 602 (1973).
78. (a) R. Sapiesko, E. Matijevic, *J. Colloid Interface Sci.* **74**, 405 (1980); (b) E. Matijevic, *Pure and Appl. Chem.* **52**, 1179 (1980).
79. K. Kandori, Y. Kawashima, T. Ishikawa, *J. Colloid Interface Sci.* **152**, 284 (1992).
80. N. Kallay, E. Matijevic, *Langmuir* **1**, 195 (1985).
81. Y. Zhang, N. Kallay, E. Matijevic, *Langmuir* **1**, 201 (1985).
82. M. Andrès Vergès, A. Mifsud, C.J. Serna, *J. Chem. Soc. Faraday Trans.* **86**, 959 (1990).
83. R.W.G. Wyckoff, *Crystal Structures*, Vol. 3, 2nd ed., Interscience Pub., New York (1965).
84. C. Kittel, *Introduction of Solid State Physics*, J. Wiley & Sons, New York (1966).
85. C.F. Baes, R.E. Mesmer, *The Hydrolysis of Cations*, J. Wiley & Sons, New York (1976).
86. E. Tronc, P. Belleville, J.P. Jolivet, J. Livage, *Langmuir* **8**, 313 (1992).
87. J.P. Jolivet, P. Belleville, E. Tronc, J. Livage, *Clays Clay Mineral.* **40**, 531 (1992).
88. T. Sugimoto, E. Matijevic, *J. Colloid Interface Sci.* **74**, 227 (1980).
89. Y. Tamaura, P.V. Buduan, T. Katsura, *J. Chem. Dalton Trans.* 1807 (1981).
90. Y. Tamaura, K. Ito, T. Katsura, *J. Chem. Dalton Trans.* 189 (1983).
91. E. Tronc, J.P. Jolivet, J. Lefebvre, R. Massart, *J. Chem. Soc. Faraday Trans I* **80**, 2619 (1984).
92. P. Belleville, J.P. Jolivet, E. Tronc, J. Livage, *J. Colloid Interface Sci.* **150**, 453 (1992).
93. M. Ozaki, E. Matijevic, *J. Colloid Interface Sci.* **107**, 199 (1985).
94. R.M. Cornell, *Clay Miner.* **23**, 329 (1988).
95. R.M. Cornell, R. Giovanoli, *Polyhedron* **7**, 385 (1988).
96. R.M. Cornell, R. Giovanoli, W. Schneider, *J. Chem. Tech. Biotechnol.* **53**, 73 (1992).
97. Z.X. Zang, C.M. Sorensen, K.J. Klabunde, G.C. Hadjipanayis, *J. Colloid Interface Sci.* **146**, 38 (1991).
98. Y. Tamaura, S. Mechaimonchit, T. Katsura, *J. Inorg. Nucl. Chem.* **43**, 671 (1981).
99. K. Kaneko, T. Katsura, *Bull. Chem. Soc. Jpn.* **52**, 747 (1979).

100. K. Kaneko, K. Takei, Y. Tamaura, T. Kanzaki, T. Katsura, *Bull. Chem. Soc. Jpn.* **52**, 1080 (1979).
101. T. Kanzaki, J. Nakajima, Y. Tamaura, T. Katsura, *Bull. Chem. Soc. Jpn.* **54**, 135 (1981).
102. Y. Tamaura, T. Katsura, *J.C.S. Dalton 825 (1980).*
103. Y. Tamaura, U. Rasyid, T. Katsura, *J.C.S. Dalton* 2125 (1980).
104. E. Matijevic, C.M. Simpson, N. Amin, S. Arajs, *Colloids and Surf.* **21**, 101 (1986).
105. B. Gillot, J.F. Ferriot, G. Dupré, A. Rousset, *Mat. Res. Bull.* **11**, 843 (1976).
106. F. Chassagneux, A. Rousset, *J. Solid State Chem.* **16**, 161 (1976).
107. A. Rousset, F. Chassagneux, B. Gillot, *Ann. Chim. Fr.* **8**, 227 (1983).
108. G. Albanese, *J. Phys.* **38**, C1 85 (1977).
109. J.C. Bernier, P. Poix, *Ann. Chim. Fr.* **4**, 460 (1979).
110. J.C. Bernier, P. Poix, M. Najmi, in *Ultrastructure Processing of Advanced Ceramics*, J.D. Mackenzie, D.R. Ulrich Eds, J. Wiley & Sons, New York (1988), p. 557.
111. J.C. Bernier, *Powder Metall. Int.* **18**, 164 (1986).
112. J. Ravez, *L'Actualité Chimique* **11**, 3 (1986).
113. D.R. Uhlman, J.M. Boulton, G. Teowee, L. Weisenbach, B.J.J. Zelinski, *Sol-Gel Optics I*, Proc. SPIE Vol. 1328, (1990), p. 270.
114. T.R. Shrout, A. Halliyal, *Am. Ceram. Soc. Bull.* 66, 704 (1987).
115. B.J. Mulder, *Ceram. Bull.* **49**, 990 (1970).
116. D. Hennings, W. Mayr, *J. Solid State Chem.* **26**, 329 (1978).
117. G. Pfaff, *J. Europ. Ceram. Soc.* **8**, 35 (1991).
118. R. Marchand, L. Brohan, M. Tournoux, *Mat. Res. Bull.* 15, 1129 (1980).
119. W. Hertl, *J. Am. Ceram. Soc.* **71**, 879 (1988).
120. K.S. Mazdiyasni, R.T. Dolloff, J.S. Smith II, *J. Am. Ceram. Soc.* **52**, 523 (1969).
121. F. Chaput, J.P. Boilot, *J. Mater. Sci. Lett.* **6**, 1110 (1987).
122. S.P. Faure, P. Barboux, P. Gaucher, J.P. Ganne, *Ferroelectrics* **128**, 19 (1992).
123. P. Griesmar, G. Papin, C. Sanchez, J. Livage, *J. Mater. Sci. Lett.* **9**, 1288 (1990).
124. J.M. Tarascon, P. Barboux, G.W. Hull, R. Ramesh, L.H. Greene, M. Giroud, M.S. Hedge, W.R. Mc Kinnon, *Phys. Rev.* B39, 4316 (1989).
125. P. Barboux, I. Campion, L. Mazerolles, D. Michel, J. Livage, *Ceram. Trans.*, Vol 18, *Superconductivity and Ceramic Superconductors II*, The American Ceramic Society, New York (1991), p. 215.
126. K.S. Mazdiyasni, C.T. Lynch, J.S. Smith, *Inorg. Chem.* **5**, 342 (1966).
127. H.H. Wang, K.D. Carlson, U. Geiser, R.J. Thorn, H.I. Kao, M.A. Beno, M.R. Monaghan, T.J. Allen, R.B. Proksch, D.L. Stupka, J.M. Williams, B.K. Flandermeyer, R.B. Poeppel, *Inorg. Chem.* **26**, 1474 (1987).
128. T. Itoh, H. Uchikawa, *J. Cryst. Growth* **87**, 157 (1987).
129. A. Manthiram, J.B. Goodenough, *Nature* **329**, 701 (1987).
130. M.E. Gross, M. Hong, S.H. Liou, P.K. Gallagher, J. Kwo, *Appl. Phys. Lett.* **52**, 160 (1988).
131. H. Nasu, H. Myoren, Y. Ibara, S. Makida, Y. Nishiyama, T. Kato, T. Imura, Y. Osaka, *Jap. J. Appl. Phys.* **4**, 216 (1988).
132. A.H. Hamdi, J.V. Mantese, A.L. Micheli, R.C.O. Laugal, D.F. Dungan, Z.H. Zhang, K.R. Padmanabhan, *Appl. Phys. Lett.* **51**, 2152 (1987).
133. Y.M. Chiang, D.A. Rudman, D.K. Leung, J.A.S. Ikeda, A. Roshko, B.D. Fabes, *Physica* C152, 77 (1988).
134. P. Barboux, J.M. Tarascon, L.H. Greene, G.W. Hull, B.G. Bagley, *J. Appl. Phys.* **63**, 2725 (1988).
135. P. Barboux, J.M. Tarascon, F. Shokoohi, B.J. Wilkens, C.L. Schwartz, *J. Appl. Phys.* **64**, 6382 (1988).
136. A. Gupta, G. Koren, E.A. Giess, N.R. Moore, E.J.M. O'Sullivan, E.I. Cooper, *Appl. Phys. Lett.* **52**, 163 (1988).

137. A. Gupta, G. Koren, *Appl. Phys. Lett.* 52, 665 (1988).
138. R.L. Henry, H. Lessof, E.M. Swiggard, S.B. Quadri, *J. Cryst. Growth* 85, 615 (1987).
139. M. Kawai, T. Kawai, H. Masuhira, M. Takahasi, *Jap. J. Appl. Phys.* 26, L 1740 (1987).
140. E.I. Cooper, E.A. Giess, A. Gupta, *Mat. Lett.* 7, 5 (1988).
141. P. Barboux, I. Campion, S. Daghish, J. Livage, J.L. Genicon, A. Sulpice, R. Tournier, *J. Non Cryst. Solids* 147–148, 704 (1992).

DropBooks

Appendix to Part I

Partial Charges Model and Applications to Aqueous Chemistry

The acid–base properties of an aquo complex stem from the polarization of the coordination water (see Chapter 1). The reactivity of complexes in nucleophilic reactions such as ligand exchange and condensation is mostly controlled by the polarity of the bonds (see Chapter 2). In order to predict the likelihood of a reaction, it is useful to know the electronic density distribution in the chemical entity, which is given by the 'partial' charges on individual atoms.

Many attempts have been made at developing such a model, but no method is completely satisfactory because it is impossible to measure the charge on an atom. The isomeric displacement measured in Mössbauer spectroscopy depends on the environment of the atom, but only the density of 's' electrons is involved since they are the only ones to have a probability of presence on the nucleus. Although some interesting correlations have been made between the isomeric displacement of an atom and its effective charge calculated from [1], Mössbauer spectroscopy does not allow a calculation of absolute charges on atoms. The same is true of NMR. The chemical shift measured depends on all the magnetic fields imposed on the nucleus, not only on those of electrons near the nucleus involved in the bonding. XPS or ESCA do not give a direct measurement of the atomic charges either.

Ab initio calculations of molecular wave functions are possible only for small, simple molecules. The relationship between the dipolar moment and the ionic character of the bonds seems like a direct method to estimate the charge distribution on atoms, using bond length and geometry. Things are somewhat more complicated, however, since the ionic moments of the bonds are only one of the contributions of the molecular dipole moment. Differences in atom size and dipole moments of free pairs must also be taken into account.

The partial charges model [2], based on Sanderson's principle [3] of electronegativity equalization in a compound, does not allow an absolutely accurate estimation of the charges, and in this respect has limitations similar to other methods. However, it is interesting to study its application to some problems of

reactivity in solution, such as the behavior of an element during hydrolysis, condensation or complexation. The model is quite simple and in some cases can bypass the absence of thermodynamic data. This appendix will describe the model and its use, and will point out some of its limitations.

A.1 IONOCOVALENT BONDING, PARTIAL CHARGES AND ELECTRONEGATIVITY

A.1.1 IONOCOVALENT BONDING AND PARTIAL CHARGES

A chemical bond between atoms may be described by molecular orbitals characterizing the situation of bonding electrons in the field created by the nucleus. In the simplest case of a molecule A–B, a bonding molecular orbital of the form

$$\Psi = a\psi_A + b\psi_B$$

describes the contribution of atomic orbitals ψ_A and ψ_B using the coefficients a and b. The charge density between nuclei resulting from the formation of the bond is given by

$$\Psi^2 = a^2\psi_A^2 + b^2\psi_B^2 + 2ab\psi_A\psi_B$$

For a molecular orbital describing an electron, factors a^2 and b^2 represent the net electron population on atoms A and B. The overlap population is given by the $2abS_{AB}$ term (S_{AB} is the overlap integral). Distributing the overlap population equally over the atoms, and assigning each part to the atoms, the global atomic populations are obtained (Mulliken populations [4]). Since atoms A and B have different abilities to attract electrons, the charge distribution between nuclei is asymetrical.

For example, formation of the HF molecule involves the 2s and 2p atomic orbitals of fluorine and the 1s of hydrogen. For isolated atoms, the population of these orbitals is, respectively, $2s^2$, $2p^5$ and $1s^1$. When the atoms are at equilibrium distance in the molecule (0.92 Å), the electronic population of fluorine is 7.46 electrons in the 2s and 2p orbitals, and hydrogen carries 0.54 electrons in the 1s orbital [5]. The transfer of 0.46 electrons from hydrogen towards fluorine indicates the ionic character of the bond. The partial charge on each atom in the combination represents the difference between the electronic populations in the isolated state and in the combined state. Thus, for hydrogen $\delta(H) = 1 - 0.54 = +0.46$; for fluorine, $\delta(F) = 7 - 7.46 = -0.46$.

In more complex structures such as the $[MnO_4]^-$ ion, the molecular orbital diagram (Figure 4.11) involves the 3d, 4s, 4p orbitals of the metal. The electron population of manganese is $3d^{5.818}\ 4s^{0.182}\ 4p^{0.344}$, or 6.344 electrons on the metal [6–8]. Compared with the configuration of the isolated atom $3d^5 4s^2$, the partial charge on the metal is $7 - 6.344 = +0.656$. The charge on each oxygen atom is therefore $(-0.656 - 1)/4 = -0.414$.

The formal charge, which corresponds to the degree of oxidation of an atom, is different from its effective or 'partial' charge in a combination—unless that combination is purely ionic. The formal charge represents the charge of the isolated atom and allows determination of the stoichiometry of a combination, assuming a -2 charge for oxygen and a $+1$ charge for hydrogen.

The partial charge of an atom in an ionocovalent compound represents the charge of the atom in its environment, taking into account the formal charge and the charge shared with the ligands (the Mulliken population). This charge is assumed to be localized on the atom, but in fact the electrons 'given' by the ligands have only a very small probability of presence on the atom considered. This assumes that no oxido-reduction takes place to decrease the partial charge of manganese in $[MnO_4]^-$ from $+7$ to $+0.656$. Similarly, in the octahedral complex $[Ni(OH_2)_6]^{2+}$, magnetic measurements show that the ion is in d^8 (t_{2g}^6, e_g^2) with a magnetic moment due to two single electrons. The electronic spectrum of the complex corresponds to transitions between the terms of the d^8 configuration in O_h symmetry. The partial covalent nature of the bond is reflected in the fact that there are different parameters for Ni^{2+} and the free ion, such as the spin–orbit coupling constant and the decrease in the interelectronic repulsion parameter (Raccah's parameter).

The ionicity of the bond is characterized by the coefficients a and b of the molecular wave functions and is directly related to the energy of valence orbitals and to the electronegativity of neutral atoms χ_A and χ_B. During the formation of the bond, the most electronegative atom attracts the bonding electrons and acquires a negative partial charge, and the least electronegative atom acquires a positive partial charge. For atoms with a large electronegativity difference, the limiting case $a = 0$ and $b = 1$ corresponds to an overlap density of zero. The molecular orbital degenerates into two atomic orbitals, one of which captures both bonding electrons, thereby forming the ionic bond. The charges are $+1$(A) and -1(B).

A.1.2 ELECTRONEGATIVITY

Introduced by Pauling [9], electronegativity is a measure of the ability of an atom in a molecule to attract electrons. There is much confusion surrounding this very flexible concept, as reflected in the many different scales proposed to characterize the same parameter. In fact, there are several definitions of electronegativity, and they do not necessarily cover similar concepts.

The total energy E of an isolated atom as a function of the number of electrons N around a nucleus of atomic number Z is shown in Figure A.1. Assuming that the variation is continuous and differentiable, Parr *et al.* [10,11] have shown that the slope $\partial E/\partial N$ is exactly equal to the chemical potential of the electrons:

$$-\mu_e = -(\partial E/\partial N)_\nu \qquad \text{(A.1)}$$

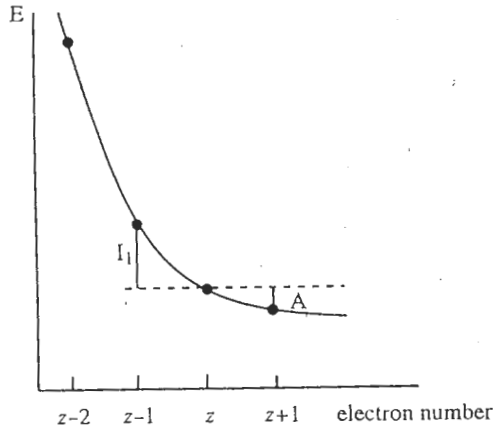

Figure A.1 Total energy of an atom (atomic number Z) as a function of the number of electrons. From [12]

Development of the expression of the energy gives [12]

$$E(N) \approx E(Z) + (N - Z)(\partial E/\partial N)_\nu + [(N - Z)^2/2!](\partial^2 E/\partial N^2)_\nu$$

The first ionization potential I and the elect affinity A can be expressed as

$$I \approx E(Z - 1) - E(Z) = -(\partial E/\partial N)_\nu + (1/2)(\partial^2 E/\partial N^2)_\nu$$

$$A \approx E(Z) - E(Z + 1) = -(\partial E/\partial N)_\nu - (1/2)(\partial^2 E/\partial N^2)_\nu$$

and hence:

$$(1/2)(I + A) \approx -(\partial E/\partial N)_\nu = -\mu_e = \chi_a \qquad \text{(A.2)}$$

In fact, Iczkowski and Margrave [13] were the first to propose that $(\partial E/\partial N) \approx (I + A)/2$ be called 'electronegativity'.

This definition introduces electronegativity as an electronic chemical potential similar to a thermodynamic chemical potential: in any system of atoms in a non-equilibrium state, there must be a flux of electronic density from the regions of high potential to the regions of lower potential.

This gives an absolute estimation of electronegativity since ionization potential and electron affinity both refer to the *fundamental state* of the atom [11].

The hardness of an atom as introduced by Pearson [11,14,15] is

$$\eta_a = (1/2)(\partial\mu/\partial N)_\nu = (1/2)(\partial^2 E/\partial N^2)_\nu = (1/2)(I - A) \qquad \text{(A.3)}$$

The hardness of an atom is directly related to its size. Here E is proportional to q^2/r (q is the electric charge and r is the distance). The hardness $\eta_a = (\partial^2 E/\partial N^2)$ is therefore proportional to r^{-1}. Hence, as a system is increasingly confined in space, its hardness increases and its polarizability decreases. In fact, hardness reflects the

resistance of the electronic chemical potential to a change in the number of electrons around the atom. It is expressed in eV, as is electronegativity. The converse of hardness is the softness $\sigma = 1/\eta$ [11].

According to the definition in equation (A.2), the absolute electronegativity of an atom is a function of its charge:

$$\chi_a = -\mu_e = -\mu_e^0 + \eta\Delta N \qquad \text{(A.4)}$$

$-\mu_e^0 (= \chi_a^0)$ relates to the neutral atom (standard state). The $\eta\Delta N$ term reflects the deviation from the standard state owing to the charge variation ΔN.

Strictly speaking, equation (A.4) can only be applied to isolated atoms. As atoms come closer together, they are subjected to an external potential due to the proximity of other nuclei and electrons. The absolute electronegativity only indicates the direction of the electron flux between two atoms, and as such reflects the chemical reactivity of *free atoms* [11]. This discussion can be applied to atoms as well as molecules.

The concept of absolute electronegativity is compatible with the MO model. Indeed, the first ionization potential of a diamagnetic molecule is the energy of the highest occupied molecular orbital (HOMO). Electron affinity is the energy of the lowest unoccupied molecular orbital (LUMO) [11]. The electronic chemical potential $\mu_\epsilon = -\chi_a$ is the average energy of these orbitals, and the hardness η is equal to half the band gap. The donor or acceptor character of a ligand on a metal or a metallic ion may therefore be indicated by comparing their respective electronegativities.

As defined by Mulliken [16], electronegativity is written using an expression similar to the absolute electronegativity:

$$\chi_M = (1/2)(I_v + A_v)$$

However, it is not the same thing, since Mulliken's definition involves the potentials I_v and A_v in the *valence state of the atom*. The valence state describes an isolated atom as if it existed in combination with other atoms [17]. Therefore, this is not the fundamental state but a statistical average of stationary states chosen to represent, *in the isolated atom*, the electronic interactions taking place when the atom is involved in a combination. The calculation of excitation energies [18] using the method of linear combination of AOs (LCAO) involves the energy contribution of spectroscopy terms for various electron configurations. The Mulliken electronegativity is an energy expressed in eV.

Electronegativity according to Mulliken is in fact a property of the orbitals. In theory, it is defined only for the bonding orbitals but it is difficult to differentiate between orbitals that are not equivalent. The absolute electronegavity, which is defined as a potential, is a property of the atom.

Many other descriptions of electronegativity have been proposed [12]. Allred and Rochow's definition [19] is based on the electrostatic interaction between electrons and nucleus Z_{eff}/r^2. Z_{eff} is the effective charge on the nucleus calculated

DropBooks

using Slater's rules, and r is the covalent radius as proposed by Pauling. Therefore, the size and shape of the atom are taken into account, and the resulting electronegativity is of the 'Mulliken type'. Gordy [20] considers the electrostatic potential between the nucleus and the outer electrons. The potential is estimated using $(n+1)/r$, where n is the number of electrons on the outer layers and r is the covalent radius.

Sanderson defined a scale of electronegativity [21] based on the assumption that the reactivity of an atom, i.e. its propensity to retain its own electrons and attract others, is linked to its compactness. The most inert elements, the rare gases, are the most compact. Therefore, a chemical combination is the result of the tendency of the atoms to attain the configuration of the most chemically inert elements. Sanderson's electronegativity is characterized by the stability ratio S, which is defined as the ratio of the compactness of an atom to that of the most inert (or compact) element I of its period—the rare gas: $S = D/D_i$, with $D = Z/V = 3Z/4\pi r^3$. Here Z is the atomic number of the atom and r is the covalent radius. Sanderson's electronegativity is a dimensionless number.

The Mulliken, Allred–Richow, Gordy and Sanderson electronegativity scales are all different but they all characterize an *atom in a combination*, and hence it is possible to convert one scale into another. The absolute electronegativity characterizes isolated atoms and their ability to react (electronic chemical potential). It does not take into account the changes in size and shape of the electron density and external potential to which electrons are subjected when the atoms combine.

Pauling's electronegativity is a different concept based on the idea that, in a heteronuclear molecule, polar bonds are stronger than purely covalent bonds. Pauling's electronegativity is a measure of the ionic resonance energy [9].

Quantum mechanics tells us that the energy of a molecule is intermediate between the energies of the limit structures liable to represent the real structure. A molecule containing a single, partially ionic bond should be more stable than the normal covalent structure without any ionic character. Assuming that the energy of a purely covalent A–B bond is approximately equal to the average of the energies of the A–A and B–B bonds, Pauling relates the energy gain to the the concept of electronegativity [9,22], and defines empirically the electronegativity difference between both atoms as the square root of the difference between the energy of the ionocovalent bond (experimental) and that of the purely covalent bond [22]:

$$\chi_A^P - \chi_B^P = [\Delta H_{AB} - (1/2)(\Delta H_{AA} + \Delta H_{BB})]^{1/2}$$

or

$$\chi_A^P - \chi_B^P = [\Delta H_{AB} - (\Delta H_{AA} \times \Delta H_{BB})^{1/2}]^{1/2}$$

For Pauling, electronegativity is a constant of the atom, irrespective of the combination in which it is involved. Pauling's electronegativities, which are obtained from thermochemical data, include the average structure effects of the atom in the combination. They have the dimension of a square root of energy. Pauling stressed

this peculiarity much later [23], pointing to the fact that if the energy of a bond A–B is developed into a Taylor series of the term $(\chi_A^P - \chi_B^P)$, the linear term is zero and the first significant term is $(\chi_A^P - \chi_B^P)^2$. This stems from the fact that the polarity of the bond should be independent of the sign of the difference $\chi_A^P - \chi_B^P$, which means that the polarity remains unchanged whether A is more electronegative than B or B is more electronegative than A. The first term in $\partial E/\partial\chi$ must therefore be zero.

Mulliken's electronegativity scale can be converted into Pauling's using the following relationship [24]:

$$\chi_M = (\chi^P/0.335) + 0.615$$

This linear combination between two quantities of different dimensions stems from uncertainties in the calculation of electronic affinities. In fact, the exact calculation of the valence states allows a precise evaluation of the ionization potential, electronic affinity and hydridation s in the valence state, leading to [18]

$$\chi^P = 1.35\chi_M^{1/2} - 1.37$$

The relationship between the Allred–Rochow scale and Pauling's scale is

$$\chi^P = (0.359Z_{eff}/r^2) + 0.744$$

A.2 PARTIAL CHARGES MODEL

Since electronegativity, defined as a potential, is a function of the charge δ [equation (A.4)], the model is used to determine this function and assumes that, in any atomic combination, the electronegativity of each atom is adjusted through variation of the charge.

A.2.1 DEPENDENCE OF ELECTRONEGATIVITY ON THE CHARGE

Let us consider neutral atoms in a combination. The absolute terms χ_a and η_a of the free atoms are subjected to a perturbation $\Delta\chi$ and $\Delta\eta$ owing to atomic changes in size and shape because of the covalence effect. The local electronic potential on each neutral atom i is $(\chi_{ai} + \Delta\chi)$.

Because of electron transfers due to the formation of a bond, partial charges on the atoms create an electrostatic potential adding itself to the local electronic potential. The electrostatic potential consists of a term $(\eta_{ai} + \Delta\eta)\delta_i$ resulting from the charge δ_i on atom i and a term $\Sigma(\delta_j/R_{ij})$ due to charges δ_j on neighboring atoms j at distances R_{ij}. The electronegativity of the combined atoms [25]

$$\chi_i = \chi_{ai} + \Delta\chi + (\eta_{ai} + \Delta\eta)\delta_i + \sum_{j\neq i, j=1}^{n} (\delta_j/R_{ij}) \qquad (A.5)$$

This expression requires knowledge of the perturbations to which the electronegativities and hardnesses are subjected in the combination. Since $\Delta\chi$ and $\Delta\eta$ are unknown, we write

$$\chi^* = \chi_a + \Delta\chi, \qquad \eta^* = \eta_a + \Delta\eta$$

In these expressions, χ^* are Mulliken-type electronegativities which consider an average environment for the atoms. Mulliken electronegativities require knowledge of the valence states of each atom and are difficult to use. The Pauling scale is inadequate because it requires knowledge of bond energies easily determined only for small elements forming small, simple molecules. Allred and Rochow's electronegativity will be used throughout the following discussion because it is easily calculated for any element.

Hardness and electronegativity are related. Since η is proportional to the reciprocal of a distance, choosing the Allred–Rochow scale ($\chi \propto Z_{eff}/r^2$) leads to the following expression [2]:

$$\eta^* = k\sqrt{\chi_i^*} \tag{A.6}$$

where k is a constant.

A.2.2 ELECTRONEGATIVITY EQUALIZATION PRINCIPLE

When two atoms A and B of different electronegativities form a bond, an electron transfer occurs, for example from A to B. The more electronegative B atom acquires a negative charge. Its electronegativity decreases. The less electronegative atom A acquires a positive partial charge. Its electronegativity increases. The electronegativities of each atom converge towards an average value χ indicating that equilibrium is attained and electron transfers are completed. This is known as the electronegativity equalization principle postulated by Sanderson [3].

Since electronegativity is defined as a potential, χ equalization is equivalent to equalization of the chemical potentials ($\mu = \partial G/\partial n$) related to transfer of matter. The direction of electron transfers is governed by the relative values of electronegativities. The intensity of these transfers is related to the hardness of the atoms involved.

The principle may be generalized to complex atomic structures and the many electron transfers involved stop when each atom in the combination has attained a common average electronegativity χ that is also the electronegativity of the group. Since the electronegativities of individual atoms converge towards an average value χ, which is a function of their partial charges, knowing this average value would allow, in principle, calculation of the partial charges.

A.2.3 CALCULATION OF THE AVERAGE ELECTRONEGATIVITY

In a first approximation, the perturbation induced on atom i by neighboring atoms is neglected compared with the perturbation caused by the charge δ_i on atom i. The

electronegativity of atom i in any combination can therefore be written [2] as

$$\chi_i = \chi_i^* + \eta_i^*\delta_i \qquad \text{with} \quad \eta_i^* = k\sqrt{\chi_i^*} \tag{A.7}$$

Calibration of the constant k is done using the charges in NaF [$\delta(Na) = -\delta(F) = 0.75$] as proposed by Sanderson [26]. Using the Allred–Rochow scale, $k = 1.36$ [1].

At equilibrium, in the combination, the equalization principle gives

$$\chi_i = \chi \qquad \text{or} \quad \chi_i^* + \eta_i^*\delta_i = \chi$$

and

$$\delta_i = \frac{\chi - \chi_i^*}{\eta_i^*} \tag{A.8}$$

or

$$\delta_i = \sigma_i^*(\chi - \chi_i^*) \tag{A.9}$$

if softness (the reciprocal of hardness) $\sigma_i^* = 1/\eta_i^*$ is used.

Charge conservation in the combination imposes

$$\Sigma_i\delta_i = z$$

and finally

$$\chi = \frac{\Sigma_i\sqrt{\chi_i^*} + 1.36z}{\Sigma_i(1/\sqrt{\chi_i^*})} \tag{A.10}$$

or

$$\chi = \frac{\Sigma_i\sigma_i^*\chi_i^* + z}{\Sigma_i\sigma_i^*} \tag{A.11}$$

χ may therefore be calculated for any atomic combination, from the composition, the charge z of the group and the electronegativity of each atom (Table A.1). It is now very easy to calculate the partial charges. Several calculations have been made in Part I.

A.2.4 APPROXIMATIONS USED IN THE MODEL

For χ_i to vary linearly with the charge δ_i according to equation (A.7) implies that the chemical composition of the structure is solely responsible for the charge distribution. This means that the model is not able to differentiate between structural isomers, which is a considerable limitation.

In the most rigorous relationship [(A.5)], which relates the electronegativity to the charge, the structure is explicitly taken into account in the sum since it involves the perturbation to which atom i is subjected owing to other charge-bearing atoms

DropBooks

Table A.1 Allred–Rochow electronegativities χ^* compiled from References [27] to [29]

H 2.10																																	He 3.20
Li 0.97	Be 1.57															B 2.02	C 2.50	N 3.07	O 3.50	F 4.10	Ne 5.10
Na 1.01	Mg 1.29															Al 1.47	Si 1.74	P 2.11	S 2.48	Cl 2.83	Ar 5.10
K 0.91	Ca 1.04	Sc 1.23	Ti 1.32	V 1.56	Cr 1.59	Mn 1.63	Fe 1.72	Co 1.75	Ni 1.80	Cu 1.75	Zn 1.66	Ga 1.82	Ge 2.00	As 2.20	Se 2.50	Br 2.69	Kr 3.10
Rb 0.89	Sr 0.99	Y 1.19	Zr 1.29	Nb 1.45	Mo 1.56	Tc 1.67	Ru 1.78	Rh 1.84	Pd 1.85	Ag 1.68	Cd 1.60	In 1.49	Sn 1.89	Sb 1.98	Te 2.15	I 2.33	Xe 2.60
Cs 0.87	Ba 0.89	*	Hf 1.36	Ta 1.50	W 1.59	Re 1.88	Os 1.99	Ir 2.05	Pt 2.00	Au 2.02	Hg 1.80	Tl 1.60	Pb 1.92	Bi 2.03	Po 2.12	At 2.28	Rn 2.30
Fr 0.86	Ra 0.95	**															

* La 1.18	Ce 1.17	Pr 1.18	Nd 1.19	Pm 1.20	Sm 1.20	Eu 1.13	Gd 1.27	Tb 1.24	Dy 1.26	Ho 1.28	Er 1.30	Tm 1.30	Yb 1.24	Lu 1.36
** Ac 1.12	Th 1.24	Pa 1.22	U 1.24	Np 1.22	Pu 1.24	Am 1.25	Cm 1.20	Bk 1.20	Cf 1.20	Es 1.20	Fm 1.20	Md 1.20	No 1.20	Lw 1.20

(δ_j) at distances R_{ij}. Calculation of the sum requires precise knowledge of the structure and results in a set of linear equations. There is a structure (or geometry)-based version of the model based on the above-mentioned calculation of the average electronegativity [30]. This calculation will not be described in detail here, even if some of its results are discussed.

In fact, in most cases, the structure of the combination is unknown, and the simplified approach assumes $\Sigma\delta_j/R_{ij} \ll \chi_i^*$, where χ^* is a Mulliken-type electronegativity. Average structural and environmental effects are taken into consideration in this term, but the results must be analyzed with caution if there are structural peculiarities. This is particularly true with π overlaps. Contributions from π and σ bonds are *a priori* taken into account simultaneously and indiscriminately in the charge calculation, and they need not be separated when π electron delocalization is present, since the bond lengths are the same. However, localized π bonds are shorter than σ bonds and it is no longer possible to obtain a correct charge distribution. Similar difficulties are encountered for atoms of identical chemical nature which are treated similarly irrespective of their formal charge or the type of atoms to which they bond.

It is also very clear that the charges obtained depend on the hardness η_i^* and the constant k. Therefore, only *relative charges* are obtained, which depend on the calibration of constant k. This calibration was obtained without taking geometric factors into account, and no geometric factor was used in the calculation of the average electronegativity either. This gross approximation must not be ignored during analysis of the charge distribution in any entity.

It must be stressed that the model does not allow for any distinction between isomers, and therefore it must not be used to identify any property related to the structure of the combination.

Although it is simple in its approach, the model is nonetheless an interesting guide for the study of reactivity in solution, and more specifically for the understanding of hydrolysis and condensation reactions.

Calculations of charge distributions usually show that, independently of the formal charge of the cation, the partial charges of cations and anions are always smaller or close to +1 and −1 when calculated with the constants of the model. Although the model can only provide for a relative idea of the charge distribution, it does appear that a bond polarity higher than one, corresponding to the departure of one electron, cannot be obtained in solution. The analysis of electron population in atomic orbitals participating in the molecular orbitals confirms these results. It also appears that the same is true in the solid state, as can be seen in electron density maps obtained by X-ray and neutron diffraction on about one hundred compounds at the present time. If the bond is very polar, it is usually destroyed by ionic dissociation (salt dissolution). Charge separation higher than one electron must cause a redox transfer. The phenomenon is associated with fast reorganiztion of the coordination sphere of the species involved in order to minimize subsequent charge separation. In the present state of the model, it is not possible to account for such

transfers. This would require taking into account structural changes in the entities involved in the activated complex [31].

A.2.5 GUIDELINES FOR THE USE OF THE MODEL

The average electronegativity of a chemical structure controls the distribution of partial charges on the constituents of this entity. Calculations show that the evaluation of partial charges is easy and fast.

The likelihood of a reaction (hydrolysis, condensation, complexation, etc.) may be predicted using very simple electrostatic criteria. Chemical equilibrium between two reactants corresponds to equalization of the average electronegativities of the products, the equalization resulting from the compositional change of the reactants.

Considering an atom or a group X in the structure, and comparing the partial charge $\delta(X)$ of the group with the formal charge p of the same group in solution, a critical state of the bond between X and the rest of the structure is attained when $\delta(X) = p$ or 0.

It is also possible to impose an average value of the electronegativity and look for a chemical composition of a particular species that will reach the imposed value. It is then possible to impose a criterion or a limiting condition for the chemical process to take place. The criteria are expressed as critical electronegativities or critical compositions calculated from the equation of charge conservation in which the constraint $\delta(X) = p$ or 0 is introduced. The criteria may also involve the stoichiometry of the species considered.

From a purely practical standpoint, calculation of the average electronegativity of any entity may be done using either (A.10) or (A.11). These relationships are easily programmable into a pocket calculator. Equation (A.11) is particularly interesting because it involves softness values, which are additive in a group of atoms. [Softness is the reciprocal of hardness, equation (A.9).] Therefore, the average electronegativity of a species

$$[M(OH)_h(OH_2)_{N-h}]^{(z-h)+}$$

according to (A.10) is

$$\chi = \frac{\sqrt{\chi(M)} + N\sqrt{\chi(O)} + (2N-h)\sqrt{\chi(H)} + 1.36(z-h)}{1/\sqrt{\chi(M)} + N/\sqrt{\chi(O)} + (2N-1)/\sqrt{\chi(H)}}$$

or according to (A.11) is

$$\chi = \frac{\sigma(M)\chi(M) + N\sigma(O)\chi(O) + (2N-h)\sigma(H)\chi(H) + 1.36(z-h)}{\sigma(M) + N\sigma(O) + (2N-1)\sigma(H)}$$

or, again, using

$$[M(OH)_h(OH_2)_{N-h}^{(z-h)+} = [M(OH_2)_N]^{z+} - hH^+$$

is

$$\chi = \frac{\sigma[M(OH_2)^{z+}]\chi[M(OH_2)^{z+}] - h\sigma[H^+]\chi[H^+]}{\sigma[M(OH_2)^{z+}] - h\sigma[H^+]} \qquad (A.12)$$

This is a considerable simplification of some expressions of the average electronegativity of complex groups, which allows, once and for all, certain calculations to be made for a given system. This type of calculation is used to describe complexation.

A.3 APPLICATION OF THE MODEL TO THE ACID–BASE PROPERTIES OF CATIONS

The acid–base properties of a solvated $[M(OH_2)_N]^{z+}$ cation in solution are reflected in the overall equilibrium

$$[M(OH_2)_N]^{z+} + H_2O \Longleftrightarrow [M(OH)_h(OH_2)_N]^{(z-h)+} + hH^+_{solvated}$$

Can we predict, under standard conditions (1 mol l^{-1} concentration and 298 K, for example), the hydrolysis ratio of the cation as a function of the acidity of the medium?

From the angle of the partial charge model, equilibrium corresponds to equalization of the average electronegativities of the reaction products. We can assume that proton exchange takes place between the solution and the cation until the average electronegativity of the hydrolyzed species, χ_h, is equal to that of the solution, χ_s. The equilibrium condition will be obtained at the value of h for which χ_h is equal to χ_s. Therefore, it is necessary to determine the average electronegativity of the medium (solvent) as a function of acidity, which means relating χ_s to the pH. Indeed, any change in pH of the solution displaces the hydrolysis equilibrium and causes a change in the average electronegativity of the medium.

Electronegativities are microscopic potentials that do not depend on macroscopic parameters such as concentration, pH or temperature. Therefore, it is necessary to establish a relationship between both sets of parameters. This can be done by considering the structure of the solvated proton (see Chapter 1, Section 1.1.2) in the 'standard' conditions as defined above.

A.3.1 pH–ELECTRONEGATIVITY RELATIONSHIP

The solvated proton in aqueous solution corresponds to the 'molecular' entity $[H_9O_4]^+$, in which the proton is coordinated to four water molecules through strong hydrogen bonds with energies of about 200 kJ mol^{-1} (see Chapter 1, Section 1.1.2). This entity is itself solvated in solution by other water molecules forming weaker hydrogen bonds with energies of about 20–30 kJ mol^{-1}.

Delocalization of the proton in water occurs through the disordered network of hydrogen bonds in the liquid. Owing to their quantum nature, protons cannot be

DropBooks

distinguished from the hydrogen atoms of the water molecules. Therefore, solvated species $[H_9O_4]^+ \cdot nH_2O$ share their protons with liquid water. In the same way that electronegativities become equal when atoms share electrons, equalization of the average electronegativities of solvated protons and water is supposed to take place though rapid proton exchange. Therefore, the average electronegativity of an aqueous solution changes with the pH, which represents the proton concentration. We can also consider that it represents the number of water molecules associated with the proton.

At the macroscopic scale, the chemical potential of the proton in solution is

$$\mu_H = \mu_H^0 + RT \ln a_H = \mu_H^0 - 0.06\,\mathrm{pH} \qquad (A.13)$$

where a_H is the activity of the proton, and $RT \ln = 0.06 \log$ at 298 K.

At the microscopic level, considering that the electronegativity represents the chemical potential of the electrons, $\chi = -\mu_e$, we may write

$$\mu_H = -k\chi_H \qquad \text{and} \qquad \mu_H^0 = -k\chi[H_9O_4]^+$$

choosing the $[H_9O_4]^+$ entity as the state of reference (pH = 0) for the solvated proton. Therefore

$$\chi_H = \chi[H_9O_4]^+ - 0.06k^{-1}\,\mathrm{pH} = \chi_s \qquad \text{with} \qquad \chi[H_9O_4]^+ = 2.621$$

We shall assume that dilution of the proton in solution amounts to delocalizing it over a large number of water molecules. Therefore, at pH = 7, the proton concentration becomes so small that we can consider the entity $[H^+, (H_2O)_n]$ in which n is very large. The value of k, which relates the pH scale to the electronegativity scale, is obtained by considering that, at pH = 7, $\chi_H = \chi_s = \chi[H_2O] = 2.491$. Finally, the following relationship is obtained:

$$\chi_s = 2.621 - 0.02\,\mathrm{pH} \qquad (A.14)$$

Therefore, the electronegativity of an aqueous solution decreases linearly from 2.621 to 2.341 as the pH varies from 0 to 14. It must be noted that the electronegativity of the solution at pH 14 is that of the molecular 'entity' $[H_7O_4]^-$ ($\chi = 2.334$), formed by the hydroxyl ion solvated through very strong hydrogen by three water molecules (cf. Chapter 1, Section 1.1.2). This is in agreement with the consideration that, at pH 7, $\chi_s = \chi[H_2O]$.

In articles preceding publication of this book ([32], for example), the reference for the solvated proton is $[H_5O_2]^+$ ($\chi = 2.732$) and equation (A.14) is $\chi_s = 2.732 - 0.035\,\mathrm{pH}$. This relationship gives similar results, but we believe that equation (A.14) is in better agreement with the structure of the solvated proton.

A.3.2 HYDROLYSIS OF CATIONS

The application of this result to the hydrolysis of a cation in solution

$$[M(OH_2)_N]^{z+} + H_2O \Longleftrightarrow [M(OH)_h(OH_2)_N]^{(z-h)+} + hH^+_{\text{solvated}}$$

is done by writing the equilibrium condition

$$\chi[M(OH)_h(OH_2)_{N-h}^{(z-h)+}] = \chi_s \qquad (A.15)$$

In accordance with the principle of electronegativity equalization, proton exchange between the metal complex and the medium takes place until their average electronegativities become equal.

Writing each expression of χ in (A.15) using (A.10) and (A.14), we easily obtain

$$h = \left[\frac{1}{1 + 0.41\,\mathrm{pH}}\right]\left[(1.36z - N)(0.236 - 0.08\,\mathrm{pH}) - \frac{2.621 - 0.02\,\mathrm{pH} - \chi_M^*}{\sqrt{\chi_M^*}}\right] \qquad (A.16)$$

At pH = 0, the hydrolysis ratio of $M(OH_2)_N^{z+}$ is

$$h = (1.36z - 0.24N) - \frac{2.621 - \chi_M^*}{\sqrt{\chi_M^*}} \qquad (A.17)$$

whereas at pH = 14 it is

$$h = (1.14z + 0.25N') - \frac{0.836(2.341 - \chi_M^*)}{\sqrt{\chi_M^*}} \qquad (A.18)$$

The value of h indicates the number of protons spontaneously released by $[M(OH_2)_N]^{z+}$ in solution. Equations (A.17) and (A.18) show that the acidity of a cation is essentially governed by three parameters: its charge z, its size (through its coordination number N) and its electronegativity. The main factor is the formal charge of the cation z. Size (through the coordination number) and nature (through its electronegativity) are parameters of lesser importance.

If the calculated values of h are negative, the aquo ion does not exhibit any acid character. However, it may be deprotonated by the addition of a base and eventually form a hydroxo complex. If h is greater than $2N$, the element exists in solution only in the aquo form and does not exhibit any basic property.

The calculated values of h need not be integer. If they are not, two species in equilibrium should be considered, and at least one of these should be a hydroxo form. These species correspond to the integer values of h that frame the calculated value. The results (Table 1.7, Chapter 1) are in good agreement with the experiments.

A.3.3 ACID–BASE PROPERTIES OF ELEMENTS IN AQUEOUS SOLUTION

One may approach the acid–base behavior of elements in water from a different angle.

Let us consider an element M^{z+} that may exist as the zero-charge molecular form MO_NH_{2N-z}. This species can have two extremely different behaviors in water:

- It may act as a strong acid:

$$[MO_NH_{2N-z}]_{aq} \longrightarrow [MO_NH_{2N-z-1}]^- + H^+_{aq}$$

- It may act as a strong base:

$$[MO_NH_{2N-z}]_{aq} \longrightarrow [MO_NH_{2N-z+1}]^+ + HO^-_{aq}$$

$$[MO_NH_{2N-z}]_{aq} \longrightarrow [MO_{N-1}H_{2N-z-1}]^+ + HO^-_{aq}$$

(a) Acid Behavior

This would correspond to the exchange of a proton between the zero-charge form and the solvent. The following transition state can therefore be considered

$$[MO_NH_{2N-z-1}]^- \cdots H^+ \cdots OH_2$$

If the charge on oxygen in water $\delta(O_w)$ is smaller (more negative) than that of oxygen in the basic form of the metal complex $\delta(O_{p-})$, $\delta(O_w) < \delta(O_{p-})$, i.e. if the average electronegativity of the basic form is such that $\chi_{p-} > \chi_w$, the proton will tend to be solvated by water. If, on the other hand, $\delta(O_{p-}) < \delta(O_w)$ and hence $\chi_{p-} < \chi_w$, the proton stays in the coordination sphere of the cation and the complex does not have any acid property. The threshold between these two situations is

$$\chi_{p-} = \chi_w = 2.49$$

This situation is reflected in the partial charges [equation (A.6)]

$$\delta(O) = -0.4, \qquad \delta(H) = +0.2, \qquad \delta(M) = \frac{2.49 - \sqrt{\chi^*_M}}{1.36\sqrt{\chi^*_M}}$$

The charge balance for the $MO_NH_{2N-z-1}]^-$ form is

$$\delta(M) + N\delta(O) + (2N - z - 1)\delta(H) = -1$$

From these relationships, a second-degree equation in $\sqrt{\chi}$ is obtained, which, for a given element, depends only on the variable z. It is now easy to calculate the critical electronegativity $\chi_{A,z}$ which gives the limit of the acid behavior of the neutral form of the cation of formal charge z:

$$\sqrt{\chi_{A,z}} = -0.136(z - 4) + \{[0.136(z - 4)]^2 + 2.49\}^{1/2} \qquad (A.19)$$

The variation in $\chi_{A,z}$ as a function of z is shown in Figure 1.8. If χ^*_M of a cation is greater than $\chi_{A,z}$, MO_NH_{2N-z} is a strong acid.

(b) Basic Behavior

There are several ways to consider the basic behavior of a species in solution. In order to establish an appropriate criterion, let us consider the exchange of an hydroxyl ion between the zero-charge species and the solution:

$$[MO_{N-1}H_{2N-z-1}]^+ \cdots OH^- \cdots OH_2$$

If the charge on hydrogen in the acid form of the complex is smaller than that on hydrogen in water $\delta(H_{p+}) > \delta(H_w)$, i.e. if $\chi_{p+} < \chi_w$, the hydroxyl ion will tend to be solvated by water. If, on the contrary, $\delta(H_{p+}) > \delta(H_w)$, or $\chi_{p+} > \chi_w$, the hydroxyl ion is better 'solvated' by the cation and the complex does not exhibit any basic property. Therefore, the criterion for basic behavior is

$$\chi_{p+} = \chi_w = 2.49$$

As seen previously, the values of the corresponding partial charges on oxygen, hydrogen and the metal are introduced in the charge balance of the $[MO_{N-1}H_{2N-z-1}]^+$ form:

$$\delta(M) + (N - 1)\delta(O) + (2N - z - 1)\delta(H) = +1$$

The critical electronegativity $\chi_{B,z}$ can now be calculated (Figure 1.8). It indicates the threshold for the strong basic behavior of the neutral form of a cation of formal charge z:

$$\sqrt{\chi}_{B,z} = -0.136(z + 4) + \{[0.136(z + 4)]^2 + 2.49\}^{1/2} \qquad (A.20)$$

If χ^*_M is smaller than $\chi_{B,z}$, MO_NH_{2N-z} is a strong base. This is the case for the $M(OH)(OH_2)_N$ forms of alkalis, in which χ^*_M is of the order of 0.9, and therefore inferior to $\chi_{B,z} = 1.00$.

A.4 APPLICATION OF THE MODEL TO THE CONDENSATION OF CATIONS IN SOLUTION

The propensity of a metal to form condensed species in solution can be described using electrostatic considerations. We have seen (Section A.3.3) that an element M^{z+} in the zero-charge molecular form MO_NH_{2N-z} can behave as a strong base or a strong acid in water. In either case, the species cannot condense because the hydroxo ligands are not 'stable' in the coordination sphere.

For example, what can be said of $[MnO_3(OH)]^0$? The critical value corresponding to acid behavior is $\chi_{A,7} = 1.459$ [equation (A.19), Figure 1.8). Since the electronegativity of manganese is 1.63, the species is a strong acid, and manganese(VII) exists in solution as $[MnO_4]^-$ at any pH [32].

For manganese(II), $\chi^*_{Mn} = 1.63 < \chi_{A,2} = 3.485$. The species $[Mn(OH)_2(OH_2)_4]^0$ does not exhibit acid character and precipitates as the hydroxide $Mn(OH)_2$ [33].

Hence, the species MO_NH_{2N-z} is able to condense, as long as the hydroxo ligand exhibits a nucleophilic character [$\delta(OH) < 0$] and as long as the cation is sufficiently electrophilic [$\delta(M) \geqslant 0.3$, see Chapter 2]. This amounts to saying that for any element M such as

$$\chi_{B,z} < \chi^*_M < \chi_{A,z}$$

DropBooks

there is a negative charge on the hydroxo ligand in the $[MO_NH_{2N-z}]^0$ form and this species is likely to condense. The reaction proceeds by olation and/or oxolation mechanism(s) depending on the value of the formal charge z.

Olation takes place only if the aquo ligand exists as such in the coordination sphere of the cation (see Chapter 2). The reaction leads to formation of a solid phase of the hydroxide $M(OH)_z$. The reaction is the only one taking place (meaning that the hydroxide is stable), as long as $\delta(H_2O)$ is negative in the solid. If $\delta(H_2O)$ is positive, oxolation by internal dehydration may become a competing mechanism.

It is possible to set the limit above which olation is the only reaction taking placeby imposing the criterion $\delta(H_2O) = 0$ and applying it to the neutral species MO_NH_{2N-z} [or to the hydroxide $M(OH)_z$]. The charge balance is

$$\delta(M) + N\delta(H_2O) - z\delta(H) = 0 \qquad \text{or} \qquad \delta(M) - z\delta(H) = 0$$

with

$$\chi_p = \chi_{H_2O} = 2.49 \qquad \text{or} \qquad \delta(H) = +0.2 \qquad \text{and} \qquad \delta(M) = \frac{2.49 - \sqrt{\chi_M^*}}{1.36\sqrt{\chi_M^*}}$$

The charge balance equation is an equation in $\sqrt{\chi}$ whose solution relates the critical $\chi_{OL,z}$ to the formal charge z of the cation:

$$\sqrt{\chi_{OL,z}} = -0.136z + [(0.136z)^2 + 2.49]^{1/2} \qquad \text{(A.21)}$$

$\chi_{OL,z}$ as a function of z is shown in Figure 2.3.

When χ_M^* is such that $\chi_{B,z} < \chi_M^* < \chi_{OL,z}$; condensation takes place by olation only, leading to the stable hydroxide $M(OH)_z$. This is the case for manganese(II), for which $\chi_{Mn}^* = 1.63 < \chi_{OL,2} = 1.766$.

If $\chi_{OL,z} < \chi_M^* < \chi_{A,z}$, the partial charge on the water molecule formed during the proton transfer is positive. Oxolation is now involved, leading to formation of an oxyhydroxide or an oxide, depending on the level of dehydration.

This reaction implies proton transfer, from the previously formed ol bridgé (in the transition state) to an adjacent hydroxo ligand, followed by elimination of the formed water molecule. Proton transfer is possible only if $\delta(OH)$ is negative on the olated species, and as long as $\delta(OH)$ remains negative during condensation, the oxide $MO_{z/2}$ may, in theory, form. As soon as $\delta(OH)$ becomes positive, at any stage of the process, the polymer behaves as an acid and forms polyanions.

Since $\delta(OH) = 0$ is the threshold value for this behavior, we may apply this criterion to the oxide $MO_{z/2}$ in order to determine a critical electronegativity $\chi_{PA,z}$ beyond which polyacids are formed:

$$\delta(M) + z/2\delta(0) = 0$$

in MO_NH_{2N-z}, with

$$\chi = \chi_{OH} = 2.711 \qquad \text{and} \qquad \delta(O) = -0.31, \qquad \delta(M) = \frac{2.711 - \chi_M^*}{1.36\sqrt{\chi_M^*}}$$

from which

$$\sqrt{\chi_{PA,z}} = -0.105z + [(0.105z)^2 + 2.711]^{1/2} \qquad \text{(A.22)}$$

If $\chi_M^* < \chi_{PA,z}$, both olation and oxolation compete. They lead, from the zero-charge form, to the formation of oxyhydroxides or hydrated oxide, either crystalline or amorphous (see Chapter 2).

A.5 APPLICATION OF THE MODEL TO THE COMPLEXATION OF CATIONS IN SOLUTION

Complexation of an aquo form of a metal cation by a monodentate species X of formal charge -1 can be written as

$$[M(OH_2)_N]^{z+} + X^- \longrightarrow [MX(OH_2)_{N-1}]^{(z-1)+} + H_2O$$

The reaction takes place by nucleophilic substitution and involves competition between the donor strengths of the X group and the leaving group H_2O. The substitution creates a new distribution of the partial charges in the complex, compared with that of the hexa-aquo complex.

The inner sphere complex may exhibit some stability if an $M \leftarrow X$ transfer takes place, allowing formation of a stable ionocovalent bond. The X^- anion must be less electronegative than the entity $[M(OH_2)_{N-1}]^{(z-1)+}$ and the partial charge $\delta(X)$ of the ligand in the complex must be greater than -1. If the anion X^- is more electronegative than $[M(OH_2)_{N-1}]^{(z-1)+}$, an electron transfer $M \rightarrow X$ should take place, which would lead to a partial charge $\delta(X)$ smaller than -1 in the complex. Unless an acid–base reaction takes place, the bond is completely ionic in nature. It dissociates in water and the anion X^- has no complexing role. At most, it acts as a counterion to the metal ion. As long as $\delta(X) > -1$, the complex will resist ionic dissociation.

Owing to its basicity, the X^- anion may attract a proton from the solution or from the coordination sphere of the cation:

$$[MX(OH_2)_{N-1}]^{(z-1)+} \Longleftrightarrow [M(XH)(OH)(OH_2)_{N-2}]^{(z-1)+}$$

The HX species may nonetheless remain coordinated to the cation if the charge $\delta(HX)$ in the complex is negative. In this case, the ligand HX maintains a higher donor strength than that of water. If the charge $\delta(HX)$ in the complex is positive, the HX ligand will probably be displaced from the complex by water molecules which will effectively replace the HX ligand because of the mass action law, in spite of the fact that they will be positively charged when coordinated to the cation. The complex will resist cation hydrolysis and anion protonation as long as $\delta(HX) < 0$. Therefore, stability of the complex in solution is connected to the double condition

$$\delta(X) = -1, \qquad \delta(HX) = 0$$

Table A.2 Average electronegativities of X^- and HX ligands, and partial charges in Fe(III) complexes for $h = 2$.

X^-	CH_3COO^-	$H_2PO_4^-$	HCO_3^-	HSO_4^-	NO_3^-	ClO_4^-
$\chi[X^-]$	×2.24	×2.49	×2.49	×2.64	×2.76	×2.86
χ[HX]	×2.49	×2.71	×2.79	×2.88	×3.08	×3.10
χ[complex]	×2.51	×2.61	×2.62	×2.66	×2.69	×2.73
$\delta(X)$	−0.14	−0.64	−0.71	−0.94	−1.10	−1.26
δ(HX)	+0.07	−0.38	−0.45	−0.65	−0.80	−0.94

Let us consider the behavior of bidendate anions towards Fe(III) for $h = 2$. The complexation of $Fe(OH)_2(OH_2)_4^+$ [$\chi = 2.61$] by a bidentate ligand X^- can be written as

$$[Fe(OH)_2(OH_2)_4]^+ + X^- \Longleftrightarrow [Fe(OH)_2X(OH_2)_2]^0 + 2H_2O$$
$$\Longleftrightarrow [Fe(OH)_3(XH)(OH_2)]^0$$

The partial charge of a few ligands X in the X and HX forms in the complex are shown in Table A.2. Ions $[NO_3]^-$ and $[ClO_4]^-$, whose partial charges are more negative than −1, do not have a complexing role for the considered form of iron. The ionic character of the bond is too strong and ionic dissociation takes place. $[NO_3]^-$ and $[ClO_4]^-$ behave as counterions. The average electronegativity of the ligand is too high compared with that of the metallic form and no M ← X transfer can occur.

The acetate ion (weak base) is protonated and a molecule of acetic acid is eliminated from the coordination sphere [$\delta(CH_3COOH) > 0$]. The excessively small average electronegativity of the acetate ion makes it susceptible to protonation. The phosphate, carbonate and sulfate ions are the only ones to resist protonation and are able to form stable complexes. The average electronegativity of these ligands is sufficiently close to that of the metallic form for the M←X transfer to occur. These conclusions are in good agreement with experimental observations [6] and may also be reached differently, since the stability criteria of a complex can be expressed directly in terms of electronegativity.

Setting a limit value of $\delta(X) = -1$ in the $[MX(OH_2)_{N-1}]^{(z-1)+}$ form amounts to considering the entity $[M(OH_2)_{N-1}]^{z+}$ of average electronegativity χ_D. If the electronegativity $\chi(X)$ of the species X^- is smaller than χ_D, the charge $\delta(X)$ on the ligand in the complex is greater than −1 and the complex is stable. χ_D imposes the stability threshold of the complex towards ionic dissociation. Similarly, setting the limit value $\delta(HX) = 0$ in $[M(XH)(OH)(OH_2)_{N-2}]^{(z-1)+}$ amounts to considering the average electronegativity χ_H of $[M(OH)(OH_2)_{N-2}]^{(z-1)+}$. If $\chi(HX)$ is greater than χ_H, the charge $\delta(HX)$ is negative. The complex can be stable. χ_H fixes the stability threshold of the complex with respect to hydrolysis of the cation or protonation of the ligand.

The criterion of complexation of a cation by a ligand X may therefore be

$$\chi(X) < \chi_D \quad \text{and} \quad \chi(HX) > \chi_H$$

In the preceding example of iron hydrolyzed at $h = 2$, we obtain

$$\chi_D = \chi[Fe(OH)_2(OH_2)_2^+] = 2.68 \quad \text{and} \quad \chi_H = \chi[Fe(OH)_3(OH_2)^0] = 2.53$$

The average electronegativities $\chi[NO_3^-]$ and $\chi[ClO_4^-]$ (Table 5.1) are greater than χ_D. The complexes will not form because of ionic dissociation. The acetate complex must be destroyed by hydrolysis because $\chi[CH_3COOH] < \chi_H$. Phosphate, carbonate and sulfate will resist hydrolysis and ionic dissociation, since, for each one of them, $\chi(X) < \chi_D$ and $\chi(HX) > \chi_H$.

This reasoning is easily extended to multivalent anions X^{n-}. Criteria controlling the complexation are obtained in a similar manner:

$$\delta(X) > -n \cdots \delta(XH_{n-x}) > -(n-x), \qquad \delta(XH_n) < 0$$

associated with corresponding values of χ_D and χ_H.

Complexation of a metal cation in solution is governed by two main variables: the acidity of the medium and the electronegativity of the complexant. The influence of medium acidity on complexation is taken into account by the nature of the cationic species considered, i.e. a form of the type $[M(OH)_h(OH_2)_{N-h}]^{(z-h)+}$ for which the hydrolysis ratio h is easily determined as a function of the acidity of the medium (see Section A.2). It is possible to establish a direct relationship between both quantities in order to determine, as a function of pH, the ability of a chemical species to act as a ligand.

In a medium of given acidity, hydrolysis of a cation $M(OH_2)_N^{z+}$ can be written as

$$[M(OH_2)_N]^{z+} + H_2O \longrightarrow [M(OH)_h(OH_2)_{N-h}]^{(z-h)+} + hH^+_{solvated}$$

This hydrolyzed form reacts with an X^{n-} ligand (of coordination mode α according to

$$[M(OH)_h(OH_2)_{N-h}]^{(z-h)+} + X^{n-} \longrightarrow [M(OH)_h(X)(OH_2)_{N-h-\alpha}]^{(z-h-n)+} + \alpha H_2O$$

The basic character of the anion, for a given pH, is reflected in the reaction with the solvation water molecules of the complex:

$$[M(OH)_h(X)(OH_2)_{N-h-\alpha}]^{(z-h-n)+} \longrightarrow [M(OH)_{h+q}(XH_q)(OH_2)_{N-h-\alpha-q}]^{(z-h-n)+}$$

and the complete reaction is

$$[M(OH_2)_N]^{z+} + X^{n-} \longrightarrow [M(OH)_{h+q}(XH_q)(OH_2)_{N-h-\alpha-q}]^{(z-h-n)+} + hH^+_{solvated} + \alpha H_2O \qquad (A.23)$$

If the cation were alone in the solution, its hydrolysis ratio would be h. Owing to complexation by a basic species, the cation undergoes an additional hydrolysis q, so that the overall hydrolysis ratio of the cation is $(h + q)$.

DropBooks

The problem is to determine the acidity range in which cation complexation by the various forms of the ligand X is effective. The approach is explained below.

The stability threshold of the protonated form XH_q with respect to ionic dissociation of the complex considered in (A.23)

$$[M(OH)_{h+q}(XH_q)(OH_2)_{N-h-\alpha-q}]^{(z-h-n)+}$$

is imposed by the condition $\delta(XH_q) = q - n$ in the complex. This amounts, as in the previous cases, to equalizing the average electronegativity of the free ligand $[XH_q]^{(q-n)+}$, χ_q to that of the entity

$$[M(OH)_{h+q}(OH_2)_{N-h-\alpha-q}]^{(z-h-q)+}$$

of average electronegativy χ_D.

Electronegativity χ_D is a function of h and q, and hence of the pH. The principle behind the calculation is to establish the relationship between the critical value of χ_q and the pH of the solution.

Using the equation

$$[M(OH)_{h+q}(OH_2)_{N-h-\alpha-q}]^{(z-h-q)+} = [M(OH)_2)_N]^{z+} - (h+q)H^+ - \alpha H_2O$$

the average electronegativity χ_D is [equation (A.12)]

$$\chi_D = \frac{\sigma_M\chi_M - (h+q)\sigma_H\chi_H - \alpha\sigma_{H_2O}\chi_{H_2O}}{\sigma_M - (h+q)\sigma_H - \alpha\sigma_{H_2O}} \qquad (A.24)$$

where σ_M and χ_M represent the softness and the average electronegativity of $M(OH_2)_N^{z+}$, respectively, and σ_H, χ_H and $\sigma_{H_2O}, \chi_{H_2O}$ represent similar quantities for the proton (H^+) and the water molecule.

From equation (A.24), we obtain

$$h + q = \frac{\sigma_M(\chi_q - \chi_M) - \alpha\sigma_{H_2O}(\chi_q - \chi_{H_2O})}{\sigma_H(\chi_q - \chi_M)} \qquad (A.25)$$

Assuming that the pH of the medium is controlled by the composition of the system, the hydrolysis ratio of the cation is that of the cation if it were alone in the solution in the absence of any complexant. Here, h (see Section A.2.5) is given by

$$h = \frac{\sigma_M(\chi_s - \chi_M)}{\sigma_H(\chi_s - \chi_H)} \qquad (A.26)$$

in which $\chi_s = 2.621 - 0.02\,\text{pH}$ [equation (A.14)].

Introducing (A.26) in (A.25) gives

$$\frac{\sigma_M(\chi_s - \chi_M)}{\sigma_H(\chi_s - \chi_H)} + q = \frac{\sigma_M(\chi_q - \chi_M) - \alpha\sigma_{H_2O}(\chi_q - \chi_{H_2O})}{\sigma_H(\chi_q - \chi_M)} \qquad (A.27)$$

Hence

$$\frac{A(M) - \alpha B(H_2O)}{(\chi_q - \chi_H)} = \frac{A(M)}{(\chi_s - \chi_H)} + C(\alpha, q) \qquad (A.28)$$

with

$$A(M) = \sigma_M(\chi_H - \chi_M)$$
$$B(H_2O) = \sigma_{H_2O}(\chi_H - \chi_{H_2O})$$
$$C(\alpha, q) = q\sigma_H + \alpha\sigma_{H_2O}$$

Terms A, B and C are constant relative to, respectively, the cation M, the medium and the anion. It is worth noting that equation (A.28) involves quantities that characterize the three partners involved in the chemical reaction.

Equation (A.28) establishes very simply the relationship between the average electronegativity of XH_q^{q-n}, χ_q, and the pH of the medium χ_s, for given values of q and α (coordination mode of the anion). Therefore, it allows a calculation of the acidity range corresponding to the metal complexation by various forms of species X, protonated or not.

For example, for aluminium:

$$\chi_M = \chi[Al(OH_2)_6^{3+}] = 2.754, \qquad \sigma_M = \sigma[Al(OH_2)_6] = 9.053$$
$$\chi_H = \chi[H^+] = 4.071, \qquad \sigma_H = \sigma[H] = 0.507,$$
$$\chi_{H_2O} = \chi[H_2O] = 2.491, \qquad \sigma_{H_2O} = \sigma[H_2O] = 1.408$$

For $q = 0$ and $\alpha = 2$:

$$A(M) = 11.922, \qquad B(H_2O) = 2.224, \qquad C(2.0) = 2.816$$

and equation (A.28) becomes

$$[7.474/(\chi_{q=0} = 4.071)] - 2.816 = 11.922/(\chi_s - 4.071)$$

For various values of χ_q, the relationship $\chi_s = 2.621 - 0.02$ pH gives the corresponding values of the threshold pH for the dissociation of the $[Al(OH)_h](X)(OH_2)_{4-h}]^{(3-h-n)+}$ complex.

For the coordination mode selected, a set of $n\,\chi_q(0 \leqslant q < n) = f(pH)$ curves is obtained, coresponding to the n value of χ_D (ionic dissociation of the complex) relative to the X^{n-} anion and its $n-1$ protonated forms XH_q^{q-n}, as well as a $\chi_{q=n} = f(pH)$ curve corresponding to the value of χ_H (dissociation of the complex via hydrolysis) for the form XH_n (Figure A.2).

For a given anion, the domain of acidity for likely complexation is found between the values corresponding to the average electronegativities of the forms X^{n-} and H_nX. Outside this range, complexes do not form because the bonds are too polar. Within this range, water is a better ligand than the acid form of the anion. This is illustrated in the case of aluminium (Figure A.2). Similar diagrams (see Figures 5.2 and 5.18) can be drawn for any cation using the set of equations in (A.28).

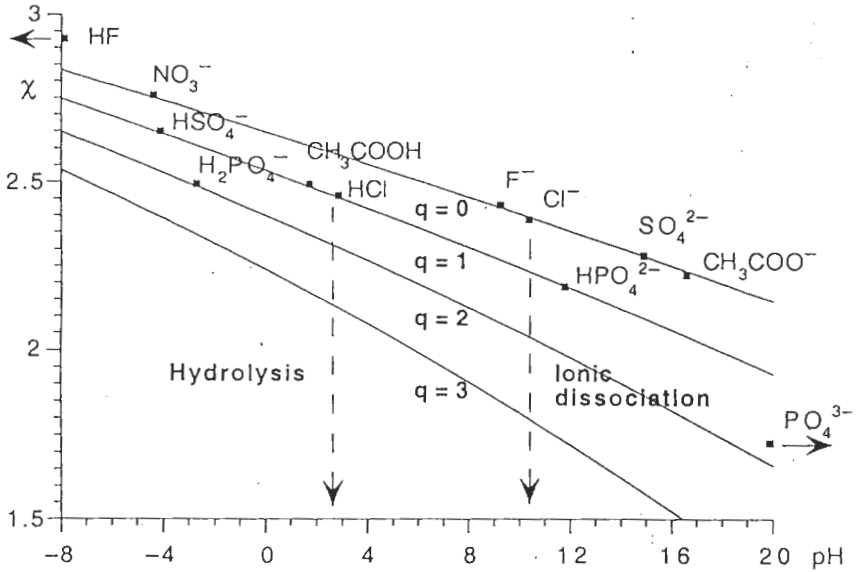

Figure A.2 Electronegativity versus pH diagram for the complexation of Al^{3+} by monodentate anions. For example, the acidity range for complexation by chloride ions is determined by the values of $\chi(Cl^-)$ and $\chi(HCl)$

Figure A.2 calls for a few remarks:

- In the preceding discussion, it was always assumed that the stoichmetry of the complexes was [1;1] it would be possible to consider the formation of complexes of various stoichiometries, but the limitations of the model would not allow a precise analysis of such species. If such complexes formed, they would do so within the stability domains of the [1;1] complexes.
- The model implies that a monoatomic anion such as Cl^-, for example, should have an extremely high complexing strength owing to its small electronegativity. This contradicts experimental results. In fact, solvation of the anion leads to the formation of $[Cl(H_2O)_N]^-$ entities with a lower complexing strength than the anhydrous form. The average electronegativity of the hexa-aquo ion [34,35] is $\chi[Cl(H_2O)_6^-] = 2.395$, which corresponds for aluminum to an ionic dissociation pH of 10.2 (Figure A.2). For the protonated form of the anion, we consider the hydrate [HCl, H_2O] for which $\chi = 2.470$, and hence pH = 2.8 for the hydrolysis of the complex, still in the case of aluminum. Therefore, it is expected that complexation of aluminum by the chloride will be observed within those two pH values, which agrees with experimental data. There are no stable chlorinated complexes with $[Al(OH_2)_6]^{3+}$, even for a high chloride concentration [36,37] or in the solid state for $AlCl_3 \cdot 6H_2O$ [38]. However, it is difficult to obtain a chloride-free precipitate of Al(OH) from $AlCl_3$ solutions [39] whereas elimination of anions through washing of the precipitate is easy with aluminum nitrate or perchlorate. Indeed, complexation of aluminum by nitrate and perchlorate occurs only in a strongly acidic medium (Figure A.2). The fluoride ion is smaller than the chloride and can only form units containing four water molecules $[F(H_2O)_4]^-$ [35] with an average electronegativity of 2.422. Since hydrofluoric acid is a weak acid, the HF species ($\chi = 2.934$) is assumed to be unsolvated. The stability domain for the complexation of aluminum by fluoride ions is much wider than in the case of the chloride, ranging from very acidic media to pH 9 (Figure A.2). A series of inner sphere complexes $[AlF_n]^{(3-n)+}$ with $n = 1-4$ has been characterized by ^{19}F NMR [40,41].
- This diagram is based on purely electrostatic criteria without consideration of any structural characteristics such as the chelate effect which stabilizes complexes, compared with monodentate ligands, or the π donor character of some ligands. Cation and ligand concentrations do not appear in the model either. Although the model agrees broadly with the experimental results, this considerable limitation should remind us that the model gives only *indications* of the possibilities of formation of a complex. Application of the model to this type of reaction only allows us to determine if a ligand is likely to enter the coordination sphere of a cation and to displace one or several aquo or hydroxo ligands, for example. In no instance does the model allow us to draw conclusions on the effective formation of a given complex, nor does it provide quantitative information on the reaction. In the absence of thermodynamic data, however, the model does provide useful information allowing us to determine whether it is reasonable or not to expect the formation of some complexes.

DropBooks

The partial charges model is a simple and convenient method for the broad prediction of the behavior of elements in solution. Electronegativity, i.e. the electronic chemical potential, seems to be an adequate and useful concept in the understanding of the direction of electron transfers between atoms. Therefore, it is a useful concept in predicting the evolution of a chemical system, since the principle of electronegativity equalization can broadly characterize an equilibrium situation.

Because of its many approximations, and mostly because it contains no concentration or structural considerations, the model is unable to provide quantitative information and may in no circumstance be a substitute for thermodynamic data. When structural issues such as the presence of multiple bonds are likely to affect the reactivity of a species, the model should be used with extreme care. In addition, the analysis of hydrolysis and condensation reactions with the partial charges model would require modifying the hardness value for each cation. This is also true for the study of complexation, which may only be treated from an extremely qualitative standpoint. However, qualitative information is better than no information at all.

In spite of these disadvantages, the partial charges model does rationalize the chemistry of cations in solution regarding hydrolysis and condensation processes. This is its main contribution.

A.6 REFERENCES

1. J.E. Huheey, J.C. Watts, *Inorg. Chem.* 10, 1553 (1971).
2. M. Henry, Thesis, Université P. et M. Curie, Paris (1988).
3. R.T. Sanderson, *Science* 114, 670 (1951).
4. W. J. Herhe, L. Radom, P.R. Schleyer, J.A. Pople, *Ab initio Molecular Orbital Theory*, J. Wiley & Sons, New York (1986).
5. E.J. Magnusson, *J. Am. Chem. Soc.* 106, 1177 (1984)
6. C.J. Ballhausen, H.B. Gray, *Molecular Orbital Theory*, W.A. Benjamin Inc., New York (1964).
7. A. Viste, H.B. Gray, *Inorg. Chem.* 3, 1113 (1964).
8. H. Basch, A. Viste, H.B. Gray, *J. Chem. Phys.* 44, 10 (1966).
9. L. Pauling, *The Nature of Chemical Bond*, 1st ed., Cornell Univ. Press, Ithaca (1939).
10. R.G. Parr, R.A. Donnelly, M. Levy, W.E. Palke, *J. Phys. Chem.* 68, 3801 (1978).
11. R.G. Pearson, *Chemtracts Inorg. Chem.* 3, 317 (1991).
12. H. Chermette, R. Lissilour, *L'Actualité Chimique* 4, 59 (1985).
13. R.P. Iczkowski, J.L. Margrave, *J. Am. Chem. Soc.* 83, 3547 (1961).
14. R.G.Pearson, *J. Am. Chem. Soc.* 85, 3733 (1963).
15. R.G. Parr, R.G. Pearson, *J. Am. Chem. Soc.* 105, 7512 (1983).
16. R.S. Mulliken, *J. Chem. Phys.* 2, 782 (1934).
17. J.H. Van Vleck, *J. Chem. Phys.* 2, 20 (1934).
18. S.G. Bratsch, *J. Chem. Educ.* 65, 34 (1988).
19. A.L. Allred, E.G. Rochow, *J. Inorg. Nucl. Chem.* 5, 264 (1958).
20. W. Gordy, *Phys. Rev.* 69, 604 (1946).
21. R.T. Sanderson, *Chemical Periodicity*, Reinhold Pub. Corp., New York (1960).
22. L. Pauling, *J. Am. Chem. Soc.* 54, 3570 (1932).
23. L. Pauling, *J. Chem. Educ.* 65, 375 (1988).
24. H.A. Skinner, H.O. Pritchard, *Trans. Faraday Soc.* 49, 1255 (1953).
25. W.J. Mortier, S.K. Ghosh, S, J. Shankar, *J. Am. Chem. Soc.* 108, 4315 (1986).
26. R.T. Sanderson, *Inorganic Chemistry*, Reinhold, New York (1976).
27. E.J. Little, M.M. Jones, *J. Chem. Educ.* 37, 231 (1960).
28. S.S. Batsanov, *Russ. J. Struct. Chem.* 37, 332 (1968).
29. Y. Zhang, *Inorg. Chem.* 21, 3886 (1982).
30. M. Henry, Thesis, Université P. & M. Curie, Paris (1993).
31. F. Basolo, R.G. Pearson, *Mechanism of Inorganic Reactions*, 2nd ed., J. Wiley & Sons, New York (1958).
32. M. Henry, J.P. Jolivet, J. Livage, *Structure and Bonding* 77, 153 (1992).
33. C.F. Baes, R.E. Mesmer, *The Hydrolysis of Cations*, J. Wiley & Sons, New York (1976).
34. J.P. Hunt, H.L. Friedman, *Prog. Inorg. Chem.* 30, 359 (1983).
35. M. Magini, G. Licheri, G. Paschina, G. Pinna, *X-Ray Diffraction from Aqueous Solutions: Hydration and Complex Formation*, CRC Press, Inc., Boca-Raton, Florida (1988), p. 160.
36. K.A. Kraus, F. Nelson, G.W. Smith, *J. Phys. Chem.* 58, 11 (1954).
37. R.E. Schuster, A. Fratriello, *J. Chem. Phys.* 47, 1554 (1967).
38. D.R. Buchanan, P.M. Harris, *Acta Cryst.* B24, 955 (1968).
39. W.B. Scott, E. Matijevic, *J. Colloid Interface Sci.* 66, 447 (1978).
40. R.E. Connick, R.E. Poulson, *J. Am. Chem. Soc.* 79, 5153 (1957).
41. J.W. Akitt, N.N. Greenwood, G.D. Lester, *J. Chem. Soc.* A, 2450 (1971).

Part II

SURFACE CHEMISTRY OF OXIDES

Oxide particles formed by precipitation or coprecipitation from solutions are usually colloidal: at least one of their dimensions is of the order of a few hundred to a few thousand ångstroms. Their specific surface area (the surface/volume or surface/mass ratio) may reach several hundred square meters per gram. This explains why the behavior of small particles is largely dominated by the physicochemical characteristics of their surface.

- The dispersion of particles in a liquid depend on the attractive or repulsive forces exerted between their surfaces. Control of the force balance allows control of the agglomeration of the particles, as well as the formation of sols or gels. It is often necessary to obtain non-aggregated systems in an aqueous or non-aqueous medium if optimum properties are desired in the dried sol or gel. If the particles have aggregated or flocculated, the performance and the mechanical properties of the final material are adversely affected owing to heterogeneities in density and porosity.
- The division state of a solid formed via precipitation is governed by the forces exerted on its surface (the interfacial tension). These forces determine the extent of the surface, and hence the size of the particles. The average size and particle size distribution are crucial parameters that must be controlled because they have direct implications on the materials from which the particles are derived: catalysts, composite materials or magnetic suspensions such as ferrofluids.
- Adsorption of ions or molecules from the dispersion medium depends on the characteristics of the surface, most particularly on the electrostatic charge density and on the structure of coordination sites. Fixation of various species on the surface of oxide particles plays a critical role in many areas: transport of matter in industrial or natural waters, catalysis or corrosion phenomena and synthesis of a stable and homogeneous dispersion.

To comprehend and control these phenomena, knowledge of the physicochemical characteristics of the surface of the particles is indispensable. Unfortunately, if

many techniques allow the characterization of cations in solution and within the solid, it is much more difficult structurally and chemically to probe the surface of nanometer-size objects. Firstly, it is very difficult to define the geometry of the surface of very small particles. Secondly, the surface often contains defects such as dislocations, stacking defects and steps, which have different reactivities. It is often very difficult to characterize the reactivity of the surface because it is hard to identify the reaction sites. The fact that few quantities are accessible to the experimentalist further complicates the research. Most of these quantities must be treated with adjustable parameters using models of different complexity.

The current state of the art does allow us to give a reasonable interpretation of experimental data. The next few chapters will introduce the reader to the fundamental concepts of the oxide–solution interface. The main factors governing its physicochemical properties are also analyzed.

DropBooks

6

Oxide–Solution Interface

A dispersion of solid particles in an aqueous solution is a two-phase system. Both phases are separated by an interface where the system is discontinuous and where matter exchange occurs between both phases. These exchanges involve chemical reactions, in a first approximation in two-dimensional space, since the thickness/surface ratio of the contact zone is very small. The behavior of reactants must be very different whether they are in the liquid phase in contact with the solid or away from the surface. Furthermore, chemical reactions involve the surface of the solid phases, whose characteristics are neither those of the bulk nor those of the metallic ion in solution. In fact, cations at the surface of oxide or hydroxide particles are immobilized and subjected to stresses owing to their proximity to the solid. These ions, which were mobile in solution prior to the formation of the particles, are now part of the solid. However, they still keep a 'memory' of their initial properties (acid–base characteristics, the ability to undergo ligand exchange) since one side of their coordination sphere is still in contact with the solution. However, their properties are now affected by the structural constraints to which they are subjected. They are also sensitive to changes in the properties of the neighboring solvent (structure, dielectric constant).

Two key points characterize the surface of oxide particles and dominate their physicochemical properties: the surface is electrically charged and it is highly hydrated.

6.1 ORIGINS OF THE SURFACE CHARGE

The charge on oxide particles results from the ionization upon contact with water of hydroxyl groups on their surface [1–3]. How are these groups formed?

From a macroscopic standpoint, there is a difference in the chemical potential of the constituents in both phases in contact. Owing to kinetics (low ionic mobility in the solid) and thermodynamics (solubility product), migration of cations towards the liquid phase and dissolution of the oxide do not occur. The difference in the chemical potential of oxygen does decrease through adsorption of water and dissociation of the adsorbed molecules, which explains the presence of hydroxyl groups on the surface.

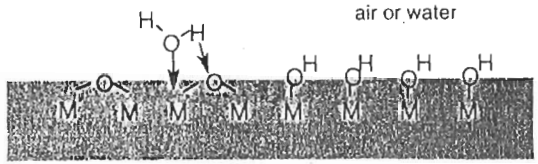

Figure 6.1 Water chemisorption on an oxide surface

From a structural standpoint, the coordination number of cations on the surface of an oxide synthesized by 'dry' techniques (CVD, electric arc, solid state reactions) is necessarily lower than that of ions within the solid. Upon exposure to ambient atmosphere, satisfying the coordination number of the surface ion is the driving force behind the chemisorption of water which causes its dissociation and combination (Figure 6.1).

When hydroxide or oxide particles precipitate in solution, surface hydroxyls are naturally present since they come from the coordination sphere of the last cations incorporated as zero-charge complexes.

Like hydroxo complexes in solution, surface groups (M–OH) ionize in contact with water:

$$M\text{–}O^- + H_3O^+ \Longleftrightarrow M\text{–}OH + H_2O \Longleftrightarrow M\text{–}OH_2^+ + HO^-$$

The charge on surface groups can be negative, positive or zero depending on the nature of the oxide, and give the surface a basic, acidic or neutral character respectively.

Acid–base properties of surface ligands are different from those of the ligand on the monomeric cation in solution. Firstly, the structure of the surface groups is variable. They may be mono, di- or tricoordinated, depending on the structure of the solid and the orientation of the crystal in the particle. Because of their proximity to one another, these groups are also subjected to short-distance electrostatic interactions. Such interactions increase the acidity of water molecules and the basicity of oxo ligands. Each type of site will behave differently depending on its own structure. As will be discussed later, the charge distribution is inhomogeneous in density and in sign, and therefore the problem requires more careful analysis. However, the net surface charge density, σ_0, is defined as

$$\sigma_0 = (F/A)([M\text{–}OH_2^+] - [M\text{–}O^-]) \qquad (6.1)$$

where A is the surface area of the particles ($m^2\,l^{-1}$) and represents the surface area per unit volume of particles, and F is the Faraday constant ($96\,500\,C\,mol^{-1}$); the quantities in brackets are the concentration ($mol\,l^{-1}$) in charged surface sites. σ_0 can be as high as $0.2–0.4\,C\,m^{-2}$. This quantity is measurable using potentiometric titration (see Section 6.3).

The surface charge on an oxide is the result of acid–base equilibria. Hence, it is a function of pH and of the ionic strength of the solution. σ_0 may be positive, negative

Table 6.1 Point of zero charge of several oxides [1]

z	Oxide	PCN
+II	MgO	≈12.5
	ZnO	9–10
+III	α-Fe_2O_3	5.5–9
	α-Al_2O_3	6.5–10
+IV	TiO_2	3.5–6.5
	SiO_2	2–4
+V	Sb_2O_5	≈0.5
+VI	WO_3	≈0.4

or zero, depending on the medium. The point of zero charge (PZC) is an important characteristic of the surface. It defines the pH of the medium for which the charge σ_0 becomes zero. Hence, the PZC is a reflection of the acidity of the surface. For pH < PCN the charge is positive, whereas for pH > PZC it is negative. The value of the PZC is directly related to the nature of the oxide and depends on several factors.

(i) *Polarization of surface groups by the cation.* This polarization is related to the size and the charge of the cation. If the cation is small and more charged, the electron transfer M ← O becomes important and the basicity of surface oxygens is small. Hence, surface groups behave as stronger acids. Table 6.1 (see also Table 7.1) gives the PZC of various oxides.

Reversal of the charge, i.e. a change in the sign of σ_0, can be obtained by modifying the pH if the PZC is neither too high nor too low. If this is not the case, the sign of the charge and its magnitude are almost independent of pH, as in the case of molecules and strongly basic or acidic ions in solution.

(ii) *Crystal structure and particle morphology.* They impose the coordination and the relative proportions of mono-, di- or tricoordinated hydroxyl surface groups. Since each type exhibits different acid–base properties, the PZC of the oxide will be dependent on the crystal structure and the particle morphology. This is why the PZC of α-FeOOH is 9.1 whereas that of γ-FeOOH is 7.4 (see Table 7.1).

(iii) *Heat treatment and physicochemical history of the oxide.* Both factors have a strong influence on the PZC. Particles fired at very high temperatures are less readily hydrated and hydroxylated. Below 200 °C, molecular water physisorbed via hydrogen bonds on surface groups is removed. The surface groups remain unaffected up to about 400 °C. At about 700 °C, hydroxyl groups dehydrate if they are adjacent to one another (two groups are required to eliminate a water molecule). When only isolated groups remain, no further dehydration can occur if the temperature is not high enough to allow their diffusion on the surface. This is the only possibility for a reaction and water elimination. This occurs at temperatures ranging from 800 to 1000 °C, depending on the oxide [4]. Rehydroxylation upon contact with water is usually slow, and oxides that have been subjected to high firing

temperatures (and hence are highly dehydrated) will exhibit a PZC significantly different from that of a fully hydroxylated material [1]. During rehydroxylation, the PZC shifts slowly back towards that of the completely hydroxylated material. This process may take several weeks or even several months. Acidity changes that parallel hydration variations may be due to changes in the coordination number of surface groups and to modification of the crystal structure in the near-surface volume of the particle [5].

The history of the particles and their morphology have a considerable influence on their surface properties. Specifically, treatments to which they have been subjected during synthesis, as well as the presence of adsorbed species, may be the reason for the various PZC values reported in the literature for 'identical' materials. For some materials, these values can differ by several pH units (Table 6.1).

6.2 SOLVATION AND STRUCTURE OF THE INTERFACE

As with ions in solution, the polarity and ionization of surface groups cause their solvation. The presence of a hydration layer on the surface of particles plays a major role in the behavior of colloidal dispersions.

6.2.1 SOLVATION OF THE PARTICLES

In an earlier section, we saw that hydrogen bonds in liquid water are responsible for a number of properties of the liquid, and that the presence of ions in the liquid does alter its local structure (see Chapter 1). The surface groups M–OH, $M–OH_2^+$ and $M–O^-$ are polarized and develop very strong interactions with water. They also have a very strong structuring effect on the liquid. Measurements of immersion and adsorption heats, as well as dielectric measurements on α-Fe_2O_3, ThO_2 or SiO_2, show that the 2–3 layers of physisorbed water adjacent to the first chemisorbed water layer are immobilized by pairs of hydrogen bonds forming an order similar to that of ice. These bonds are still present at room temperature [3,6–8] (Figure 6.2).

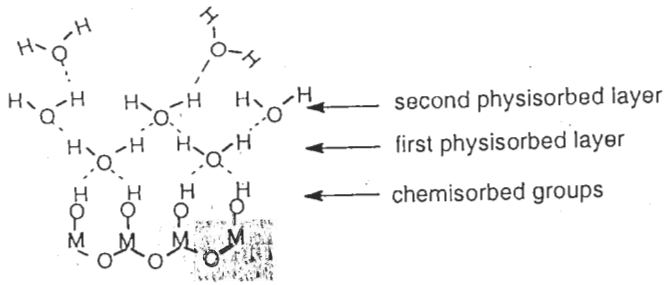

Figure 6.2 Adsorption of water on an oxide surface. From [6] by permission

The ordering of solvation layers disappears away from the surface. Beyond a distance ranging between a few ångstroms to a few tens of ångstroms, depending on the nature of the oxide, water recovers its liquid characteristics [9]. Large amounts of water may participate in the solvation of a surface. The hydrodynamic size of the particles, measured by quasi-elastic light diffusion, is very frequently greater than the size observed by SEM or XRD. The 80 Å γ-Fe_2O_3 particles (as measured by microscopy and XRD) have, at pH≈2 (positively charged surface), a hydrodynamic diameter of approximately 140 Å. Therefore, a 30 Å thick layer of water is transported with the particles in their movement within the suspension.

The thickness of the highly structured hydration layer is usually a few molecular diameters. It increases with increasing polarity of the surface and increasing surface charge density. This solvation water constitutes the 'Stern compact layer'. Its characteristics (thickness, dielectric constant) are difficult or impossible to determine experimentally, but its presence allows the differentiation of interactions between surface and several electrolytes: proton, hydroxyl ion and ions that are inactive from acid–base standpoints (see below).

The transition zone between the ordered layers of solvent, the first of which are strongly attached to the surface, and 'liquid' water is characterized by the 'destructuring' of the solvent. It is a process similar to that around ions in solutions. Water molecules within this zone are subject to competing forces: forces due to neighboring molecules in the solution, and forces due to orientation imposed by the surface of the particle. Within this zone the viscosity of the solvent is minimal, and this is where the solvent 'glide' or 'shear' takes place when the particles moves [9]. The structure imposed in the solvation layers influences the forces exerted at short distance between hydrated surfaces [10,11].

DropBooks

6.2.2 SURFACE–ELECTROLYTE INTERACTIONS

The presence of a network of hydrogen bonds in the entire liquid phase, including the solvation layers of the particles, allows easy diffusion of H^+ and HO^- ions towards the oxide surface. These ions participate in chemical reactions taking place on hydroxyl groups, and the structure of water near the surface does not hinder their movement. Of these two ions, the proton is the only one truly chemisorbed since it forms OH or OH_2 ligands. HO^- ions deprotonate surface ligands to form water. These ions are responsible for the charge σ_0 [equation (6.1)], and for the potential created by this charge. Protons and hydroxyl ions are called potential-determining ions, or PDIs.

The non-specific electrostatic forces caused by the surface charge attract ions of opposite sign (counterions) and repel ions of same charge (co-ions). Depending on the nature of the counterions, their interaction with the surface will be more or less strong.

Ions of relatively weak charge density {ions such as Cs^+, $[N(CH_3)_4]^+$, $[ClO_4]^-$, see Chapter 1} cannot penetrate the strongly structured water layer near the oxide

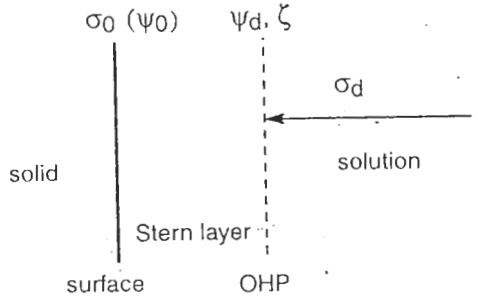

Figure 6.3 Oxide–aqueous solution interface

surface. The minimum distance they are able to reach corresponds to the thickness of the Stern layer. This limit is called the outer Helmholtz plane, or OHP, and corresponds to the glide plane of the solvent (Figure 6.3).

When subjected to electrostatic attraction and thermal agitation, counterions form a diffuse layer in the solution, beyond the OHP. The electric potential ψ_d caused by the surface charge and measured at the OHP (at the limit of the diffuse layer) is the zeta potential, ζ, which is calculated from the electrophoretic mobility. This is the only measurable potential for oxide particles. The charge of the diffuse layer, σ_d, represents the countercharge of the particle (Figure 6.3). Since it compensates for the surface charge, electroneutrality imposes $\sigma_0 + \sigma_d = 0$.

Some ions are attracted towards the surface by electrostatic forces and have a particular affinity for the solvation layer. With oxides, the structuring ions penetrate the ordered solvent layer most easily because they have a tendency to preserve local order in the zone. Alkalis, for example, are adsorbed on negatively charged oxide surfaces in the following sequence $Li^+ > Na^+ \gg Cs^+$. This order is due to the fact that water molecules are poorly mobile near the surface and compensate the entropy loss by an increase in bond energy with the most strongly hydrated cations [11] (see also the study on flocculation in Section 8.1.5). On the other hand, AgI colloids adsorb more specifically on destructuring ions [12]. Ag^+ and I^- are also destructuring and do not cause strong solvation of the surface.

The mobility of ions within the solvation layers is limited by the strong structuring of the layer and the strong electrostatic forces near the surface. This was clearly demonstrated in NMR investigations of the relaxation times of ^{23}Na adsorbed on the surface of silica [13]. The relaxation time of adsorbed Na^+ is longer for ions in solution, but does not allow the formation of ion pairs or complexes with negatively charged sites on the surface. The solvation layers of the adsorbed Na^+ do not appear to be affected and, since these ions are only subjected to non-specific electrostatic forces, they are only constrained not to diffuse outside the solvation layer of the particles. The chemical component of the free enthalpy of adsorption of these ions is zero. Their bonding energy is of the order of a few kT [14]. Interactions between

the ion and the surface probably occur via hydrogen bonding between charged groups and solvated surface groups as in

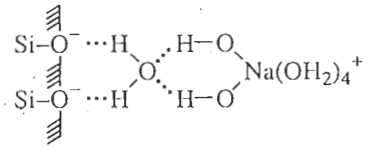

The role of the counterions on a charged surface is not limited to maintaining the electroneutrality of the dispersion. Since these ions are near the surface, they also shield electrostatic repulsions between charged groups, which modifies the surface charge. At a given pH sufficiently far from the PZC, the number of charged sites is limited by their mutual repulsion. Attenuation of this repulsion by the counterions adsorbed in the solvation layer allows an increase in the surface charge. Therefore, the surface depends, for a given pH, on the concentration of counterions, and hence also on the level of shielding. This is the salt effect, which is used in the experimental measurement of the PZC (see Section 6.3).

Some ions or molecules are attracted to the surface by non-specific electrostatic attractions and are able to penetrate the Stern layer and bind chemically on surface sites. Most often, these ions are complexing anions, easily hydrolyzable cations or neutral molecules forming true coordination complexes with surface groups. Depending on the strength of the interaction between the adsorbed species and the surface, inner sphere or outer sphere complexes are formed. These species are called physisorbed or chemisorbed respectively. This phenomenon is known as 'specific' adsorption, or surface complexation, and a chemical term appears in the free enthalpy of adsorption. Specific adsorption is further discussed in Chapter 9.

6.3 EFFECT OF IONIC STRENGTH AND DETERMINATION OF THE PZC

The net surface charge $\sigma_0 = (F/A)\,([MOH_2^+] - [MO^-])$ is a function of the acidity of the medium. pH measurements and titration curves give access to the amount of protons or HO^- ions consumed after known additions of acids or bases to the colloidal suspension. They allow calculation of the charge of the particles [2,15,16] (Figure 6.4). Since the absolute value of the charge is not known *a priori*, a single acid–base titration curve does not allow determination of the PZC. Therefore, the electrostatic shielding effect of charged surface sites by the ions in the electrolyte is used.

At a given pH, the net surface charge increases with increasing electrolyte concentration, as shown in Figure 6.4. Electrolyte ions accumulating at the OHP or penetrating further into the Stern layer (cations if the charge is negative, anions if it is positive) shield on the one hand the repulsions between charged surface sites, and

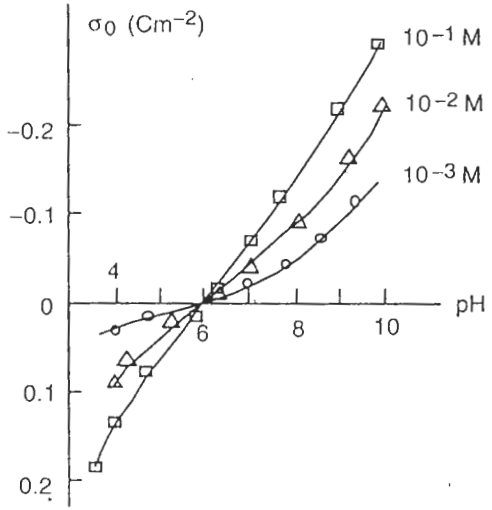

Figure 6.4 Variation in the surface charge of TiO_2 anatase as a function of the pH of NaCl solutions for several concentrations. Reproduced by permission of Academic Press from [17]

on the other hand the repulsions between the surface and the PDIs (protons, hydroxyl ions). The latter become less repulsed by the surface. With the addition of the electrolyte, more sites are ionized and the surface charge increases. At the PZC, the electrolyte has no effect. This is why all curves have a common intersection indicating the PZC, or point of zero salt effect [18].

The sol or suspension is at equilibrium for a given pH, for example basic, in the presence of an electrolyte that does not adsorb specifically (KNO_3, for example) (point 1, Figure 6.5). It is subsequently titrated until point 2. At this point, more electrolyte is added. The pH increases and the positive charge increases until point 3. The suspension is then titrated by a base until point 4. More electrolyte is added (point 5) and an additional titration by a base is carried out (point 6). If indeed the electrolyte is indifferent, which means that its ions are subject only to the electrostatic constraints, all curves will intersect at the PZC. At the onset of the experiment, the surface charge is unknown and the first curve cannot be placed on the y axis. But the intersection point of all subsequent curves, indentified as the PZC, allows a determination of the origin of the charge axis. Hence, if for a given oxide and several electrolytes of varying concentration the same intersection point $\sigma_0 = f(pH)$ is obtained, it is clear that this point is the PZC and that no specific adsorption takes place.

If the electrolyte contains an ion specifically adsorbed, the intersection point of the $\sigma_0 = f(pH)$ curves shifts and no longer represents the PZC determined with 'indifferent', or non-specifically adsorbed ions. Specific adsorption of cations shifts the intersection towards lower pH; anions shift it towards higher pH. For example,

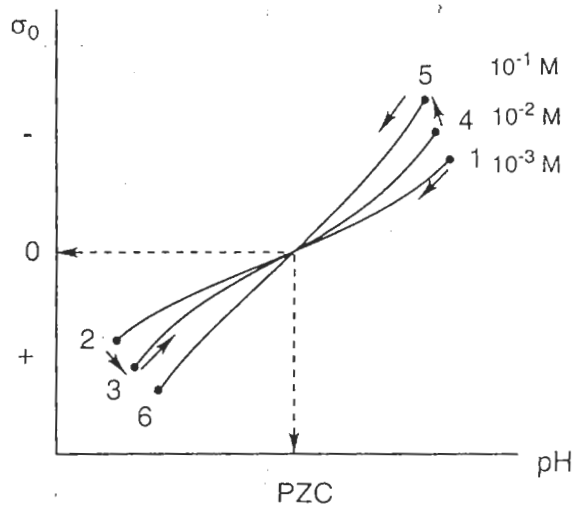

Figure 6.5 Proton titration curve of an oxide suspension for various electrolyte concentrations. Reproduced by permission of Academic Press from [18]

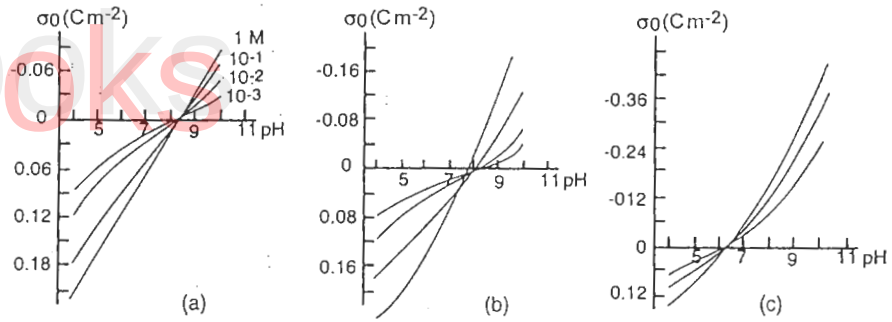

Figure 6.6 PZC for hematite, α-Fe_2O_3, as a function of the electrolyte: (a) KCl, (b) LiCl, (c) $Ca(NO_3)_2$. The PZC shift is more pronounced with Ca^{2+} since it is more strongly adsorbed than Li^+. From [19] by permission

specific adsorption of Ca^{2+} on α-Fe_2O_3 shifts the PZC from 8.5 to 6.5 (Figure 6.6), whereas adsorption of SO_4^{2-} increases it from 8.5 to 9.5 [19–21].

Specific adsorption of cations near a negatively charged surface shields the negative charges and promotes desorption of protons on adjacent sites. Cancelling the charge requires a pH lower than in the absence of any adsorption, causing a decrease in the PZC. Similarly, anions adsorbed on a positive surface increase the PZC. In this case, $\sigma_0 = f(pH)$ curves for various electrolyte concentrations no longer have a common intersection point. The greater the affinity of the ion for the surface, the greater the shift in PZC. If the ion affinity is very high, the surface may

DropBooks

be saturated at very small concentrations. In this case, the $\sigma_0 = f(pH)$ curves do have a common intercept but it does not shift with electrolyte concentration. This is why it is necessary to use several electrolytes to measure the actual position of the PZC.

6.4 COMPONENTS OF THE SURFACE COUNTERCHARGE

When particles are suspended in a medium of given acidity, they acquire, in the presence of an electrolyte that does not adsorb specifically, a positive charge for pH < PZC, or a negative charge for pH > PZC. How is this surface charge compensated for in the solution and how can the shielding effect of counterions be measured?

Shielding of charged surface sites is described quantitatively by the Esin–Markov coefficient, β [18,22]. This coefficient was introduced initially in the case of the mercury/electrolyte interface. It represents the variation in applied potential required to maintain a constant surface charge when electrolyte acitivity increases:

$$\beta = \frac{\partial E}{\partial(\ln \gamma c)_\sigma}$$

where E is the applied external potential and γ is the electrolyte activity coefficient at concentration c.

The surface potential of oxides is related to the concentration of PDIs, and hence it is also related to the pH. Therefore, β can also be expressed as

$$\beta = \frac{\partial \mathrm{pH}}{\partial(\log \gamma c)_\sigma}$$

Experimentally, β is determined using the $\Delta \mathrm{pH}/\Delta \log \gamma c$ ratio, which represents the horizontal distance between the curves in Figure 6.4 for a given spread in ionic activity of the medium. The usefulness of this parameter is that it allows a calculation of the components of the countercharge of the colloid.

If σ^- and σ^+ are the respective contributions from anions and cations to the surface countercharge, then $\sigma^- + \sigma^+ = -\sigma_0$, where σ_0 is the net surface charge.

Thermodynamic considerations [19] show that in the case of an electrolyte $[z^+ : z^-]$

$$\beta = -\frac{1}{z^+} - \frac{z^+ + z^-}{z^+ z^-}\left(\frac{\partial \sigma^-}{\partial \sigma_0}\right)_a = +\frac{1}{z^-} + \frac{z^+ + z^-}{z^+ z^-}\left(\frac{\sigma^+}{\sigma_0}\right)_a$$

where a is the ionic activity.

For a [1 : 1] electrolyte, integration of these expressions gives

$$\sigma^+ = -\frac{\sigma_0}{2} + \frac{1}{2}\int_0^{\sigma_0} \beta \, d\sigma + \sigma^+_{PZC} \qquad \sigma^- = -\frac{\sigma_0}{2} + \frac{1}{2}\int_0^{\sigma_0} \beta \, d\sigma + \sigma^-_{PZC}$$

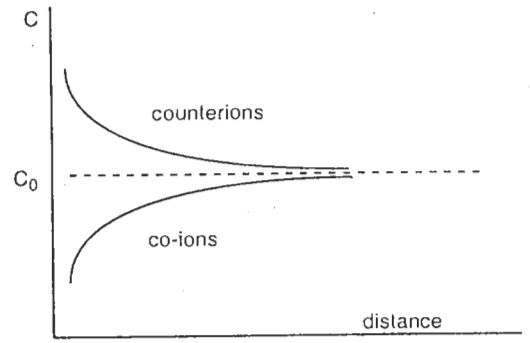

Figure 6.7 Concentration profile of the constituents to the surface countercharge near the PZC

where $\sigma^+_{PZC} + \sigma^-_{PZC} = 0$. Here σ^+_{PZC} and σ^-_{PZC} are the contributions of the cations and anions to the countercharge at PZC ($\sigma_0 = 0$).

If there is no specific adsorption and if the number of ionized sites is zero at PZC (see Section 7.1.3), then $\sigma^+_{PZC} = \sigma^-_{PZC} = 0$ and $\beta = 0$ at the PZC.

Near the PZC ($\beta \approx 0$), we may write $\partial\sigma^-/\partial\sigma_0 \approx \partial\sigma^+/\partial\sigma_0 \approx -1/2$ and

$$\sigma^- \approx \sigma^+ \approx -\sigma_0/2$$

This shows that cations and anions have an equal contribution to the compensation for the surface charge. At the PZC, there is no charge and no countercharge, but if σ_0 becomes slightly positive, for example, half the charge σ_0 is compensated for by excess anions from the electrolyte (counterions attracted by the surface), and the other half is provided by a deficit in cations (co-ions repelled by the surface). The ionic concentration profile is shown in Figure 6.7.

If the surface charge increases, the β coefficient increases in absolute value towards ± 1. If $\sigma_0 < 0$, β decreases towards -1, σ^- towards 0 and σ^+ towards $-\sigma_0$. If $\sigma_0 > 0$, β increases towards $+1$, σ^+ towards 0 and σ^- towards $-\sigma_0$. Essentially, the electric charge is compensated for by ions of opposite charge [22,23]. Ions of the same charge as the surface are repelled and their concentration is negligible near the surface.

6.5 REFERENCES

1. G.A. Parks, *Chem. Rev.* 65, 177 (1965).
2. G.A. Parks, P.L. De Bruyn, *J. Phys. Chem.* 66, 967 (1962).
3. F.J. Micale, D. Kiernan, A.C. Zettlemoyer, *J. Colloid Interface Sci.* 105, 570 (1985).
4. G.Y. Onoda, J.A. Casey, *Ultrastructure Processing of Ceramics, Glasses and Composites*, L.L. Hench, D.R. Ulrich Eds, John Wiley & Sons, New York (1984), p. 374.
5. D. Mc Robinson, J.A. Pask, D.N. Fuerstenau, *J. Am. Ceram. Soc.* 47, 516 (1964).
6. E. McCafferty, A.C. Zettlermoyer, *Disc. Faraday Soc.* 52, 239 (1971).

7. H.F. Holmes, E.L. Fuller, C.H. Secoy, *J. Phys. Chem.* **72**, 2095 (1968).
8. M.L. Hair, W. Hertl, *J. Phys. Chem.* **73**, 4269 (1969).
9. Y.G. Bérubé, P.L. De Bruyn, *J. Colloid Interface Sci.* **28**, 92 (1968).
10. B.W. Ninham, *Pure and Appl. Chem.* **53**, 2135 (1981).
11. J. Israelachvili, *Intermolecular and Interface Forces*, Academic Press (1985).
12. J. Lyklema, *Pure and Appl. Chem.* **53**, 2199 (1981).
13. H.M. Jang, D.W. Fuerstenau, *Langmuir* **3**, 1114 (1987).
14. G.Y. Onoda, P.L. De Bruyn, *Surf. Sci.* **4**, 48 (1966).
15. Y.G. Bérubé, P.L. De Bruyn, *J. Colloid Interface Sci.* **27**, 305 (1968).
16. L.G. Fokking, A. De Keizer, J. Lyklema, *J. Colloid Interface Sci.* **118**, 454 (1987).
17. R. Sprycha, *J. Colloid Interface Sci.* **102**, 173 (1984).
18. J. Lyklema, *J. Colloid Interface Sci.* **99**, 109 (1984).
19. A. Breeuwsma, J. Lyklema, *Disc. Faraday Soc.* **52**, 324 (1971).
20. A. Breeuwsma, J. Lyklema, *J. Colloid Interface Sci.* **43**, 437 (1973).
21. J. Lyklema, *Croat. Chem. Acta* **60**, 371 (1987).
22. J. Lyklema, *J. Electroanal. Chem.* **37**, 53 (1972).
23. R. Sprycha, M. Kosmulski, J. Szczypa, *J. Colloid Interface Sci.* **128**, 88 (1989).

DropBooks

7

Modeling of the Oxide–Solution Interface

To the previous phenomenological considerations, it is necessary to add a quantitative approach that could link the characteristics of the medium with those of the surface. More specifically, the acid–base characteristics of the surface and the charge variation as a function of pH must be characterized. Unfortunately, very few surface-specific experimental quantities are accessible to experiment, and the structural details of the surface are usually unknown or impossible to determine. Building a model of the oxide–solution interface is therefore required in order to understand the behavior of particles in suspensions.

7.1 SURFACE ACIDITY

Is it possible quantitatively to describe the variation in the surface charge of an oxide with the acidity of the medium and predict the value of the PZC?

Structural considerations aside, surface group acidity can be characterized by the following equilibria:

$$-\mathrm{MOH}_2^+ \Longleftrightarrow -\mathrm{MOH} + \mathrm{H}_s^+, \qquad K_+^0 = \frac{[-\mathrm{MOH}][\mathrm{H}_s^+]}{[-\mathrm{MOH}_2^+]} \tag{7.1}$$

$$-\mathrm{MOH} \Longleftrightarrow -\mathrm{MO}^- + \mathrm{H}_s^+, \qquad K_-^0 = \frac{[-\mathrm{MO}^-][\mathrm{H}_s^+]}{[-\mathrm{MOH}]} \tag{7.2}$$

The constants K_+^0 and K_-^0 involve the local proton concentration $[\mathrm{H}_s^+]$ in equilibrium with surface groups in their immediate environment. These protons are subjected to the electrical charge of the surface. In order to relate the local proton concentration to the proton concentration in the solution in zones unaffected by the surface charge, we must consider their electrochemical potential.

The electrochemical potential μ_i^* of ion i of charge z_i subjected to a local electrostatic field ψ is expressed as a function of its chemical potential μ_i as

$$\mu_i^* = \mu_i + z_i F\psi$$

where F is the Faraday constant, $96\,500\,\mathrm{C\,mol^{-1}}$. For the i species distributed between two phases A and B, the equilibrium condition is

$$\mu^*_{i\mathrm{A}} = \mu^*_{i\mathrm{B}}$$

or

$$\mu^0_{i\mathrm{A}} + RT\ln C_{i\mathrm{A}} + z_i F\psi_{\mathrm{A}} = \mu^0_{i\mathrm{B}} + RT\ln C_{i\mathrm{B}} + z_i F\psi_{\mathrm{B}}$$

where $C_{i\mathrm{A}}$ and $C_{i\mathrm{B}}$ are the concentrations of ion i in both phases ($c_i = C_i/N_{\mathrm{A}}$, with C_i being the concentration in $\mathrm{mol\,l^{-1}}$, and N_{A} Avogadro's number).

Assuming that the standard chemical potentials μ^0_i are the same in both phases, and that the electrical potential is zero in one of them ($\psi_{\mathrm{B}} = 0$), we can write

$$C_{i\mathrm{A}} = C_{i\mathrm{B}}\exp(-z_i F\psi_{\mathrm{A}}/RT)$$

This is Maxwell–Boltzmann's equation, in which ψ_{A} is the electrical potential at the point where $C_{i\mathrm{A}}$ is measured. If $C_{i\infty}$ is the concentration in ion i far from the particle, in the zone not affected by surface electrical charge, the concentration of i at a distance r is

$$C_{ir} = C_{i\infty}\exp(-z_i F\psi_r/RT) \tag{7.3}$$

For the protons subjected to the electrical potential ψ_0 at the surface of the particles, we can write

$$[\mathrm{H}^+_s] = [\mathrm{H}^+]\exp(-F\psi_0/RT) \tag{7.4}$$

$[\mathrm{H}^+]$ is the proton concentration in the solution, far from the interface (which controls the pH). Using (7.4) in (7.1) and (7.2) gives

$$K^0_+ = \frac{[-\mathrm{MOH}][\mathrm{H}^+]}{[-\mathrm{MOH}^+_2]}\exp(-F\psi_0/RT), \qquad K^0_- = \frac{[-\mathrm{MO}^-][\mathrm{H}^+]}{[-\mathrm{MOH}]}\exp(-F\psi_0/RT)$$

or

$$K^0_+ = K^+\exp(-F\psi_0/RT), \qquad K^0_- = K^-\exp(-F\psi_0/RT) \tag{7.5}$$

In these expressions, K^+ and K^- are the affinity ratios. They are called the intrinsic constants and characterize the acidity of surface groups in the absence of an electric field ($\psi_0 = 0$).

One of the main difficulties in understanding the physicochemistry of particles is the identification of the reaction sites on the surface. Most often, the effective structure of the surface is unknown. The solid may be amorphous or, if it is crystallized, the identification of faces and their relative amounts cannot be known. The morphology of the particles is also difficult to determine and it is not necessarily uniform. Electrophoretic measurements allow the determination of the acidity ranges in which particles carry a positive or negative charge. With this technique it is also possible to determine when the sign of the surface charge changes. Since more detailed information is not available, we are limited to considering an average

behavior of the surface, with one type of amphoteric surface sites. This means that the sites involved in equilibria (7.1) and (7.2) are *the same* as those involved in equilibria (7.5). It is obvious that this description of the surface sites is chemically unrealistic, because *two* protons reacting on the *same* ligand would involve considerable electrostatic repulsions. For monomeric species in solution, the same cation cannot successively exhibit the three aquo, hydroxo and oxo forms. For surface sites, the constraints that limit acid–base equilibria are even stronger.

In the absence of a good technique able to characterize reaction sites, surface acidity is considered to be an average value. The constants K^0_+ and K^0_- (or K^+ and K^-) related to amphoteric sites are often treated as adjustable parameters in models of the oxide–solution interface. A model of multiple site complexation has recently allowed a better description of the surface of oxide colloids, as well as an interpretation of their behavior.

7.1.1 SURFACE ACIDITY INTRINSIC CONSTANTS: THE MULTISITE COMPLEXATION (MUSIC) MODEL [1,2]

The model is partially derived from analyses by Kossiakoff and Harker [3] and by Parks [4]. The model assumes that it is possible quantitatively to assess the strength of oxyacids using electrostatic considerations.

The acid–base character of oxygenated surface groups is a function of the degree of compensation for the charge on oxygen by the surrounding cations. In an ionic solid, electroneutrality results from the mutual and local compensation for the charge of ions surrounding themselves with ions of the opposite charge. In order to account for the geometry of the ionic arrangement, Pauling introduced the concept of formal bond valence, $v = z/N$, defined as the ratio of the charge of the cation z to its coordination number N. It expresses the degree of charge compensation for a bond. For example, in $\mathrm{Al(OH)_3}$, gibbsite, the +3 charge of aluminum in coordination 6 is compensated for by that of six $\mathrm{OH^-}$ ions. The bond valence of the cation is $v = z/N = 3/6 = 1/2$. In other words, the charge of each $\mathrm{HO^-}$ in the solid is compensated for by a fraction of the charge of two $\mathrm{Al^{3+}}$. The charge of the anion is equal to the sum of the bond valences around it, and the compound can be formally written $\mathrm{Al(OH)_{6/2}}$.

Compensation for the negative charge of surface oxygens by coordinated cations is not always complete. A formal partial charge δ may remain on the surface ligands. For example, for singly coordinated OH ligands, the formal charge δ can be variable:

Si–OH	$v = 4/4 = 1$	$\delta = 1 - 2 + 1 = 0$	$\mathrm{Si–OH^0}$
Ti–OH	$v = 4/6 = 2/3$	$\delta = 2/3 - 2 + 1 = -1/3$	$\mathrm{Ti–OH^{-1/3}}$
Al–OH	$v = 3/6 = 1/2$	$\delta = 1/2 - 2 + 1 = -1/2$	$\mathrm{Al–OH^{-1/2}}$
Mg–OH	$v = 2/6 = 1/3$	$\delta = 1/3 - 2 + 1 = -2/3$	$\mathrm{Mg–OH^{-2/3}}$

For a doubly or triply coordinated OH:

Al_2–OH	$v = 1/2$	$\delta = 2 \times 1/2 - 2 + 11 = 0$	Al_2–OH^0
Al_3–OH	$v = 1/2$	$\delta = 3 \times 1/2 - 2 + 1 = +1/2$	Al_3–$OH^{+1/2}$

The charge $\delta = nv - 2 + p$ (p is the number of protons of the surface ligand) on the oxygen atoms causes them to exhibit an acid–base character. Their protonation equilibria are

$$M_n\text{–}O^{(nv-2)} + H^+ \Longleftrightarrow M_nOH^{(nv-1)}, \qquad K_{n,1} \tag{7.6}$$

$$M_n\text{–}OH^{(nv-1)} + H^+ \Longleftrightarrow M_nOH_2^{(nv)}, \qquad K_{n,2} \tag{7.7}$$

For consistency with the previously defined constants, the intrinsic dissociation constants are

$$K_{n,1} = \frac{[M_nO^{(nv-2)}][H^+]}{[M_nOH^{(nv-1)}]} \quad \text{and} \quad K_{n,2} = \frac{[M_nOH^{(nv-1)}][H^+]}{[M_nOH_2^{(nv)}]}$$

Since the acidity of a group increases with increasing positive formal charge, the MUSIC model allows a simple calculation of acidity constants, starting from electrostatic considerations.

The change in free enthalpy of reactions (7.6) and (7.7) includes a purely electrostatic component ΔG^0_{el} corresponding to the electrical energy involved as the proton comes closer to the surface, and other 'chemical' components ΔG^0_{ch}:

$$\Delta G^0 = \Delta G^0_{el} + \Delta G^0_{ch} \tag{7.8}$$

The calculation consists in calculating the electrostatic term and in describing explicitly the parameters involved in the constants $K_{n,p}$. The use of the bond valence concept simplifies the calculation by providing a way of removing the influence of other ligands in the coordination sphere.

Assuming point charges, the term ΔG^0_{el}, is due to the approach of the proton and to O–H or OH–H and M–H interactions:

$$\Delta G^0_{el} = \frac{Z_H Z_{O(H)} Ne^2}{4\pi\varepsilon_1 r} + \frac{nZ_H vNe^2}{4\pi\varepsilon_2 L} \tag{7.9}$$

where L is the M–H distance, r is the O–H distance (Figure 7.1), $Z_H = 1$, $Z_O = -2$ and $Z_{OH} = -1$. Here ε_1 and ε_2 are the microscopic effective dielectric constants, and ε_2 has no real physical significance owing to the simplicity of the model. It is involved in only one term representing a sum of electrostatic interactions.

Taking into account K as the dissociative constant of the considered reactions, the equilibria constant is

$$\Delta G^0 = -RT \ln(1/K) = \Delta G^0_{el} + \Delta G^0_{ch} \tag{7.10}$$

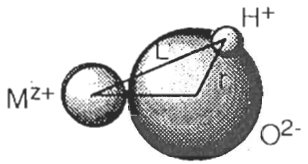

Figure 7.1 Geometry of the –M–OH surface groups

or

$$-RT \ln(1/K) = \Delta G^0_{ch} + \frac{Z_H Z_{O(H)} Ne^2}{4\pi\varepsilon_1 r} + \frac{nZ_H vNe^2}{4\pi\varepsilon_2 L} \tag{7.11}$$

or again

$$\log(1/K) = pK = A - \frac{Bnv}{L} \tag{7.12}$$

with

$$A = -\frac{Z_H Z_{O(H)} Ne^2}{2.3RT4\pi\varepsilon_1 r} - \frac{\Delta G^0_{ch}}{2.3RT} \quad \text{and} \quad B = \frac{Z_H Ne^2}{2.3RT4\pi\varepsilon_2}$$

where A and B are constants which can be estimated using solution chemistry data. They are needed in the calculation of the intrinsic constant K, using v and L.

The protonation of oxo or hydroxo monomers in solution:

$$M\text{–}O^{(v-2)} + H^+ \Longleftrightarrow MOH^{(v-1)}, \qquad K^m_{1,1} \tag{7.13}$$

$$M\text{–}OH^{(v-1)} + H^+ \Longleftrightarrow MOH_2^{(v)}, \qquad K^m_{1,2} \tag{7.14}$$

is characterized by equilibrium constants [5] which are indeed correlated to the v/L ratio for elements of similar electronic structure. This is true for a wide range of formal charges (1–5) and coordination numbers (4–8) (Figure 7.2). The intrinsic constants $K^m_{1,x}$ in the protonation equilibria of monomers can therefore be written as

$$\log(1/K^m_{1,x}) = pK^m_{1,x} = A' - \frac{Bv}{L} \tag{7.15}$$

which is analogous to (7.12) for $n = 1$.

The parallel straight lines in Figure 7.2 indicate that the successive protonation constants of oxo and hydroxo species are about 14 units apart. This difference is roughly the same for water couples (H_3O^+/H_2O, pK = 0, H_2O/HO^-, pK = 14). This difference is quite large because the protonation steps take place on the same ligand and involve strong H–H repulsions. In polyacids, successive pK values are distant by about 5 pK units [6].

One may assume that for surface reactions the main difference with monomeric species in solution is the ΔG^0_{ch} term in the expression for the intrinsic constant

DropBooks

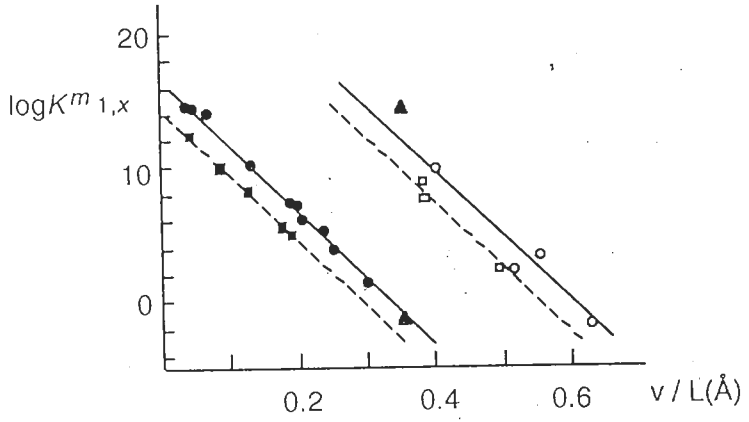

Figure 7.2 Protonation constants of hydroxo and oxo monomer complexes as a function of the bond–valence/M–H distance ratio. ● is for the protonation of neutral hydroxo complexes of metals with a rare gas configuration ($\log K^m_{1,2}$); ○ is for the protonation of oxo forms of the same elements ($\log K^m_{1,1}$). Constants $\log K^m_{1,1}$ and $\log K^m_{1,2}$ of d^{10} elements are denoted by ■ and □, and those of water (OH and H_2O) are labeled ▲; L values are estimated from ionic radii. Reproduced by permission of Academic Press from [1]

[equation (7.11)], assuming that the difference between $K_{n,1}$ and $K_{n,2}$ remains the same. For aluminum, the protonation constant of the $Al(OH)_3$ monomer, $K^m_{1,2}$, is 5.7 [5]. In gibbsite $Al(OH)_3$, a material well defined structurally and involving monocoordinated surface groups $-Al(OH)^{-1/2}$, the experimentally determined $K_{1,2}$ is 10 ± 0.5 [1]. The difference between pK values is caused by the structural and proximity constraints to which the protonable groups are subjected.

In order to obtain the pK of surface groups, it is necessary to change the A' term in (7.15), i.e. effectively shift the straigtht lines in Figure 7.2. Using the experimentally determined value of the protonation constant of simply coordinated Al–OH groups, one obtains average values $A = 34.06$ and 20.16 (for $K_{n,1}$ and $K_{n,2}$ steps respectively) and $B = 52.7$ (L is in angstroms). Used in (7.12), these values allow the calculation of protonation constants of singly, doubly or triply coordinated groups. The M–H distance, L, which varies in each case, is obtained from crystallographic data. A few examples are given below.

Gibbsite $Al(OH)_3$ particles look like hexagonal platelets (Figure 7.3). The large faces 001 only exhibit doubly coordinated OH groups (density is 13.8 groups/nm^2). The sides of the particles ($hk0$ faces) contain single and doubly coordinated OH groups (9.6 and 4.8 groups/nm^2 respectively). For singly coordinated groups, the $L_{(M-H)}$ distance is 2.59 Å [2]. Equation (7.12) gives

$$pK_{1,2} = 20.16 - 52.7 \times 0.5/2.59 = 9.98$$

$$-Al\text{–}OH^{-1/2} + H^+ \Longleftrightarrow -Al\text{–}OH_2^{+1/2}, \qquad pK_{1,2} = 10$$

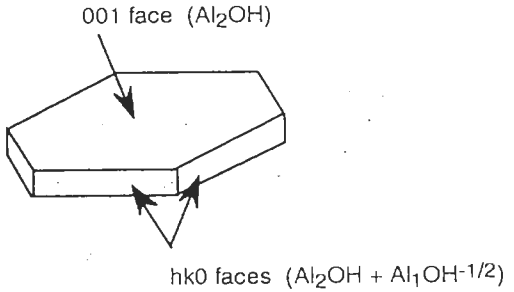

Figure 7.3 Gibbsite particle $Al(OH)_3$

For doubly coordinated groups [$L_{(M-H)} = 2.43$ Å], a similar calculation gives

$$pK_{2,1} = 34.06 - 52.7/2.43 = 12.37$$

$$-Al_2\text{–}O^- + H^+ \Longleftrightarrow -Al_2\text{–}OH, \qquad pK_{2,1} = 12.3$$

and

$$pK_{2,2} = 20.16 - 52.7/2.43 = -1.53$$

$$-Al_2\text{–}OH + H^+ \Longleftrightarrow -Al_2\text{–}OH_2^+, \qquad pK_{2,2} = -1.5$$

The pK of the $-AlO^-/-AlOH^{-1/2}$ equilibrium ($pK_{1,1} = 23.88$) is very high and the singly coordinated groups are therefore present only as $-Al\text{–}OH^{-1/2}$ or $-Al\text{–}OH_2^{+1/2}$, depending on the pH. Doubly coordinated groups exist only as $-Al_2\text{–}OH$ within the usual pH ranges.

Acicular particles of goethite α-FeOOH have three types of face. The 100 faces bear singly (I), doubly (II) and triply coordinated (III) OH ligands (Figure 7.4). The density of all three types is the same (3.3 groups/nm^2), as calculated using the dimensions of the unit cell. The 010 and 001 faces carry type (I) and type (II) groups (7.1 and 8.6 groups/nm^2 respectively).

The calculated protonation constants are

$$-Fe\text{–}OH^{-1/2} + H_s^+ \Longleftrightarrow -FeOH_2^{+1/2} \qquad pK_{1,2} = 10.7$$

$$-Fe_2 - O^- + H_s^+ \Longleftrightarrow -Fe_2\text{–}OH \qquad pK_{2,1} = 13.7$$

$$-Fe_2\text{–}OH + H_s^+ \Longleftrightarrow -Fe_2\text{–}OH_2^+ \qquad pK_{2,2} = 0.1$$

$$-Fe_3\text{–}O^{-1/2} + H_s^+ \Longleftrightarrow -Fe_3\text{–}OH^{+1/2} \qquad pK_{3,1} = 4.3$$

The $-Fe_2\text{–}OH$ groups are chemically inert and do not contribute to the charge within usual pH ranges. Figure 7.5 shows the degree of protonation of various surface groups as a function of the acidity of the solution.

CeO_2 is also a good example [7]. The 100 faces of the particles carry doubly coordinated groups Ce_2–OH (6.8 groups/nm^2). The 111 faces carry tricoordinated Ce_3–OH and singly coordinated Ce–OH groups in equal amounts (7.9 groups of

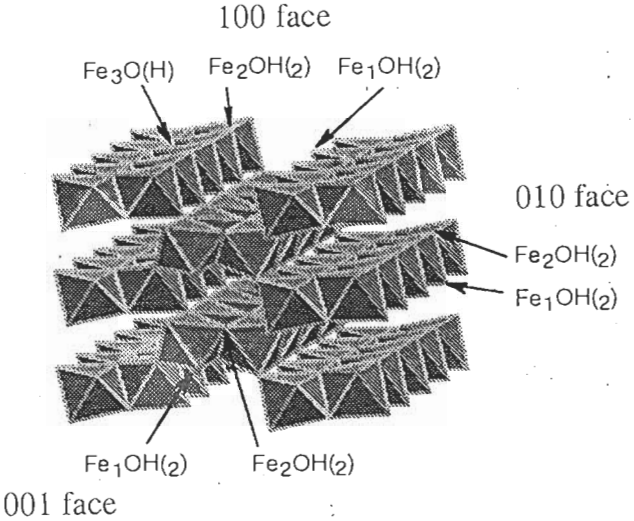

Figure 7.4 Crystal of goethite showing the surface structure of faces 100, 001 and 010

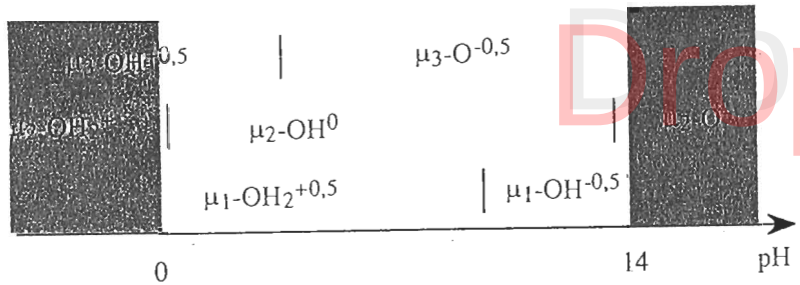

Figure 7.5 Protonation range of various groups on the surface of goethite

each type/nm^2). The same is true for the 110 faces (9.6 groups/nm^2). Their calculated acidity constants are

$$Ce_1{-}O^{-3/2} + H^+ \Longleftrightarrow Ce_1{-}OH^{-1/2} \quad pK_{1,1} = 23 \quad (a)$$

$$Ce_1{-}OH^{-1/2} + H^+ \Longleftrightarrow Ce_1{-}OH_2^{+1/2} \quad pK_{1,2} = 9.2 \quad (b)$$

$$Ce_2{-}O^- + H^+ \Longleftrightarrow Ce_2{-}OH^0 \quad pK_{2,1} = 14 \quad (c)$$

$$Ce_2{-}OH^0 + H^+ \Longleftrightarrow Ce_2{-}OH_2^+ \quad pK_{2,2} = 0 \quad (d)$$

$$Ce_3{-}O^{-1/2} + H^+ \Longleftrightarrow Ce_3{-}OH^{+1/2} \quad pK_{3,1} = 4.2 \quad (e)$$

$$Ce_3{-}OH^{+1/2} + H^+ \Longleftrightarrow Ce_3{-}OH_2^{+3/2} \quad pK_{3,2} = -9.8 \quad (f)$$

Table 7.1 Characteristics of the hydroxylated groups on the surface of aluminum oxide Al_2O_3

Surface groups	$-Al{-}OH^{-1/2}$	$-Al_2{-}OH$	$-Al_3{-}OH^{+1/2}$
Calculated $pK_{n,1}$	24	12.3	1.6
Bond energy of the proton (eV) [8]	21	19.4	17.7
Infrared absorption frequency (cm^{-1}) [9]	3785–3800	3740–3745	3700–3710

Equilibria (a), (c), (d) and (f) do not occur within usual acidity ranges. The only surface groups present are $Ce_1{-}OH^{-1/2}$, $Ce_2{-}OH^0$ and $Ce_3{-}OH^{+1/2}$.

The 100 faces, which carry only doubly coordinated groups [equilibria (c) and (d)], remain practically unchanged in the entire acidity range. Faces 111 and 110 are always unchanged at any pH [equilibria (b) and (e)]. The PZC of these faces (which is in fact an isoelectric point, see Section 7.1.3) is close to 7 since they have both types of group. Therefore, when the morphology of the particles and the crystal structure of the faces are known, it is possible to calculate the charge as a function of solution pH, and to calculate the PZC (see Section 7.3.3).

The calculated values of the equilibrium constants are quite reasonable (see Section 7.3.3). The acidity of surface groups increases notably with the degree of coordination of the hydroxylated groups. This effect can also be shown by calculating the bond energy of the proton in the hydroxyl groups coordinated to the surface of model clusters [8]. The bond energy decreases with increasing coordination of oxygen (Table 7.1). The weakening of the O–H bond with the coordination number of the hydroxyl ligand is also reflected in the decrease in its infrared resonance frequency [9] (Table 7.1).

It is interesting to note that, in these examples, no group exhibits amphoteric character, in spite of the fact that some faces of the particles might be positively or negatively charged. Each type of group is only involved in one protonation equilibrium over the entire pH range. Therefore, *the successive involvement of two protons on the same group* appears completely unrealistic. This seems to be a general property of the surface of oxide particles that is contrary to widely held beliefs [10].

A thorough analysis of the origin of the electrostatic charge can explain the preferential development of some faces of a crystal. It also explains, to a certain extent, the irreversible and ordered aggregation which leads to the formation of tactoids [11] (see Chapter 8).

7.1.2 EVALUATION OF THE PZC

If details of the morphology and structure of the particles are unknown, surface acidity and PZC can be characterized only using average values of the equilibrium constants. It is assumed that surface groups are able to react with two protons at most, to form a molecule of coordination water, which leaves an uncompensated charge $+v$ on the metal [12]. The approach taken by Parks [4] and the

DropBooks

MUSIC model allows us to write the following equilibrium:

$$M{-}O^{(2-v)-} + 2H_s^+ \Longleftrightarrow M{-}OH_2^v \tag{7.16}$$

characterized by the intrinsic dissociation constant

$$K = \frac{[MO^{(2-v)-}][H^+]^2}{[MOH_2^v]} \tag{7.17}$$

At the PZC, the overall neutrality of the surface imposes

$$(2 - v)[MO^{(2-v)-}] = v[MOH_2^v]$$

The constant in (7.17) may therefore be expressed as

$$K = \frac{v[H^+_{PZC}]^2}{2 - v}$$

or

$$pK = \log \frac{2 - v}{v} + 2PZC \tag{7.18}$$

Substitution of (7.17) in (7.12) gives

$$PZC = A - B\frac{v}{L} - \frac{1}{2}\log \frac{2 - v}{v} \tag{7.19}$$

In this equation, the A and B terms are constants analogous to the constants in equation (7.12). In this case, both protons are treated as a single point charge +2; L is the M–H distance.

Constants A and B are calculated using the experimental values of the PZC of α-Al_2O_3 (PZC = 9.1) and MgO (PZC = 12.4) [12]. The calculated values of the PZC for oxides and hydroxides are generally in good agreement with experimental data (Table 7.2) [4,12].

Since A and B are calculated with 6-coordinated elements (7.19), there is a large difference for compounds with a coordination number different from 6. In solids containing hydrogen bonds, the experimental PZC is lower than the calculated one because hydroxyl ions in the lattice tend to anchor hydroxyl ions of the solution within the surface layer [4]:

$$-M{-}OH + OH^- \longrightarrow -M{-}OH\cdots OH^-$$

This anchoring is not dissociative. Corrective terms must be added to equation (7.19) for elements stabilized by the crystal field because the CFSE is involved in the ΔG^0_{ch} term of equation (7.12).

This model of the PZC and surface acidity constants appears to provide us with a rather simple and accurate characterization of the mechanism by which an oxide or hydroxide surface acquires a charge in an aqueous solution. In the absence of structural data, the reversal of the surface charge is explained by considering an

Table 7.2 Calculated and experimental data for the PZC of various solids [12] (the solids containing hydrogen bonds are in italics)

	Coordination					PZC	
Material	z	M	Ligand	v	v/L	calc.	exp.
MgO	2	6	6	1/3	0.107	12.4	12.4
$Mg(OH)_2$	2	6	3	1/3	0.109	12.3	12
ZrO_2	4	8	4	1/2	0.153	12.1	10–11
ZnO	2	4	4	1/2	0.167	×9.3	×9.3
$Zn(OH)_2$	*2*	*4*	*2*	*1/2*	*0.169*	×9.2	×7.8
α-Al_2O_3	3	6	4	1/2	0.171	×9.1	×9.1
α-AlOOH	*3*	*6*	–	*1/2*	*0.170*	×9.2	×7.7
γ-AlOOH	*3*	*6*	–	*1/2*	*0.171*	×9.1	×8.3
α-Fe_2O_3	3	6	4	1/2	0.164	×9.4	×9.4
α-FeOOH	*3*	*6*	–	*1/2*	*0.164*	×9.5	×9.1
γ-FeOOH	*3*	*6*	–	*1/2*	*0.166*	×9.4	×7.4
ThO_2	4	8	4	1/2	0.145	10.5	×9–9.3
Y_2O_3	3	6	4	1/2	0.152	10.1	×9.0
SnO_2	4	6	3	2/3	0.218	×6.7	×6.6
TiO_2	4	6	3	2/3	0.224	×6.3	×6.2
WO_3	6	6	2	1	0.340	×0.3	×0.5
SiO_2	4	4	2	1	0.382	−1.8	×1.8

average reaction site involving two steps of protonation:

$$M{-}O^- + 2H^+ \Longleftrightarrow M{-}OH + H^+ \Longleftrightarrow M{-}OH_2^+$$

This corresponds, in the MUSIC model, to $nv = 1$ (groups $Si{-}OH^0$, $Al_2{-}OH^0$, or $Fe_2{-}OH^0$, for example). If one of the values of pK is outside the range of pH accessible in solution, a single equilibrium occurs and PZC = pK. In some models, changes in surface charges with pH are analyzed with equilibrium constants that are mere tuning parameters and have no structural significance to the mechanism of charge acquisition (see Section 7.3.2).

7.1.3 POINT OF ZERO CHARGE OR ISOELECTRIC POINT?

These terms are used routinely in the literature, most often indiscriminately, to describe conditions in which the surface charge on colloidal particles is zero. However, they are two different concepts that must be defined clearly.

The surface charge of an oxide may be zero for two reasons:

- absence of positive or negative charges. The surface is characterized by a PZC. This is the case of the 001 faces of gibbsite (see Section 7.1.1).
- equal amounts of positive and negative charges. The IEP (isoelectric point) is the pH at which positive and negative charges compensate each other exactly (*hk*0 faces of gibbsite).

The difference between PZC and IEP is the fraction of ionized sites when the net charge is zero. This fraction depends on the relative strengths of the acids MOH_2^+ and MOH, and on that of the bases MOH and MO^-. (The previous model illustrates these concepts quite clearly.) This fraction can be calculated from the intrinsic constants of surface equilibria [equation (7.5)]:

$$pK^- - pK^+ = \Delta pK = \log \frac{[MOH]^2}{[MOH_2^+][MO^-]} \tag{7.20}$$

If ΔpK is high ($\Delta pK > 4$), $[MOH] \gg [MOH_2^+] = [MO^-]$. The acid MOH_2^+ is much stronger than the acid MOH, and the base MO^- is much stronger than the base MOH. The predominant species is MOH and the number of ionized species is very small. In this case, the PZC is used.

If ΔpK is small, the MOH_2^+ and MOH acids have similar strength. The same is true for bases MO^- and MOH. The number of charged groups MOH_2^+ and MO^- is large. The oxide is characterized by an IEP.

More quantitatively, if N is the total number of surface groups and $2N'$ is the number of charged groups when the net charge is zero, we have

$$N = [MOH_2^+] + [MOH] + [MO^-]$$
$$N' = [MOH_2^+] = [MO^-]$$

The fraction of positive or negative groups, $\theta = N'/N$, is

$$\Delta pK = 2 \log \frac{1 - 2\theta}{\theta}$$

The change in θ with ΔpK is given in Table 7.3.

In the case of ionic solids like AgI, all sites are charged when the net charge is zero ($\theta = 0.5$). In this case, the IEP is used. For most oxides, $\Delta pK > 2$–3. The fraction of ionized groups is small when the charge is zero, and the PZC concept should be used.

At the PZC of the oxide $[MO^-] = [MOH_2^+]$. The PZC is therefore defined as

$$PZC = 1/2(pK^+ + pK^-) = 1/2(pK_+^0 + pK_-^0) \tag{7.21}$$

This is of course a very general approach applicable only in the case of a two-pK system (two protons involved per surface group, see Section 7.1.2). A more refined analysis such as the MUSIC model shows that, in most cases, a single protonation equilibrium must be considered per surface group. The pH at which the net charge

Table 7.3

ΔpK	6	4	2	0
θ	9.9×10^{-4}	9.8×10^{-3}	8.3×10^{-2}	0.33
		PZC		PIE

is zero depends on the relative fractions of each type of group, as well as on their respective pK. For many oxides, cancellation of the global charge takes place through compensation, and most often, such surfaces are characterized by an IEP (see Section 7.1.1).

7.2 SURFACE CHARGE–POTENTIAL RELATIONSHIP

In order to improve the description of the electric charge distribution around particles, it is useful to divide the analysis into two parts: a study of the inner zone (the compact layer) and a study of the outer, or diffuse, zone of the double layer. The particles are assumed to be isolated and unable to interact with each other.

7.2.1 INNER PART OF THE DOUBLE LAYER

The ionization of surface MOH groups is characterized by the local equilibria (7.1) and (7.2). Under fixed acidity conditions, the net surface charge density σ_0 is

$$\sigma_0 = (F/A)([MOH_2^+] - [MO^-])$$

where A is the total surface area in $m^2\,l^{-1}$. Considering the total number of surface groups per unit area, N_s (in mol m^{-2}):

$$N_s = ([MOH_2^+] + [MOH] + [MO^-])/A$$

we can write

$$\sigma_0 = FN_s \frac{[MOH_2^+] - [MO^-]}{[MOH_2^+] + [MOH] + [MO^-]} \tag{7.22}$$

which, taking into account (7.5), may be rewritten as

$$\sigma_0 = FN_s \frac{([H^+]/K^+)\exp(-F\psi_0/RT) - (K^-/[H^+])\exp(F\psi_0/RT)}{1 + ([H^+]/K^+)\exp(-F\psi_0/RT) + (K^-/[H^+])\exp(F\psi_0/RT)} \tag{7.23}$$

which is the equation of state of the surface [13]. It links the charge σ_0 to the potential ψ_0 (at the surface) at a given pH.

The surface potential of an oxide ψ_0 is not directly accessible to experiment because no reversible electrode is able to carry out this measurement. However, it would be useful to know if a Nernst-type equation is likely to link the potential ψ_0 to the activity of the PDIs in solution. This is the case for the ionic solid AgI: the surface charge is acquired via adsorption of PDIs which also form the lattice. The adsorption equilibrium of Ag^+ ions, for example, is characterized by the equalization of the electrochemical potentials of these ions in the solid phase and in the solution:

$$(\mu_{Ag}^*)_c = (\mu_{Ag}^*)_s$$

DropBooks

The indices c and s refer to the crystal and the solution. Therefore

$$(\mu^0_{Ag})_c + RT\ln(a_{Ag})_c + F\psi_c = (\mu^0_{Ag})_s + RT\ln(a_{Ag})_s + F\psi_s \tag{7.24}$$

Far from the particle in the solution, $\psi_s = 0$, and when the net charge is zero (IEP), $\psi_c = 0$. Therefore

$$(\mu^0_{Ag})_c + RT\ln(a^*_{Ag})_c = (\mu^0_{Ag})_s + RT\ln(a^*_{Ag})_s + F\psi_s \tag{7.25}$$

The a^* refer to the activities at the IEP. Subtracting one equation from the other, we obtain

$$RT\ln(a_{Ag}/a^*_{Ag})_c + F\psi_c = RT\ln(a_{Ag}/a^*_{Ag})_s$$

Assuming that the activity of Ag^+ is constant in the crystal even as the charge changes, we can write

$$(a_{Ag})_c = (a^*_{Ag})_c \qquad \text{and} \qquad \psi_c = \frac{RT}{F}\ln(a_{Ag}/a^*_{Ag})_s$$

or

$$\psi_c \approx \frac{RT}{F}\ln\frac{[Ag^+]}{[Ag^+]_{PZC}} = 2.3\frac{RT}{F}(pAg_{PZC} - pAg) \tag{7.26}$$

This is the Nernst equation. It is valid assuming that the activity of Ag^+ on the surface of the particle is independent of the charge [14,15]. This is a valid assumption since, when the charge is zero (IEP), there is a large amount of Ag^+ (and I^-) ions on the surface ($\theta = 0.5$). Therefore, the development of the net surface charge does not significantly alter the number or the surroundings of Ag^+ ions on the surface.

For an oxide in which the PDIs are the protons, a relationship similar to (7.26) may be written:

$$\psi_N = \frac{2.3RT}{F}(PZC - pH) \tag{7.27}$$

Should we assume that the activity of charged surface sites remains constant when the pH of the solution changes (during the charging process)? Does the potential ψ_N, as defined above, effectively represent the surface potential ψ_0? [10,13,16].

From equations (7.1), (7.2), (7.4) and (7.21), we may write

$$\psi_0 = \frac{2.3RT}{F}(PZC - pH) - \frac{RT}{2F}\ln\frac{[MOH_2^+]}{[MO^-]}$$

or

$$\psi_0 = \psi_N + \frac{RT}{2F}\ln\frac{[MO^-]}{[MOH_2^+]} \tag{7.28}$$

Here $\psi_0 - \psi_N$ is a function of the ratio of the amounts of charged surface sites and becomes smaller as $[MO^-]/[MOH_2^+]$ becomes closer to 1. If ΔpK is high, the number of charged groups is small near the PZC [equation (7.20)]. When a net charge is acquired, the terms $[MOH_2^+]$ or $[MO^-]$ change with respect to each other, and the reaction of the surface to changes in pH no longer follows a Nernst-type relationship. However, if ΔpK is small, the number of charged groups is high at the PZC. The relative variation in $[MOH_2^+]$ and $[MO^-]$ is small during the development of the charge, and the surface does exhibit 'Nernstian' behavior [14,15,17]. Although Nernst's law does not rigorously apply to oxide surfaces, it is a good approximation when the difference between the pK values of surface equilibria is small.

7.2.2 DIFFUSE PART OF THE DOUBLE LAYER

The electrical charge of the particle surface creates, in its immediate surroundings in the electrolyte, an electrical perturbation attracting ions of opposite charge and repelling ions of identical charge. Counterions are subjected to the surface potential as well as to thermal agitation. They are distributed in a diffuse layer whose charge σ_d compensates for the surface charge σ_0. It is possible to determine the charge σ_d and to determine its distribution near the surface.

The net charge of the diffuse layer is

$$\sigma_d = \int_d^\infty \rho_r\, dr^3 \tag{7.29}$$

where d is the thickness of the Stern layer and ρ_r is the net charge density at a point r in the solution. This charge is related to the potential at the same point through Poisson's equation [18]:

$$\nabla^2\psi_r = -\rho_r/\varepsilon$$

where ε is the dielectric permittivity of the medium. It is the product of the relative permittivity of water (the dielectric constant), $\varepsilon_{water} = 78.5$, and the permittivity of vacuum, $\varepsilon_0 = 8.854 \times 10^{-10}\,C^2\,J^{-1}\,m^{-1}$. Hence, $\varepsilon_{water}\varepsilon_0 = 6.954 \times 10^{-10}\,C^2\,J^{-1}\,m^{-1}$.

For the sake of simplicity, the surface is often assumed to be planar, and we can write

$$d^2\psi_r/dr^2 = -\rho_r/\varepsilon \tag{7.30}$$

For a symmetrical electrolyte [z : z] of concentration C, the charge density ρ_r is expressed using equation (7.3):

$$\begin{aligned}\rho_r &= \Sigma z_i F C_{ir} = zF(C_r^+ - C_r^-) = zFC[\exp(-zF\psi_r/RT) - \exp(zF\psi_r/RT)] \\ &= 2zFC\sinh(-zF\psi_r/RT)\end{aligned} \tag{7.31}$$

(The charge density is the number of particles per unit volume, in moles per m^3.)

Hence, the Poisson–Boltzmann equation

$$d^2\psi_r/dr^2 = (2zec_\infty/\varepsilon)\sinh(-ze\psi_r/kT) \tag{7.32}$$

with the following boundary conditions: $\psi = \psi_d$ when $r = d$, the thickness of the Stern layer, and $\psi = 0$ ($d\psi/dr = 0$) when $r \to \infty$ (the surface is isolated).

Therefore, the charge of the diffuse layer [equation (7.29)] is

$$\sigma_d = \varepsilon \int_{\infty}^{d} (d^2\psi_r/dr^2)dr = \varepsilon[d\psi_r/dr]_{r=d} \tag{7.33}$$

Multiplying both sides of equation (7.32) by $2d\psi/dr$ gives

$$2(d\psi/dr)(d^2\psi_r/dr^2) = (4zFC/\varepsilon)\sinh(zF\psi_r/RT)[d\psi/dr]$$

which, after integration, gives

$$(d\psi/dr)^2 = (4CRT/\varepsilon)\cosh(zF\psi_r/RT) + \text{constant}$$

Because of boundary conditions, constant $= 4CRT/\varepsilon$, and hence

$$(d\psi/dr)^2 = (4CRT/\varepsilon)[\cosh(zF\psi_r/RT) - 1]$$

which can be rewritten as

$$(d\psi/dr)^2 = (2CRT/\varepsilon)[\exp(zF\psi_r/2RT) - \exp(-zF\psi_r/2RT)]^2$$

and hence

$$(d\psi/dr) = \pm(8CRT/\varepsilon)^{1/2}\sinh(zF\psi_r/2RT) \tag{7.34}$$

A negative sign is chosen since the absolute value of $(d\psi/dr)$ always decreases when ψ is positive, and vice versa. The absolute value of ψ always decreases as the distance from the surface increases. If (7.34) is introduced into (7.33), we obtain

$$\sigma_d = -(8\varepsilon CRT)^{1/2}\sinh(zF\psi_d/2RT) \tag{7.35}$$

which is Grahame's relation. In water at 25 °C, the charge of the diffuse layer is (for a symmetrical electrolyte [z : z] of concentration C)

$$\sigma_d = -0.1173\sqrt{C}\sinh(19.48z\psi_d) \tag{7.36}$$

with σ_d in C m^{-2}, C in mol l^{-1} and ψ_d in volts. Equation (7.36) shows that a variation in electrolyte concentration creates a variation in σ_d and/or in ψ_d. In order to calculate the size of the diffuse layer, i.e. the zone affected by electrical perturbations, we must know the dependence of ψ with the distance r. A second integration of the Poisson–Boltzmann equation (7.32) gives [18,19]

$$\psi_r = \frac{2RT}{\varepsilon}\ln\frac{1 + \gamma\exp[-\kappa(r-d)]}{1 - \gamma\exp[-\kappa(r-d)]} \tag{7.37}$$

with

$$\gamma = \frac{\exp(zF\psi_d/2RT) - 1}{\exp(zF\psi_d/2RT) + 1}$$

and $\kappa = (F^2\Sigma C_i z_i^2/\varepsilon RT)^{1/2} = (2F^2 I\, 10^3/\varepsilon RT)^{1/2}$, where I is the ionic strength, $I = (1/2)\Sigma z_i^2 c_i$. The 10^3 factor is due to the conversion from mol m^{-3} to mol l^{-1}.

For weak potentials, the electrical energy is small compared with thermal energy. Therefore, $zF\psi_d/2RT \ll 1$ or $z\psi_d \ll 50$ mV, and $\exp(zF\psi_0/2RT) \approx 1 + (zF\psi_0/2RT)$. Equations (7.36) and (7.37) can now be written, respectively, as

$$\sigma_d = -\varepsilon\kappa\psi_d \tag{7.38}$$

$$\psi_r = \psi_d \exp[-\kappa(r-d)] \tag{7.39}$$

The most important parameter in equations (7.37) to (7.39) is κ, which has the dimension of the reciprocal of length. In water at 25 °C, $\kappa = 0.329\sqrt{I}$ Å^{-1}. Distance κ^{-1} is the 'Debye–Hückel length' and represents the 'thickness' of the diffuse layer. This happens to be a misnomer because, over distance κ^{-1}, the potential decreases only by $\psi_d/\exp(1) = \psi_d/2.7$, but, in the weak potential approximation, the diffuse layer [equation (7.38)] can be treated as a parallel-plate capacitor $C_d = \varepsilon\kappa$ with plates separated by distance κ^{-1}. The variation in the potential in the solution, as a function of the distance from the surface, depends on the concentration and the charge of the ions present in the electrolyte (Figure 7.6).

The main observations from Figure 7.6 are:

- The size of the electrically affected zone is of the same order of magnitude of the size of the colloidal particles: $\kappa^{-1} = 30$ Å for a [1 : 1] electrolyte of concentration $C = 10^{-2}$ mol l^{-1}.
- The thickness of this zone is very sensitive to the concentration and the charge of ions in the electrolyte, i.e. very sensitive to the ionic strength. As these increase, the diffuse layer is compressed (κ^{-1} is small).

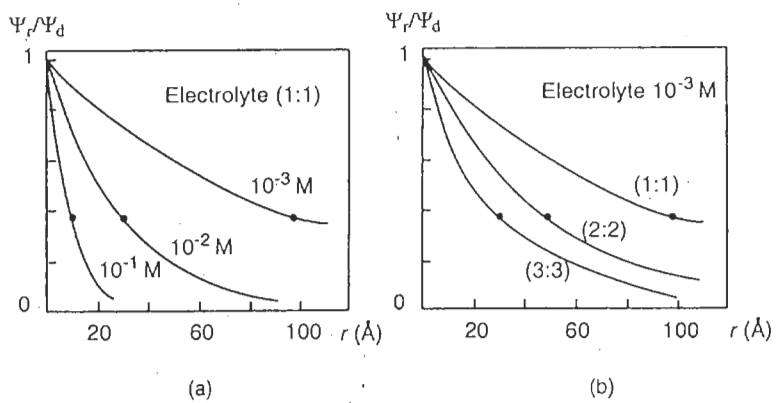

Figure 7.6 Variation in the potential in the diffuse layer, as a function of distance, calculated from the OHP (weak potential approximation). Influence of (a) electrolyte concentration (1:1) and (b) charges of ions in the electrolyte (z:z). Marker • indicates the distance κ^{-1}. Data from [18]

DropBooks

- The response of the double layer to a change in ionic strength is a change in the charge and/or the potential [equation (7.36) or (7.38)].

These observations will be particularly useful when we discuss interactions between colloidal particles.

7.2.3 INTERFACIAL CAPACITANCE

The potential ψ_0 on the surface of an oxide is an unknown and non-measurable quantity since there is no reversible electrode capable of measuring it. In addition, there is no simple analytical relationship between the charge and the surface potential. These two quantities may, however, be linked if the interface is assumed to be a capacitor of capacitance $K = \sigma_0/\psi_0$ [20]. In principle, the double-layer capacitance is a measure of the shielding effect of the surface charge by the countercharge: the better the shielding, the higher is σ_0 for a given potential ψ_0.

From a practical standpoint, the differential capacitance is considered, $C = d\sigma_0/d\psi_0$. It represents the slope of the curves $\sigma_0 = f(\psi_0)$ or $\sigma_0 = f(pH)$ for a given ionic strength [14,17]. This value is accessible experimentally from measurements of the change in surface charge as a function of pH [21]. It is assumed that the surface potential obeys Nernst's law. Both capacitances are related by the expression $C = K + \psi_0(dK/d\psi_0)$ [20] and they are equal for weak surface potentials.

If the Stern layer is distinguished from the diffuse layer in the interfacial zone, the surface potential may be written as

$$\psi_0 = (\psi_0 - \psi_d) + \psi_d$$

or

$$\frac{\psi_0}{\sigma_0} = \frac{\psi_0 - \psi_d}{\sigma_0} + \left(\frac{\psi_d}{-\sigma_d}\right)\left(\frac{-\sigma_d}{\sigma_0}\right) \tag{7.40}$$

If there is no specific adsorption, $\sigma_0 = -\sigma_d$, and hence

$$\frac{\psi_0}{\sigma_0} = \left(\frac{\psi_0 - \psi_d}{\sigma_0}\right) + \left(\frac{\psi_d}{-\sigma_d}\right) \quad \text{or} \quad \frac{1}{K} = \frac{1}{K_s} + \frac{1}{K_d}$$

The latter expression represents two capacitors in series. Here, K_s and K_d are the integral capacitances of the Stern layer and of the diffuse layer respectively. A similar expression is true for the differential capacitances:

$$\frac{1}{C} = \frac{1}{C_s} + \frac{1}{C_d} \tag{7.41}$$

The magnitude of C_s is typically around $1\ F\,m^{-2}$, and may be obtained from the total capacitance C (obtained experimentally) and from the capacitance of the diffuse layer, $C_d = \varepsilon/\kappa^{-1}$ [obtained with equations (7.38) and (7.35)] [21,22]. Assuming that ε' is the permittivity of the Stern layer of thickness d, then $C_s = \varepsilon'/d$. It was shown [22] that, for high ionic strengths (e.g. $1\ mol\,l^{-1}$), C_s is almost independent of the surface charge or electrolyte concentration. The variation in C_s for low ionic strengths should, in principle, account for some specific effects such as the penetration of counterions in the Stern layer, or a change in the orientation of water molecules in the solvent layer adjacent to the surface. However, the capacitance of the diffuse layer is very sensitive to electrolyte concentration [κ is proportional to $\sqrt{I}$, equation (7.37)]. Therefore, any factor increasing the ion concentration in the diffuse layer (potential and/or high ionic strength) also increases its capacitance. The $1/C_d$ term becomes small because the system behaves as if the capacitance were constant and equal to the capacitance of the internal layer.

If specific adsorption occurs, the adsorbed ions are assumed to be located on an average plane b within the Stern layer. This plane is called the inner Helmholtz plane (IHP) (see Section 7.3.2). The adsorbed ions develop a charge σ_b and are subjected to a potential ψ_b. The surface potential may therefore be written as

$$\psi_0 = (\psi_0 - \psi_b) + (\psi_b - \psi_d) + \psi_d \tag{7.42}$$

Dividing by σ_0 gives

$$\frac{\psi_0}{\sigma_0} = \frac{\psi_0 - \psi_b}{\sigma_0} + \left(\frac{\psi_b - \psi_d}{-\sigma_d}\right)\left(\frac{-\sigma_d}{\sigma_0}\right) + \left(\frac{\psi_d}{-\sigma_d}\right)\left(\frac{-\sigma_d}{\sigma_0}\right) \tag{7.43}$$

or

$$\frac{1}{C_t} = \frac{1}{C_1} + \frac{1}{C_2}\left(\frac{-\sigma_d}{\sigma_0}\right) + \frac{1}{C_d}\left(\frac{-q_d}{\sigma_0}\right) \tag{7.44}$$

where C_t is the total capacitance of three capacitors in series, C_1 and C_2 being the capacitance of the zones between the surface and the b plane (IHP), and between the b plane and the OHP, zones with permittivities ε_1 and ε_2 respectively; C_d is the capacitance of the diffuse layer.

Taking $R = (-\sigma_b/\sigma_0)$ and using $\sigma_0 + \sigma_b + \sigma_d = 0$, we get:

$$\frac{1}{C_t} = \frac{1}{C_1} + \left(\frac{1}{C_2} + \frac{1}{C_d}\right)(1 - R) \tag{7.45}$$

In the absence of specific adsorption, $\sigma_b = 0$, and $-\sigma_d = \sigma_0$, and hence

$$\frac{1}{C_t} = \frac{1}{C_1} + \frac{1}{C_2} + \frac{1}{C_d} \quad \text{with} \quad \frac{1}{C_1} + \frac{1}{C_2} = \frac{1}{C_s}$$

which are the results of equation (7.4).

7.3 MODELS OF THE OXIDE–SOLUTION INTERFACE

In order to explain the experimental data, i.e. obtain an accurate description of the change in surface charge as a function of the acidity of the medium ($\sigma_0 = f(pH)$ curves), many models have been developed [23,24]. All of them describe the surface reactions using mass-action laws and matter balances, with the surface potential being linked to the surface charge using an electrostatic model. The models differ in

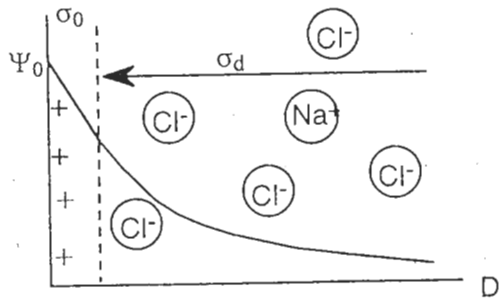

Figure 7.7 Two-layer model and the variation in the potential through the interface

where they place species in the interfacial zone, as well as in the equations used to link potential and surface charge. A description of the most frequently used models follows.

7.3.1 BASIC MODEL (TWO-LAYER)

In the most simple approach, we assume that the surface charge that developed as a result of acid–base reactions is compensated for by anions or cations from the electrolyte, which constitute the diffuse layer. The Stern layer is considered empty of any ion and is characterized by a differential capacitance C_s (Figure 7.7) [24,25].

Equations (7.23) and (7.36) express the relationship between charge and potential:

$$\sigma_0 = FN_s \frac{([H^+]/K^+)\exp(-F\psi_0/RT) - (K^-/[H^+])\exp(F\psi_0/RT)}{1 + ([H^+]/K^+)\exp(-F\psi_0/RT) + (K^-/[H^+])\exp(F\psi_0/RT)} \quad (7.23)$$

$$\sigma_d = -0.1173\sqrt{C}\sinh(19.5\psi_d) \quad (7.36)$$

These two equations involve four interfacial variables (σ_0, σ_d, ψ_0, ψ_d), two variables characterizing the medium (pH and electrolyte concentration C) and quantities specific to the surface (acidity constants K^+ and K^- and the total group density N_s).

The quantities accessible to the experiment are the surface charge σ_0 as a function of pH, the potential of the diffuse layer ψ_d, assimilated to the electrokinetic potential ζ, and the total density of reactive sites N_s. The equilibrium constants K^+ and K^- are determined graphically or numerically (see Section 7.3.2.) from the pH, σ_0 and N_s for various electrolyte concentrations and types. The MUSIC model (see Section 7.1.1) allows simplification in the calculation of the intrinsic constants K^+ and K^-.

The equations of the system are:

- The equation of state of the surface [equation (7.23)].
- The expression for the charge of the diffuse layer [equation (7.36)].
- The electroneutrality of the system: $\sigma_0 + \sigma_d = 0$.
- The capacitance $C_s = \sigma_0/(\psi_0 - \psi_d)$; C_s is obtained graphically or fitted and is of the order of $0.2–2\,F\,m^{-2}$.

This system of equations is resolved graphically and allows the calculation of the $\sigma_0 = f(pH)$ curves. A semiquantitative agreement with experimental data accounts for the position of the PZC of the oxide [25]. However, it is not possible properly to fit the curves $\sigma_0 = f(pH)$ and $\zeta = f(pH)$ with the same set of parameters. Generally speaking, the calculated surface charges σ_0 are much smaller than those measured via titration. This would suggest that the surface charge is partially compensated for by a charge located inside the Stern layer which contributes to a decrease in the electrokinetic potential.

7.3.2 SITE COMPLEXATION MODEL (TRIPLE-LAYER)

The concept used in this model is the idea that the surface charge, which is due to adsorption/desorption of protons, is partially shielded from the solution by the presence of counterions in the Stern layer [26,27]. This is confirmed experimentally (see Section 6.3.3). These ions are supposed to form 'complexes' with the surface groups. These complexes can be treated as ion pairs, but no specific bond type is defined in the model. This is why these ions are said to be specifically adsorbed, only to indicate that they can penetrate the Stern layer, whether the interactions are specific or not.

Specifically adsorbed ions are difficult to locate. They are supposed to be on an average plane b within the Stern layer, and hence the need for the introduction of a third layer. This plane is called the inner Helmholtz plane (IHP) and carries a charge σ_b (Figure 7.8), where adsorbed ions are subjected to a potential ψ_b. The b plane is separated from the surface by a distance of the order of the ionic radii of the adsorbed ions [26].

DropBooks

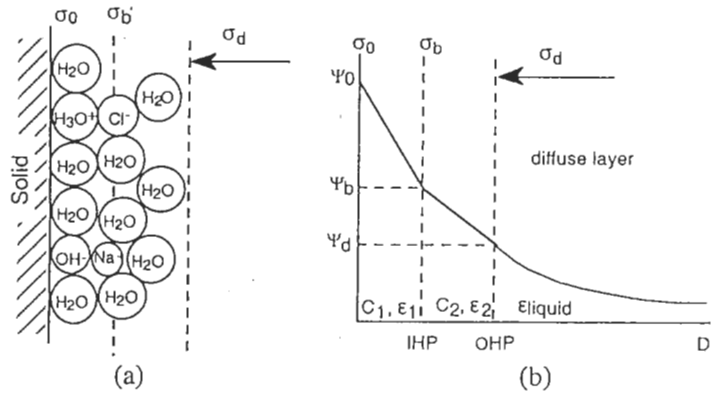

Figure 7.8 Oxide–solution interface with (a) the position of charged species on ideal planes and (b) the decrease in the potential starting from the surface. Reproduced by permission of Academic Press from [26]

The model considers that the surface charge is acquired owing to adsorption/desorption of protons:

$$-MOH_2^+ \Longleftrightarrow -MOH + H_s^+, \qquad K_+^0 = \frac{[-MOH][H^+]}{[-MOH_2^+]} \exp(-F\psi_0/RT) \quad (7.1)$$

$$-MOH \Longleftrightarrow -MO^- + H_s^+, \qquad K_-^0 = \frac{[-MO^-][H^+]}{[-MOH]} \exp(-F\psi_0/RT) \quad (7.2)$$

but also by complexation equilibria of cations or anions:

$$-MO^- + C_s^+ \Longleftrightarrow -MO^-C^+ \qquad -MOH_2^+ + A_s^- \Longleftrightarrow -MOH_2^+A^-$$

which may be combined with the former to give

$$-MOH + C_s^+ \Longleftrightarrow -MO^-C^+ + H_s^+$$

$$K_C = \frac{[-MO^-C^+][H^+]}{[-MOH][C^+]} \exp[-F(\psi_0 - \psi_b)/RT) \quad (7.46)$$

$$-MOH_2^+A^- \Longleftrightarrow -MOH + A_s^- + H_s^+$$

$$K_A = \frac{[-MOH][A^-][H^+]}{[-MOH_2^+A^-]} \exp[-F(\psi_0 - \psi_b)/RT) \quad (7.47)$$

Equilibria (7.46) and (7.47) account for the fact that complexation is related to acid–base reactions, and that it is involved in the mechanism of charge generation, with proton adsorption/desorption equilibria. The charge σ_0, obtained by proton titration, represents the number of protons released or consumed in all reactions within the Stern layer, and not only the protons involved in the formation of the MO^- and MOH_2^+ species. Hence, all ions participating in the creation of charges σ_0 and σ_b are called potential-determining ions (PDIs), although this name is very often reserved for H^+ and HO^-.

Charge σ_0 can be written as

$$\sigma_0 = (F/A)([-MOH_2^+] + [-MOH_2^+A^-] - [-MO^-] - [-MO^-C^+]) \quad (7.48)$$

and the charge 'shielded' by the complexation, σ_b is

$$\sigma_b = (F/A)([-MO^-C^+] - [-MOH_2^+A^-]) \quad (7.49)$$

The remainder of the charge is compensated for by that of the diffuse layer:

$$\sigma_d = -(F/A)([-MOH_2^+] - [-MO^-]) \quad (7.50)$$

which may also be calculated from equation (7.35).

Electroneutrality imposes

$$\sigma_0 + \sigma_b + \sigma_d = 0 \quad (7.51)$$

The total density of charged sites, which includes all possible forms of these groups, expressed in units of charge density, is

$$N_s = (F/A)N_s$$
$$= (F/A)([-MOH_2^+] + [-MOH_2^+A^-] + [-MO^-] + [-MO^-C^+]) \quad (7.52)$$

The potentials ψ_0 and $(\psi_0 - \psi_b)$ are related to the surface charge through the interfacial capacitance [equation (7.44)].

The 11-equation system (in the case of a single electrolyte) is solved numerically [26,23,17] to fit experimental curves $\sigma_0 = f(pH)$ and $\zeta = f(pH)$ from experimental data on pH, electrolyte concentration, total density of surface sites, total area A and temperature. The other necessary parameters are the differential capacitances, which are considered to be constant in the various zones of the interface, and the equilibria constants (7.4), (7.5), (7.46) and (7.47). The capacitance C_2 is considered equal to $0.2\,F\,m^{-2}$ and the adjustable parameter is C_1. The equilibria constants are determined graphically or numerically (see below) from the experimentally obtained N_s and $\sigma_0 = f(pH)$ curves obtained for several electrolyte concentrations.

The fit of experimental curves $\sigma_0 = f(pH)$ for non-porous crystalline oxides (TiO_2, Al_2O_3, SiO_2) is quite good.

For example, in TiO_2 (Figure 7.9), the ΔpK between the acidity constants is 6.4 and that of the complexation constants of the electrolyte is 2.6. C_1 calculated by the model ranges from 1 to $1.4\,F\,m^{-2}$, depending on the nature of the oxide and that of the ions adsorbed. These values are in agreement with experimental data obtained

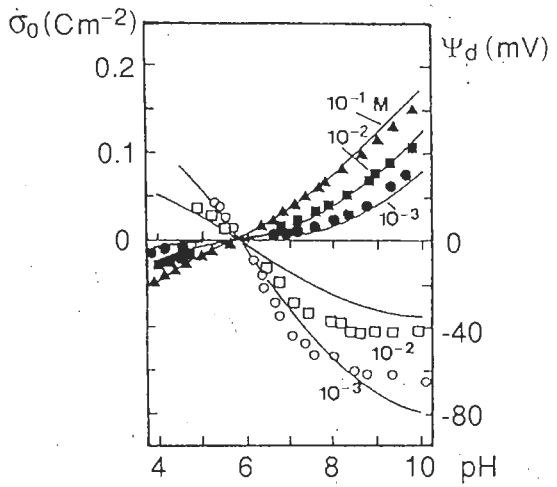

Figure 7.9 Surface charge and diffuse layer potential for TiO_2 as a function of pH and for several electrolyte concentrations. The continuous lines are derived from the model. Reproduced by permission of Academic Press from [26]

from the $\sigma_0 = f(pH)$ curves [21] and allow an estimation of the average distance of approach of adsorbed ions near the surface sites: 1–1.5 Å.

The main difficulty in the implementation of this model is the large number of variables involved, particularly in the calculation of the equilibrium constants of surface ionization.

(i) *The graphical optimization method* is based on the calculation of intrinsic adsorption 'constants'. They depend on the surface charge and hence on the pH, and they are calculated by extrapolation at pH = PZC and zero electrolyte concentration.

The intrinsic constants $K^{\pm}$, Q_A and Q_C are obtained from (7.5), (7.46), (7.47) as

$$K^{+} = \frac{[-MOH][H^{+}]}{[-MOH_2^{+}]} = K_{+}^{0} \exp(F\psi_0/RT) \tag{7.53}$$

$$K^{-} = \frac{[-MO^{-}][H^{+}]}{[-MOH]} = K_{-}^{0} \exp(F\psi_0/RT) \tag{7.54}$$

$$Q_C = \frac{[-MO^{-}C^{+}][H^{+}]}{[-MOH][C^{+}]} = K_C \exp[F(\psi_0 - \psi_b)/RT] \tag{7.55}$$

$$Q_A = \frac{[-MOH][A^{-}][H^{+}]}{[-MOH_2^{+}A^{-}]} = K_A \exp[F(\psi_0 - \psi_b)/RT] \tag{7.56}$$

From (7.45), we can write

$$K^{+} = K_{+}^{0} \exp[(FN_s\sigma_{max}/RTC_t)(\sigma_0/N_s)]$$
$$K^{-} = K_{-}^{0} \exp[(FN_s\sigma_{max}/RTC_t)(\sigma_0/N_s)]$$
$$Q_A = K_A \exp[(FN_s\sigma_{max}/RTC_1)(\sigma_0/N_s)]$$
$$Q_C = K_C \exp[(FN_s\sigma_{max}/RTC_1)(\sigma_0/N_s)]$$

These last four equations show the explicit dependence of the affinity ratios $K^{\pm}$ and Q on the surface charge.

$\log K^{\pm}$ is plotted as a function of pH, i.e. as a function of the ratio $\sigma_0/N_s = \alpha$ and for several electrolyte concentrations c according to $\log K^{\pm} = f(\alpha + \sqrt{c})$. A double extrapolation at $\alpha = 0$ (PZC) and $c = 0$ allows the calculation of the equilibrium constant and the total capacitance C_t (Figure 7.10).

For the complexation constants, the variation in $\log Q$ with $(\alpha \pm \log c)$ is doubly extrapolated at $\alpha = 0$ and $c = 1$. The choice of electrolyte concentration function, either $\sqrt{c}$ or $\log c$, is purely arbitrary and made for technical convenience.

The data available for the calculation of $K^{\pm}$ are σ_0 and N_s. In order to calculate these values, we must assume that for pH $\geqslant$ PZC, $[MOH_2^{+}]$ and $[MOH_2^{+}A^{-}]$ are negligible compared with $[MO^{-}]$ and $[MO^{-}C^{+}]$ (the reverse is true for pH $\leqslant$ PZC). This imposes a very high $\Delta pK = pK^{-} - pK^{+}$ ($\Delta pK > 4$, see Section 7.1.3) in order for the approximation to be valid over the entire pH range. Unfortunately, this hypothesis cannot be verified internally because the method always gives a high value of ΔpK [17]. In addition, these extrapolations are sometimes not at all linear (Figure 7.11) and may result in several sets of parameters.

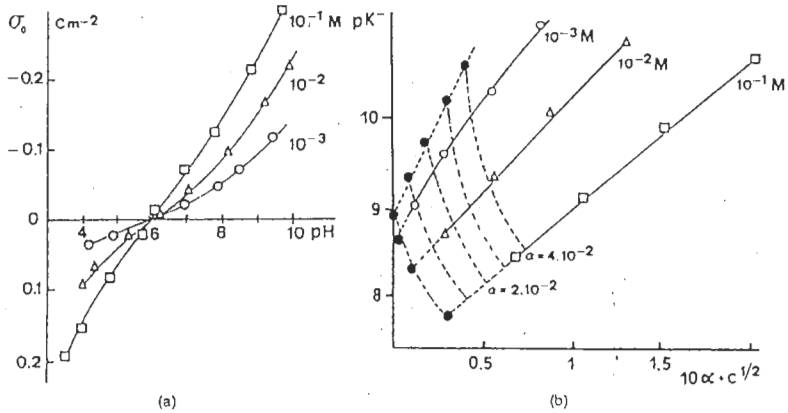

Figure 7.10 (a) Variation in the surface charge of TiO_2 anatase with NaCl concentration and (b) determination via double extrapolation of the affinity ratio pK^{-}. Extrapolations are the dashed lines and filled markers. Reproduced by permission of Academic Press from [28]

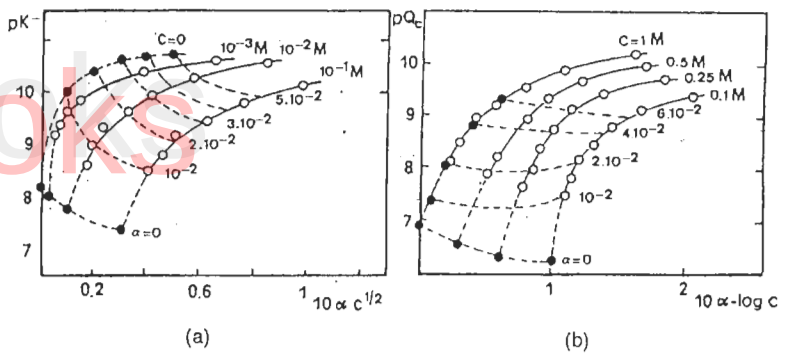

Figure 7.11 Calculation of affinity ratios pK^{-} (a) and pQ_C (b) by the double extrapolation method for SiO_2–NaCl. Reproduced by permission of Elsevier Science Ltd from [29]

(ii) *The numerical optimization method* has the advantage of not requiring any hypothesis. It consists in minimizing the difference

$$[\Sigma(\sigma_{exp} - \sigma_{calc})^2/(n - m - 1)]^{1/2}$$

where n is the number of experimental data points and m is the number of parameters to be calculated (K_{+}^{0}, K_{-}^{0}, K_C, K_A and C_1) using standard procedures [17,23]. The method gives a good fit of the $\sigma_0 = f(pH)$ and $\zeta = f(pH)$ curves, but, here again, more than one set of parameters is obtained. Some initial values must be introduced in the calculation. The method can accommodate small or large values of ΔpK [17].

DropBooks

In fact, confidence in the results can only be ensured if additional information can confirm the order of magnitude of ΔpK. Such information may be obtained from experimental measurement of the differential capacitances $C_t^* = -d\sigma_0/dpH = (d\sigma_0/d\psi_0)(-d\psi_0/dpH)$ near the PZC [14,17]. Equation (7.28)

$$\psi_0 = \frac{2.3RT}{F}(PZC - pH) - \frac{RT}{2F}\ln\frac{[MOH_2^+]}{[MO^-]}$$

may be rewritten as

$$\sigma_0 = \frac{2.3RTC_t}{R}(PZC - pH) - \frac{RTC_t}{2R}\ln\frac{[MOH_2^+]}{[MO^-]}$$

For small ΔpK, near the PZC, the term $\ln([MOH_2^+]/[MO^-])$ is negligible and $C_t^* = 2.3RTC_t/F$. For large values of ΔpK, $[MO^-] \gg [MOH_2^+]$ for a pH slightly larger than the PZC, and therefore

$$C_t^* = \frac{2.3RTC_t}{F} - \frac{d\ln[MO^-]}{dpH}$$

High values of C_t^* suggest small values of ΔpK, i.e. a Nernstian behavior of the surface.

Figure 7.12 illustrates these considerations. It shows the components of the surface charge as determined by application of the triple-layer model on a real system for

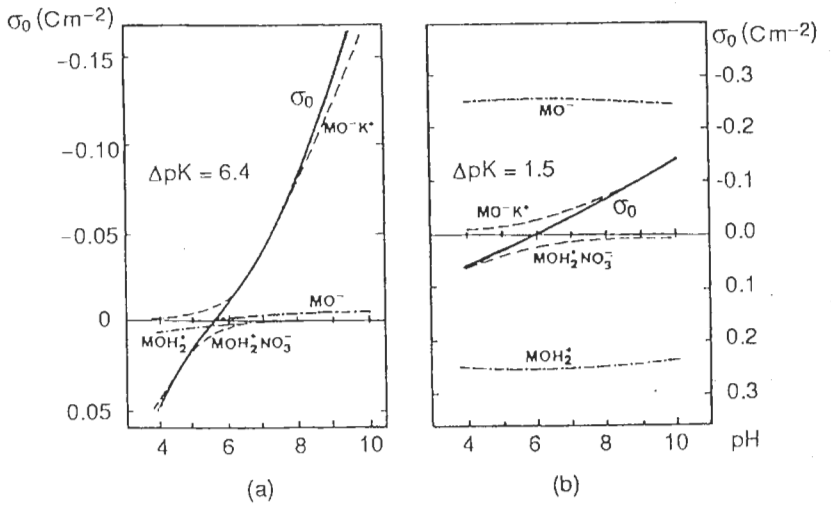

Figure 7.12 TiO_2–10^{-1} mol l^{-1} KNO_3 system. Constituents of the charge, calculated with the triple-layer model, with constants obtained by (a) graphic extrapolation (ΔpK = 6.4, $pK^+ = 2.6$, $pK^- = 9$, $pK_C = 7.1$, $pK_A = 4.6$) and (b) numerical optimization (ΔpK = 1.5, $pK^+ = 5.1$, $pK^- = 6.6$, $pK_C = 5.1$, $pK_A = 6.6$). Reproduced by permission of Academic Press from [17]

both small and large ΔpK. Changes in the quantities of various surface sites show that a large ΔpK satisfies the conditions required for the graphical extrapolation method ($[MOH_2^+]$ and $[MOH_2^+A^-] \ll [MO^-]$ and $[MO^-C^+]$ at pH ≥ PZC), whereas a small ΔpK corresponds to a pseudo-Nernstian behavior of the surface, requiring a large number of charged sites near the PZC.

The advantage of this method is that it takes into account the influence of the ionic strength on the charge of the particles. The model also simultaneously accounts for the variations in charge and electrokinetic potential with pH, for reasonable values of system parameters. Nevertheless, the position of the ions through the interface must be considered carefully.

7.3.3 APPLICATIONS OF THE MUSIC MODEL

In the previous models, the surface acidity constants are obtained by fits of experimental data. Let us look at what happens when the intrinsic acidity constants are obtained using the MUSIC model (see Section 7.1.1).

Surface acidity constants $K_\pm^0$ are obtained by incorporating the Boltzmann accumulation factor $\exp(-F\psi_0/RT)$ into the calculated intrinsic constant. The charge and surface potential are related using a classical two-layer model [$\sigma_0 = C(\psi_0 - \psi_d)$], with the charge of the diffuse layer given by equation (7.35) [30]. Specific adsorption of the electrolyte is taken into account by the formation constants of ion pairs [2,30].

The charge on each type of face of gibbsite $Al(OH)_3$ particles (see Section 7.1.1) is calculated as a function of pH [2] (Figure 7.13a). The large faces containing

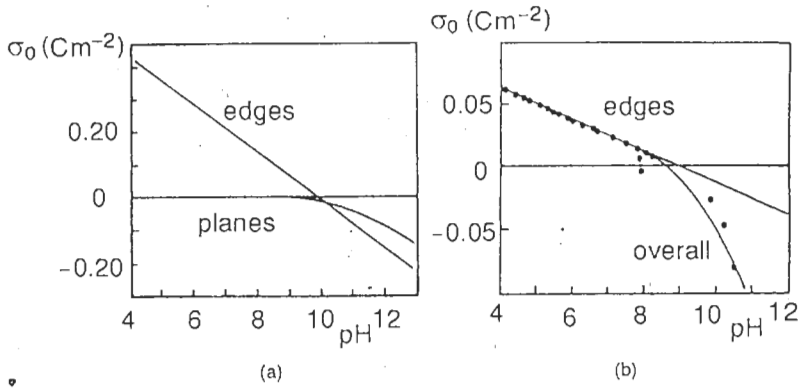

Figure 7.13 (a) $\sigma_0 = f(pH)$ curves calculated for the large faces and the edges of gibbsite particles, for an NaCl concentration of 0.5 mol l^{-1} and a Stern layer capacitance fixed at 1.4 F m^{-2}. The adsorption constants of electrolyte ions are $pK_A = pK_C = 0.1$. (b) Overall $\sigma_0 = f(pH)$ curves calculated for gibbsite. The specific surfaces of the edges and the large faces are 3.4 and 16.4 m^2/g. The parameters used for the calculation are the same as in (a). The markers show experimental data. Reproduced by permission of Academic Press from [2]

doubly coordinated groups are not charged except for high pH, in agreement with the predictions of the calculations of intrinsic constants. However, the edges of the particles are reactive over the entire pH range owing to the presence of singly and doubly coordinated groups. The global charge of the particle (Figure 7.13b) is in good agreement with potentiometric measurements [2,30].

The same analysis has been made for goethite FeOOH. We have seen (see Section 7.1.1) that the charge on the 010 and 001 faces is due to the mono-coordinated groups Fe_1–OH. The charge on the 100 face is due to singly and triply coordinated groups. Doubly coordinated groups can be considered chemically inert in the range pH 3–11.

The variation in the charge of different faces, calculated as a function of pH, is shown in Figure 7.14. The charge of the 100 faces is zero over a wide pH range. This is not due to an absence of charged species but to the exact compensation for the charge of different sites (Figure 7.14b). This is a clear illustration of the

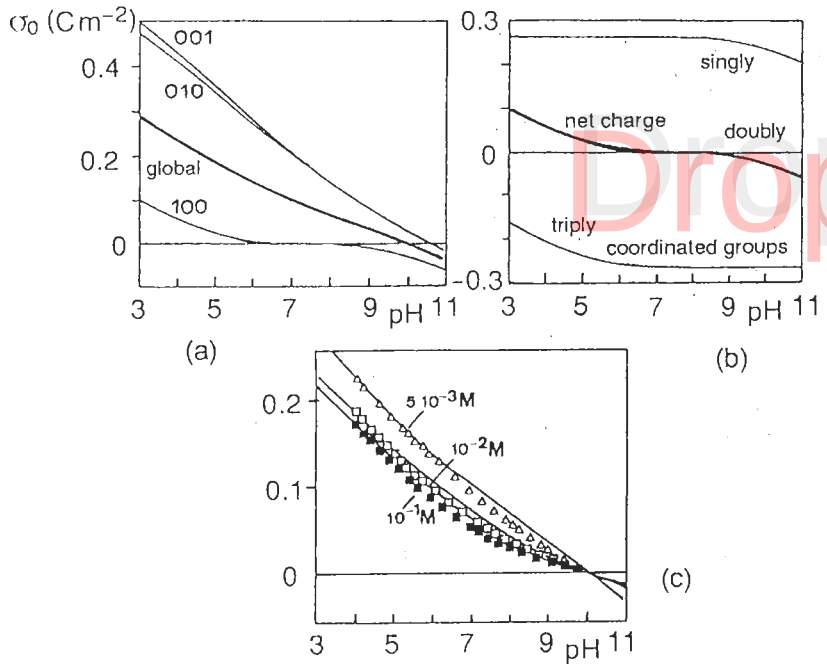

Figure 7.14 (a) $\sigma_0 = f(pH)$ curves calculated for the 001, 010 and 100 faces of goethite ($NaNO_3$ 0.1 mol l^{-1}, Stern layer capacitance 1.54 F m^{-2}, $pK_C = pK_A = 0.75$, specific surface area of the three types of face 5, 45 and 50 m^2/g respectively). (b) Calculated contributions of several types of site to the charge of 100 faces with the same parameters as for (a). (c) Global $\sigma_0 = f(pH)$ curve for various $NaNO_3$ concentrations. The calculated curves are shown in solid lines, experimental data points are shown using markers. Reproduced by permission of Academic Press from [2]

concepts of IEP and PZC. The overall behavior of goethite particles can eventually be calculated using an averaged sum of the charge on the different faces. The fit of the experimental data is excellent (Figure 7.14c).

The use of this model requires precise knowledge of some structural information of the system studied. The system must include particles of well-defined shape, size and structure. The 'sensitive' parameters are the total density of active surface groups N_s and their mode of coordination.

The results given by all these models are strongly dependent on many physico-chemical characteristics (preparation techniques, impurities, particle size distribution, crystal structure of the surface, preferential growth of some faces, etc.). These parameters have an influence on the PZC and on the values of the ionization equilibrium constants. They must be carefully determined for each type of particle. Because of the large number of particles involved, and because of approximations in the models and in the experimental measurements, the results do not always lead to singular solution. Although site complexation models remain one of the best descriptions of the oxide–solution interface, it is not possible to identify the exact nature of the complexes involved. The reactions are selected to fit the experimental data with a given model, and the model controls the values of the parameters. This is why surface complexation models should be treated as fitting models rather than models able to describe chemical processes at the interface.

Furthermore, these models are usually applicable only to 'model' systems: non-porous crystallized materials such as SiO_2 quartz, TiO_2, rutile, FeOOH rutile, aluminum oxides or hydroxides [Al_2O_3, $Al(OH)_3$], etc. In all these cases, the interface is assumed to be completely polarizable, i.e. mass transfer takes place between the surface (planar and ideal) of the particles and the solution only. Recent work [31–33] takes into account some heterogeneities on the surface such as sites of various energies uniformly distributed or grouped in zones.

DropBooks

7.3.4 OTHER MODELS OF THE OXIDE–SOLUTION INTERFACE

(a) Gel Models

In gel models (or porous layer models), one fraction of the surface charge is assumed to diffuse inside the solid, in a highly hydrated zone of a structure comparable to that of a gel [34–37]. Therefore, it is assumed that acid–base reactions causing the charges take place within a volume of the solid of finite thickness also permeable to counterions. With the gel model, it is possible to explain the kinetic character of PDI adsorption. During the addition of an acid or a base during proton titration, the pH of the suspension changes rapidly but slowly recovers its initial value. The process can take weeks or months. This phenomenon has been studied extensively in Fe_2O_3 [38], TiO_2 [21] and ZnO [39]. It has been linked to the formation of a layer of α-FeOOH goethite on the surface of Fe_2O_3 or to a ligand exchange reaction

between surface HO^- and anions from the electrolyte [21,39]. The mathematical treatment of this type of model is particularly complex [36,37].

(b) Model with Variable PZC

Owing to the small solubility of oxides, there are too few metal ions in solution for their transfer to affect the surface charge. However, the reaction

$$O^{2-}_{solid} + 2H^+ \Longleftrightarrow H_2O$$

does assume reversible transfer of O^{2-} between the solid and the solution [40]. This is, in addition to acid–base reactions on the surface, a second mechanism of charge generation, because of the non-stoichiometry of the transfer of ions from the solid (an excess or deficit of O^{2-} ions with respect to metal ions). This O^{2-} transfer affects the pH of the solution and titration curves and has the same effect as the adsorption or desorption of two H^+, depending on whether O^{2-} is lost or gained by the lattice. Since ions from the lattice are located below the surface, they are involved in much slower reactions than surface acid–base reactions, which means that they can play a role in the kinetic effect observed during potentiometric titrations.

The partial reversibility of the oxide–solution interface (the way it is used for AgI, i.e. transfer of ions from the *network* through the interface), means that a composite system must be considered, in which two mechanisms create the charges σ_H and σ_0 located on different planes H (the surface plane) and O below the surface (Figure 7.15).

The net charge density σ_H resulting from ionization of surface sites is given by equations (7.23) and (7.28) (neglecting specific adsorption) and can be written as

$$\sigma_H = \sigma_T \frac{\delta \sinh[(-F\psi_H/RT) + 2.3(pH_K - pH)]}{1 + \delta \cosh[(-F\psi_H/RT) + 2.3(pH_K - pH)]} \tag{7.57}$$

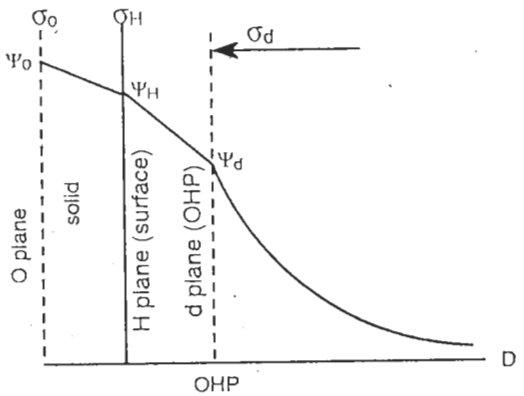

Figure 7.15 Charge distribution on ideal planes and decrease in the potential from the O plane. Reproduced by permission of John Wiley & Sons from [25]

where σ_T is the density of surface sites, $\delta = 2(K^-/K^+)^{1/2}$, $pH_K = (1/2)(pK^+ + pK^-)$. Here, pH_K is the pH value for which $\sigma_H = 0$ and represents the PZC of the completely hydrated (hydroxylated) oxide.

Reversible transfer of O^{2-} ions consumes (or releases) protons in solution and creates the charge σ_0. The corresponding potential ψ_0 is linked to the pH of the solution in the Nernst equation:

$$\psi_0 = \frac{2.3RT}{F}(pH_0 - pH) \tag{7.27}$$

where pH_0 is the pH for which $\sigma_0 = 0$; pH_0 represents the PZC of the anhydrous oxide.

The charge σ_d of the diffuse layer is given by (7.35) and the potential ψ_d is exerted on the outer plane (OHP) (Figure 7.15). The capacitance of the various zones are

$$C_0 = \frac{\sigma_0}{\psi_0 - \psi_H} \quad \text{and} \quad C_H = \frac{\sigma_0 + \sigma_H}{\psi_H - \psi_0} \tag{7.58}$$

System electroneutrality imposes $\sigma_0 + \sigma_H + \sigma_d = 0$.

Because of the existence of two types of surface charge, the surface must be characterized by an IEP. At the electrokinetic isoelectric point, pH = IEP, and $\sigma_d = 0$. Therefore, $\sigma_0 = -\sigma_H$ and $\psi_H = 0$.

The charge σ_H can be expressed, using (7.58), (7.27), (7.57), by the two independent equations

$$\sigma_H = (2.3RT/F)C_0(pH - pH_0) \tag{7.59}$$

$$\sigma_H = \sigma_T \frac{\delta \sinh[2.3(pH_K - pH)]}{1 + \delta \cosh[2.3(pH_K - pH)]} \tag{7.60}$$

Equation (7.59) is a straight line passing through pH_0 at $\sigma_H = 0$ (positive slope) (Figure 7.16). Equation (7.60) is a curve passing through pH_K at $\sigma_H = 0$ (negative slope).

The IEP is the intersection point of the curves of Figure 7.16. It is always found between the limit values pH_0 and pH_K. It is a function of σ_T and is given by

$$\frac{C_0}{\sigma_T} = \frac{\delta \sinh[2.3(pH_K - PIE)]}{1 + \delta \cosh[2.3(pH_K - PIE)]} \left[\frac{1}{(2.3RT/F)(PIE - pH_0)}\right]$$

This relationship shows that, when σ_T is large, IEP $\rightarrow pH_K$. If σ_T is small, then IEP $\rightarrow pH_0$ (Figure 7.17). Since σ_T is related to the hydroxylation of the surface, any change in hydration of the oxide creates a change in the IEP.

Therefore, during hydration of an oxide in aqueous medium, the slow evolution of the PZC can be ascribed to the contribution of O^{2-} ions (and/or metal ions) from the network. The transfer of O^{2-} must probably occur if the surface charge is the result of adsorption/desorption equilibria of hydroxylated complexes [41]. It is also involved in the behavior of colloidal magnetite Fe_3O_4 in a weakly acidic medium which gives rise to the desorption of Fe^{2+} from the lattice [42] (see Section 9.1.3).

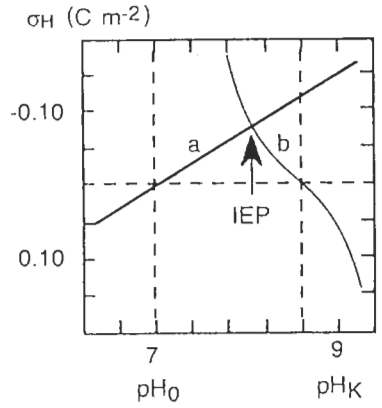

Figure 7.16 Graphic determination of the IEP using the intersection of (7.59) (a) and (7.60) (b). System parameters: $K^+ = 10^7$, $K^- = 10^{-11}$, $pH_0 = 7$, $pH_0 = 7$, $pH_K = 9$, $C_0 = C_H = 1\,F\,m^{-2}$, $\sigma_T = 2\,C\,m^{-2}$. Reproduced by permission of Academic Press from [40]

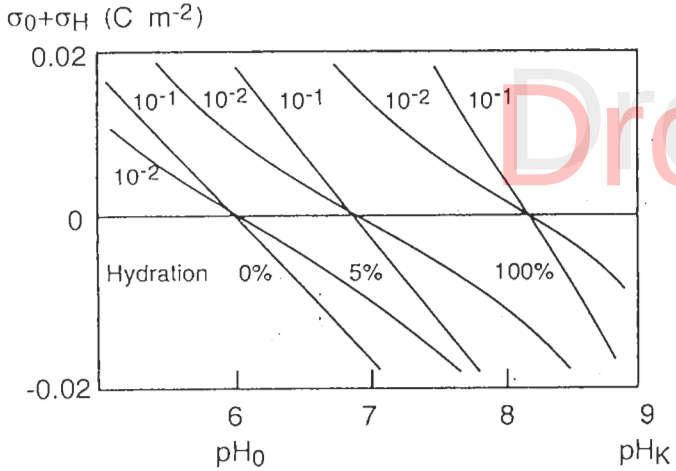

Figure 7.17 Relationship between the IEP and the hydration of an oxide surface. The system constants are those listed in Figure 7.16 using values of 0, 0.1 and 0.2 $C\,m^{-2}$ for σ_T. The ionic strength is indicated on the figure. Reproduced by permission of John Wiley & Sons from [25]

7.4 REFERENCES

1. T. Hiemstra, W.H. Van Riemsdijk, G.H. Bolt, *J. Colloid Interface Sci.* 133, 91 (1989).
2. T. Hiemstra, J.C.M. De Wit, W.H. Van Riemsdijk, *J. Colloid Interface Sci.* 133, 105 (1989).
3. A. Kossiakoff, D. Harker, *J. Am. Chem. Soc.* 60, 2047 (1938).

4. G.A. Parks, *Chem. Rev.* 65, 177 (1965).
5. C.F. Baes, R.E. Messmer, *The Hydrolysis of Cations*, J. Wiley & Sons, New York (1976).
6. C.S.G. Phillips, R.J.P. Williams, *Inorganic Chemistry*, Vol. 1, Oxford University Press, London (1965), p. 529.
7. O. Spalla, Thesis, Université P. & M. Curie, Paris (1991).
8. H. Kawakami, S. Yoshida, *J. Chem. Soc. Faraday Trans. II* 81, 1117 (1985).
9. H. Knözinger, P. Ratnasamy, *Catal. Rev. Sci. Eng.* 17, 31 (1978).
10. T.W. Healy, L.R. White, *Adv. Colloid Interface Sci.* 9, 303 (1978).
11. W. Heller, Ordered and disordered aggregation of colloidal particles and macromolecules. *Polymer Colloids II*, E. Fitch Ed., Plenum Press, New York (1980).
12. R.H. Yoon, T. Salman, G. Donnay, *J. Colloid Interface Sci.* 70, 483 (1979).
13. T.W. Healy, D.E. Yates, L.R. White, D. Chan, *J. Electroanal. Interface Electrochem.* 80, 57 (1977).
14. S. Levine, A.L. Smith, *Disc. Faraday Soc.* 52, 290 (1971).
15. A.L. Smith, *J. Colloid Interface Sci.* 55, 525 (1976).
16. M.A. Blesa, N. Kallay, *Adv. Colloid Interface Sci.* 111 (1988).
17. L.K. Koopal, W.H. Van Riemsdijk, M.G. Roffey, *J. Colloid Interface Sci.* 118, 117 (1987).
18. P.C. Hiemenz, *Principles of Colloid and Surface Chemistry*, M. Dekker Ed. (1977), p. 366.
19. D.J. Shaw, *Introduction to Colloid and Surface Chemistry*, 3th ed., Butterworths (1980), p. 152.
20. J. Lyklema, in *Colloidal Dispersions, Fundamentals of Electrical Double Layers in Colloidal Systems*, J.W. Goodwin Ed., The Royal Society of Chemistry, London (1982).
21. Y.G. Bérubé, P.L. De Bruyn, *J. Colloid Interface Sci.* 27, 305 (1968).
22. Y.G. Bérubé, P.L. De Bruyn, *J. Colloid Interface Sci.* 28, 92 (1968).
23. J. Westall, H. Hohl, *Adv. Colloid Interface Sci.* 12, 265 (1980).
24. A. Haworth, *Adv. Colloid Interface Sci.* 32, 43 (1990).
25. G.Y. Onoda, J.A. Casey, *Ultrastructure Processing of Ceramics, Glasses and Composites*, L.L. Hench, D.R. Ulrich Eds, J. Wiley & Sons, New York (1984), p. 374.
26. J.A. Davis, R.O. James, J.O. Leckie, *J. Colloid Interface Sci.* 63, 480 (1978).
27. D.E. Yates, S. Levine, T.W. Healy, *J. Chem. Soc. Faraday Trans.* 70, 1807 (1974).
28. R. Sprycha, *J. Colloid Interface Sci.* 102, 173 (1984).
29. S.K. Milonjic, *Colloids and Surf.* 23, 301 (1987).
30. T. Hiemstra, W.H. Van Riemsdijk, M.G.M. Bruggenwert, *Neth. J. Agric. Sci.* 35, 281 (1987).
31. W.H. Van Riemsdijk, G.H. Bolt, L.K. Koopal, J. Blaakmeer, *J. Colloid Interface Sci.* 109, 219 (1986).
32. A.W.M. Gibb, L.K. Koopal, *J. Colloid Interface Sci.* 134, 122 (1989).
33. L.K. Koopal, W.H. Van Riemsdijk, *J. Colloid Interface Sci.* 128, 188 (1989).
34. A. Breeuwsma, J. Lyklema, *Disc. Faraday Soc.* 52, 324 (1971).
35. J. Lyklema, *Electroanal. Chem.* 18, 341 (1968).
36. J.W. Perram, *J. Chem. Soc. Faraday Trans. II* 993 (1973).
37. J.W. Perram, R.J. Hunter, H.J.L. Wright, *Aust. J. Chem.* 27, 461 (1974).
38. G.Y. Onoda, P.L. De Bruyn, *Surf. Sci.* 4, 48 (1966); 8, 448 (1967)
39. L. Blok, P.L. De Bruyn, *J. Colloid Interface Sci.* 32, 527 (1970).
40. G.Y. Onoda, J.A. Casey, *J. Colloid Interface Sci.* 103, 590 (1985).
41. G.A. Parks, P.L. De Bruyn, *J. Phys. Chem.* 66, 967 (1962).
42. J.P. Jolivet, E. Tronc, *J. Colloid Interface Sci.* 125, 688 (1987).

DropBooks

8

Stability of Colloidal Dispersions

The stability of colloids in water has several aspects, depending on whether one considers the permanence of the dispersion of the particles or the division of the solid.

If the particles are small enough in mass and size, they are subjected to Brownian motion and can form a stable, homogeneous suspension. In this sol, the particles repel each other and disperse spontaneously in the liquid. If, however, they attract each other and aggregate, they separate from the liquid and flocculate. The stability of a sol imposes repulsion forces so that a kinetic energy barrier prevents them from getting too close to each other. These forces may be caused by electrostatic forces on the surface. In this case, the pH of the solution and the nature and concentration of the electrolytes must be considered. The stability of the dispersion may also be due to adsorption of macromolecules, causing steric effects on the surfaces. The strength of the surface–macromolecule interaction and the coverage of the particles influence the dispersion in an aqueous or non-aqueous medium.

Another aspect is the stability of the size, structure and morphology of the particles, which is not always guaranteed. Ostwald ripening involves a series of transformations causing the initial particles to evolve into a more stable thermodynamic state (Section 2.3.4). The driving force is the oxide–solution interfacial tension which allows, through a change in surface area of the system, a decrease in its free enthalpy. Stabilization of the particles towards ageing requires control of the interfacial tension. This stabilization is directly linked to adsorption phenomena, which are themselves controlled by the pH and the ionic strength of the solution. This is called *thermodynamic* stabilization.

These two aspects of stability involve very different forces controlled by the same parameters: pH and ionic strength. It is crucial to understand the influence of these parameters since even a small variation can cause drastic changes in the particles because of the large surface area involved. To reflect such properties, De Gennes used the term 'matière molle' ('soft matter') to describe such systems [1].

8.1 KINETIC STABILITY OF THE DISPERSIONS. CONTROL OF PARTICLE AGGREGATION

The stability of dispersed particles towards aggregation and flocculation is described by the DLVO (Dejarguin, Landau, Verwey, Overbeek) theory. Taking into account all forces applied on the particles, the theory allows a calculation of the energy barrier to avoid permanent contact. This is what is meant by 'kinetic' stability of the dispersions. The forces involved are of two kinds:

- Repulsive forces caused by the interaction between electrical double layers and controlled by the physicochemical parameters of the system. In Section 6.2, we saw that the surface charge and the size of the counterion diffuse layer are linked to the pH and to the ionic strength of the solution.
- Attractives forces, which are always present (London–Van der Waals forces) and are a sole function of the materials involved.

How are such forces involved as the particles come together during Brownian collisions? This is indeed a complex problem because the interaction energies depend on the transient behavior of the double layers during the collisions. A quantitative treatment of this problem is beyond the scope of this book. However, it is probably useful to give a qualitative description of the phenomena involved.

8.1.1 ELECTROSTATIC FORCES

When two charged particles come together, the interpenetration of the diffuse parts of the double layers causes a local increase in ionic strength, I, in the zone between the particles. The diffuse layers are made of identical counterions and repel each other, but their repulsion domain κ^{-1} decreases because κ is proportional to $\sqrt{I}$ (see Section 7.2.2). Therefore, the Stern layers interact with each other.

(a) Static Aspect of the Interactions

Let us assume that oxide particles are dispersed in a solution of given pH containing an electrolyte [1 : 1] of concentration c. What happens when two particles, previously sufficiently distant not to affect each other, come closer to a separation distance D? This can be modeled using the variation in the charge and potential as a function of the distance between surfaces. This analysis is simplified assuming planar surfaces and the validity of Poisson's equation for the entire space between particles.

Since the particles are initially far from each other, the surface charge density σ_0 is linked to the surface potential ψ_0 for any pair of dissociation constants (K^+, K^-) and for any pH:

$$\sigma_0 = FN_s \frac{([H^+]/K^+)\exp(-F\psi_0/RT) - (K^-/[H^+])\exp(F\psi_0/RT)}{1 + ([H^+]/K^+)\exp(-F\psi_0/RT) + (K^-/[H^+])\exp(F\psi_0/RT)} \qquad (7.23)$$

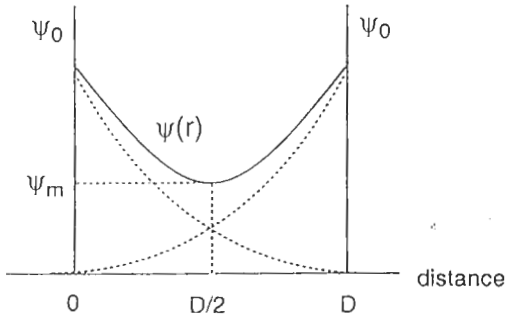

Figure 8.1 Variation in the potential (solid line) between two charged surfaces, resulting from the overlap of the diffuse layers (dotted lines)

The countercharge density at a given point between the surfaces is given by equation (7.31):

$$\rho_r = FC_\infty[\exp(-zF\psi_r/RT) - \exp(zF\psi_r/RT)] \tag{7.31}$$

It is related to the potential ψ_r at this point by the Poisson equation:

$$d^2\psi_r/dr^2 = -\rho_r/\varepsilon \tag{7.30}$$

for which the boundary conditions in the zone between surfaces are $[d\psi_r/dr]_{r=d} = \sigma_d = -\sigma_0$ and $[d\psi_r/dr]_{r=D/2} = 0$ because of the symmetry of the system [2,3].

As the particles come closer together, the overlap of the diffuse layers causes an increase in the potential in the zone between the surfaces (Figure 8.1). To a first approximation, this potential at a given point is equal to the sum of the potentials caused by each surface. Therefore, within this zone of the solution, the counterion density increases as the particles come closer to each other. As a result, an osmotic pressure develops which tends to repel the particles [2–4].

If the approach is slow enough as to maintain equilibria between surfaces and solution, the increase in potential near the surface tends to force a decrease in PDI concentration [equation (7.4)]:

$$[H_s^+] = [H^+]\exp(-F\psi/RT) \tag{7.4}$$

The stability of the equilibria causes deprotonation (pH < PZC) or protonation (pH > PZC) of surface groups, which decreases the net charge and decreases the potential between surfaces. If the particles touch, their charges may, in theory, cancel each other.

When oxide particles come together, the surface charge and potential change *simultaneously*. The charge variation (or dissociation ratio of the surface groups) as a function of the distance between particles is calculated using equations (7.23) and (7.31) for given values of the pH, electrolyte concentration and boundary conditions. The mathematical solution is complex [5–7]. The main results are shown in

Figure 8.2, for particles with surfaces characterized by various pairs of K^+ and K^- constants. Therefore, during the interaction between particles, changes in the surface potential are regulated by variation in the charge.

The efficiency of the regulation depends on the ability of the surface to respond, through charge variation, to the pH variations near the surface (pH_s). This ability is itself proportional to the difference $\Delta pK = pK^- - pK^+$ between the acidity constants of the surface sites (Figures 8.2 and 8.3). A small ΔpK increases the

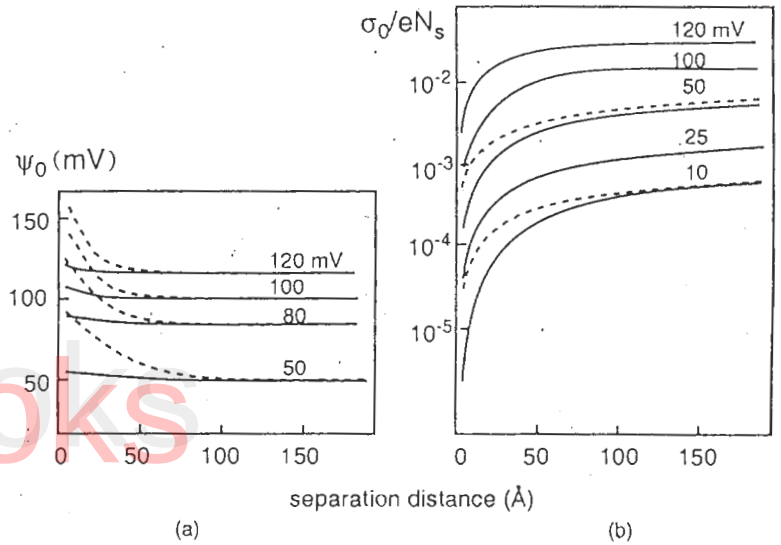

Figure 8.2 Variation in the potential ψ_0 (a) and in the charge σ_0 (b) as a function of the distance between two surfaces of PZC = 7 and $\Delta pK = 3$ (solid lines) and 6 (dotted lines). Electrolyte concentration 10^{-3} mol l^{-1} ($\kappa^{-1} = 96$ Å). The potentials are given for an infinite separation distance. Reproduced from [5] by permission

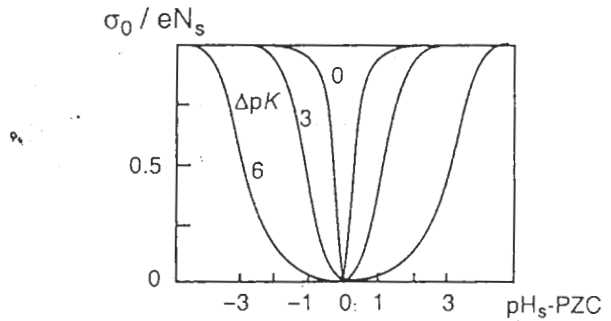

Figure 8.3 Surface charge σ_0 as a function of surface pH [equation (7.23)] for various values of ΔpK. Reproduced from [5] by permission

DropBooks

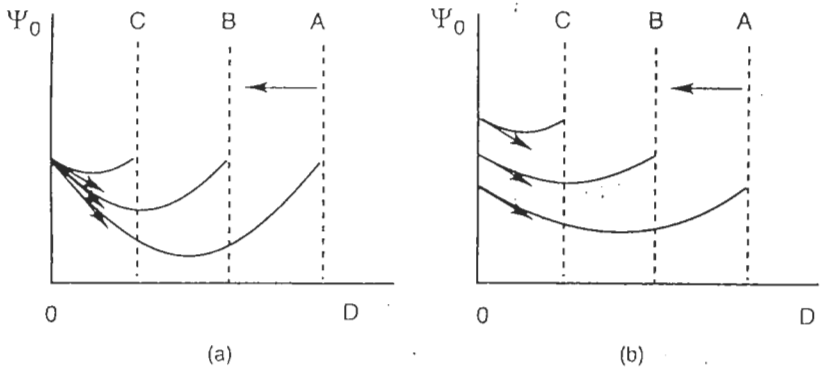

Figure 8.4 Surface potential as a function of the separation distance in the case of an interaction (a) at constant potential and (b) at constant charge. One of the surfaces is displaced from A towards C. σ_0 is indicated by the slope of the tangent at the origins of the potential variation with distance $[\sigma_0 = -\varepsilon(\mathrm{d}\psi/\mathrm{d}r)_{r=0}]$. In case (a) the decrease in the slope indicates a gradual decrease in the surface charge

ability of the surface to regulate the potential, i.e. to decrease the charge during the interaction (Figure 8.3). If ΔpK is small, the surface carries only few non-charged groups at any pH (see Section 7.1.3). For example, for a positively charged surface, a decrease in the concentration of protons near the surface decreases the charge because of the decrease in the number of $M-OH_2^+$ groups and the increase in the number of $M-O^-$ groups. If ΔpK is large, the charge decrease occurs only through a decrease in the number of $M-OH_2^+$ groups. Therefore, σ_0 is increasingly sensitive to pH variations as ΔpK becomes smaller ($\mathrm{d}\sigma/\mathrm{dpH}$ increases) (Figure 8.3).

When ΔpK increases, the pH range for which $\mathrm{d}\sigma/\mathrm{dpH}$ is maximum moves away from the PZC, and controlling the potential becomes increasingly difficult because $\mathrm{d}\sigma/\mathrm{dpH}$ is smaller (Figures 8.2 and 8.3). The limiting case is the 'constant potential' interaction (Figure 8.4). In fact, this is a case of perfect regulation taking place for reversible surfaces for which the surface charge is caused by preferential adsorption of ions from the network. AgI is a good example. For such surfaces, the amount of non-charged sites is zero and the surface follows Nernst's equation for all conditions. Since the surface potential $\psi_0 \rightarrow \psi_N$ (Nernst potential) when $D \rightarrow 0$ [equation (7.27)], the interaction between surfaces carrying charged sites only takes place at constant potential [5]. The $\Delta pK = 0$ case is not a case of perfect regulation since the fraction of zero-charge sites is not zero.

If $pH_s \gg pK^-$ or $pH_s \ll pK^+$, the charge σ_0 is maximum and becomes quasi-independent of the pH. The interaction takes place under 'constant charge' conditions (Figure 8.4) until very small separation distances, where the charge must cancel out abruptly by adsorption (or desorption) of protons, or by compensation and readsorption of counterions. At this point, there is no longer a relationship between the surface potential and the pH of the solution.

The calculation of electrostatic repulsion energy between surfaces for which charge relaxation is incomplete is not trivial [8]. In the limiting cases (constant charges and potentials) and for small surface potentials, approximate expressions for the interaction energies of spheres of radius a are, respectively [3,8,9]:

$$V_R^{(\psi)} = 2\pi\varepsilon a\psi_d^2 \ln[1 + \exp(-\kappa D)] \tag{8.1}$$

$$V_R^{(\sigma)} = -2\pi\varepsilon a\psi_d^2 \ln[1 - \exp(-\kappa D)] \tag{8.2}$$

In these expressions, the potential ψ_d at the Stern layer is approximated by the electrokinetic potential ζ.

For large distances ($D \gg \kappa^{-1}$), both expressions give

$$V_R^{(\psi)} = V_R^{(\sigma)} = 2\pi\varepsilon a\psi_d^2 \exp(-\kappa D) \tag{8.3}$$

and if the weak potential approximation is not valid, equation (8.3) becomes [9]

$$V_R = \frac{32\pi\varepsilon a k^2 T^2 \gamma^2}{e^2 z^2} \exp(-\kappa D) \tag{8.4}$$

where z is the charge of the counterions and

$$\gamma = \frac{\exp(ze\psi_d/2kT) - 1}{\exp(ze\psi_d/2kT) + 1}$$

The repulsion energies V_R corresponding to various types of interaction are clearly different for small distances only (Figure 8.5). The case of charge regulation (which depends on the value of ΔpK) is always found between the constant potential (perfect regulation) and constant charge (no regulation) limits. The two parameters that have the greatest influence on V_R are the surface potential ψ_0 (or ψ_d) and the concentration and nature of the electrolyte (c, z), which are reflected in κ.

(b) Dynamic Aspect of the Interaction

Studies of the stability of colloids usually assume that the double layers are permanently at equilibrium (constant charge) or, on the contrary, independent from the medium (constant charge). The constant potential environment concerns only systems with complete relaxation of the double layer, such as reversible colloids of the AgI type. When the superficial charge is the result of the near-complete ionization of surface sites of weak acid–base nature (clays, latex), there is no mechanism for a decrease in surface charge, aside from readsorption of counterions. The interaction takes place at constant charge and the double layers do not relax at all.

Oxide colloids exhibit an intermediate behavior between both limiting cases because charge acquisition involves protonation or deprotonation equilibria. The dynamic nature of the chemical equilibria allows regulation of the interaction. In addition, aggregation and flocculation are obviously kinetic phenomena involving several processes, each taking place at its own rate. It is perhaps useful to consider their respective time-scales [8].

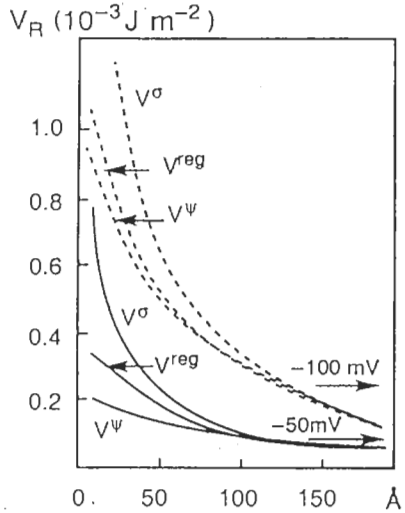

Figure 8.5 Electrostatic interaction energy V_R as a function of the separation distance for constant potential, constant charge interactions and under regulation conditions $\Delta pK = 6$ (dotted lines), $\Delta pK = 3$ (solid lines). Ionic strength 10^{-3} mol l^{-1}. The potentials shown on each curve are for an infinite separation distance. Reproduced from [5] by permission

The duration of a Brownian collision, τ_B, may be estimated by considering the time required to cover a distance $2\kappa^{-1}$ (interaction distance) for particles of diffusion coefficient $D_p = kT/6\eta\pi a$ (η is the viscosity of the solvent, and a is the radius of a spherical particle):

$$\tau_B = (2\kappa^{-1})^2/2D_p = 12\pi\eta a/\kappa^2 kT$$

For particles of 500 Å radius, in water at 25 °C and for a salt concentration of the order of 10^{-1}–10^{-3} mol l^{-1}, κ^{-1} ranges between 10 and 1000 Å and $\tau_B \approx 10^{-5}$–10^{-7} s. The diffusion of particles is not completely free, however, since at short separation distances they are slowed by hydrodynamic interactions. This effect is difficult to quantify because the movement is not uniform. The probable duration of this interaction seems to be of the order of 10^{-4} s [10].

Relaxation of the double layers involves two characteristic times, one related to the relaxation of the diffuse layer (τ_D), the other concerning the relaxation of the Stern layer (τ_S).

The relaxation time of the diffuse layer represents the average displacement time of ions (of diffusion coefficient D_i) over the distance κ^{-1}: $\tau_D = (\kappa^{-1})^2/D_i \approx 10^{-8}$ s. One may consider that the diffuse part of the double layer is always fully relaxed as particles come closer together.

There are several mechanisms by which the ions can move within the Stern layer [10]: diffusion in solution, lateral diffusion in the Stern layer and surface conductivity. To our knowledge, little information has been published on this topic [11,12], and none of it deals specifically with oxides. The speed of the process is controlled by the surface discharge current i. Considering a surface charge density σ_0 of about 0.1 C m^{-2} and current densities of the order of 1–10^{-10} A cm^{-2}, the relaxation time of the compact layer $\tau_S = \sigma_0/i$ ranges from 10^{-5} to 10^5 s [8].

Relaxation measurements on AgI colloids destabilized by coulostatic impulses (using Ag–AgI electrodes) have shown durations of the order of 1 ms [10]. This would seem to indicate that relaxation in the Stern layer is slower than Brownian motion. The issue has not been resolved for oxides. One may expect shorter relaxation times because of the fast diffusion of the proton and the OH^- ion in the strongly structured surface hydration layer.

Comparing the time-scales of the various processes involved does not allow a clear description of the behavior of the Stern layer as the particles come closer to one another. It is likely that, if relaxation occurs, it does so—at least partially—during the collision. It is very important to take this behavior into account, since it is likely to influence the reversibility of flocculation.

8.1.2 VAN DER WAALS FORCES

These forces are always present and always attractive between particles of the same nature. They are the result of fluctuations in the dipolar interactions at the molecular level [2,3,13]. The potential energy of this interaction is a function of the separation distance r between dipoles, and has an r^{-6} dependence. The sum of the interactions between macroscopic objects (as far as molecular dimensions are concerned) yields an interaction energy that is a function of r^{-2}.

Assuming two identical spheres of radius a, with surfaces separated by a distance D (center-to-center separation distance $R = D + 2a$), the potential energy is [8]

$$V_A = -\frac{A}{6}\left(\frac{2a^2}{R^2 - 4a^2} + \frac{2a^2}{R^2} + \ln\frac{R^2 - 4a^2}{R^2}\right) \tag{8.5}$$

where A is the effective Hamaker constant for the system. It is a function of the Hamaker constants for the particles and the dispersion medium. For objects interacting in a vacuum, the Hamaker constant is [2,3,13]

$$A = \pi^2 C \rho_1 \rho_2$$

where ρ_1 and ρ_2 are the number of atoms per unit volume in each object, and C is the coefficient of the potential interaction of atom pairs ($V = -Cr^{-6}$). For particles 1 in a medium 2, an approximate expression of the effective Hamaker constant is

$$A \approx (\sqrt{A_1} - \sqrt{A_2})^2 \tag{8.6}$$

Typical values of A are usually of the order of a few kT (3.5–8×10^{-20} J for oxides, 3.7×10^{-20} J for water) [2,3,13].

DropBooks

For small separation distances ($D/a \ll 1$), an approximate expression of the interaction energy is [8]

$$V_A = -\frac{A}{12}\left(\frac{L}{D} + 2\ln\frac{D}{L}\right) \tag{8.7}$$

where $L = a + 3D/4$.

For large separation distances (10–100 nm), intermolecular London–Van der Waals forces vary with the −7th power of the distance (the retardation effect). This retardation effect is due to the fact that intermolecular interactions propagate as a complex electromagnetic field [3]. A dipole oscillating in a molecule A emits a field propagating at the speed of light towards a molecule B where it induces an oscillating dipole which in turn emits a field towards A. If the time between emission from A and reabsorption of the field reflected from B is negligible compared with intramolecular motion, A finds itself in the same configuration during emission and reabsorption, and the interaction energy is maximum. If the propagation time of the field is comparable with that of changes in internal configuration, the interaction energy is smaller. The main consequence of the retardation effect is a decrease in the reach of the Van der Waals forces. This effect does not play any role at moderate distances.

In a first approximation, the influence of the electrolyte on the potential energy V_A is not taken into consideration. Therefore, this potential energy depends only on the nature of the particles and on the dispersion medium (Hamaker constant), as well as on the particle size and their separation distance. The attractive character of the interaction is reflected in the fact that V_A is negative.

8.1.3 TOTAL POTENTIAL ENERGY OF THE INTERACTION

The calculation of the total potential energy V_T of the interaction between particles is the foundation of DLVO theory [14]. The total interaction energy is the sum of the repulsion and attraction energies $V_T = V_A + V_R$ (Figure 8.6).

Energy V_R varies exponentially with the distance between surfaces. It is a function of the pH and the ionic strength reflected in the potential ψ_0 (or ψ_d) and in κ. Energy V_A, in a first approximation, is insensitive to the physicochemical conditions of the medium and varies with the reciprocal of the distance. Therefore, V_A is always predominant at small separation distances, and for short distances (1–2 nm) the interaction energy falls drastically and causes V_T to approach minus infinity. In fact, for very short distances, the repulsive forces due to the interpenetration of strongly oriented solvent layers (structural forces) and to the overlap of electron clouds (Born forces) become stronger than the Van der Waals forces [15–17]. As a result, a primary minimum appears on the curve of V_T as a function of distance (Figure 8.6).

Depending on the physicochemical characteristics of the dispersion (pH, ionic strength), several situations must be considered. For highly charged surfaces in the

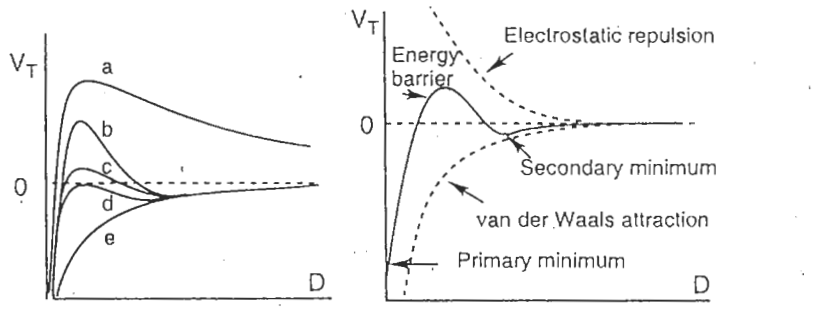

Figure 8.6 Interaction energy $V_T = V_A + V_R$ as a function of distance: (a) the surfaces repel each other strongly; (b) the surfaces are in stable equilibrium in the secondary minimum if it is sufficiently deep; (c), (d) the surfaces in unstable equilibrium cause limited aggregation and slow flocculation of the particles; (e) the surfaces are strongly attracted to one another and the particles flocculate rapidly

presence of a dilute electrolyte, hence for large Debye lengths κ^{-1}, the particles repel each other more intensely as they come closer to one another. The energy barrier, which corresponds to a V_T maximum (Figure 8.6a), can reach from a few tens of kT to 100 kT and thus prevents the aggregation of the particles which are maintained in a kinetically stable dispersed state. If the surface charge is small and the ionic strength is high, the interaction energy is close to the variation in Van der Waals energy (Figure 8.6e). This is an attractive system for any distance between particles, and their flocculation is fast. For highly charged surfaces in the presence of a concentrated electrolyte, the total energy exhibits a small minimum (secondary minimum) prior to the barrier (Figure 8.6b). The particles repel one another at short distances, but they can remain at a given equilibrium distance corresponding to the secondary minimum, without flocculating. This is probably the process of formation of physical gels. In the gel state, particle aggregates form a loose network which traps the solvent. The presence of the solvent prevents the collapse of the aggregates (flocculation) and the system forms a semi-rigid medium with unique rheological properties [18].

As the energy barrier decreases, the stability of the dispersion decreases and aggregation becomes possible or even favored. Cases c and d in Figure 8.6 illustrate the kinetically unstable critical state for which coagulation is slow. The sol may appear kinetically stable because of the establishment of temporary stationary states in which aggregation is partially compensated for by dispersion. These stationary states allow the formation of aggregates of various sizes without complete flocculation of the sol. This regime is called kinetically limited [19,20].

For a given particle size, the height of the energy barrier depends essentially on the following factors:

- *The concentration and charge of the ions in the electrolyte* (Figure 8.7a). An increase in these parameters causes a decrease in V_R through the decrease in the

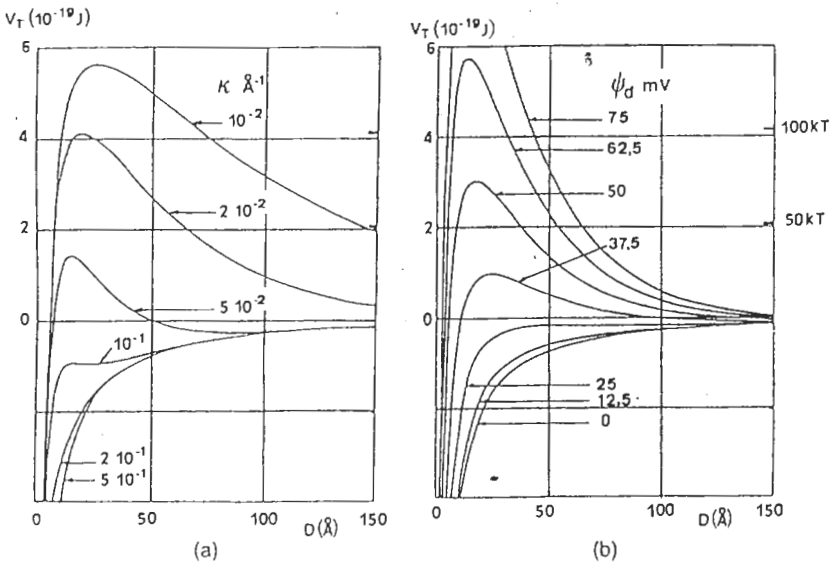

Figure 8.7 Interaction energy V_T between two spherical particles of radius $a = 100$ nm with $T = 298$ K and $z = 1$ as a function of (a) electrolyte concentration through the term κ ($\psi_d = 50$ mV) and (b) potential ψ_d ($\kappa = 3 \times 10^8$ m^{-1}). Hamaker constant 6.1×10^{-20} J, $\varepsilon = 78.5$. V_R and V_A are calculated from equations (8.4) and (8.5). Reproduced by permission of Butterworth-Heinemann Publishers, a division of Reed Educational & Professional Publishing Ltd from [9]

Debye length κ^{-1} (κ is proportional to $z\sqrt{c}$). An electrolyte will be increasingly flocculating with increasing charge and concentration of the ions it contains (Schulze–Hardy rule [21], see Section 8.1.5). This explains the flocculation of muds carried by rivers (freshwaters) when they come in contact with salt water in the ocean. It also explains the presence of lime in clay soils: the bivalent Ca^{2+} ions cause the aggregation of clay particles into grains, which make the soil less compact and more amenable to water circulation.

• *the surface charge, and therefore the potential* (Figure 8.7b). A high potential increases V_R without changing V_A and therefore increases the position of the maximum V_M. Figure 8.8 shows the increase in the aggregation with pH in sols of γ-Fe_2O_3 particles. Limited aggregation, which does not cause complete flocculation of the particles, probably takes place in the secondary minimum.

An increase in the Hamaker constant A makes V_A increasingly negative and the V_M maximum decreases. This factor should not be taken into account in the analysis of the stability of a system, because the value of A is fixed since it is a function of the characteristics of the materials. The same is true for particle size. If phenomena such as Ostwald ripening do not occur, the particle size is constant for any given system. However, it should be pointed out that the energy of Van Der Waals forces

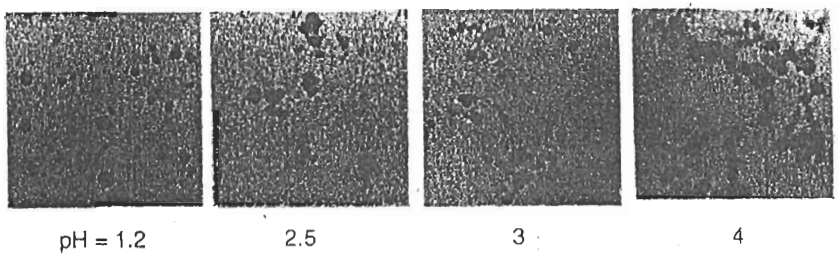

Figure 8.8 TEM micrographs showing the aggregation of iron oxide particles (γ-Fe_2O_3, average diameter 90 Å, PZC = 8) in a cationic sol at various pH. Polyvinyl alcohol introduced in the sol prior to drying allows the preservation of the dispersion on the grid [22]

will increase with the size of the particles. This would explain why, in polydispersed systems, flocculation of a fraction of the distribution may occur at any pH. One should not forget that if the goal is to form a stable sol through an increase in surface charge caused by an increase between pH and PZC by acidification or the addition of a base, an opposite effect is usually obtained owing to the increase in ionic strength of the medium.

Interaction energy diagrams (Figures 8.6 and 8.7) show that, if the particles reach small separation distances (through a decrease in the charge or the addition of an electrolyte), the system reaches an energy wall and dispersion should no longer be possible. Elimination of the electrolyte through dialysis, and/or an increase in surface charge, increases the energy barrier which no longer allows dispersion of the particles. Peptization of flocculates is frequently used in the synthesis of sols. For redispersion to take place, the surface charge must be compensated for, rather than cancelled out, by counterions pressed against the surface, between flocculation and redispersion. Direct contact between particles must be avoided in order to limit Van der Waals forces. The minimum distance between particles must therefore remain at least equal to the Stern layers, so that the particles may keep their strongly structured hydration sphere intact [8,23,24]. Diagrams corresponding to the flocculation and repeptization of the colloids (Figure 8.9) differ from those of Figures 8.6 and 8.7 in the absence of a deep minimum owing to a larger minimum separation distance, which is limited to twice the thickness of the Stern layer.

The important parameter in Figure 8.9 is the total energy V_T^0 at the shortest separation distance between particles. If V_T^0 is negative (Figure 8.9a) there is no energy barrier and the coagulation of the colloids is fast. A decrease in electrolyte concentration by dilution or dialysis and/or recharging of the surface by a modification of the pH would increase V_T^0, but the energy curve does not exhibit a sharp maximum (Figure 8.9b). Therefore, the flocculate must repeptize rapidly. This assumes that desolvation and the mechanism of potential regulation at the expense of the charge do not take place [24,25].

Therefore, the smaller the ΔpK of the oxide, the greater is the rate at which peptization must take place, otherwise it must be carried out under such acid

DropBooks

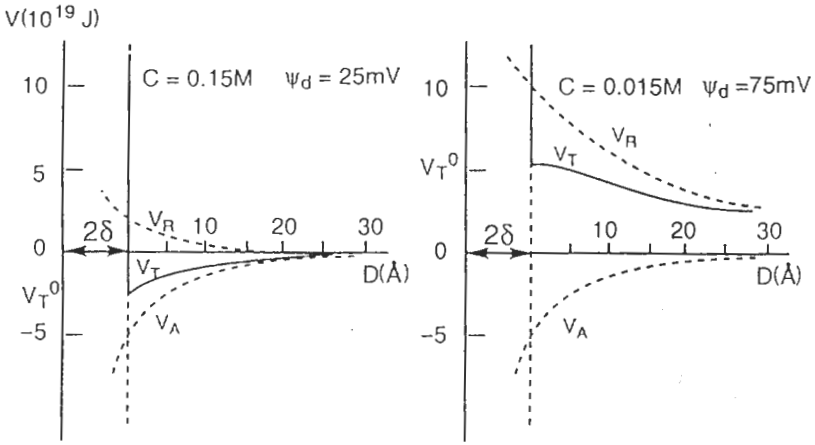

Figure 8.9 Total interaction energy V_T for (a) flocculation and (b) peptization. Thickness of the Stern layer $d = 2$ Å; radius of the particles $a = 500$ Å; effective Hamaker constant $A = 5 \times 10^{-20}$ J; the concentration c of a [1 : 1] electrolyte and the diffuse layer potential ψ_d are shown on the figure. Reproduced by permission of Academic Press from [23]

conditions that the surface charge is maximum and cannot be regulated easily. These diagrams are also valid for swelling clays which always keep a small quantity of water intercalated between sheets. Flocculation is reversible. Rehydration on contact with water occurs spontaneously and sheet separation, which increases with the dilution, may go as far as delamination or formation of sols.

8.1.4 KINETICS OF FLOCCULATION

The efficiency of the energy barrier against flocculation (or coagulation) is characterized by the stability ratio W [26,8]:

$$W = \int_{2a}^{\infty} x^{-2} \exp[V(x)/kT]\,dx \tag{8.8}$$

where $V(x)$ is the total interaction energy $V_T = V_R + V_A$, at distance $x = D + 2a$ between two spherical particles of radius a.

The largest contribution to the Fuchs integral [equation (8.8)] comes from the range of distances in which $V(x)$ exhibits a positive maximum, and therefore equation (8.8) can be simplified [27] into

$$W \approx (1/2\kappa a)\exp(V_M/kT) \tag{8.9}$$

In the absence of a maximum in the variation of $V(x)$, W is close to 1. Under these conditions, coagulation of the sol is fast. The flocculation rate is limited only by the

diffusion of particles towards one another by Brownian motion. For particles of radius a, diffusion coefficient D and concentration n_0, the number of collisions is given by the flux J_0 of particles whose centers pass through each sphere of radius $R = 2a$ surrounding the central particle. The flux (in s^{-1}), calculated using Fick's law, is given by

$$J^0 = 8\pi Dan_0$$

This relationship gives only the number of pairs formed by collisions, and it would be more accurate to take into account the formation of multiplets. The time of formation of doublets in the regime of fast coagulation is given by $t_{1/2} = 1/J^0$ or, calculating the diffusion coefficient by the Stokes–Einstein law $D = kT/6\pi a\eta$, we obtain $t_{1/2} = 3\eta/4n_0kT$. In the case of water, at 25 °C, $t_{1/2} = (2 10^{11}/n_0)$ s if n_0 is given in the number of particles per cm^3. A moderately concentrated sol ($n_0 = 10^{14}$ particles per cm^3, i.e. a concentration of metallic elements of about 10^{-2} mol l^{-1}) has a coagulation time of about a millisecond.

The presence of an energy barrier decreases the number of effective collisions, and the coagulation rate becomes proportional to the flux:

$$J_a = J^0/W$$

The stability ratio thus expresses the ratio of the number of collisions due to Brownian motion per unit time to the number of effective collisions leading to flocculation. For an energy barrier of 20 kT and particles for which $\kappa a = 2$ ($a = 100$ Å, $\kappa^{-1} = 50$ Å for example), the stability ratio calculated using (8.9) is of the order of 10^8. For the previously considered particles, the coagulation time is about 1.5 days. This time would be increased to 7 months for a barrier of 25 kT.

A change in electrolyte concentration (at constant pH) allows a modification of the height of the energy barrier [equation (8.3)] and therefore allows a variation in the stability ratio W. In the slow coagulation regime (charged particles, moderate salt concentration), an increase in salt concentration decreases the energy barrier and $\log W$ varies linearly with $\log c$ [27] until the rapid coagulation regime is attained, where $\log W$ remains zero (Figure 8.10).

The intersection of the two linear parts of the diagram is the limit concentration beyond which the energy maximum V_M of the energy barrier disappears. From a practical standpoint, the stability ratio W is the ratio of the fast flocculation rate of a sol in the presence of excess electrolyte to its flocculation rate at a given electrolyte concentration. The ratio is determined by the ratio of the initial coagulation rates, as observed by spectrophotometry for example [28–31].

Like flocculation, peptization (redispersion) can be characterized by a factor W' [20]:

$$W' = \int_{2a}^{\infty} x^{-2} \exp(V'(x)/kT)\,dx = W[\exp(V_T^0/kT)]^{-1}$$

where $V'(x) = V(x) - V_T^0$, and V_T^0 is the depth of the primary minimum (Figure 8.9).

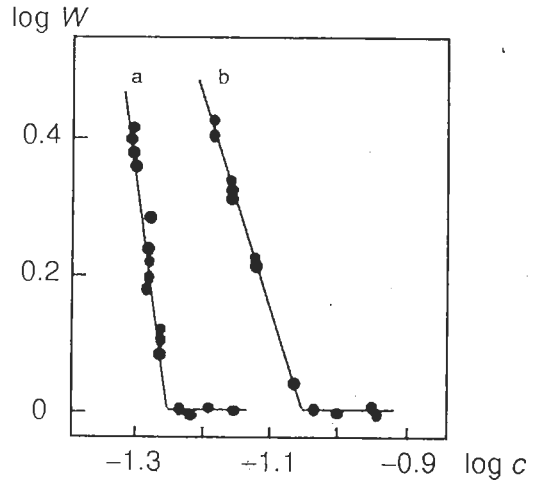

Figure 8.10 Influence of the electrolyte concentration on the flocculation rate of hematite particles (α-Fe_2O_3) of average diameter 47.5 nm and PZC = 8.2 (a) at pH 11.8 with counterions K^+ and (b) at pH 4 with counterions ClO_4^-. Reproduced from [28] by permission

The peptization rate is: $J_p = J^0/W'$ and the overall rate of aggregation is

$$J = J_a - J_p = (J^0/W)[1 - \exp(V_T^0/kT)]$$

The expression of the effective stability $W_{eff} = W[1 - \exp(V_T^0/kT)]^{-1}$ shows that aggregation is slower, or even zero, as V^0 is increasingly positive (Figure 8.9). It is therefore understandable that a system could be maintained in a state of limited aggregation (which is often observed in sols) when both $(V_M - V_T^0)$ and V_T^0 are small, of the order of a few kT.

It is interesting to note that the particle size has no influence on the interaction energy diagrams. When the radius of the particle (assumed spherical) is very large compared with the distance between surfaces ($D/a \ll 1$), both V_R and V_A are proportional to the radius and therefore the shape of the diagram does not change. In particular, the sign of V_T^0 is independent of size [24].

Depending on the flocculation rate, the structure of the aggregates can differ. When the particles aggregate slowly, the aggregates are compact and frequently non-redispersable because there is enough time for desolvation and relaxation of the double layers to take place. The aggregate is highly compact because, in such a situation, the particles can increase the attractive Van der Waals energy by increasing the number of contact points. However, if flocculation is fast, aggregates usually exhibit a loose and voluminous structure because of the large amount of trapped solvent. The fast flocculation rate also prevents particles from organizing themselves within the aggregate. This aggregate is frequently peptizable, as long as the relaxation of double layers is not appreciable. If left unperturbed for a long

time, the aggregate becomes progressively irreversible. The charge is no longer screened or compensated and tends to decrease or even become zero. Therefore, peptization of small particles should take place immediately after their flocculation.

8.1.5 CHARACTERIZATION OF THE OXIDE–SOLUTION INTERFACE BY THE FLOCCULATION KINETICS

The $\log W/\log c$ diagrams are a simple source of information on the behavior of ions near surfaces and on the properties of the surfaces themselves. An excellent example is the study of hematite sols (α-Fe_2O_3) prepared by thermohydrolysis (100 °C) of $Fe(NO_3)_3$ solutions aged at pH 1.6 for 2 weeks [28,32]. The PZC of the material ($\approx$8.2) allows the formation of sols in an acidic or alkaline medium.

The critical salt concentrations, (C_{lim}), corresponding to rapid coagulation have been determined, at fixed pH, for various monovalent ions (anions at pH < PZC, cations at pH > PZC). They are obtained from the diagrams in Figure 8.10 and transferred on to Figure 8.11. The flocculating strength of anions in an acidic medium ($IO_3^- > F^- > CH_3CO_2^- > CH_2ClCO_2^- > CHCl_2CO_2^- > Br^- > NO_3^- > Cl^- > ClO_4^- \approx I^-$) and that of the cations in an alkaline medium ($Li^+ > Na^+ > K^+ \approx Cs^+$) follow the same order as the structuring role of these ions on water, as determined by the viscosity of aqueous solutions or hydration heats [34] (see Section 1.1.3c). Since a small limit concentration is the reflection of strong adsorption, the surface of hematite particles is strongly structuring towards water.

The surface of an oxide will adsorb an ion strongly if their behavior in water are similar [33] (see Section 6.3.3). Hence, structuring ions IO_3^-, F^-, Li^+ and Na^+ are

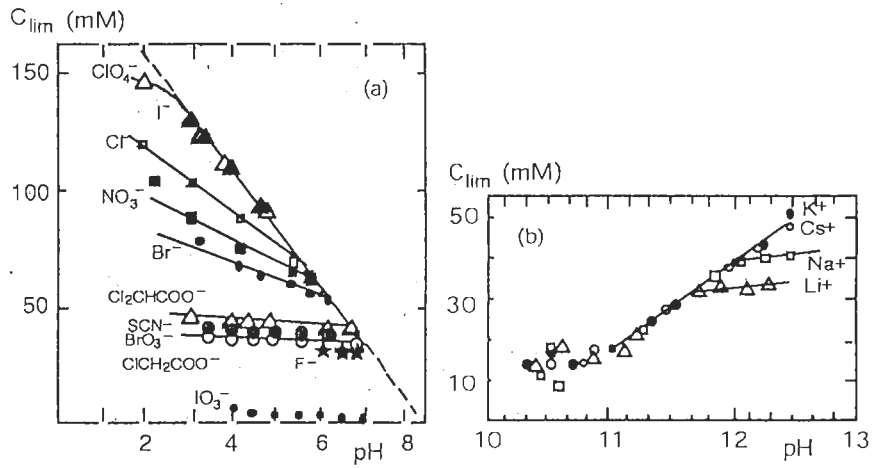

Figure 8.11 Critical flocculation concentrations for hematite particles as a function of pH for anions (a) and cations (b). Reproduced from [28] by permission

DropBooks

Table 8.1 Flocculation sequence of several oxides

Oxide	PCN	Sequence	Oxide	PCN	Sequence
WO_3	0.5	$Cs^+ > Li^+$	TiO_2	6	$Li^+ > Cs^+$
V_2O_5	1–2		Cr_2O_3	7	
δ-MnO_2	1.5		β-MnO_2	7.3	
SiO_2	2–3		ZnO	8	

strongly adsorbed when the surface is positively and negatively charged, respectively, whereas destructuring ions such as ClO_4^-, I^-, Cs^+ and K^+ are not adsorbed. Using flocculation sequences, or immersion heats [35], it is possible to distinguish the destructuring oxides (PZC < 4) from the structuring ones (Table 8.1).

Values of c_{lim} for α-Fe_2O_3 in an acid medium are 80–150 mmol l^{-1}, and 20–50 mmol l^{-1} in an alkaline medium. Electrokinetic potentials at flocculation are also higher in an alkaline medium (25–28 mV) than in an acidic medium (8–14 mV) [32]. This shows that, in spite of a weaker surface potential, a positively charged surface is more stable towards flocculation, and therefore that attractive van der Waals forces are weaker than between negatively charged surfaces. The attraction energy depends on the nature and size of the surfaces, not on the sign of the charge or on the electrolyte concentration. The decrease in interparticle attraction appears to be due only to the screening of these attractions by water molecules, which are more strongly adsorbed on a positive, more structuring surface than on a negative surface. The center-to-center distance between particles at flocculation is therefore greater in an acidic medium than in an alkaline medium. This also explains why, soon after flocculation in an acidic medium, particle peptization is observed after a simple dilution. This is not the case for negatively charged and less hydrated particles. The distance between flocculated particles is immediately very short and the Van der Waals energy is much higher (of the order of 20 kT). Figure 8.11a shows two regimes in the variation of the limit flocculation concentration as a function of pH. The linear part, common to all ions, is extrapolated to the PZC of the oxide (obtained independently by varying the electrokinetic potential as a function of pH): the ions behave non-specifically in this range. The break in the curve, which corresponds to deviation from the general behavior of ions, may be considered as the specificity threshold beyond which ions penetrate the Stern layer under the influence of the surface potential ψ_0. The measured values of ψ_d at the specificity threshhold, plotted as a function of the surface potential ψ_0 [calculated with the Nernst equation (7.27)] (Figure 8.12), show that specific adsorption takes place at higher potentials if the structuring (destructuring) strength of the ions decreases (increases).

Specific adsorption phenomena are more pronounced for multivalent ions because of their higher structuring strength. Their flocculating strength is also markedly higher than that of monovalent ions, and the Schultze–Hardy rule stipulates that the $c_{lim} \cdot z^6$ product is constant [21,24].

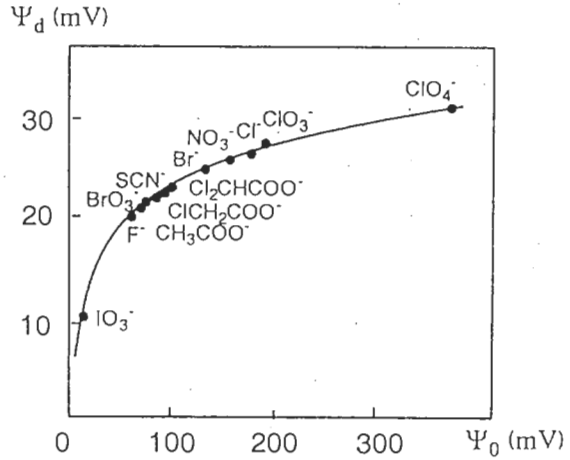

Figure 8.12 ψ_d as a function of ψ_0 at the specificity threshold for various anions adsorbed on α-Fe_2O_3. Reproduced from [28] by permission

It is also interesting to note that peptization by dilution of sols flocculated in an acid medium, is immediate if they have not aged more than 2 min. Beyond 15 min evolution, ultrasonic irradiation must be used. It is difficult to repeptize sols flocculated in an alkaline medium, independently of ageing time [32]. This clearly illustrates the effect of the relaxation of the solvation layer in flocs. Elimination of adsorbed water allows sharing of solvation layers, a decrease in interparticle distance and hence an increase in attraction energy, making peptization more difficult.

8.2 THERMODYNAMIC STABILITY OF THE DISPERSIONS. CONTROL OF PARTICLE SIZE

The classical analysis of nucleation and growth phenomena (see Section 2.3) involves the concentration of precursor of the solid phase as the main parameter controlling the particle size, because it regulates the relative importance of each reaction step and their possible overlap. During Ostwald ripening, the system reaches thermodynamic equilibrium. However, for a given concentration of the solution, the particle size decreases as the difference between PZC and the precipitation pH of the cation increases. Under such conditions, Ostwald ripening is almost non-existent. The fact that the divided state of the solid may be limited permanently makes the thermodynamic stability of oxide particles a reality from a dimensional point of view.

This concept can be applied to microemulsions [36]. Microemulsions are homogeneous, transparent dispersions of water, oil (toluene or cyclohexane, for example) and surfactant. These micellar systems form spontaneously and are very stable. Since the phases in contact are fluid and since the molecular interactions are weak,

such systems are very labile and a change in composition or temperature can easily cause a change in the size or the structure of the particles [37]. Such systems can probably be treated as colloidal systems from a thermodynamic standpoint as well as from a kinetic standpoint. The reactivity of oxides is much lower than that of microemulsions since breaking a metal–oxygen bond requires a large activation energy. The spontaneous division of solids caused by the modification of a parameter of the dispersion is usually not observed, at least in short times. However, since it is possible significantly to affect the particle size without involving Ostwald ripening by changing some synthesis conditions (acidity, ionic strength of the medium, concentration, temperature, etc.), it is possible to assume that thermodynamic equilibrium is reached in these systems.

In the classical treatment of precipitation, the surface energy of the solid is considered constant. This constant is related to the chemistry of the system, and the fact that this energy is also a function of the chemical composition of the oxide–solution interface is ignored. In turn, we have seen that the characteristics of the interface are closely related to the acidity and the ionic strength of the solution (see Chapter 6), i.e. to the physicochemical conditions of the synthesis. The growth of particles of any substance depends on the ability of the system to decrease its surface area. This ability is characterized by the surface energy (or tension), γ also involved in the change in free enthalpy of formation of the dispersion. Since the interfacial energy depends on the chemical composition of the interface, it would be expected that thermodynamic criteria would control the stability of the size of oxide colloids. This problem is different from the stability of a dispersion towards aggregation, which is characterized by a kinetic energy barrier (Fuchs' integral) similar to the activation energy of a chemical reaction involving deformation of molecules within an activated complex.

In the expression of the interfacial energy, $\gamma = (\partial G/\partial A)_{P,T,n}$ (see Section 8.2.2), we observe that if γ in a two-phase system is positive, spontaneous evolution ($\partial G < 0$) tends to decrease the extent of the interface ($\partial A < 0$). This is what happens to a drop of water in air, to two immiscible liquids or during the growth of particles during ageing (Ostwald ripening). If γ is negative, the interface must spontaneously expand ($\partial A > 0$). If γ is zero (or slightly positive owing to the contribution of entropy to the free enthalpy of formation of the dispersion [36,41]), equilibrium is reached. This postulate, which explains the formation and stability of microemulsions, can be applied without obstacles to oxide particles. It does not necessarily imply the spontaneous division of the solid, which would involve elevated activation energies, but it allows for an understanding of the reasons why the size and stability of particles during ageing can be regulated by the physicochemical conditions of the precipitation medium.

In order to explain the influence of these parameters on the size and stability of the particles, and in order to understand if it is possible effectively to control the dispersion of a solid during precipitation, it is useful to understand how the interfacial energy relates to the physical chemistry of such systems.

8.2.1 SURFACE ENERGY (TENSION) AND INTERFACIAL ENERGY

Within a liquid, there are isotropic attractive forces between molecules (Van der Waals, hydrogen bonds, etc.), but the molecules located on the surface of the liquid are subjected to uncompensated forces which tend to attract them towards the inside of the liquid. Therefore, as many molecules as possible leave the surface for the interior of the liquid, and the surface tends to contract spontaneously. The surface energy represents the difference in interaction energy between particles, depending on whether they are located on the surface or within the condensed phase. Assuming that in a condensed phase the interactions between nearest neighbors dominate, and that all interaction energies, $v(r)$, can be added to each other, the potential energy per molecule within the liquid is [3,9]

$$E_{A\,liq} = 1/2 z_{AA\,liq} \times v_{AA}(r_m)$$

where $z_{AA\,liq}$ is the number of neighbors of the molecules in the liquid at a distance r_m.

The potential energy per surface molecule is also given by

$$E_{A\,surf} = 1/2 z_{AA\,surf} \times v_{AA}(r_s)$$

where r_s is the distance between molecules on the surface. Assuming that $r_m = r_s$ and $z_{AA\,surf} = 1/2 z_{AA\,liq}$, we have

$$E_{A\,surf} - E_{A\,liq} = v_{AA}(r_m) \times (z_{AA}/2)(1/2 - 1)$$

Since v_{AA} is negative, the difference $E_{A\,surf} - E_{A\,liq}$ is positive. It is necessary to provide energy in order to form a surface.

When two liquids A and B are in the presence of one another, any A molecule leaving the bulk of the liquid for the interface progressively loses about half of its interactions with other molecules, but it also gains about the same number of interactions with B molecules. The potential energy of an A molecule at the interface can be written as

$$E_{A\,surf} = 1/2 z_{AA\,surf} \times v_{AA}(r_{AA\,surf}) + 1/2 z_{AB\,surf} \times v_{AB}(r_{AB\,surf})$$

For A and B molecules of similar sizes

$$z_{AA\,surf} + z_{AB\,surf} = z_{AA\,liq} = z_{BB\,liq}$$

If $v_{AB}(r_{AB}) > v_{AA}(r_{AA})$, $E_{A\,surf} > E_{A\,liq}$, and if $v_{AB}(r_{AB}) < v_{AA}(r_{AA})$, $E_{A\,surf} < E_{A\,liq}$. The same is true for B molecules. Therefore, in order to create a surface, A and B molecules must be brought towards the interface and the energy change per molecule is

$$\Delta E = (E_{A\,surf} - E_{A\,liq}) - (E_{B\,surf} - E_{B\,liq})$$

If ΔE is positive, the interface must shrink as much as possible, whereas if ΔE is negative, the interface must expand and allow mixing of the two liquids. It is also necessary to take into account the entropy change, which favors dispersion, even if ΔE is slightly positive.

DropBooks

Table 8.2 Surface tension and interfacial tension for a few liquids (in $mN\,m^{-1}$ or $mJ\,m^{-2}$ at 20 °C)

Interface	Liquid/vapor	Water/liquid
Water	×72.75	—
Benzene	×28.88	×35
CCl_4	×26.77	×45
Hg	476	375

The contribution of surface energy to the total energy becomes important if there is no change in energy within the liquid, or if the system is sufficiently divided for the surface energy to be comparable with the energy within the liquid. The work W necessary for the creation of the surface is proportional to the number of molecules brought from within the liquid to its surface, e.g. it is proportional to the area δA of the newly created surface, $\delta W = \gamma \delta A$. The proportionality factor γ represents the surface energy (or tension) in the case of a liquid/gas or solid/gas interface. It is called the interfacial energy (or tension) in the case of a liquid/liquid or liquid/solid interface. It has the dimension of $[MT^{-2}]$ and is expressed in $mJ\,m^{-2}$ or $erg\,cm^{-2}$. It is the energy required for an increase of the surface, reversibly and isothermally, by one unit. If ∂G is the change in free enthalpy associated with the formation of a surface ∂A, then $\gamma = (\partial G/\partial A)_{P,T,n}$. For liquids, γ is usually expressed as a force per unit length (surface 'tension'), given in $mN\,m^{-1}$ or dyne cm^{-1}. It is worth noting that all units of γ have the same dimension $[MT^{-2}]$ and that the numerical values of γ are the same [2,3].

The surface tension of liquids is measurable experimentally. A few values are given in Table 8.2. The surface tension of solids is not measurable directly because their small lability does not allow them to reach equilibrium, but it can be calculated [2,38–40]. It varies from 50 to a few hundreds $mJ\,m^{-2}$.

8.2.2 DECREASE IN INTERFACIAL ENERGY OWING TO ADSORPTION

The free enthalpy of a system may be divided into two components associated with its bulk (c) and its surface (s): $G = G^c + G^s$. The terms may be expressed as

$$G^c = U + PV - TS + \Sigma \mu_i n_i, \qquad G^s = U^s + \gamma A - TS^s + \Sigma \mu_i n_i^s$$

Within the two-dimensional space that is the surface, the PV term and its differential $V\,dP$ have no physical significance and may be neglected. Differentiating G^s gives

$$dG^s = -S^s\,dT + A\,d\gamma + \gamma\,dA + \Sigma \mu_i\,dn_i^s + \Sigma \mu n_i^s\,d\mu_i \qquad (8.10)$$

From both principles of thermodynamics, we may write

$$dG = (\partial G/\partial T)\,dT + (\partial G/\partial P)\,dP + (\partial G/\partial n)\,dn$$

or

$$dG^s = -S^s\,dT + \gamma\,dA + \Sigma \mu_i\,dn_i^s \qquad (8.11)$$

Subtracting (8.11) from (8.10), we obtain: $A d\gamma + \Sigma n_i^s\,d\mu_i = 0$, an expression more widely known as

$$d\gamma = -(\Sigma n_i^s/A)\,d\mu_i = -\Sigma \Gamma_i\,d\mu_i \qquad (8.12)$$

where Γ_i is the adsorption density of the ith constituent on the surface. Equation (8.12) is the Gibbs adsorption equation. It shows the influence of the composition of the zone near the surface on the interfacial tension. This relationship is analogous to the Gibbs–Duhem relationship, $\Sigma n_i\,d\mu_i = 0$, obtained in a similar manner from the expression

$$dG^c = V dP - S dT + \Sigma \mu_i\,dn_i + \Sigma n_i\,d\mu_i$$

which applies to bulk phases and does not take surface energy into consideration.

Equation (8.12) shows that adsorption of substances (increase in Γ) decreases interfacial tension. This is why molecules of fatty acids or alcohols that exhibit a polar hydrophilic head and a hydrophobic tail are called surfactants. These amphiphilic molecules are soluble in water and in hydrocarbons. They prefer to segregate at the water/air interface or at the water/oil interface as monolayers, since this situation is energetically favorable compared with complete solubilization into one phase or the other. The decrease in surface energy of alcoholic solutions in water (Figure 8.13a) shows that the tendency of alcohol molecules to occupy the water/air interface increases with the length of the hydrocarbon chain. Conversely, the surface energy of water increases with the concentration of ionic solutes (Figure 8.13b). The water–ion attractive forces are stronger than the water–water

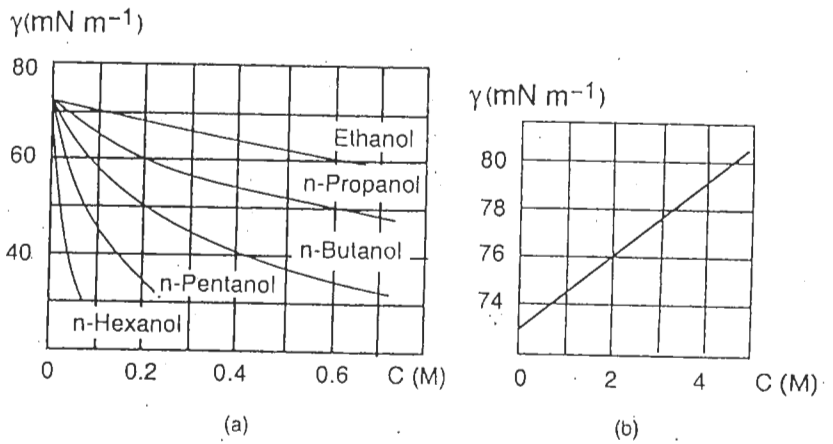

Figure 8.13 Surface energy of aqueous solutions as a function of concentration in (a) alcohol and (b) sodium chloride at 20 °C. Reproduced by permission of Butterworth-Heinemann Publishers, a division of Reed Educational & Professional Publishing Ltd from [9]

interactions, and the ions migrate towards the bulk of the solution. The adsorption is negative and γ increases.

The adorption of surfactants (wetting agents) decreases the interfacial tension of water and promotes expansion of the interface. If, through the adsorption of such molecules, the interfacial tension between two non-miscible liquids is sufficiently decreased or becomes negative, emulsification is spontaneous since the interface may expand without increase in free enthalpy. This explains schematically the formation of microemulsions.

In the case of oxides, the Gibbs adsorption equation (8.12) gives the variation in interfacial tension of particles in the presence of a basic solution XOH (or an acidic solution HY) and an electrolyte XY [39–41]:

$$d\gamma = -(\Gamma_H - \Gamma_{OH})\, d\mu_{XOH} - (\Gamma_X - \Gamma_Y)\, d\mu_{XY} \qquad (8.13)$$

where Γ, the adsorption density, is expressed in number of moles adsorbed per unit area.

Since the adsorption takes place on a charged surface, the electrochemical potential of the adsorbed species, μ_i^*, must be taken into consideration ($\mu_i^* = \mu_i + z_i F\psi$). Neglecting the specific adsorption of X^+ and Y^- ions, for an elevated and constant ionic strength ($[XY] \gg [XOH]$, $d\mu_X = 0$), (8.13) becomes

$$d\gamma = -(\Gamma_H - \Gamma_{OH})\, d\mu_{OH}^* \qquad (8.14)$$

The surface charge is $\sigma_0 = F(\Gamma_H - \Gamma_{OH})$ and (8.14) becomes

$$d\gamma = -(\sigma_0/F)\, d\mu_{OH} - \sigma_0\, d\psi_0 \qquad (8.15)$$

where ψ_0 is the surface electrical potential.

Equation (8.15) shows that, on the one hand, the interfacial tension is maximum at the PZC, for which σ_0 and ψ_0 are both zero, and, on the other hand, there are both a chemical and an electrical contribution to the decrease in interfacial tension. Since the charge and the surface potential are directly related to the pH and the ionic strength of the medium, the surface energy of the solid is certainly controlled by these parameters.

The *variation* in the interfacial tension of various oxides is calculated from the integration of $\sigma = f(pH)$ curves for different ionic strengths (Figure 8.14) [39–40]. The variation is similar to that calculated after integration of equation (8.15) [41], by calculating the chemical contribution $d\mu_{OH}$ using the Langmuir model, and evaluating the electrical contribution using the Grahame equation (7.35). A large decrease in oxide–solution interfacial tension, reaching zero or even negative values, is therefore predicted for high ionic strengths and far from the PZC of the oxide.

Since adsorption causes a decrease in interfacial energy, and since spontaneous dispersion of the systems occurs for $\gamma < 0$, the stability criterion, $\gamma = 0$, must be associated to the pH value corresponding to the point of zero surface tension PZST [41]. Two PZST can be defined since adsorption of PDIs may take place on either side of the PZC (Figure 8.14).

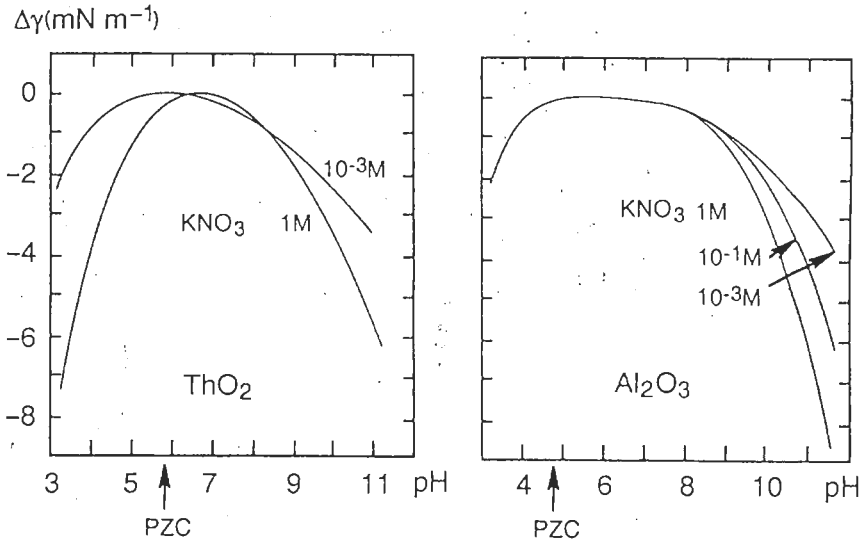

Figure 8.14 Surface energy as a function of pH, calculated from $\sigma = f(pH)$ curves, for ThO_2 and Al_2O_3 at various ionic strengths. Reprinted with permission of from [40]. Copyright 1969 American Chemical Society

DropBooks

The PZST is calculated by integration of equation (8.15) [42]. This integration will not be discussed here.

Depending on the value of γ_0 (surface energy at PZC usually between 50 and 300 mJ m^{-2}), and for given experimental conditions (I, pH), a two-phase macroscopic system will be obtained in which the minimum interface is reached (PCN $\leqslant$ pH < PZST in the case of a negatively charged surface, $\gamma > 0$) or, if pH $\geqslant$ PZST, $\gamma \approx 0$, a thermodynamically stable dispersion is obtained in which the particle size does not change during ageing.

8.2.3 CONTROL OF THE PARTICLE SIZE OF OXIDES

Magnetite Fe_3O_4 is an interesting oxide because spheroidal particles crystallize almost immediately during precipitation at room temperature (see Sections 3.5 and 5.6.1). Figure 8.15 shows the change in particle size for particles formed via coprecipitation of a stoichiometric mixture $FeCl_3 + 0.5FeCl_2$ in anaerobic conditions, in a basic solution where the pH is maintained constant with an automatic potentiometric apparatus, and in which the ionic strength is stabilized by an electrolyte [43]. The higher the pH and ionic strength I, the smaller are the particles. In addition, for a given ionic strength, there is a critical pH, pH*, defining a pH (pH > pH*) with which particle size does not change during ageing (Figure 8.16). If pH < pH*, the particles tend to become coarser after their formation.

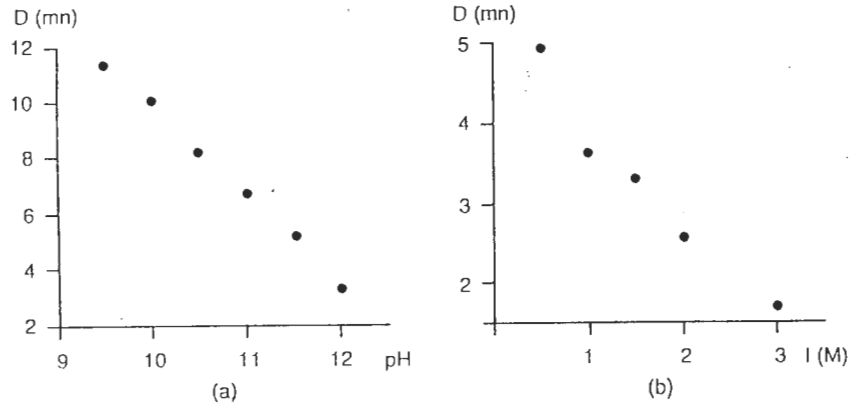

Figure 8.15 Average size of Fe_3O_4 particles formed (a) at various pH ($I = 0.5$M) and (b) at various ionic strengths (pH = 12) after 8 day ageing at 25 °C. Reproduced with kind permission from Kluwer Academic Publishers from [43]

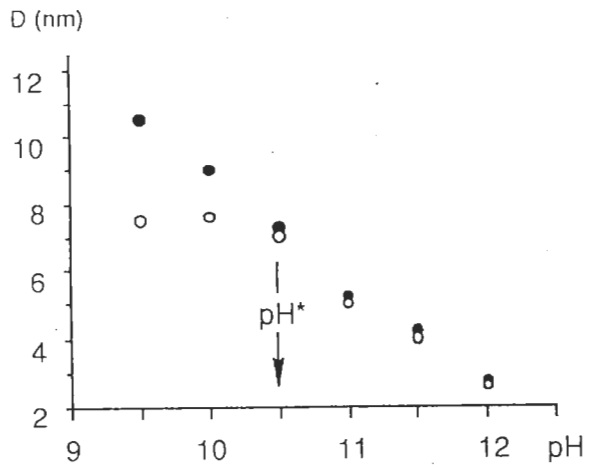

Figure 8.16 Average size of Fe_3O_4 synthesized at various pH, (25 °C, $I = 0.5$M) immediately after precipitation (○) and after 8 day ageing (●). Reproduced with kind permission from Kluwer Academic Publishers from [43]

The chemical composition and electrostatic charge of the surface of the particles are determined by the pH and the ionic strength of the solution. The pH influences the protonation–deprotonation equilibria of the surface hydroxylated groups (magnetite is negatively charged at pH > PCN ≈ 8). The ionic strength I ensures shielding between the charged groups on the surface and, at a given pH, the surface charge increases with I (see Section 6.3). The increase in surface charge by proton

desorption decreases the interfacial tension compared with its maximum value obtained at the PZC of the oxide [equations (8.12) and (8.15)].

Above the critical pH, pH*, which can be assumed equal to the PZST, the particle size seems to be controlled by the difference $\Delta pH = pH - pH^*$ and does not change with time (Figures 8.15 and 8.16). This suggests that particles form in conditions in which the surface is electrostatically saturated and in which the very weak interfacial tension allows an increase in surface area at little energy expense. The larger the difference $\Delta pH = pH - pH^*$, the smaller the particles since an increase in the number of charged sites leads to an increase in the size of the interface. The nucleation activation energy decreases when γ decreases [equation (2.4)]. Under such conditions, dissolution–crystallization phenomena do not take place since the driving force for the reduction of surface area is very small (the $\gamma\, dA$ term has almost no influence on the free enthalpy of formation of the dispersion). If the precipitation pH is lower than the critical pH*, the surface is not electrostatically saturated and the interfacial tension remains strongly positive. The system tends spontaneously to reduce its interfacial area. Secondary growth via Ostwald ripening must take place and the final particle size depends mostly on the lability of the dissolution–crystallization equilibria.

The interfacial tension should therefore not be treated as a constant for an oxide, and it appears that it is probably the most relevant parameter in particle size control. It is easy to understand why, from this standpoint, pH and ionic strength are major parameters affecting precipitation. Although little data are currently available, the example of magnetite can probably be extended to other oxides. The effect of medium acidity, for a given ionic strength, on the growth or stability of the solid phase is shown in Figure 8.17.

When PZC < pH < PZST (zone A), particle growth is not limited during synthesis (the surface charge is not saturated). Kinetically stable dispersions may exist in

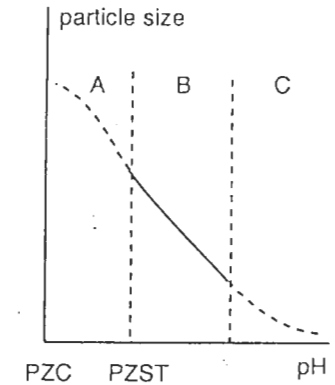

Figure 8.17 Variation in particle size as a function of precipitation pH (pH ≥ PZC, surface charge ≤ 0)

this domain, but some evolution in the size of the particles is possible (Ostwald ripening) in order to minimize the interfacial area. The B zone characterizes thermodynamically stable dispersions (pH > PZST, saturated surface charge). The particle size is determined by the difference pH – PZST. (Research is under way in order to determine the particle size variations within this pH range [42].)

Within zone C, pH ≫ PZST, solid particles cannot form. The solution is homogeneous and contains mono- or polynuclear complexes owing to the dissolution of oxides or hydroxides in a strongly acidic or basic medium.

When an oxide is formed under the conditions of zone A (non-limited growth), it might be expected that a change in the pH or ionic strength would bring the system back into zone B, leading to spontaneous division and thermodynamic equilibrium. The height of the activation energy barrier limits the evolution of the system in most cases. Under more extreme conditions (pH very distant from the PZST, i.e. a strongly acidic or alkaline madium), the oxide is dispersed through a 'dissolution' mechanism.

8.3 REFERENCES

1. P.G. De Gennes, *Rev. Modern Phys.* **64**, 645 (1992).
2. J.N. Israelachvili, *Intermolecular and Interface Forces*, Academic Press (1985).
3. R.J. Hunter, *Foundations of Colloid Science*, Vol. I, Clarendon Press, Oxford (1987).
4. T.W. Healy, D. Chan, L.R. White, *Pure and Appl. Chem.* 52,1207 (1980).
5. D. Chan, J.W. Perram, L.R. White, J.W. Healy, *J. Chem. Soc. Faraday Trans. I* 71, 1046 (1975).
6. B.W. Ninham, V.A. Parsegian, *J. Theor. Biol.* 31, 405 (1971).
7. D. Chan, P.M. Pashley, L.R. White, *J. Colloid Interface Sci.* **77**, 283 (1980).
8. J. Th. Overbeek, *J. Colloid Interface Sci.* **58**, 408 (1977).
9. D.J. Shaw, *Introduction to Colloid and Surface Chemistry*, Butterworths (1980).
10. J. Lyklema, *Pure and Appl. Chem.* **52**, 1221 (1980).
11. S.S. Dukhin, J. Lyklema, *Langmuir* 3, 94 (1987).
12. C.F. Zukoski IV, D.A. Saville, *J. Colloid Interface Sci.* **114**, 32 (1985).
13. P.C. Hiemenz, *Principles of Colloid and Surface Chemistry*, M. Dekker (1977).
14. J. Th. Overbeek, *Adv. Coll. Interface Sci.* 16, 17 (1982).
15. B.W. Ninham, *Pure and Appl. Chem.* **53**, 2135 (1981).
16. J. Israelachvili, *Adv. Coll. Interface Sci.* **16**, 31 (1982).
17. D.L. Feke, N.D. Prabhu, J. Adin Mann Jr, J. Adin Mann III, *J. Phys. Chem.* **88**, 5735 (1984).
18. C.J. Brinker, G.W. Scherer, *Sol Gel Science*, Academic Press, San Diego (1990).
19. T. Gillespie, *J. Colloid Sci.* **15**, 313 (1960).
20. B.V. Derjaguin, *Disc. Faraday Soc.* **65**, 306 (1978).
21. J. Th. Overbeek, *Pure and Appl. Chem.* **52**, 1151 (1980).
22. J.P. Jolivet, E. Tronc, Unpublished results.
23. G. Frens, J. Th. Overbeek, *J. Colloid Interface Sci.* **38**, 376 (1972).
24. G. Frens, *Disc. Faraday Soc.* **65**, 146 (1978).
25. D.W. Weaver, D.L. Feke, *J. Colloid Interface Sci.* **103**, 267 (1985).
26. N. Fuchs, *Z. Phys.* **89**, 736 (1934).
27. J. Th. Overbeek, in *Colloid Science*, Vol. I, H.R. Kruyt Ed., Elsevier, Amsterdam (1952).

28. F. Dumont, A. Watillon, *Disc. Faraday Soc.* **52**, 352 (1971).
29. A. Watillon, A.M. Joseph-Petit, *Disc. Faraday Soc.* **42**, 143 (1966).
30. G. Frens, *Kolloid Z.* **250**, 736 (1972).
31. A.M. Joseph-Petit, F. Dumont, A. Watillon, *J. Colloid Interface Sci.* **43**, 649 (1973).
32. F. Dumont, D. Van Tan, A. Watillon, *J. Colloid Interface Sci.* **55**, 678 (1976).
33. Y. Bérubé, P.L. De Bruyn, *J. Colloid Interface Sci.* **28**, 92 (1968).
34. E. Nightingale, in *Chemical Physics of Ionic Solutions*, B.E. Conway, R.G. Barradas Eds, J. Wiley & Sons, New York (1964).
35. T.W. Healy, D.W. Fuerstenau, *J. Colloid Interface Sci.* **20**, 376 (1965).
36. J.Th. Overbeek, *Faraday Disc. Chem. Soc.* **65**, 7 (1978).
37. K. Ogino, M. Abe, *Surface and Colloid Science*, Vol 15, E. Matijevic Ed., Plenum Press, New York (1993), p. 85.
38. E.N. Dalal, *Langmuir* 3, 1009 (1987).
39. S.M. Ahmed, *Can. J. Chem.* **44**, 1663 (1966).
40. S.M. Ahmed, *J. Phys. Chem.* **73**, 3546 (1969).
41. R.J. Stol, P.L. De Bruyn, *J. Colloid Interface Sci.* **75**, 185.81 (1980).
42. L. Vayssières, C. Chanéac, E. Tronc, J.P. Jolivet, *J. Colloid Interface Sci.* (in press).
43. J.P. Jolivet, E. Tronc, L. Vayssières, in *Nanophase Materials*, G.C. Hadjipanayis, R.W. Siegel Eds, NATO ASI Series, Series E, Vol. 260, Kluwer Academic Pub., Dordrecht (1994), p. 45.

DropBooks

9

Interface Reactions and Adsorption

The surface of oxide particles in water is a privileged reaction zone. Dissolved species such as metal cations, anions, neutral molecules or polymers are likely to attach themselves and adsorb on it. Owing to the large surface area of colloidal suspensions this phenomenon can have significant magnitude, and adsorption plays a role in many different processes such as matter transport in natural or industrial waters, in geochemistry, catalysis and stabilization of dispersed media. Adsorption of polymers on oxide particles also allows the fabrication of organic–inorganic hybrids. Adsorption (or 'sorption' if more than a monolayer of matter is attached) is a very important phenomenon and it would be useful to understand the interaction mechanism between oxide particles and species in solution.

Hydroxylated groups, which are the cause of the surface charge (see Chapter 6), may also act as coordination sites for dissolved cations, or may be substituted by anions (surface coordination). They may also act as nucleation sites for a solid phase in the case of surface precipitation. Therefore, several possible mechanisms should be considered in the overall phenomena of adsorption, and most of them may be described in terms of the classical concepts of coordination chemistry. However, adsorption exhibits some specific characteristics because one of the partners is a solid with structural and physical properties that may play an important role. Although adsorption often involves only the surface of the particles, if the solid exhibits appreciable ionic mobility (in the case of an ion-exchange material), or electronic mobility (for a mixed-valence material), acid–base surface reactions may trigger various phenomena in the core of the particles, reactions which in turn may cause ionic and/or electron transfers through the solid–solution interface.

9.1 ADSORPTION OF METAL CATIONS

Oxide particles suspended in an aqueous medium carry hydroxylated groups bearing positive or negative charges that modify the properties of water in the solvation sphere. These characteristics, which are related to the pH of the solution,

cause an interaction between the surface and cations in solution. Like many other phenomena we discussed, adsorption is closely linked to the acidity of the medium, for any oxide or cation in solution [1]. This is because the pH of the suspension controls both the hydrolysis of the cation and the surface charge of the oxide. However, there are several types of interaction, depending on the nature of the bond between the adsorbed ion and the surface.

9.1.1 ELECTROSTATIC INTERACTION AND OUTER SPHERE COMPLEXES

Non-hydrolyzable, non-structuring cations, such as Li^+ or Na^+, adsorb on oxides when the surface is negatively charged (pH > PZC). Ions are attracted towards the surface by 'non-specific' forces: electric charge, preferential solvation within the heavily structured hydration sphere of the surface (see Sections 6.2.2 and 8.1.5). Such ions are called 'physisorbed' since they are restricted to the solvation layer and they exhibit reduced mobility. This is the case for Na^+, whose relaxation time (determined by ^{23}Na NMR) is longer near the surface of silica than in solution [2]. Preferential solvation of structuring cations within the hydration sphere of the surface is clearly shown by the adsorption sequence $Li^+ > Na^+ > K^+ > Cs^+$ (see Section 8.1.5).

A similar interaction occurs with the very stable complexes of various cations such as Cu^{2+}, Ni^{2+} or Co^{2+}. At high ammonia concentration (pH > 8), $[M(NH_3)_6]^{2+}$ complexes dominate in solution and are adsorbed on various substrates [3]. The UV-visible characteristic absorption of the nickel amino complex is not shifted upon adsorption on silica [4]. Adsorption of these complexes does not cause a shift in the intersection point of the proton titration curves (i.e does not cause a shift in the PZC of the oxide [5]). The negatively charged surface of the oxide acts as the counterion of the cation complex $[M(NH_3)_6]^{2+}$ ($M = Cu^{2+}$, Ni^{2+}, Co^{2+}), leading, at the most, to the formation of ion pairs:

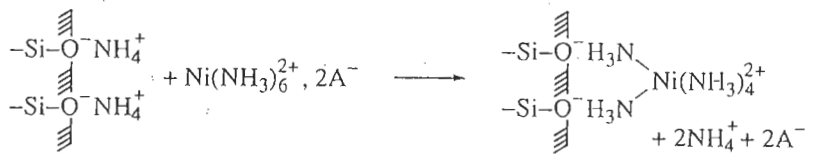

Some very stable metal complexes with very bulky ligands (phenanthroline, bipyridyl) may appear specifically adsorbed without modification of their coordination sphere [5]. The large size of the ligands and their polarizability allow a significant contribution of Van der Waals forces to the energy of adsorption.

Some aquo cations may be adsorbed non-specifically. This is the case for Cu^{2+} in an acid medium (pH < 3) impregnated in porous silica, where the pores are small (< 6 nm). The EPR spectrum of copper is characteristic of hexa-aquo ions $[Cu(OH_2)_6]^{2+}$ exhibiting axial symmetry [6], but their rotation and reorientation

time is 1.5 times longer than that of ions in aqueous solution. Their mobility is strongly affected by the structuring of water near the surface. The cations appear trapped within 8–10 layers of solvation, forming a 'vitreous' matrix filling the small pores. With larger-pore silica, the water filling the pores is not so strongly structured, and a second EPR signal characteristic of $[Cu(OH_2)_6]^{2+}$ ions in solution is observed [6].

Oxides more strongly basic than SiO_2, such as MgO and Al_2O_3, develop stronger interactions with $[Cu(OH_2)[6]^{2+}$ ions. The EPR spectrum of copper is similar to that of the solid [6]. Although the cupric ions are not desolvated, the $[Cu(OH_2)_6]^{2+}$ are immobilized on the surface. A similar situation is encountered when they are adsorbed at pH 2.7 on TiO_2 [7], i.e. well below the PZC of the oxide (pH = 6.2). Although the ions cause an increase in the electrophoretic mobility of the oxide (see below) because they increase the surface charge, their 'static' EPR spectrum is typical of cupric ions hydrated in a distorted octahedral environment. This means that the axis of the tetragonal distortion does not change at the time-scale of EPR spectroscopy.

In this type of interaction, there is no change in the coordination sphere of the adsorbed cations. In fact, their solvation by the surface hydration layer is higher than with 'liquid' water. From a coordination chemistry standpoint, sodium and cupric ions form ion pairs with the surface (the surface is negatively charged), or perhaps outer sphere complexes [8] probably involving hydrogen bonds between surface hydroxyl groups and the coordination water, through the bridging ligand $[H_3O_2]$ [9,10]:

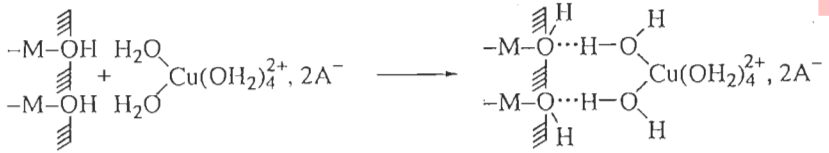

In fact, in the process of 'physisorption', the surface acts as a solvating agent for the cations. At most, the cations shield the surface charges without modifying the PZC of the oxide.

9.1.2 CHEMISORPTION AND INNER SPHERE COMPLEXES

Cations that hydrolyze easily, such as Zn(II), Cd(II), Hg(II), Pb(II) and Al(III), and transition metals have a strong affinity for oxide surfaces, and adsorption may occur against electrostatic forces, and for pH values inferior to the PZC of the oxide. Adsorption of these cations is a strong function of the pH, since there is a narrow pH range, usually 1–2 units, for which the adsorption rate (the degree of saturation of the surface) changes from 0 to 100% (Figure 9.1).

The pH for the onset of this phenomenon is always lower than the pH at which the cations alone in solution would hydrolyze or precipitate. This brings about the

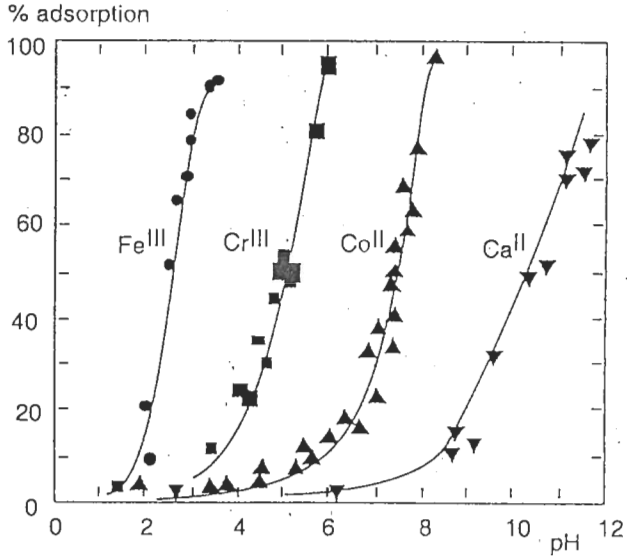

Figure 9.1 Adsorption isotherms at 25 °C for Fe(III) (1.2×10^{-4}M), Cr(III) (2×10^{-4}M), Co(II) (1.2×10^{-4}M) and Ca(II) (1.4×10^{-4}M) on SiO_2 as a function of pH. Reproduced by permission of Academic Press from [11]

DropBooks

issue of the adsorption mechanism for such cations [1,12,13]. The process may occur via adsorption of previously hydrolyzed complexes

$$\underset{(nHO^-)}{[M(OH_2)_6]^{z+}} + nH_2O \Longleftrightarrow [M(OH)_n\underset{(nH_2O)}{(OH_2)_6}]^{(z-n)+} + nH_3O^+$$

that physisorb on the surface:

$$S\text{–}OH + [M(OH)_n(OH_2)_{6-n}]^{(z-n)+} \rightleftharpoons S(OH)_m, [M(OH)_n(OH_2)_{6-n}]^{(z-n)+} + mH_2O$$

An equivalent process with regards to the stoichiometry of proton exchange may also involve hydrolysis of complexes by the surface:

$$S\text{–}OH + [M(OH_2)_6]^{z+} \rightleftharpoons S(O)_n, M(OH_2)_{6-n}]^{(z-n)+} + nH_3O^+$$

The issue is to determine whether cation hydrolysis precedes and enhances their ability to adsorb, or whether hydrolysis is a consequence of adsorption. In the first scenario, we are dealing with physisorption of hydrolyzed complexes whose coordination sphere is not affected by adsorption. In the second scenario, penetration

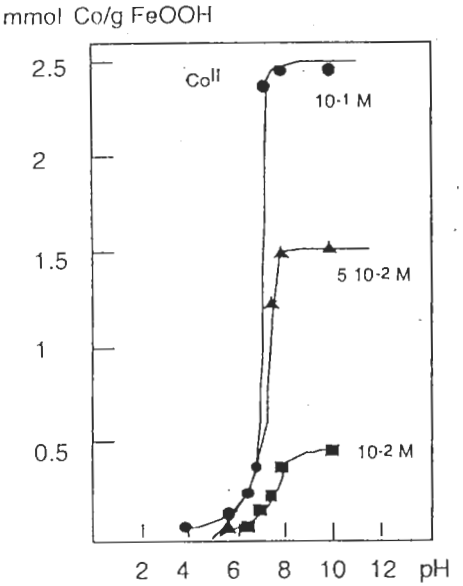

Figure 9.2 Adsorption of Co(II) on α-FeOOH for various concentrations. (1 g solid in 200 ml solution). Reproduced by permission of Academic Press from [14]

of the coordination sphere of the cation by oxo or hydroxo ligands causes their chemisorption as inner sphere complexes.

In fact, although the adsorption isotherm cannot predict this, both mechanisms occur, depending on the pH of adsorption, as shown in the following examples.

(a) Structural Considerations

Adsorption of Co(II) on α-FeOOH goethite occurs between pH 6 and 7 [14] (Figure 9.2). If alone in solution, Co^{2+} forms the $[Co(OH)(OH_2)_5]^+$ complex around pH 7. At a concentration of 0.1 mol l^{-1}, the hydroxide precipitates around pH 8 [15].

XPS spectroscopy shows that adsorbed Co(II) exists under various forms depending on the pH of the reaction [14]. At pH < 6.5, cobalt is adsorbed as the hexa-aquo ion. Since the PZC of the surface is 6.5, aquo ions form outer sphere complexes with the neutral and negatively charged groups of the surface ($-Fe_2OH_0$, $-Fe_3O^{\delta-}$, see Section 7.1.1). The adsorption density is small because the surface is charged positively.

Between pH 6.5 and 7.5, XPS parameters of adsorbed Co are very similar to those of the hydroxide $Co(OH)_2$. Since, in a solution of the same concentration, cobalt alone hydrolyzes only at pH > 7.4, it is very likely that hydrolysis of Co(II) is induced by surface groups rather than by the acidity of the solution. Surface

hydroxyls act as hydrolyzing ligands, and cobalt chemisorption is the result of the formation of inner sphere complexes.

If adsorption takes place at pH > 8, XPS data show the presence of $Co(OH)_2$ and CoO(OH) on the surface. These forms are also identified by XRD and XPS in the precipitates formed at the same pH in solutions containing Co alone. This strongly suggests that hydrolysis and precipitation of cobalt occur in solution, and the precipitated particles are later physisorbed on goethite.

Therefore, three adsorption mechanisms seem to take place, depending on the pH of the medium. A similar behavior is observed for the adsorption of Co(II) on SiO_2 and TiO_2 [11], on ZrO_2 and Al_2O_3 [16] and for the adsorption of Zn(II), Cd(II) Cu(II) and Pb(II) on amorphous ferric oxyhydroxide [17,18].

The hydrolyzing role of oxide surfaces is very elegantly shown in Mössbauer investigations of the adsorption of ^{57}Fe(III) on hematite α-$^{56}Fe_2O_3$ [19]. Since ^{56}Fe is Mössbauer-inactive, the spectrum of ferric ions is not obfuscated by that of the particles.

At pH 2.5, the oxide surface is positively charged and ferric ions are present in dilute solution (10^{-3} mol l^{-1}) as $[Fe(OH_2)_6]^{3+}$ (70%), $[Fe(OH)(OH_2)_5]^{2+}$ (20%), $[Fe(OH)_2(OH_2)_4]^+$ (3%) and $[Fe_2(OH)_2(OH_2)_8]^{4+}$ (6%). Mössbauer spectra of the suspension (Figure 9.3a), which exhibit a sextuplet, show that all adsorbed ferric ions interact magnetically with the substrate. The parameters of the adsorbed ions (isomeric shift, average hyperfine field) are very similar to those of solid hematite. Within the adsorbed layer, ferric ions occupy sites characteristic of the structure of hematite, and hence the layer is an extension of the crystalline network of the

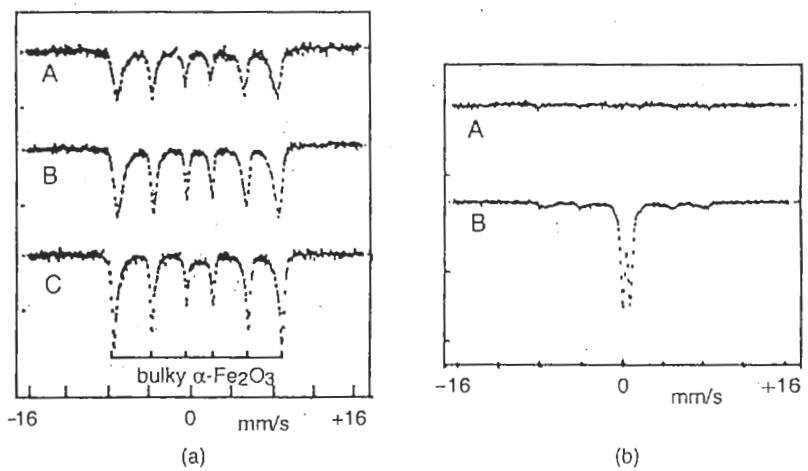

Figure 9.3 Mössbauer spectra at room temperature for ^{57}Fe(III) ions adsorbed on hematite particles α-$^{56}Fe_2O_3$ (a) at pH 2.5 (A suspension; B after drying; C after heating at 600 °C for 6 h; D after heat treatment at 600 °C for 6 h) and (b) at pH 6 (A suspension; B after drying). Reprinted with permission from [19]. Copyright 1990 American Chemical Society

particles. In this acidity range, ferric ions are not able to nucleate on the solid, and most certainly not on the corundum structure (see Section 3.2.3), and therefore they are hydrolyzed by hydroxyl groups and chemisorbed on the oxide surface.

If adsorption takes place at pH 6, no Mössbauer signal is observed. After drying, a strong quadrupolar doublet is observed along with a weak magnetic component (Figure 9.3b). In this acidity range, iron forms a ferric gel physisorbed on the substrate, with no strong chemical bond. The lack of a signal is due to the very weak absorption of γ-rays by the gel weakly bonded to the surface of the particles. Dehydration at room temperature decreases the mobility of the physisorbed gel, generating a Mössbauer spectrum similar to that of amorphous ferric gels. At pH 4, adsorption involves both mechanisms.

Adsorption of hydrolyzable ions takes places through various mechanisms in which hydrolysis by surface nucleophilic groups and hydrolysis by the solution itself (OH^-, water molecules) compete. Therefore, as long as the hydrolysis and precipitation pH is not reached, the surface is likely to behave as a ligand, leading to chemisorption through a true substitution reaction:

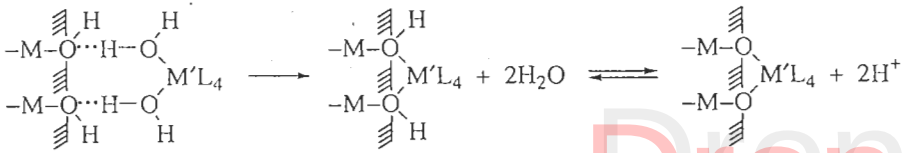

This reaction is analogous to olation and oxolation reactions between hydrolyzed species. It involves, at pH $\geqslant$ PZC, oxo or hydroxo ligands from the surface acting as nucleophiles within the coordination sphere of the adsorbed ion. This reaction is also responsible for the adsorption of mixed aquo–amino complexes of nickel. Washing silica suspensions which have adsorbed hexamino nickel(II) complexes leads to the formation of tetra-amino complexes. The shift in the UV-visible absorption towards lower frequencies makes it possible to follow the level of replacement of NH_3 by H_2O, and then of water by SiO^- [4,10]:

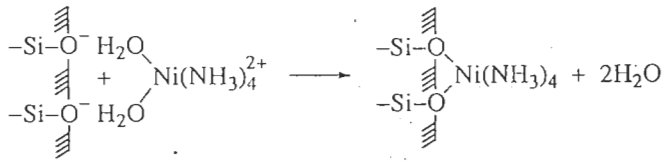

The presence of removable aquo ligands in the coordination sphere of the nickel causes an increase in the adsorbed amounts. The same phenomenon takes place with $[Cu(OH_2)_n(NH_3)_m]^{2+}$ complexes formed at pH < 9 [10,20].

(b) Electrophoretic Mobility

The various regimes of interaction between ions in solution and the surface, as a function of pH (chemisorption of the cations, physisorption of the oxide or the

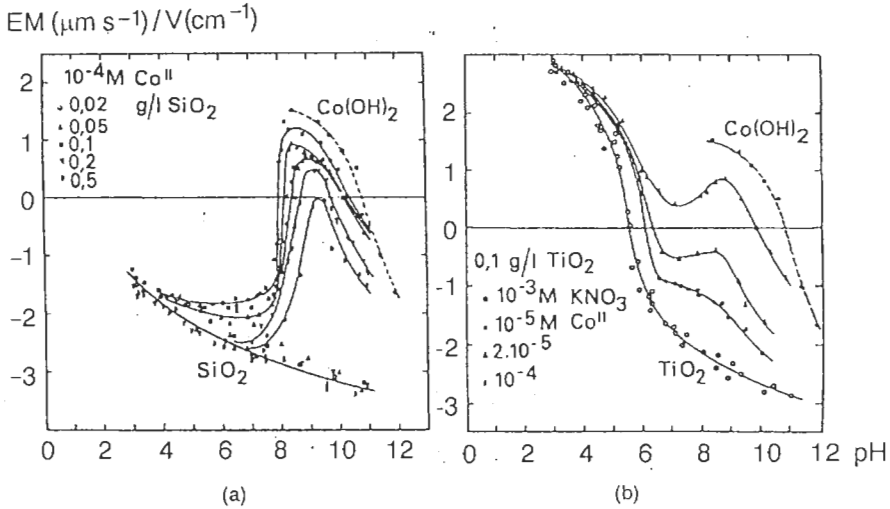

Figure 9.4 Electrophoretic mobility (a) for various SiO_2 amounts and (b) for TiO_2 in the presence of $Co(NO_3)_2$. Reproduced by permission of Academic Press from [22]

hydroxide) are measurable on the electrophoretic mobility of the suspensions. The mobility m_E of the particles is defined as $m_E = v_E$, where v_E is the velocity of the particles under an electric field E [21]. Depending on the sign of the particles, the particles move in the direction of the field or in the opposite direction. At pH = PZC, the mobility is zero.

Adsorption of a hydrolyzable cation in large enough concentration completely to cover the available surface area of the suspension can modify the electrophoretic behavior of the particles. Three charge reversals (CR) are observed as the pH increases (Figure 9.4).

Reaching the PZC (or the IEP, isoelectric point), causes CR_1 ($\pm$). It is close to pH 2 for SiO_2 and 5.5 for TiO_2 (Figure 9.4). Adsorption of positively charged entities (aquo ions, hydroxylated complexes) progressively compensates for the negative charge on the surface, leading to CR_2 ($\pm$) around pH 8 (Figure 9.4). As the pH increases, the positive charge on the adsorbed species decreases, and CR_3 indicates the PZC of the adsorbed layer (pH 11). The position of CR_2 and CR_3 depends on the number of ions that have been adsorbed. When coverage of the surface is complete, CR_3 is identical to the PZC of the hydroxide or oxide formed by the adsorbed cation alone. CR_2, which is inferior to the precipitation pH of the cation alone in solution, marks, in fact, the pH of the onset of precipitation on the almost completely covered surface [22,16].

This variation in electrophoretic mobility reflects the progressive change in nature of the surface during adsorption, assuming a homogeneous distribution of the ions on the surface. It turns out that this behavior is not generalized because the

DropBooks

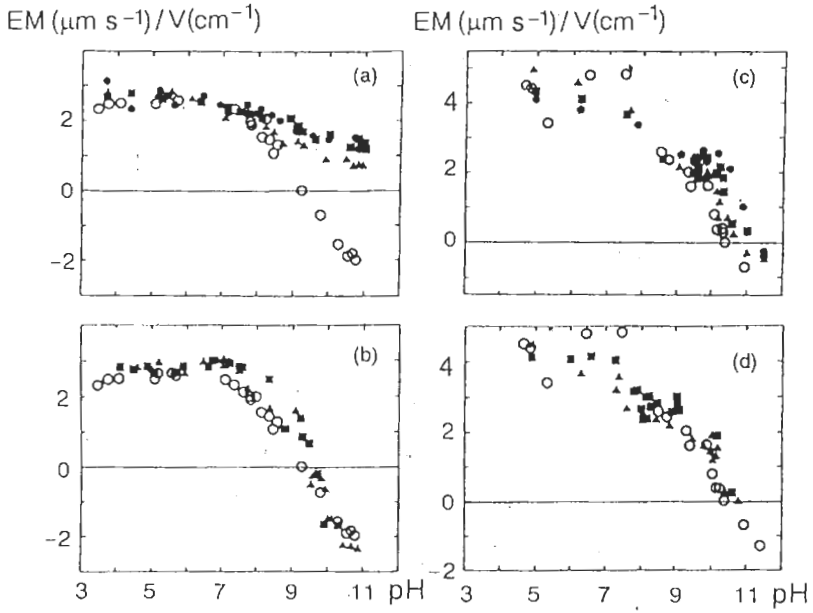

Figure 9.5 Electrophoretic mobility (EM) of goethite particles ($20\,m^2/l$) adsorbed at various concentrations (solid markers): (a) Mg(II), (b) Mn(II); boehmite ($20\,m^2/l$) having adsorbed (c) Mg(II) and (d) Mn(II). Open markers indicate the electrophoretic mobility of both solids measured in the presence of $NaClO_4$. Reproduced by permission of Academic Press from [23]

adsorption mechanism depends on the nature of the surface as well as on that of the adsorbed ions.

For example, adsorption of Mg(II) on goethite, α-FeOOH, begins below the PZC, and a 10–25% coverage is sufficient to bypass the CR_1 of goethite (Figure 9.5a) [23]. However, adsorption of Mg(II) on boehmite, γ-AlOOH, is complete at the PZC and modifies only slightly the position of the CR_1 (Figure 9.5b). Adsorption of Mn(II) on both oxyhydroxides also does not affect the position of their PZC (CR_1) (Figure 9.5c, d).

EPR studies of manganese adsorbed on boehmite show that Mn(II) ions form an antiferromagnetic material analogous to $Mn(OH)_2$ [23]. Since the amount of adsorbed Mn(II) would be sufficient to form several compact layers of the hydroxide, the lack of influence on the electrophoretic mobility seems to indicate that manganese hydroxide is adsorbed as clusters that do not cover the boehmite surface very uniformly. The surface remains largely exposed to the solution and is able to maintain its physicochemical characteristics. This must also be the case during adsorption of manganese on goethite because no effect is observed on the CR_1 of goethite. Manganese might form very small clusters $Mg(OH)_2$ which would

exhibit a strongly widened EPR signal owing to the local magnetic field produced by ferric ions near the surface [23].

However, adsorption of Mg(II) on goethite takes place homogeneously on isolated sites of the surface, thereby preventing reversal of the surface charge.

This difference in behavior can probably be explained by the difference in the energy of adsorption for the ions and that of the nucleation of the hydroxide on the surface of the adsorbant. If the adsorption energy is larger than the nucleation energy, homogeneous coverage of the surface is favored. If the opposite is true, heterogeneous nucleation of the hydroxide can take place. In other words, the nucleophilic strength of oxo or hydroxo ligands of the boehmite surface is not as high as that of the surface groups on goethite. The surface groups on boehmite ($PZC \approx 10$) are less acidic, and therefore less nucleophilic or complexing, than on goethite ($PZC \approx 8$–9). This is in agreement with the results of the MUSIC model (see Section 7.1.1). Mg(II) ions cannot nucleate the hydroxide on goethite and are adsorbed as inner sphere complexes. Mn(II) ions are more readily hydrolyzable than Mg(II) ions and condense preferentially in solution, before adsorbing as $Mn(OH)_2$ clusters on both surfaces.

The magnetic behavior of Mn(II) and Cu(II) adsorbed at $pH > 6$ on TiO_2 shows that they also form hydroxide or hydrated oxide clusters on the surface of TiO_2 [7].

(c) Adsorption Isotherms

Another useful technique for the study of various adsorption regimes is the use of isotherms linking the adsorption density Γ (the amount of cations adsorbed per unit surface area) to the cation concentration C in solution at equilibrium.

Isotherm models initially used for adsorption of gas molecules on to solids can now be applied to adsorption in solution. Two such models are most widely used [13]:

- The Langmuir isotherm:

$$\Gamma = \Gamma_{max} \frac{kC}{1 + kC}$$

where k the adsorption equilibrium constant and Γ_{max} is the maximum adsorption density. The fundamental hypotheses of the model are that all adsorption sites are equivalent, and that the adsorption energy is not a function of the extent of surface coverage. This means that there is no interaction between adjacent species adsorbed on the surface. Γ is proportional to C at low concentrations and reaches a maximum Γ_{max} at high concentration.

- The Freundlich isotherm:

$$\Gamma = kC^{1/n} \qquad \text{with } n > 1$$

This purely empirical model assumes that adsorption energy decreases logarithmically with adsorption density, and hence there is no linear relationship between Γ and C. Adsorption density is, in principle, not limited.

Usually, Langmuir isotherms describe experimental data reasonably well for small adsorption densities and pH lower than the precipitation pH of the cation alone in solution, when the cations are adsorbed in monolayers. Plots of $\log \Gamma = f(\log[M^{z+}]_{eq})$ are linear with a slope of 1. This is the case for adsorption at pH $\leqslant$ 6.4 of Cd(II), Zn(II) or Cu(II) on amorphous iron oxyhydroxide at a concentration smaller or equal to 10^{-6} mol l^{-1} [18]. It is also true at pH $\leqslant$ 7 for Co(II) and Ni(II) on SiO_2 [24], for Co(II) on Fe_3O_4, Al_2O_3 and MnO_2 [25] and for Ag^+ on TiO_2 anatase [26]. However, at high cation concentration, or for a pH higher than the precipitation pH, adsorption data are better described by the Freundlich isotherm. The $\log \Gamma = f(\log[M^{z+}]_{eq})$ plots are linear and their slopes are smaller than 1 (adsorption on amorphous iron oxyhydroxide of Cd, Zn and Cu at $C > 10^{-6}$ mol l^{-1} [18] and Ag at pH 8 [27]). In this case, adsorption is not limited to a monolayer, which was a restriction imposed by the Langmuir isotherms.

These behavior differences are often explained by the heterogeneity of adsorption sites [18,13], and composite isotherms can be used to fit experimental data [28].

(d) Models

Many models try to provide a quantitative analysis of adsorption phenomena on oxide surfaces. Most of these models are based on the formation of surface complexes [1,13,29]. They consider the competition between the variation in free enthalpy due to chemical and electrostatic interactions and the variation in solvation energy of the adsorbed cations [30]. Some models also consider equilibrium constants derived from the mass-action law (the triple-layer model) [31,32]. Combining surface complexation and precipitation of cations in solution is a way of treating the problem continuously over a very wide range of concentrations [33].

The models fit experimental data quite well without identifying or describing the surface complexes chemically. In fact, these models often look more like 'tuning' exercises than real tools improving our understanding of interfacial phenomena. For example, identical data are sometimes remarkably fitted using very different 'chemical' parameters [29]. Therefore, the physical significance of these models is highly questionable.

Surface heterogeneities are often invoked to explain a change in regime of the adsorption mechanism. However, taking such heterogeneities into account does not significantly change the results of adsorption simulation [34]. Since various mechanisms and various 'types' of adsorption (homogeneous layers formed via chemisorption, physisorbed surface clusters—see sections a and b) can occur, it is not surprising that a single model cannot describe all the phenomena observed over a wide range of concentrations. It seems logical to assume that adsorption of cations by the formation of inner sphere complexes cannot be treated like the precipitation or physisorption of a hydroxide. The required change in approach is indeed related to the fact that the chemistry of the system is dominated by surface properties in the case of complexation, and by the chemistry of the cation in solution in the case of precipitation.

9.1.3 CATION ADSORPTION AND INTERFACE TRANSFERS

Cation chemisorption on many oxides comprises various mechanisms that involve the adsorbing surface without involving the core of the particles. The interface is polarizable, and there is no exchange of matter between the inside of the solid and the solution.

The high room-temperature electronic mobility of mixed-valence oxides such as Fe_3O_4, Mn_3O_4, MnO_2 and $V_2O_5 \cdot xH_2O$ makes these materials particularly interesting in suspension. Acid–base surface reactions and cation adsorption may cause a redox response inside the colloid as well as ionic or electronic transfers through the solution–solid interface. A few examples related to iron oxide spinels are discussed in this section.

Rapid electronic exchange takes place in Fe_3O_4 magnetite at room temperature (see Section 3.5). Mössbauer spectroscopy gives an average valence of 2.5 for the cations in the octahedral sublattice, which justifies the use of the formula $[Fe^{3+}]_{Td}[Fe_2^{2.5+}]_{Oh}O_4$. Oxidation of magnetite into maghemite γ-Fe_2O_3 preserves the inverse spinel structure, but the octahedral sublattice now contains vacancies: $[Fe^{3+}]_{Td}[Fe_{5/3}^{3+}V_{1/3}]_{Oh}O_4$, where V are the cation vacancies. Colloidal magnetite can be converted easily into maghemite in various ways. The conversion is apparently reversible. These properties are due in large part to the electronic mobility.

(i) Colloidal magnetite oxidizes readily in air, or in a neutral or alkaline suspension, by chemisorption of oxygen:

$$[Fe_{3+}][Fe_2^{2.5+}]O_4 + 0.25O_2 \longrightarrow 1.125[Fe^{3+}][Fe_{5/3}^{3+}V_{1/3}]O_4$$

Mobile electrons are trapped by adsorbed oxygen. The excess positive charge in the lattice forces migration of excess ferric ions towards the surface in order to coordinate the O^{2-} ions formed on the surface. They form new cation sites that extend the crystalline lattice (cf. Figure 9.7). These new sites participate in electron transfers and allow the reaction to proceed until complete oxidation of the oxide. Overall, the migration of Fe^{3+} and electrons towards the surface is compensated for by the migration of cation vacancies towards the inside of the particle. Because of the small size of the particles, approximately 8 nm in diameter, and their large specific surface area, the reaction kinetics are fast.

(ii) In a suspension acidified with $HClO_4$ to about pH 2, and in the absence of oxidizing agents, the same transformation takes place by elimination of ferrous ions from the lattice of the particle [35]. The titration curves of suspensions containing various acid concentrations exhibit two equivalent points (Figure 9.6).

The first equivalent point around pH 4 corresponds to an excess of free acidity. The second point corresponds to the end of precipitation of ferrous ions as $Fe(OH)_2$.

ProbBooks

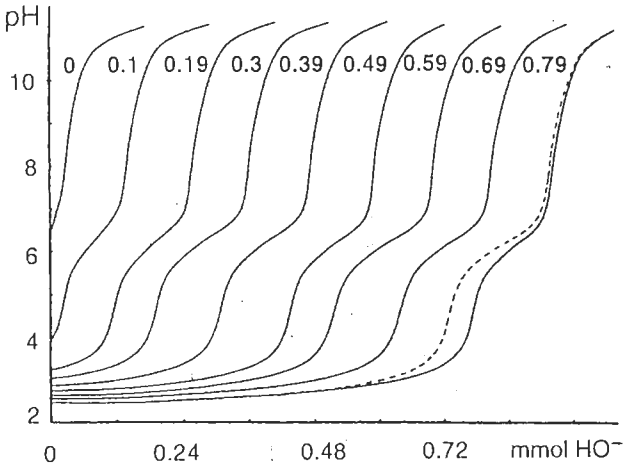

Figure 9.6 Titration of $Fe_3O_4 + HClO_4$ by $N(CH_3)_4OH$. The ratios $[H^+]_{added}/Fe(II)_{initial}$ are indicated on the curves. Titrations are carried out 5 min after acidification. Dashed line: titration 45 min after acidification. Reproduced by permission of Academic Press from [35]

The total reaction balance involves consumption of two protons for one Fe(II) released into the solution.

The protonation of surface hydroxyl groups causes localization of mobile electrons from the lattice, and the formation of ferrous ions will compensate locally for the charge of protonated sites on the surface. This, in turn, causes a lengthening of the O–Fe(II) bonds compared with O–Fe(III) bonds, and, under such conditions, unstable surface Fe(II) ions go into solution as solvated species:

$$Fe^{2.5+}\text{–O–}Fe^{2.5+}\text{–OH} \xrightarrow{H^+} Fe^{3+}\text{–O–}Fe^{2+}\text{–}O^{+}H_2$$

$$\xrightarrow{H^+} Fe^{3+}\text{–OH} + [Fe(OH_2)_6]^{2+}_{aq}$$

The mobile electrons from the lattice renew the surface ferrous sites, which are now eliminated from the lattice, but, under these conditions of acidity, no ferric ion appears in the solution. Migration of Fe(II) (more probably as Fe(III) $+e$) towards the surface and the formation of vacancies enable the excess positive charge to be resorbed in the solid. Hence, there is an interface transfer of electrons and ions towards the solution, combined with migration of vacancies towards the core of the particles. The net reaction is

$$[Fe^{3+}][Fe_2^{2.5+}]O_4 + 2H^+ \longrightarrow 0.75[Fe^{3+}][Fe_{5/3}^{3+}V_{1/3}]O_4 + Fe^{2+} + H_2O$$

Ferrous ions are desorbed with an equivalent amount of oxygen, according to

$$[Fe(II), O^{2-}]_{solid} + 2H^+ \longrightarrow Fe(II) + H_2O$$

This transformation is characteristic of the small size of the particles and observed to a much lower extent in micrometer-size particles. It occurs in two consecutive steps. The first step, elimination of surface ferrous ions (i.e. formation of cation vacancies near the surface), is almost immediate. The second step is slower and must be limited by the diffusion coefficient of ferric ions in the lattice. Although diffusion takes place between nearest neighbors by a cooperative process, it is a relatively slow phenomenon. In small particles of high surface/volume ratio, the net diffusion involves the addition of rather short distances. The conversion of magnetite into maghemite is therefore compatible with reasonable observation time-frames (a few days at room temperature), without a measurable reduction in particle size.

The same transformation is observed if the acidification around pH 2 is made by the addition of a solution of ferric ions. However, the phenomena are more complex and the characterization of the solution [by titration of excess Fe(III) as $Fe(OH)_3$ and titration of the released ferrous ions as $Fe(OH)_2$] shows that in this case some ferric ions are fixed by the particles, and that ferrous ions are released into the solution in the stoichiometry $[Fe(II)_{solution}]/[Fe(III)_{fixed}] = 1.5$ [35]. The main effect of the Fe(III) addition is the significant structural disorder on the surface, unlike in the case of the acidification of suspensions with $HClO_4$ (Figure 9.7). The stoichiometry of the reaction is

$$[Fe^{3+}][Fe_2^{2.5+}]O_4 + 2/3Fe^{3+} \longrightarrow [Fe^{3+}][Fe_{5/3}^{3+}V_{1/3}]O_4 + Fe^{2+}$$

The structural disorder on the surface implies that adsorbed ferric ions are not reduced, or at least not completely, by electrons migrating from the inside of the particles and subsequently released into the solution. In fact, fast protonation of the surface owing to the presence of ferric ions leads, as with $HClO_4$, to desorption of Fe(II). Ferric forms are simultaneously hydrolyzed by the surface and chemisorbed in a more or less crystalline order, bringing enough protons (from water molecules and hydroxyl groups) for the desorption of ferrous ions to proceed further.

If ferric ions are precipitated at pH 8 in the presence of colloidal magnetite, a ferric gel forms immediately. Gel particles are physisorbed on the magnetite and are identified in Mössbauer spectroscopy by a quadrupolar doublet superimposed on two sextuplets of magnetite due to Fe^{3+} and $Fe^{2.5+}$ respectively [36]. During ageing of the suspension, the intensity of the doublet decreases and the relative intensity of the Fe^{3+} sextuplet increases compared with the $Fe^{2.5+}$ sextuplet (Figure 9.8), which indicates formation of non-stoichiometric magnetite.

Investigations of the structure and amount of ferric gel show that the adsorbed gel slowly forms a spinel layer by epitaxy on the lattice. Electron transfer through the surface of the magnetite particles forms ferrous ions locally, which induce crystallization of the gel, in a process similar to the co-precipitation of ferric and ferrous ions (see Section 3.5).

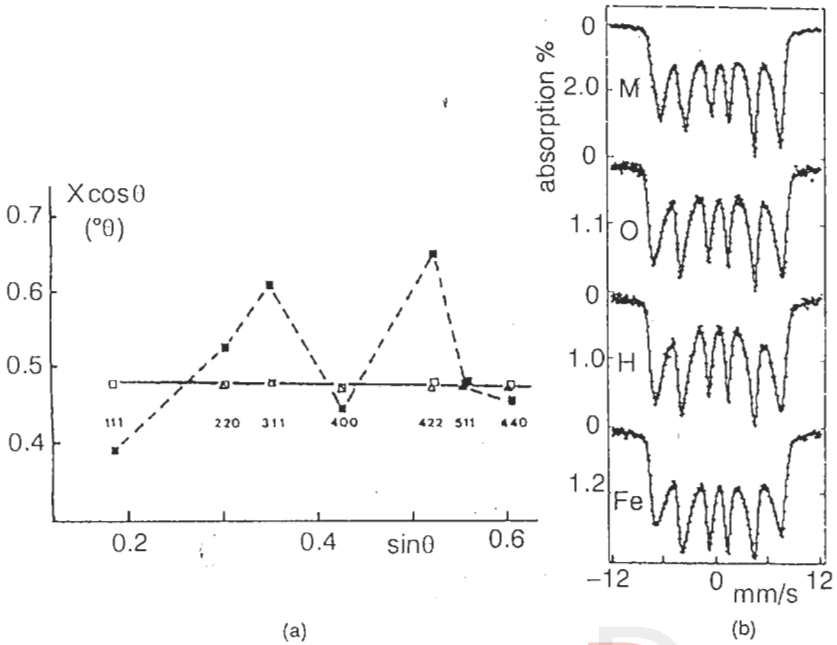

Figure 9.7 (a) Variation in the width L of XRD peaks and (b) Mössbauer spectra (300 K) of freshly prepared colloidal magnetite (average particle diameter 8 nm): △, M; treated with $HClO_4$: □, H; treated with $Fe(NO_3)_3$: ■, Fe; and oxidized in air: ○, (diffraction data for particles oxidized in air and treated in an acidic medium are indistinguishable. Reproduced by permission of Academic Press from [35]

(iii) Adsorption, around pH 6, of easily reduced ions such as Ag^+, Pt^{2+}, Pd^{2+}, Cu^{2+} on colloidal magnetite causes reduction of the cations and formation of metallic particles (Ag, Pt, Pd) or the formation of hydroxide Cu(OH). Conversion of magnetite into maghemite occurs in this case without iron desorption from the particles [37,38]. Around pH 6, the cation adsorbed on surface hydroxylated sites forces (as does the proton) the localization of a mobile electron from the lattice, but it also traps the electron. The cation can now be reduced without Fe(III) desorption. The excess positive charge in the lattice is still compensated by the migration of ferric ions towards the surface. These ions increase their coordination by hydroxylation:

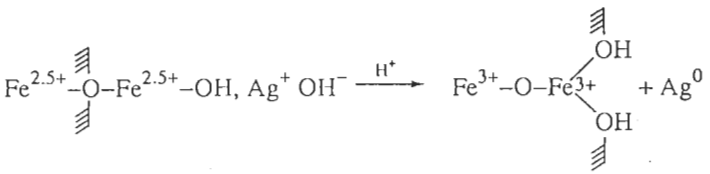

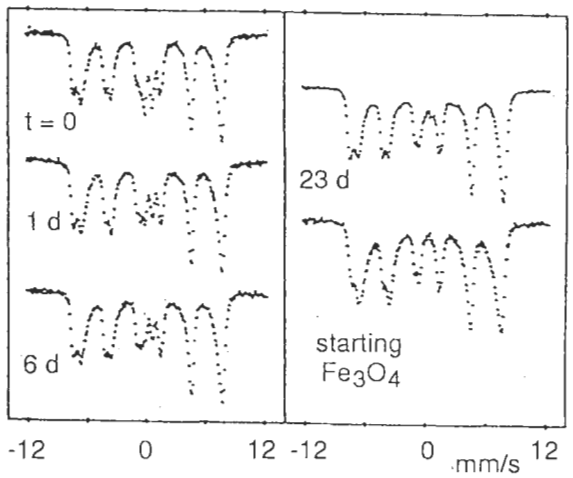

Figure 9.8 Evolution of Mössbauer spectra (300 K) for magnetite particles in the presence of ferric gel ('$Fe(OH)_3$'/Fe_3O_4 = 2.25) during ageing of the suspension. Reproduced by permission of Academic Press from [36]

The net reaction involves consumption of a hydroxyl ion by an electron removed from the solid:

$$[Fe^{3+}][Fe_2^{2.5+}]O_4 + Ag^+ + OH^- \longrightarrow 1.125[Fe^{3+}][Fe_{5/3}^{3+}V_{1/3}]O_4 + Ag^0 + 0.5H_2O$$

This transformation only involves a transfer of electrons near the interface compensated by adsorption of OH^-.

(iv) When magnetite has been converted into γ-Fe_2O_3 in acidic medium, via Fe^{2+} desorption, the latter may be readsorbed through an increase in the pH (pH $\geqslant$ 6), but the 'reduction' process is not, strictly speaking, the reverse of the proton 'oxidation' described in (ii) [39]. In the presence of the colloids, ferrous ions precipitate at a much lower pH than if they are alone in solution (Figure 9.9, a curves). The amount of adsorbable Fe(II) corresponds to a $Fe(II)/Fe(III)_{initial}$ ratio of 1/2. Beyond 1/2, Fe(II) precipitates as if it were alone in solution (curves b, Figure 9.9). Although the stoichiometry of the adsorption is 2 mol HO^- per mol Fe^{2+}, the iron adsorbed does not exist as $Fe(OH)_2$. A layer of magnetite forms by epitaxy on the γ-Fe_2O_3 particles. Crystallization of the adsorbed layer stems from the coexistence of ferric and ferrous ions, the latter being formed by electron transfer from the adsorbed layer towards the inside of the particle. The reaction stops when half the octahedral sites within the initial colloid are equally populated by ferric and ferrous ions. This corresponds to the net stoichiometry $Fe(II)_{adsorbed}/Fe(III)_{total} = 1/2$. The kinetics of the reaction is fast, and suggests that charge compensation in the solid takes place by proton incorporation rather than by iron diffusion.

DropBooks

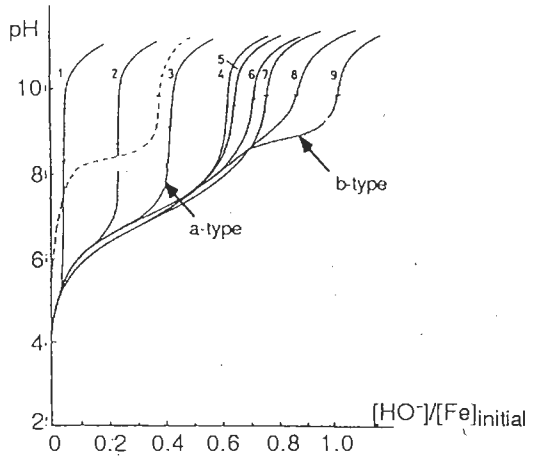

Figure 9.9 Titration of γ-Fe_2O_3 by $N(CH_3)_4OH$ in the presence of ferrous ions. The ratio $[Fe^{2+}]_{added}/[Fe^{3+}]_{initial}$ is shown on the curves. The dashed curve shows the titration of Fe^{2+} alone. Reproduced from [39], by permission

Adsorption of Fe(II) occurs within a pH range inferior by two points to the range of precipitation of $Fe(OH)_2$ (Figure 9.9). This shows the role of the oxide surface as a hydrolyzing and condensation agent. The increase in pH necessary for iron adsorption also leads predominantly to the creation of nucleophilic sites on the surface. These sites ($-OH, -O^{\delta-}$) penetrate the coordination sphere of $Fe(OH_2)_6^{2+}$ ions by substitution. The pH increase does not lead to adsorption via hydrolysis and decreases its charge. Adsorption of Co(II) on to γ-Fe_2O_3 is very limited and the surface hydrolysis of Fe_2CoO_4 is greatly reduced at pH 2 [35]. The spectacular difference in behavior of the colloid with Fe(II) or Co(II) is due to the lack of electron transfer between Co(II) and Fe(III). Therefore, it is clear that electron delocalization plays a fundamental role in surface phenomena. The behavior of colloids of iron oxide spinel is similar to that of microbatteries discharging and recharging themselves by acid–base reaction on the surface. Various recharging processes by 'reduction' of the colloids are possible, either through the formation of a stoichiometric material (chemical reduction of γ-Fe_2O_3 by organic compounds such as dimethylformamide) or by preservation of metal vacancies (electrochemical reduction in an alkaline medium) [40]. All these reactions, including oxidation of magnetite in air, stem from the same electronic process: transfer through the interface towards (or from) an adsorbed layer, relayed by a transfer though the particle (Figure 9.10). The intrinsic mechanism is the same, even if the phenomena that induce the transfer through the interface, and even if external conditions governing the behavior of surface Fe(II), are very different. Ion and/or electron exchange reactions between the colloid and its surroundings underline the importance of the spinel structure in the use of iron oxide in applications such as heterogeneous catalysis.

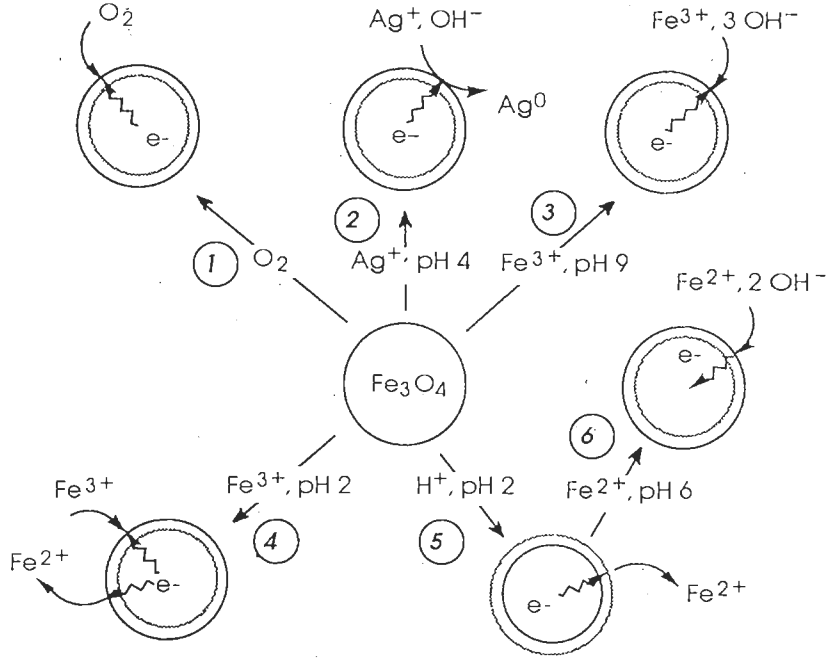

Figure 9.10 $Fe_3O_4 \rightarrow \gamma$-$Fe_2O_3$ transformations induced by adsorption of various species. Dashed circles represent the intial size of the colloid in each transformation. In each case, adsorption is assisted by outward electron transfers within the particle, which renew the reactive chemical species on the surface (Fe^{2+} ions). The surface may be oxidized *in situ* (steps 1 to 3) or desorbed (steps 4 and 5) depending on the physicochemical characteristics of the medium. In all steps, electron transfers are associated with migration of Fe^{3+} from the octahedral sublattice towards the surface of the particle, causing formation of cation vacancies. Step 5 is apparently reversible. Adsorption of Fe^{2+} and HO^- (step 6) is also assisted by electronic and ionic (H^+) inward transfers, but without appreciable Fe migration. This results in the epitaxial growth of an Fe_3O_4 layer

9.2 ANION ADSORPTION

Whereas the surface of oxides may act as a ligand for cations in solution, the *specific* adsorption of anions or weak acids occurs by substitution of aquo or oxo ligands on the oxide surface.

Infrared absorption spectra show that the oxalate, benzoate and phosphate replace mono-coordinated groups on the surface of goethite, ferric gels or gibbsite. Such ligands have a bridging coordination mode for small adsorption levels and at around pH 3–4 [41–43] (Figure 9.11).

Only the monocoordinated hydroxo groups of these surfaces are replaced. The characteristic infrared absorption band of Fe_1–OH at 3840 cm^{-1} (2584 cm^{-1} for

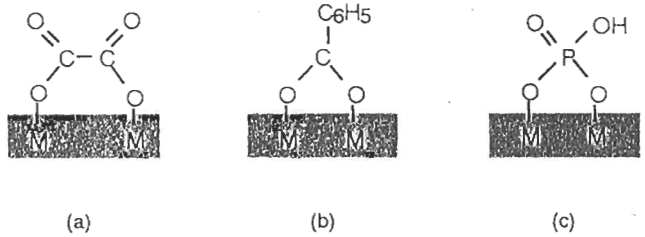

Figure 9.11 Coordination (a) of oxalate, (b) of benzoate and (c) of phosphate on the surface of oxides or hydroxides

Fe_1–OD) decreases with increasing adsorption. The presence of oxalate on the surface causes only minor alteration of the 3660 cm^{-1} band characteristic of doubly and triply coordinated OH groups (2702 cm^{-1} for deuterated groups). Phosphate replaces all monocoordinated groups on the surface because it is a stronger complexant of Fe than oxalate. The exclusive replacement of monocoordinated OH groups by the oxalate is clearly observed in gibbsite. The adsorption corresponds exactly to the number of such groups present only on the sides of the particles shaped as hexagonal platelets (see Figure 7.3) [42]. The absence of replacement of Al_2–OH groups by the oxalate is also confirmed by the weak adsorption on imogolite, an aluminosilicate of tubular morphology that has only doubly coordinated OH groups on its surface [44].

The reactivity of surface hydroxylated groups towards anion substitution decreases as the acid character of these groups increases. Doubly and triply coordinated groups are more acidic and carry negative charges which do not favor electrostatic attraction with anions. In addition, these groups form bonds with surface cations that are more covalent in nature than the bonds formed with monocoordinated groups. Their replacement is therefore more diffcult.

The symmetry and the charge of the anion play an important role in its adsorption and its mode of coordination. This has been clearly demonstrated in infrared spectrocopy investigations of various anions on a ferric gel [45]. In air-dried suspensions, nitrate ions preserve the D_{3h} symmetry of the free nitrate. Vacuum dehydration forces an interaction with the surface, and nitrate ions adopt a C_{2v} symmetry characteristic of monocoordinated nitrates. The carbonate ion (D_{3h} symmetry when free) is monocoordinated (C_{2v} symmetry) to surface groups even in the air-dried, hydrated gel. The carbonate ion is more strongly adsorbed than the nitrate: the higher charge on the carbonate reinforces the interactions with the surface. Similar phenomena are observed with ions of tetrahedral symmetry in the free configuration. The interaction between the perchlorate ion and the surface of the dried gel is purely electrostatic in nature. After vacuum drying, the ion is coordinated to the surface in a monodentate mode. Sulfate and selenate ions, on the other hand, are already doubly coodinated (C_{2v}) on the surface of the hydrated gel.

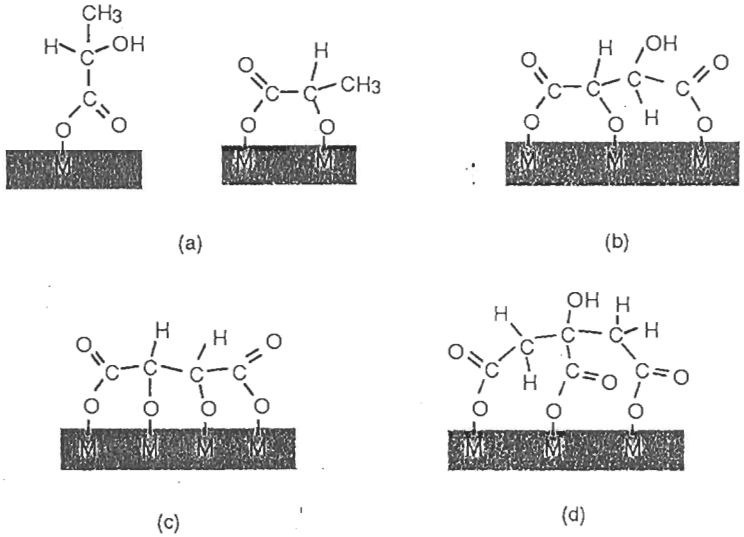

Figure 9.12 Coordination of (a) lactate, (b) l-tartrate, (c) mesotartrate and (d) citrate on oxide or hydroxide surfaces

Because of their small size, these anions can chelate cations on the surface of the oxide. Polycarboxylate anions such as oxalates or hydroxycarboxylates act as bridges. These ions are able to adsorb themselves by forming, in addition to a bond via the carboxylate groups, an alcohol group which may deprotonate and coordinate the surface. This effect depends on the structure of the ligand and on the nature and geometry of the groups to be replaced on the surface. This has been observed with mesotartrate on goethite, and with lactate and l-tartrate on ferric gels [46] (Figure 9.12).

This effect seems to be specific to surface coordination because it is not observed with mononuclear complexes in solution [47]. The molecular structure of the citrate group, coordinated by its three carboxylate functions, does not allow the alcohol group to participate.

Specific adsorption of anions is a surface complexation reaction and, as a rule, anions do absorb more efficiently if their complexing nature is high in solution [1,48–51]. The complexing nature depends to a large extent on the structure and geometry of the anion, which define its mode of coordination. The chelating or bridging effect, which reinforces the complexing nature of the anion in solution, also stimulates its adsorption. Some chelating anions such as EDTA and aminocarboxylates may form soluble complexes more stable than the oxide, and may prevent cation precipitation in some pH ranges. They also allow dissolution of small oxide particles [52] (see below). For example, these ligands are used in the clean-up of industrial facilities for the dissolution of corrosion products.

DropBooks

Adsorption of anions or neutral molecules on oxides is controlled by the same parameters (pH, concentration, temperature) as those involved in complexation of cations in solution. The pH of the suspension imposes both the level of protonation of the anion and the surface charge of the oxide. As in the case of cation complexation in solution (see Chapter 5), there is an optimum pH range for anion adsorption. Adsorption is characterized by complexation equilibrium constants, determined using an approach similar to the calculation of complexation constants in solution from acid–base titration of suspensions [48–51].

Some models try to explain the variations in surface charge and potential on the basis of a specific model of the interface [53–55], but some do not use such models [56]. Various models provide good fits of experimental adsorption curves as a function of pH and ionic strength. These models are not described here because of some of the remarks expressed above: their ability to fit experimental data does not necessarily reflect their ability fully to describe the mechanisms involved in adsorption phenomena. The models usually do not take into account any structural specificity. The type of complexes formed, the position of ions and the characteristics of the interface are usually imposed by the parameters used to fit the data.

It is interesting to examine some characteristics of anion adsorption on oxide surfaces.

i *Adsorption and magnetic behavior*

The behavior of small magnetic particles is usually different from the behavior of the bulk. This behavior is a function of particle size and may be influenced by surface effects or interactions between particles.

If the dimensions are smaller than 20–50 nm, the particle is a single magnetic domain. The anisotropy energy is proportional to the volume of the particle and, for very small ($\leqslant 10$ nm) particles, may be comparable with thermal energy even below room temperature. Under such conditions, the magnetization is no longer pinned in an easy magnetization axis as in a macroscopic crystal, but may fluctuate from one easy magnetization axis to another. This phenomenon is called superparamagnetic relaxation.

The magnetic anisotropy energy is a measure of the energy required to make the magnetization vector switch direction. It has many contributions. The most important ones, for a macroscopic crystal, are the magnetocrystalline energy and the shape anisotropy. The lower symmetry of surface atoms, compared with that of atoms in the bulk, generates another type of magnetic anisotropy. This surface anisotropy can be neglected in macroscopic crystals but becomes appreciable in nanoparticles because of the large number of atoms located near the surface. It also depends on the geometry of the surface and may be sensitive to the presence of adsorbed species. If the particles are close to one another, their magnetic moments may interact. This gives rise to the anisotropy of interaction. The interaction may be long

range (magnetic dipolar) or short range (exchange, superexchange from surface to surface). The latter are strongly influenced by phenomena at the interface.

We have seen that the aggregation of γ-Fe_2O_3 particles in water can be controlled by tuning the acidity of the medium (see Section 8.1.3 and Figure 8.8). Aggregates of various sizes and shapes can be formed. Dipolar magnetic interactions ($\approx$ kT), much weaker than electrostatic interactions (≈ 10 kT), should not contribute to aggregation but instead may cause magnetic coupling which affects superparamagnetic relaxation, and it has been shown that the magnetic behavior of the particles is correlated with the configuration of the cluster [57] (Figure 9.13a). Small, linear aggregates (≈ 5 particles), sufficiently distant from one another, give spectra (A) characteristic of superparamagnetic relaxation. Branching and intertwining of chains of particles causes an increase in dipolar interactions and faster relaxation (spectrum B). A similar effect is observed when small clusters are concentrated. The cancellation of the surface charge on the particles causes the formation of very large three-dimensional aggregates with strong surface/surface coupling, and the superparamagnetic relaxation is blocked (spectrum C).

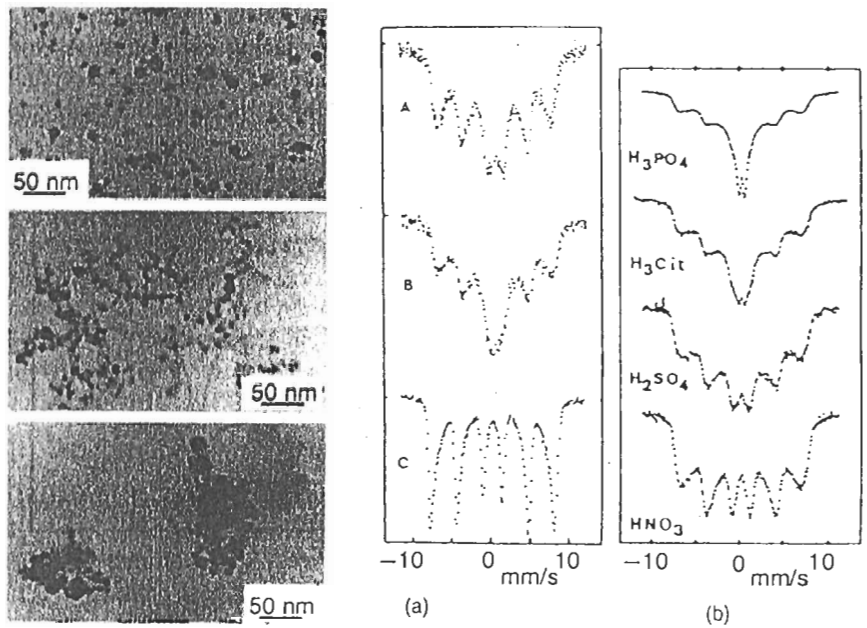

Figure 9.13 (a) SEM micrographs and Mössbauer spectra (300 K) of γ-Fe_2O_3 colloids. The samples are sols stabilized using a polymer, containing aggregates of various sizes and morphology. They were obtained through modification of the surface charge. (b) Mössbauer spectra (290 K) of γ-Fe_2O_3 particles (powder) flocculated with various acids. Reproduced by permission of Elsevier Science Ltd from [59]

Adsorption of ions or molecules can affect surface anisotropy and interactions between particles because the surfaces are separated by counterions, adsorbed ions and hydration water. Coupling of surface spins decreases as the affinity of the adsorbed species for the surface increases. The decrease in magnetic coupling, which follows the sequence $NO_3^- < SO_4^{2-} < HCitr^{2-} < HPO_4^{2-}$, is parallel to the increasing complexation of ferric ions (Figure 9.13b). The citrate and phosphate ions have a higher complexing nature and form paramagnetic surface complexes. The corresponding spectra exhibit a quadrupolar doublet superimposed with the magnetic component [57–59].

ii *Adsorption and thermal stabilization*

Surface effects play a spectacular role in the thermal stabilization of the spinel structure. The thermal stability of the adsorbed layer is an important factor in the increase in the temperature of the $\gamma \rightarrow \alpha$-$Fe_2O_3$ transition [60a,b] (Figure 9.14a). With an adsorbed layer of citrate, the transformation occurs as early as 300 °C after extended heating (Figure 9.14b), but it does not occur until 800 °C with the phosphate.

After the adsorbed layer has decomposed, sintering occurs by the formation of oxo bridges during dehydration of hydroxyl groups facing each other. As local structural constraints develop, particularly near the contact zones, local recrystallization takes place which eventually expands to all the particles in the aggregates,

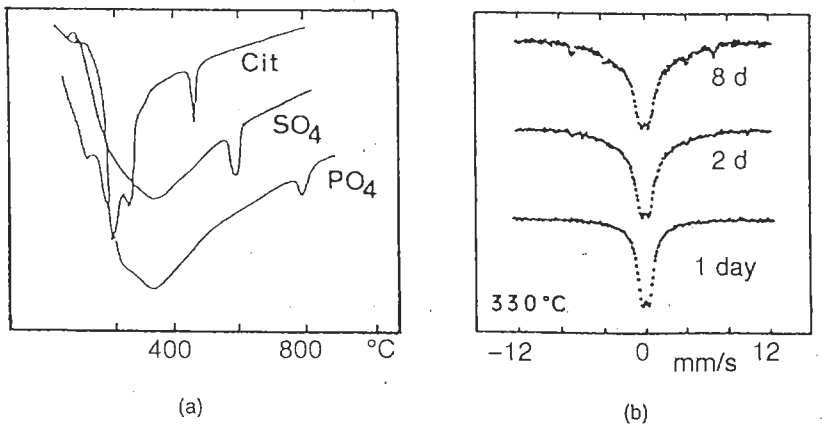

Figure 9.14 (a) Differential thermal analysis of γ-Fe_2O_3 particles (10 nm). The endotherm shows the $\gamma \rightarrow \alpha$-$Fe_2O_3$ transition. (b) Mössbauer spectra of γ-Fe_2O_3 particles heated at 330 °C for various times, after decompostion of the adsorbed citrate. The sextuplet of hematite appears at 330 °C after 8 days of heat treatment. Reproduced with kind permission from Kluwer Academic Publishers from [60a]

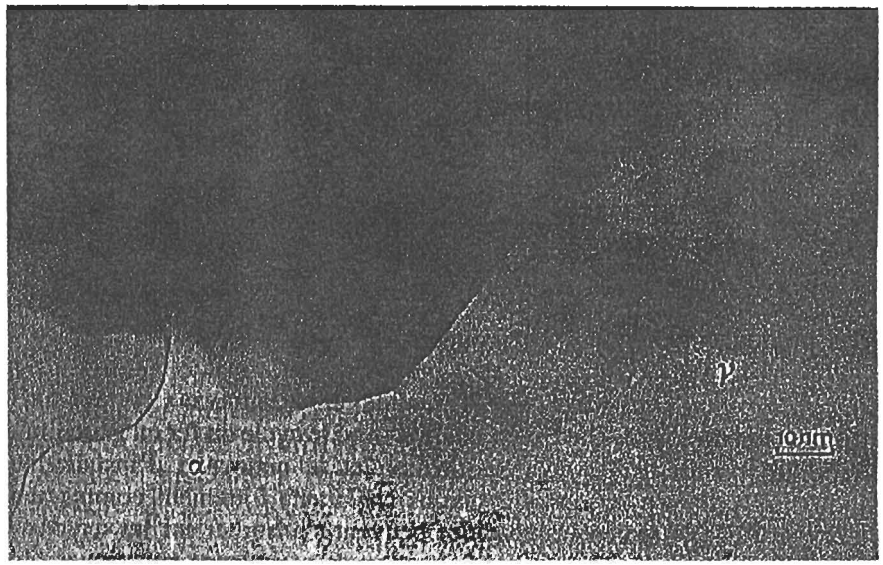

Figure 9.15 Hematite particles formed via thermal conversion of small γ-Fe_2O_3 particles [61]

DropBooks

forming large monocrystalline domains [60b] (Figure 9.15). The phosphate acts as an anti-sintering agent.

Some condensed phosphates such as the tripolyphosphate $[P_3O_{10}]^{3-}$ or the hexametaphosphate $[PO_3]_6^{6-}$ are less complexing than the monophosphate but bulkier and also prevent sintering of goethite particles during the preparation of γ-Fe_2O_3 by the formation of Fe_3O_4 in the dehydration–reduction–reoxydation process [62]. Condensed phosphates, when adsorbed on goethite, allow the initial acicular particles to maintain their geometry during heat treatment, thereby allowing an increase in the coercive forces in the resulting particles.

iii *Adsorption and dissolution*

Much work has been published on the dissolution of iron oxides in connection with the iron cycle in geochemistry, decontamination processes or the clean-up of industrial facilities. We have already seen that strong chelating agents such as EDTA or amino acids can adsorb on the surface of oxides and promote their dissolution because they can form anion complexes that are more stable than the oxide [52,63,64]. Citrates and oxalates, among others, act in a similar way [65].

Dissolution of oxides is markedly accelerated if oxidation-reduction processes occur in conjunction with anion adsorption [66]. The adsorption of ascorbate on hematite is a good example [67] (Figure 9.16). The reduction of ferric ions is shown

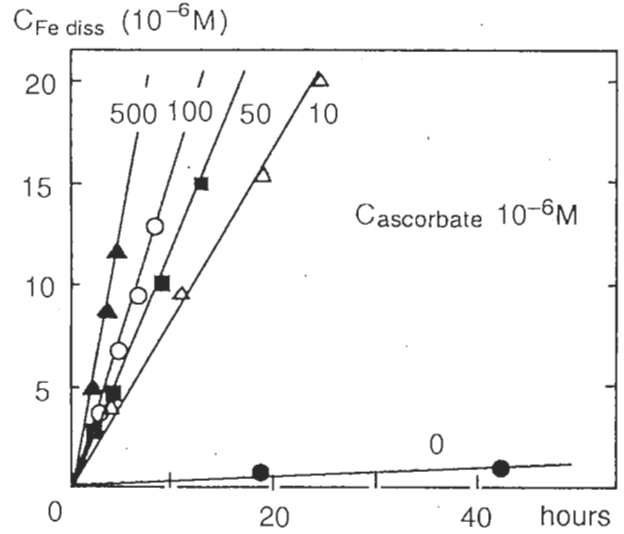

Figure 9.16 Dissolution of hematite in the presence of ascorbate at pH 3. In the absence of ascorbate, Fe(III) concentration. Reprinted with permission from [67]. Copyright American Chemical Society

by titration of the ferrous ions in solution. Three steps are involved in the dissolution process:

- adsorption of the ascorbate by formation of a surface ferric complex,
- electron transfer through the surface complex and formation of a ferrous ion,
- desorption of the ferrous complex, which is unstable within the acidity range required by the ascorbate adsorption ($2 \leqslant pH \leqslant 4$). The solubility of the reduced and complexed surface ions is higher because Fe(II)–O bonds are more labile than Fe(III)–O bonds. In fact, the process is similar to the oxidation of magnetite by elimination of ferrous ions in the same acidity range (see Section 9.1.3).

A similar mechanism can occur with sulfur and reducing compounds such as thioglycolate [68].

The reduction of surface ferric ions may also occur through other mechanisms. Adsorption of ferrous complexes (oxalate, malonate) causes an electron transfer through the ferrous–ferric surface complex [67]:

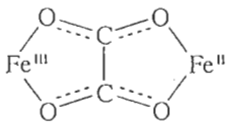

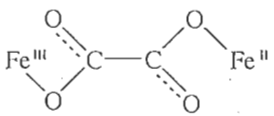

The reducing strength of complexes of ferrous ions is higher than that of aquo complexes $[Fe(OH_2)_6]^{2+}$, but the electron transfer through the surface complex is

possible (or favored) if the ligand can form a conjugated system after adsorption. This is the case for citrates, oxalates, malonates, etc. This occurs in the dissolution of goethite [67] and in the dissolution of magnetite by ferrous oxalate [69] or by the EDTA–Fe(II) complex [70] and by ferrous sulfate [71]. The tris(picolinato)V(II) complex promotes the dissolution of $NiFe_2O_4$ through the same mechanism [72].

The reduction process may be initiated by UV irradiation of photosensitive anions such as EDTA [73], citrates [74] or mercaptocarboxylates [75,76]. The reduction mechanism takes place by injection of electrons into the solid, through excitation of the charge transfer bands in the ferric surface complex. Free radicals generated by radiolysis (γ-ray irradiation) of the suspensions also causes reduction of the surface ions. Hematite, goethite and magnetite dissolution can therefore be obtained using viologen radicals [77] or $(CH_3)_2C^{\cdot}OH$ [78], but the reduction is limited by the recombination of the radicals.

A reverse mechanism may occur upon irradiation (photolysis or radiolysis) of a semiconducting oxide (hematite, magnetite, TiO_2, ZnO, WO_3, etc.) [79]. Electron–hole pairs are created in the colloid and sent into the conduction band. Fast recombination can be prevented by adsorbed species such as anions or neutral molecules acting as traps for electrons or holes. Polyvinyl alcohol strongly adsorbed on TiO_2 traps the holes, and the lifetime of the electron in the colloid ranges from minutes to hours. They can react with species in solution and, for example, reduce tetranitromethane [80]:

$$C(NO_2)_4 + e^- \longrightarrow C(NO_2)_3^- + NO_2$$

The citrate ion and the thiocyanate ion SCN^- (which oxidizes into $(SCN)_2^-$) also act as hole traps. The efficiency of the trap depends on the ability of the ion to adsorb and oxidize.

Species prone to reduction may adsorb on the colloid and prevent electron–hole recombination by trapping the electrons. Methylviologen MV^{2+} is strongly adsorbed on TiO_2 at $pH > 6$. Immediately after flash irradiation, it is reduced to MV^+ with a characteristic optical absorption at 392 nm. Holes can oxidize HO^- ions into H_2O_2 and O_2, and the carbonate ion into the CO_3^- radical, and can also oxidize various organic compounds [80]. Similar reactions have been observed in other colloidal oxides. Since photoelectrochemistry is outside the scope of this book, it might be best to refer the reader to Henglein's excellent papers [79,80] on the subject.

9.3 POLYMER ADSORPTION

Adsorption of macromolecules on the surface of oxides is perhaps the most ancient technique used for the stabilization of small particles. In Ancient Egypt, for the production of ink, carbon particles were stabilized in water using arabic gum. Adsorption of polymers on many types of particle is of considerable industrial

interest today, and is the object of much research. For example, it is at times desirable to prevent aggregation and adhesion of particles during rehydration of stored dried particles. On the contrary, it might be necessary to use polymers as binders in the production of glues or coatings.

The physics and chemistry of these systems is complex, essentially because of the many possible adsorption mechanisms involved. It is also difficult to determine the internal structure of the adsorbed layers or what interactions might develop between them. There are a few excellent review papers on these topics [81–84]. We shall only briefly describe here the main interaction mechanism between the surface of oxides and various macromolecules.

9.3.1 NON-IONIC MACROMOLECULES

Polymers such as polyethylene oxide, polyacrylamide and polyvinyl alcohol are linear, flexible molecules with no charge, which adsorb non-specifically on the surface of oxides. Interaction with the surface takes place though hydrogen bonds between polar functional groups of the polymer chain and the hydroxylated and protonated groups on the surface [85]. In polyacrylamide for example, adsorption is due to interactions between the oxygen of the carbonyl group and the protons of the surface group, rather than from the interaction between the proton of the nitrogen and the negatively charged sites:

$$MOH/MOH_2^+ \cdots O{=}C{-}(NH_2) \qquad MO^- \cdots H_2N{-}C{=}O$$
$$\qquad\qquad\quad | \qquad\qquad\qquad\quad |$$
$$\qquad -(CH{-}CH_2)- \qquad\qquad -(CH{-}CH_2)-$$

Indeed, although the polymer is not charged, adsorption density decreases with increasing pH, irrespective of the nature of the oxide. Surface sites are much better proton donors than the amide group, and hence the surface charge plays an important role in the adsorption mechanism. Since this mechanism involves hydrogen bonds, it must compete with surface solvation processes. The affinity of the polymer for the surface will be weaker when the surface sites are more prone to solvation. Adsorption density on the polymer decreases in the sequence Fe_2O_3, Cr_2O_3, Al_2O_3, TiO_2 (anatase), SnO_2, SiO_2, which is also the increasing sequence of solvation energy [85]. The particle–polymer interactions compete with the particle–water interactions. The term adsorption is used if the surface prefers the polymer to the solvent, and depletion is used if the opposite is true.

Although the interaction energy between surface and each chain segment is very small (smaller than kT), chains adsorb very well because of the large number of contact points: the affinity of the macromolecule for the surface usually increases with its molecular weight [86]. Nonetheless, the interaction of the polymer with the surface remains rather weak because it may be desorbed easily by adsorption of low molecular weight molecules (acetone, butanol). For these smaller molecules the entropy loss due to conformation changes is smaller [86].

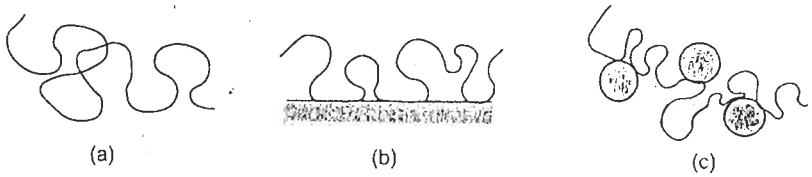

Figure 9.17 Conformation of a non-ionic polymer (a) in solution; (b) adsorbed on an oxide surface and (c) adsorbed and acting as a bridge between particles

The configuration of adsorbed chains is difficult to determine [87,88]. Upon saturation, adsorption does not dramatically alter the radius of gyration of the macromolecule, which is neither inflated nor collapsed owing to adsorption [89,90]. The conformation of the adsorbed polymer remains similar to that of a free macromolecule in a good solvent, and exhibits tails and loops between contact points (Figure 9.17). The adsorbed layer provides excellent steric protection against aggregation [81,83,91].

When the surface is not polymer-saturated, adsorbed chains have a 'flatter' appearance. The thickness of the polyethylene oxide layer adsorbed on silica particles is about 6 times smaller at half-saturation than at saturation [89]. Under such conditions, a few chains can bridge several particles and cause flocculation of the colloid [81].

DropBooks

9.3.2 CHARGED POLYMERS

Polyelectrolytes and ionic surfactants adsorb more strongly than neutral macromolecules on charged surfaces, because the adsorption energy contains an electrostatic contribution from sites of opposite charge on the polymer and on the oxide [84,92]. The nature of the adsorbed layer can lead to large variations in the behavior of the particles.

The polyelectrolyte, such as polyvinyl chloride, polyvinylpyridine or polyethyleneimine, is a flexible chain bearing many charged sites (Figure 9.18a). The polymer is 'flattened' against the surface of the particles, and no tails and loops are created because of the repulsion between sites of similar charge on the chain [84,88] (Figure 9.18b). In a sense, the polyelectrolyte acts as a counterion and causes flocculation of the colloid [91]. If the chains are long, they may also act as a bridge between several particles.

Surfactant molecules such as sodium dodecylsulfate SDS^-Na^+ or dodecyltrimethylammonium bromide $DTAB^+Br^-$ have a structure consisting of a carbon chain with a single polar head group. The surfactant is attached to the surface of the particle through electrostatic interactions between the head and charged sites on the surface (Figure 9.18c). As in the case of polyelectrolytes, the adsorption density depends on the sign and number of surface charges.

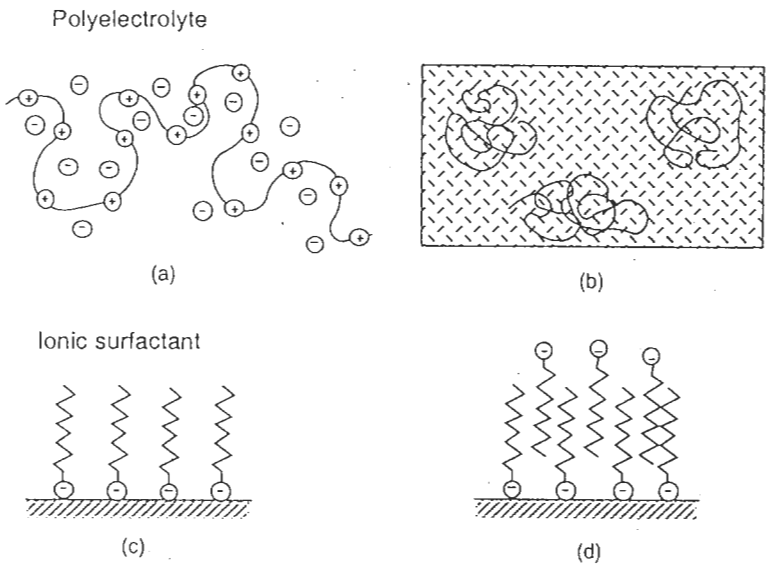

Figure 9.18 Polyelectrolyte (a) in solution and (b) adsorbed on a charged surface. Adsorption of an amphiphilic ionic surfactant, forming (c) a hydrophobic monolayer and (d) a hydrophilic double layer

Table 9.1 Adsorption of surfactants on TiO_2 powders (PZC = 4.7) [93]. Aqueous dispersion at 100 g/l TiO_2, SDS 1 mmol l^{-1}, DTAB 8 mmol l^{-1}, NaCl 0.01 mol l^{-1}

		Charge sign		
	pH	Surfactant	Surface	Adsorption density (mmol m^{-2})
SDS^-	×2	—	+	0.61
	×6.7	—	—	0.11
	11	—	—	0
$DTAB^+$	×2	+	+	0
	×6.8	+	—	0.23
	11	+	—	1.2

Since they contain only one ionized group, surfactants cannot act as bridges between particles. However, the oxide particles flocculate in water because the tail of the surfactant is hydrophobic. With the surfactant, the particles can be dispersed in a non-aqueous, non-polar solvent able to solvate the tail of the surfactant. Non-ionic surfactants [alkyl ethers of epolyethylene glycol of general formula $C_mH_{2m+1}O(CH_2CH_2O)_nH$ with $m = 18$, $n = 12$–98] or long-chain monoacids [oleic acid $CH_3(CH_2)_7CH{=}CH(CH_2)_7COOH$, lauric acid $CH_3(CH_2)_{10}COOH$, stearic acid $CH_3(CH_2)_{16}COOH$] play a similar role. Fatty acids are used in the preparation of ferrofluids, in the dispersion of magnetite or maghemite particles in kerosene or various oils [94].

Dispersion of particle–surfactant systems in water occurs through the formation of a double layer, according to a surface micellization process [95] (Figure 9.18d). The tails of a second layer of surfactants interact with those of the adsorbed molecules, so that the double layer formed at the surface is once again hydrophilic. This approach is used in the fabrication of magnetic ink for ink jet printers: oleic acid is adsorbed on the surface of magnetite or maghemite particles [96]. After the particles have been rendered hydrophobic by oleic acid, they can be dispersed in water after subsequent adsorption by a surfactant [Triton N-101, $C_9H_{19}C_6H_5O(CH_2CH_2O)_9H$] in the presence of PEG, glycerol or monobutylether.

9.3.3 POLYMER GRAFTING

Polymers and ionic or non-ionic surfactants may be desorbed by a change in the pH or competitive adsorption from small molecules. Anchoring the adsorbed layer may be greatly reinforced if chemical bonds are created through grafting reactions. This allows greater stability of dispersions, as well as the formation of protective layers on corrosive materials. It can also render surfaces hydrophobic and non-wetting, or allow fabrication of organic–inorganic hybrids.

Several grafting techniques can be used [97]. They usually involve polymerizing monomers on the surface of the oxide, or the reaction between surface sites and a polymer containing a chemically reactive group. In polymerization reactions, the surface must participate in one step of the reaction. *Initiation* of the reaction may occur on functional sites of the surface acting as catalysts in the polymerization process:

$$-X^{\bullet} + \text{monomer} \longrightarrow -X-\text{polymer}$$

Propagation of the reaction may take place on groups bound to the surface acting as monomers or co-monomers. Some surface sites may also deactivate chain growth and ensure *termination* of the polymerization:

$$-Y + {}^{\bullet}\text{monomer} \longrightarrow -\text{polymer} + Y^{\bullet}$$

The surface sites required to ensure incorporation of the particle into the macromolecule must be created prior to the grafting reaction. Surface hydroxylated groups are used, usually replaced by chlorine or a benzene ring in the case of silica. The proton may be replaced by alkyl groups.

It is sometimes easier to activate the polymer rather than the oxide. Surface OH groups can react with chlorosilanes or alkoxysilanes incorporated into the polymer chain (styrene, methylmetacrylate, for example) in a toluene or xylene solution [97]:

$$-M-OH + X-Si-[CH-CH_2]_n-R \longrightarrow -M-O-Si-[CH-CH_2]_n-R + HX$$

(the Ø substituent is attached to the CH group in each chain)

Such grafts have been made on various oxides: SiO_2, TiO_2, Cr_2O_3, Fe_2O_3, ZnO, etc. The main parameters in the reaction are the reaction time, the polymer and oxide concentrations, the size of the macromolecule and the chemical nature of the oxide, on which the type and number of surface hydroxyl groups depend. Generally speaking, the amount of grafted polymer increases with increasing temperature (which increases chain mobility) and decreases with the size of the macromolecule owing to steric effects.

Another grafting technique, used for example in the case of TiO_2, involves the use of a coupling agent such as titanium alkoxide $Ti(OR')_2(OR)_2$ bearing several alkoxy groups, such as $R' = -CH(CH_3)_2$ or $R = -COC_{17}H_{35}$ [98]. The synthesis medium is chloroform, dichloromethane or diethylether. The R′ groups are more ramified and polar than R groups and readily hydrolyze with surface OH and adsorbed water, and the alkoxide condenses on the oxide surface. The synthesis of ordered multilayers of phosphonate of zirconium on silica is a very elegant illustration of this technique [99]. The process involves functionalization of silica in a phosphonic acid containing silyl groups (Figure 9.19), followed by immersion of the silica in zirconium oxychloride. The surface is subsequently treated with another phosphonic acid solution. The process is repeated several times to form a crystallized multilayer film.

Polymer adsorption on an oxide surface is of great interest. The technique allows stabilization of dispersions in various aqueous or non-aqueous media; it also allows

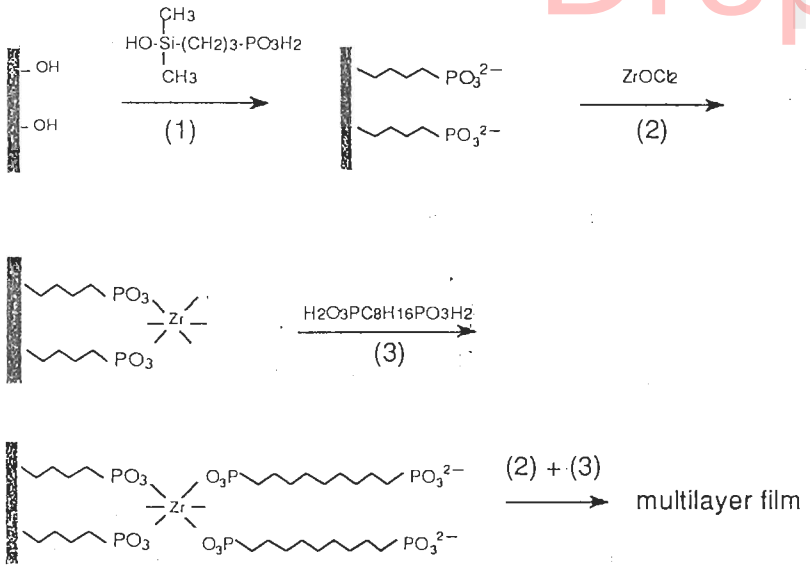

Figure 9.19 Formation of multilayer films on the surface of silica particles. Reprinted with permission from [99]. Copyright 1991 American Chemical Society

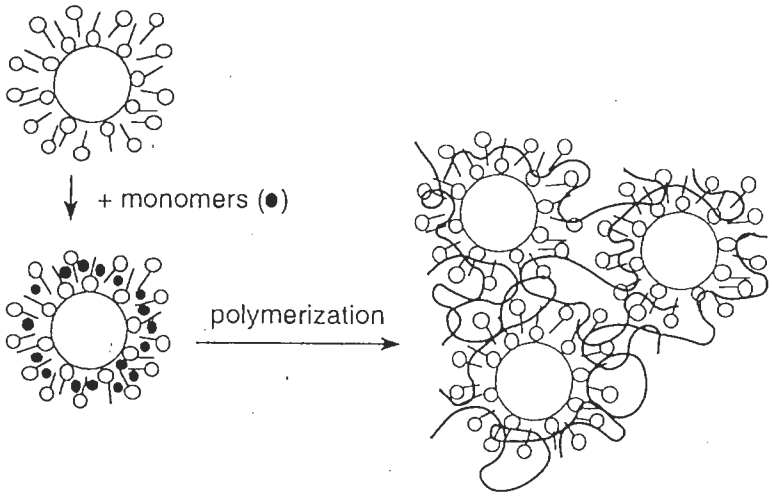

Figure 9.20 Encapsulation of oxide particles through monomer polymerization in a double layer

the synthesis of organic–inorganic hydrids for various applications, or polymer encapsulation of particles. A surfactant adsorbed on the oxide, or on a grafted polymer, forms a double layer which stabilizes the particles against aggregation in water. Monomers 'dissolve' preferentially in the double layer and can be polymerized *in situ* using a water-soluble initiator. The polymer thus formed is bound to the surface of the particles by the entanglement of its chains with those of the double layer [93,98] (Figure 9.20).

The surface of oxide particles is not always as inert as is often assumed. In many respects it does play a role similar to that of discrete species in solution. The wide diversity of the phenomena observed implies a very rich surface chemistry that clearly demonstrates the unique nature of the oxide–liquid interface. In many instances, a complete description of its behavior requires the combination of concepts from solid state chemistry with concepts from solution chemistry. Much research is still necessary to understand completely the reactivity of this very unique space.

9.4 REFERENCES

1. P.W. Schindler, W. Stumm, in *Aquatic Surface Chemistry, Chemical Processes at the Particle–Water Interface*, W. Stumm Ed., J. Wiley & Sons, New York (1987).
2. H.M. Jang, D.W. Fuerstenau, *Langmuir* 3, 1114 (1987).
3. D.W. Fuerstenau, K. Osseo-Asare, *J. Colloid Interface Sci.* 118, 524 (1987).
4. L. Bonneviot, O. Legendre, D. Olivier, M. Che, *J. Phys. Chem.*
5. W. Stumm, H. Hohl, F. Dalang, *Croat. Chem.* Acta, 48, 491 (1976).
6. V. Bassetti, L. Burlamacchi, G. Martini, *J. Am. Chem. Soc.* 101, 5471 (1979).

DropBooks

7. W.F. Bleam, M.B. McBride, *J. Colloid Interface Sci.* **110**, 335 (1986).
8. F. Basolo, R.G. Pearson, *Mechanisms of Inorganic Reactions*, J. Wiley & Sons, New York (1958).
9. M. Ardon, A. Bino, *Structure and Bonding*, Vol. 65, Springer-Verlag, Berlin (1987), p. 1.
10. M. Che, L. Bonneviot, *Pure Appl. Chem.* **60**, 1369 (1988).
11. R.O. James, T.W. Healy, *J. Colloid Interface Sci.* **40**, 42 (1972).
12. R.O. James, P.J. Stiglich, T.W. Healy, *Disc. Faraday Soc.* **59**, 142 (1975).
13. A. Haworth, *Adv. Colloid Interface Sci.* **32**, 43 (1990).
14. C.V. Schenk, J.G. Dillard, J.W. Murray, *J. Colloid Interface Sci.* **95**, 398 (1983).
15. C.F. Baes, R.E. Mesmer, *The Hydrolysis of Cations*, J. Wiley & Sons, New York (1976).
16. P.H. Tewari, W. Lee, *J. Colloid Interface Sci.* **52**, 77 (1975).
17. D.T. Harvey, R.W. Linton, *Colloids Surf.* **11**, 81 (1984).
18. M.M. Benjamin, J.O. Leckie, *J. Colloid Interface Sci.* **79**, 209 (1981).
19. S. Ambe, F. Ambe, *Langmuir* **6**, 644 (1990).
20. O. Clause, L. Bonneviot, M. Che, *Catalysis Today* **6**, 39 (1989).
21. D.J. Shaw, *Introduction to Colloid and Interface Chemistry*, 3rd ed., Butterworths, London (1980).
22. R.O. James, T.W. Healy, *J. Colloid Interface Sci.* **40**, 53 (1972).
23. W.F. Bleam, M.B. McBride, *J. Colloid Interface Sci.* **103**, 124 (1985).
24. G.C. Bye, M. McEvoy, M.A. Malati, *J. Chem. Soc. Faraday Trans I* **79**, 2311 (1983).
25. P.H. Tewari, A.B. Campbell, W. Lee, *Can. J. Chem.* **50**, 1642 (1972).
26. D.N. Misra, *J. Colloid Interface Sci.* **28**, 24 (1968).
27. W. Dyck, *Can. J. Chem.* **46**, 1441 (1968).
28. D.G. Kinniburg, J.A. Barker, M. Whitfield, *J. Colloid Interface Sci.* **95**, 370 (1983).
29. G. Sposito, *J. Colloid Interface Sci.* **91**, 329 (1983).
30. R.O. James, T.W. Healy, *J. Colloid Interface Sci.* **40**, 65 (1972).
31. J.A. Davis, J.O. Leckie, *J. Colloid Interface Sci.* **67**, 90 (1978).
32. K.F. Hayes, J.O. Leckie, *J. Colloid Interface Sci.* **115**, 564 (1987).
33. K.J. Farley, D.A. Dzombak, F.F. Morel, *J. Colloid Interface Sci.* **106**, 226 (1985).
34. W.H. Van Riemsdijk, J.C.M. De Wit, L.K. Koopal, G.H. Bolt, *J. Colloid Interface Sci.* **116**, 511 (1987).
35. J.P. Jolivet, E. Tronc, *J. Colloid Interface Sci.* **125**, 688 (1988).
36. P. Belleville, J.P. Jolivet, E. Tronc, J. Livage, *J. Colloid Interface Sci.* **150**, 453 (1992).
37. J.P. Jolivet, E. Tronc, C. Barbé, J. Livage, *J. Colloid Interface Sci.* **138**, 465 (1990).
38. J.P. Jolivet, M. Richart, E. Tronc, unpublished results.
39. E. Tronc, J.P. Jolivet, R. Massart, J. Lefebvre, *J. Chem. Soc. Faraday Trans I* **80**, 2619 (1984).
40. P. Belleville, Thesis, Université P. et M. Curie, Paris (1991).
41. R.L. Parfitt, V.C. Farmer, J.D. Russel, *J. Soil Sci.* **28**, 29 (1977).
42. R.L. Parfitt, A.R. Fraser, J.D. Russel, V.C. Farmer, *J. Soil Sci.* **28**, 40 (1977).
43. R.J. Atkinson, R.L. Parfitt, R.S.C. Smart, *J. Chem. Soc. Faraday Trans. I* **70**, 1472 (1974).
44. P.D.G. Cradwick, V.C. Farmer, J.D. Russel, C.R. Masson, K. Wada, N. Yoshinaga, *Nature* **240**, 187 (1972).
45. J.B. Harrison, V.E. Berkheiser, *Clays Clay Miner.* **30**, 97 (1982).
46. R.M. Cornell, P.W. Schindler, *Colloid Polym. Sci.* **258**, 1171 (1980).
47. C.F. Timberlake, *J. Chem. Soc.* 5078 (1964); 1229 (1964).
48. W. Stumm, R. Kummert, L. Sigg, *Croat. Chem. Acta* **53**, 291 (1980).
49. W. Stumm, B. Wehrli, E. Wieland, *Croat. Chem. Acta* **60**, 429 (1987).
50. R. Kummert, W. Stumm, *J. Colloid Interface Sci.* **75**, 373 (1980).
51. P.W. Schindler, B. Fuerst, R. Dick, P. Wolf, *J. Colloid Interface Sci.* **55**, 469 (1976).
52. H.C. Chang, E. Matijevic, *J. Colloid Interface Sci.* **92**, 479 (1983).

53. J.A. Davis, J.O. Leckie, *J. Colloid Interface Sci.* **74**, 32 (1980).
54. K.F. Hayes, C. Papelis, J.O. Leckie, *J. Colloid Interface Sci.* **125**, 717 (1988).
55. N.J. Barrow, J.W. Bowden, *J. Colloid Interface Sci.* **119**, 236 (1987).
56. N. Kallay, E. Matijevic, *Langmuir* **1**, 195 (1985).
57. E. Tronc, J.P. Jolivet, *J. Phys.* **49** C8, 1823 (1988).
58. E. Tronc, J.P. Jolivet, *Hyperf. Interactions* **28**, 525 (1986).
59. E. Tronc, J.P. Jolivet, in *Magnetic Properties of Fine Particles*, J.L. Dormann, D. Fiorani Eds., North-Holland, Amsterdam (1992), p. 199.
60. (a) E. Tronc, J.P. Jolivet, in *Nanophase Materials*, G.C. Hadjipanayis, R.W. Siegel Eds, NATO ASI Series, Series E, Vol. 260, Kluwer Academic Pub., Dordrecht (1994), p. 23 ; (b) E. Tronc, J.P. Jolivet, J. Livage, *Hyperf. Interactions* **54**, 737 (1990).
61. E. Tronc, J.P. Jolivet, unpublished results.
62. E.M. Ceresa, *IEEE Trans. Mag.* MAG-17, 3023 (1981).
63. H.C. Chang, E. Matijevic, *Finn. Chem. Lett.* 90 (1982).
64. J. Eisenlauer, E. Matijevic, *J. Colloid Interface Sci.* **75**, 199 (1980).
65. Y. Zhang, N. Kallay, E. Matijevic, *Langmuir* **1**, 201 (1985).
66. M.A. Blesa, A.J.G. Maroto, *J. Chim. Phys. Paris* **83**, 757 (1986).
67. D. Suter, S. Banwart, W. Stumm, *Langmuir* **7** , 809 (1991).
68. M.A. Blesa, A.J.G. Maroto, P.J. Morando, *J. Chem. Soc. Faraday Trans. I* **82**, 2345 (1986).
69. M.A. Blesa, H.A. Marinovitch, E. Baumgartner, A.J.G. Maroto, *Inorg. Chem.* **26**, 3713 (1987).
70. E.B. Borghi, A.E. Regazzoni, A.J.G. Maroto, M.A. Blesa, *J. Colloid Interface Sci.* **130**, 299 (1989).
71. V.I.E. Bruyère, M.A. Blesa, *J. Electroanal. Chem.* **182**, 141 (1985).
72. M.G. Segal, R.M. Sellers, *J. Chem. Soc. Faraday Trans. I* **78**, 1149 (1982).
73. M.I. Litter, M.A. Blesa, *J. Colloid Interface Sci.* **125**, 679 (1988).
74. T.D. Waite, F.M.M. Morel, *J. Colloid Interface Sci.* **102**, 121 (1984).
75. T.D. Waite, A. Torikov, J.D. Smith, *J. Colloid Interface Sci.* **112**, 412 (1986).
76. T.D. Waite, A. Torikov, *J. Colloid Interface Sci.* **119**, 228 (1987).
77. P. Mulvaney, R. Cooper, F. Grieser, D. Meisel, *Langmuir* **4**, 1206 (1988).
78. G.V. Buxton, T. Rhodes, R.M. Sellers, *J. Chem. Soc. Faraday Trans. I* **79**, 2961 (1983).
79. A. Henglein, *Pure Appl. Chem.* **56**, 1215 (1984).
80. A. Henglein, *Mechanism of Reactions on Colloidal Microelectrodes and Sizes Quantization Effects. Topics in Current Chemistry*, Vol. 143, Springer Verlag, Berlin (1988), p. 113.
81. D.H. Napper, *Polymeric Stabilization of Colloidal Dispersions*, Academic Press, London (1983).
82. M.A. Cohen Stuart, T. Cosgrove, B. Vincent, *Adv. Colloid Interface Sci.* **24**, 143 (1986).
83. P.G. De Gennes, *Adv. Colloid Interface Sci.* **27**, 189 (1987).
84. M.A. Cohen Stuart, G.J. Fleer, J. Lyklema, W. Norde, J.M.H.M. Scheutjens, *Adv. Colloid Interface Sci.* **34**, 477 (1991).
85. L.T. Lee, P. Somasundaran, *Langmuir* **5**, 854 (1989).
86. J. Lyklema, G.J. Fleer, *Colloids Surf.* **25**, 357 (1987).
87. L. Auvray, P.G. De Gennes, *Europhys. Lett.* **2**, 647 (1986).
88. J.M.H.M. Scheutjens, G.J. Fleer, M.A. Cohen Stuart, *Colloids Surf.* **21**, 285 (1986).
89. F. Lafuma, K. Wong, B. Cabane, *J. Colloid Interface Sci.* **143**, 9 (1991).
90. O. Spalla, Thesis, Université P. et M. Curie, Paris (1991).
91. E. Dickinson, L. Ericsson, *Adv. Colloid Interface Sci.* **34**, 1 (1991).
92. T.K. Wang, R. Audebert, *J. Colloid Interface Sci.* **121**, 32 (1991).
93. M. Hasegawa, K. Arai, S. Saito, *J. Polym. Sci.* **A25**, 3231 (1987).
94. S.W. Charles, J. Popplewell, Ferromagnetic liquids. In *Ferromagnetic Materials*, Vol. 2, E.P. Wohlfarth Ed., North Holland (1980), p. 509.

95. Y.M. Glazman, G.D. Botsaris, P. Dansky, *Colloids Surf.* **21**, 431 (1986).
96. C.J. Sambuccetti, *IEEE Trans. Mag.* Mag-16, 364 (1980).
97. R. Laible, K. Hamann, *Adv. Colloid Interface Sci.* **13**, 65 (1980).
98. C.H.M. Caris, L.P.M. Van Elven, A.M. Van Herk, A.L. German, *British Polym. J.* **21**, 133 (1989).
99. H.G. Hong, D.D. Sackett, T.E. Mallouk, *Chem. Mat.* **3**, 521 (1991).

DropBooks

Index

Adsorption isotherms 293
Affinity ratio 224
Aging 39, 45, 87
Aggregation 46, 47, 168, 267, 270
Akageneite, *see* Iron: β-FeOOH
Aluminum
  $Al(OH)_3$ 59, 67, 68, 228, 249, 302
  α-AlOOH 47, 67, 233
  γ-AlOOH 67, 68, 233
  Al_2O_3 69, 233
  complexation in solution 206
  polycations 63, 64
Aluminosilicates 101, 302
Anatase, *see* Titanium dioxide
Antimony
  antimonic acid 36, 105, 152
  antimonates 105, 152
  phosphatoantimonates 152

Barium hexaferrite 173
Bayer process 78
Bayerite, *see* Aluminum: $Al(OH)_3$
Bond valence 225
Boron
  boric acid 108
  borates 37, 108
  oxide 111
  polyborates 110
Brucite 77, 80

Cassiterite, *see* Tin oxide
Catalysis
  of the oxolation reaction 94, 99, 116
  of nucleation 41
Cation acidity 12, 15, 197
Charge–electronegativity diagram 19, 35
Charge–pH diagram 14, 34
Chemisorption 212, 217, 286, 295
Chromium
  chromate 32, 96, 112, 148
  α-CrOOH 75, 76
  Cr_2O_3 74, 163
  ferrites 172
  hydroxides 33, 59, 73
  polycation 54, 57, 60
Complexation
  on surfaces 225, 243, 285
  in solution 141, 142, 201
Coordination number 9, 212
  change of 27, 111
  decrease of 15
  sphere 9, 16
Copper
  cuprates 176
  hydroxide, oxide 80
  polycations 79
Clays 102, 103, 261, 268
Critical flocculation concentration 271

Debye–Hückel length 239
Dehydration 32, 213
Diaspore, *see* Aluminum: α-AlOOH
Diffuse layer 216, 237
Dissolution–crystallization 44, 54, 72, 83, 88, 108
Double-layer model 242
DLVO model 257, 264

Electrical double-layer 216, 235
Electronegativity 185
Electronegativity–pH diagram 144, 146, 163, 206
Electrophoretic mobility 290
Esin–Markov coefficient 220

Ferrites
barium hexaferrite 173
hexagonal 173
spinel 171
Flocculation 268, 271
kinetics 271
sequence 272
Freundlich isotherm 293
Fuchs integral 268, 274

Gibbs, adsorption equation 277, 278
Gibbs–Kelvin equation 41, 45
Gibbsite, *see* Aluminum: $Al(OH)_3$
Goethite, *see* Iron: α-FeOOH
Grahame relation 238
Growth 38, 42

$H_3O_2^-$ ligand 29, 55, 61, 73
Hamaker constant 263
Hardness 186, 190, 193
Helmholtz plane 216, 235, 241, 243
Hydration
of the surface 212, 214, 271
of ions 9
Hydrogen bond 6, 8, 19, 55, 73, 120, 161, 214, 217, 275, 310
Hydrothermal conditions 20

Inner sphere complexes 286
Interfacial capacitance 243, 253
Isoelectric point 233, 251, 253
Iron
α-FeOOH 69, 161, 167, 174, 213, 229, 233, 250, 288, 301, 309
β-FeOOH 48, 69, 160, 161, 167
γ-FeOOH 161, 171, 213, 233
α-Fe_2O_3 48, 69, 71, 214, 233, 270, 271, 289
γ-Fe_2O_3 86, 171, 215, 267, 295, 305
Fe_3O_4 46, 86, 171, 279, 295, 309
ferric gel 69, 87, 290, 297
hydroxides 33, 59, 69
lability of the coordinated water 18
polycations 63, 66

Kinetic stability 257

Langmuir isotherm 293
Lepidocrite, *see* Iron: FeOOH

Maghemite, *see* Fe_2O_3
Magnetite, *see* Fe_3O_4
Maxwell–Boltzmann equation 224
Molybdenum
hydrates 132, 134
molybdenates 112, 125
oxides 134
Multisite complexation (MUSIC) model 225

Nernst equation 236, 253, 260
Nickel
ferrite 172
polycation 78
Nucleation 37, 39
heterogeneous 43, 44, 167, 293
homogeneous 37, 39
Nucleophilic addition 27, 113
Nucleophilic substitution 28, 53, 94

Olation 29, 53
Ostwald ripening 39, 46, 83, 273, 281
Outer sphere complexes 285
Oxolation 29, 93
Oxonium ion 7

Palladium oxide 80
Partial charges model 183
Peptization 267, 269
Perovskites
oxides 174
structure 175
synthesis 175
Phosphate 30
complexation 149
Phosphatoantimonates 151
Phosphatotungstates 152
π-bond 15, 108, 112, 131, 137, 149, 193
Platinum oxide 80
Poisson–Boltzman equation 237
Point of zero surface tension 278
Polymers
adsorption 309
grafting 313
Potential
surface 235
electrochemical 223
electrokinetic 216, 272

Regulation of the surface charge 258
Relaxation
of the double layer 258, 262
superparamagnetic 305
Rutile, *see* Titanium oxide

Salt effect 217
Segregation 172
Shielding 217, 280
Shulze–Hardy rule 266, 272
Silica 36, 47, 96, 213, 216, 233, 286, 314
Silicates 94, 96, 101
Solvated proton 7
Solvation 4
of surfaces 212, 213, 267
of cations 9, 11
Specific adsorption 218, 243, 271, 284
of anions 301
of cations 284
of polymers 309
Spinel 86, 88, 171, 295
Stability
of dispersions 256
ratio 268, 269
thermodynamic 257, 273
Stern layer 216, 240, 242, 262, 272
Stokes–Einstein law 269
Stranski rule 47
Structuring ions 11, 216, 271
Surface
acidity 212, 213, 223, 255
acidity constant 223, 224, 246
charge 211, 216, 220, 235, 243, 248
energy 40, 42, 47, 274
equation of state 235, 242
tension 40, 275, 276
Surfactant 273, 277, 311

Template effect 103, 122, 124, 156, 167
Tenorite, *see* Copper oxide
Thermohydrolysis 20, 51, 58, 74, 166
Tin
oxide 47, 83, 107, 233
stannate 36, 83, 93, 107
Titanium
oxide 33, 47, 161, 176, 233, 245, 248, 309, 314
polycations 81
titanates 174
Triple layer model 243
Tungsten
tungstic acid 132
oxide, hydrates 132, 233, 309
phosphatotungstates 152, 184
tungstates 152, 182

Vanadium
oxide 119
vanadates 111, 114, 121
vanadic acid 118
vanadic cation 17
vanadyl cation 17
van der Waals forces 263, 275

Zeolites 103
Zinc oxide 169, 233
Zirconia, *see* Zirconium oxide
Zirconium
basic salts 145
hydroxide 33, 84
oxide 33, 84, 233
oxyhydroxide 33, 84
phosphate 150
polycation 82